

**A Conceptual Electrical Energy Storage (EES) Receiver
for Solar Parabolic Trough Collector (PTC) Power Plants**

PhD Thesis

Presented by

Deju Denton St. Leo Nation

Submitted in accordance with the requirements for the degree of
Doctor of Philosophy

The University of Leeds

Energy Research Institute (ERI)
Faculty of Engineering

October 10, 2013

Intellectual Property and Publication Statement

The candidate hereby confirms that the work submitted in this thesis is his own and that appropriate credit has been given where reference has been made to the work of others.

The reader is supplied this copy with the understanding that it is copyright material and that no quotation from the thesis may be published without proper acknowledgement of the author.

Assertion of moral rights:

The right of Deju Denton St.Leo Nation to be identified as author of this work has been asserted by him in accordance with the Copyright, Designs and Patents Act 1988.

© 2013 The University of Leeds and Deju Denton St. Leo Nation

Acknowledgements

The completion of this work has been a very rewarding, but quite challenging task, one which would not have been possible without the support of so many people. Firstly I must thank my PhD supervisors, Prof. Peter J. Heggs and Dr. Darron Dixon-Hardy here at the Energy Research Institute (ERI), University of Leeds, for their wisdom, support and guidance in successfully completing my research work. Many thanks to my employer Northern Caribbean University Jamaica, for their primary sponsorship of my studies here in the U.K.

Special thanks to the following individuals and or companies:

- Dr. John Blackburn and Mr. F. Michael Stackpool of Ionotec Ltd. U.K, for providing at no charge, the NaS cells used for my experimental work.
- Mr. Berrel Oude Egbrink and Mr. Andrew Mackney of Solutia Europe BVA/SPRL, for also providing at no charge, the 10 L of Therminol 66 HTF required for use in the experimental rig.
- All of the Lowe Engineering team (Tony a.k.a “*yeah-mon*”, Graeme, Steve, Andrew, Joe, Rob, Wayne and Dave) for building my experimental rig. You all made me feel as if I was on the payroll! I really had loads of fun working with you all of you on the project and will keep the fond memories!
- Mr. Paul Harris (of Leeds College of Building), for your massive help, encouragement and advice in building my experimental rig.
- Mr. Ed Woodhouse and Mr. Matthew Buckley (ERI Technicians) for help and advice in preparing my experimental rig for operation in the lab.

To my church family at home in Jamaica and also here in Leeds, your love and support has made the difference. To my dear friend Rebecca “*Becky*” Bembridge, thanks so much for your patience and understanding when my rent was overdue!! To Samantha “*Sparkle*” Bembridge, Unessa “*Lady P*” James and Rochelle Brown, thanks for your love, friendship and your dinner invitations!! To Father and Mother Brown my adopted parents here in Leeds, I could not have made it without your love and care. You have treated me as your blood and I will miss you dearly.

Finally, this work is dedicated to my parents Denton and Paulette Nation, my siblings and to all the outstanding teachers I have had in my early life (especially at Appleton Basic and Siloah Primary Schools). You all with the help of God provided me with a solid educational foundation, the only reason why this work exists today. Finally, supreme thanks to The Father for His wisdom and strength in conceptualizing and modelling a novel energy storage concept that could one day enhance the operation of solar PTC power plants globally.

Abstract

This work outlines the conceptualization, modelling and design of a novel electrical energy storage (EES) receiver for use in solar parabolic trough collector (PTC) power plants. A hybridization of sodium sulphur (NaS) battery and parabolic trough collector (PTC) Technologies, the EES receiver concept could one day enable PTC power plants to operate 24 hrs using solar energy only, while simultaneously providing them significant ancillary power benefits.

Modelling of the EES receiver operation is achieved using of a system of ten steady state (algebraic) equations and two transient (partial differential) temperature dependent equations. The method of solving the system consisted of precedence ordering and back substituting of the steady state equations to develop a single complex and highly non-linear algebraic equation, in terms of the main process heat flux $\dot{q}'_{cond,at}$. This equation was solved with the assistance of the Microsoft Excel goalseek tool.

For the partial differential equations, a one dimensional finite difference approximation, consisting of a forward difference predictor, and a modified central difference corrector was used in discretization. Visual Basic code was then written to solve the system at each increment, each time utilizing the solution obtained for the complex non-linear algebraic equation in $\dot{q}'_{cond,at}$. This allowed investigation of the initial heat-up and charge/discharge function of the conceptual solar field.

Results of simulations indicate the concept is both promising and implementable and that the slightly higher heat losses in the order of 400 – 600 W/m (a direct result of the unavoidably larger size of the conceptual receiver), are seen to be insignificant when compared to the possible energy storage and power support benefits. Though NaS batteries are currently expensive, this condition is thought to be ephemeral, since cells are made from low cost and widely available materials. Thus falling battery prices (with future mass production) could make this novel energy storage concept worthy of evaluation in a prototype PTC power plant.

Keywords: *solar thermal, parabolic trough collector (PTC), sodium sulphur (NaS) batteries, charge, discharge, energy storage, receiver tube, heat collecting element (HCE), power plant, renewable energy, heat transfer, numerical simulation, mathematical modelling, lumped capacitance model, annulus, annular flow*

Relevant Published Work and Presentations

In regards to this thesis, the works listed below contain an initial description of the conceptual EES receiver system presented in Chapter 3 and certain aspects of the mathematical models presented in Chapter 4. All presentations are the work of the author, as well as the publication mentioned below, with the co-authors (supervisors of this thesis) serving in an editorial role.

Publication and Conference Presentation

1. Nation D.D., Heggs P.J, Dixon-Hardy D.W. *“A conceptual Photo-Electro-Chemical-Thermal (PECT) receiver for a net zero CO₂ emissions SPTC plant”*. Paper published in: Conference Proceedings, 30th ISES Biennial Solar World Congress 2011, SWC 2011, August 28, 2011 - September 2, 2011, 2011; Kassel, Germany.

Presentations

1. Nation D.D., *“An experimental rig design for a prototype Photo-Electro-Chemical-Thermal (PECT) receiver”*. Presented at: 8th SolNet SolNet PhD Course on Advanced applications of Solar Thermal Systems, August 23-27, 2011, Institute of Thermal Engineering, Kassel University, Germany.
2. Nation D.D., *“An overview of current PhD research in the modelling of a Conceptual Energy Storage Receiver (EES) for use in Parabolic Trough Collector (PTC) power plants”*. Presented at: 9th SolNet SolNet PhD Course on Advanced applications of Solar Thermal Systems, July 16-20, 2012, Institute for Construction and Material Engineering, University of Innsbruck, Austria.

Table of Contents

Important Abbreviations	xxiii
Glossary of Important Terms.....	xxiv
Chapter 1 A General Overview of this Thesis.....	29
The Aims and Scope of this Work	31
Chapter 2 Energy Storage Options for Solar Thermal Power Plants: A Review.....	33
Introduction	33
The importance of Energy Storage.....	37
2.1 Tank based Thermal Storage Systems	42
2.1.1 The Two-Tank Thermal Storage System.....	43
2.1.1.1 Literature Survey: Two-Tank Storage Systems	47
2.1.2 The Single Tank “Thermocline” Storage.....	48
2.1.2.1 Literature Survey: Single Tank “Thermocline”	51
2.1.2.2 Filler Material Selection and Analysis	54
2.1.2.3 General Modelling of Thermocline.....	57
2.1.2.4 Investigating Thermal Ratcheting	64
2.1.2.5 Investigating Viscous Channelling problems	69
2.2 Solid Media Thermal Storage	71
2.2.1 Recent research work in Solid Media Storage for CSP Plants	73
2.2.1.1 The WESPE Project	73
2.2.1.2 The WANDA Project.....	77
2.2.1.3 The ITES Project	82
2.3 Latent Heat Storage.....	88
2.3.1.1 Solid-Solid and Solid-Liquid type PCM’s.....	91
2.3.1.2 A review of PCM Storage for CSP Power Plants	94
2.4 Thermo-chemical Energy Storage.....	107
2.4.1 Ammonia based Thermo-chemical Storage Systems .	108
2.4.2 Research in Ammonia Storage Systems for CSP	109
2.4.3 Research in Gas-Solid Storage Systems for CSP	111
2.4.4 Solar Energy Storage by Fuel Production (H ₂ , Syngas).....	112

2.4.4.1 Solar Thermolysis	113
2.4.4.2 Solar Thermochemical Cycles	113
2.4.4.3 Fossil Fuel Decarbonization	118
2.5 Other Energy Storage Options.....	124
Chapter Summary	131
Chapter 3 Design of the Conceptual EES Receiver	132
Introduction	132
3.1 Description of the Conceptual EES Receiver	135
3.2 Design of the EES Receiver	139
3.2.1 The EES Receiver Prototype.....	142
3.3 Design of the EES Receiver Experimental Rig	147
3.4 EES Receiver and Rig Construction	151
3.4.1 EES Receiver Construction Photos.....	151
3.4.2 EES Rig Construction Photos.....	157
Chapter Summary	163
Chapter 4 Modelling the Conceptual EES Receiver	164
Introduction	164
4.1 Operation of the EES Receiver in a PTC Solar Field.....	166
4.2 Optics of the PTC collector	170
4.3 Fluxes, Parameters and Correlations used in the EES Receiver Heat Transfer Model.....	173
4.3.1 Definition of Heat Fluxes.....	173
4.3.2 Dimensionless Numbers and Correlations used in the EES Receiver Model	177
4.3.2.1 Turbulent Heat Transfer -HTF Annulus	179
4.3.2.2 Convective Heat Transfer to the Ambient	181
4.4 Modelling of Heat Transfer to the NaS Cell	182
4.4.1 Assumptions used in Heat Transfer Modelling.....	182
4.4.2 The NaS Cell Lumped Capacitance Model and Nodular Heat Transfer	183
4.4.3 Solving the Steady-State System of Equations.....	191
4.4.4 Reference Frame Transformation for the Transient Equations of the Heat Transfer Model	197

4.4.5	Discretization and Numerical Solution of the Partial Differential Equations.....	200
4.4.6	Assessment of the Numerical Method	203
	Chapter Summary	205
Chapter 5	Simulation of the operation of the Conceptual EES Receiver in a typical 50 MWe PTC Power Plant	206
	Introduction	206
5.1	Key Comparison of the EES Receiver Model Outputs	207
5.1.1	Receiver Heat Loss per metre length (W/m).....	208
5.1.2	Collector Efficiency with HTF temperature above the ambient.....	209
5.1.3	Useful Energy Gain of the HTF	210
5.1.4	HTF Temperature Profile along Flow Loop	211
5.1.5	Phase Change Temp.Validation using experimental data from the constructed prototype EES Receiver	212
5.2	Setting up the Model for the Solar Field of the Conceptual EES Receiver	214
5.2.1	Physical Specifications of the system	215
5.2.2	Setting up the EES Receiver Model.....	219
5.3	Model Simulations of the initial heating-up of the EES Receiver Solar Field.....	222
5.3.1	Operating Profiles for Heat loss, Efficiency and Useful Energy Gain for selected HTF's at rated temperature	243
	Chapter Summary	246
Chapter 6	Charge and discharge simulation in the conceptual EES receiver: Results and discussion	248
	Introduction	248
6.1	The Charge/Discharge Concept for the EES Solar Field...	252
6.1.1	The Potential Energy Storage Capacity of the Tepco T5 NaS Cells.....	255
6.2	Charging of the NaS Batteries during daylight hours	257
6.3	Discharging of the NaS cells during no-sun hours	268

6.3.1 Simulation of the Discharging Operation	272
6.4 A possible approach to cooling the NaS batteries	278
Chapter Summary	280
Chapter 7 Thesis Summary, Recommendations, and Conclusion	282
Introduction	282
7.1 Thesis Summary	283
7.2 Recommendations for Future Work	284
Concluding Remarks for this Thesis	286

Reference Section	288
References	289
Appendices Section	313
Appendix A: Hydraulic Analysis of the EES Rig.....	314
Appendix B: Calculating the Volume of Fluid in Hydraulic Circuit	320
Appendix C: Heating Design Calculations for the EES Heating Rig	325
Appendix D: Calculation of the required Pipe-work Insulation for the EES Heating Rig at an Operating Temperature of 350°C.....	327
Appendix E: Solving the Quartic Glass Tube Temperature Equation	337
Appendix F: Sample Check of the MS Excel calculation by a Binary Search Method	342
Appendix G: System Advisor Model (SAM) – Exploring costs.....	346
Appendix H: Microsoft Visual Basic (VB) code used for model solution.....	359
Appendix I: Convergence check for temperature calculation with decreasing step size.....	373
Appendix J: DNI data used in simulation – Kramer Junction, USA.....	374
Appendix K: Ambient temperature data used in simulation – Kramer Junction, USA.....	375
Appendix L: Wind Speed Data used in Simulation – Kramer Junction, USA.....	376
Appendix M: Section A, graph of NaS Cell Temperature Coefficient of Cell Voltage	377
Appendix N: Section B, Graph of NaS Cell Temperature Coefficient of Cell Voltage	378
Appendix O: Section C, Graph of NaS Cell Temperature Coefficient of Cell Voltage	379

Appendix P: Graph of Tepco T5 NaS Cell Charge Resistance with Depth of Discharge.....	380
Appendix Q: Graph of Tepco T5 NaS Cell Charge Resistance with Depth of Discharge.....	381
Appendix R: (Thermal Cond.) - Dowtherm/Syl. HTF.....	382
Appendix S: (Dyn. Visc.) - Dowtherm A/Syltherm HTF.....	384
Appendix T: (Specific Heat) - Dowtherm A/Syltherm HTF	385
Appendix U: (Density) - Syltherm 800 HTF.....	387
Appendix V: Rig Assembly Views (SolidWorks 2011 CAD).....	388
Appendix W: Main EES Receiver Drawings (SolidWorks 2011 CAD)	390
Appendix X: Electrical Wiring Plan and Parts Info - EES Rig.....	391
Appendix Y: Main Parts Info. Sheet for EES Experimental Rig	392
Appendix Z: Risk Assessment for EES Experimental Rig.....	396

List of Tables

Table 2-1: Five major benefits of energy storage to CSP plants.	38
Table 2-2: Important properties of Therminol VP-1, Hitec XL and OnimBF4 ionic fluid	46
Table 2-3: Recent research work in Thermocline Tank Design	52
Table 2-4: Summary of thermocline tank efficiencies (First Law, Second Law and Temperature Criterion) for different external loss conditions (Nu_w) and filler granule diameter (d_s)	63
Table 2-5: Summary of cases considered by Flueckiger <i>et al.</i> (2011) for differing tank wall composite layer thicknesses and heat loss conditions.....	66
Table 2-6: Material properties of storage materials - DLR.....	76
Table 2-7: Effect of graphite content on PCM composite thermal properties	101
Table 2-8: Thermal properties of PCM composites,(2008)	102
Table 4-1: Definition of heat fluxes	175
Table 4-2: Definition of key parameters.....	176
Table 4-3: A summary of the stability of Linear Finite Difference Schemes	204
Table 5-1: Model parameters used in EES receiver solar field simulation	219

List of Figures

Figure 1-1: (a) Block diagram of a typical solar parabolic trough collector (PTC) power plant and (b) Section through a standard sodium sulphur (NaS) cell.	29
Figure 1-2: Diagram showing the main types of solar thermal energy systems (Source: ¹)	30
Figure 1-3: Schematic showing PTC receiver absorbing incident solar radiation.....	31
Figure 2-1: Common energy storage approaches used in engineering today.....	33
Figure 2-2: Schematic showing the four major CSP technologies (a) Parabolic Trough Collector (PTC); (b) Linear Fresnel Reflector (LFR); (c) Power Tower (PT) and (d) Dish-Engine (Adapted: ^[30])	34
Figure 2-3: CSP plants in operation worldwide – 2013 (Based on data from NREL ^[31-45])	36
Figure 2-4: Energy storage in operational CSP plants (worldwide) in 2013 (Based on data from NREL ^[31-45])	36
Figure 2-5: Viable energy storage approaches for solar power plants 37	
Figure 2-6: Effects of storage on a solar power plant. (Source: ^[48]).....	39
Figure 2-7: Estimated hourly distribution of integration costs in \$ million and \$/MWh, caused by wind and solar resources in California under 33% RPS (Source: ^[26])	40
Figure 2-8: Stabilizing effect of energy storage on power output of a 125 MWe solar plant (Adapted: ^[49])	40
Figure 2-9: Thermal storage options for PTC power plants. (Adapted: ^[49]).....	42
Figure 2-10: Schematic illustration of “direct” thermal storage in a solar power tower plant (Source: ^[51]).....	44
Figure 2-11: Schematic illustration of “indirect” thermal storage in a solar PTC plant (Source: ^[51]).....	44
Figure 2-12: Schematic showing shortened structural formula for OnimBF ₄ ionic liquid (Source: ^[64])	46
Figure 2-13: Section showing internal constriction of the optimized molten salt tank (Source: ^[68])	48
Figure 2-14: Schematic illustrating the difference between ideal and real thermocline systems (Adapted: ^[71])	49

Figure 2-15: Section through Solar One thermocline tank (source: [74])	50
Figure 2-16: Schematic illustrating Floating Barrier Thermocline Tank (Source: [77])	51
Figure 2-17: Illustrative charts of thermocline tank energy delivery effectiveness for various discharge time periods (Πd) but at constant τr (developed by Li, Van Lew, Karaki <i>et al.</i> , 2011) (Source: [71])	53
Figure 2-18: Effect of Re and H on thermocline tank discharge efficiency (source: [73])	54
Figure 2-19: Schematic of the 2.3 MWh _{th} thermocline flow loop used by Pacheo et. al (Source: [54])	55
Figure 2-20: Pacheo and Hassani's model comparison with discharge and cool down tests results of Solar One thermocline tank (Source: [81])	58
Figure 2-21: Yang and Garimella - Effect of tank wall conditions on Thermocline Tank flow field (Source: [57])	61
Figure 2-22: Outflow temperature history of thermocline tank discharge for different tank wall conditions and granule diameter (source: [79])	62
Figure 2-23: Schematic illustration of thermocline tank with a composite wall of firebrick (1), steel (2) and ceramic (3). (Source: [89])	65
Figure 2-24: Hoop stress profile along the filler bed for cases 1-7.(Source: [89])	67
Figure 2-25: Solar One thermo cline tank hoop stress (simulation and measured) (Source: [70])	68
Figure 2-26: Illustration of viscous channelling effect in a porous medium when hot fluid displaces cold fluid (Source: [92])	69
Figure 2-27: Schematic illustrating the development of a viscous channel in at the hot-cold fluid interface in a porous bed (Source: [92])	70
Figure 2-28: Solid media heat exchanger modules under construction for the WESPE project, Plataforma Solar de Almeria (PSA), Spain. (Source: [93])	74
Figure 2-29: Schematic showing the integration of storage modules into the PTC test loop at PSA; P1 – P4 mark the axial position of thermocouples. (Source: [93])	75
Figure 2-30: Curves of charge/discharge for both oil and storage module along with oil mass flow rate. (Source: [93])	76

Figure 2-31: Specific heat capacity as a function of total tube length for different conductivities (W/m.K) and distance of tubes (cm). (Source: ^[97]).....	79
Figure 2-32: Schematic illustrating (a) standard storage integration (reference) versus (b) modular storage integration into the plant power cycle for both charging and discharging operations. (Source: ^[97])	80
Figure 2-33: Simulated results for electric work provided during storage operation of a 50 MW power plant for various configurations of energy storage. (Source: ^[97]).....	81
Figure 2-34: Finished concrete test module developed during the ITES project (without thermal insulation). (Source: ^[98])	82
Figure 2-35: Results of initial heating-up period from April 21-28, 2008 with the expulsion of water from the concrete module – temperature of the thermal oil at the inlet/outlet (Pt100 MQ1/Pt100 MQ4) and of concrete in the core of the storage module (MQ1 – 6 6 4, MQ4 – 6 6 4) on the left axis and vapour pressure on the right axis. (Source: ^[98]).....	83
Figure 2-36: Comparison of power measured in reference steady state cycles (24 h charging from a storage temperature of 350°C to 390°C) (Source: ^[98]).....	84
Figure 2-37: Test plot showing compressive strength of HT concrete with heat treatment cycles (Source: ^[17])	86
Figure 2-38: Schematic showing setup of 1100 MWh concrete storage using 252 basic storage modules (Source: ^[17]).	87
Figure 2-39: Concrete heat transfer enhancements with graphite foil (Source: ^[17]).....	88
Figure 2-40: Schematic showing various PCM categories (source: ^[101])	90
Figure 2-41: Comparison between SLPCM's and SSPCM's (Adapted: ^[101])	91
Figure 2-42: Schematic illustrating solid-liquid phase change in a solid crystal (Adapted: ^[101])	92
Figure 2-43: Cyclic illustration of an encapsulated PCM undergoing phase change. (Source: ^[107]).....	92
Figure 2-44: PCM encapsulation using sacrificial polymer (Source: Terrafore, USA, ^[77])	93
Figure 2-45: Schematic illustration of a PCM composite.	94
Figure 2-46: Chart of PCM storage concepts investigated in the DISTOR project, February 2004 – September 2007. (Source: ^[9])	96

Figure 2-47: Steinmann and Tamme (2008): Integration of PCM store into PTC plant (Source: ^[9])	97
Figure 2-48: The effect of thermal conductivity on the number of tubes required in PCM storages that use parallel tube heat exchangers, for three levels of specific volume thermal power during charge/discharge (Source: ^[9])	98
Figure 2-49: Images of (a) finished macrocapsules (b) cross section through a capsule tested in DISTOR (Source: ^[106])	98
Figure 2-50: Cold compressed PCM-graphite composite, NaNO ₃ /KNO ₃ eutectic showing drilled holes for heat exchanger tubes (Source: ^[110])	99
Figure 2-51: PCM sandwich concept with integrated PCM and fins (Source: ^[77])	99
Figure 2-52: Configuration of PCM composite storage modelled by Morrisson <i>et al.</i> (2008) (Source: ^[111])	100
Figure 2-53: Charge time for a test store with various fin materials and thickness (Source: ^[106])	103
Figure 2-54: Photograph of sandwich PCM storage module tested at DLR (Source: ^[106])	104
Figure 2-55: Chart showing various methods to enhance PCM performance (Source: ^[10])	105
Figure 2-56: Schematic illustration of cascade of 5 PCM units (Source: ^[11])	106
Figure 2-57: Schematic illustrating a thermo-chemical energy store system (Source: ^[77])	107
Figure 2-58: Schematic of solar driven ammonia dissociation process (Source: ^[77])	109
Figure 2-59: Photograph of 400 m ² thermochemical ammonia dissociation dish system at ANU (Source: ^[130])	110
Figure 2-60: Schematic illustrating various routes to solar energy storage as fuels (Source: PSI, ^[132])	112
Figure 2-61: Process flow for hydrogen generation in a CSP powered thermo-chemical cycle (Adapted: ^[133])	114
Figure 2-62: Schematic illustrating thermo-chemical metal oxide cycle or hydrogen generation (Source: ^[132])	115
Figure 2-63: Variation of ΔG for water decomposition with (i) FeO (ii) MnO and (iii) CoO with temperature at 1 bar (Source: ^[133])	116
Figure 2-64: The two cavity reactor for Carbo-thermal Reduction of ZnO in SOLZINC Project (Source: ^[132])	117
Figure 2-65: Solar decarbonisation of fossil fuels using (a) cracking (b) reforming (Source: ^[132])	118

Figure 2-66: Schematic representation of (a) indirect and (b) direct solar NG reformers (Sources: ^[132, 149])	120
Figure 2-67: Schematic illustrating concept of a chemical heat pipe (Source: PSI, ^[132])	121
Figure 2-68: Schematic showing experimental setup for CAMF absorber by Kodama <i>et al.</i> (Source: ^[151])	122
Figure 2-69: Schematic showing layout of a DSG Solar Tower Plant with a Steam Accumulator Storage System (Source: ^[77])	123
Figure 2-70: Schematic illustrating storage systems discharge time vs. storage capacity (Source: ^[163])	124
Figure 2-71: Schematic showing layout of a compressed air storage system (Source: ^[27])	125
Figure 2-72: Schematic of a pumped hydro system (Source: Better Green, ^[165])	126
Figure 2-73: Schematic illustrating a flywheel energy storage system (Source: ^[27])	127
Figure 2-74: Supercapacitors (Source: Shanghai Green Tech Co., Ltd)	128
Figure 2-75: Schematic illustrating the operation of the flow battery (Source: ^[27])	129
Figure 2-76: Schematic showing section down a NaS cell and the typical arrangement of a 50 kWh NaS battery module (Source: ^[166])	130
Figure 3-1: Parabolic trough collector and receiver tube (source: NREL)	132
Figure 3-2: Schematic illustrating (a) A conventional PTC receiver and (b) The conceptual EES receiver	134
Figure 3-3: Schematic showing longitudinal section through the Conceptual EES Receiver	136
Figure 3-4: Schematic showing internal assembly of tubes tube within the EES Receiver	137
Figure 3-5: Schematic showing a more detailed longitudinal section of EES Receiver near an End Cap	138
Figure 3-6: Schematic showing section through a HP-4 10Ah NaS Cell (Source: Ionotec Ltd. UK)	140
Figure 3-7: Schematic showing potential shorting problem in series connection of HP-4 NaS Cells	140
Figure 3-8: Schematic showing intended use of Cell Inter-connect	141
Figure 3-9: Schematic showing final manufacturing drawing of the Conceptual EES receiver	143

Figure 3-10: Schematic showing some internal components near End Caps of the EES Receiver	144
Figure 3-11: Schematic showing angled view of EES Receiver	145
Figure 3-12: Schematic showing section through angled view of EES Receiver.....	146
Figure 3-13: Schematic showing initial concept for EES Rig process layout.....	148
Figure 3-14: EES system process flow loop.....	149
Figure 3-15: Schematic showing flow resistance network and “rough” pipe-work for ESS Rig	150
Figure 3-16: Photograph showing the Receiver End Cap, and Absorber Tube with internal Battery Tube	152
Figure 3-17: Photograph showing the NaS cells fitted into the EES Receiver	152
Figure 3-18: Photograph showing insertion of Battery Interconnect and NaS Cell into Ceramic Tube.....	153
Figure 3-19: Photograph showing insertion of Mullite Ceramic Tube into Battery Tube.....	153
Figure 3-20: Photograph showing tight fitting between inner tubes and central NaS Cell	154
Figure 3-21: Photograph showing end caps at both ends of the EES Receiver.....	154
Figure 3-22: Electrical testing of the NaS battery assembly	155
Figure 3-23: EES receiver screw on End-Cap.....	155
Figure 3-24: Fully assembled EES Receiver.....	156
Figure 3-25: Photograph of Expansion Tank during construction.....	157
Figure 3-26: Photograph showing connection of EES Receiver into Rig pipe-work	158
Figure 3-27: Photograph showing Rig Frame under construction with section of pipe-work mounted	158
Figure 3-28: Photograph showing mounted of Expansion Tank and hanging of pipe-work using insulative High Temperature Pipe Wrap	159
Figure 3-29: Photograph showing skid mounting of the Rig Frame.....	159
Figure 3-30: Photograph showing insulated pipe-work and Expansion Tank	160
Figure 3-31: Photograph showing central heating pump used in the ESS Receiver Rig.....	161
Figure 3-32: Photograph showing relief valve and drain pipe.....	161

Figure 3-33: Photograph of EES rig control box	162
Figure 4-1: Schematic showing block layout of a standard PTC Power Plant (Source: ^[183])	164
Figure 4-2: East-West tracking of a parabolic trough collectors (Adapted: ^[187])	165
Figure 4-3: Schematic illustrating the NaS and HTF temperature profiles	167
Figure 4-4: Schematic representation of the conceptual EES HTF loop	168
Figure 4-5: Thermal resistance model of heat flow in the EES receiver (night time).....	169
Figure 4-6: Parabolic trough collector system (Source: ^[191])	171
Figure 4-7: Schematic illustrating important optical characteristics of PTC collector.....	172
Figure 4-8: Schematic showing heat fluxes in the EES receiver cross section	174
Figure 4-9: Schematic illustrating lumped thermal capacitance of NaS cell.....	184
Figure 4-10: Schematic showing inner construction and heat transfer to a 300 Ah central sodium NaS cell (Adapted: ^[201])	184
Figure 4-11: Schematic showing thermal resistance between HTF and NaS Cell	185
Figure 4-12: Schematic illustrating comparison between Jefferson correction model, exact transient heat conduction and lumped capacitance model for heat transfer to solid object in a fluid	186
Figure 4-13: Thermal resistance model of heat flow in the EES receiver (day time).....	189
Figure 5-1: South facing view of the 50 MWe Andasol-1 Solar PTC plant in Granada, Spain (Source: ^[206])	206
Figure 5-2: Absorber heat loss per metre length vs. absorber tube temperature.....	208
Figure 5-3: Collector efficiency vs. HTF temperature above the ambient (°C)	210
Figure 5-4: Useful energy gain of the HTF with operating temperature.....	211
Figure 5-5: Simulated tube temperature profiles with HTF loop position	212
Figure 5-6: Tube temperature profiles along the experimental EES receiver	213

Figure 5-7: Plot illustrating temperature difference between HTF and NaS temperatures	214
Figure 5-8: Illustration of the integration of the EES receiver in a typical PTC solar field. (Adapted: PVTECH)	215
Figure 5-9: Sketch of cross section through a typical Tepco T5 NaS cell.....	216
Figure 5-10: Image showing the end of the industry standard Schott PTR-70 PTC receiver tube (Source: Schott Solar).....	216
Figure 5-11: Schematic showing cross section of the conceptual EES Receiver/Collector system	217
Figure 5-12: Schematic showing cross section of a standard PTR-70 Receiver and LS-2 Collector combination	218
Figure 5-13: Collector dimensions used in simulation of the EES Receiver solar field.....	219
Figure 5-14: Weather data at SEGS VI power plant, Kramer Junction, California on July 18, 1991 (Source: ^[205]).....	222
Figure 5-15: Temperature profiles during the “zero pass” through the HTF loop	223
Figure 5-16: Temperature profiles during the “first pass” through the HTF loop	224
Figure 5-17: Schematic illustrating the layout of an Andasol-1 type PTC solar field (Adapted: ^[218]).....	225
Figure 5-18: Second pass of Therminol VP-1 HTF through a representative loop in the solar field.....	229
Figure 5-19: Third pass of Therminol VP-1 HTF through a representative loop in the solar field.....	231
Figure 5-20: Fourth pass of Therminol VP-1 HTF through a representative loop in the solar field.....	232
Figure 5-21: Fifth pass of Therminol VP-1 HTF through a representative loop in the solar field.....	233
Figure 5-22: Sixth pass of Therminol VP-1 HTF through a representative loop in the solar field.....	234
Figure 5-23: Seventh pass of Therminol VP-1 HTF through a representative loop in the solar field.....	235
Figure 5-24: Eighth pass of Therminol VP-1 HTF through a representative loop in the solar field.....	236
Figure 5-25: Ninth pass of Therminol VP-1 HTF through a representative loop in the solar field.....	237
Figure 5-26: Tenth pass of Therminol VP-1 HTF through a representative loop in the solar field.....	238

Figure 5-27: Eleventh pass of Therminol VP-1 HTF through a representative loop in the solar field.....	239
Figure 5-28: Twelfth pass of Therminol VP-1 HTF through a representative loop in the solar field.....	240
Figure 5-29: Thirteenth pass of Therminol VP-1 HTF through a representative loop in the solar field.....	241
Figure 5-30: Fourteenth and final pass of Therminol VP-1 HTF through a representative loop in the solar field.....	242
Figure 5-31: Tube temperature profiles along HTF loop length.....	243
Figure 5-32: NaS cell temperature profile along HTF loop length.....	244
Figure 5-33: Glass tube temperature profiles for use of various HTF's in the EES receiver.....	244
Figure 5-34: Glass tube heat losses along HTF loop.....	245
Figure 5-35: Useful energy gain of the various HTF's used in simulation.....	245
Figure 5-36: EES collector efficiency for the various HTF's used in simulation.....	246
Figure 6-1: NaS cell EMF with depth of discharge (D.O.D).....	249
Figure 6-2: NaS cell voltage temperature coefficient with depth of discharge (D.O.D).....	250
Figure 6-3: Plot showing the three sections of the original dE/dT profile used for fitting of a mathematical model.....	251
Figure 6-4: A PTC receiver solar field showing SCA loops (Source: SHAMS-1 PTC power plant).....	253
Figure 6-5: Schematic illustrating a conceptual setup for the EES receiver charge/discharge control operation in a typical solar field.	254
Figure 6-6: Battery charge capacity and current with charging cycles	258
Figure 6-7: A representative NaS battery charging profile and the associated cell charging resistance within a single SCA.....	259
Figure 6-8: Simulated profiles results for 1 st NaS battery charge cycle at 600 A.....	260
Figure 6-9: Simulated profiles results for 2 nd NaS battery charge cycle at 600 A.....	261
Figure 6-10: Simulated profiles results for 3 rd NaS battery charge cycle at 600 A.....	262
Figure 6-11: Simulated profiles results for 4 th NaS battery charge cycle at 600 A.....	263

Figure 6-12: Simulated profiles results for 5 th NaS battery charge cycle at 216 A.....	264
Figure 6-13: Simulated useful energy gain profiles results for NaS battery and HTF during the 5 th charge cycle at 216 A.	265
Figure 6-14: Simulated collector efficiency of EES collector using solar salt HTF.....	266
Figure 6-15: The effect of current spikes on the NaS battery temperature profile.....	267
Figure 6-16: Plot showing natural HTF temperature decay during night time hours with NaS cells held under adiabatic conditions.....	269
Figure 6-17: Heat losses from EES receiver during night-time operation.....	270
Figure 6-18: Overnight fall-off in molten salt HTF temperature with plant storage capacity (Source: ^[224]).....	271
Figure 6-19: Effect of NaS cell thermal capacitance in reducing HTF temperature fall-off.....	271
Figure 6-20: Simulated profile results for the 1 st NaS battery discharge cycle at 50 A.....	272
Figure 6-21: Simulated profile results for the 2 nd NaS battery discharge cycle at 50 A.....	273
Figure 6-22: Simulated profile results for the 3 rd NaS battery discharge cycle at 50 A.....	274
Figure 6-23: Simulated profile results for the 4 th NaS battery discharge cycle at 50 A.....	275
Figure 6-24: Simulated profile results for the 5 th NaS battery discharge cycle at 0 A.....	277
Figure 6-25: The temperature reducing effect of flow reversal.....	278
Figure 6-26: Plots illustrating the NaS temperature profile equalization effect of two flow reversals.....	279

Important Abbreviations

Term	Meaning
CAISO	California Independent System Operator
CB	Carbon Black
CLFR	Compact Linear Fresnel Reflector
CLHS	Cascaded Latent Heat Systems
CSP	Concentrating Solar Power
EES	Electrical Energy Storage
HCE	Heat Collecting Element
LCA	Life Cycle Assessment
LFR	Linear Fresnel Reflector
LHS	Latent Heat Systems
NaS	Sodium Sulphur
PCM	Phase Change Materials
PTC	Parabolic Trough Collector
STES	Solar Thermal Energy System
LCOE	Levelized Cost of Energy
RPS	Renewable Portfolio Standard

Glossary of Important Terms

For the purpose of the “*general reader*”, some basic definitions are provided for the key terms used throughout this work

1. *Analytical Solution* *A closed form mathematical solution, for an unknown quantity which isolated on one side of an equation is explicitly expressed in terms of a known variables and common mathematical functions on the other side.*
2. *Ancilliary Service* *A secondary “power generation or power supporting” action provided by special generator systems in electric power plants, usually in respose to stabilizing output power and frequency fluctuations.*
3. *Base Load Plant* *A power plant that is used to supply a rated power capacity constantly to the utlity grid for serving the continous non-peak power demand.*
4. *Battery Polarization* *This refers to the process of producing a partial or complete separation of positive and negative electric species in an electrochemical reaction system.*
5. *Capacity Factor* *The ratio of the actual output of a power plant over a given period of time, to the output that would be achieved when operating at the full nameplate capacity over the same period.*
6. *Differential Equation* *A mathematical equation for an unknown function given in one or more variables in terms of the function itself and derivates of this function of various orders.*

7. *Doping* *The act of adding an impurity into a substance (usually chemical) in order to change its electrovalent or electrical properties.*
8. *Efficiency* *A ratio used to describe the ratio between the energy or work out versus the energy or work put into the system for a given thermodynamic process.*
9. *Effusion* *A process in which individual fluid molecules flow through an opening, without collision between individual molecules.*
10. *Endothermic Process* *A processs in which a reaction system absorbs heat from the external environment.*
11. *Energy Dispatch* *Delivery of required power output to the grid as per utility contract for agreed time duration.*
12. *Entropy* *A thermodynamic term that is commonly used to define the “unavailable” energy of a system, which cannot be used for useful work, a measure of system disorder.*
13. *Exothermic Process* *A processs in which a reaction system releases heat energy to the external environment.*
14. *Exergy* *A thermodynamic term used to refer to the “maximum useful work possible” during the process of bringing a system into equilibrium with its environment.*
15. *Eutectic* *A term used to describe a special mixture of two or more compounds which has a single melting below that of the constituent compounds or any other mixture of them.*

16. *Heat Exchanger* *A physical device designed to effect the transfer of thermal energy from one part of a system to another by means of a temperature difference between the source and sink.*

17. *Interstitial* *Of or pertaining to a small gap or empty space between two regions that are full of matter (known as an interstice).*

18. *Latent Heat* *Heat flow associated with the change of a substance from one physical phase to another, without temperature change.*

19. *Numerical Solution* *An approximate solution to an analytical solution, obtained usually through model discretization at a finite number of points and the use of mathematical differencing schemes, implemented in computational algorithms.*

20. *Ordinary Differential Equation* *A mathematical equation comprising a function of one independent variable and its derivatives.*

21. *Peak Power Plant* *A power plant that is used to supply a rated power capacity intermittently to the utility grid solely for servicing the peak demand periods of grid energy consumption*

22. *Partial Differential Equation* *A differential equation given in terms of unknown multivariate functions and their partial derivatives.*

23. *Renewables* *A term used to describe a range of power generating services driven by natural cycles or sources that are constantly replenished and therefore non-fossil or non-nuclear energy based.*
24. *Sensible Heat* *Heat energy flow associated with a change in temperature or with a temperature difference*
25. *Sequestration* *The act of isolating or keeping apart one substance or chemical species from another.*
26. *Solar Insolation* *A measure of the solar energy incident on, or received by a given surface over a certain time period.*
27. *Thermal Boundary Layer* *A thin layer of fluid in the immediate vicinity of a wall or bounding surface, where the effects of fluid viscosity are pre-dominant.*
28. *Thermodynamics* *A branch of science concerned with the analysis of heat flow and its relationship with work and energy.*

(This page is intentionally left blank)

Chapter 1

A General Overview of this Thesis

This thesis explicates the modelling of a conceptual “*Electrical Energy Storage (EES) Receiver*” for use in the solar field of a solar parabolic trough collector (PTC) power plant. Essentially, this conceptual receiver hybridizes PTC technology for power generation (Figure 1-1a) with sodium sulphur (NaS) battery technology (Figure 1-1b) for electrical energy storage, and consequently describes “*a new energy storage strategy*” for exploration by existing PTC plant operators. This becomes especially important in light of a forecasted demand for more robust, green energy storage options.

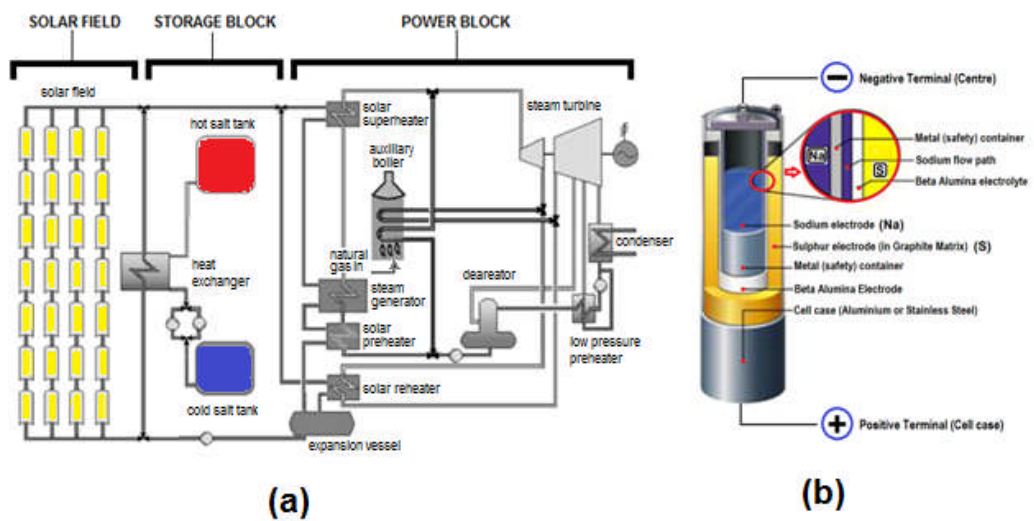


Figure 1-1: (a) Block diagram of a typical solar parabolic trough collector (PTC) power plant and (b) Section through a standard sodium sulphur (NaS) cell.

The modelling of the operation of the EES receiver, the focal point of this work, is essentially the modelling of a “*Solar Thermal Energy System (STES)*” using mathematical models which describe solar energy conversion and heat transfer. Solar thermal energy systems (STES) are “*Energy Conversion Systems*” that change solar energy into

useful thermal energy for heating, cooling or electrical power generation (Figure 1-2). They are composed of integrated networks of active and passive energy absorbing, transferring and processing components that perform the electro-chemical, mechanical and thermodynamic functions of the energy conversion process.

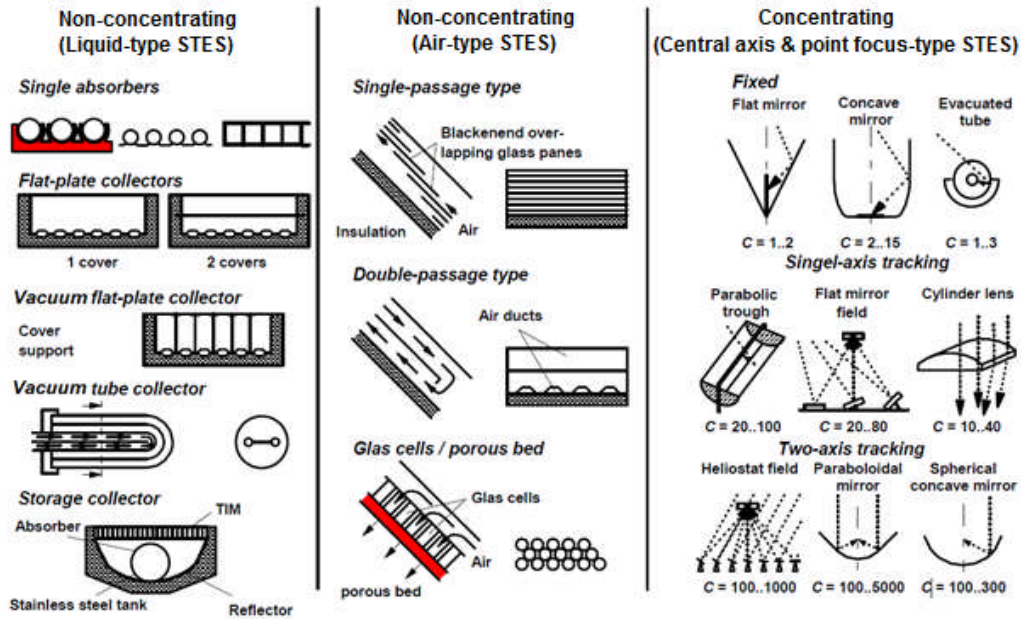


Figure 1-2: Diagram showing the main types of solar thermal energy systems (Source:¹⁾

The component of the STES responsible for absorbing the collected energy is commonly referred as the “Receiver” or “Heat Collecting Element (HCE)”. For solar parabolic trough collector plants (PTC), this receiver typically comprises a 4 metre steel pipe with a selective cermet outer coating for absorbing maximum solar radiation and whose inner surface transfers absorbed solar energy (Figure 1-3) in the form of heat o a working fluid ^[2-3].

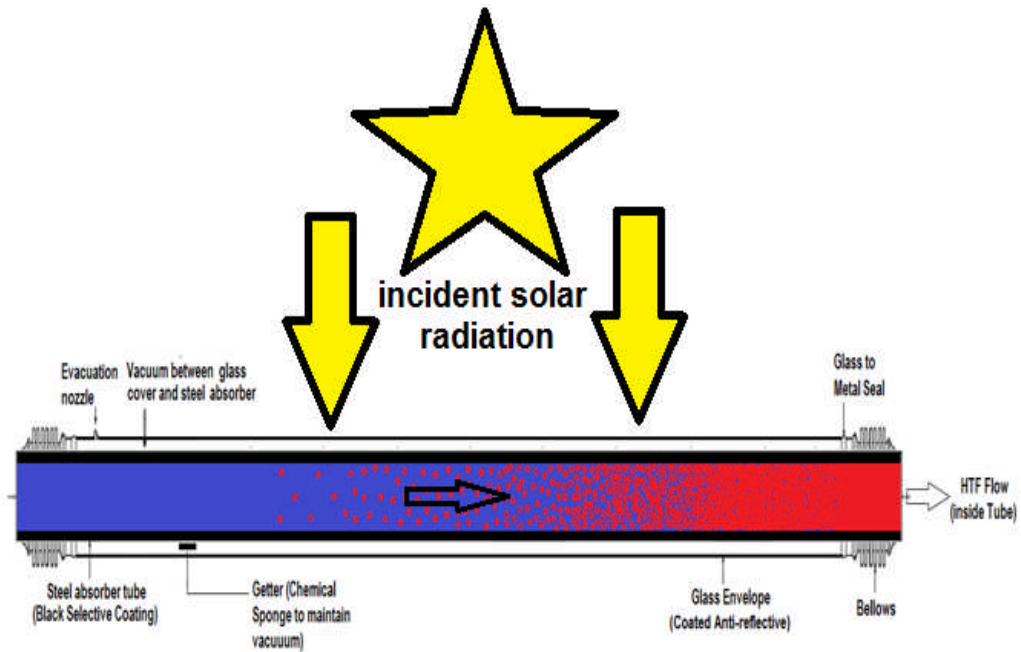


Figure 1-3: Schematic showing PTC receiver absorbing incident solar radiation

Though applied particularly to parabolic trough collector (PTC) technologies in this work, the EES receiver concept here described may find applications in other solar thermal energy (STE), applications, especially in regards to concentrating solar power (CSP) systems.

The Aims and Scope of this Work

The two fundamental aims of this work are:

- a) To explore by simulation and experimentation, key aspects of a conceptual "*NaS battery based, electrical energy storage approach*" for complementary operation with the existing thermal storage of current PTC power plants.
- b) To aid future implementation of this concept through design and modelling of the "*EES receiver*" on which this storage approach is based.

With regards to the scope of this work, the next chapter (Chapter 2) provides a review of the state of the art of the energy storage methods currently available to CSP plants. It provides a detailed summary of the

current literature related to these concepts and of CSP storage technology in general.

In Chapter 3 the conceptualization, design and construction of a conceptual EES receiver and of an experimental rig for investigating the phase change heating profile of the NaS batteries used in the system is presented.

Chapter 4 follows by outlining the mathematical models used in the simulation of the EES receiver solar field. The models develop the appropriate heat transfer relationships into a complete system that describe heat transfer processes in the EES receiver as internal temperatures increase from their start-up value to that of steady state operation.

Chapter 5 explores by simulation the initial heating of the conceptual EES receiver in the solar field similar of an Andasol-1 type (50 MWe) PTC power plant, using the system of mathematical models developed in Chapter 4. The results provide insight into the possible thermal performance of an EES receiver based PTC plant.

Analysis is extended in Chapter 6 to explore the associated NaS battery charge/discharge operation of the conceptual solar field using the models of Chapters 4 and the results of Chapter 5.

The concluding chapter (Chapter 7) presents the summary points of this work along with some important recommendations for future research. It then provides the concluding remarks.

It is hoped that the ideas presented on these pages and particularly the list of recommendations found in the concluding chapter will serve to inspire other engineers and researchers in the field to investigate and to further develop on any perceived merits in this novel concept.

Chapter 2

Energy Storage Options for Solar Thermal Power Plants: A Review

Introduction

Concomitant with the global thrust towards CO₂ reductions and climate change mitigation, power plant operators are today facing increasingly onerous pressure from the collective action of governments, fastidious environmental bodies and international agencies to constantly increase the share of renewables in their power generation portfolio [4-5]. In recent years, this has led to a phenomenal growth in “green power generation”, with analysts forecasting sustained grid penetration by these power sources in the coming years [6].

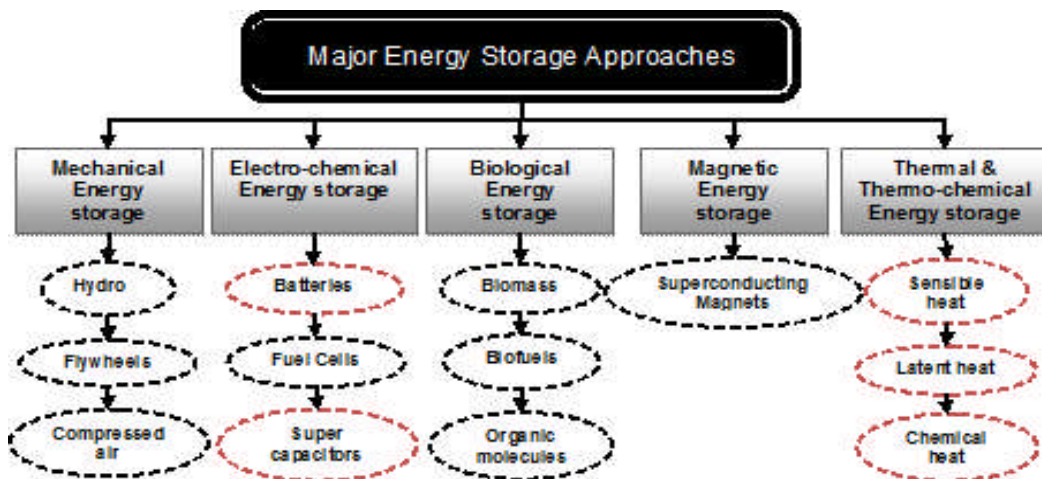


Figure 2-1: Common energy storage approaches used in engineering today

Though positive from an environmental or sustainable perspective, one real problem that arises from this trend is “increasing variability and uncertainty” in grid power generation [7]. This is directly a result of the variable and intermittent nature of renewables derived power and

certainly runs at cross purposes to the mandate of the power plant operator, who is forced to find cost effective solutions.

Amelioration of the status quo reveals two available options: (a) fossil power generator support and (b) energy storage. In light of the global climate change mitigation and CO₂ reduction targets mentioned earlier, along with caps on fossil fuel derived energy, solutions utilizing energy storage, are being increasingly demanded.

Energy storage offers the potential to deliver electricity without fossil fuel backup as well as to meet peak demand, independent of weather fluctuations [8-29]. Consequently, it is a key factor closely linked with any future growth in renewable such as photovoltaic (PV) and wind technologies; a factor of critical importance not to be underestimated.

However, a survey of the renewables industry will reveal that for PV and wind systems, energy storage technologies are not currently mature. They are typically very expensive, of low energy density (eg. standard battery storage for solar PV) and consequently still require significant research and development.

Concentrating solar power (CSP) technologies (Figure 2-2) however are one exception. Of all the competing renewable energy technologies CSP has from its inception, demonstrated a proclivity for supporting cost effective energy storage solutions.

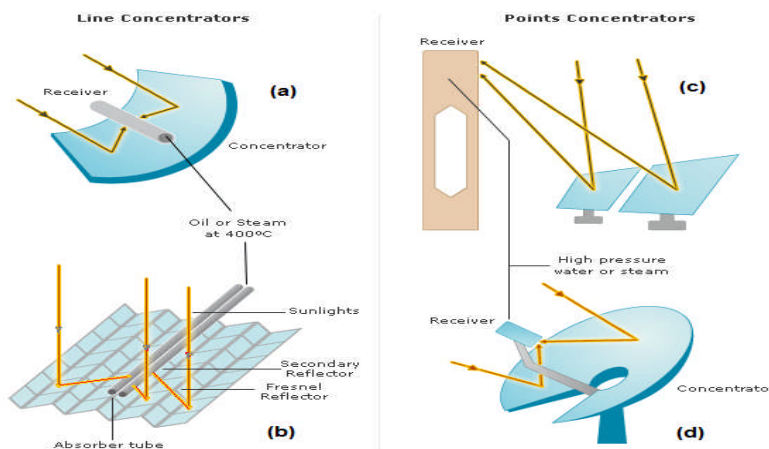


Figure 2-2: Schematic showing the four major CSP technologies (a) Parabolic Trough Collector (PTC); (b) Linear Fresnel Reflector (LFR); (c) Power Tower (PT) and (d) Dish-Engine (Adapted:^[30])

In an effort to provide the reader with an overview of the CSP plants and storage systems in current operation globally, data collated at the time of writing of this work, revealed that there are currently 88 grid connected CSP plants worldwide (Figure 2-3), representing a total installed global capacity of 3.0563 GW_e.

The countries Spain and the U.S.A account for 71% and 17% of this installed capacity respectively ^[31]. Approximately 85% of the 88 plants are based on parabolic trough collector (PTC) technology, 10% on power tower (PT) and 5% on linear Fresnel collector (LFR) technologies. The only grid connected dish-engine power plant, (the Maricopa Solar Project) was decommissioned in 2011, when the plant developer, Sterling Energy Systems filed for bankruptcy. Thus dish-engine CSP technology continues to struggle in a solar market dominated by low cost photo-voltaics and well proven PTC solar thermal technology.

PTC plant deployment has increased significantly in recent years, owing largely to the rapid and phenomenal growth of the Spanish CSP market, which now constitutes 71% of installed global capacity. It is important to note that this entire market share has been achieved only since 2007. The US market on the other hand, has had 68% of its current capacity in operation since 1991, showing very little growth over an even longer time period.

However, 3.98 GW_e of new CSP capacity is under construction in the U.S.A in contrast to 0.42 GW_e in Spain. Most of these projects are scheduled for completion by 2017, by which time both countries are expected to have roughly 4GW_e of installed capacity, which projects a global installed capacity close to 9 GW_e in the very near future ^[31-45].

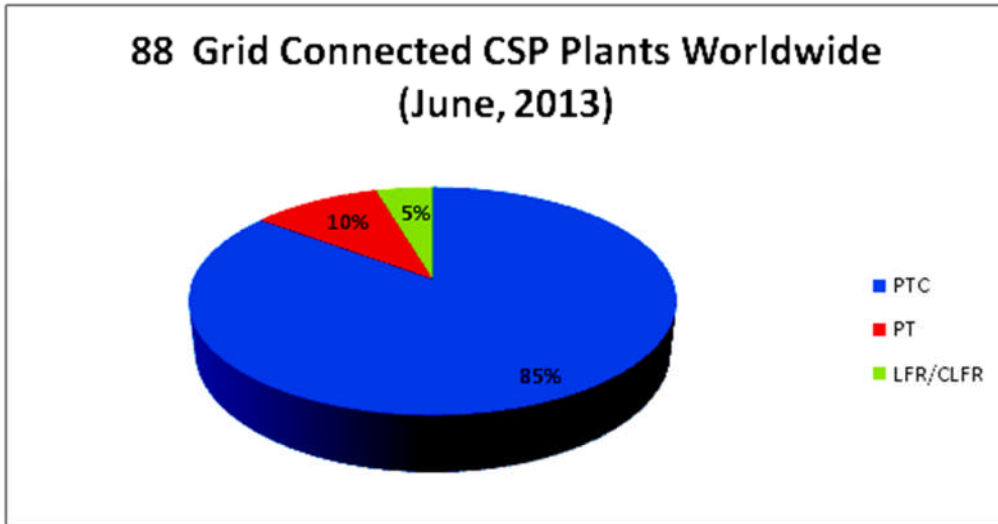


Figure 2-3: CSP plants in operation worldwide – 2013 (Based on data from NREL [31-45])

For CSP plants in current operation globally, roughly one in every four PTC plants, two of every three PT plants and one of every two LFR/CLFR plants has installed storage capacity (Figure 2-4). This storage capacity (thermal) may range from 0.5 - 10 hours depending on the power production/purchase agreements of the power plants and the local utility companies.

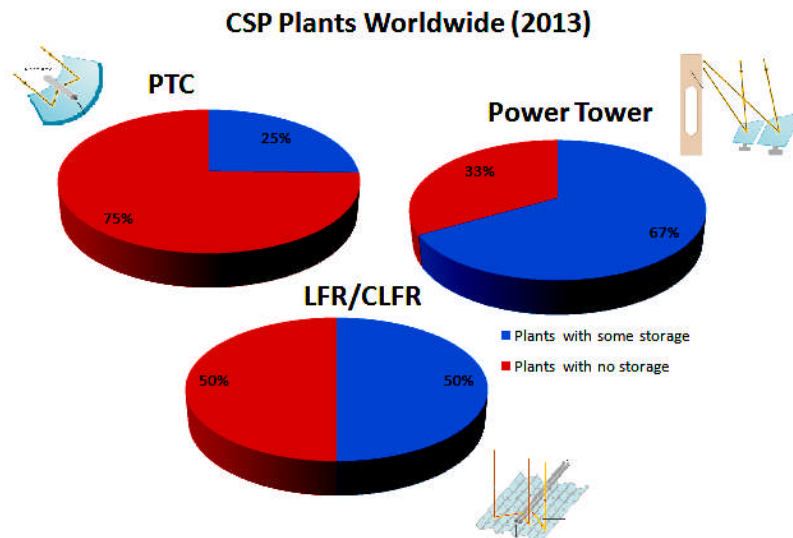


Figure 2-4: Energy storage in operational CSP plants (worldwide) in 2013 (Based on data from NREL [31-45])

Despite the various storage options available to CSP plants, these options can be divided into roughly three main groups; thermal, electrical and chemical energy storage (Figure 2-5). Combinations of these options are also possible as hybridized thermo-chemical, thermo-electrical and electro-chemical storage systems. Of the three major storage options, plant operators have traditionally chosen thermal storage, as this approach to date has proved the most economical [46].

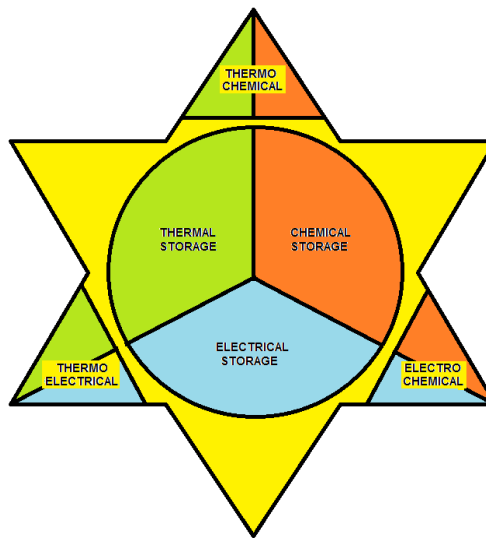


Figure 2-5: Viable energy storage approaches for solar power plants

The importance of Energy Storage

A PTC power plant with storage capacity has certain advantages over erstwhile ones without storage. These important advantages, a direct result of energy storage (Table 2-1) are outlined in the CSP Alliance Report [29], of December 2012.

The critical importance of storage for PTC technologies is also highlighted by the International Energy Agency (IEA) World Energy Outlook 2010, which makes the following statement.

“Even more fundamental to the economics of CSP is increasing its availability, through the integration of storage...while this significantly increases the upfront investment costs ... it can be more than offset by the value of the increased hours of operation per day.” [47]

Table 2-1: Five major benefits of energy storage to CSP plants (Source: [26]).

AREA	BENEFIT
Energy	Hourly optimization of energy schedules Sub-hourly energy dispatch Ramping reserves
Ancillary services (for secondary frequency control)	Regulation 10 minute spinning reserves Operating reserves on greater than 10 minute time-frames from synchronized generator
Power quality and other ancillary services	Voltage control Frequency response Blackstart
Capacity	Generic MW shifted to meet evolving system needs Operational attributes
Integration and curtailment costs compared to solar Photo-voltaics (PV) and wind	Reduced production forecast error and associated reserve requirements Reduced curtailment due to greater dispatch flexibility without production losses Ramp mitigation

Energy storage is of critical importance to CSP plants because it enables power delivery beyond sunshine hours. Each day the solar power collected follows a “bell curve” distribution (Figure 2-6) with the peak occurring at solar noon. The design point for solar power plants however is not this peak value, for in that case power would be produced only at solar noon. Rather the design point is some nominal level which ensures that rated power is available for most of the daylight hours.

Here an energy store is vital. Not only does it improve plant efficiency by harvesting energy that would be otherwise lost, it also allows extends power production beyond daylight hours (Figure 2-6) when the stored energy is dispatched to the grid. This action provides a revenue boost for the operator as energy dispatched during this period usually coincides with the “evening peak” and fetches a higher price.

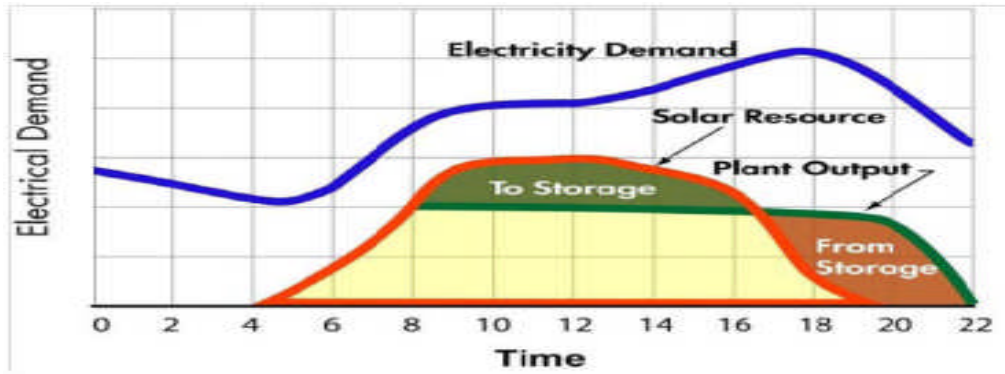


Figure 2-6: Effects of storage on a solar power plant. (Source: ^[48])

This act of extending power delivery is commonly referred a “*capacity factor*” benefit. With respect to a power plant, “*capacity factor*” as defined by the International Renewable Energy Agency (IRENA) is:

“The number of kWh produced each year divided by the product of nominal capacity of the plant multiplied by 8760, (the number of hours in the year).” ^[21]

We can therefore cogently conclude that “*an increase in capacity factor*” really means that the plant is able to dispatch its rated power, for longer, resulting in power generation beyond daylight hours. When there is no energy storage, a typical PTC plant has a capacity factor of between 0.20 and 0.25. With thermal storage this factor rises to between 0.40 and 0.53. Naturally associated with this benefit is a higher initial capital outlay for the proposed plant.

Storage systems also reduce the “*integration and curtailment*” cost of the power plant. Significant penetration by wind and solar generation creates new integration requirements for existing power systems. Solar energy like wind energy, is an intermittent source of power, which is highly subject to variation over any given time period. This leads to higher forecasting errors in power generation when compared to conventional fossil-fired power plants.

Most importantly since these intermittent sources cannot be actively controlled or dispatched, there is naturally a loss of power production and more importantly revenue, if demand does not match supply, a loss which is described as “*curtailment loss*”. Curtailment here refers to the

act of “getting rid of” or “dissipating” any excess energy produced by the plant in periods of low energy demand.

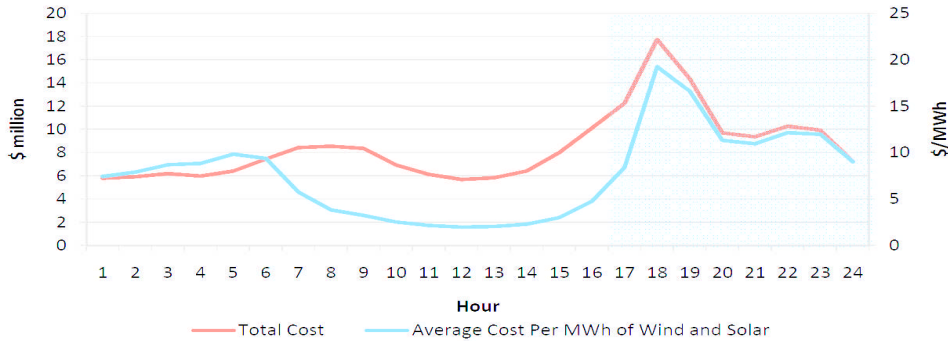


Figure 2-7: Estimated hourly distribution of integration costs in \$ million and \$/MWh, caused by wind and solar resources in California under 33% RPS (Source: [26])

Since the plant is “integrated with” or “tied to the grid”, the operator makes a loss whenever excess energy has to be “curtailed”, an action that is inimical to plant profitability. Solar PV and wind energy technologies for example, suffer high integration costs in the afternoon peak (Figure 2-7) when demand is high and they are not able to supply rated power to the grid.

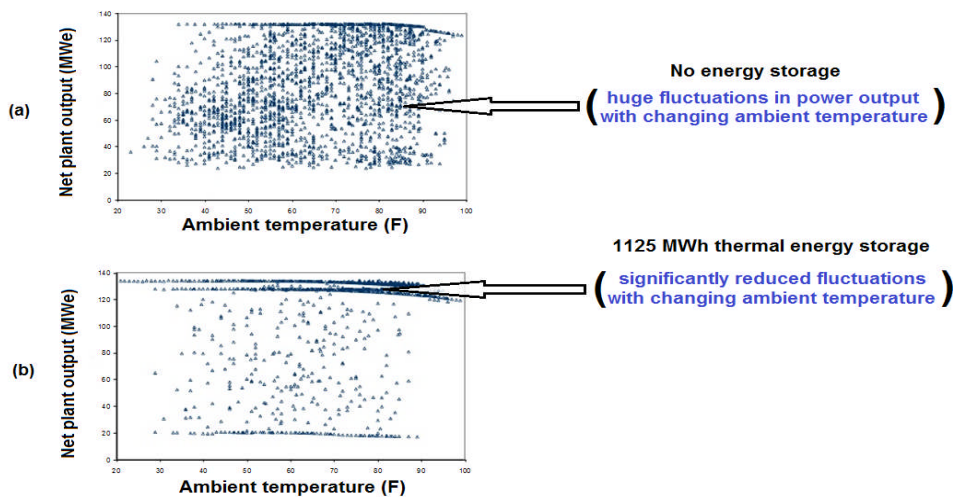


Figure 2-8: Stabilizing effect of energy storage on power output of a 125 MWe solar plant (Adapted: [49])

A storage system reduces or eliminates curtailment costs because excess energy is harvested and stored for dispatch when needed, especially during peak periods where the plant operator will generate the most revenue. A reduction in curtailment cost translates to a reduction in integration costs. In this regard not only is the storage system a cost reducer, it is also a revenue enhancer.

The effects of a store on power quality and stability can be illustrated (Figure 2-8) by considering the buffering effect of a thermal store on the performance of a 125 MWe solar power plant. Without any form of storage, the ambient temperature induced variation in absorbed solar energy (a change in the input driving force) is almost perfectly replicated minus some delay, in the plant's power output (Figure 2-8a).

However, adding a 1125 MWh thermal store (9 hrs of storage capacity) to the same plant, results in a dramatic power quality improvement and the output becomes relatively stable despite driving force variations (Figure 2-8b). Thus energy storage significantly minimizes or even eliminates power quality problems, while at the same time "firming-up" power plant output. This significantly reduces the stresses on generator components and increases their useful working life ^[48,50].

Finally, storage of solar energy by PTC power plants reduces green house gas emissions. This results from the fact that energy generation can be shifted to evening and nighttime hours where fossil fuel powered boilers would normally be brought online. Thus in this respect energy storage provides a "*green house gas displacement effect*" ^[6].

Green house emissions are also displaced when energy storage "*prevents construction*" of new fossil fired plants. For example the California Energy Commission estimates that as California moves astutely towards a 33 % renewable portfolio standard (RPS) in 2020, half of this energy is projected to be provided by intermittent sources such as solar and wind. In this respect the California Independent System Operator (CAISO) predicts that without energy storage the state will have to add 4800 MW of "*load following*" fossil powered

generating capacity (generation that comes online in response to grid demand) to meet the projected demand [26]. Clearly this is one example where energy storage can play a key role in “preventing deployment” of the required fossil fired “generation support” thus potentially lowering green house gas emissions and supporting a sustainable future for all.

This introductory section has presented a brief overview of the critical importance that energy storage will play in CSP power plants of the future. The rest of this chapter is divided into five main sections which review the current state art with respect to energy storage approaches for CSP power plants. Each section will discuss an energy storage option currently under research, or possessing potential application to CSP power plants. Finally the chapter summary provided at the end of these sections serves to recap the main points developed in the chapter.

2.1 Tank based Thermal Storage Systems

The traditional energy storage approach for PTC plants has been essentially thermal, owing to the relatively low cost of implementing this solution when compared to other storage approaches (namely electrical or chemical). Thermal storage options are themselves quite varied, with current options in use today, illustrated by the tree diagram of Figure 2-9.

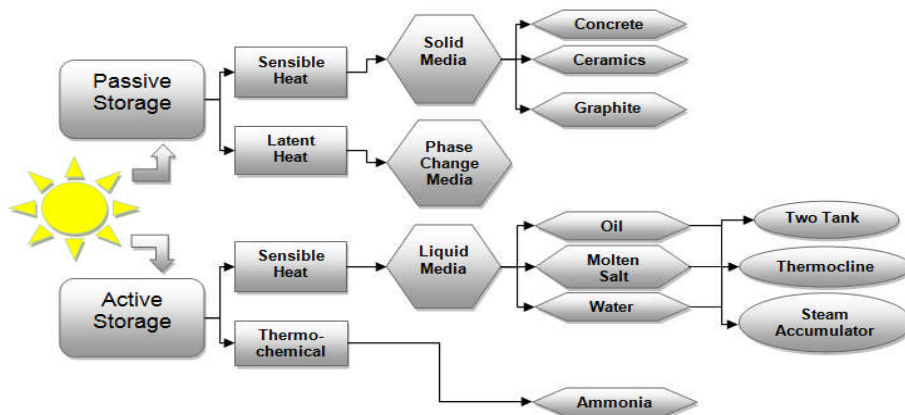


Figure 2-9: Thermal storage options for PTC power plants. (Adapted: [49])

As illustrated (Figure 2-9), thermal storage may be active or passive. In passive storage devices there is no mass motion of matter in the store but rather, heat transfer occurs by conduction through a thermal boundary. In active storage devices however, heat sinked across the thermal boundary of a heat exchanger is transferred by mass motion within the storage media in the form of natural and/or forced convection currents. This is what effects heat transfer in the active storage system.

Passive storage media may be grouped into sensible or latent heat categories and involve energy storage in either solid or phase change media. Active storage may be either sensible or thermo-chemical and involves energy storage in liquid media contained in a holding vessel or tank.

A review of the CSP power plants currently operating worldwide reveals universal usage of a thermal storage approach based on the two-tank molten salt system discussed in the next section.

2.1.1 The Two-Tank Thermal Storage System

The two-tank thermal storage system is currently the state of art for CSP thermal storage systems. In this system, one tank stores hot HTF while the other stores “cold” or spent HTF. There are two versions of this system: (a) the direct and (b) the indirect storage system.

Two-tank “direct” systems are so called because thermal energy from the solar field is transferred by the hot HTF passing directly through the storage system (Figure 2-10) during thermal charging, without use of a heat exchanger. This is possible because the solar field and the storage system both use the same heat transfer fluid. A good example of this is the 19.9 MW_e Terresol Gemasolar power tower CSP plant in Seville, Spain ^[51].

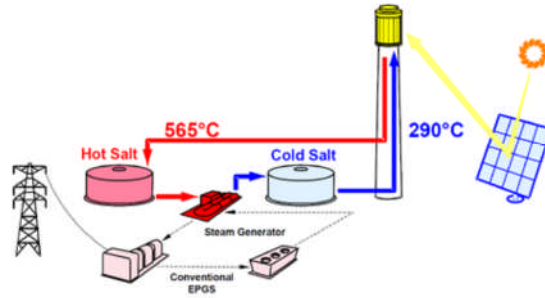


Figure 2-10: Schematic illustration of “direct” thermal storage in a solar power tower plant (Source:[51])

In the “*indirect*” system, the solar field HTF and tank storage medium are not the same and so the hot tank must be charged from the solar field by specialized heat exchangers integrated with the tank system (Figure 2-11). A good example of this system can be found in the Andasol-1 PTC plant in Spain [51].

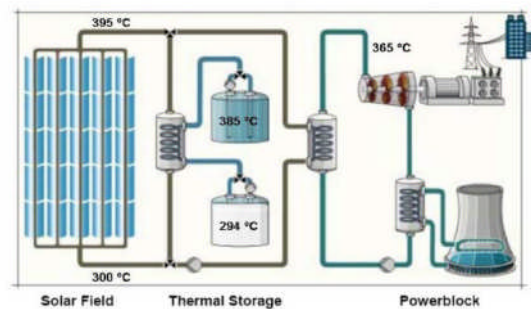


Figure 2-11: Schematic illustration of “indirect” thermal storage in a solar PTC plant (Source:[51])

The first of the commercial CSP plants to be built in the early 1980’s (SEGS-1, California USA) used low cost mineral oil as the solar field HTF [52]. Since mineral oil was relatively low cost, it was also used as the tank storage medium, thereby allowing a “*direct*” charging operation.

However, later SEGS plants sought to improve thermodynamic cycle efficiencies by achieving higher HTF temperatures in the solar field. This was made possible through the use of the more expensive synthetic oil HTF’s, now common to most PTC power plants today.

As continuation of the “*direct*” thermal storage approach, meant the storage tanks had to be filled with expensive synthetic oil, system economics has forced current plants to adopt the “*indirect*” storage approach consisting of a low cost storage medium charged through an intermediate heat exchanger.

Whether direct or indirect, the principle of operating the thermal store is always the same. In periods of high solar radiation, when excess energy is produced in the solar field, the hot HTF is used to charge the store, storing thermal energy for later dispatch.

If energy from the solar field is low, or no longer available, the hot tank is discharged directly or indirectly by heat exchangers, to the power block. The “*cooled HTF*” is not returned to the hot tank, but rather transferred to the cold tank for storage, where it is later reheated by hot HTF from the solar field. It is important to note that these storage tanks are well insulated and are able to maintain an average operating temperature for long periods (even weeks) ^[53-58].

Significant work has been done in recent years in relation to the engineering of heat transfer fluids for use in tank storage systems. Much work has been done in the area of molten salt HTF development, so as to increase their upper operational limits (for higher Rankine cycle temperatures) and to decrease their melting points (to prevent HTF freezing in the pipe work overnight).

Kearney *et al.* (2003), Bradshaw *et al.* (2009) and Gomez *et al.* (2013) investigated nitrate salts such as solar salt (a binary salt consisting of 60% NaNO₃ and 40% KNO₃), HitecXL (a ternary salt consisting of 48% Ca(NO₃)₂, 7% NaNO₃, and 45% KNO₃) and similar nitrate salts, for operation in CSP systems up to 450°C ^[53, 59-60].

Wang (2012a,b) reported on a new quaternary LiNO₃-NaNO₃-KNO₃-KNO₂ molten salt which showed a lower freezing temperature (124°C) than Hitec XL or Solar Salt. Hussain *et al.* (2012) synthesized and characterized a nano-HTF consisting of a mixture of eutectic nitrate salt

doped with 0.5% by mass of silica nanoparticles. This salt was reported to have an even lower freezing point of 120°C [61-63].

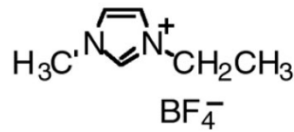


Figure 2-12: Schematic showing shortened structural formula for OnimBF4 ionic liquid (Source: [64])

Especially since 2000, ionic liquids (salts that are liquid at or near room temperature) have been researched as potential candidates for use as HTF's in CSP storage systems and as a general heat carrier. Moens *et al.* (2003) investigated "room temperature" ionic liquids and provided an overview of issues surrounding their development and deployment. A potential ionic fluid called oniMBF4 (Figure 2-12) was reported and a useful comparison (Table 2-2) of the liquid's physical properties with standard PTC HTF's such as Therminol VP-1 synthetic oil and Hitec XL molten salt was also provided in this work [65].

Table 2-2: Important properties of Therminol VP-1, Hitec XL and OnimBF4 ionic fluid (source: [64])

Properties @ 25°C (or other T)	VP-1™	Hitec XL™	Ionic Liquid
Freezing point (°C)	13	120	
Max. applicable T (°C)	400	500	400–450
Density ρ_f (kg/m ³)	815	1992 (300°C)	1400
Specific thermal capacity C_p (J/kg K)	2319 (300°C)	1447 (300°C)	2500
Vapor pressure	>1 atm above 257°C)	Nil	Nil
Storage density (MJ/m ³ K)	1.9 (300°C)	2.9 (300°C)	3.5
Thermal conductivity k (W/mK)	0.098479 (304°C)	0.519 (300°C)	Tbd
Viscosity (cP)	0.2 (300°C)	6.27 (300°C)	Tbd
Cost (\$/kg)	3.96	1.19	4.57 ^a
Heat capacity cost (\$K/Mbtu) Solar field inlet T=300°C			
ΔT 100	17	8.8	19.28
ΔT 125	-	7.04	15.42
ΔT 150	-	5.9	12.83

^aSum of raw materials cost

Reddy (2003) also analyzed the thermal stability and corrosivity of these fluids. TGA analysis of the tested liquids revealed that operating

temperatures over 400°C were possible and tests with 316 stainless steel and 1018 carbon steel showed excellent corrosion resistance ^[66]. Valkenburg (2005) also did similar evaluation of the compatibility of ionic liquids with certain metals, along with their thermal and chemical properties, concluding that ionic liquids had favourable thermal properties for solar collector applications ^[67].

2.1.1.1 Literature Survey: Two-Tank Storage Systems

Today research is also aimed at reducing the operational and investment costs of existing two-tank systems, the most widely deployed CSP storage technology of today.

Research by Herrmann *et al.* (2003) investigated two tank systems for potential cost reductions and operational improvements ^[56] during a time period when plant operators had switched to synthetic oil HTF's and were beginning to search for low cost storage solutions. It was recommended that system costs could be significantly reduced to approximately US\$ (30 – 40)/kWh_{th}, provided that low cost molten salts were used to replace the expensive synthetic oil tank storage medium, with tanks charged indirectly through oil to salt heat exchangers. This approach has now been adopted in the CSP industry as the state of art ^[68-70].

Other methods of improving these two tank systems involved optimizing the design of the tank itself. Gabrielli and Zamparelli (2009) presented an optimal design procedure for traditional carbon steel molten salt storage tanks with internal insulation (Figure 2-13). In this work, vessel size, insulation walls and roof design were optimized by minimizing the total investment cost subject to three constraints:

- (a) Abiding within the maximum allowable values of temperature
- (b) Abiding within the maximum allowable values of stress and
- (c) Disallowing excessive cooling (and hence possible solidification of the molten salt) over long periods of “no-sun”.

The procedure was developed into an iterative step-wise optimization procedure which integrated the thermal, mechanical and economic aspects of the system and was used in the case study of a 600 MWh thermal storage system. The case results revealed that the optimal design was an internally insulated carbon steel storage tank of height 11 m and diameter 22.4 m. The total investment cost of the optimized system was found to be 20% lower than a corresponding 321H stainless steel tank system without insulation or internal protection [68].

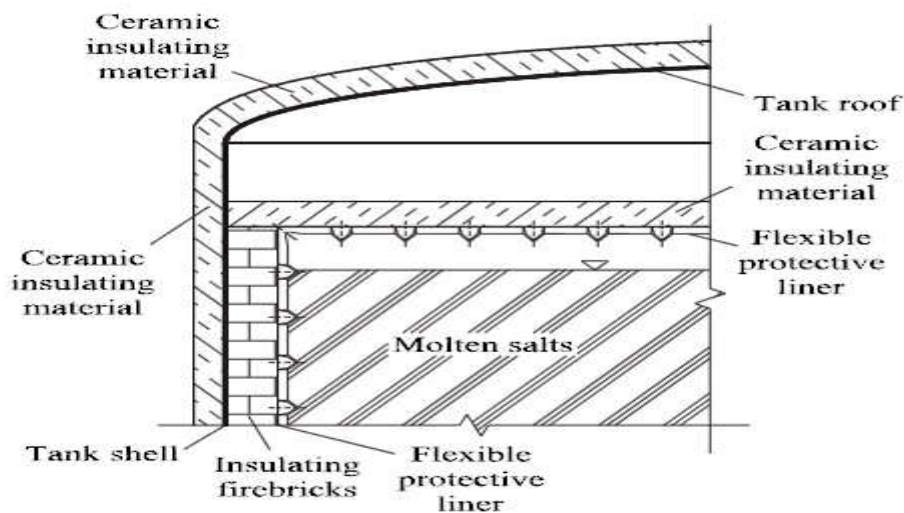


Figure 2-13: Section showing internal construction of the optimized molten salt tank (Source: [68])

2.1.2 The Single Tank “Thermocline” Storage

In recent years however, storage tank research has shifted focus to a more promising concept, the single tank “*thermocline*” system. In the thermocline, both the cold and hot salt are contained in a single tank which is only marginally larger than one of the tanks in an equivalent two-tank system [69].

The term “*thermocline*” refers to the sharp temperature gradient (Figure 2-14) that exists between the two fluid regions and which serves as the boundary of separation. Separation between “hot” and “cold” fluid is

maintained by the combined effect of buoyancy induced stratification within the storage medium and the effect of gravity on a bulk solid filler material used in the tank ^[70]. The thermocline is also sometimes called the “*heat exchange region*” since a gradual mixing of hot and cold fluid occurs in this region over time, but this is relatively small compared to the total tank volume. Due to this slow heat exchange, fluid in the thermocline region is not available for process heat transfer and consequently represents “*lost tank capacity*”.

In the theoretical system (Figure 2-14), where hot and cold fluid regions are separated by a movable baffle under adiabatic conditions, there is no such loss, and 100% thermal capacity would be available. The size and stability of the thermocline region is therefore essential to maintaining thermal stratification within the storage tank.

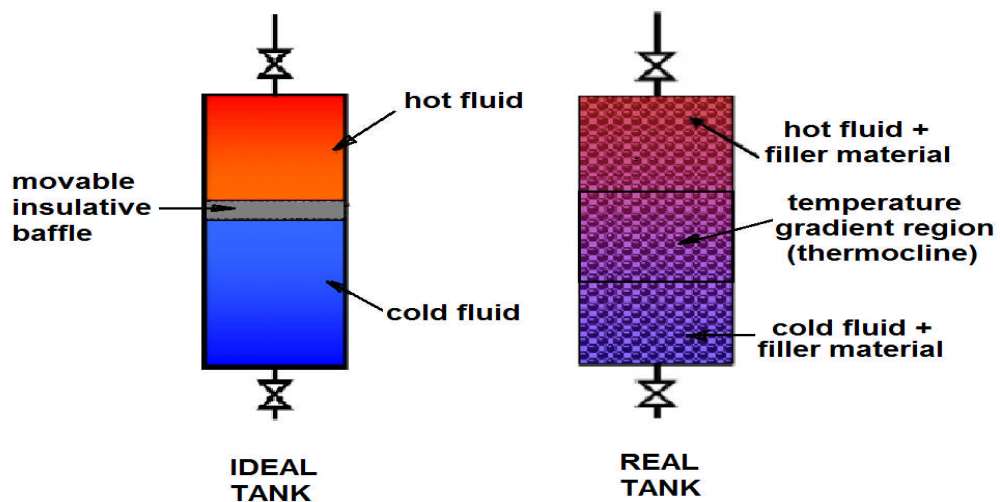


Figure 2-14: Schematic illustrating the difference between ideal and real thermocline systems (Adapted: ^[71])

There are currently two approaches to thermocline tank design. The first and the most researched approach, consists of a single tank system containing a two phased storage medium. One of these phases is a cheap filler material (usually a rock and sand mixture) used to pack the bulk of the tank and to provide the primary thermal capacitance of the store. The other phase, a liquid HTF (usually molten salt or oil) fills the void fraction of the tank and effects heat transfer between the tank

and some thermal load [54, 72-73]. The Solar One thermocline tank (Figure 2-15) which operated from 1982 to 1986 and used Caloria HT-43 mineral oil as the HTF was constructed in this manner [73].

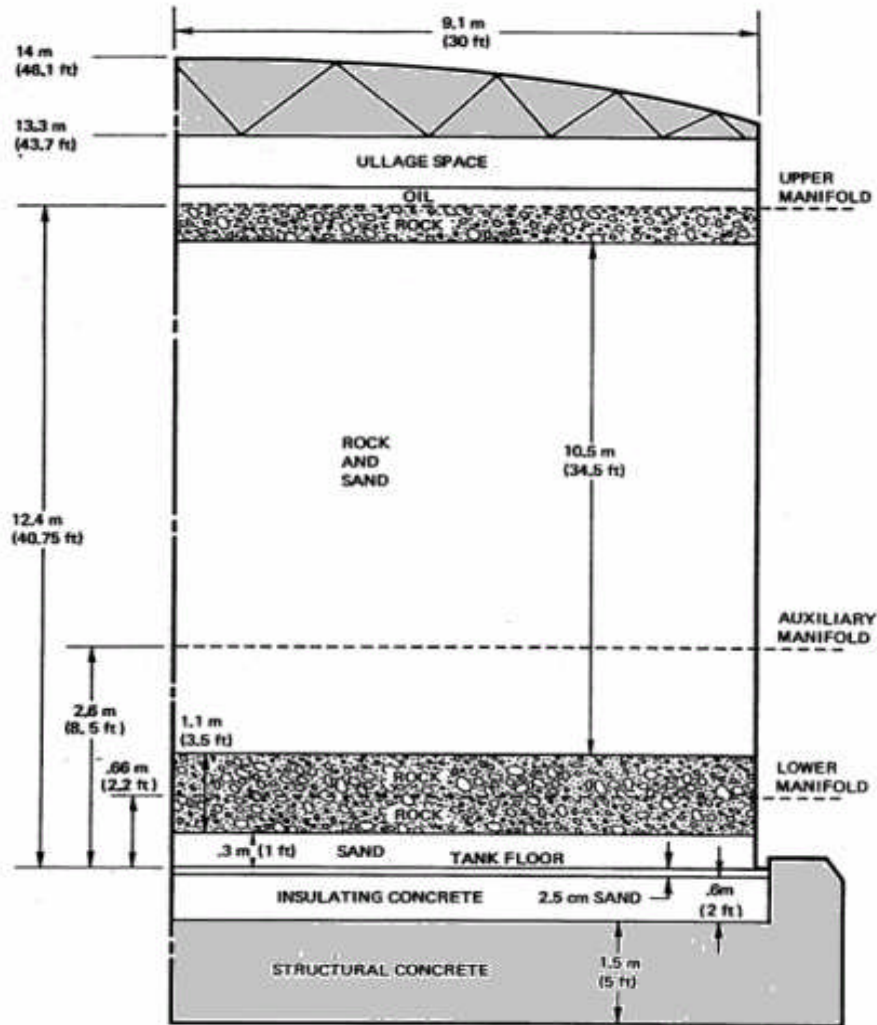


Figure 2-15: Section through Solar One thermocline tank (source: [74])

Another single tank system has been proposed and developed by the global engineering firm SENER, that utilizes a “floating barrier” (Figure 2-16) for separation of hot and cold storage fluids. In a recent report [75], Dunn (2012) stated that SENER has already deployed this tank system as 24 MWh_{th} prototype that currently operates at the Terresol Valle 2 PTC plant in Spain [76].

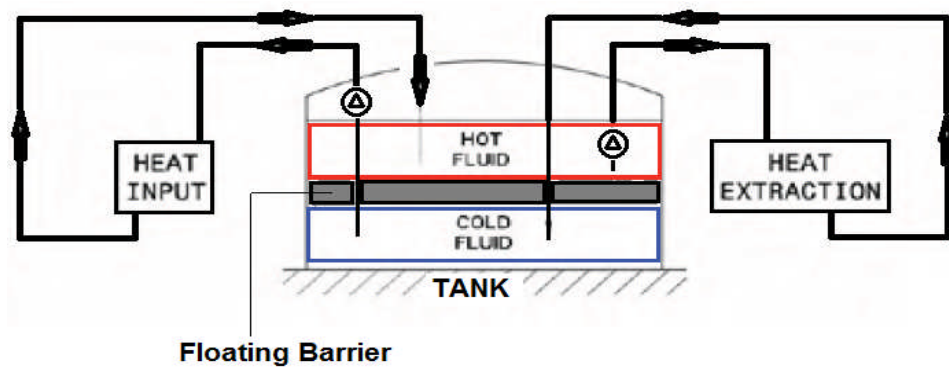


Figure 2-16: Schematic illustrating Floating Barrier Thermocline Tank (Source: [77])

Provided, the floating barrier is leak free and of low thermal conductivity, heat transfer between the hot and cold regions of the tank should be significantly reduced and this could be a promising design approach. Also the fact that the material is of very low thermal conductivity (very high thermal resistance) results in almost full utilization of the tank's thermal capacity, and consequently increases the charge/discharge efficiency.

Whichever single tank design prevails in the end, there is general agreement within the CSP industry that such single tank systems have the potential of significantly reducing storage investment and operational costs. According to Pacheco *et al.* (2002), an equivalent thermocline system could be built for only 66% of the cost of a conventional two tank system [54].

2.1.2.1 Literature Survey: Single Tank “Thermocline” Systems

A review of the literature on single tank thermocline systems reveals that current research is divided into four main areas. These are:

- Optimization of tank design
- Filler material selection and analysis

- General thermocline system modelling
- Investigating thermal ratcheting and viscous channelling problems

Research in thermocline tank design for CSP applications is a relatively new topic and consequently research of significance is all post the year 2010. Table 2-3 summarizes the major publications in this area since this time.

Table 2-3: Recent research work in Thermocline Tank Design

Themocline Tank Design	
Publication	Summary of key findings
<p>Yang and Garimella (2010) ^[69]</p> <p><i>“Thermal analysis of solar thermal energy storage in a molten-salt thermocline”</i></p>	<p>A thermocline tank design procedure was formulated for engineers. The procedure reduced complex numerical computation to nine simple steps. Inputs of required tank diameter d, filler particle type and filler size size d_s were given in step one Through a series of simple calculations, the required outputs of required tank height (h) and discharge efficiency (η) were obtained in the final steps.</p>
<p>Li, Van Lew, Karaki et al. (2011a) ^[71]</p> <p><i>“Generalized charts of energy storage effectiveness for thermocline heat storage tank design and calibration”</i></p>	<p>In follow up to the work of Yang and Garimella (2010), a chart based approach was developed (Figure 2-17) by Li <i>et al.</i>, which field engineers can conveniently use to design and calibrate the dimensions of thermocline storage tanks. In these charts, energy storage effectiveness is represented as a function of four dimensionless parameters that are grouped and which comprise all the given parameters of thermocline tanks. They are generally applicable for any given practical thermocline tank storage design application ^[71].</p>
<p>Li, et al. (2011b) ^[78]</p>	<p>In this work Li <i>et al.</i> (2011b) extended the previous analysis ^[71] to systems comprising “direct storage of HTF only” in containers and systems with “HTF pipes passing through filler materials, single or multi-phased” ^[78].</p>

From Table 2-3, the main benefit of the procedure developed by Yang, Garimella and Li *et al.* (Figure 2-17) is that it now enables system designers to easily evaluate various thermocline designs in terms of the important operational parameter, tank discharge efficiency η defined as:

$$\eta = \frac{\text{Output energy with } \theta_1 > \theta_0}{\text{Total initial energy stored in the thermocline}} \quad \text{(Equation 2-1)}$$

Where θ_1 is the temperature of the output HTF at the desired high temperature level and θ_0 is the low temperature cutoff value which occurs when the thin “thermocline gradient zone” reaches the top of the tank (discharge port).

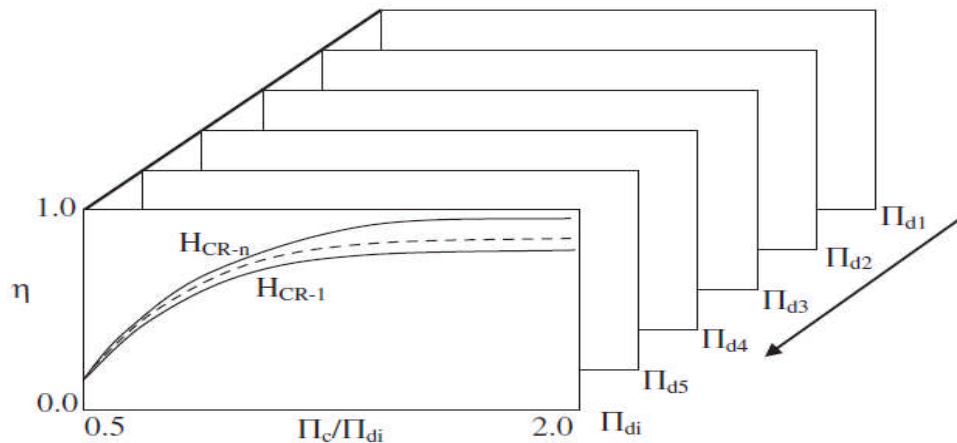


Figure 2-17: Illustrative charts of thermocline tank energy delivery effectiveness for various discharge time periods (Π_d) but at constant τ_r (developed by Li, Van Lew, Karaki *et al.*, 2011) (Source: [71])

It is clearly evident however that any value obtained for η is directly dependent on the value chosen for θ_0 . Yang and Garimella (2010b) used a value of $\theta_0 = 0.95$, designating that only temperatures above 95% of the total operating range should be considered useful for power generation. Since the value was *ad hoc* [79], It was therefore not clear what value is optimal for calculation purposes.

As an alternative, Flueckiger *et al.* (2011) recommended the “quality of the tank outflow” be measured using the thermodynamic definition of “exergy”, the destruction of which is directly related to entropy generation within the tank due to destratification from by heat transfer effects. Consequently it was recommended that the first and second laws of thermodynamics be used as an alternative metric for assessing

outflow quality ^[79]. This matter is discussed in the sub-section to come on general thermocline modelling.

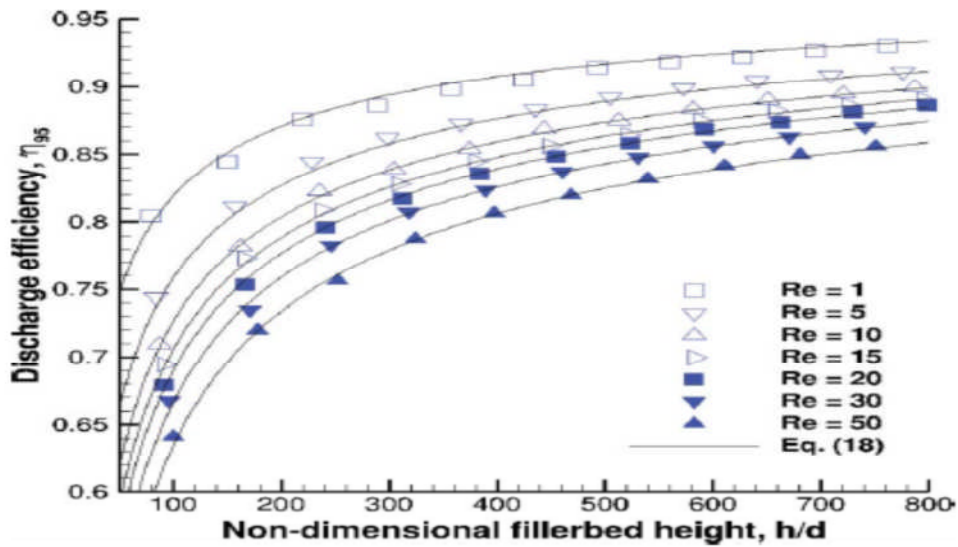


Figure 2-18: Effect of Re and H on thermocline tank discharge efficiency (source: ^[73])

Flueckiger (2013) also deduced that tank height plays a major role in determining tank efficiency. Larger tank height relative to cross sectional area extends the discharge time during which the tank's HTF is maintained at a high temperature. It was found that discharge efficiency (Figure 2-18) is affected by both the Reynold's number "Re", and the non-dimensional tank height "H" (actual tank height/filler particle diameter) ^[73]. This summarizes the key research on tank design and the section which follows next discusses work on filler materials.

2.1.2.2 Filler Material Selection and Analysis

Pacheo *et.al* (2001) of Sandia National Laboratories, U.S.A., conducted experiments to evaluate potential tank filler materials for lowering system cost through displacing the use of more expensive HTF ^[54]. The ideal filler material needed to be inexpensive, widely available, have a high heat capacity, a low void fraction (to reduce required HTF volume), be compatible with the HTF (in Pacheo's case, molten nitrate salts) and be non-hazardous. Seventeen materials were surveyed for testing,

(including anhydrite, fluorapatite, hydroxyapatite, illemerite, limestone from Kansas and New Mexico, magnasite, marble, quartzite, taconite and witherite) and subjected to various thermal cycling tests ^[54].

After a specified number of thermal cycles (typically 350) the testing process was stopped and samples were removed for testing. Of the entire 17 samples, quartzite rock and silica filter sand showed the greatest resistance to the stresses of thermal cycling. Pacheo *et. al* then proceeded to test these materials material in a 2.3 MWh_{th} pilot thermocline tank (Figure 2-19), which also confirmed the superior thermal stability characteristics of these materials in the extended cycling applications of a thermocline tank ^[54].

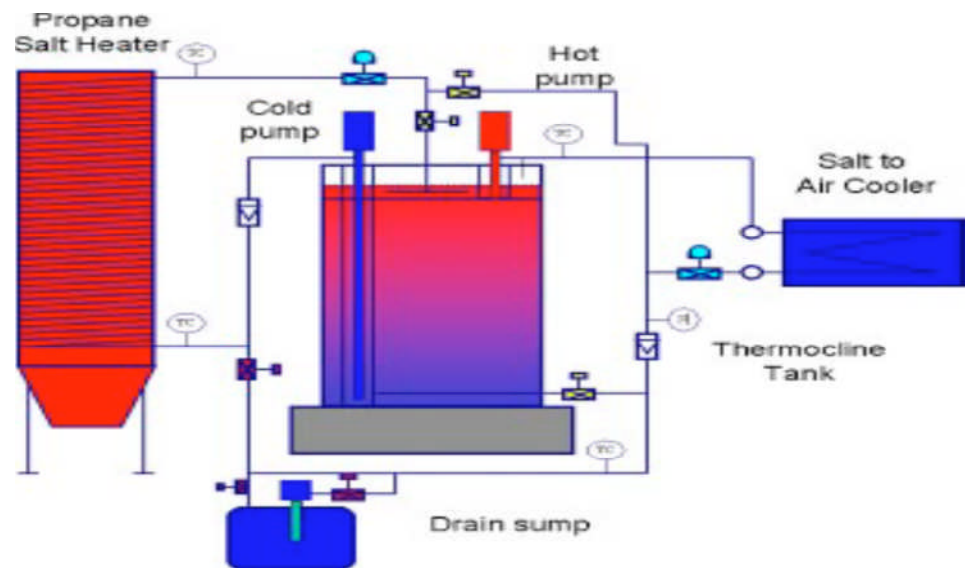


Figure 2-19: Schematic of the 2.3 MWh_{th} thermocline flow loop used by Pacheo *et. al* (Source: ^[54])

Brosseau *et al.* (2005) also of Sandia National Laboratories conducted similar research ^[72] in an attempt to extend the work done by Pacheo *et al.* The objective was to expand the series of isothermal and thermal cycling tests done by Pacheo in order to demonstrate the durability of these filler materials in molten nitrate salts over a range of temperatures, for extended time frames. Results obtained from these tests re-confirmed the ability of quartzite rock and silica sand to

withstand extended cycling while showing no signs of deterioration or reduction in performance characteristics. Therefore Brosseau *et al.* concluded that the CSP industry had indeed found an appropriate filler material for use in large scale commercial thermocline systems.

In the area of heat transfer between the HTF and filler materials, Karaki *et al.* (2010) using a Laplacian transformation to analytically solve the previously mentioned Schumann equations ^[80] did further investigation into charge/discharge cycles with respect to day-to-day tank operation.

Solving the coupled Schumann partial differential equations in this manner allowed a very flexible investigation using constant, linear or exponential initial tank temperature distributions typical of actual day-to-day operation ^[80]. Results from this analytical model were in good agreement with an earlier numerical model developed by the said authors and further established the potential of the suitability of the filler materials proposed by Pacheco *et al.* (2002) for a real tank system.

Flueckiger and Garimella (2012) conducted numerical simulations to investigate the effects of different filler granule diameters and diabatic boundary conditions along the tank wall. Performance of the thermocline was assessed with three particular metrics:

- (a) Outflow temperature with discharge time,
- (b) Entropy generation inside the filler bed
- (c) Net cycle efficiency.

It was found that thermocline tanks with small granules exhibit narrower heat-exchange regions relative to tanks with larger granule sizes, an effect which improves thermal stratification and yields higher outlet temperatures during discharge. Also, thermocline efficiency was reported (in terms of energy, exergy and outlet temperature) to be relatively higher for smaller granule diameters ^[79].

A tradeoff however has to be made at some point, as smaller granule diameters also cause lower bed permeability, thus requiring additional pumping power. As such, future work is required to determine the

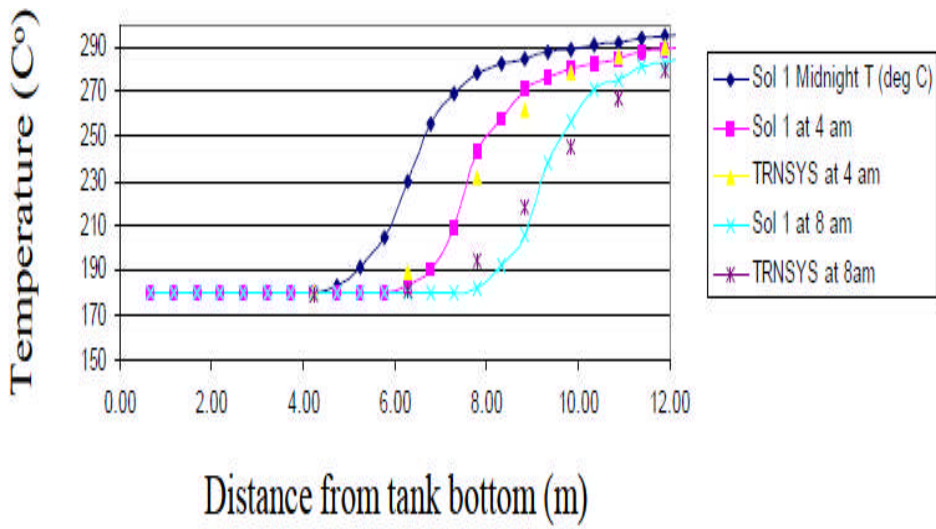
optimal granule diameters in the context of pump driving power and system efficiency. Finally, the results from Flueckiger and Garimella (2012) also revealed that entropy generation inside the tank fillerbed is a function of the external boundary conditions at the tank wall.

2.1.2.3 General Modelling of Thermocline Storage Systems

Kolb and Hassani (2006) developed a TRNSYS based model that evaluated the time dependent performance of a potential thermocline storage system for the 1MWe Saguaro PTC plant in Arizona, U.S.A ^[81]. This was influenced by a recommendation from energy company Nextant, that Saguaro's performance could be improved by a thermal storage system comprising a 330 m³ scaled down version of the Solar One thermocline tank (Figure 2-15) but with an increased H/D ratio of 1.2 ^[81-83].

Kolb and Hassani's modelling of the Nextant proposal in the TRNSYS simulation environment yielded positive results regarding the benefits of the proposed thermocline storage system ^[81]. The model input consisted of an hourly insolation and weather file based on a typical meteorological year, while the model output consisted of temperatures, flows, turbine power and other related process variables. In an attempt to improve the accuracy of results, this model included the effects of thermal conduction between control volumes, thermal losses through the tank walls, roof and floor, along with the thermal inertia of the tank's concrete foundation, factors ignored for simplicity in the earlier model by Pacheo *et al.* ^[81]. With these modifications, simulated results showed good agreement with Solar One test data both for tank discharge ^[84] and for a 16.5 day tank cool down period ^[85], with the exception that the thermocline slope of the actual data was slightly steeper than that predicted in the TRNSYS model (Figure 2-20).

Discharge Test



16.5 Day Cooldown of Solar One Thermocline Storage

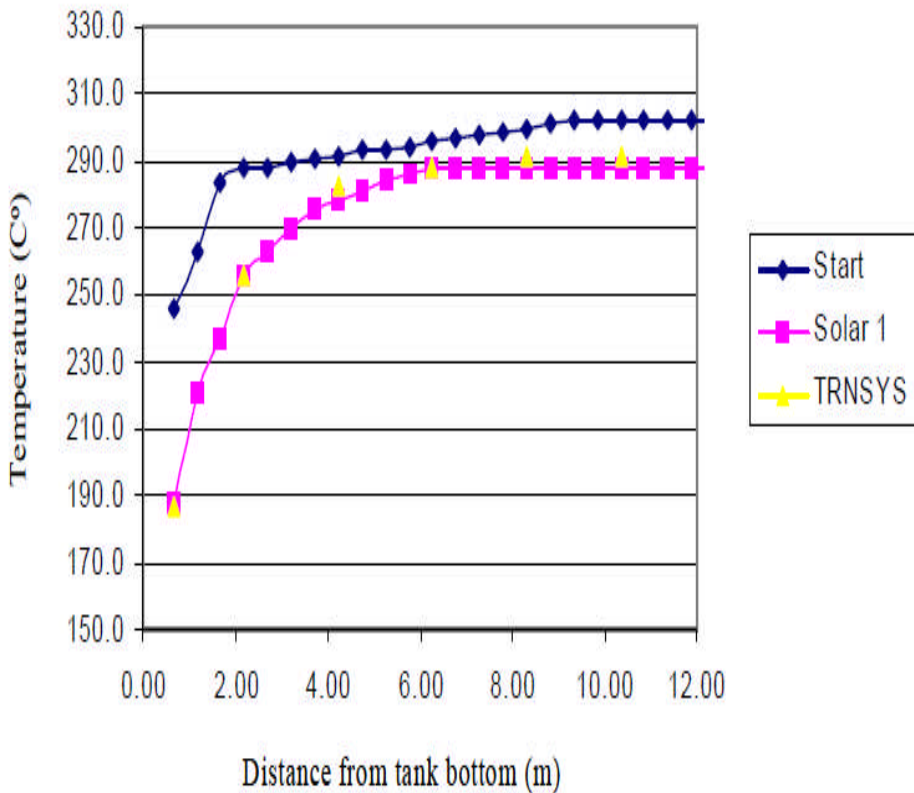


Figure 2-20: Pacheo and Hassani's model comparison with discharge and cool down tests results of Solar One thermocline tank (Source: [81])

The authors provided no explanation for this difference, which could very well have resulted from slight differences between the actual and simulated interparticle conductive effects, and some of the “assumed” thermophysical properties for the actual tank and the material contents.

The validated model was scaled in accordance with the Nextant recommendations and an annual simulation of Siguario’s operation was performed in TRNSYS. Results of annual simulations performed with and without storage revealed that though overall efficiency would only be increased by 0.1%, adding the thermocline tank as recommended by Nextant would more importantly increase the plant’s capacity factor from 23% to 42%.

This would require some capital expenditure as the solar field would have to be increased by approximately 55% to operate the storage system. However the gains of increased revenue earning potential derived from an almost doubled capacity factor were generally expected to outweigh this cost. It would have been interesting to see whether or not economic analysis corroborated this point.

Still other researchers such as Yang and Garimella (2010a) set out to obtain a better understanding of certain unexplained charge/discharge characteristics ^[69], reported by previous researchers including those previously mentioned with regards to the work of Kolb and Hassani (2006). Their work was therefore aimed at developing a two-temperature model (HTF and filler) that could accurately predict tank charge/discharge efficiency and by extension, develop useful guidelines for designing the molten-salt thermocline tank system described in the previous section.

A numerical model of the tank discharge process was developed and validated with experimental data obtained from the work of Pacheo *et al.* (2002). It was found that discharge efficiency increases with tank height and decreases with Reynolds number. More importantly Yang and Garimella developed a correlation to predict discharge efficiency

based on Reynolds number and non-dimensional tank height H , as follows:

$$\eta = 1 - 0.1807\text{Re}^{0.1801}(H/100)^m \quad \text{(Equation 2-2)}$$

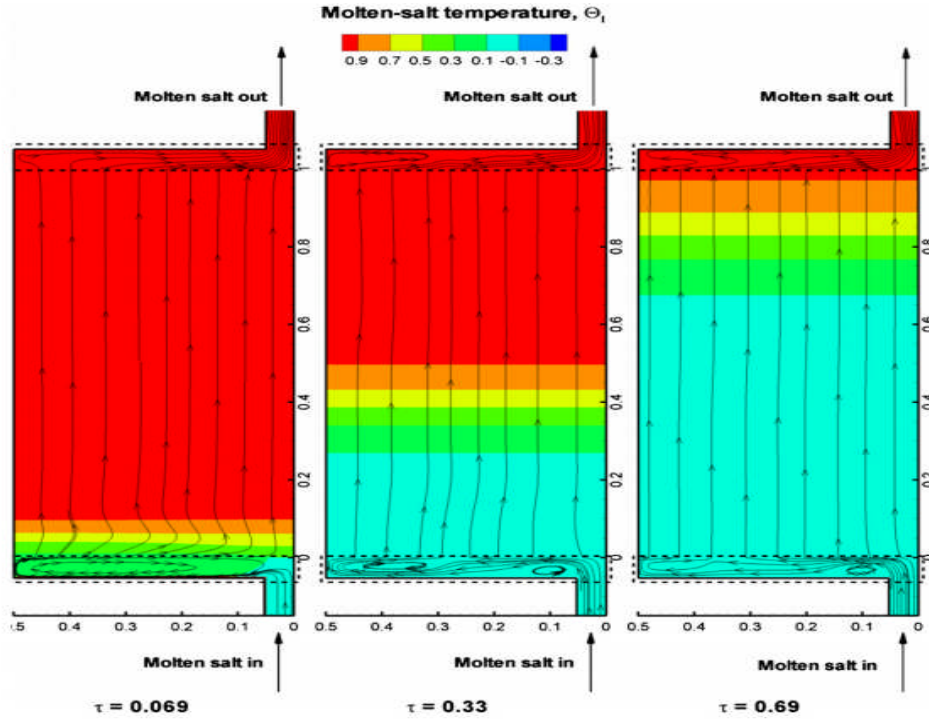
where $m = 0.00234\text{Re}^{0.1801} + 0.00055\text{Re} - 0.485$

This correlation was capable of predicting the numerical data of the model within a maximum error of 1% for Reynolds (Re) and non-dimensional height (H) numbers ranging from 1 to 50 and 10 to 800 respectively. Model results also indicated that, during discharge, the heat-exchange (thermal gradient) zone of a thermocline tank expands with both time and Reynolds number (Re). It was also revealed that the rate of travel is both constant and precisely predictable by appropriate numerical models [69].

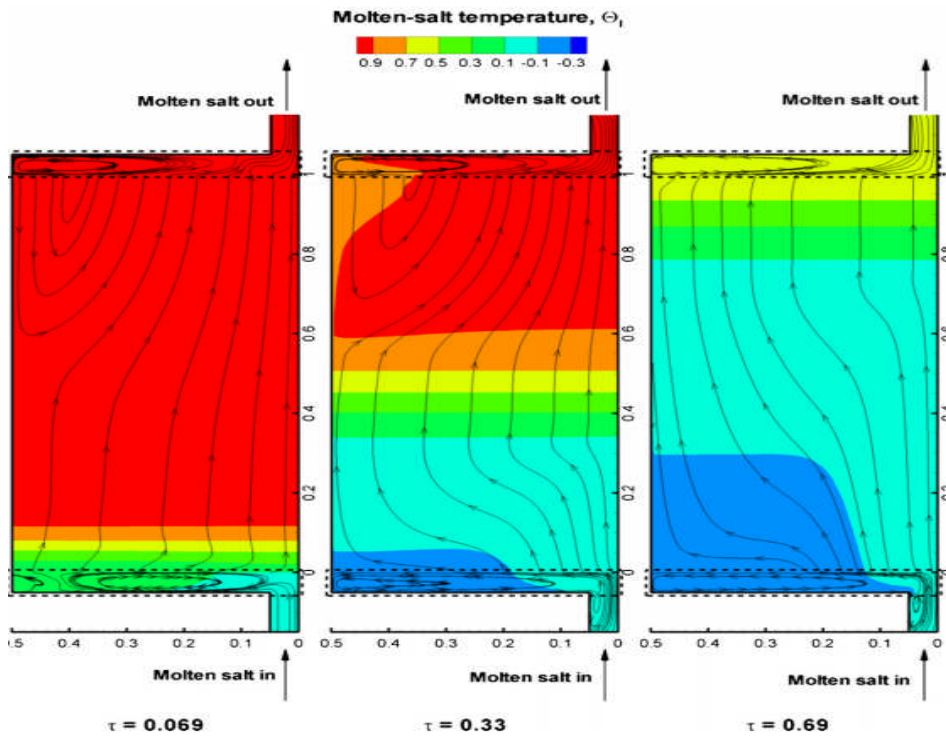
Yang and Garimella (2010b) also developed a numerical model to investigate the effects of distributors on tank flow characteristics at either end of the tank filler bed [57]. In their previous model [69], which investigated tank discharge and cycle efficiencies, tank walls were assumed adiabatic. However in this model heat transfer effects and fluid flow along a diabatic tank wall were included.

Model results revealed that imposing adiabatic tank wall conditions resulted in a uniform flow field (Figure 2-21a), but with a diabatic wall the streamlines were distorted (Figure 2-21b). With respect to the effect of the flow distributors, it was found that for both boundary conditions, distributors were effective in maintaining thermal stratification in the tank for $\text{Nu}_{\text{wall}} = 1.6 \times 10^5$.

Van Lew *et al.* (2010 and 2011) non-dimensionalized the Shumann based model used for modelling the tank charge/discharge process, in an attempt to reduce model computational time accuracy and efficiency.



(a) adiabatic tank wall



(b) diabatic tank wall

Figure 2-21: Yang and Garimella - Effect of tank wall conditions on Thermocline Tank flow field (Source: [57])

This effective approach compressed all the influential model parameters into just two representative parameters $\tau_r = f(x) \cdot n. (\rho_f, C_{p,f}, R, U, H, h, S_r, \varepsilon)$ and $H_{CR} = f(x) \cdot n. (\rho_f, C_{p,f}, C_{p,r}, \varepsilon)$ [86-87]. The first parameter τ_r , is a non-dimensional time constant describing the interaction between the non-dimensional temperatures (θ_r and θ_f) for the filler particle and fluid respectively (Figure 2-22). The other parameter H_{CR} is the fractional ratio of fluid and filler heat capacitances.

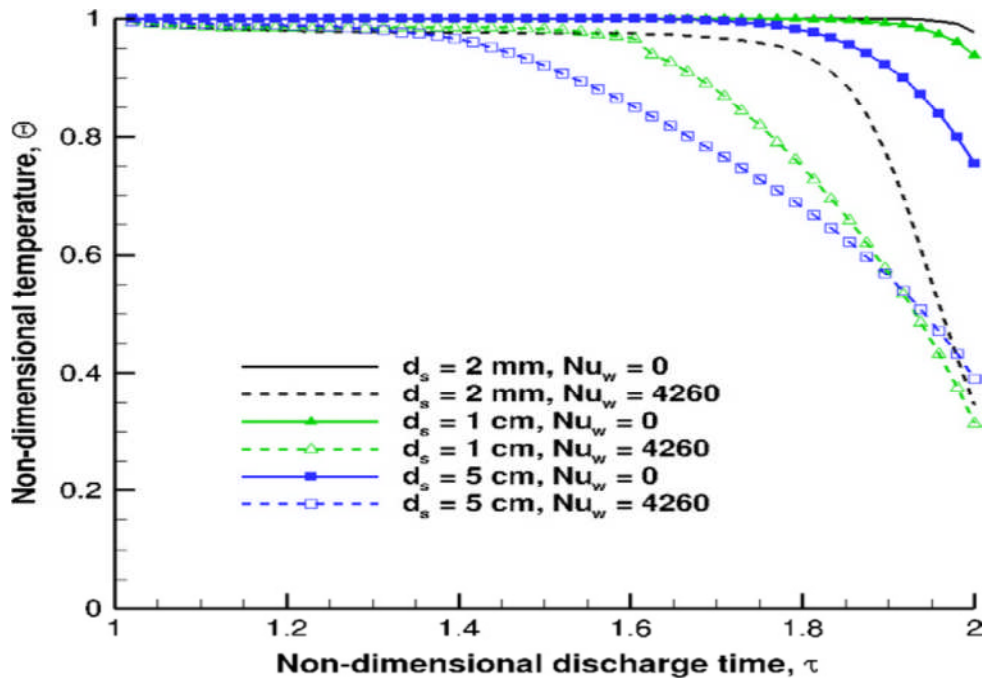


Figure 2-22: Outflow temperature history of thermocline tank discharge for different tank wall conditions and granule diameter (source: [79])

This approach by Van Lew *et al.* provided researchers in the field with a better understanding of the link between the mathematics and fluid dynamics of the thermocline model and allowed a very efficient and powerful model solution through use of the “*Method of Characteristics*”.

Consequently, this introduced a certain level of model flexibility with regards to handling nonlinear initial conditions, along with varying boundary conditions of the inlet. There was also the added benefit of significantly reduced computational times [87]. Of all the models

developed for thermocline tank analysis to date, this approach is considered the most efficient and is therefore the preferred method ^[71].

The problem of assessing the limits of useful tank energy outflow for power generation as discussed in the earlier section on tank design was evaluated using the “*ad hoc*” outflow temperature metric suggested by Yang and Garimella (2010a). Here Yang and Garimella (2010a) had suggested that system designers allow tank outlet temperatures no lower than 95% of the system’s operating range in order to provide a quality steam temperature for the power block. However Flueckiger and Garimella (2011) argued that this metric was overly conservative, limiting the exergetic content of the tank ^[79].

Flueckiger and Garimella argued that when this temperature criterion is reached, the tank still contains recoverable exergy that could be utilized if the power block was made to operate at a slightly lower thermal efficiency, thus improving the overall discharge efficiency. The example of the SEGS VI power plant was cited in this regard as possessing the capacity to operate as low as 90 K below its nominal design point.

Table 2-4: Summary of thermocline tank efficiencies (first law, second law and temperature criterion) for different external loss conditions (Nu_w) and filler granule diameter (d_s) (Source:^[79])

Case	d_s (cm)	Nu_w	$\eta_{1st\ Law}$	$\eta_{2nd\ Law}$	$\eta_{1,95\% out.temp}$
1	0.2	0	0.975	0.975	0.975
2	0.2	4260	0.940	0.923	0.748
3	1	0	0.975	0.974	0.964
4	1	4260	0.921	0.893	0.597
4	5	0	0.966	0.961	0.840
6	5	4260	0.903	0.868	0.426

Their model results revealed that tank losses to the ambient, create small but almost immediate drops in outflow temperature at the start of tank discharge which inhibit the sustained delivery of HTF temperatures

above the 95% threshold previously mentioned, resulting in temperature criterion efficiencies as low as 0.426 (Table 2-4).

Finally, Bayon and Rojas (2013) developed a one-dimensional model ^[55] called CIEMAT1D1SF for simulating thermocline storage tanks with an effective storage medium consisting of either a liquid or a liquid and packed bed. The model is reported to be a simplified version of previous models and is said to have been validated with experimental data from literature. The model used the dimensionless approach for solving the governing equations presented earlier by Van Lew *et al.* but expressed the parameters governing the thermocline thermal behaviour in terms of a dimensionless velocity referred to as $v^* = f \cdot x \cdot n \cdot (\rho_f, C_{p,f}, L, v_m, k_{eff})$. Results indicated that thermocline thickness decreased with increasing v^* , obtaining a minimum value when $v^* \geq 2350$. The opposite was reported to happen with tank efficiency, whose value increased with increasing v^* up to a maximum of 87.3%, also for $v^* \geq 2350$.

From these results Bayon and Rojas (2013) reported that it was possible to establish an equation for practical design of thermocline storage tanks with maximum theoretical efficiency. This equation was reported as linking tank dimensions, storage medium effective conductivity, temperature interval and thermal power. This mirrored the report mentioned earlier by Valmiki *et al.* (2012) that mathematically linked energy storage effectiveness to the following tank design parameters: fluid and solid material properties, tank dimensions, packing schemes of the solid filler material, and the durations of the charge and discharge times ^[88].

2.1.2.4 Investigating Thermal Ratcheting problems in Thermocline Tanks

Thermal ratcheting is a destructive phenomenon associated with the cyclic temperature operation of the dual medium (HTF and filler material) thermocline tank storages discussed earlier. It specifically

refers to the outwardly expansive action of mechanical stress from the tank filler material on the tank wall. When a thermocline tank heats up during the charging period of its thermal cycle, it expands horizontally, resulting in a slightly larger tank diameter. The height of the solid filler packing within the tank thus decreases as the filler particles fill this newly created void.

During the discharge period however, as the tank cools down and contracts horizontally, the filler particles cannot be easily displaced upwards due to the effects of gravity, inter-particle friction and packing resistance, and so the tank cannot shrink back to its original dimensions [89]. This effect is compounded with the normal tank cycling, resulting in a build up of mechanical stresses that cause the tank wall to grow or “ratchet” outward with time. If at any point this stress exceeds yield stress of the tank wall, plastic deformation occurs. Further cycling from this point onwards eventually leads to tank rupture.

Thermal ratcheting of pressure vessels has been explored in other works [90-91], however its effects in relation to thermocline storages was not clearly understood. Flueckiger *et al.* (2011) therefore conducted a thermal and mechanical investigation [89] in respect of potential tank wall failure due to thermal ratcheting.

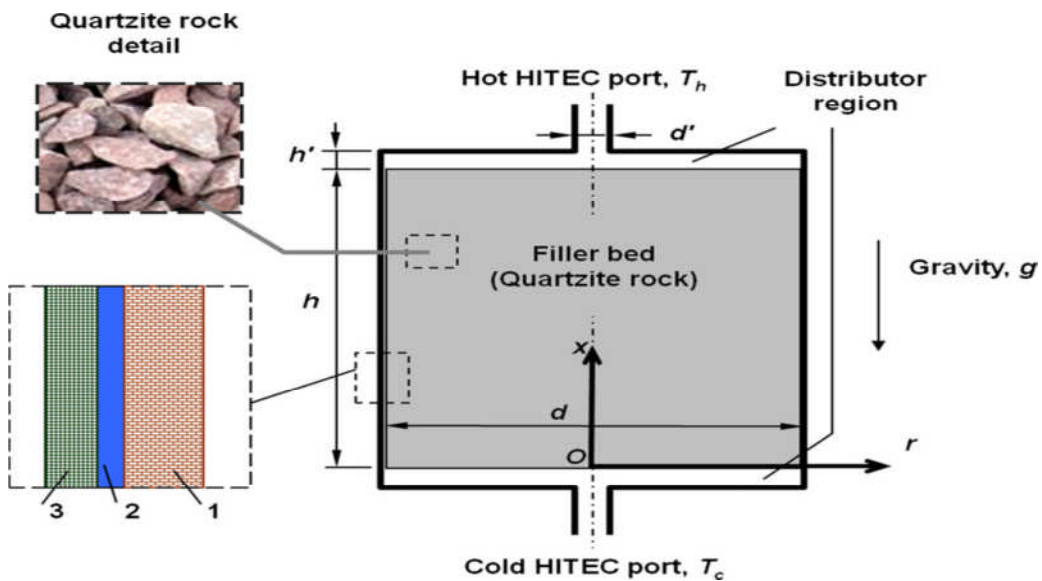


Figure 2-23: Schematic illustration of thermocline tank with a composite wall of firebrick (1), steel (2) and ceramic (3). (Source: [89])

The results confirmed hoop stress in the tank steel shell is a direct consequence of thermocline cycling. The effects of cyclic changes on the stresses were shown to be dampened by increasing either the surface heat losses or the insulation resistance between the internal filler material and the steel shell (Figure 2-23).

Seven cases were investigated (Table 2-5) with different ratios for composite wall thicknesses and differing heat loss rates. In cases 1-4 , tank wall conditions were held constant while heat loss rates were varied, while in cases 5 -7 wall composite thickness ratios were varied at constant heat loss.

Table 2-5: Summary of cases considered by Flueckiger *et al.* (2011) for differing tank wall composite layer thicknesses and heat loss conditions. (Source: ^[89])

Case	$h(W/m^2K)$	ϵ_r	$\delta_{fb} (m)$	$\delta_{cs} (m)$	$\delta_{cer} (m)$
1	5	1	0.1	0.02	0.05
2	10	1	0.1	0.02	0.05
3	5	0.5	0.1	0.02	0.05
4	10	0.5	0.1	0.02	0.05
5	5	1	0.2	0.02	0.05
6	5	1	0.1	0.02	0.05
7	5	1	0.1	0.02	0.025

In cases 1-4, the normalized stress value (Figure 2-24) was shown to be inversely proportional to tank heat loss as stress values for cases 1 and 3 are greater than those of cases 2 and 4 respectively where the heat loss was twice as great. Of these set of cases, case 2 (thin black line), produces the lowest normalized stress value since it had the highest of all the heat losses.

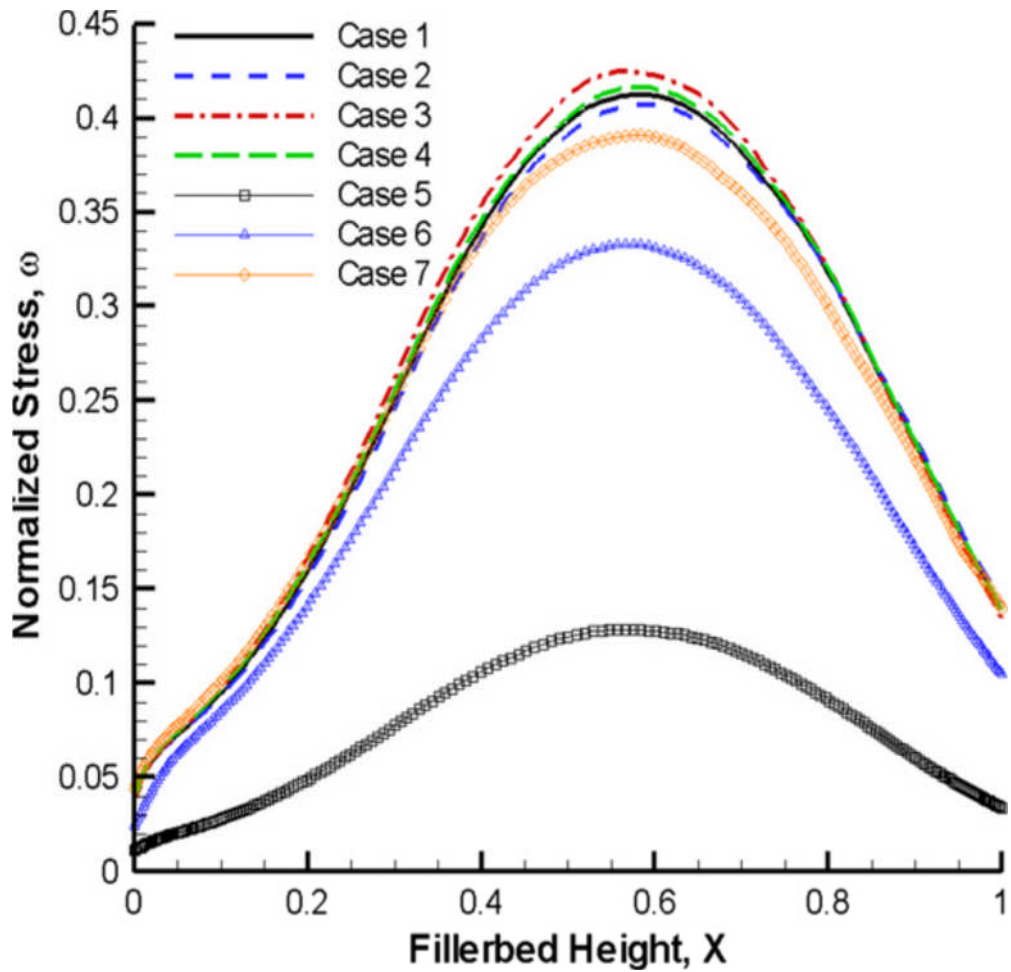


Figure 2-24: Hoop stress profile along the filler bed for cases1-7.(Source: ^[89])

With regards to cases 5-7, where heat loss was fixed, case 5 showed the lowest normalized stress value as the fire brick insulation layer was twice the thickness of the other cases modelled in the group.

Cases 1-4 therefore demonstrated the effect of heat loss in reducing tank wall stresses while cases 5-7 showed that a relative increase in insulation thickness also reduces the stresses linked to thermal ratcheting. Since heat loss from the tank is not desirable, Flueckiger *et al.* (2011) therefore recommended an increase in the internal firebrick insulation between filler material and the steel shell. Tank wall stresses were also shown to be lowered by increasing the steel shell thickness but it was noted that this could result in impractical aspect ratios or excessive radial temperature gradients, which are both undesirable ^[89].

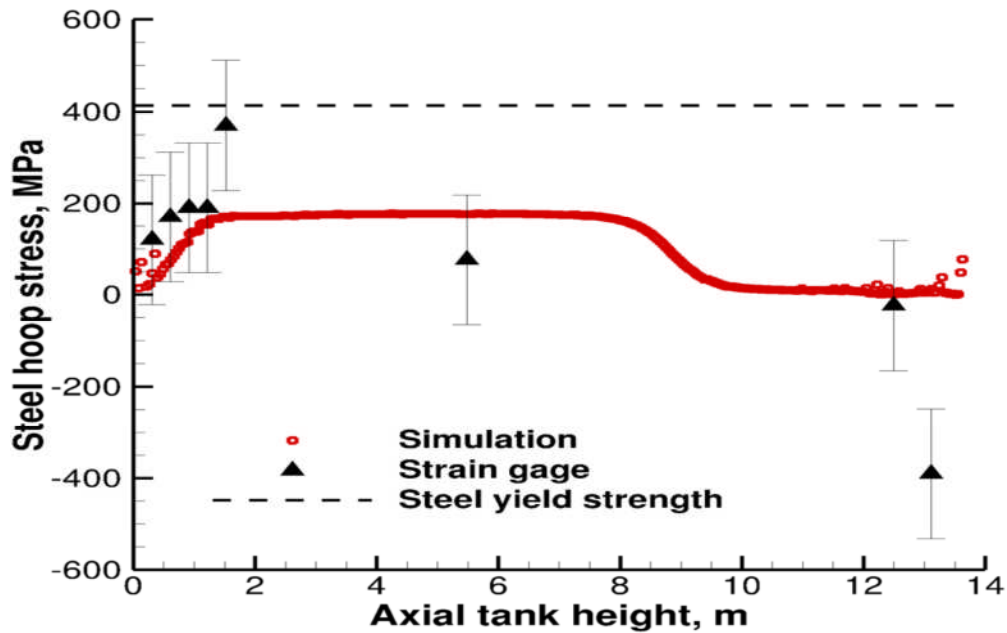


Figure 2-25: Solar One thermo cline tank hoop stress (simulation and measured) (Source: ^[70])

Flueckiger *et al.* (2012), conducting follow up work in this regard, constructed a detailed CFD model of the original Solar One thermocline tank in order to validate a model for the determining the hoop stress and thermal ratcheting potentials of normal tank cycling. It was found from this model (assuming infinite filler particle rigidity) that hoop stress in the tank's steel shell is readily determined from periodic temperature profiles, which directly determine the maximum permanent deformation of the structure. The results predicted a wide band of maximum hoop stress across the lower half of the thermocline tank, which was attributed to the moving heat exchange (thermocline) region inside the tank during operation. The predicted stresses of the numerical model were reported to agree with Solar One test data within 6.8% and proved to be lower than the yield strength of the steel shell (Figure 2-25), thus avoiding potentially catastrophic thermal ratcheting ^[70].

2.1.2.5 Investigating Viscous Channelling problems in Thermocline Tanks

Another undesired phenomenon in relation to the mixing of fluids in porous media has been discovered in recent decades and is thought to be a factor affecting the stability of the thermocline. It is commonly known as viscous “channelling” or “fingering” and is directly attributed to the displacing motion between hot and cold fluid occurring when fluid is pumped into, or drawn from the tank.

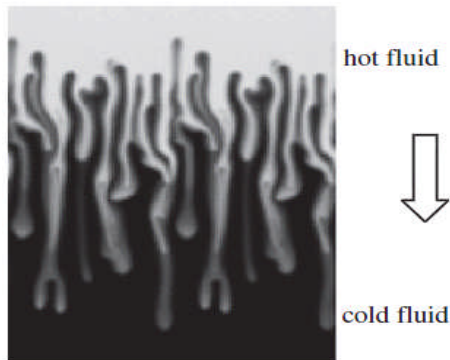


Figure 2-26: Illustration of viscous channelling effect in a porous medium when hot fluid displaces cold fluid (Source: ^[92])

In viscous channelling the growth of “finger like projections” or “channels” of mixed fluid (Figure 2-26) occurs in the thermocline region, disturbing thermal stability (thermal gradient region) and increasing system entropy.

Qin *et al.* (2012) conducted research to investigate the effects of viscous channelling on the thermal stability of the thermocline and reported that it can be prevented under certain hydrostatic and hydrodynamic conditions in a porous medium ^[92] .

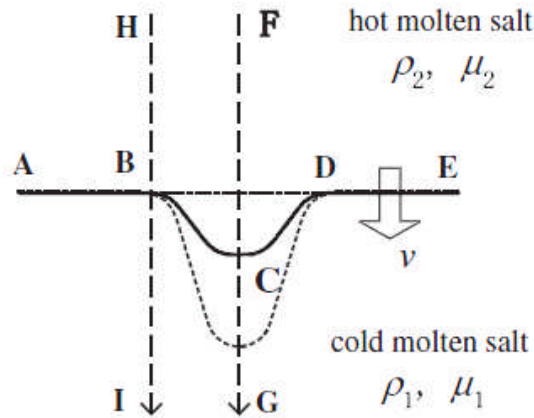


Figure 2-27: Schematic illustrating the development of a viscous channel in at the hot-cold fluid interface in a porous bed (Source: [92])

Modelling the thermocline stability criteria required the evaluation of the interstitial and critical flow velocities which are important to the definition of stability criteria. The interstitial velocity (v) refers to the velocity of fluid flowing into a small gap (“BCD” in Figure 2-27) created by some random disturbance at the interface between hot and cold fluid in the filler material of a porous bed.

The critical velocity is given as:

$$v_c = gK \frac{\rho_1 - \rho_2}{\mu_1 - \mu_2} \quad \text{(Equation 2-3)}$$

Where μ_2 and μ_1 are the viscosities of the displacing and displaced fluid respectively; ρ_2 and ρ_1 are their respective densities; K is a constant defining the permeability of the porous medium and g is acceleration due to gravity.

As far as the surveyed literature reveals, Qin *et al.* (2012) were the first to investigate thermocline stability criterion in this regard and presented four stability criteria as follows:

- **Criterion 1:** Hot HTF with less density must sit on top of the cold HTF allowing a stable hydrostatic state.

- **Criterion 2:** When hot HTF is displacing cold from the top down as in charging a TES tank, the interstitial flow velocity must be less than the critical velocity to prevent viscous fingering.
- **Criterion 3:** If cold HTF is displacing hot HTF from the bottom up as in the discharging phase, there is no interstitial flow velocity limit. On the other hand, when cold HTF is displacing hot from the top down, the interstitial velocity must exceed the critical velocity.
- **Criterion 4:** The mobility ratio $\left(M = \frac{K_2/\mu_2}{K_1/\mu_1}\right)$ when charging the TES tank is naturally greater than 1. This means that the thermocline is intrinsically unstable and therefore the interstitial flow velocity must be controlled to a value below the critical velocity given in criterion 2, unless the displacement occurs under a gradient porosity packed bed. During discharge, the mobility ratio is less than 1 and consequently displacement of cold HTF to hot from the bottom up, is intrinsically stable. Therefore there is no interstitial flow velocity limit except if displacement occurs in reverse.

If it is therefore anticipated that observation of these criteria will significantly reduce the potential for occurrence of viscous channelling in thermocline tank systems.

So far, this section has provided a useful overview of the major issues currently being addressed in thermocline tank research work. The next section discusses another option currently being explored known as solid media thermal storage.

2.2 Solid Media Thermal Storage

Solid media sensible heat storage is also another promising storage option currently under development for CSP power plants, particularly PTC plants ^[93]. Relative to the other storage options, solid media storage of sensible heat offers the potential of lowering storage investment costs, due to its high availability, durability, thermal stability,

mechanical strength, heat capacity, operational safety, and ease of processing.

In this type of storage, the temperature dependent thermo-physical properties of the storage material that is used are critically important [17]. Such properties include the thermal conductivity (k), thermal diffusivity (α), specific heat capacity (C_p) and the density (ρ) which relate to each other in the equation:

$$k_{(T)} = \alpha_{(T)} \cdot \rho_{(T)} \cdot C_{p,(T)} \quad \text{(Equation 2-4)}$$

High thermal diffusivity (α), improves transient heat transfer, thus reducing the time constant during charge/discharge cycles of the heat store. High volumetric heat capacity ($\rho \cdot C_p$) reduces the storage volume. The variation of density with temperature is represented by the coefficient of thermal expansion (CTE), whose design value should be similar to that of the metallic HTF pipework embedded in the solid media [17].

Current research work in concrete storage systems has had an epicentre based in Germany at the DLR (German Aerospace Center) developing in recent years over a number of phases consisting of [8, 94]:

- (a) **Phase 1** - Concept development and study phase from 1988 – 1992.
- (b) **Phase 2** - Lab scale development and testing at research centers DLR (German Aerospace Center) and Zentrum für Sonnenenergie- und Wasserstoff-Forschung (ZSW) until 1994.
- (c) **Phase 3** - A period of dormancy during 1995 – 1999, generally with little or no government funding procurement. However in a report by Geyer (1999) it was evinced that the “*Concrete Thermal Energy Storage for Parabolic Trough Plants*” (CONTEST) programme of the European Union was effective in encouraging collaboration between key research bodies and industrial partners, during this period thus keeping interest alive in this area [95].

- (d) Phase 4 - A “resurgence” of activities from the year 2000 which resulted in the WESPE (11/2001 – 12/2003), WANDA (03/2004 – 09/2006) and ITES (2007 – 2009) projects funded by the German government in collaboration with industrial partners, and other current research work.

A number of potential solid storage media have been tested. Generally these media have consisted of a mixture of aggregates and small amounts of auxiliary materials held together by a binder which together forms a stable matrix. From a review of the literature, it can be seen that current research work in solid media sensible heat storage centres on the following key areas:

- High temperature concretes
- Castable ceramics
- Graphite

2.2.1 Recent research work in Solid Media Storage for CSP Plants

The Institute of Technical Thermodynamics at the German Aerospace Center (DLR) has been at the forefront of research and certain researchers at this institute (Meyer, G., Laing, D., Steinmann, W., Tamme, R., and Richter, C.) over the last decade have conducted significant work in this area. The aim of research activities at this Institute is to develop new innovative concepts and approaches to energy storage for CSP with thermal efficiencies greater than 90%, a minimum lifetime of 30 years. Specific costs of less than 20 €/kWh of thermal capacity and less than 0.01 €/kW electric are also targeted ^[93].

2.2.1.1 The WESPE Project

Solid media sensible heat stores were developed in the project “*Midterm Storage Concepts – Further Development of Solid media Storage Systems*” (PARASOL/WESPE) funded by the German government from December 2001 until December 2003. It was aimed at

developing an efficient and cheap sensible heat storage media, based on the optimization of a tube register heat exchanger which was to be experimentally demonstrated with a 350 kWh test unit ^[93]. Two parallel storage materials were developed for testing: a high temperature concrete and a castable ceramic. These materials each consisted of a binder system along with aggregates such as iron oxides and a small quantity of auxiliary materials ^[96].

According to Laing *et al.* (2006) two 350 kWh ceramic storage modules and two high temperature concrete modules with approximately 20% lower storage capacity were constructed in the WESPE project. The heat exchanger in these modules consisted of 36 tubes of high temperature steel with a outer diameter of 21 mm x ½” nominal bore. The tubes running down the axial length of the module (Figure 2-28) were arranged in a square format of 6 tubes x 6 tubes. Flow distributors and collectors were designed such that there was a uniform flow distribution through all the tubes in the modules.



Figure 2-28: Solid media heat exchanger modules under construction for the WESPE project, Plataforma Solar de Almeria (PSA), Spain. (Source: ^[93])

Each storage module of dimensions $(0.48 \times 0.48 \times 23) \text{ m}^3$, was fitted with 208 thermocouples cast into the structure, 2 flow meters, 2 differential pressure sensors and 8 Pt-100 thermocouples for measuring oil temperatures. They operated up to a maximum temperature of 390°C and were cycled with a temperature difference of 40 K.

The modules were tested at the Plataforma Solar de Almeria (PSA) test facility in Spain by integration into a parabolic trough collector test loop (Figure 2-29) consisting of 50 m LS-3 and 75 m Eurotrough collectors.

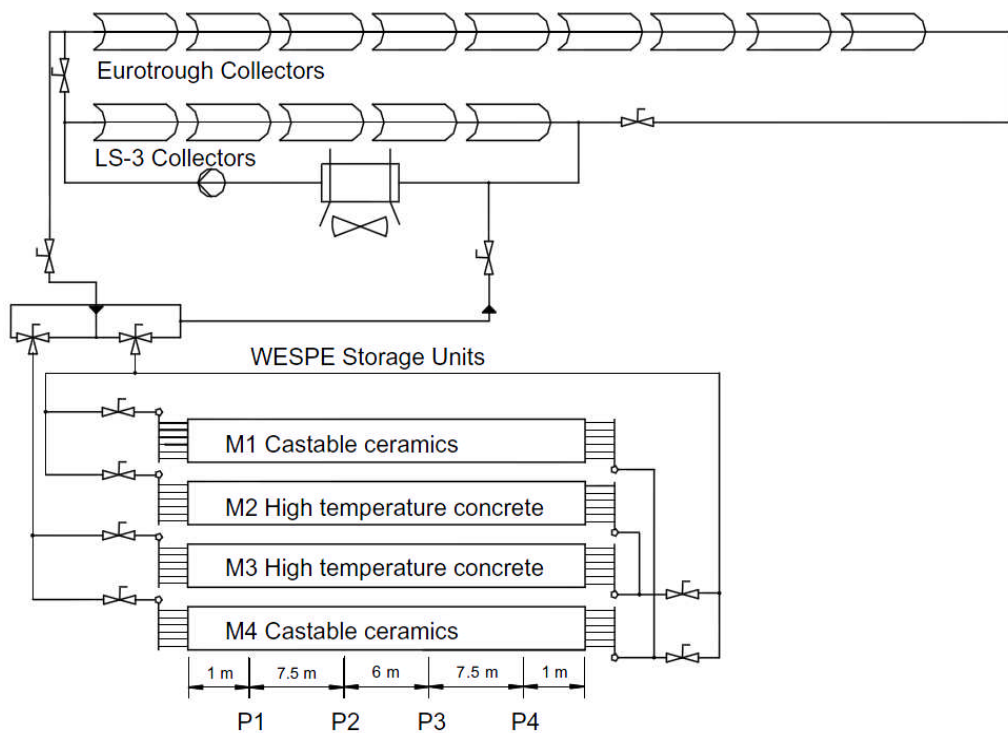


Figure 2-29: Schematic showing the integration of storage modules into the PTC test loop at PSA; P1 – P4 mark the axial position of thermocouples. (Source: [93])

However, before operational testing had begun, damage to the LS-3 collector loop rendered it unusable, forcing operation at a lower power of 300 kW from the Eurotrough collectors alone. In the entire set of tests performed, mass flows and oil inlet temperatures to both modules were kept constant.

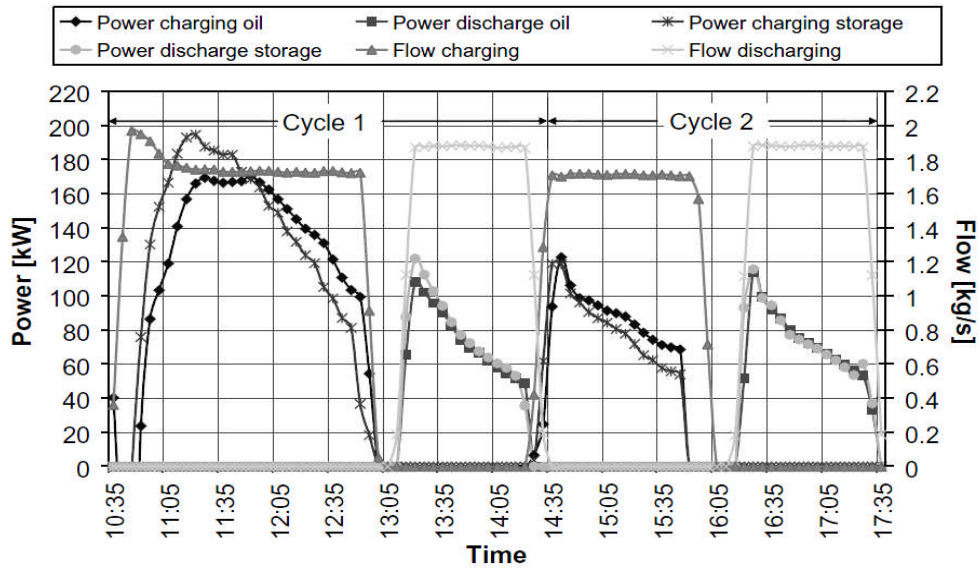


Figure 2-30: Curves of charge/discharge for both oil and storage module along with oil mass flow rate. (Source: [93])

An integration of the resultant curves for charge and discharge power (cycles 1 and 2) in the M1- ceramic module (Figure 2-30) revealed that 216 kWh of thermal energy was transferred to the module over a period of 7 hours.

Table 2-6: Material properties of storage materials developed at DLR. (Source: [93])

Material	Castable ceramic	High temperature concrete
Density (kg/m ³)	3500	2750
Specific heat capacity at 350°C (J/kg.K)	866	916
Thermal conductivity at 350° C (W/m.K)	1.35	1.0
Coefficient of thermal expansion at 350°C (10 ⁻⁶ /K)	11.8	9.3
Material strength	Low	Medium
Crack initiation	Hardly no cracks	Several cracks

During this time the temperature rose from 122°C to 169°C, a calculated capacity increase of 192 kWh with respect to the thermal properties of the ceramic material (Table 2-6). This suggested that the

difference of 24 kWh was the net heat loss of the storage unit during the same time.

When compared with each other it was found that for similar temperature increases in both the ceramic and concrete storage modules, 25% more power was transferred to the ceramic module, which is directly attributable to its higher heat capacity.

Due to the problems with the LS-3 collector, storage temperatures of only 325°C could be reached during the time of the WESPE test project, and the cycle tests for the 340-390°C range had to be postponed to a later date. However the project was still able to demonstrate the high suitability of these two materials in a practical storage application. There was no reported degradation in either the HTF or storage module material during any of the 60 thermal test cycles. High power levels were realized during cooling and high temperature differences were managed without difficulties.

Laing *et al.* (2006) reported that charging results from the WESPE test showed good agreement with performance predictions of the simulation environment “*StorageTech-Thermo*” developed by DLR and described in detail by Tamme *et al.* (2004). There were however some deviations for the discharging tests at low temperature which was attributed to the fact that oil temperature properties are significantly different in this range and this effect was not accounted for in the model ^[93].

The general conclusion from this first test project in solid media storage was that the target investment cost of less than 20€ /kWh could be realized and that castable ceramic and high temperature concrete are both suitable storage media. However of the two, high temperature concrete was favoured owing to a lower cost, high material strength and easier handling properties ^[93].

2.2.1.2 The WANDA Project

To continue the work started in WESPE, the WANDA project began with the aim of exploring pre-commercial development of WESPE

technology for use in ANDASOL-type power plants. Also funded by the German government, the WANDA project focused on the analysis of various design concepts to further reduce storage costs and also on the analysis of modular storage concepts to increase the utilization factor of the thermal storage system^[97].

In relation to this project Laing *et al.* (2008) commented that since a major part of the storage costs was due to the tube register, various concepts could be explored to reduce this cost. The concepts explored were^[97]:

- (a) Tubeless design, (pressure resistant storage medium, direct contact)
- (b) Encapsulated design, (direct contact)
- (c) Optimization of the tube register design (Heat transfer enhancement)

In the tubeless design concept, a prefabricated, pre-stressed concrete storage tank was directly in contact with the HTF. The design was low cost and allowed direct heat transfer. However despite being pre-stressed the concrete modules under test in the WANDA project showed permeability to HTF in the form of oil leaks^[97].

The encapsulated design consisted of preformed concrete units in a container. The HTF flowed directly over and through these units which resulted in effective heat transfer. The concrete however partially absorbed the HTF, which forecasted potential disposal problems. Special steel containers (ST 35.8, 15 Mo3 or equivalent quality standard) were needed to house the concrete units and to contain the HTF. For the pipe/container no complicated collector or distributor assembly was necessary, and a single flanged end connection was possible. However the high cost of the steel container was the main disadvantage to this approach.

Since the tubeless and encapsulated design options did not produce the expected techno-economic advantages, a third approach, the optimizing of the tube register design was explored. Optimization

effects of heat transfer enhancement both inside the storage material and on the heat transfer structures were analyzed.

Results revealed that the thermal conductivity of the storage material had a significant impact on tube register design. Distances between tubes within the storage media could be thus increased and consequently the number of tubes required for the module reduced [97].

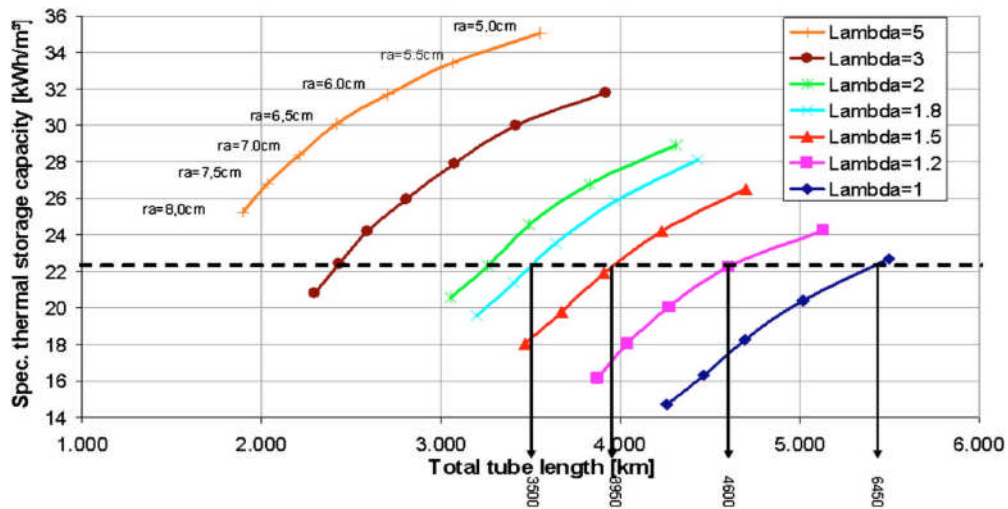


Figure 2-31: Specific heat capacity as a function of total tube length for different conductivities (W/m.K) and distance of tubes (cm). (Source:[97])

It was found that for a 950 MWh_{th} storage system charged and discharged with oil inlet temperatures of 390°C and 290°C respectively, an increase in solid media thermal conductivity from 1 to 1.8 W/mK resulted in a tube length reduction of approximately 46% (Figure 2-31) [97].

In an attempt to improve thermal conductivity within the storage media, metal and graphite splinters were added in the castings, and for graphite splinters it was found that thermal conductivity increased by 15%. However the cost of this enhancement was found to outweigh the benefits [97].

In regards to storage material heat capacity versus cost, it was found that a concrete containing quartz aggregates and a low level of binder

made from blast furnace cement and flue ash is lower in cost while displaying almost equivalent thermo-physical properties to the concrete used in the WESPE project and other test concretes. It was also found that the higher heat capacity resulting from use of a concrete with iron oxide aggregates also produces cost reductions in comparison to standard concrete. This was a result of less HTF pipes being required per module, due to a higher heat density.

To improve heat transfer effects between the tube register and storage media, Laing *et al.* (2008) also explored the addition of axial fins to tube registers. FEM modelling reported in later work (2012) revealed a heat transfer enhancement that could result in a 47% reduction in the number of tubes, but the additional cost and workmanship involved proved this enhancement uneconomical.

It was therefore concluded that the conventional tube register of the WESPE project was still the ideal design with respect to cost, simplicity of production and the safe operation achieved by the division of energy storage and transport functions between the concrete structure and the tube register assembly respectively [17].

Finally Laing *et al.* (2008) explored the system aspects of the storage system design by investigating the potential benefits of a modular storage arrangement (Figure 2-32) on plant performance, in contrast to the conventional layout [17, 97].

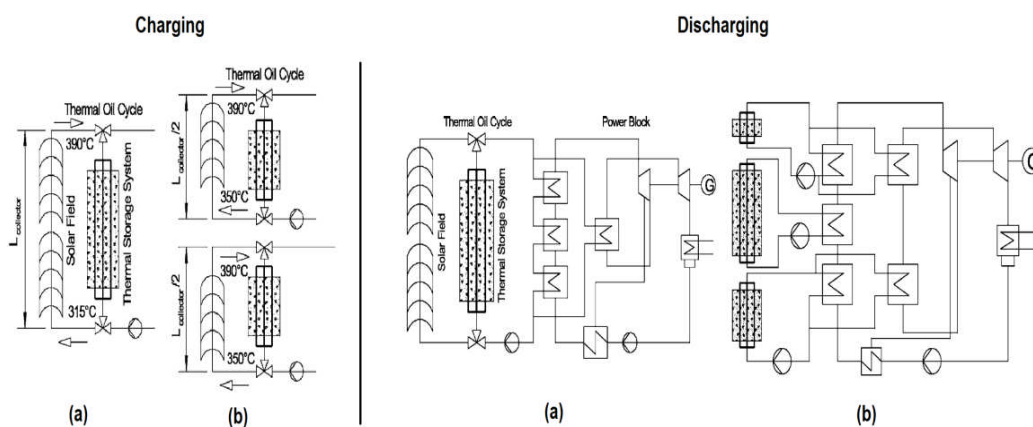


Figure 2-32: Schematic illustrating (a) standard storage integration (reference) versus (b) modular storage integration into the plant power cycle for both charging and discharging operations. (Source: [97])

Transient simulations performed with “*MODELICA software*” revealed that the storage module configuration and operation strategy were important factors that greatly impacted storage capacity.

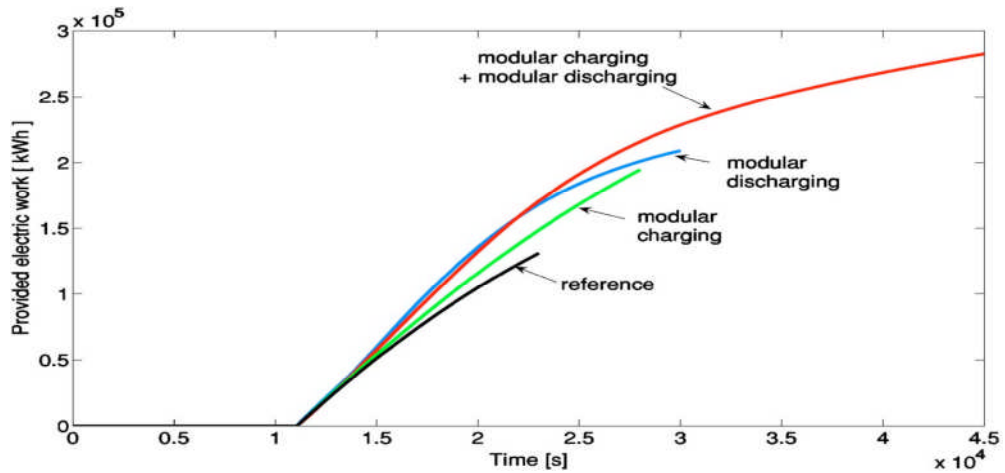


Figure 2-33: Simulated results for electric work provided during storage operation of a 50 MW power plant for various configurations of energy storage. (Source: [97])

Results for a simulated 50 MW power plant with storage system operating between 350°C and 390°C showed that a modular storage layout produced an increased electrical power output (Figure 2-33) compared to the standard layout [97]. A combination of modular charging and discharging was reported to produce an increase of 115% in electrical work compared to the reference layout. It was also reported that system performance could be further enhanced by combining sequential discharging and feed water preheating.

Despite these benefits however, a modular storage approach could have proved more expensive and more technical to implement. A cost benefit analysis was therefore required for a correct assessment of the reported modular storage improvements. In this respect Laing *et al.* (2010) conducted an economic analysis and life cycle assessment (LCA) of concrete TES for an Andasol-1 type PTC power plant. Results suggested that a 2-3% reduction in the levelized cost of energy (LCOE) could result from use of this modular storage approach.

However depending on the error margin in these simulations, the results may not be highly reliable, especially since LCA simulations

were based solely on a “hypothetical” concrete storage system, not a real test model. Results reported a 7% reduction in environmental impact for delivery of 1 kWh to the electric grid and a 9.5% reduction in the emissions related to power production ^[16].

2.2.1.3 The ITES Project

Though successful in establishing that the use of a normal tube register assembly was still the best option, the WANDA project encountered some problems which needed to be addressed. Firstly, due to low concrete permeability, an excessive vapour pressure build-up caused failure of the first WANDA test module indicating that module thermo-physical characteristics and operating strategy required re-engineering. Secondly, optimization was needed in the areas of storage capacity and thermal conductivity. Finally demonstration of module operation at elevated temperatures up to 400°C had still not materialized, and this was critically important in demonstrating any potential applicability to real PTC plants such as Andasol-1.

Consequently the German government funded ITES, a follow up project aimed at addressing these issues. It involved collaboration between the Institute of Technical Thermodynamics at the German Aerospace Center (DLR), the construction company Ed Züblin AG and the energy company Siemens AG and other partners ^[98].



Figure 2-34: Finished concrete test module developed during the ITES project (without thermal insulation). (Source: ^[98])

For the ITES project a new test module (Figure 2-34) was designed in accordance with operation conditions that would be typical of its integration into a typical PTC plant. The design temperature and pressure were 400°C, and 25 bar respectively with 6 hour cycling conditions using thermal oil HTF. The overall module length was 10 m, while the concrete casting length and cross sectional area were 8.60 m and (1.70 x 1.30) m² respectively [98].

To prevent the permeability problems encountered in the WANDA project, Laing *et al.* (2009) reported that special fibres were added in the concrete mixture to improve permeability [98]. It is not stated however what these fibres were and what impact their inclusion would have on the overall module cost.

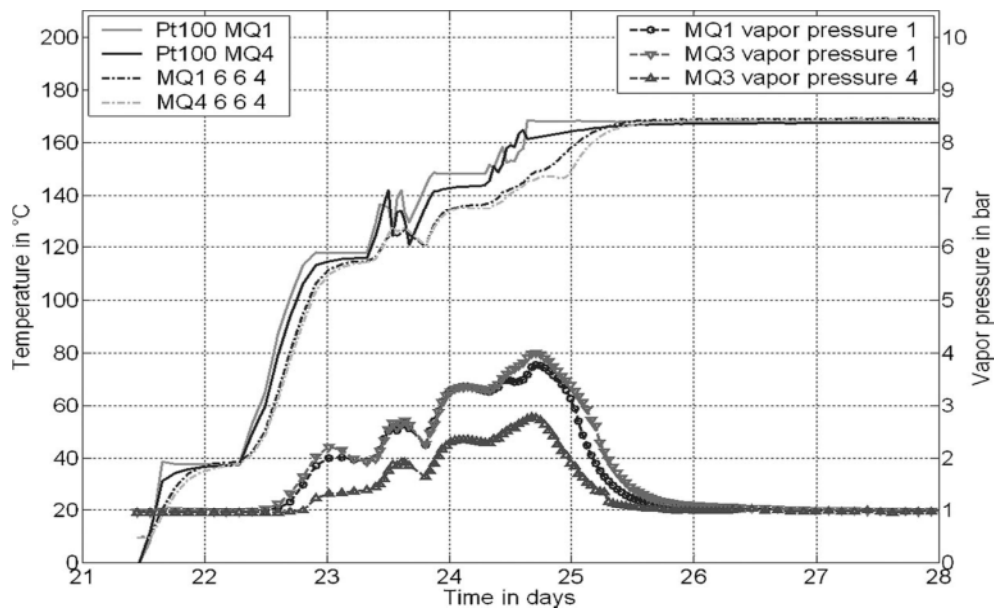


Figure 2-35: Results of initial heating-up period from April 21-28, 2008 with the expulsion of water from the concrete module – temperature of the thermal oil at the inlet/outlet (Pt100 MQ1/Pt100 MQ4) and of concrete in the core of the storage module (MQ1 – 6 6 4, MQ4 – 6 6 4) on the left axis and vapour pressure on the right axis. (Source: [98])

Permeability problems were also linked to the water vapour content of the module. Most of the water content in a new concrete module is expelled during the first heating process, with a corresponding build up

of vapour pressure within the concrete pores. If vapour pressure exceeds a critical value with respect to the tensile properties of the concrete, major damage may occur to the module. Therefore the initial heating of the ITES module from ambient to an operating temperature of 400°C, was closely monitored so as to prevent a dangerous vapour pressure build-up. The temperature was increased in steps, allowing the corresponding increases in vapour pressure to fall off in time before the next temperature step ^[98]. Over a period of seven days, all the water vapour was effectively expelled when an average module temperature of approximately 170°C was reached (Figure 2-35). A little over two weeks later, the module reached the target temperature of 400°C.

From this point, the module was subjected to long charge/discharge (24 h/24 h) cycles (which Laing *et al.* referred as “steady state” since thermal equilibrium was achieved at the end of each step) and also to short “accelerated” charge/discharge cycles (6h/6h) to determine module dynamics. A 40K temperature difference was used in all cycling tests. By the end of November 2008, the module had accumulated about 5 months of operation between 300 and 400°C and completed almost 100 cycles ^[98]. This was an average of about 1 cycle per day.

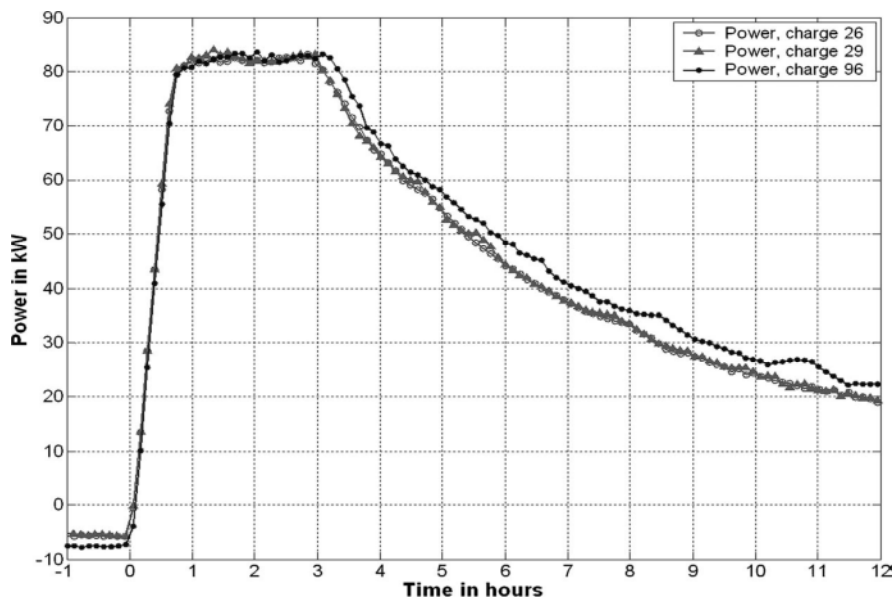


Figure 2-36: Comparison of power measured in reference steady state cycles (24 h charging from a storage temperature of 350°C to 390°C) (Source: ^[98])

Results indicated (Figure 2-36) that after extended cycling in the high temperature range of 350-400°C, (one of the main objectives of the ITES project) there was no discernable degradation in module performance as the charge cycles at both beginning and end were similar. However slightly less power was delivered to the module during charge 96 which Laing *et al.* (2009) attributed to increased heat loss from the module wing to a significantly lower ambient temperature in November. Notably, module storage efficiency was a low 67% which Laing *et al.* attributed to the unfavourable ratio of “*module surface area to volume*” for the small test unit and suggested that this should not be confused with the 90-95 % value expected in a plant scale system with significantly better ratios ^[98].

Overall, the ITES project proved successful as the target goals of the project were largely realized. It served to bolster confidence that with modular construction, a larger scale system could be readily constructed for an Andasol-1 type power plant. For such a plant, a 1100 MWh_{th} storage capacity would be needed, requiring a concrete volume of 50,000 m³. Laing *et al.* (2009) suggested that this could be provided by building 252 of the ITES project storage modules at a system investment cost of €38 million ^[98].

Laing *et al.* (2012) conducted further modelling and experimentation to determine the thermal operating characteristics of the ITES model up to an increased working temperature of 500°C ^[17]. Earlier in the ITES project as has been previously discussed, it was found that initial heating up to temperatures within the 150 -170°C range resulted in concrete mass losses dominated by expulsion of water vapour from the concrete pores. A smaller mass loss, resulting from the ejection of chemically combined water of hydration occurs at more elevated temperatures in the range of 150 - 400°C, representing an average weight loss of 1.1% ^[17]. Further testing by Laing *et al.* (2012) at higher temperatures revealed that there was an additional 0.8 % weight loss in the heating 450 – 500°C range.

Laing *et al.* (2012) finally concluded that mass losses on heating are attributable to loss of (free) evaporable water vapour, dehydration of hardened cement paste and mass losses of the aggregates.

Since the concrete module is mainly comprised of aggregate, it was suggested that mass loss in the 450 – 500°C range was therefore dominated by aggregate mass loss, but an explanation to justify this conclusion was not provided. It was reported that no further mass loss occurred when the temperature was held at 500°C, however it is highly likely that mass losses albeit smaller could continue to occur above 500°C.

It is possible that the observed mass loss is attributable to thermal decomposition of module binder components rather than aggregate which is naturally more thermally resistant. Since the binder material holds the aggregate together, a chemical breakdown in binder would naturally reveal itself as a loss in module strength under compression. This view is supported by the results of compressive strength tests conducted by Laing *et al.* (2012) which showed a loss in material strength with heating ^[17].

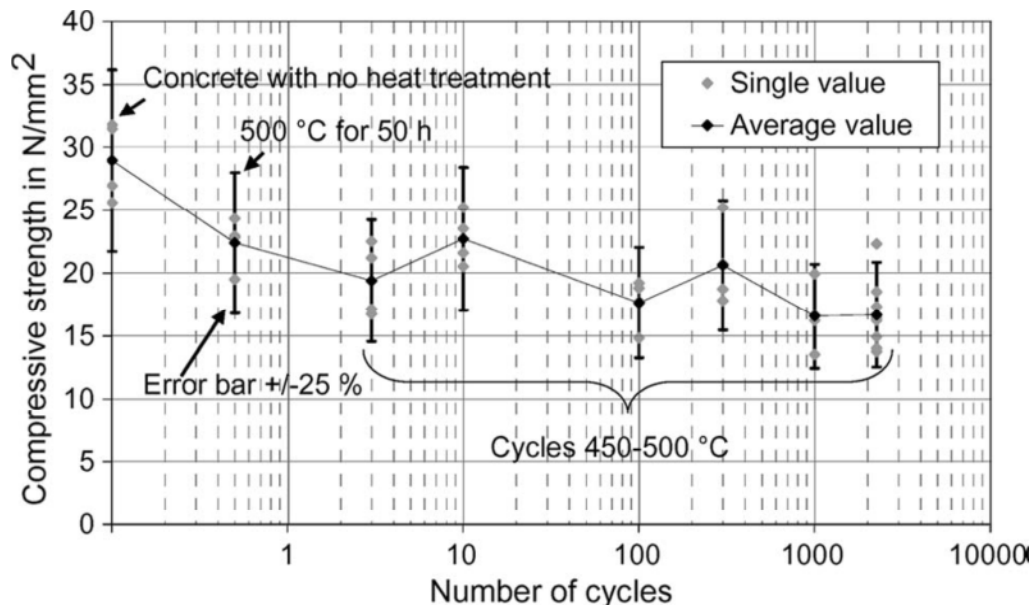


Figure 2-37: Test plot showing compressive strength of HT concrete with heat treatment cycles (Source: ^[17])

Compression test results indicate (Figure 2-37) that the initial strength value of the hardened concrete drops from approximately 29 to 22 N/m² after a 50 hour heat treatment at 500°C with a less significant effect during thermal cycling ^[17]. However if cycling was conducted at 500°C or higher, the module strength value could have continued to fall at or near the initial rate, provided thermally unstable material was still present. Therefore it would have been very interesting to see the effect of thermal cycling even in a small temperature range of at least 10°C, just over 500°C.

Average module energy storage was reported as 1148 kWh, which for the dimensions of the module and the 100K cycle resulted in a specific energy storage value of 0.63 kWh/ (m³K). This translated to a working heat capacity of 1.008 J/gK and compared well with the reference value of 1.05 J/gK at 400°C for N4 concrete ^[17].

One of the most important aims of this study by Laing *et al.* (2012) was to evaluate the annual electricity generation of an Andasol-1 type power plant equipped with a 1100 MWh_{th} concrete storage system, composed of 252 of the basic storage modules (Figure 2-38) as discussed earlier ^[17].

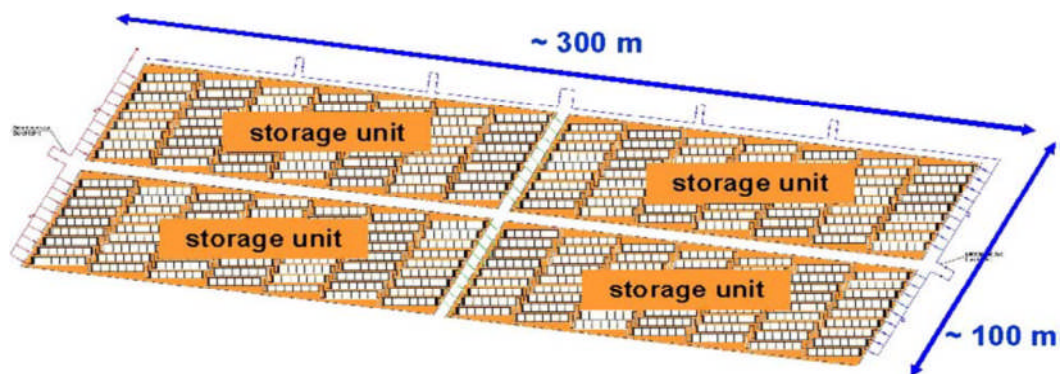


Figure 2-38: Schematic showing setup of 1100 MWh concrete storage using 252 basic storage modules (Source: ^[17]).

Simulations of electricity production for an entire year were performed using the Modelica and Dyloma software packages, with year 2005 weather data for Guadix Spain. Results indicated that over the year the

storage system alone would generate 30% of the total annual electric power. It was also reported that optimal control of mass flows through the storage system could increase energy accumulation by 2.5% and electricity generation by 8.4% [17].

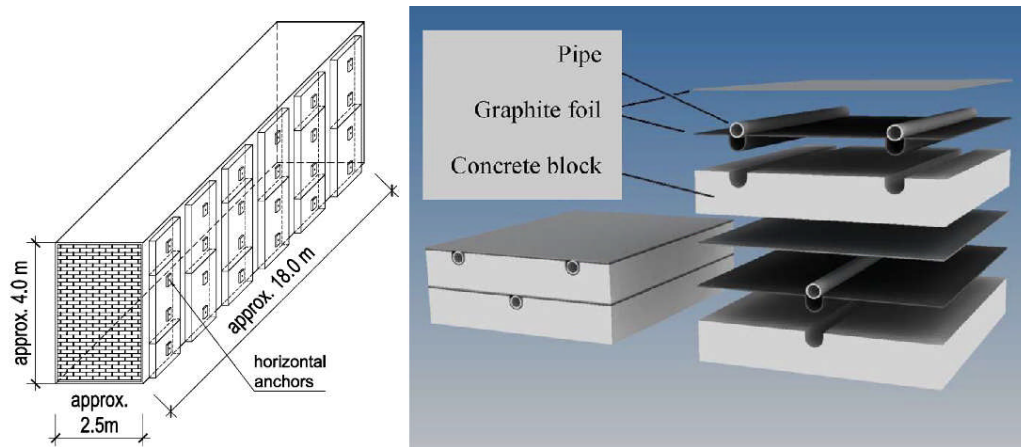


Figure 2-39: Concrete heat transfer enhancements with graphite foil (Source: [17])

Finally Laing *et al.* (2012) designed a new module in an effort to improve the heat transfer characteristics of the ITES module. It was constructed from concrete blocks prefabricated with a pipe channel, high thermally conductive sheeting and tube registers in a stacked arrangement.

The conductive sheeting of graphite or aluminium sheet (Figure 2-39) was formed over the horizontal block surface followed by the laying of the tube registers. Conductive sheets were also placed at the sides of the blocks for adjacent interconnection and anchors were installed to fix the module in position [17]. A 40% reduction in tube quantity was reported due to the heat transfer enhancements of this modification; however there was no discussion of

2.3 Latent Heat Storage

Latent heat storage (LHS) is another promising energy storage option, currently under investigation for CSP power plants. Unlike the sensible heat storage methods described earlier, latent heat storage entails the “*absorption or release*” at “*constant temperature*”, of a material’s “*phase*

transition energy". Such materials are commonly known as "phase change materials" (PCM's).

Energy can be stored nearly isothermally in PCM's as latent heat of fusion (in a solid-liquid transition), latent heat of vaporization (in a liquid-vapour transition) or heat of solid-solid crystalline phase transformation [46]. PCM's offer a higher material energy density compared to sensible heat materials, gained from utilization of their heat of fusion energy. Near iso-thermal operation results in very small charge/discharge stream temperature differences and lower heat losses.

Phase change materials (PCM's) that undergo solid-liquid transitions with latent heat flow are currently the most tested types [28]. It should be noted that PCM storage can also be integrated with the conventional two tank storage system for PTC power plants, providing a reduction in the volume of expensive HTF required.

Some advantages that PCM thermal storage potentially brings to CSP systems are [99-100]:

- A 30% reduction in HTF volume
- A 60% reduction in container size
- A 2-3% improvement in overall system efficiency
- Flexibility to operate with different steam cycles
- Flexibility to store energy when collection temperature is less than the desired high temperature
- Potential to reduce the levelized cost of energy (LCOE) by 6 – 9%

Today PCM systems are widely applied in building construction, cooling systems, solar water heating, waste heat recovery and solar power generation [101]. Sokolov and Keizman (1991) were among the first to suggest the potential use of phase change materials (PCM's) for energy storage application in solar collector systems [102]. Many different types of PCM's are now currently used in industry, but they all fall into one of

three main groupings (Figure 2-40): organic, inorganic or a combination of both.

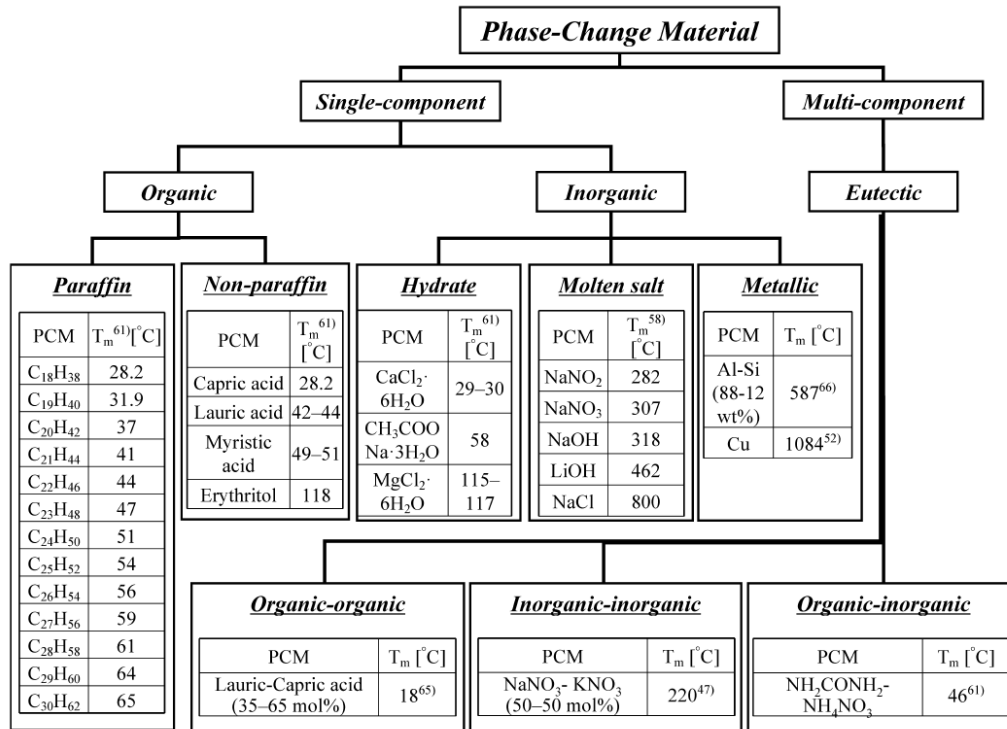


Figure 2-40: Schematic showing various PCM categories (source: [101])

Recent advances in PCM technology have also attracted significant interest in recent years, especially since 2005 [101]. This has been especially influenced by the unprecedented global growth in solar thermal systems deployment and its associated requirement for appropriate thermal energy storage. Most of this research has been targeted at PCM stores for water heating systems operating in the 20 – 60°C temperature range. However since 2006, there has been a significant increase in research for higher temperature PCM systems signifying some shift in focus from residential to industrial applications [101]. Detailed reviews of PCM development and applications can be obtained from recent works by Zalba *et al.* (2002), Sharma *et al.* (2007), Nomura *et al.* (2010), and Liu *et al.* (2012) [15, 101,103,180].

2.3.1.1 Solid-Solid and Solid-Liquid type PCM's

In solid-solid PCM's (Figure 2-41), heat is stored or released when a solid crystal makes a transition from one crystalline structure to another [103]. Consequently the PCM encapsulation, required for leakage containment in solid-liquid PCM's is not required for this type of PCM.

Solid-solid PCM's therefore offer the potential to reduce material costs and recover the volumetric capacity lost to encapsulation. They also exhibit very small volumetric changes during transition, which is desirable from a system design perspective, but their energy storage capacity is typically one order of magnitude lower than that of solid-liquid PCM's [101].

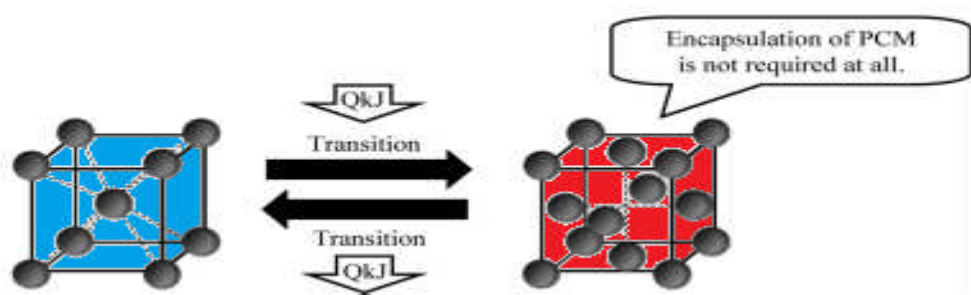


Figure 2-41: Comparison between SLPCM's and SSPCM's (Adapted: [101])

Solid-liquid PCM's (Figure 2-42) on the other hand, physically change between solid and liquid states whenever they absorb or release latent heat of fusion energy. Therefore encapsulation of the PCM is necessary to avoid leakage during solid to liquid transitions. Despite the current research interest, the concept of encapsulation itself is not new, as Lane (1986) explored the pros and cons of potential encapsulation materials, their geometries, and potential PCM compatibilities over two decades ago [104].

Regin *et al.* (2009) recommended that containment mechanisms should: (a) meet the requirements of strength and flexibility (b) act as a barrier to protect the PCM from harmful interactions with the process environment (c) provide adequate heat transfer and (d) provide structural stability and easy handling [105].

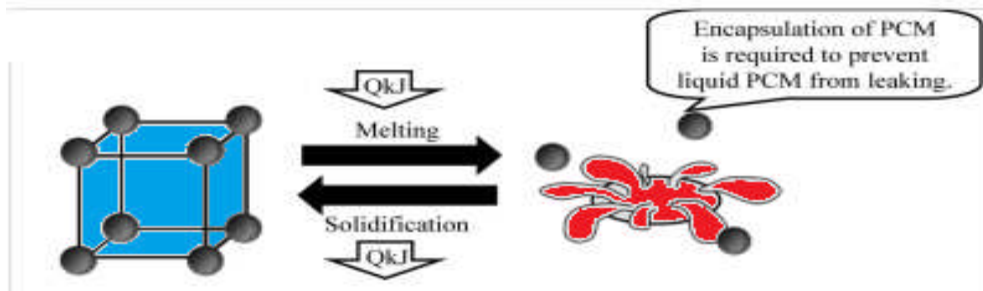


Figure 2-42: Schematic illustrating solid-liquid phase change in a solid crystal (Adapted:^[101])

PCM encapsulation (Figure 2-43) is the process of containing the solid form of a PCM (usually spherical), within a protective capsule shell. This makes it possible to reduce the average distance for heat transfer within the particles of the bulk storage material ^[106]. Ideally, the protective shell only allows heat transfer, protects the PCM by inhibiting all harmful interactions with the process environment and contains the PCM during liquefaction. Two types of PCM capsules currently exist: macrocapsules and microcapsules. Macrocapsules are encapsulated PCM solid spheres, typically 3-5 mm in diameter, whereas microcapsules are substantially smaller spheres of 15-25 microns ^[107].

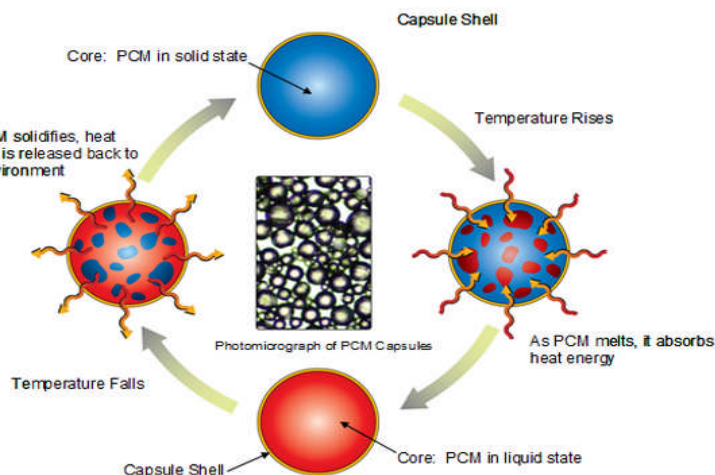


Figure 2-43: Cyclic illustration of an encapsulated PCM undergoing phase change. (Source:^[107])

Macro-encapsulation of solid-liquid PCM's is the more conventional of the two methods ^[77]. Various capsule shell materials have been

reported in literature. These include metals and plastics, formed into cylindrical or spherical shapes ^[101]. Matthur (2009 and 2011) reported on a new encapsulation method (figure 44) developed by the technology consulting company Terrafore, MN, USA and based on the use of a sacrificial polymer ^[99-100].

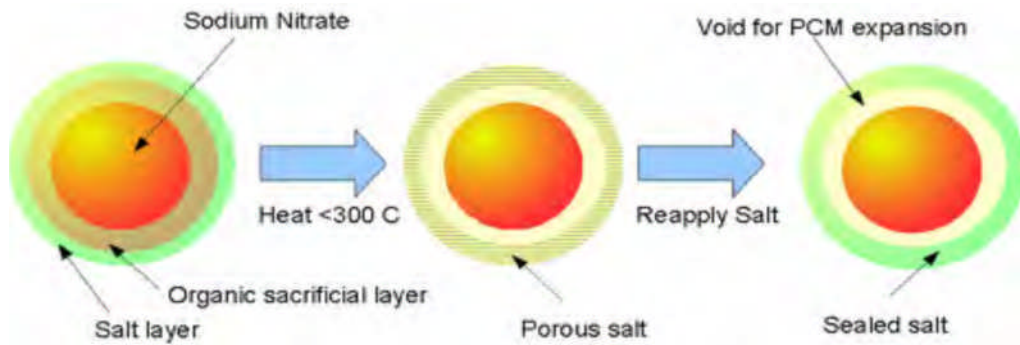


Figure 2-44: PCM encapsulation using sacrificial polymer (Source: Terrafore, USA, ^[77])

In the last decade however, significant interest has been generated in the potential of solid-liquid PCM microcapsules, which based upon their increased surface area, may reduce unwanted reactivity between the PCM and process, increase PCM heat transfer properties and better manage frequent volumetric changes ^[101].

Despite the need for encapsulation, which is an added system cost, solid-liquid PCM storage systems are still the most widely deployed PCM type. This is due to the fact that they possess greater latent energy capacity than solid-solid types and do not undergo the huge volumetric changes associated with the phase transitions of solid-gas PCM's. They also adapt easily to most process design applications and despite their encapsulation requirements, are generally low cost, ^[101, 103].

To address the inherent low thermal conductivity problems of most PCM's ($\lambda_{\text{typical}} < 0.5\text{ W/mK}$) ^[9,101], materials known as "PCM composites" are now being developed. PCM composites describe specially engineered and highly conductive solid structures, which contain porous cavities filled with PCM material (Figure 2-45).

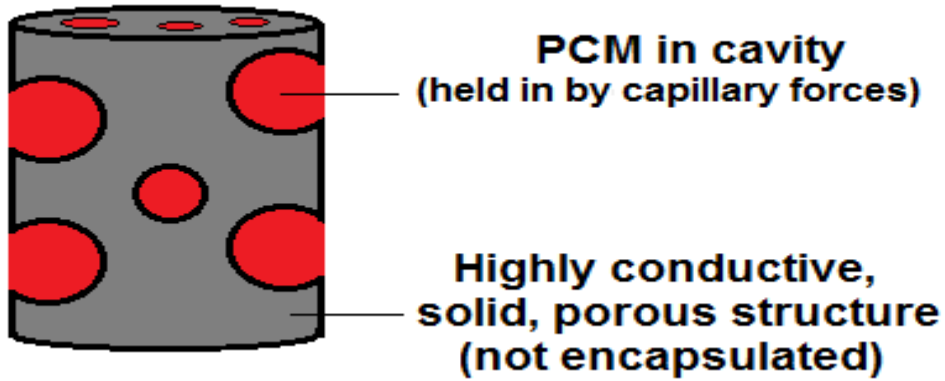


Figure 2-45: Schematic illustration of a PCM composite.

PCM contained in these cavities does not leak during phase change due to capillary action within the porous structure. Consequently, these structures do not need encapsulation, and provide the added benefit of high thermal conductivity relative to other PCM types. A detailed list of recently developed PCM composites and their applications has been compiled in the work of Nomura *et al.* (2010) ^[101].

2.3.1.2 A review of PCM Storage for CSP Power Plants

The foundation for the current research in PCM storage for CSP applications goes back to the 1980's and 90's. Due to the large scope of this review and space constraints it is not possible elaborate on all the work in this period. However, a brief overview of current PCM research specifically applied in CSP systems, and therefore work cited since the year 2000 provides a good background from which to begin. We now begin with the work of Hoshi *et al.* (2005).

Hoshi *et al.* (2005) numerically modelled and analyzed the operating parameters, charge/discharge characteristics, of various high temperature PCM's for use in Compact Linear Fresnel Reflector (CLFR) and Multi-Tower Solar Array (MTSA solar) power plants. The results of this study revealed five important points:

- (a) Molten salts with melting points within the 500 – 1300 K range showed good potential for use in high temperature latent heat thermal energy systems (LHTES).
- (b) The thermal conductivity of the PCM would be a critical factor in high temperature LHTES and that some materials (eg. Na_2CO_3) with high melting points also possess high thermal conductivities.
- (c) Large CLFR plants with low pressure turbines could successfully integrate with a LHTES system by using low cost PCM salts such as NaNO_2 .
- (d) Zinc (Zn) could be used as a cost effective PCM for PTC systems using high boiler temperatures (up to 700 K).
- (e) Implementation of LHTES systems into CSP power plants would require resolution of numerous design issues in relation to thermal conductivity, vessel corrosion and vessel integrity with regards to PCM freezing.

Bauer (2006) reported on work at the Institute of Technical Thermodynamics, DLR in developing high temperature PCM composites of graphite and alkali nitrate salts for use in high temperature CSP storage systems ^[108]. These composites were manufactured by infiltration/impregnation of PCM within a porous graphite structure, dispersion of graphite mechanically within the PCM, or by compressing together pre-mixed graphite and PCM materials.

Results indicated that the effective thermal conductivity of the dispersion composites is dictated by the thermal conductivity of the graphite structure, with little influence from the changes in the PCM properties. However, with regards to compressed composites, thermal conductivity was found to be influenced by the melting/solidification cycles of operation. Overall, compression was reported to be significantly more effective for heat transfer enhancement, than dispersion, with the added benefit of being moulded into any shape ^[10].

In an attempt to resolve the thermal conductivity, heat transfer and corrosion problems identified earlier by Hoshi *et al.* (2005) and to

achieve actual deployment of LHTES systems in CSP plants, the DISTOR (Energy Storage for Direct Steam Solar Power Plants) project [9] funded by the EC Sixth Framework Programme, began in February 2004. This project ran until September 2007 and was instrumental in the development of promising PCM storage concepts for CSP energy storage applications.

DISTOR's primary project objective was the development of high temperature phase change materials (PCM's) for energy storage in direct steam generation (DSG) power plants operating at saturation temperatures of 235 – 310°C and operating pressures of 30 - 100 bar [9, 109]

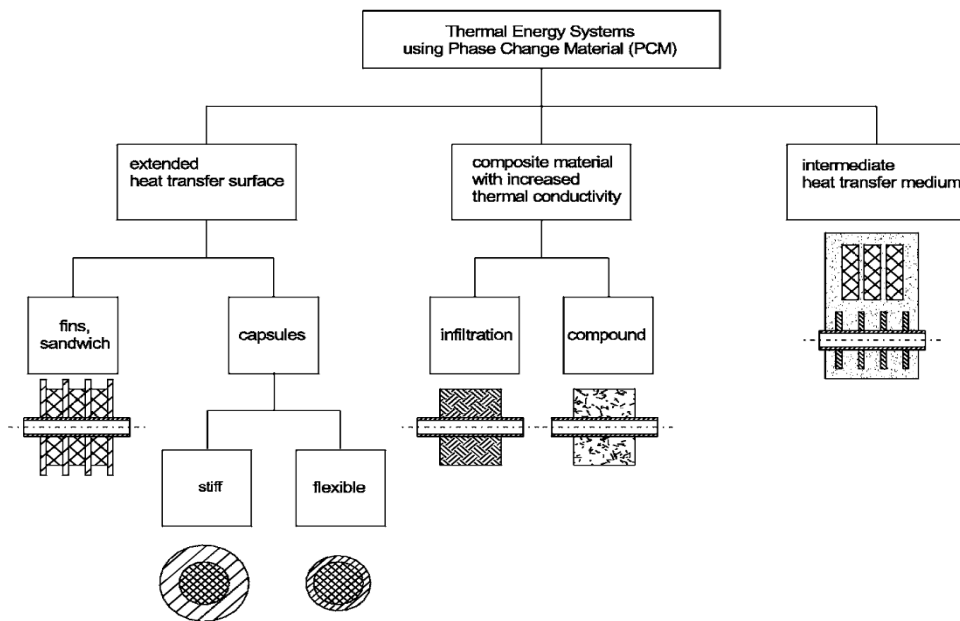


Figure 2-46: Chart of PCM storage concepts investigated in the DISTOR project, February 2004 – September 2007. (Source: [9])

Thirteen research based institutions from five countries under the leadership of the Institute for Technical Thermodynamics, German Aerospace Institute (DLR), conducted parallel research in various conceptual areas for PCM innovation (Figure 2-46). It was organized into three phases:

- (a) Fundamentals: PCM identification, characterization and development
- (b) Laboratory scale testing of the four most promising PCM's in the 5 – 10 kW power range.
- (c) Selection of the best PCM technology for testing under actual working conditions at the DISS test facility at Plataforma Solar de Almeria, Spain.

Steinmann and Tamme (2008) who were key researchers in DISTOR, modelled and analyzed the theoretical performance of PCM energy storage required for the isothermal steam production requirements of DSG (direct steam generation) power plants. The layout for this investigation (Figure 2-47) consisted of a solar field charging cycle and a power block discharging cycle coupled by a cascaded block of PCM stores operating at preheating, evaporating and superheating cycle temperatures.

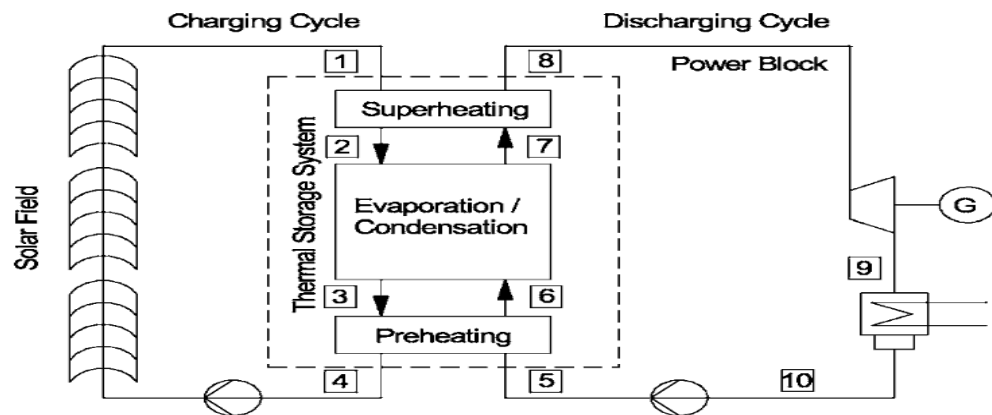


Figure 2-47: Steinmann and Tamme (2008): Integration of PCM store into PTC plant (Source: [9])

For a PCM store consisting of parallel tubes running through a tank filled with PCM material, Steinmann and Tamme reported that the required number of tubes in such a store would be significantly reduced (Figure 2-48) if average thermal conductivity within the store could be increased just one order of magnitude (from 0.5 – 5 W/mK) [9].

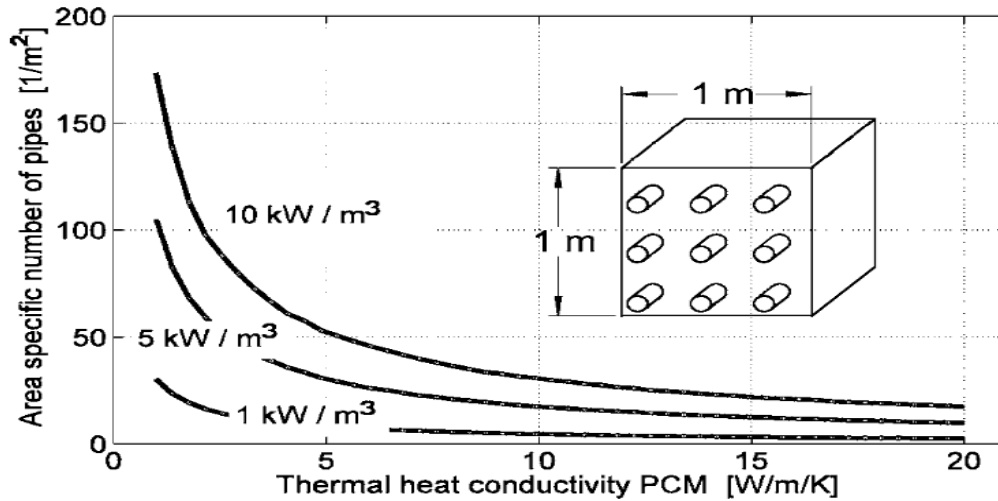


Figure 2-48: The effect of thermal conductivity on the number of tubes required in PCM storages that use parallel tube heat exchangers, for three levels of specific volume thermal power during charge/discharge (Source: [9])

Finally, Steinmann and Tamme (2008) provided an overview of the outcomes from DISTOR-Phase 1, identifying concepts for further investigation (illustrated in the images that now follow).

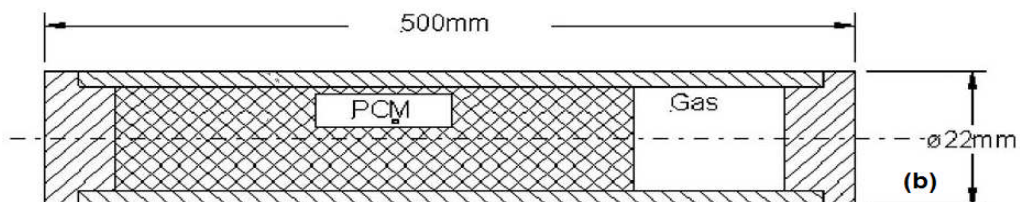
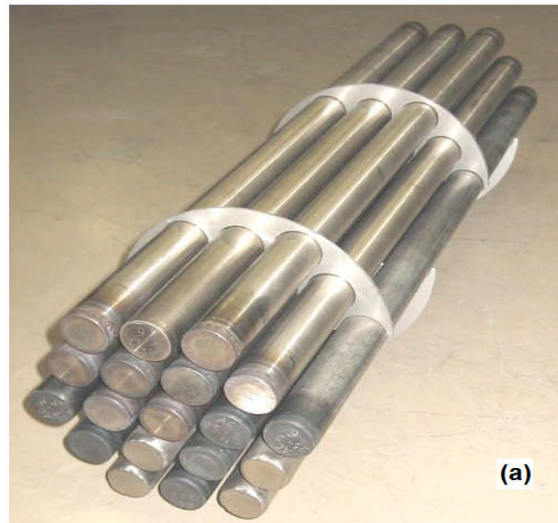


Figure 2-49: Images of (a) finished macrocapsules (b) cross section through a capsule tested in DISTOR (Source: [106])



Figure 2-50: Cold compressed PCM-graphite composite, NaNO₃/KNO₃ eutectic showing drilled holes for heat exchanger tubes (Source: ^[110])

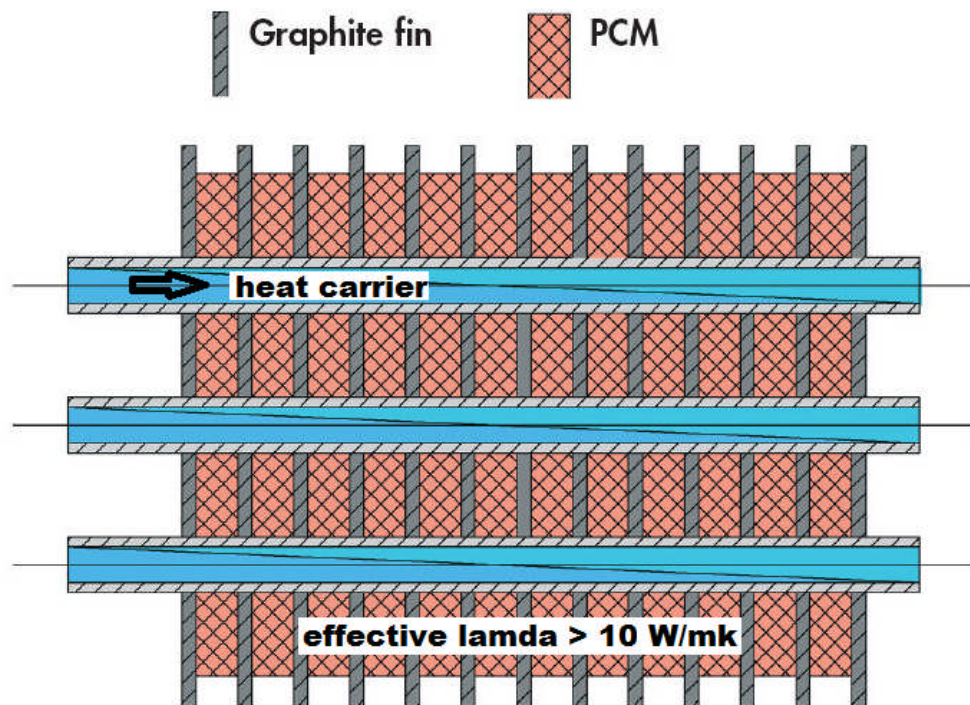


Figure 2-51: PCM sandwich concept with integrated PCM and fins (Source: ^[77])

As part of the DISTOR project, Morrison *et al.* (2008) also conducted practical investigations in LHTEs for DSG applications.

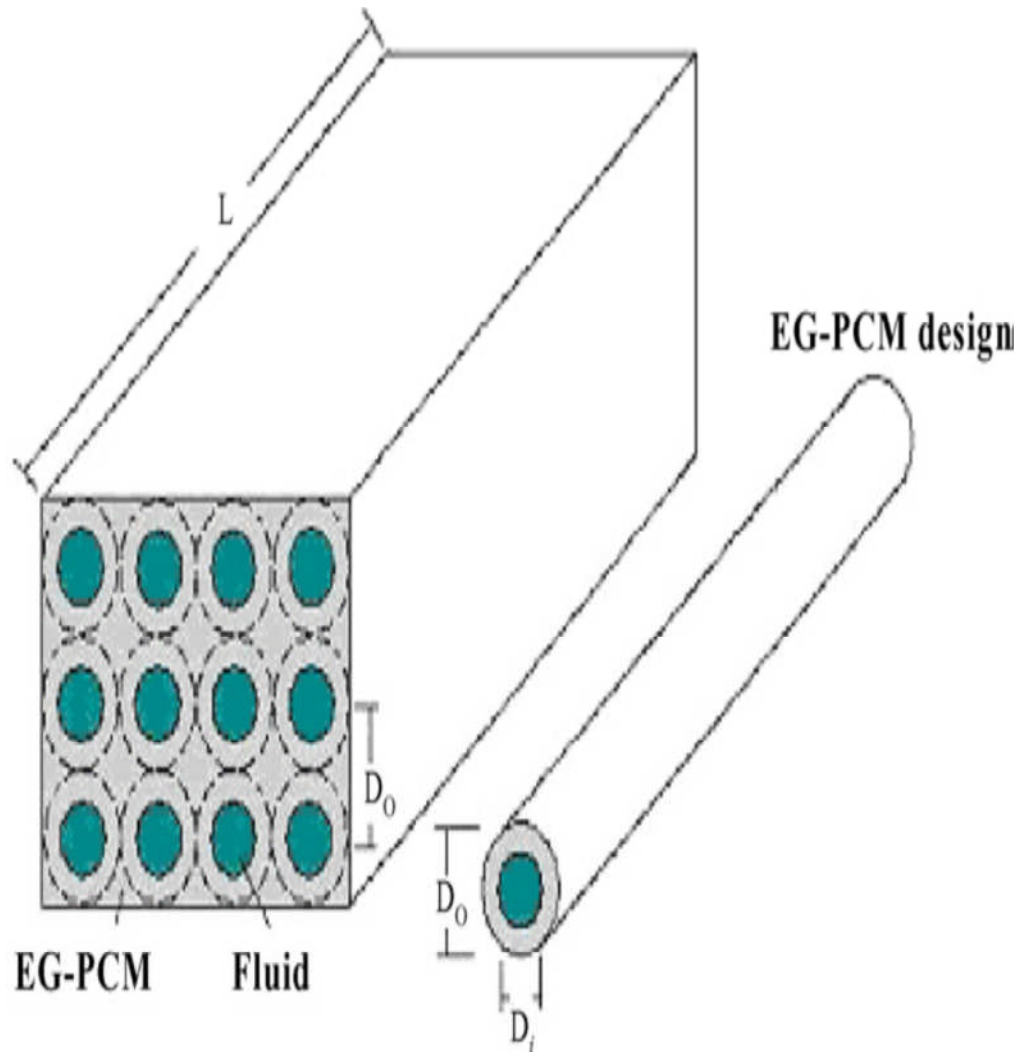


Figure 2-52: Configuration of PCM composite storage modelled by Morrison *et al.* (2008) (Source: [111])

Of the concepts identified for investigation, the four promising ones chosen for laboratory testing under the next project phase (DISTOR-Phase 2) were as follows:

- (a) Macro-encapsulated PCM's (Figure 2-49)
- (b) Graphite PCM composites (Figure 2-50)
- (c) PCM's integrated with graphite foil fins (Figure 2-51)

(d) PCM's with an intermediate heat transfer medium, where both PCM and heat exchanger are housed in a container filled with intermediate liquid or gaseous medium of heat transfer.

A detailed heat transfer and fluid flow model for analyzing the performance of a new PCM composite storage (Figure 2-52) unit made from graphite and nitrate salts was presented. The PCM composite consisted of naturally expanded graphite matrix (CEG) made by cold compression of graphite powder with binary eutectic $\text{KNO}_3/\text{NaNO}_3$ in a cubic mould, since infiltration of the graphite by the salt is not possible [106, 111].

One main objective in the engineering of these new composites was to increase the thermal conductivity of the PCM. Results (Table 2-7) indicated that composites containing a small percentage of graphite (less than 8%) had significantly improved thermal conductivities (250% increase, axial) with only a relatively small decrease in the overall heat storage capacity (7.4%) [111].

Table 2-7: Effect of graphite content on PCM composite thermal properties (Source: [111])

Material	Pure Salt	CEG salt composite (3.96% mass graphite)	CEG salt composite (5.27% mass graphite)	CEG salt composite (7.35% mass graphite)
Axial thermal conductivity (W/mK)	0.8	1.6	2.6	2.8
Radial thermal conductivity (W/mK)	0.8	4.1	5.65	8.2
Apparent latent heat of fusion (J/kg)	94250	90500	89300	87300
Apparent density of CEG (kg/m^3)	-	75	100	140

This was found to result in increased charge/discharge rates, along with increased unit power and steam production rates. It was also found that

using the new graphite PCM composite in a storage system allowed a reduction in the overall lengths of steel tubes in the storage unit, thereby reducing system costs^[111].

Table 2-8: Thermal properties of PCM composites, Pincemin *et al.* (2008) (Source: ^[110])

Material	$T_m(^{\circ}C)$	$L(kJ/kg)$	$\rho(kg/m^3)$	$\lambda@40^{\circ}C(W/mK)$
(PLAIN EUTETIC SALT) Na/K/NO3 E (Laboratory grade)	216	105	1920	1.1
(PLAIN EUTETIC SALT) Na/K/NO3 E (Industrial grade)	222	112	1920	0.56
(PCM-SALT COMPOSITE 3) Na/K/NO3 E (Industrial grade+10% GFG)	210	80	1923	11.7
(PCM-SALT COMPOSITE 2) Na/K/NO3 E (Industrial grade+20% GFG)	223	67.6	1955	40
(PCM-SALT COMPOSITE 3) Na/K/NO3 E (Industrial grade+30% GFG)	220	42.5	1989	51.5

Pinceman *et al.* (2008) also working in DISTOR project, investigated PCM composites made of eutectic mixtures of $NaNO_3/KNO_3$ and prepared using the methods of dispersion, impregnation and cold compression. Test results (Table 2-8) also showed a thermal conductivity enhancement using the graphite PCM composites^[110].

A composite of 10% grounded expanded graphite powder (GFG) resulted in a thermal conductivity increase of over 2000%, with only a 29% reduction in heat capacity. Larger graphite compositions also continued to increase thermal conductivity, but at a significantly reduced rate, while considerably reducing the composite's thermal capacity. An optimization study would have been useful in accessing the most cost effective graphite percentage composition of the PCM.

One of the PCM integration concepts that showed good potential during the DISTOR project was the “sandwich” concept (Figure 2-51).

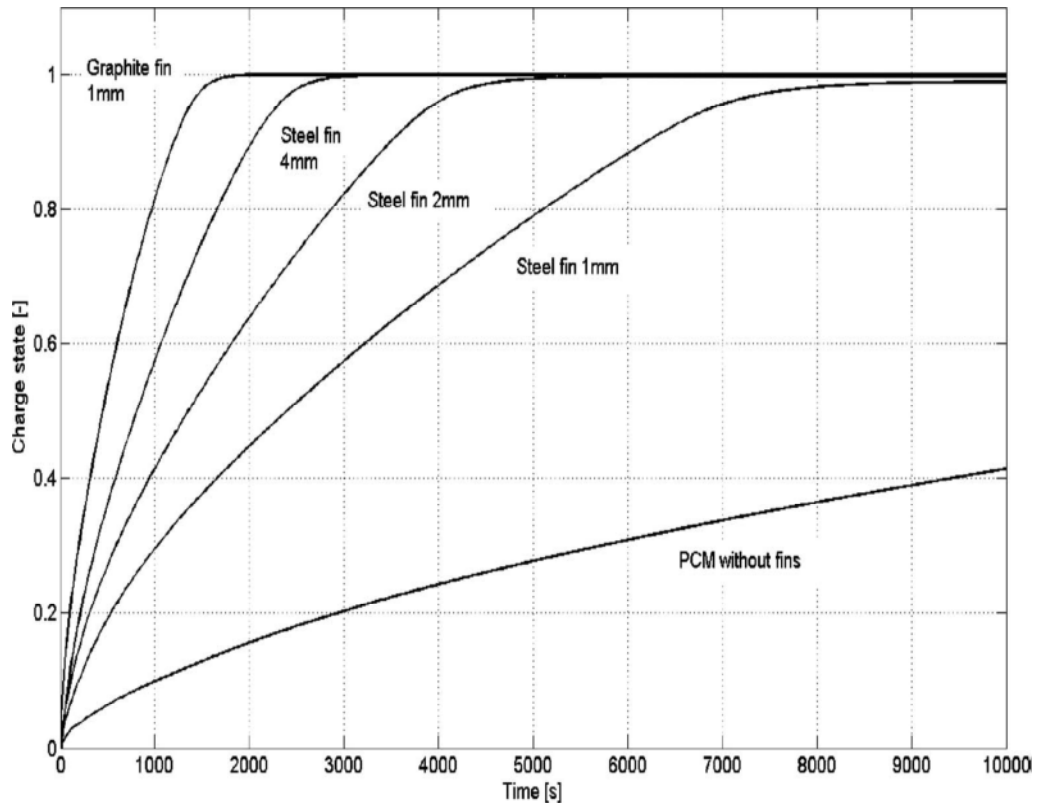


Figure 2-53: Charge time for a test store with various fin materials and thickness (Source: [106])

Steinmann *et al.* (2010) who had investigated this concept reported the test results of three such storage units ranging from power levels of 2 – 100 kW and operating at melting temperatures of 145 – 225°C.

Firstly, the model results of Steinmann *et al.* (2010) indicated that heat transfer fins of the sandwich concept significantly increased the heat transfer rates. With no fins, after 10,000 s, only 40% of the PCM store was charged (Figure 2-53). With the addition of steel fins, there was a significant improvement. Graphite fins were found to be the best option for sandwich systems since they cost less, have higher thermal conductivity and also provide good corrosion resistance to nitrate salts. However, since graphite was only found to be stable with nitrates at temperatures below 250°C, metallic fins were recommended for higher operating temperatures [106].

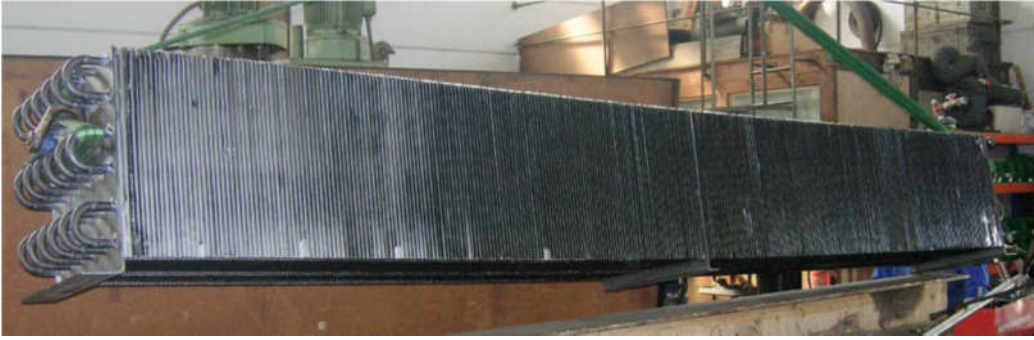


Figure 2-54: Photograph of sandwich PCM storage module tested at DLR (Source: ^[106])

A DISTOR experimental sandwich test module (Figure 2-54), constructed in a similar manner with 1 mm graphite fins and $\text{KNO}_3/\text{NaNO}_3$ eutetic PCM was tested in a DSG loop at the Plataforma Solar de Almeria test facility by CIEMAT. This test proved the feasibility of the sandwich concept at higher power levels of up to 150 kW

Complementary investigations into the sandwich concept had also been done by Guo *et al.* (2008). Numerical simulations and parametric analysis of DSG using sandwich PCM structures distributed with aluminium foils for heat transfer enhancement indicated that the discharging process is significantly accelerated by adding aluminium foils ^[158]. Simulations indicated that the total discharge time for the aluminium sandwich PCM was only 1756 s in contrast to 504 s for a PCM control test without enhancement. It was also shown that heat transfer and discharge times are affected by changes in geometry of the aluminium foil, thermal conductivity of the PCM, tube radius and boundary conditions of the storage module.

Kenisarin (2010) in his comprehensive review of PCM's operating the 120 – 100°C operating range confirmed the benefits of the enhancement mechanisms so far discussed ^[112]. He however stated the potential of using the latent heat of fusion energy in metallic alloys of iron, nickel, zirconium and titanium for energy storage could be promising and needs further investigation. This is due to the fact that although metal alloys have lower energy densities, they do not suffer

the problems of low conductivity, corrosion and volumetric change typical of eutectic salts [112].

Laing *et al.* (2012) conducted material investigations of NaNO₃ based PCM's operating at a transition temperature of 306°C. The thermal stability of these PCM's was experimentally investigated by kinetic and long duration testing, in regards to thermal decomposition to nitrites.

Though some nitrite formation occurred during testing, the level was insignificant and did not practically affect the performance of the PCM storage system. Further testing in this regard however, would be useful in further exploring the effect of thermal cycle lengths and nitrate concentrations on the level of decomposition to nitrites.

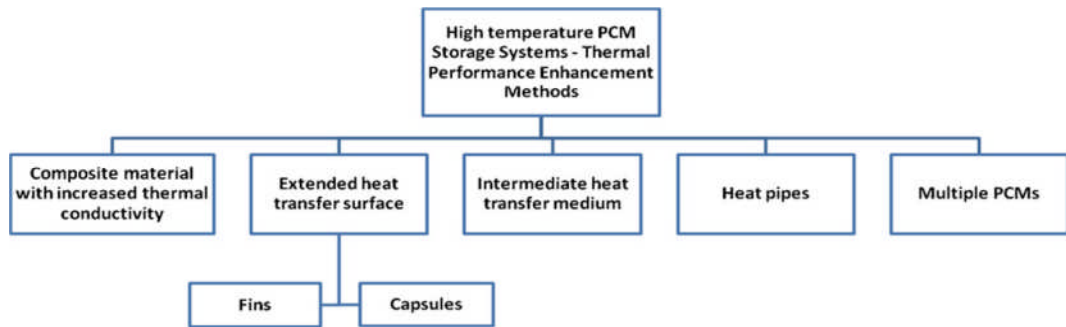


Figure 2-55: Chart showing various methods to enhance PCM performance (Source: [10])

Thus far all the literature presented has focused on performance enhancement mechanisms for PCM materials (Figure 2-55). However, enhancements pertaining to the layout of the PCM storage system or process can also prove beneficial.

One way of achieving higher PCM utilization and higher exergetic efficiency in tank based storage systems is to break the tank's temperature gradient into ranges that can be assigned to a cascade of smaller PCM tanks. This concept was numerically modelled in the work of Michels and Pitz-Paal (2007) who investigated the performance enhancement of "Cascaded Latent Heat Systems (CLHS)" (Figure 2-56) [11], using earlier recommendations from the works of

Haslett *et al.* (1978), Steiner *et al.* (1982) and Dinter *et al.* (1991) [113-115].

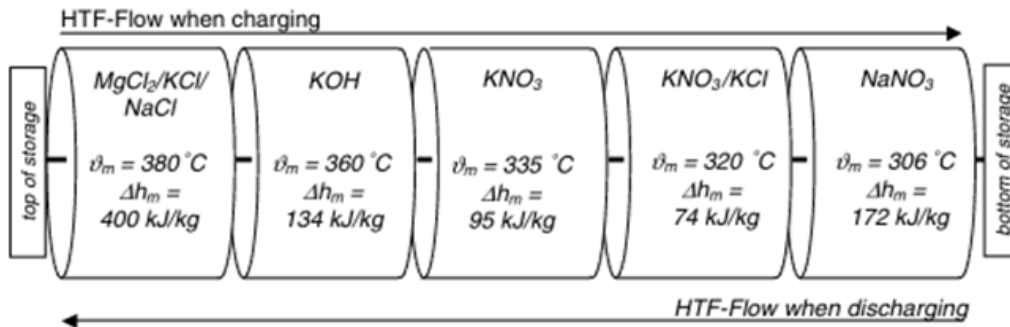


Figure 2-56: Schematic illustration of cascade of 5 PCM units (Source: [11])

Simulations suggested that with a CLHS system, a storage capacity of 875 MWh_{th} could be achieved by using only 22,000 tonne of salt compared to 26,000 in an uncascaded store. However this finding was predicated on the supposition that the PCM's thermal conductivity was equal to 2 W/mK.

As stated earlier in this review, standard eutectic nitrate salt PCM mixtures have thermal conductivities in the region of 0.5 W/mk, which therefore means that some heat transfer enhancement of the PCM would be first required for the cascaded system. Though a material reduction of 4000 tonne is meaningful, a more credible analysis would also include the additional material cost involved in implementing the cascade and also the related thermal conductivity enhancement that would be required in the system.

This now concludes the chapter section on latent heat storage. Although this review was by no means exhaustive, it will have provided the reader a fairly good overview of the current and relevant research topics with regards to PCM storage applications for CSP power generation.

2.4 Thermo-chemical Energy Storage

The final storage method to be discussed and which is also currently being explored for CSP applications is thermochemical energy storage. It involves the utilization of heat from reversible chemical reactions (Figure 2-57) for heating or cooling a HTF directly or indirectly through a heat exchanger, to produce steam for power generation. The direction of the chemical reaction (which determines whether the store is charged or discharged) is adjusted, controlled or catalyzed in order to achieve a target charge/discharge rate. This form of energy storage has the potential to provide higher energy densities than standard sensible heat storages (eg. molten salt tanks), because energy is stored in the chemical bonds of a substance rather than in sensible form. It also has the potential for application over a wide temperature range (50 – 1000°C), providing loss-free transportation of energy that is locked in chemical bonds.

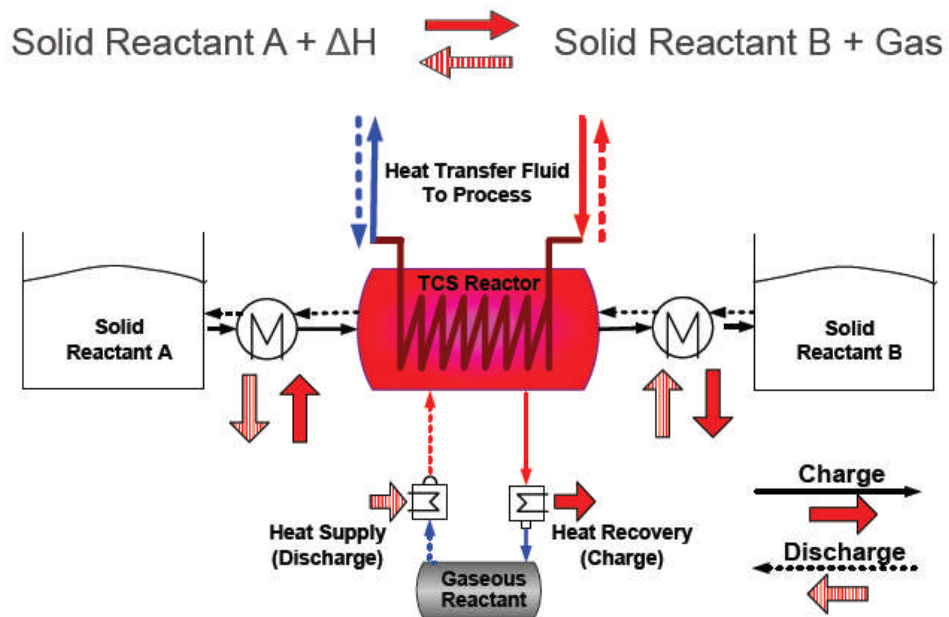


Figure 2-57: Schematic illustrating a thermo-chemical energy store system (Source: ^[77])

Despite this fact however, thermo-chemical energy storage faces some challenges causing it to be the least mature of the energy storage options available to CSP systems. This is largely due to the fact that

with respect to the state of the art, it is a much more technical storage process, comparatively harder to implement, operate and control.

Current challenges are related to: (a) reaction system stability, equilibrium and kinetics (b) process design heat transfer, parasitics, reactor operation and control (c) process integration with CSP technology and modes of operation ^[77]. With economics also an issue, significant research and development will be required to make this technology competitive with state of the art molten salt tank storage.

Research work in this area is currently focused in the following areas:

- (a) Thermal decomposition of ammonia, metal hydroxides, carbonates, hydrides and sulphates
- (b) Methane reforming for solar enhancement of natural gas
- (c) Hydrogen production
- (d) Solar fuel production using metal oxide cycles involving zinc, tin, cerium, iron oxides and mixed metal ferrites
- (e) Redox reactions with metal oxides

2.4.1 Ammonia based Thermo-chemical Storage Systems

Ammonia based thermo-chemical storage systems are based on the reversible dissociation of ammonia, given by the following chemical reaction.



The process involves the passage of a fixed quantity of ammonia between energy storing (solar dissociation) and energy releasing (synthesis) reactors, which are both catalyzed ^[77]. At 300 K and 20 MPa the specific energy of the reaction is 1.09 kWh per kg of ammonia. When coupled to a steam power cycle, the energy content of the reaction is large enough to produce base load power to the grid.

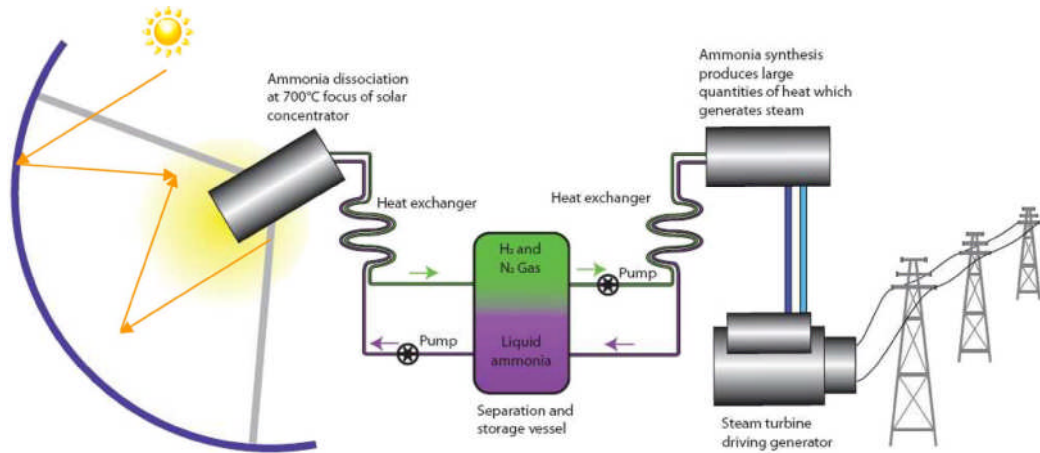


Figure 2-58: Schematic of solar driven ammonia dissociation process (Source: [77])

In a typical system (Figure 2-57) a two-axis tracking paraboloidal dish focuses solar radiation onto a cavity receiver/reactor through which anhydrous ammonia circulates over a catalyzed bed. In the presence of the concentrated solar energy and the catalyst, the ammonia dissociates into gaseous hydrogen and nitrogen. The gases are stored for later use in a standard Haber-Bosch ammonia synthesis reactor to release heat for power generation, thus recovering the dissociated ammonia [77]. The most current research work in these areas since the year 2000, will now be examined.

2.4.2 Research in Ammonia Storage Systems for CSP

The ammonia based energy storage concept for CSP applications was first proposed by P. Carden in 1974 at the Australian National University (ANU), with an initial assessment of the theoretical limits of thermal efficiency and useful work [116-117]. It was established in this work, that the process had a maximum conversion efficiency limit of 54% at 30 MPa. Parallel investigations were also carried out in the late 1970's by researchers at the Colorado State University, Fort Collins that involved system design, receiver design, and research into nickel-on ammonia catalysts [118].

Following this initial work, the period of the 1990's saw significant research work by K. Lovegrove who began to lead research in this area at the Australian National University (ANU) ^[119]. Publications involved analysis of work recovery, investigation of reactor designs and exergetic efficiency. A “pseudo-homogeneous” packed bed reactor numerical model was largely used in these investigations ^[120-129], which Lovegrove and fellow researchers calibrated using a 1 kW_{chem} electrically heated dissociation reactor at ANU.

The model was then used to successfully predict various outputs such as system temperature profiles and mass flows ^[119]. One of the main conclusions drawn from the works of Lovegrove *et al.*, was the possibility of these systems to achieve exergetic efficiencies of up to 71% and overall solar to electric conversion efficiencies of 20% ^[119].

Solar paraboloidal dishes have been identified as the most ideal CSP technology for providing homogeneous heating of the ammonia reactor. A 20 m² dish system was installed at ANU which together with a 400 m² prototype (Figure 2-59) installed in 1994, provided experimental data for much of the work done by Lovegrove *et al.* over the past two decades.



Figure 2-59: Photograph of 400 m² thermochemical ammonia dissociation dish system at ANU (Source: ^[130])

Dunn *et al.* (2012) also of ANU, completed a recent review of these systems ^[119]. One of the points raised in this work was the fact that it is still yet to be conclusively established whether ammonia based storage systems are economically competitive with the state of the art storage systems. Also reported was the fact that though these systems are capable of even 24 h base load operation, they do not handle power ramping requirements well, due to the power response limitations of the chemical reactions in the process ^[119].

It is highly unlikely that these systems will become competitive with the state of art, at least not in the short term, primarily due to the significant cost incurred in designing pressurized reactors and the ramping power limitations of the process. However, with larger energy densities compared to sensible heat storages, future innovations to reduce system installation and operating costs, and ramping power limitations could one day make this system competitive with state of the art storage.

2.4.3 Research in Gas-Solid Storage Systems for CSP

Thermal energy storage by reversible gas-solid reactions also has the potential of achieving high storage densities and of being adjusted to various CSP plant configurations ^[131]. Calcium hydroxide/ calcium oxide [Ca(OH)₂/CaO] reaction systems have been explored as one option for future research and development. The chemical reaction for this process is given as:



Storage densities above 300 kWh per m³ are reported to be achievable, when operating within a temperature range between 400 and 600°C. Storage systems may directly produce steam for the required power cycle or indirectly by heat exchanger.

Schaube *et al.* (2011) developed a one dimensional finite element model of this system using direct heat transfer to the power cycle ^[131].

The objective of this investigation was to classify the parameters that limit the reactor discharge process. Limiting factors that were investigated included solid-gas heat transfer, the heat capacity of mass flows in the reactor, particle size and reaction. Results indicated that for the theoretical 1 MW/10 MWh reactor unit, the energetic losses due to pressure drop are less than 10%. It was also found that at higher power levels up to 100 MW/1 GWh storage, larger particle diameters up to 40 mm are required.

2.4.4 Solar Energy Storage by Fuel Production (H₂, Syngas)

Solar energy storage through fuel production (hydrogen, syngas) is another storage pathway that has been investigated over the last two decades ^[132]. There are three possible routes (Figure 2-60) that can be taken: (a) water splitting by thermolysis or thermochemical cycles (b) electrolysis and (c) decarbonisation of fossil fuels.

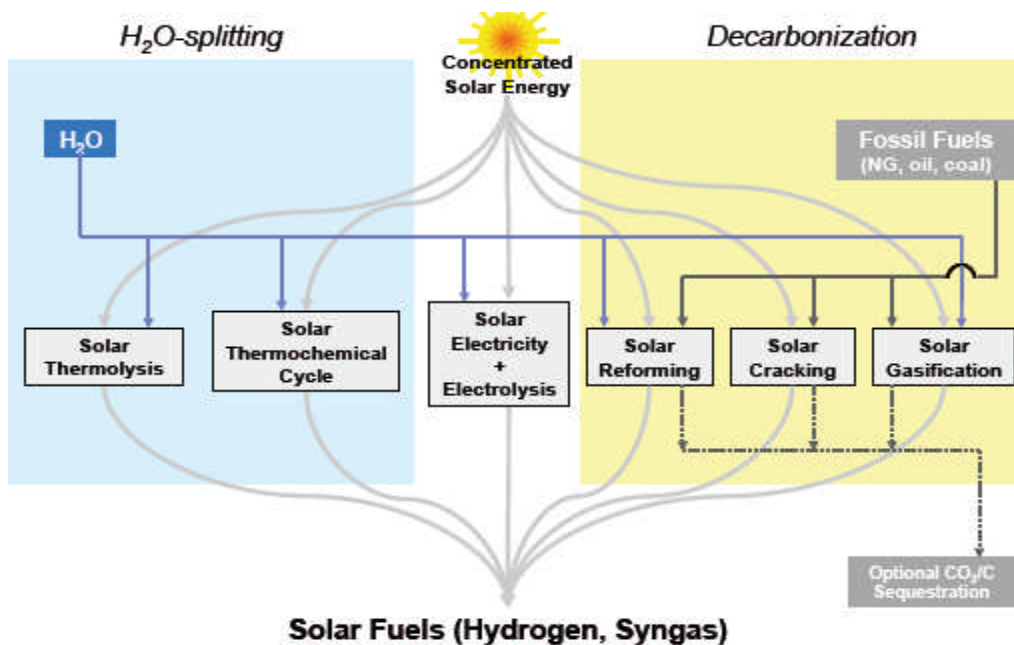


Figure 2-60: Schematic illustrating various routes to solar energy storage as fuels (Source: PSI, ^[132])

In the electro-chemical route, electricity generated directly by photovoltaic (PV) cells or indirectly by solar thermal power plants is used to produce hydrogen by the electrolysis of water at overall efficiencies of 12-16%^[132].

2.4.4.1 Solar Thermolysis

Thermolysis is the thermal dissociation of H₂O into H₂ and O₂ in a high temperature heating chamber. Though conceptually simple, it is a very challenging engineering process as the heat chamber must achieve temperatures over 2200°C to achieve any economic level of dissociation. As an example, a 64% dissociation level at atmospheric pressure requires an extreme temperature of 2725°C.

Therefore, achieving separation of the H₂ and O₂ gases to avoid explosion and finding suitable stable materials to operate continuously at these temperatures is a challenge. Proposals for separating the product gases include (a) effusion separation (passing one molecule at a time through a selective membrane) and (b) electrolytic separation.

Although ceramic membranes such as zirconia and other high temperature ceramics have been tested, they fail to cope with the serious thermal shocks of very high solar flux concentrations. Consequently, despite small advances, thermolysis still remains a theoretical concept for CSP based direct hydrogen generation^[132].

2.4.4.2 Solar Thermochemical Cycles

With respect to the use of thermo-chemical cycles for fuel production, Kadoma and Gokon (2007) presented a general review of this energy storage approach. In these systems receivers focused with concentrated solar radiation are used to produce hydrogen from water thermo-chemically by high temperature water splitting. Whichever the CSP technologies are, the thermo-chemical process flow (Figure 2-61) can be summarized as follows^[133]:

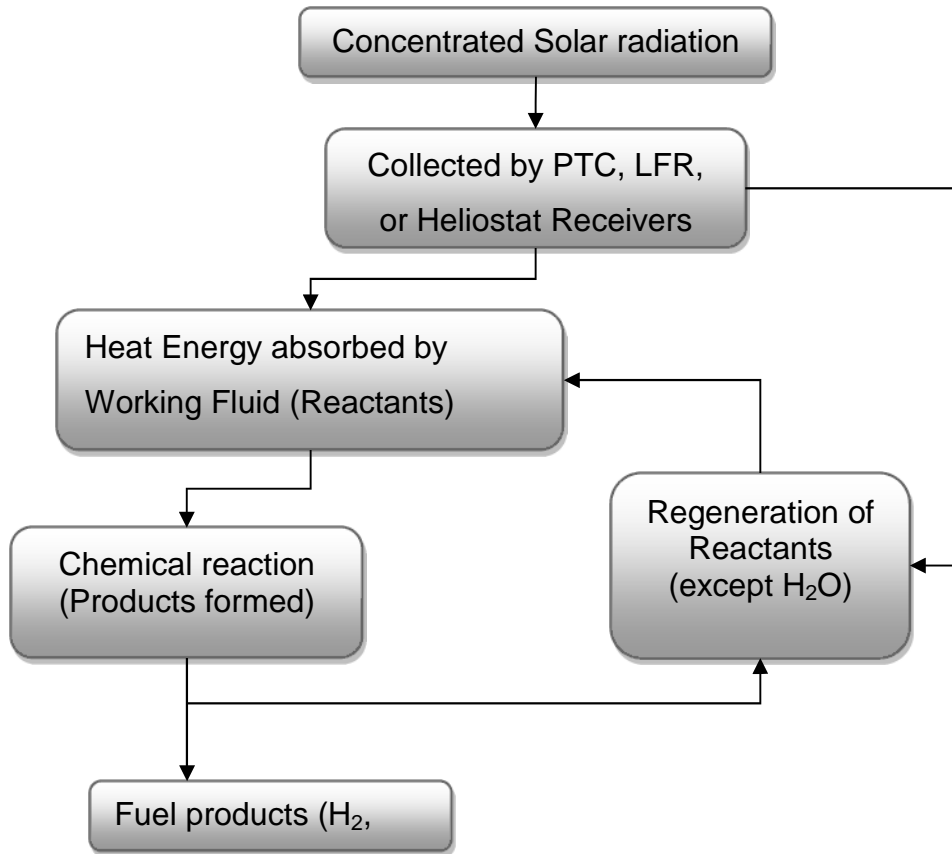


Figure 2-61: Process flow for hydrogen generation in a CSP powered thermo-chemical cycle (Adapted:^[133])

Kadoma summarized the oxide, hydride and hydroxide reaction routes to hydrogen production for two step reactor processes as follows:

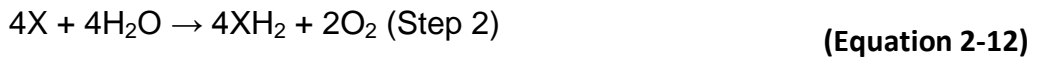
(a) Metal Oxide Type - Reaction



(b) Hydride Type - Reaction



(c) Hydroxide Type - Reaction



The concept of a two-step thermo-chemical water splitting process was first proposed by Nakuramura (1977) ^[133].

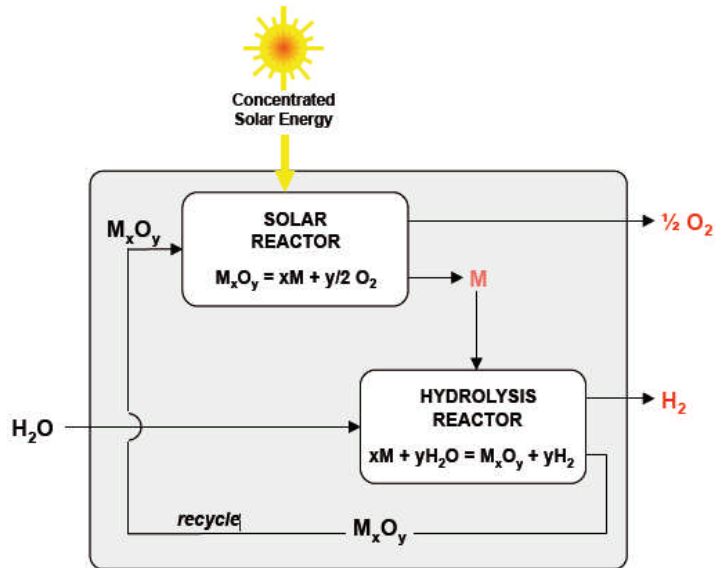


Figure 2-62: Schematic illustrating thermo-chemical metal oxide cycle or hydrogen generation (Source: ^[132])

A two step sequence involving the reduction of metal oxides (Figure 2-62) is also another thermo-chemical path to hydrogen generation, and is more efficient than three and four step processes. In the first of these steps, the metal oxide is reduced to base metal in the solar reactor chamber and in the final step the metal is hydrolysed to reform a metal oxide and liberate hydrogen gas. It is evident that hydrogen and oxygen are both formed in separate steps and this eliminates the need for a gas separation system, as required by the thermolysis approach ^[132].

Theoretical analysis performed by Kadoma and Gokon on standard Fe, Mn and Co based two step processes revealed that concentration temperatures for step 1 need to be above 2500 K at a pressure of 1 bar

and for step 2, the hydrolysis reaction thermodynamically proceeds at temperatures below 1000 K (Figure 2-63).

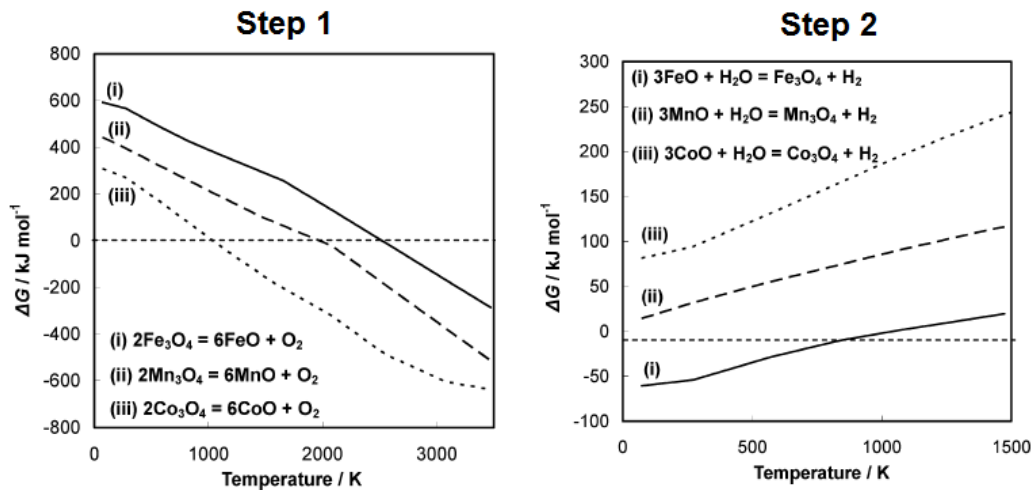


Figure 2-63: Variation of ΔG for water decomposition with (i) FeO (ii) MnO and (iii) CoO with temperature at 1 bar (Source: ^[133])

Other thermo-chemical cycles for hydrogen production may involve more than two steps. Examples include:

- (a) A three step sulphur-iodine cycle based involving thermal decomposition of sulphuric acid at a temperature of 850°C, as demonstrated in the work of Thomey *et. al* (2012) ^[134], Tarquini *et al.* (2007) ^[135].
- (b) A four step cycle involving the hydrolysis of calcium at 750°C and iron bromide at 600°C ^[132].

Other researched metal oxide reduction cycles include: Zn/ZnO and Sn/SnO₂ (eg. a 10 kW reactor prototype, operating at 1700°C at PSI's solar furnace in Switzerland and a 1 kW reactor prototype operating at 1500°C at Odeillo, France respectively).

Processes using other redox pairs such as manganese oxide, cobalt oxide, ferrites, mixed oxide and hydride pairs have also been investigated or modelled by various researchers (Roeb *et al.*, Charvin *et al.*, Neises *et al.*, Alvani *et al.*, Diver *et al.*, Karagiannakis *et al.*, Villafa

n-Vidales *et al.*, Abandes *et al.*, Coker *et al.*, Neises *et al.*, Krishnan *et al.*, Harries *et al.*) [22, 136-146]. Practical demonstrations of these reactors include the 10 kW_{th} reactor of the EU's "Hydrosol 1 and 2" research and development project (years: 2002-2009) [132].



Figure 2-64: The two cavity reactor for Carbo-thermal Reduction of ZnO in SOLZINC Project (Source: [132])

In all these processes as outlined in the various chemical reactions (usually catalyzed), hydrogen production occurs at moderately high temperatures (950-1200°C) in specially constructed receiver-reactors. This occurs as the reactants flow through a catalyzed reactor chamber/cavity that is heated directly or indirectly by CSP collectors or heliostats.

Solar "Carbo-thermal Reduction" of metal oxides is another reduction process but operates at lower temperatures and produces metal and syngas. Steinfeld *et al.* (1998) were the first to conduct experimental work in this regard, with the construction of a 5 kW reactor at the High Temperature Solar Laboratory, Paul Scherrer Institute (PSI), Switzerland. The reactor operated at 1000 – 1600 K and achieved up to 90% zinc conversion in a single pass system [147].

In the EU's "Solzinc" project (2001-2005) a similar "two cavity" 300 kW_{th} solar reactor (Figure 2-64) was also tested at PSI, Switzerland. Test results from this project which used zinc oxide as a reactant,

revealed zinc production of 95% purity at rates of 50kg/hr with reactor temperatures of 1000 – 1200°C. Overall conversion efficiency was reported to be 30% [132]. Similar tests of a 300 kW_{th} reactor directly heated to temperatures of 1000 – 1200°C at the WIS Solar Tower facility in Israel showed the process yielded 50 kg per hour of high purity zinc and had an energy conversion efficiency of 30% [132, 148].

2.4.4.3 Fossil Fuel Decarbonization

Solar energy storage for CSP plants is also possible with solar decarbonisation of fossil fuels. Decarbonisation of fossil fuels can occur through: (a) cracking, (b) reforming and (c) gasification.

In the cracking process (Figure 2-65a), the fossil feedstock is thermally converted into H₂ and carbonaceous products at high temperature. The carbonaceous solid products can be sequestered without releasing CO₂, used as a material commodity in other processes or as a reducing agent in other chemical reactions [132]. Rodat *et al.* (2010) reported on a 10kW prototype reactor for thermal decomposition (cracking) of natural gas to form hydrogen and carbon black (CB), a high value nano-material, all with zero CO₂ emission [149]. Operating at temperatures of 1740 – 2070 K, analysis showed that a 55 MW solar tower plant based on this concept would produce 1.7 tonnes per hour of hydrogen and 5 tonnes per hour of carbon black [149].

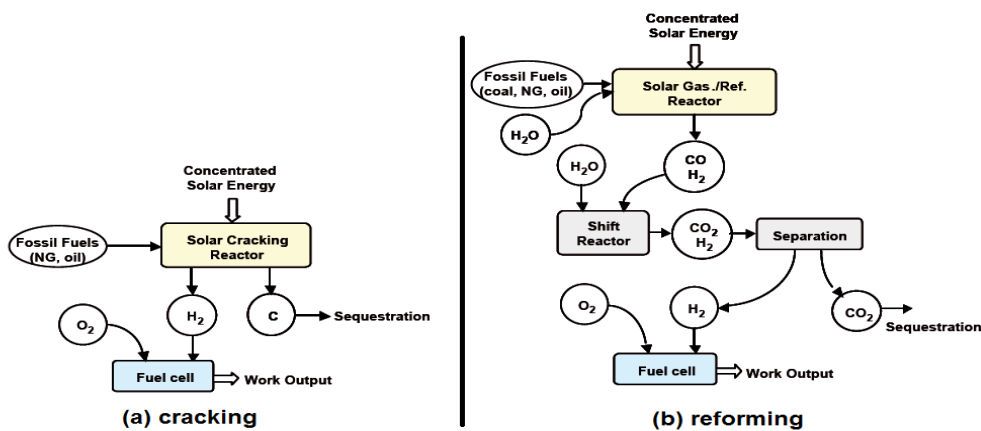


Figure 2-65: Solar decarbonisation of fossil fuels using (a) cracking (b) reforming (Source: [132])

Solar reforming of natural gas (mainly composed of methane) is one such decarbonising process and therefore another promising energy storage approach. The word “*reforming*” describes a process that comprises several parallel and consecutive reactions ^[150]. In this process natural gas, along with other light gaseous fractions are converted with water and/or carbon dioxide to synthesis gas (syngas, a mixture of hydrogen, carbon monoxide and carbon dioxide), at a high temperature in a presence of special catalysts.

The thermodynamics of the reaction is such that reforming of natural gas occurs at temperatures of 900-1100 K with a maximum efficiency in the range of 50-60% ^[150]. Reforming is a particularly useful process for upgrading the value of hydrocarbons. In the reforming process, concentrated solar radiation is used to increase the calorific value of the natural gas in reactions 1 to reaction 2.



$$(\Delta H_{298\text{K}} = 206.25 \text{ kJ/mol})$$

These reactions are then accompanied by the “*water gas shift*” reaction:



$$\Delta H_{298\text{K}} = -41.03 \text{ kJ/mol}$$

As can be seen from the enthalpies, the overall reaction is highly endothermic. In conventional reforming processes, the heat input required by the endothermic reaction is usually supplied by the incineration of natural gas or waste refinery fuels, but in solar reforming processes, this heat is provided by concentrated solar radiation. The syngas (mixture of carbon monoxide and hydrogen) that is produced has a greater calorific value than the initial methane by about 25% ^[151], and can be used directly for electric power generation by combusting in a gas turbine or combined cycle at high conversion efficiencies (up to 55% in combined cycles). Also, it may be used as an intermediate

reactant for the production of other compounds such as hydrogen, ammonia, methanol and oxo-products [150].

Two main reactor types (a) indirect and (b) direct reformers (Figure 2-66) are used in the reforming process. In the indirect reactor the reacting gases flowing inside the four graphite tubes are mostly indirectly heated by a cubic graphite cavity chamber that is exposed to concentrated solar radiation passing through a hemispherical quartz window.

In the direct reactor, a porous ceramic absorber containing a Rhodium catalyst is directly exposed to concentrate radiation. A concave quartz window minimizes reflective losses and permits operation at elevated pressures. This results in higher conversion efficiency for the direct reactor.

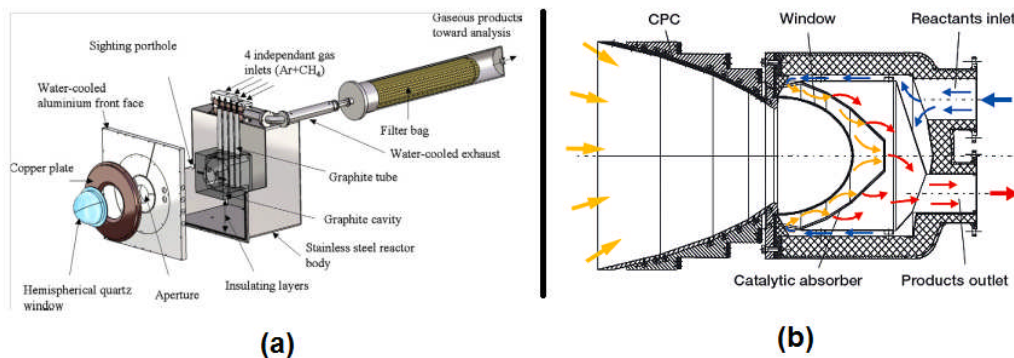


Figure 2-66: Schematic representation of (a) indirect and (b) direct solar NG reformers (Sources: [132, 149])

Solar reforming of methane with CO₂ using a direct receiver/reactor was promoted by work done at DLR and Sandia National Laboratories in 1990, using a direct absorption solar reactor system concept in which receiver and reformer are packaged in the same unit. The ASTERIX project undertaken in collaboration between DLR, Germany and CIEMAT, Spain in 1993 used a 170 kW reformer heated directly by hot air delivered from a 270 kW ceramic GAST tubular receiver and produced syngas of industrial quality [150].

Various research institutions (Sandia National Laboratories-USA, DLR-Germany, Weizmann Institute-Israel, etc.) have been involved in reactor designs over the last 20 years. Also, several researchers (Buck, Muir, Hogan, Kadoma, Gokon, Yamawaki, Nakazawa, Anikeev, De Falco, Parmon, Kirrollov etc.) have done significant work in this area. Much of the solar methane reforming processes are based upon the use of “Catalytically Activated Ceramic Absorbers” in volumetric reactors. One of the main objectives of research in this area is to achieve higher solar-chemical conversion efficiencies (η_{chem}) for a given target solar power density (P_d).

Dry reforming of natural gas with CO_2 instead of steam is also possible using a chemical heat pipe (Figure 2-67). Residence times for this conversion process are in the order of 10 milliseconds and temperatures of approximately $1700^\circ C$ with typical methane and CO_2 conversion efficiencies of 70 and 65% respectively achieved without use of catalysts^[132].

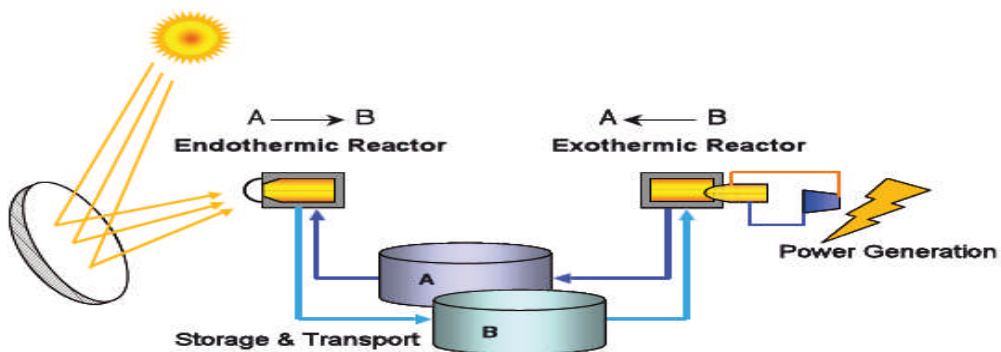


Figure 2-67: Schematic illustrating concept of a chemical heat pipe (Source: PSI,^[132])

In this regard, a sodium reflux chemical heat-pipe receiver reformer built by Sandia National Laboratory, was tested using a 15 kW solar furnace at the Weizmann Institute, Israel. Tests confirmed the feasibility of the concept. According to Diver *et al.* (1990), this work ended prematurely due to system failure caused by a reactor air leak^[152]. Shortly after, direct irradiation testing of tubular receivers in Israel was reported by Levy (1993)^[148].

Several efforts have been made to improve these reactor systems, in order to improve conversion efficiency. Kodama *et al.* (2003) experimented with an active catalytically activated metal foam (CAMF) absorber for use in direct methane reforming reactors (Figure 2-68) that used relatively low flux concentration of solar energy ^[151]. This Ru/Al₂O₃/Ni-Cr-Al-foam absorber was reported to have a light to chemical conversion efficiency of 50% at a low solar irradiation density of 180 kW/m² on the absorber. It would have been interesting to see the effect on conversion efficiency of higher irradiation density values, especially in light of the higher anticipated heat losses.

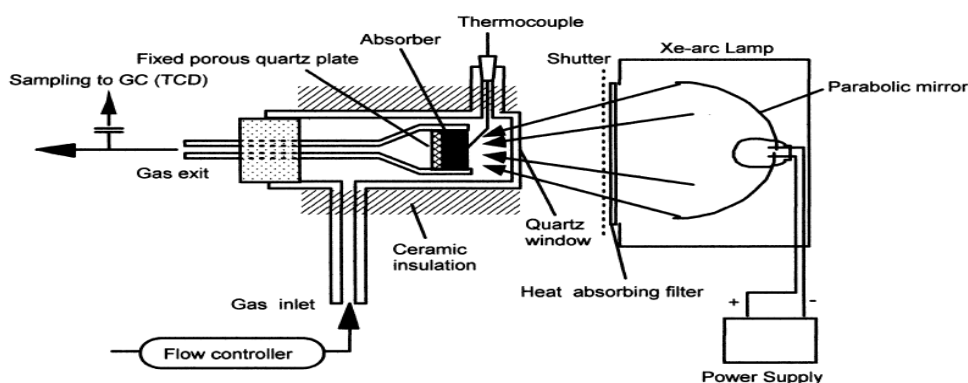


Figure 2-68: Schematic showing experimental setup for CAMF absorber by Kodama *et al.* (Source: ^[151])

Gokon *et al.* (2010) investigated a Ni/MgO-Al₂O₃ catalyzed foam absorber which was reported to be more cost effective than the Ru-based catalyzed absorber reported by Kodama (2003) as it was able to achieve an equivalent 50% solar-to-chemical conversion efficiency using a larger foam absorber which reformed more methane. Several different reactors for these processes have been presented in literature ^[153].

One such reactor is the Solar reactor with multichannel honeycomb support developed by DLR, Cologne Germany ^[133]. For the design of these reactors, Tescari *et al.* (2010) developed a simplified method for their geometrical optimization at a given incident flux ^[154]. Finally in regard to thermochemical reactor hybridization, De Falco and Piemonte (2011) reported on a reactor design for producing solar enriched

methane (mixture of methane and hydrogen) by use of a steam reforming process in a novel hybrid CSP plant.

Up until now, all of the thermal storage systems discussed have used only one dedicated storage option. However there are also cases where hybrid systems comprising two or more of the general storage options discussed have been implemented.

In this regard several hybrid storage options have also been reported in literature: Kaushika *et al.* (2005) modelled the operation of a solar biomass hybrid co-generation plant ^[155]; Guo *et al.* (2008), Steinmann *et al.* (2008), Morisson *et al.* (2008), Birnbaum *et al.* (2010), Laing *et al.* (2010), Feldhoff *et al.* (2012), all investigated DSG using PCM with molten salt sensible heat storage ^[9, 111, 156-159]. Laing *et al.* (2011) modelled high temperature concrete storage with PCM in DSG ^[160]; Zhuang (2011) modelled oil tank storage systems with buffer steam accumulators (Figure 2-69) ^[161]; and Adinberg (2010) reported a novel reflux heat transfer storage concept based on PCM storage ^[162]. These citations represent some of the most recognized work in the area of hybrid energy storage.

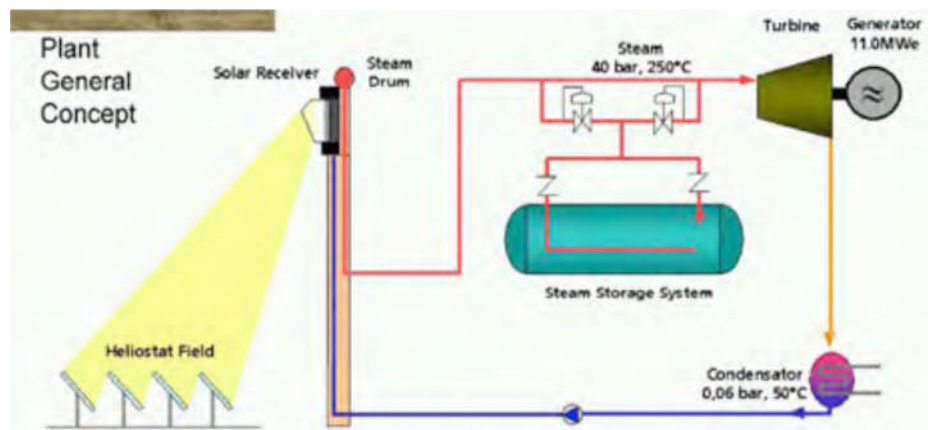


Figure 2-69: Schematic showing layout of a DSG Solar Tower Plant with a Steam Accumulator Storage System (Source: ^[77])

The final section of this chapter which follows next, describes briefly other storage technologies not currently applied to CSP plants. While

some of these storage solutions are more appropriate than others, some could provide useful solutions in the future. The potential utilization of one of these technologies, sodium sulphur battery storage is the main focus of work in this thesis and will be specifically mentioned.

2.5 Other Energy Storage Options

Thus far, the energy storage options that have been reviewed for CSP plants either represent the state of the art, or are currently in developmental stage as pilot or laboratory models. Despite this however, other non-conventional storage approaches are still open to exploration for CSP power plants.

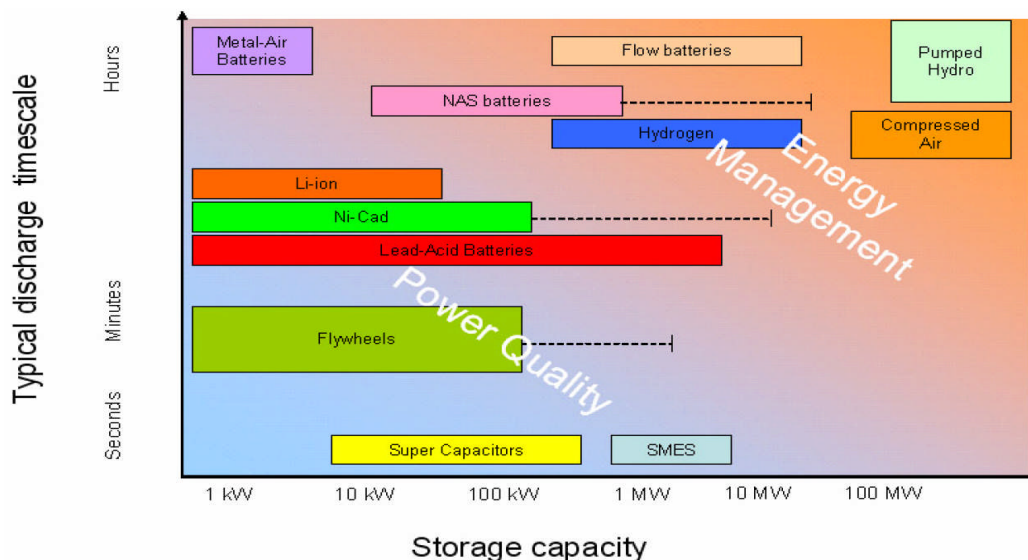


Figure 2-70: Schematic illustrating storage systems discharge time vs. storage capacity (Source: [163])

Some of these storage approaches are already in use, with regards to other renewable energy technologies while others are still in the early stages of development.

Examples of these storage options (Figure 2-70) include: compressed air systems for storage of wind energy; sodium sulphur batteries for wind energy storage and grid support/back-up applications; super capacitors for power quality support; flywheels for mechanical energy

storage on rotating electrical machines; flow batteries and fuel cells for power generation.

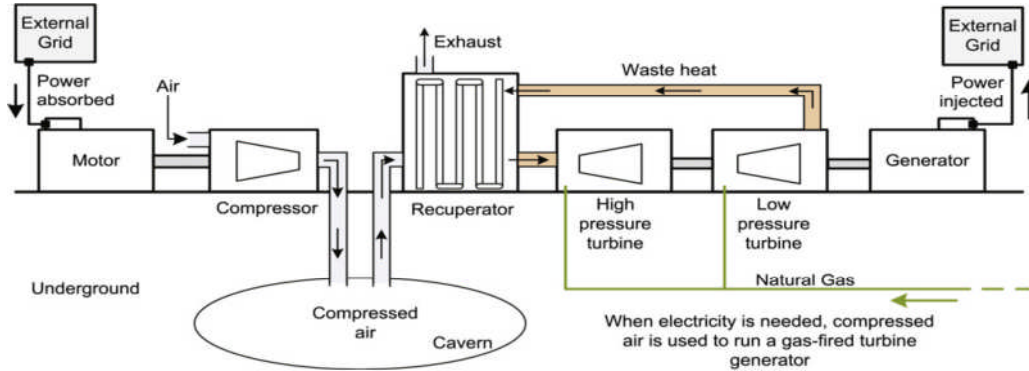


Figure 2-71: Schematic showing layout of a compressed air storage system (Source: [27])

Compressed air systems (Figure 2-71) are not yet widely used today, even though they possess the capability for grid scale energy storage. To date only two plants have been constructed worldwide. One of these plants (290 MW), is located in Germany, and the other (11 MW) is located in the United States [27]. However there is increasing interest in applying this technology for renewable energy applications. One good example of this is the current development of the 2700 MW Iowa Stored Energy Park scheduled for completion by 2015 [164].

The system will operate by using low cost electricity, obtained from the grid, along with excess generating capacity from an adjacent wind farm to compress air for storage in an underground geological formation. During peak demand, the compressed air is released and used with natural gas to drive a turbine generator, sending electrical power back to the grid.

The benefit of this system lies in the fact that the process uses much less energy compared to a conventional natural gas fired generator for producing the same rated power output. Consequently, the process reduces fossil fuel utilization and cuts CO₂ emissions. Solar energy from CSP plants could be therefore suitably stored in such compressed air systems.

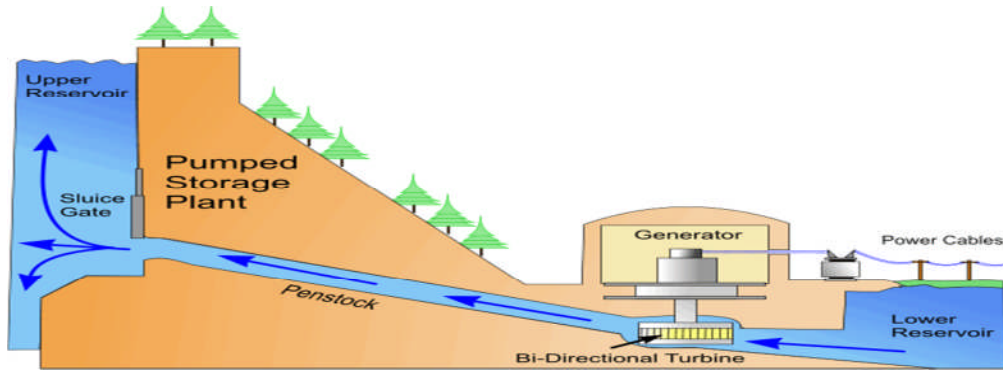


Figure 2-72: Schematic of a pumped hydro system (Source: Better Green, ^[165])

Pumped hydro energy storage (Figure 2-72) is also a well known storage option. It is not currently used with any CSP plants due to the fact that it is a geography specific application, and CSP systems are normally suited to geographic climates (deserts) where hydro systems could never naturally operate.

If it were possible however, CSP plants could store solar energy in gravitational potential form by pumping readily available water from a low level reservoir to a high level reservoir during periods of low energy demand. When power is needed, the water would be returned to the low level reservoir where the potential energy is converted to work by driving an electrical turbine generator. The Dinorwig plant in Wales, UK is a good example of this system in operation, being able to respond to a 1320 MW demand in 12 seconds. In general pumped hydro storage has a proven ability to provide large scale, high power storage in the MW and GW range, operating at efficiencies between 65-75% and with systems lasting for 30 - 50 years ^[27].

Short term ancillary power services (in the order of minutes) for CSP plants can be provided by electromechanical flywheels, and may already be in use in some power plants. In this system, a mass, the flywheel is supported on two magnetic bearings (in order to reduce friction at high speed) and is coupled to a generator. The system is enclosed within a vacuum to reduce energy losses. Whenever there is an increase in electrical/mechanical drive energy, the flywheel accelerates

thus storing the energy in kinetic form. When this energy is recovered from the flywheel it decelerates, discharging the energy back to the electrical/mechanical load. The energy stored in the flywheel is a function of its inertia and the square of its rotational speed.

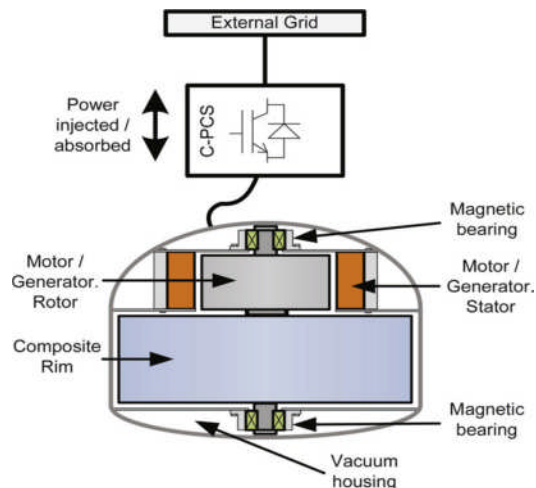


Figure 2-73: Schematic illustrating a flywheel energy storage system (Source:^[27])

Flywheels (Figure 2-73) have a typical efficiency of about 90% at rated power, but they suffer relatively large standing losses, with self discharge rates of 20% of stored capacity per hour. Therefore flywheels cannot act as long term energy storage devices, but are good for generator ride-through power support applications ^[27]. The largest commercial flywheel system is manufactured by Piller Power Systems and operates within a speed range of 1500-3600 rpm, with an energy capacity of 19 MWs ^[27].

Electrical energy storage is another storage concept made possible with a range of different battery systems. Conventional lead acid batteries are currently used for on-site storage to support small photovoltaic or wind renewable systems, but cannot be used for grid support due to low efficiencies, high self discharge and low energy densities. Nickel and Li-ion type batteries are under development for high power applications, but are more suited to the electrical vehicles market.

Supercapacitors or ultracapacitors (Figure 2-74) store energy in the electric field between a pair of charged plates. These devices have a significantly enlarged electrode surface area when compared to normal capacitors, and instead use a liquid electrolyte and polymer membrane. They are suited to very fast charge/discharge cycles, have a high cycle lifetime and show little degradation over this time. They also have high efficiencies (85 -98%) and very good energy densities (5 – 60 Wh/kg). Improvements in energy density are also regularly reported.



Figure 2-74: Supercapacitors (Source: Shanghai Green Tech Co., Ltd)

Today supercapacitors are mainly used for starting diesel trucks and railroad locomotives, actuator systems, transient load levelling and brake energy regeneration in eclectic hybrid vehicles. In recent years they have also been used for supporting starting and load levelling applications in renewable power battery storage systems.

Flow battery technology (Figure 2-75) on the other hand is relatively new. These batteries operate based on reversible electrochemical reactions that occur in a large electrochemical cell. They differ from conventional batteries in that the battery electrolyte is stored in two separate tanks, outside the cell's electrochemical reaction chamber^[27].

During normal operation, the aqueous electrolyte solutions are pumped through the cell reaction chamber where an electrochemical (Redox) reaction occurs, producing electricity. There are three types of flow cells: Vanadium Redox Battery (VRB), Zinc Bromide Battery (ZBB) and Polysulphide Bromide Battery (PBB). Cell power capacity is related to

the size of the reaction chamber and electrodes, therefore the system can be easily sized or scaled.

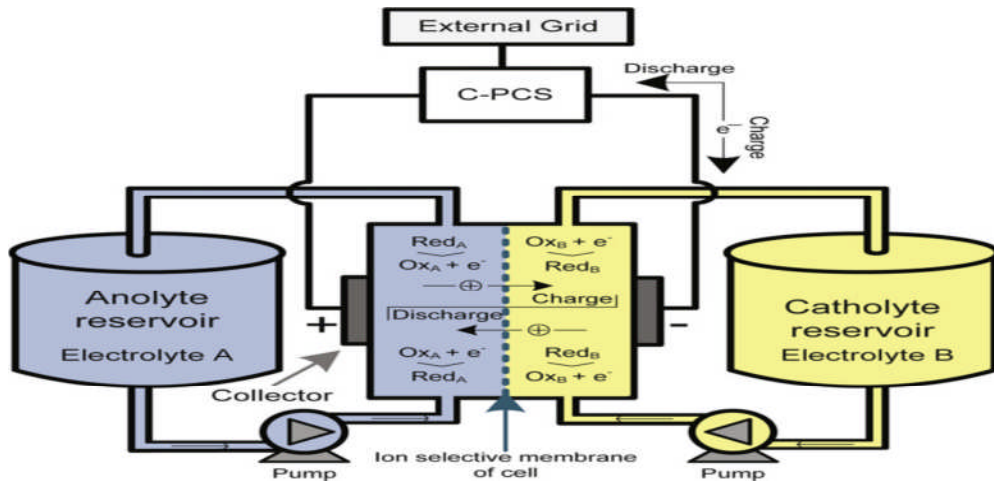


Figure 2-75: Schematic illustrating the operation of the flow battery (Source: [27])

Other positives include the ability of these batteries to reach full charge without damage, and experience very low self discharge, due to the separation of electrolytes in separate storage tanks. When charged, they have the potential to store electrical energy for CSP plants in the MW range and could be used to provide ancillary services and general grid power support. System life is said to be 15-20 years. However, these systems are still in the developmental stages and must still address issues with regards to environmental impact and operational safety [27].

There is one final storage system that will be briefly mentioned in this chapter, but discussed in detail in the next. It is a promising large scale electrical storage application which happens to be the main subject of work in this thesis, the "Sodium Sulphur Battery" (Figure 2-76). Sodium sulphur (NaS) batteries have about four times the energy density of traditional lead acid batteries but must be kept at an operating temperature between 300 – 400°C.

As a result of their high energy density, high efficiency, zero self-discharge, long life (20 years or more), they are currently used for power back-up, power quality and power storage solutions in the MW

range for both photovoltaic and wind power applications. The special temperature requirements for operation have limited the use of these promising batteries to industrial and commercial power applications. All NaS battery modules are built up from individual cells (Figure 2-76) and typically packed into a sand filled insulated enclosure equipped with an electrical heater and a temperature control system [166].

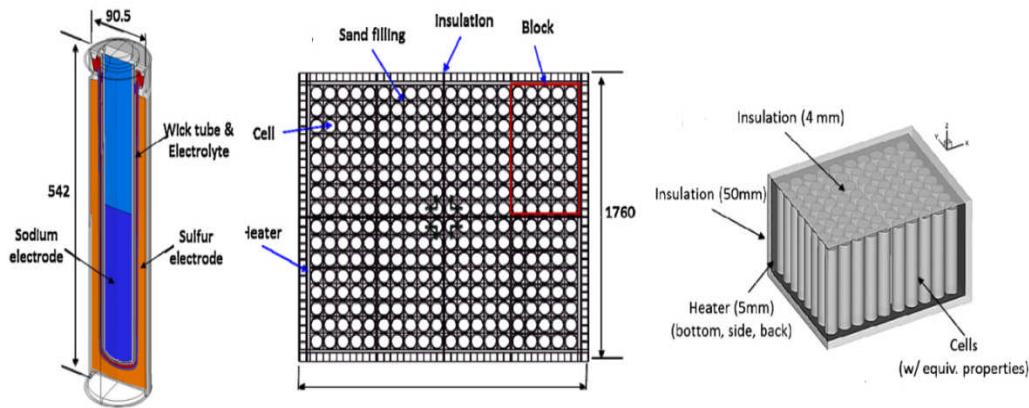


Figure 2-76: Schematic showing section down a NaS cell and the typical arrangement of a 50 kWh NaS battery module (Source: [166])

In this thesis, a novel way of utilizing these cells in PTC power plants for energy storage purposes is proposed, and this will be discussed in detail in the next chapter. It will be seen that the hybridization of NaS battery storage into a PTC system provides not only storage benefits, but also helps to solve some of the operating problems of current PTC plants.

Though currently a more expensive storage option (USD \$500/kWh) [226] compared to €20/kWh for molten salt thermal energy storage (MSTES), NaS batteries are manufactured from cheap, readily available materials (sodium, sulphur and steel). The technology itself though not widely deployed is very mature, with a proven record of performance over the past two decades.

It is therefore envisioned that with widespread utilization and economies of scale, the cost of this storage option could one day drop significantly to a point which allows it to compete with, or exceed the cost-performance benefits of the state of the art.

Chapter Summary

With the increasing penetration of renewable forecasted for power grid, a method of handling the intermittent nature of these resources must be found. The two options available to plant operators are fossil powered back-ups or storage of renewable energy. As discussed at the start of this chapter, experts suggest that in the context of widely debated climate change and the thrust towards 100% renewable power in the developed world, the latter option of energy storage is the only option that will be accepted by the policy makers of tomorrow [6, 12, 23-24, 26-28, 49, 103, 111, 163, 167-182]

Concentrating solar power systems (CSP) can play a significant role in this area. Of all renewable technologies, CSP it is the only one that naturally lends itself to energy storage, especially in thermal form. In this regard, it is able to support an increased integration of other renewable into the grid, when part of the operator's renewable energy portfolio. Storage options such as thermocline tanks, solid media and latent heat storage systems all offer the potential for more cost effective CSP storage systems in the future.

Thermochemical storages will need significant cost reductions and process enhancements to compete with the other storage options and with the state of art. Research and development aimed at improving and enhancing promising storage options will prove beneficial for all renewable technologies and for the general uptake of renewable energy by the electric grid. To this end is the effort of this current work.

Consequently, the next chapter outlines a novel method for hybridizing or integration promising sodium sulphur (NaS) battery technology into state of the art PTC power plants, in the design of a conceptual receiver. This provides an advanced storage solution, which when used with existing thermal storage, could provides the added benefits of power quality enhancement, rapid ramping response and improved thermodynamic performance.

Chapter 3

Design of the Conceptual EES Receiver

Introduction

Solar parabolic trough collector (PTC) power plants are an interesting topic for energy related research work. This is largely due to the fact that they produce large amounts of “green” electric power on a grid scale, through the thermo-electrical conversion of concentrated solar radiation by precisely engineered solar collector/receiver assemblies (Figure 3-1).

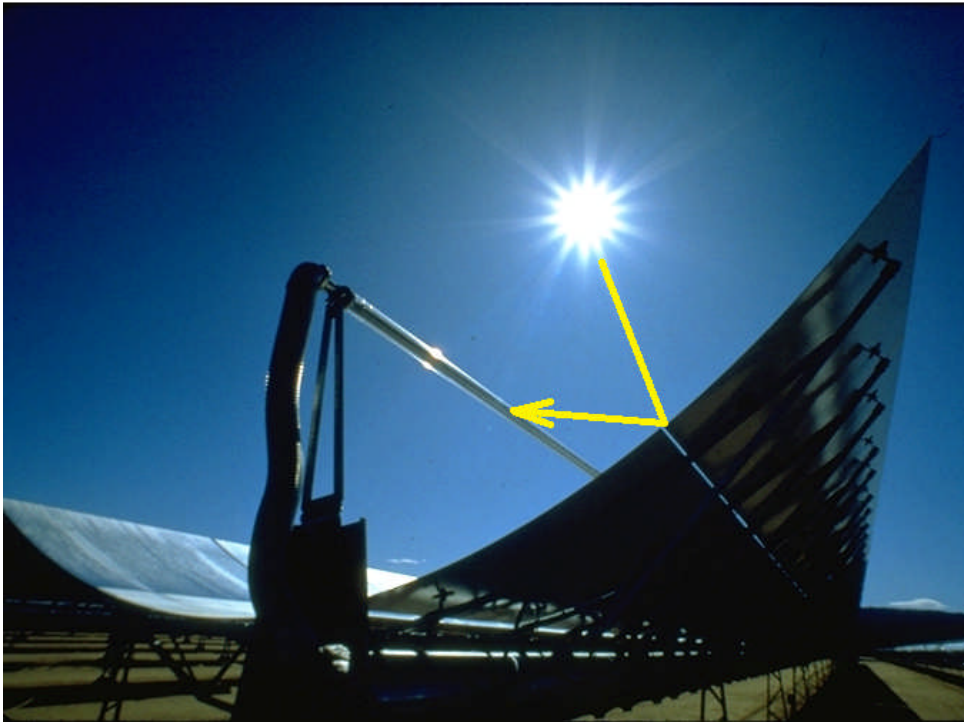


Figure 3-1: Parabolic trough collector and receiver tube (source: NREL)

However, a survey of widely available literature on renewables in the public domain will reveal that commercial deployment of PTC technology in recent years has been adversely affected by falling prices in photovoltaic technology, its main competitor. If PTC

technology is to become a more attractive to investors in a market swamped with low cost photovoltaics, new ways must be found to leverage or enhance a key advantage of this technology, “*energy storage capability*”.

Various approaches for enhancement of this energy storage advantage were explored while going through the initial stages of identifying a focus for this research. While examining storage options, it was discovered that high energy density “*Sodium Sulphur (NaS)*” batteries were being deployed for electrical energy storage applications in wind and PV plants worldwide.

It was also realized that these battery systems were widely used for grid support applications in Japan, providing power outputs in the MW range for over 6-8 hour durations. It is this 6-8 hour power supply duration that initially attracted the interest in these battery systems, as it is identical to the average power supply duration of a PTC plant thermal storage system. Also the fact that NaS batteries are thermal batteries and must be heated up to temperature before they can be used led to the realization that both the NaS battery and a standard PTC power plant operated in a similar temperature range of 300 – 400°C.

This immediately suggested that it would be possible to heat the NaS batteries using the HTF from the solar field, a completely different method to the standard approach of heating batteries in a sand filled module equipped with an electrical heater and a temperature control system.

It also became apparent that the tubular nature of the NaS cells would allow them to be easily placed inside a standard PTC receiver tube for heating. All that would be required was a special modification of the receiver tube internals to allow for HTF flow between the main receiver tube and the internal batteries (annular flow) rather than traditional pipe flow. This sequence of initial thought processes is the genesis of the design, modelling and analysis presented in this thesis as the “*Conceptual EES Receiver*”.

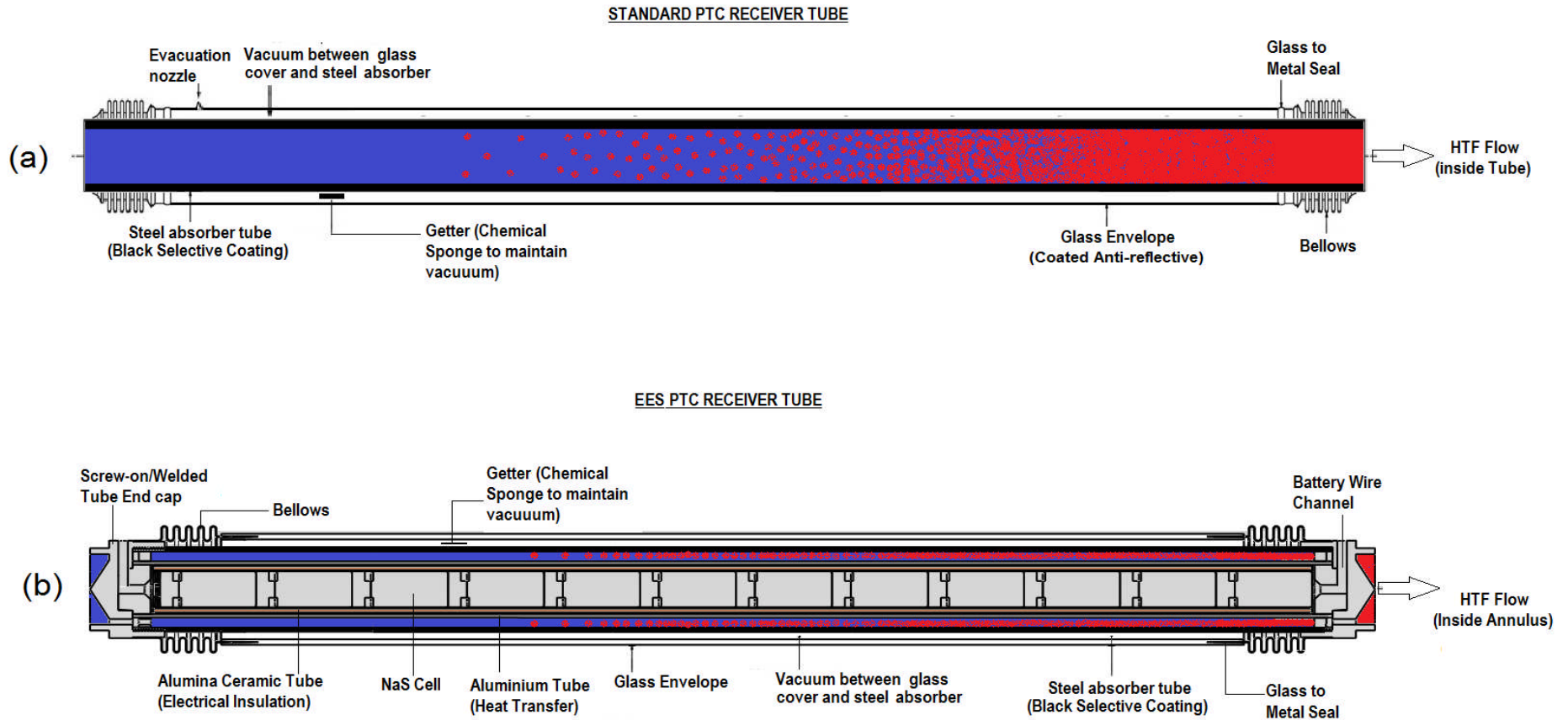


Figure 3-2: Schematic illustrating (a) A conventional PTC receiver and (b) The conceptual EES receiver

The EES receiver can therefore be described as a hybrid solar heat collecting element (HCE) for parabolic trough collectors with built in electrical storage. The objective behind the design of the EES receiver was to create a solar receiver for use in PTC power plants that could help to solve challenge of energy storage by incorporating *“built in energy storage”*.

Unlike the traditional receiver (Figure 3-2a) used in a PTC power plant, the conceptual EES receiver (Figure 3-2b) would provide the functions of a traditional PTC receiver along with the added benefit of electrical energy storage in the form of sodium sulphur batteries. A detailed explanation of the receiver’s construction is given in section 3.1. Although technically speaking, *“a battery is an electrical connection of two or more cells”*, throughout this thesis the terms *“NaS battery”* and *“NaS cell”* will be used interchangeably, as referring to *“a single NaS storage element”*.

As this introductory section is now ended, the reader will find four content sections to follow in this chapter. Sections two to four discuss important design aspects of the conceptual EES receiver and of an associated heating rig built for an experimental receiver prototype. As images generally convey much more information than written text, section five provides the reader with a photographic highlight of the construction phases of the prototype EES receiver and the experimental heating rig. Finally, the chapter summary presents a recap of the key points of all chapter sections.

3.1 Description of the Conceptual EES Receiver

The conceptual design of the EES receiver (Figure 3-3) highlights the fundamental difference of the EES receiver with respect to a standard PTC receiver. This difference lies in its internal construction.

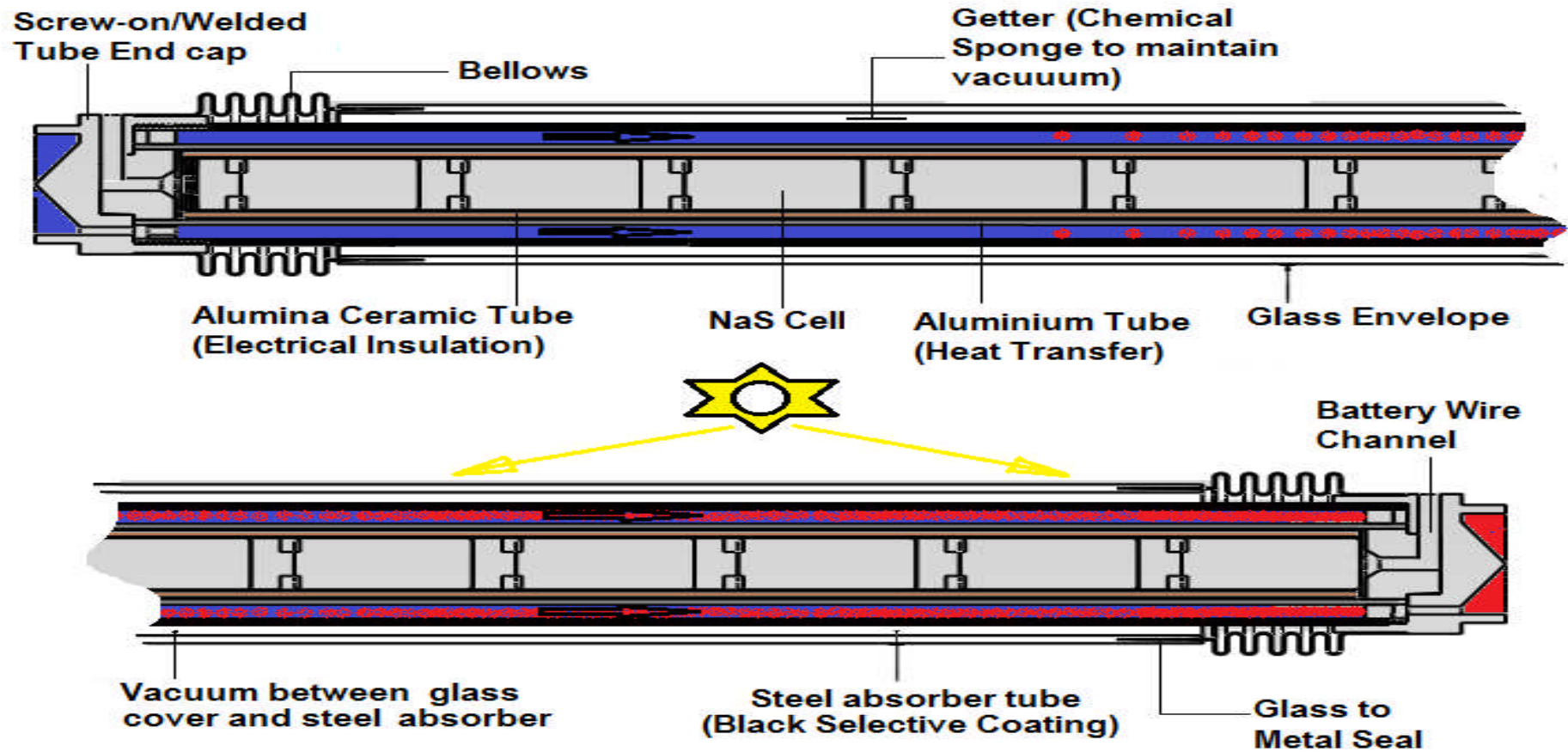


Figure 3-3: Schematic showing longitudinal section through the Conceptual EES Receiver

Like a traditional receiver (e.g Schott PTR-70), the EES receiver consists of a selectively coated steel absorber tube enclosed within an evacuated borosilicate glass cover, with glass and metal tube ends joined together through use of thermally expandable steel bellows and glass-metal seals. The glass cover itself has high transmittivity to solar flux ($\tau_g > 0.97$) and also has an anti-reflective coating to reduce reflective losses.

Vacuum enclosure of the absorber tube protects the selective coating from degradation and virtually eliminates convective heat loss. Special chemical getters (molecule sponges) placed within the evacuated space, absorb gas molecules left after sealing and also indicate via colour change, whether tube vacuum has been lost. All of the above is typical of a commercial PTC receiver.

However, unlike the traditional receiver, the EES receiver contains an internal tube or “battery tube” (Figure 3-4). The HTF therefore flows in the “*concentric annular space*” between the absorber and battery tubes.

Heat is transferred via forced convection from the HTF to the battery tube wall, which should be made of a highly thermally conductive material such as aluminium, capable of the process duty (temperature and pressure). For higher temperature systems ($T > 500^\circ\text{C}$) a steel battery tube would be required.

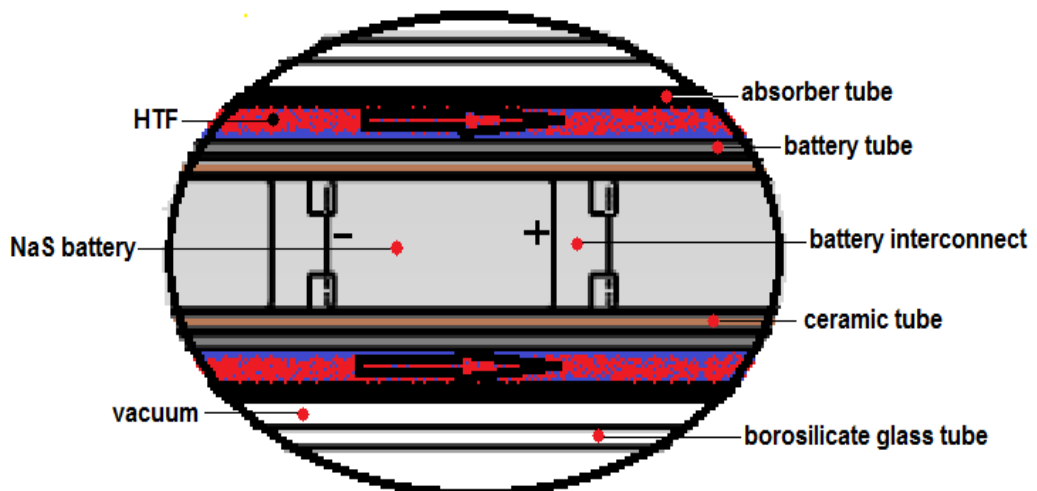


Figure 3-4: Schematic showing internal assembly of tubes tube within the EES Receiver

Inside the battery tube, is a special ceramic tube (Figure 3-4) which houses the NaS batteries. This fundamental purpose of this tube is to electrically insulate NaS batteries from each other and from the rest of the receiver, so as to prevent short circuiting. Therefore this tube should be electrically non-conductive, but also should possess good thermal conductivity.

However, since it must also transfer heat from the battery tube to the NaS cells it should also have good thermal conductivity. A low cost ceramic material which serves this purpose well is mullite alumina, which unlike silicon carbide (another low cost material that was considered) is electrically non-conductive. It is also important to note that for effective heat transfer, the battery tube, ceramic tube and NaS cells must be in good physical contact, albeit within the limits allowed for differences in thermal expansion.

Individual NaS cells within the ceramic tube are linked electrically and physically with metallic interconnects, connecting opposite poles (+ with -) of adjacent batteries. Cells in a standard 4 m receiver would be all connected in series. However, practical receiver modules could also be connected in parallel to increase the current capacity of the NaS battery storage system.

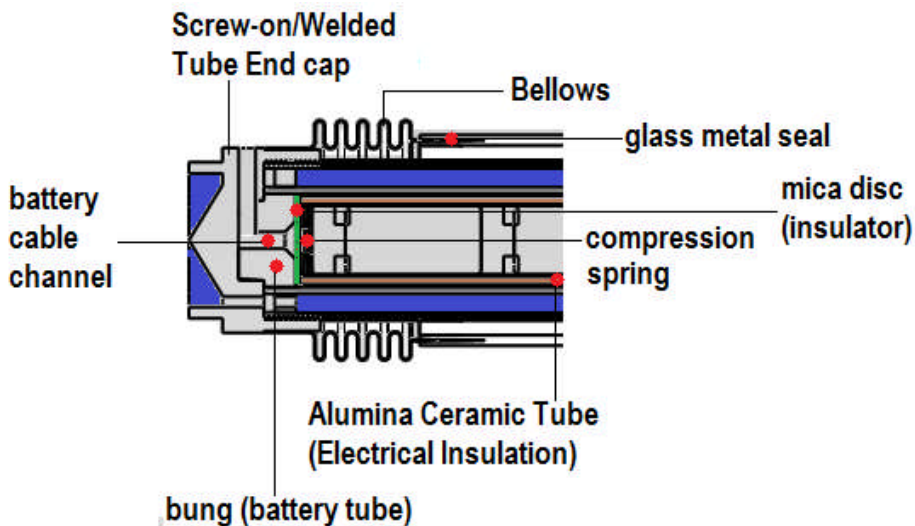


Figure 3-5: Schematic showing a more detailed longitudinal section of EES Receiver near an End Cap

Finally specially designed “end caps” (Figure 3-5) are either screwed on with thread sealant or welded in place at both receiver ends to hold the whole tube assembly together. These end caps have special holes or slots for the passage of HTF into the flow channel, and another channel orthogonal to the flow for feeding of the battery cable into the battery tube for connection with the internal NaS batteries.

A special bung on the inside of the endcap seals the entrance of the battery tube and prevents HTF from entering the battery compartment. The NaS batteries are electrically insulated from the internal face of this bung and the rest of the receiver body, by a special mica disc. This completes the general description of the components making up the conceptual EES receiver, along with their intended functionality. The next section now discusses the design procedure of a prototype receiver that was constructed for experimental investigation during the course of this study.

3.2 Design of the EES Receiver

The design of a prototype EES receiver is dictated by the physical dimensions of the cells it must contain, the rated annular flow at design point and the operating duty (temperature and pressure). With this in mind, the first task in designing an experimental prototype was identifying and acquiring the NaS cells to be used in the receiver.

After an online search, a local UK based company called Ionotec Ltd. was discovered. Ionotec Ltd. is successor of the former Chloride Silent Power Company, which conducted major research and development in sodium sulphur battery technology in the 1970's and 80's. Ionotec's management team was subsequently contacted and after a series of discussions, twelve 10 Ah HP-4 Nas cells (Figure 3-6) were obtained for the project.

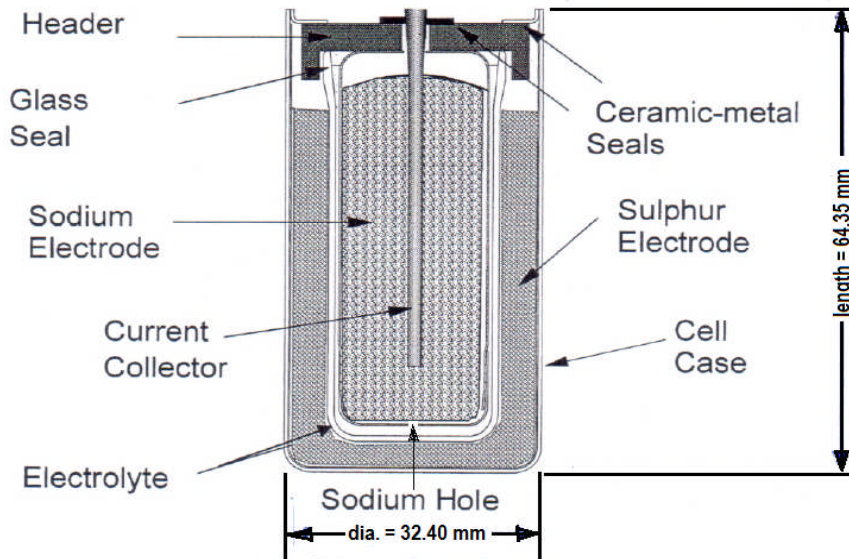


Figure 3-6: Schematic showing section through a HP-4 10Ah NaS Cell (Source: Ionotec Ltd. UK)

The HP4 NaS cells however were designed to be operated vertically, as the hole by which sodium leaves to wet the β -alumina electrolyte (Figure 3-6) was made at the bottom of the sodium container. This suggested that the EES receiver in the experimental rig had to be mounted vertically and not horizontally as would be the case in an actual PTC solar field.

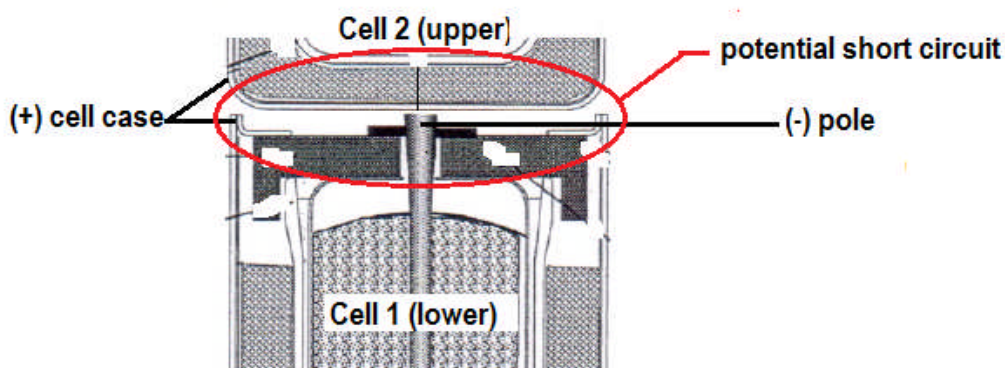


Figure 3-7: Schematic showing potential shorting problem in series connection of HP-4 NaS Cells

It was decided that the conceptual EES receiver would have similar dimensions in diameter (approx. 70 mm) to a commercial PTC receiver, but would be only 1 m in length. This is a quarter of the length of a

standard PTC receiver tube and would allow for a smaller experimental rig, whose results could be easily scaled for comparison with a standard receiver.

One problem that had to be solved however was the interconnection of the NaS cells. Connecting cells in series (Figure 3-7) without an intermediate connector would cause shorting of the NaS cells as the positive (+) and negative poles (-) of a cell would be bridged together. Therefore use of the HP4 cells in an EES receiver application would require special metal cell interconnects to be machined for “standing off” the inner negative (-) pole from the positive (+) cell case.

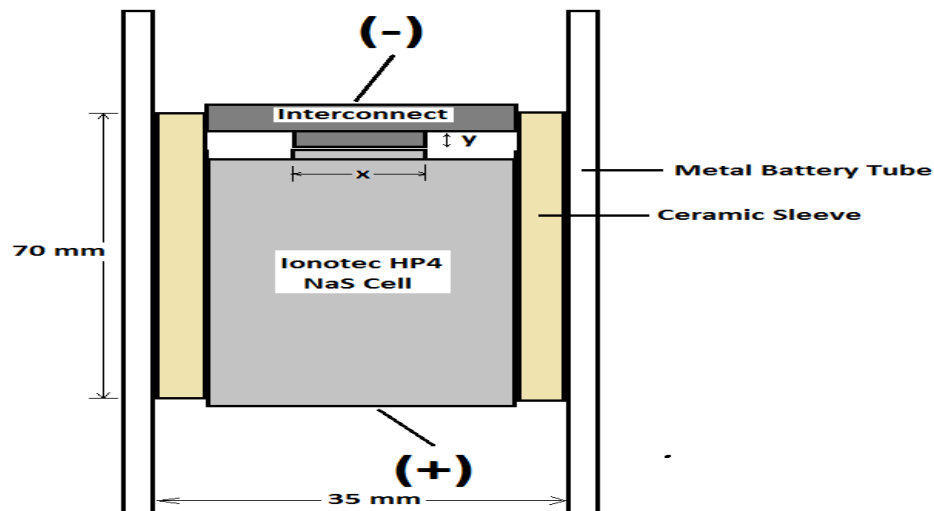


Figure 3-8: Schematic showing intended use of Cell Inter-connect

As stated earlier, a tubular ceramic sleeve material (Figure 3-8) would be also required to electrically insulate the NaS cells from the battery tube wall, which is another potential source of “cell shorting”. In addition to being a good electrical insulator, this material also at the same time needed to be a good thermal conductor.

Several potential ceramics were explored such as aluminium and boron nitride, which are of very high thermal conductivity, but rather expensive to machine. Acting on a supervisor’s recommendation, the use of low cost mullite alumina ceramic tube proved most cost effective for this application.

Finally, the duty parameters chosen for operation were a temperature range of 120 – 350°C at a maximum of 2.5 bar, parameters typical of a lab scale heating rig. After selecting the duty parameters, the next step was finalizing a technical design for the receiver. This is presented in the next sub-section.

3.2.1 The EES Receiver Prototype

The finalized design drawing for the conceptual EES receiver is given in Figure 3-9. As mentioned earlier, the receiver is an assembly of glass and metal tubes, held in place by two machined carbon steel end caps at either end. Each end cap was machined with two flats on the circumferential surface for tightening with an adjustable wrench. An 2-1/2" ANSI-150 slip-on flange was welded onto the collar of the end caps, so that the EES receiver could be integrated into the pipe-work of an experimental rig.

Angled views of the conceptual EES receiver (Figures 3-11 and 3-12) provides a better view of how the HTF flows in and out of the receiver. It can also be seen that the glass tube was designed with a special glass segment. This was to be coated with a cold mirror filter so that it reflected the visible solar spectrum onto parallel positioned photovoltaic cells which would be used to charge the NaS cells. Also, the space between glass and absorber tube was to be partially evacuated using a vacuum pump, with a pressure gauge fitted to indicate the strength of the vacuum.

Owing to time and resource constraints however, these concepts could not be integrated into the final experimental prototype. More detailed drawings of EES receiver components are available in the appendices section of this work. In the next subsection which follows, the design of an experimental heating rig for the prototype receiver is presented.

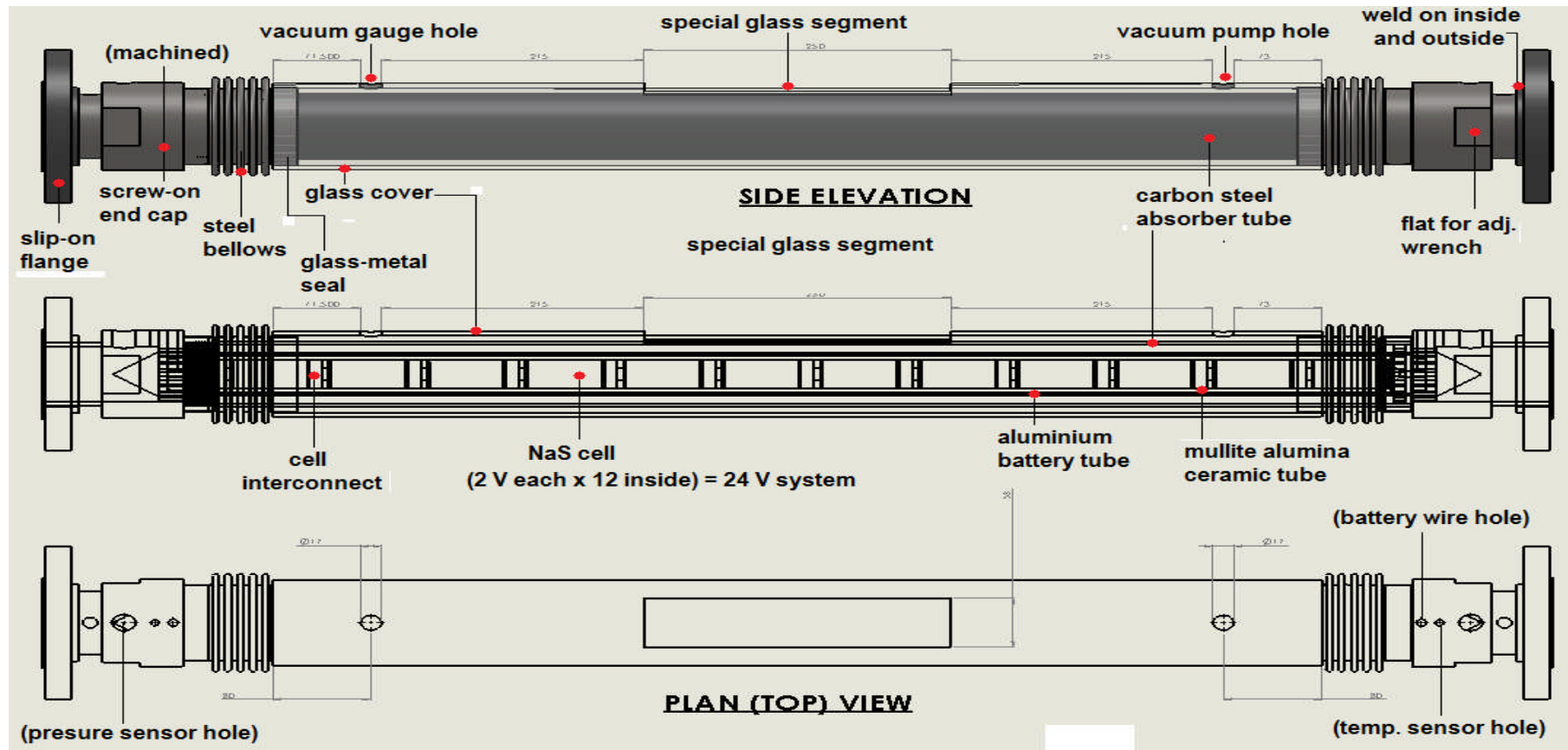


Figure 3-9: Schematic showing final manufacturing drawing of the Conceptual EES receiver

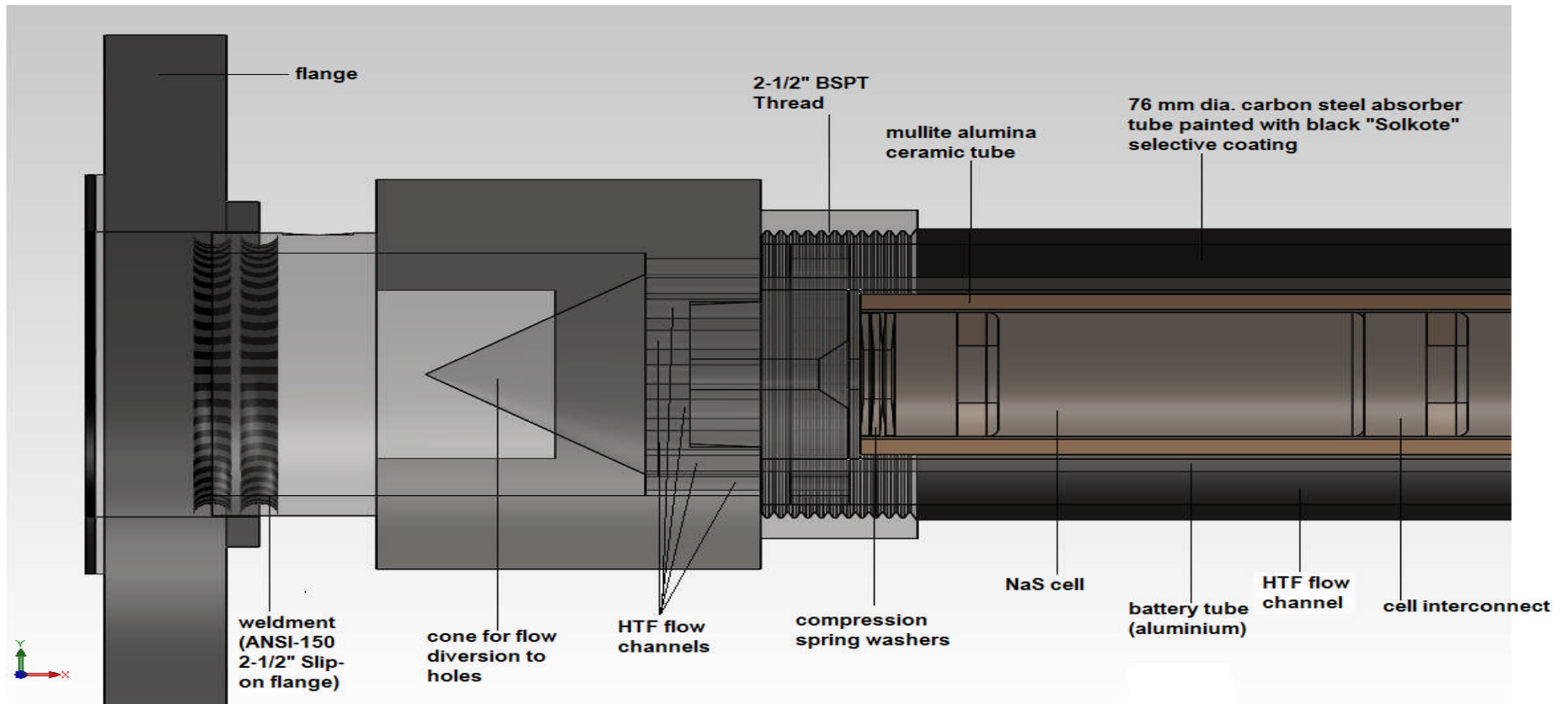


Figure 3-10: Schematic showing some internal components near End Caps of the EES Receiver

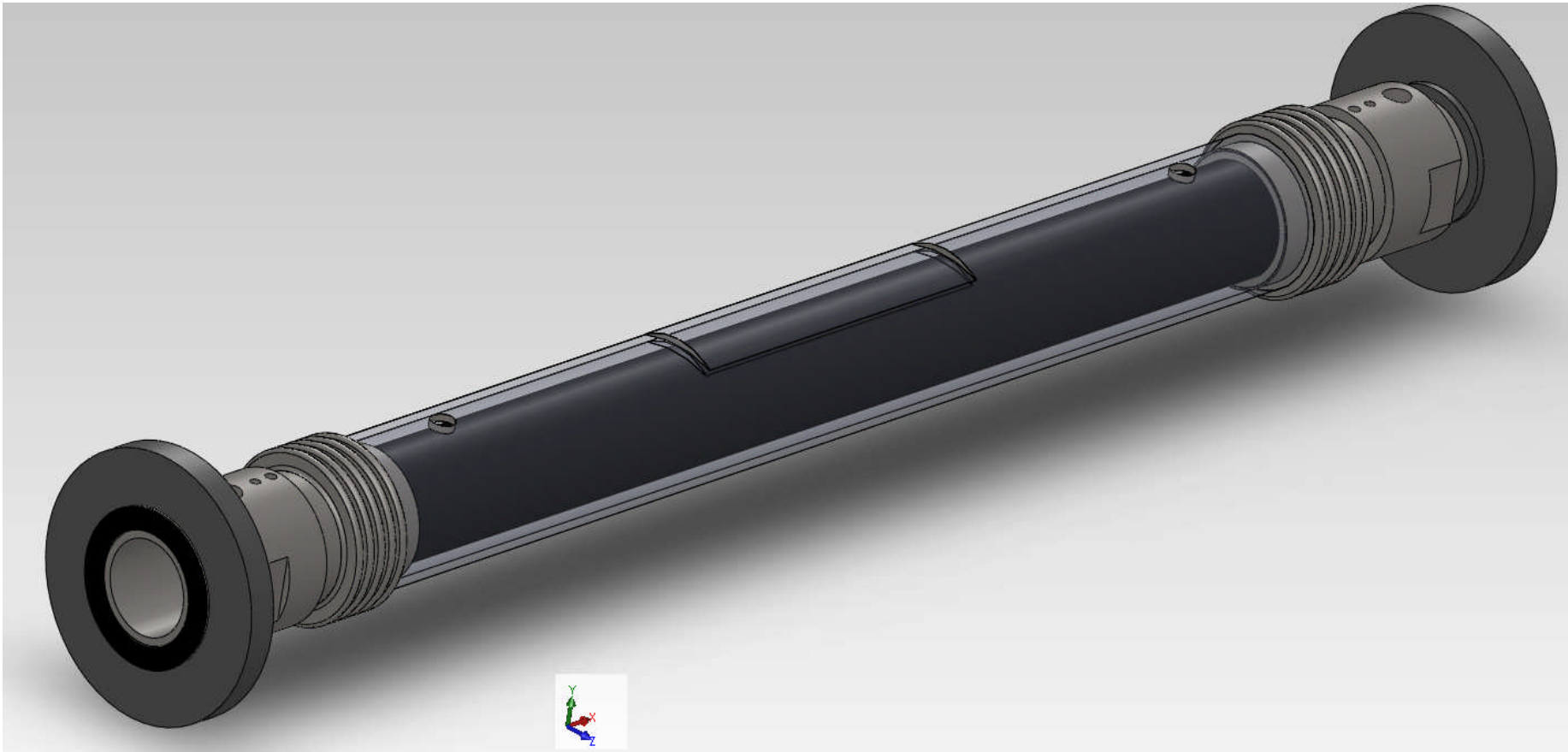


Figure 3-11: Schematic showing angled view of EES Receiver

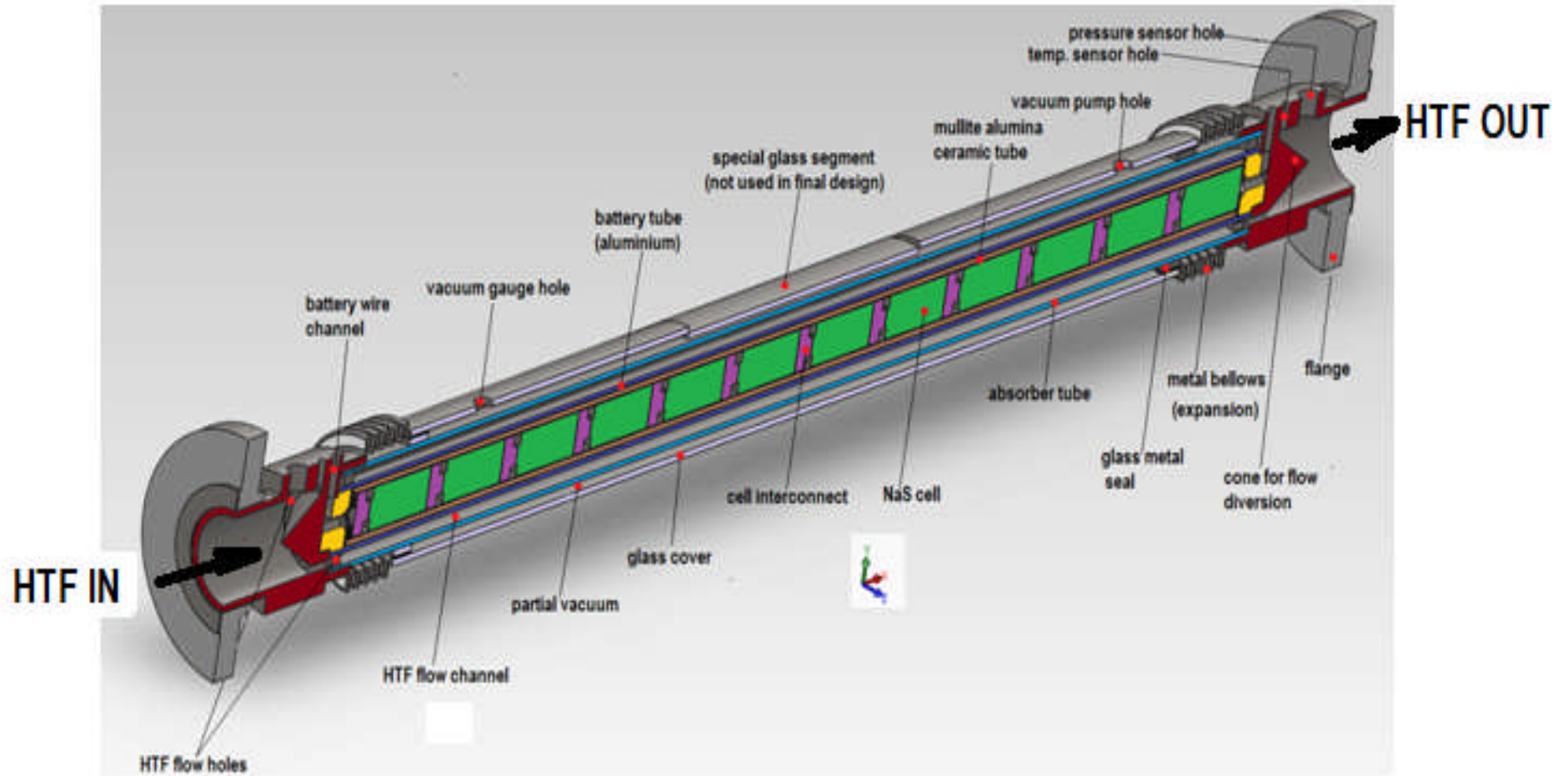


Figure 3-12: Schematic showing section through angled view of EES Receiver

3.3 Design of the EES Receiver Experimental Rig

Following the design of the prototype EES receiver, the next task was the design of a heating rig for experimental testing of the receiver. The rig design had to meet the following criteria:

- (a) Operate up to a temperature of 350°C and pressure of 2.5 bar gauge
- (b) Allow relatively easy connection of the EES receiver mounted in a vertical orientation
- (c) Allow the flow through the EES receiver to be varied, and monitored for temperature (°C) and differential pressure (bar) at high temperatures up to 350°C
- (d) Mount and connect to a selected high temperature pump
- (e) Be implemented in a skid mounted frame, hence movable
- (f) Allow for easy frame disassembly, and recycling, hence constructed from a bolted-up frame
- (g) Allow for expansion of HTF and rig pipework up to operating temperature in the region of 300-350°C
- (h) Accommodate blanketing of HTF in expansion tank with nitrogen gas from an external gas line
- (i) Minimize heat losses to ambient and provide safe working surfaces over pipework, through appropriate insulation selection
- (j) Thermally insulate the pipework from the rig frame.
- (k) Possess a simple, isolatable heat exchanger for cooling the HTF if required
- (l) Heat the HTF *“indirectly”* as is standard practice, via the pipework
- (m) Electrically operate and control the heating process safely, and connect with appropriate data logging equipment.
- (n) Implement steps a-m for the least possible cost, subject to the project budget.

Therefore, from requirement a-m, it became clear that at minimum the rig needed to have:

- (a) A flow branch for EES receiver process flow
- (b) A parallel branch for the connection of a heat exchanger which could be “dropped in/out” the network via isolation valves
- (c) Band heaters for clamping to the pipework
- (d) A specially designed expansion tank for operation up to 350°C

This led to a sketch of the prospective process layout as given in Figure 3-13.

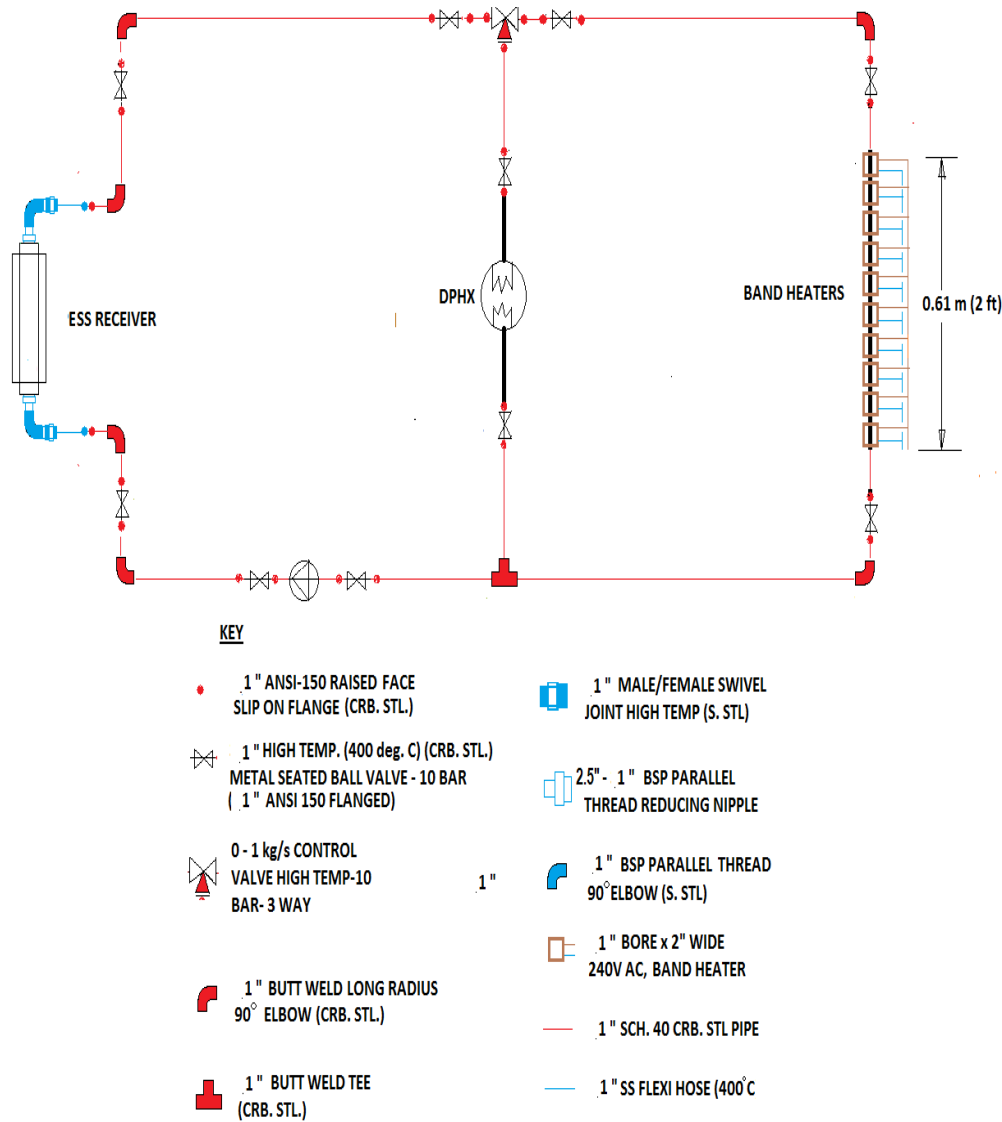


Figure 3-13: Schematic showing initial concept for EES Rig process layout

Although the EES receiver end connections were 2-1/2” ANSI flanges, the decision was made to reduce the size of the connecting pipework to readily 1” or 3/4” piping which would also greatly reduce the volume of the

expensive HTF required in the hydraulics. This meant that a 2-1/2" to 1" concentric reducer would be required at both ends.

With regards to the HTF flow rate, it was determined that the maximum flow rate would be 1 kg/s as this would allow experimental data to be easily scaled to actual flows in PTC solar fields of 9 -10 kg/s, while requiring significantly less pump power and hence lower pump costs.

In order to determine whether 1" or 3/4" piping should be used, as well as to determine the required pump pressure for the target flow, it was necessary to perform a hydraulic analysis. This required sketching of the potential process hydraulics diagram shown in Figure 3-14.

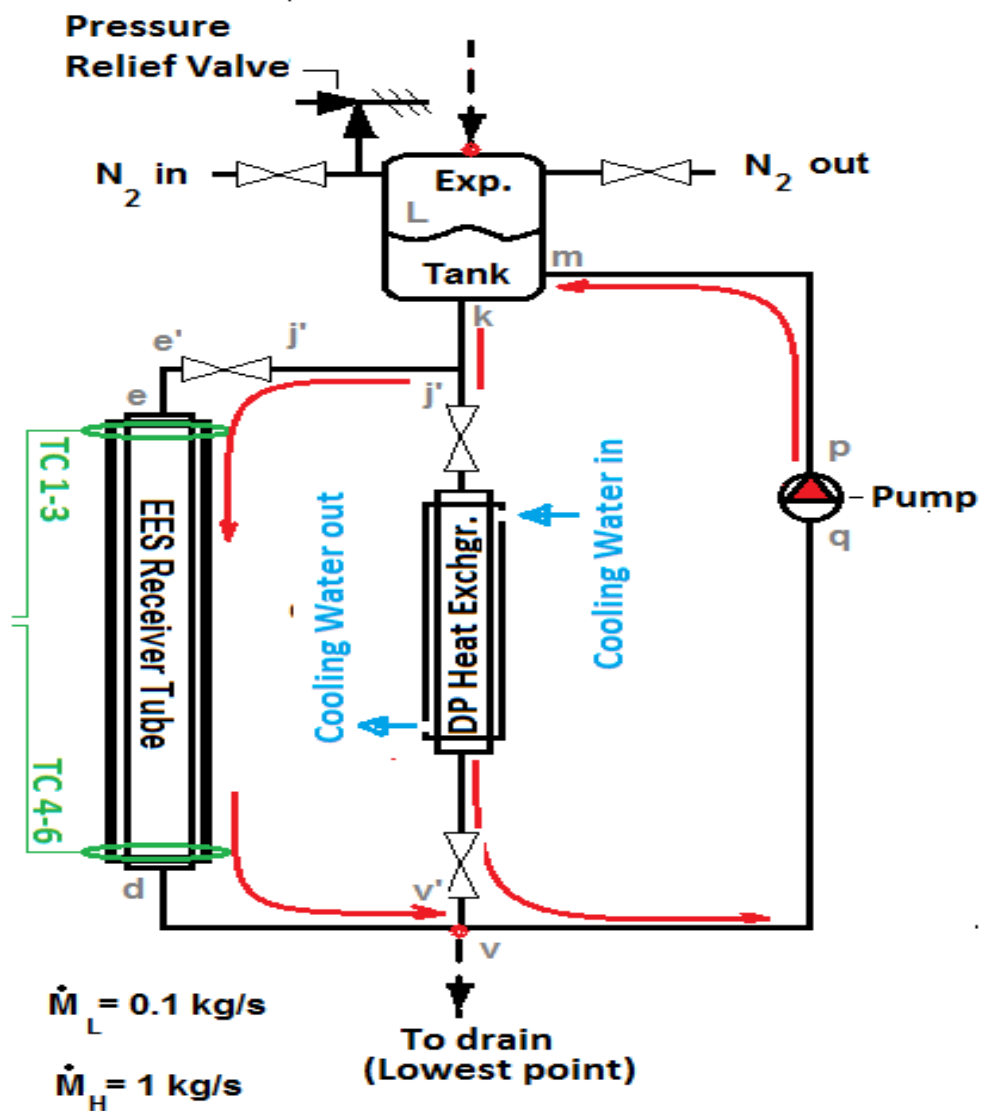


Figure 3-14: EES system process flow loop

This process hydraulic loop was used to draw up a “rough” version of the EES rig pipework using Solid Works 3D CAD software. The node letters correspond to the node letters given in the hydraulic loop (Figure 3-15). In consultation with the supervisors of this work however, it was recommended that the pump be relocated from the position shown in the process flow loop and positioned horizontally in the rig close to the “v” node to allow a “pump through” operation rather than a “suck through” operation. The hydraulic loop pipework and components were then converted to a flow resistance circuit as shown in Figure 3-15. Hydraulic analysis was then performed on this network to determine the required discharge and suction pressures of the pump.

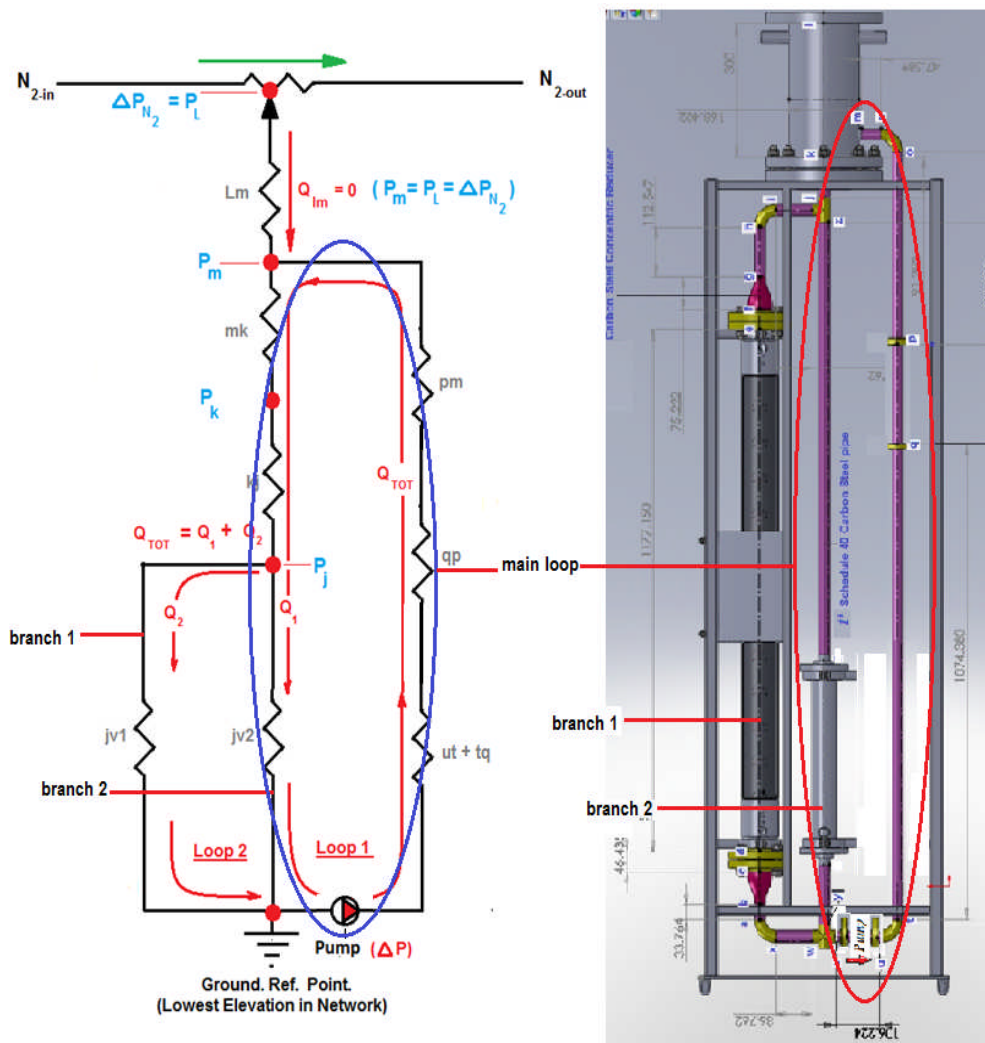


Figure 3-15: Schematic showing flow resistance network and “rough” pipe-work for ESS Rig

Using Bernoulli's principle, hydraulic analysis was performed to determine the required suction and discharge pump pressures for the heating rig at the required flow. Calculations showed that the total pressure drop around the HTF loop for 1" pipe-work and connecting valves would be approximately 2.00 bar at the required flow of 1 kg/s.

Since the vapour pressure of the Therminol 66 HTF was close to 0.3 bar at 300°C a pump suction pressure of 0.5 bar was chosen to provide a margin of safety against cavitation, the required pump discharge pressure was therefore $2.0 + 0.5 = 2.5$ bar. Details of these calculations are provided in Appendix A.

Using the internal volume of the pipe-work, the volume of HTF required to fill the rig was calculated to be approximately 7.7 litres. The related calculation details are provided in Appendix B. In relation to rig heating requirements, a 2 kW heater was found to be adequate, and specifics of these heating calculations are provided for the purpose of the reader in Appendix C. Finally a pipework insulation thickness of 40 mm was determined to be adequate for ensuring a safe temperature of 45°C and these calculation details are given in Appendix D.

3.4 EES Receiver and Rig Construction

In this final section, a brief overview of the key aspects of EES rig construction is provided through photographs. The design of the EES receiver is first illustrated and is followed by that of the EES rig.

3.4.1 EES Receiver Construction Photos

In the process of constructing the prototype EES receiver, the first parts to be machined were the two receiver end caps (Figure 3-16). While these parts were being machined, the absorber tube, battery tube and ceramic tube were simultaneously manufactured. Once completed the end caps and tubes were taken to Ionotec Ltd., where the NaS cells (Figure 3-17), were selected and test fitted. The photographic highlights which now follow, recap the key stages in this process.



Figure 3-16: Photograph showing the Receiver End Cap, and Absorber Tube with internal Battery Tube

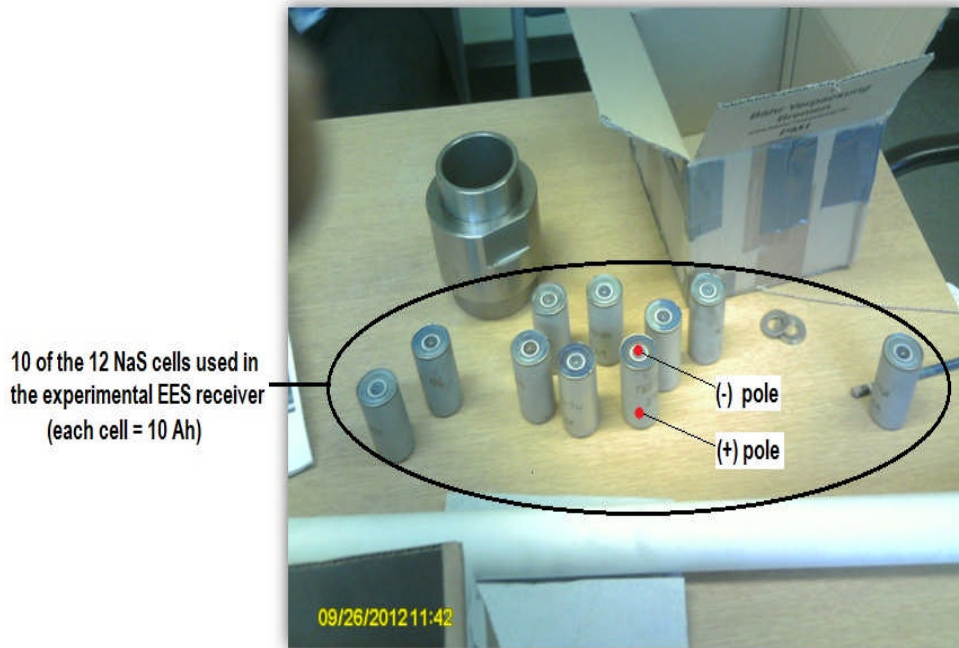


Figure 3-17: Photograph showing the NaS cells fitted into the EES Receiver

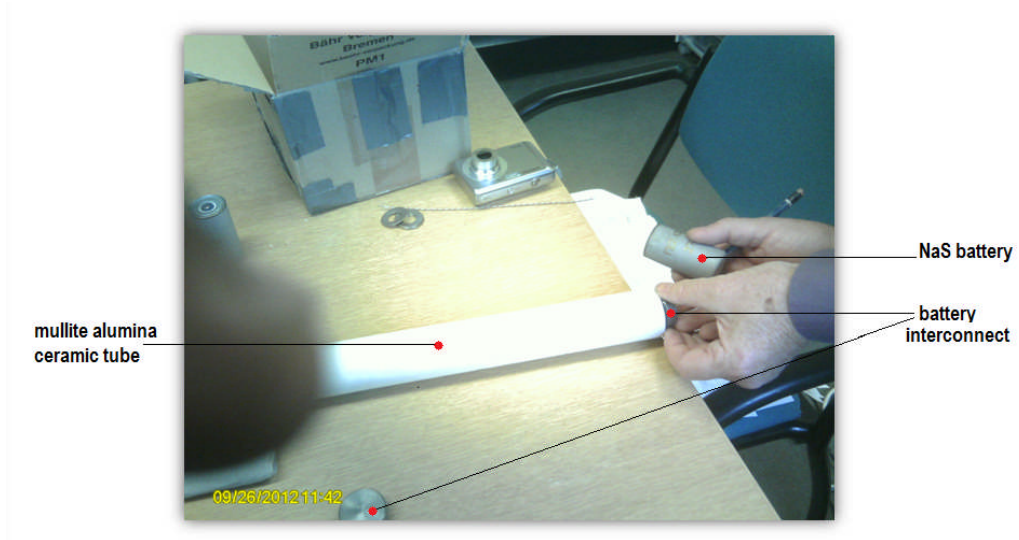


Figure 3-18: Photograph showing insertion of Battery Interconnect and NaS Cell into Ceramic Tube

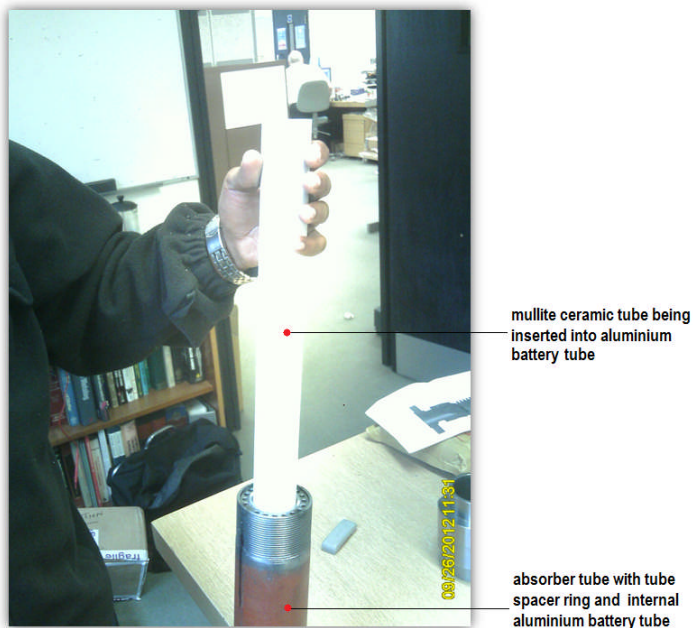


Figure 3-19: Photograph showing insertion of Mullite Ceramic Tube into Battery Tube

Although the ceramic tube was inserted directly into the aluminium battery tube (Figure 3-19) during initial test assembly at Ionotec Ltd, in the final assembly of the receiver, both the NaS cells and the ceramic tube were wrapped with aluminium foil adhesive tape in order to fill the small gaps

between contact surfaces. This would ensure good heat conduction from HTF to the NaS cells placed inside the ceramic tube (Figure 3-20).

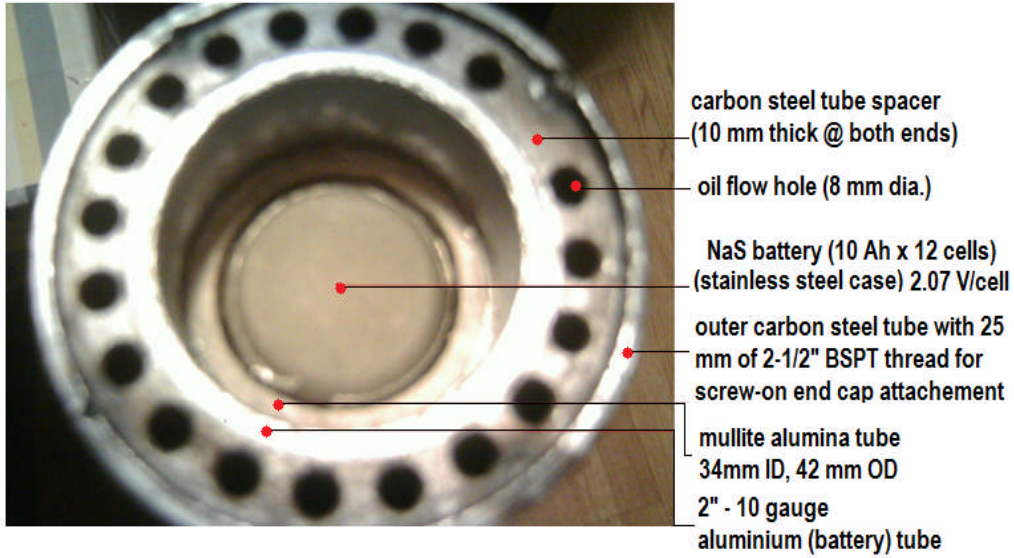


Figure 3-20: Photograph showing tight fitting between inner tubes and central NaS Cell

The receiver end caps on either end of the EES receiver (Figure 3-21) were next fitted with slip-on flanges (Figure 3-22) for connection to the EES rig pipework.



Figure 3-21: Photograph showing end caps at both ends of the EES Receiver



Figure 3-22: Electrical testing of the NaS battery assembly



Figure 3-23: EES receiver screw on End-Cap

For the electrical connection to the EES receiver, the NaS battery wire (type K thermocouple wire) was run from outside the end cap, through the 90 degree bend of the battery channel, attached to the battery/cell connectors (Figure 3-23) in the centre of both end caps, above the battery tube bung. Once connected, they were secured and sealed into position.

One of the major challenges involved in this part of the assembly was preventing the battery wire from snapping while the end caps (1" thread) were screwed onto the absorber tube during final assembly. Two ways of dealing this problem were coiling the wire in the opposite direction to the screw-on motion, and/or leaving the wire coil inside the battery tube, and using a flexible wire hook to pull it out after the end cap was securely screwed into position. A combination of these two methods is what proved successful in the end.

The absorber tube was painted with special Solkote selective solar paint, which has high absorptivity to solar radiation, but low emissivity of long wave radiation. Once the paint had dried (overnight), the other internal tubes, along with the NaS cells were inserted. Next the glass cover and expansion bellows were installed over the absorber tube and then the other endcaps were fitted, completing the receiver assembly (Figure 3-24).



Figure 3-24: Fully assembled EES Receiver

The glass and bellows assembly however was later removed as it became unnecessary when time and resource constraints ruled out outdoor solar heating tests. Thus experimentation was confined to an indoor heating operation using electrical band heaters clamped directly to the outer surface of the main absorber tube.

In the next sub-section the construction of the EES heating rig, is illustrated by means the images and the brief comments which now follow.

3.4.2 EES Rig Construction Photos

This section contains a selection of photos outlining various aspects of the rig construction for the ESS receiver. The main tasks involved in this part of the project were:

- cutting, fitting and welding the pipework with the ESS receiver
- building the double pipe heat exchanger
- building the expansion tank
- constructing the rig frame
- Hanging the pipework securely in the rig frame.

All these tasks were undertaken by Lowe Engineering, Leeds, U.K. A photographic overview of the main phases of construction is given in Figures 3-25 through to 3-28 which now follow.



Figure 3-25: Photograph of Expansion Tank during construction



Figure 3-26: Photograph showing connection of EES Receiver into Rig pipe-work

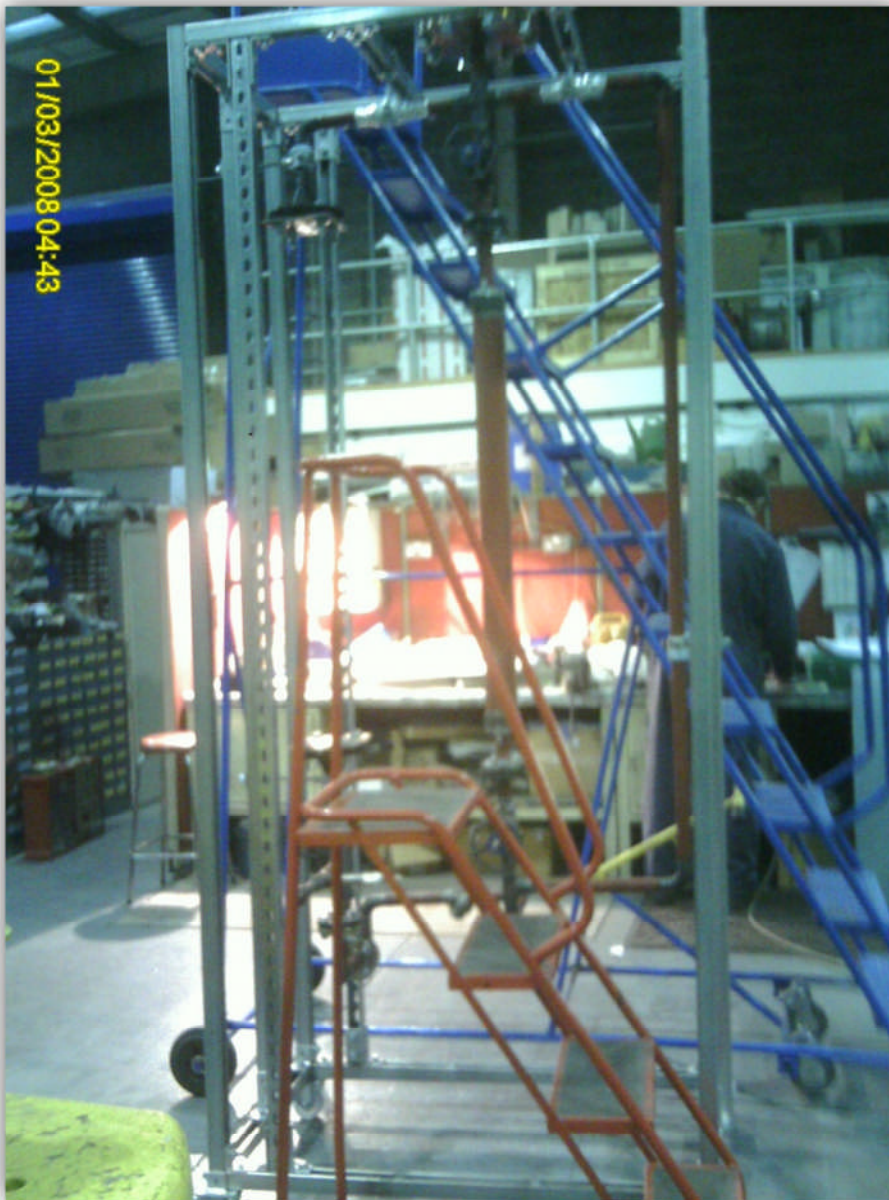
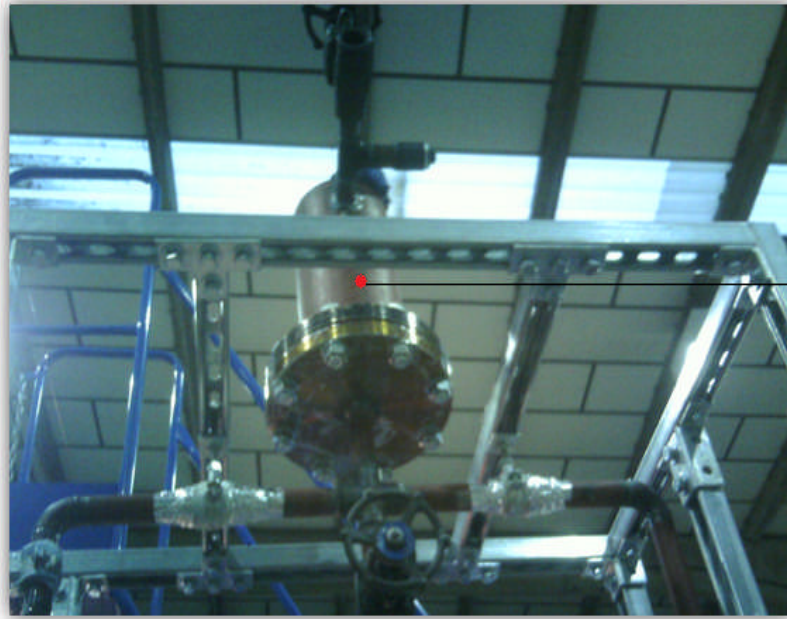


Figure 3-27: Photograph showing Rig Frame under construction with section of pipe-work mounted



Expansion tank
bolted into EES
receiver rig
pipework

Figure 3-28: Photograph showing mounted of Expansion Tank and hanging of pipe-work using insulative High Temperature Pipe Wrap



Figure 3-29: Photograph showing skid mounting of the Rig Frame

After the pipe-work was fitted, the instrumentation devices such as thermocouples, and gauges were connected and the pipe-work was insulated (Figure 3-30). High temperature rock wool (up to 700°C) pipe sections were used for this purpose.

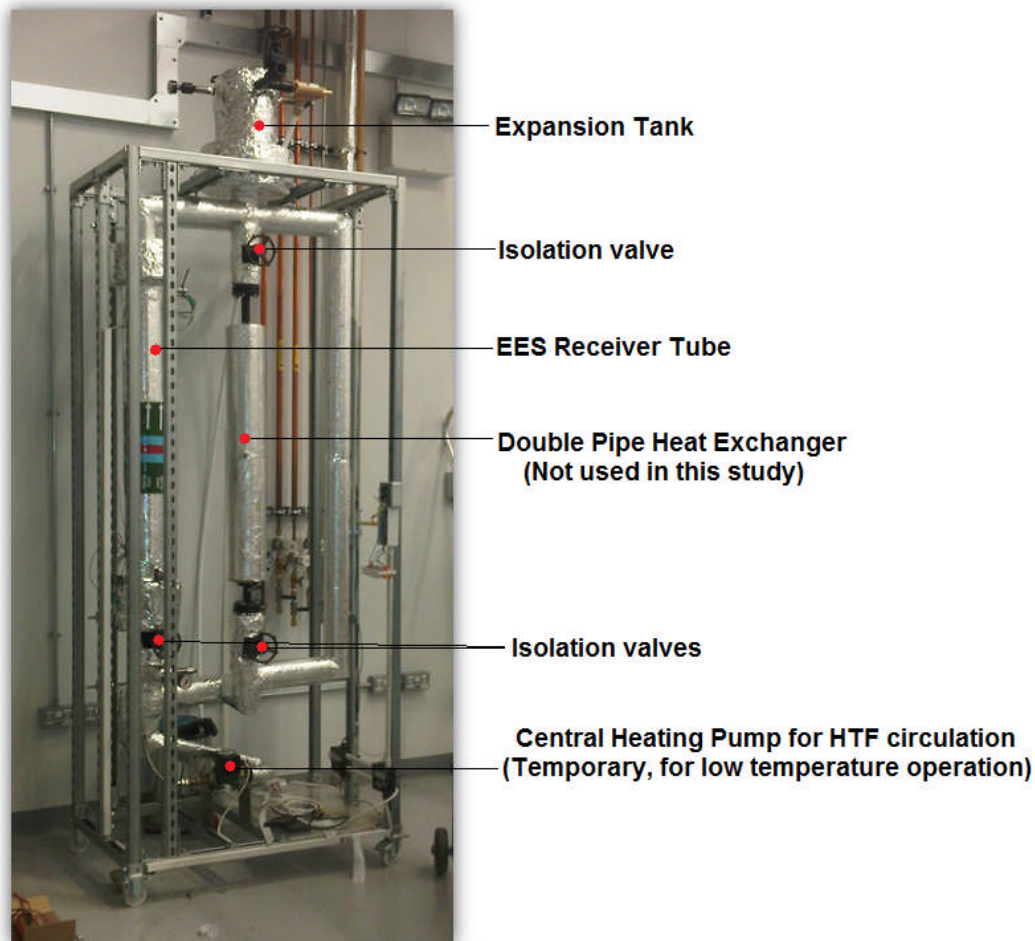


Figure 3-30: Photograph showing insulated pipe-work and Expansion Tank

Although a reasonably priced high temperature pump was identified from March May Pumps, U.K., it could not be obtained in the time frame required for conducting experiments. Consequently the operation of the rig was limited to observing of the initial heating from an ambient up to a NaS cell phase change temperature of close to 120°C. This allowed the use of a simple central heating pump (Figure 3-31) for circulating the Therminol 66 HTF donated to the project by Solutia U.K.



Figure 3-31: Photograph showing central heating pump used in the ESS Receiver Rig.

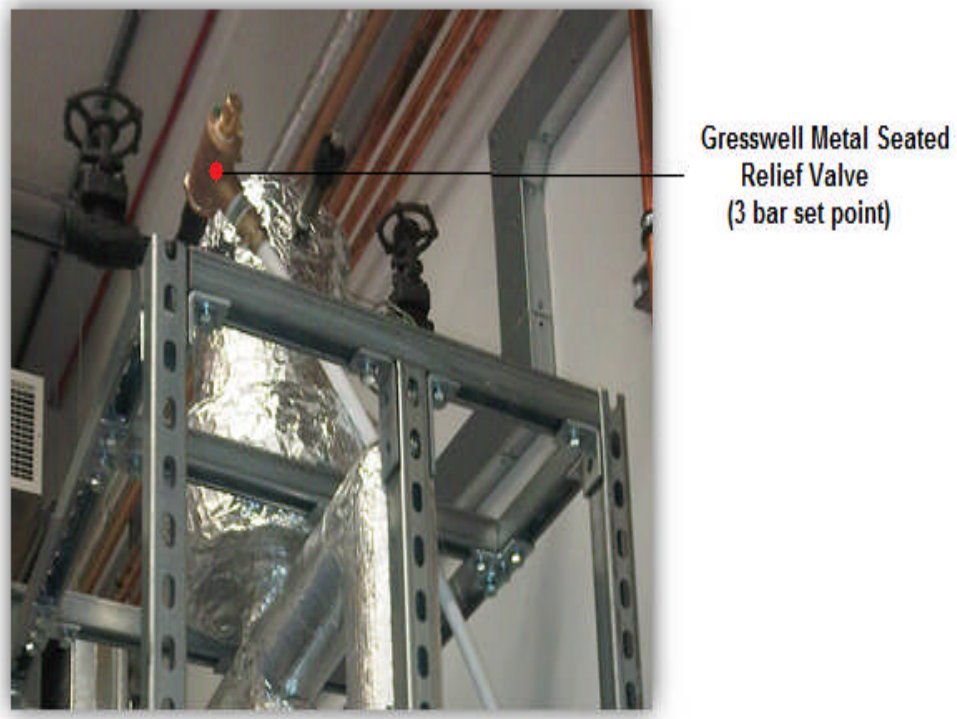


Figure 3-32: Photograph showing relief valve and drain pipe

For safety purposes, the tank relief valve (Figure 3-32) was fitted with a drain pipe that lead down to an oil sump below the EES rig.

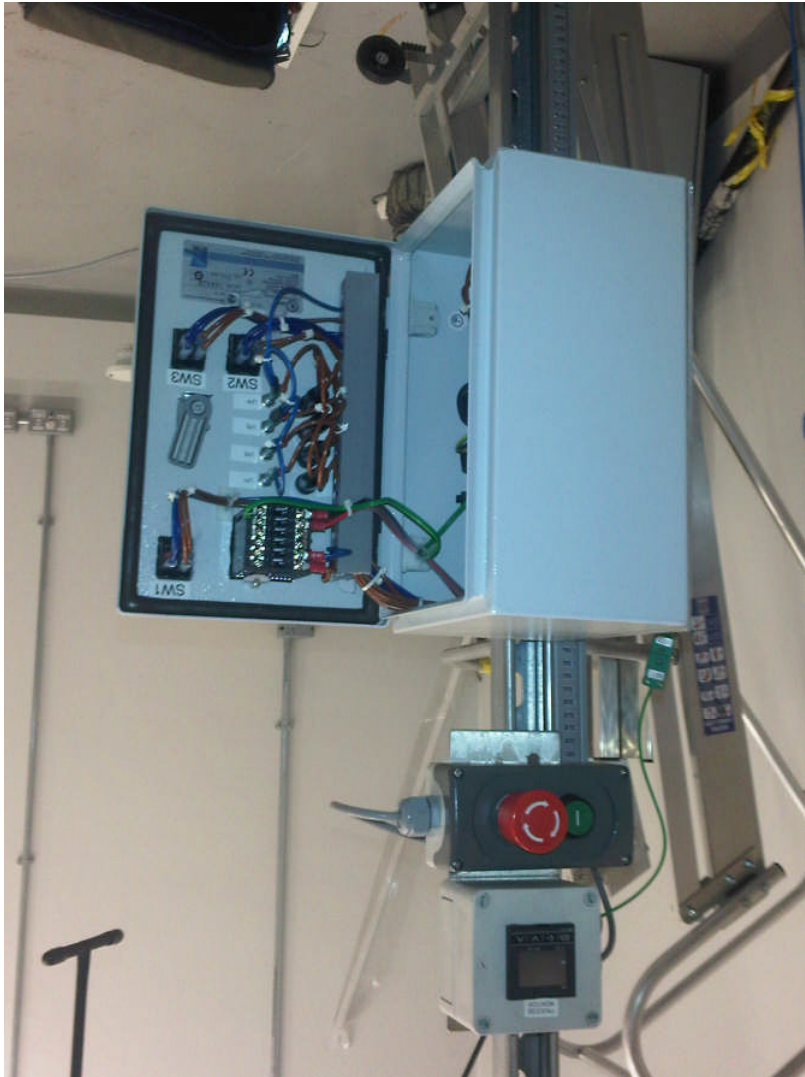


Figure 3-33: Photograph of EES rig control box

The rig was then completed with the fitting of the control box, process monitor and emergency stop switch (Figure 3-33). The electronics and controls were also specially designed as a part of this research work, and the reader will find these details in Appendix X.

Finally the entire rig was electrically tested and certified for operation in the Future Fuels laboratory of the Energy Research Institute (ERI) at the University of Leeds, UK.

This now concludes an overview of the key highlights of the construction phases of the EES receiver and rig, used in the experimental work of this study.

Chapter Summary

In this chapter the design and construction of a conceptual EES receiver and its associated operating rig have been presented. The rig has been conceptually designed to operate at a maximum duty of 350°C and 2.5 bar, with a maximum flow rate of 1kg/s.

However, in context of this current work, financial and time constraints dictated, that maximum temperature be limited to 120°C. This limitation allowed experimental observation of only the initial heating-up of the EES receiver to the phase change temperature of the NaS cells. With the acquisition of a high temperature pump, the heating of the NaS cells up to their full operating temperature of 350°C will be possible. Further still, the charge/discharge operations on the NaS cells, which are permitted only at temperatures above 300°C will also become possible.

Herein concludes the collective presentation of both physical and design details for the conceptual EES receiver and the associated experimental rig. In the next chapter, the EES receiver concept is further developed, by explicating the important mathematical models used for simulating the basic operation of the system.

Chapter 4

Modelling the Conceptual EES Receiver

Introduction

This chapter concerns the modelling of heat transfer processes in the conceptual electrical energy storage (EES) receiver previously described in Chapter 3, primarily for use in parabolic trough collector (PTC) power plants.

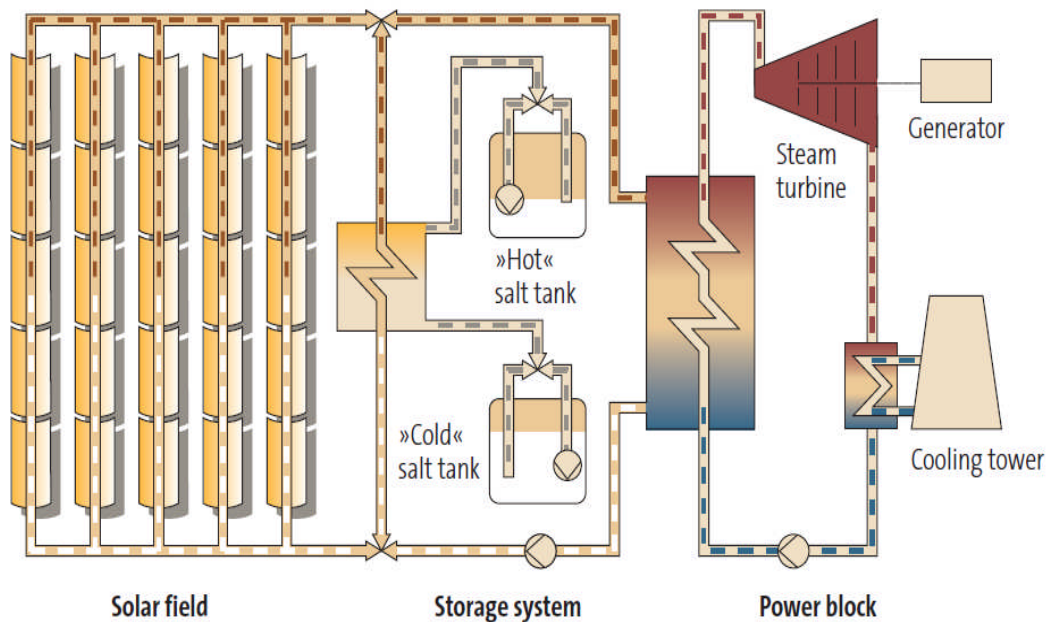


Figure 4-1: Schematic showing block layout of a standard PTC Power Plant (Source: ^[183])

A typical PTC power plant layout (Figure 4-1) comprises three main parts: a solar field, a thermal storage block and a power block. The solar field consists of long rows of highly reflective parabolic trough mirrors, ^[184] arranged in loops, and attached to large rotatable tracking platforms. These platforms are oriented axially along the north-south line where they track the sun along an east to west path (Figure 4-2). Incoming solar “beam” radiation is concentrated by a factor of 20 - 80 suns unto a selectively coated black absorber tube, at the focal axis of the trough. Typical solar to electrical conversion efficiencies of 24% ^[185] are standard

for today's commercial PTC plants, a value significantly higher than the efficiency value (20%) of the best photo-voltaic modules available in the commercial solar market ^[186].

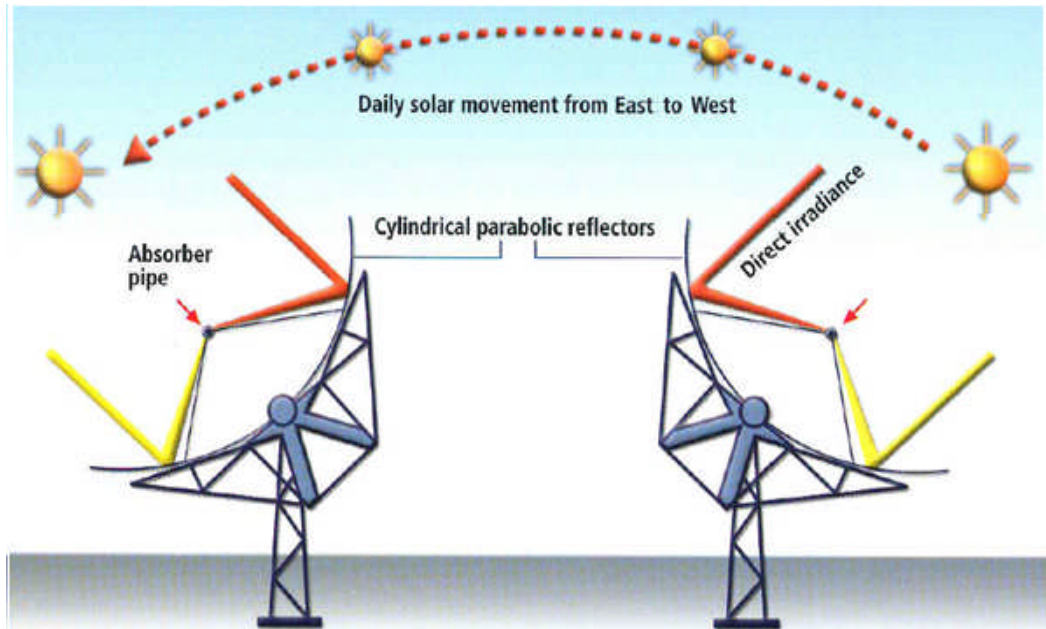


Figure 4-2: East-West tracking of a parabolic trough collectors (Adapted:^[187])

The concentrated solar radiation absorbed by the PTC receiver typically heats a special fluid (HTF) circulating inside (at 8-9 kg/s) up to a working temperature of about 393°C ^[188]. The hot fluid is then pumped into the plant's power block, where it exchanges heat to produce superheated steam (100 bar, 371°C) for driving a Rankine power cycle ^[189] steam turbine, which is mechanically coupled to an electric generator. Once through the power block, the cooled HTF is pumped back into the solar field for the cyclic reheating process.

PTC technology is also the most widely deployed and proven CSP technology with a track record of performance going back the early SEGS plants of the 1980's ^[189]. As explained earlier in this thesis, PTC technology can make an important contribution to the renewable power grid of the future by aiding the integration of other renewables such as wind and photovoltaics, primarily because of an inherent energy storage

capability. Consequently, any effective method of enhancing the energy storage ability of these plants is consequently an aid to general mass integration of renewables into the energy grid of tomorrow. In this regard, the conceptual EES receiver, based on hybridization of NaS battery and PTC technologies is proposed as one such method.

Bearing in mind this introductory background to PTC power plants and the associated relevance of the EES receiver concept in mind, the first chapter section (which follows next), outlines exactly how the conceptual receiver would be operated in a typical PTC solar field. The second continues by explaining the important solar optics required for system analysis. The third defines the important fluxes, parameters and correlations used in the model. Finally, the fourth section presents the heat transfer models used for system description and their method of solution. A chapter summary then recaps the key points discussed.

4.1 Operation of the EES Receiver in a typical PTC Solar Field

The hybridizing of NaS and PTC technologies to build a conceptual EES PTC power plant is possible because of the following reasons.

- a) The 300-400°C operating temperature range of both technologies [4, 190] is naturally complementary.
- b) The layout of the conceptual EES PTC plant would be identical to that of an existing PTC power plant, requiring only a special modification of the receiver in the solar field.
- c) The modification required for production of the EES receiver will affect chiefly the diameter (cross sectional) of the traditional receiver and therefore should adapt itself easily to existing operating facilities.

Some important conditions identified for the operation of this conceptual PTC plant are as follows:

- a) The volume of the HTF annulus and/or mass flow in the EES receiver must be correctly sized to maintain the heat transfer/enthalpy requirements of the PTC plant.
- b) The HTF mass flow and heat exchange, along with NaS cell charge/discharge must be controlled as required to maintain the NaS cell temperatures ideally within the 300-450°C operating range.
- c) The NaS cells should ideally be charged during the main daylight hours, storing available solar energy in electrical form for discharge during evening and night-time hours, when the sun is unavailable and energy demand peaks.
- d) In the situation that the cells reach full charge during the daylight hours, the endothermic heat flux normally absorbed during the charging process will become zero. Consequently, if solar flux continues to pass into the cells, cell temperatures could rise above the maximum operating value and cause cell failure. Therefore, HTF mass flows must be controlled such that the temperature of the HTF in the annulus around the cell always stays within the 300-450°C operating range. As long as this condition is satisfied, the NaS cell temperature will only approach (Figure 4-3), but never exceed HTF operating temperature range, with flux into the cells becoming zero as $\bar{T}_{NaS} \rightarrow T_{htf}$.

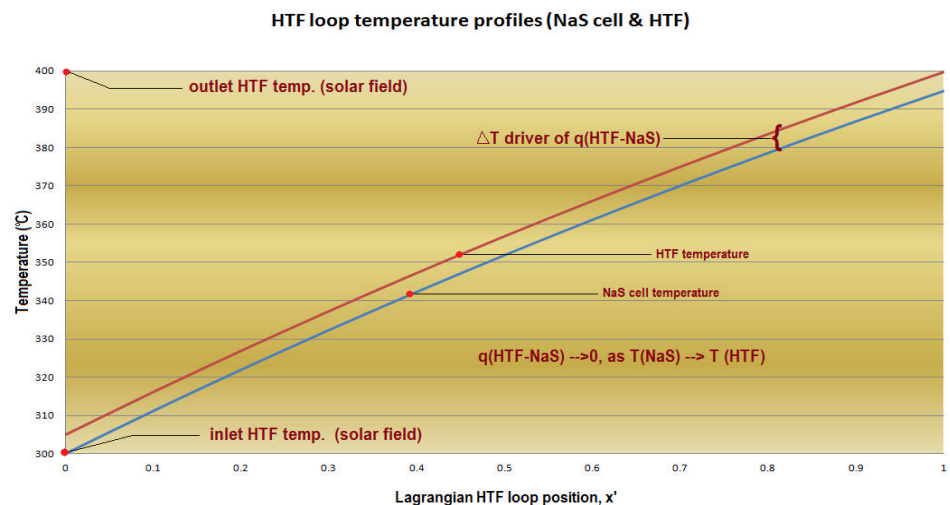


Figure 4-3: Schematic illustrating the NaS and HTF temperature profiles

- e) Fully charged cells should NOT be discharged for extended periods during daylight hours, since the discharge process is exothermic. However, if this must be done outside of night time hours (eg. to provide ramping reserves and other ancillary power support services), EES receivers should be partially or totally defocused from the incident solar radiation as required to stay within cell operating temperature limits.

In addition, the HTF temperature and mass flow in the EES HTF loop (Figure 4-4) must be controlled so that the heat generated during cell discharge is sunk from the NaS cells into the power plant block, or into the thermal storage tanks.

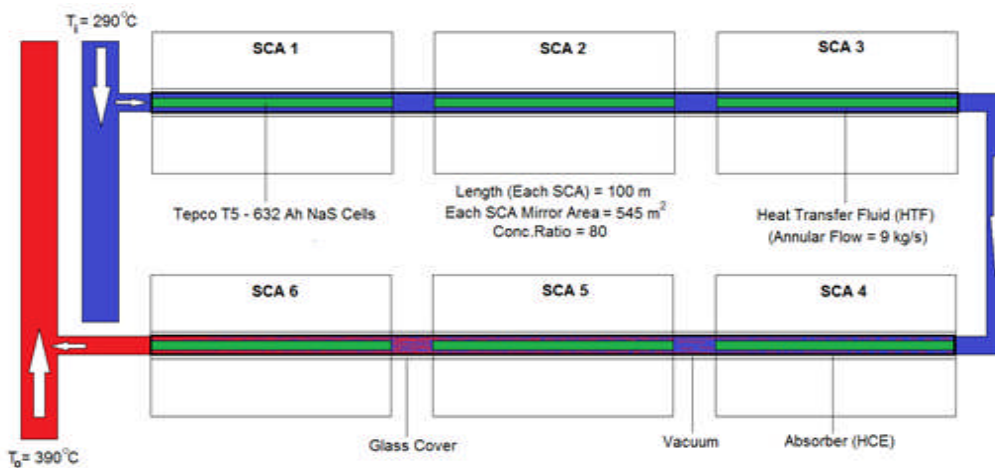


Figure 4-4: Schematic representation of the conceptual EES HTF loop

Heat transfer in the EES receiver comprises:

- Heat transfer from the sun to the working fluid
- Heat losses from the EES receiver to the ambient
- Heat transfer from the working fluid to the NaS cells
- Heat transfer from the NaS cells to the working fluid (occurs during electrical discharge)

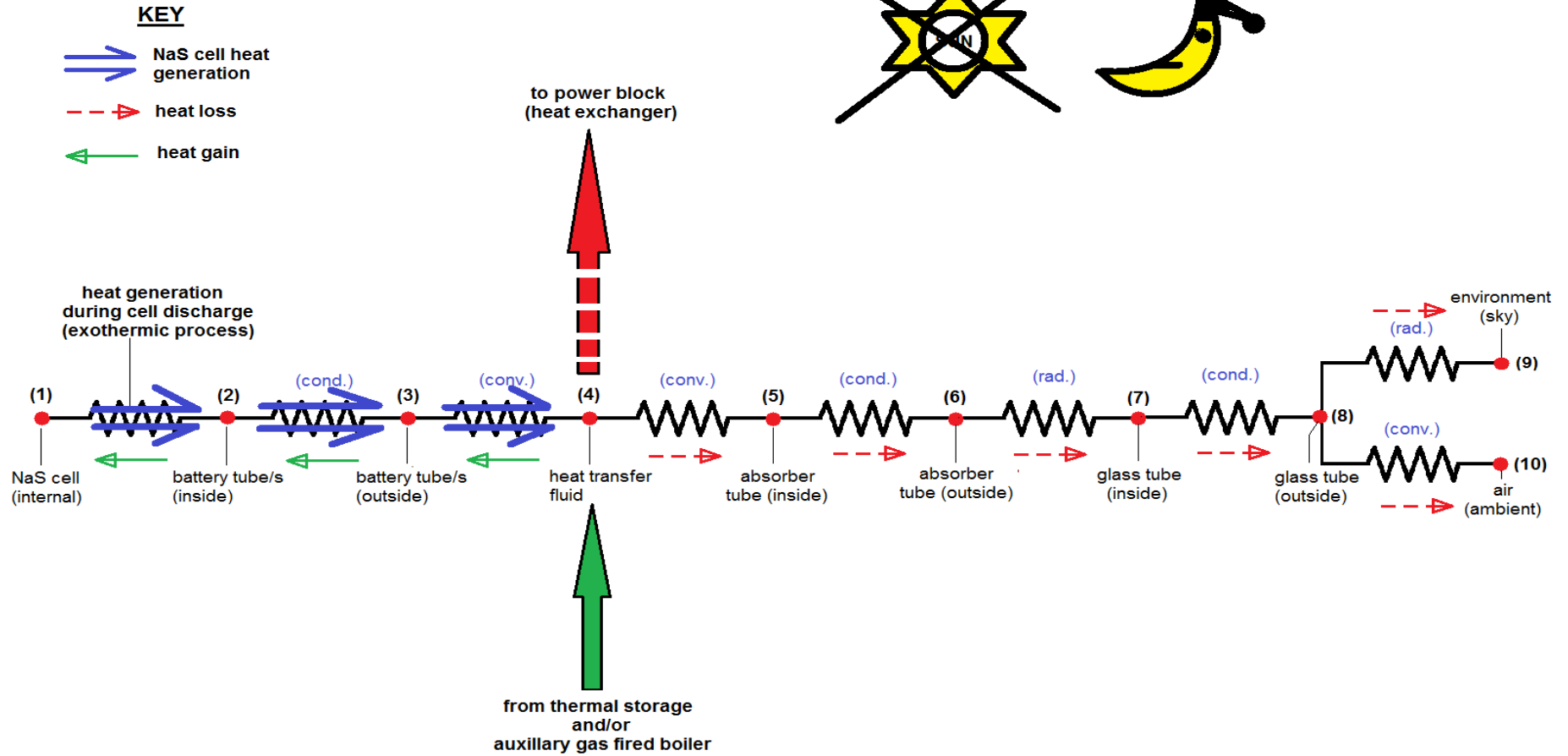


Figure 4-5: Thermal resistance model of heat flow in the EES receiver (night time)

During daytime hours, solar radiation is used to:

- a.) Heat the NaS cells in the EES receiver up to a working temperature of between 300°C (HTF inlet temp.) and 400°C (HTF outlet temp.).
- b.) Raise the HTF up to a typical working temperature of about 400°C for driving the Rankine steam cycle of the power plant.
- c.) Charge the thermal energy storage system (molten salt tank).

The EES power plant could also provide another very significant advantage over the conventional plant during night time operation. With much lower ambient temperatures, an absence of solar radiation, and possibly clear skies at night time, the temperature of HTF in the solar field will gradually fall and freezing could occur. This is largely owing to heat radiation to the sky and convection to the ambient by the receivers (Figure 4-5). This problem is solved in conventional PTC plants by circulating the HTF through an auxiliary heat exchanger powered by a gas fired boiler.

In the EES power plant, the NaS cells would be discharged during night time hours for power generation. NaS cell discharge is an exothermic process, and with appropriate controls, the heat generated during night time discharge could prove effective in maintaining the HTF temperature of the solar field, without requiring auxiliary power. More will be said about this in Chapter 6.

Now that the method of operation the EES receiver has been presented, the next section (Section 4.2) explains briefly the important solar optics needed to visualize the physics behind the mathematical models about to be discussed in this chapter.

4.2 Optics of the PTC collector

PTC power plants function primarily to convert solar radiation concentrated onto a special receiver tube, into electrical energy for supply to the grid. The section of the PTC plant responsible for collecting this

energy is known as the solar field, which is made up of long rows of “parabolic shaped” collectors (Figure 4-6) .

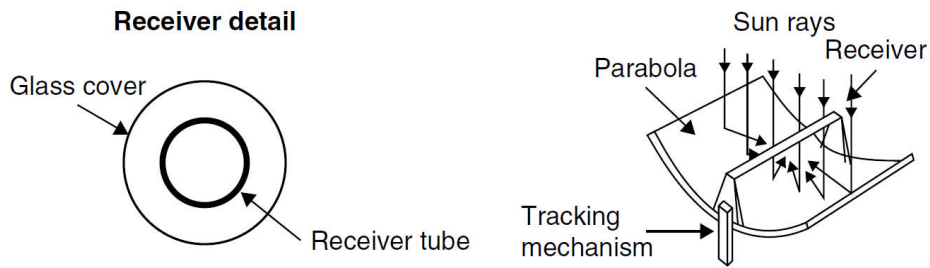


Figure 4-6: Parabolic trough collector system (Source: [191])

The magnitude of concentration of a parabolic trough collector is given by the “Concentration Ratio (CR)”. The most commonly used ratio is the “geometric” concentration ratio defined as:

$$CR_{geometric} = \frac{\text{Collector aperture (width)}}{\text{Absorber diameter}} \quad \text{(Equation 4-1)}$$

This ratio is useful mainly for quoting the concentrating “physics” of a PTC system. For purposes of analysis and simulation however, the “Flux Concentration Ratio” should be used. This term effectively describes the ratio of the parabolic surface area (of the trough collector) to the circumferential absorber area (of the receiver tube) and is given as:

$$CR_{flux} = \frac{\text{Collector aperture (W)} - \text{Collector shading}(D_{abs})}{\text{Absorber circumference } (\pi D_{abs})} \quad \text{(Equation 4-2)}$$

As explained earlier, direct normal solar radiation (DNI) reflected from a parabolic mirror of the trough collector is concentrated onto a linear receiver tube running down the centre line of the trough (Figure 4-6). The radiation intercepted is here referred as “direct” because the rays travel a straight line path from the sun, directly to the receiver. Concentrating systems can focus only this form of solar radiation, and consequently the other type of solar radiation known as “diffuse” or “scattered” radiation is not included in PTC optical analysis.

In addition to being “*direct*”, the solar radiation should also be “*normal*” to the receiving surface to achieve a proper focus. This means that the angle of incidence, (angle between the incoming solar ray and the centre line of the trough) should be ideally zero, a task assigned to the trough’s tracking system. However, no practical collector system is able to achieve a 100% focus accuracy, and therefore in optical analysis an “*incidence angle modifier*” must be used. In this work the PTC incidence angle modifier determined from experimental tests by Dudley *et.al* at the Sandia National Laboratory was used and is given as:

$$K = \cos(\theta_i) + 0.000884\theta_i - 0.00005369\theta_i^2 \quad \text{(Equation 4-3)}$$

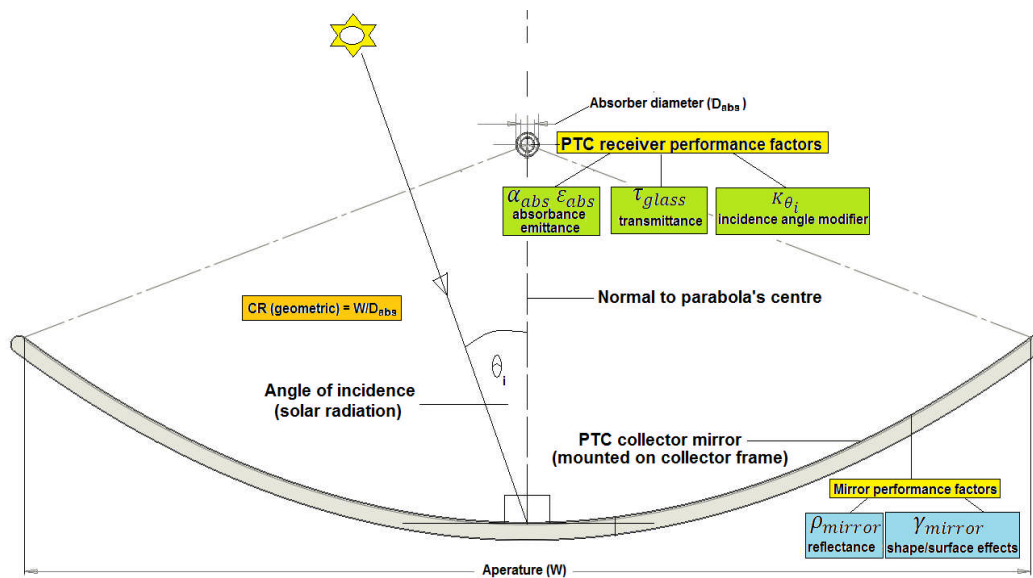


Figure 4-7: Schematic illustrating important optical characteristics of PTC collector

The optical efficiency of the collector and receiver combination used in a PTC solar field is one of the most significant factors in determining the overall efficiency of a PTC power plant (Equation 4-4).

$$\eta_{total} = \eta_{solar\ field,(optical)} \times \eta_{power\ block,(thermoelectrical)} \quad \text{(Equation 4-4)}$$

Consequently precision engineering is required in the design and manufacture of the receiver and concentrating mirror units that make up the PTC solar field. Still yet, real world collector and receiver assemblies

can only approach ideal performance. This is due primarily to inefficiencies (Figure 4-7) in the performance of mirrors, (*reflectance* $\rho_m < 1$); the glass cover, (*transmittance* $\tau_{gc} < 1$); and the inner absorber tube, (*absorbance* $\alpha_{abs} < 1$, and *emittance* $\varepsilon_{abs} > 0$).

Finally, two other important deviations from ideal performance, are with respect to heat losses:

- (a) Through the annular space between the glass cover and the inner black absorber tube.
- (b) At each of the tube support points along the length of the trough.

In real world receivers, the annular space between absorber and glass cover is not a perfect vacuum, and there is also significant heat loss at the tube support points, exacerbated especially by wind effects.

This now concludes a very elementary overview of the important optics of the PTC collector/receiver system, particularly limited to only what was necessary for the general reader (not the expert) to follow in this chapter. The next section presents the important fluxes, parameters and correlations used in the description of the conceptual system. It is also the final descriptive section of this chapter, just before the general presentation of the models used in this work.

4.3 Fluxes, Parameters and Correlations used in the EES Receiver Heat Transfer Model

The first sub-section which now follows, briefly defines the heat fluxes used in the heat transfer models.

4.3.1 Definition of Heat Fluxes

For heat transfer analysis of the EES receiver, the important fluxes described in the mathematical models are defined in Table 4-1. They are also illustrated with the aid of Figure 4-8 (on the next page), a schematic which provides an arbitrary cross sectional view along the length of the collector/receiver assembly.

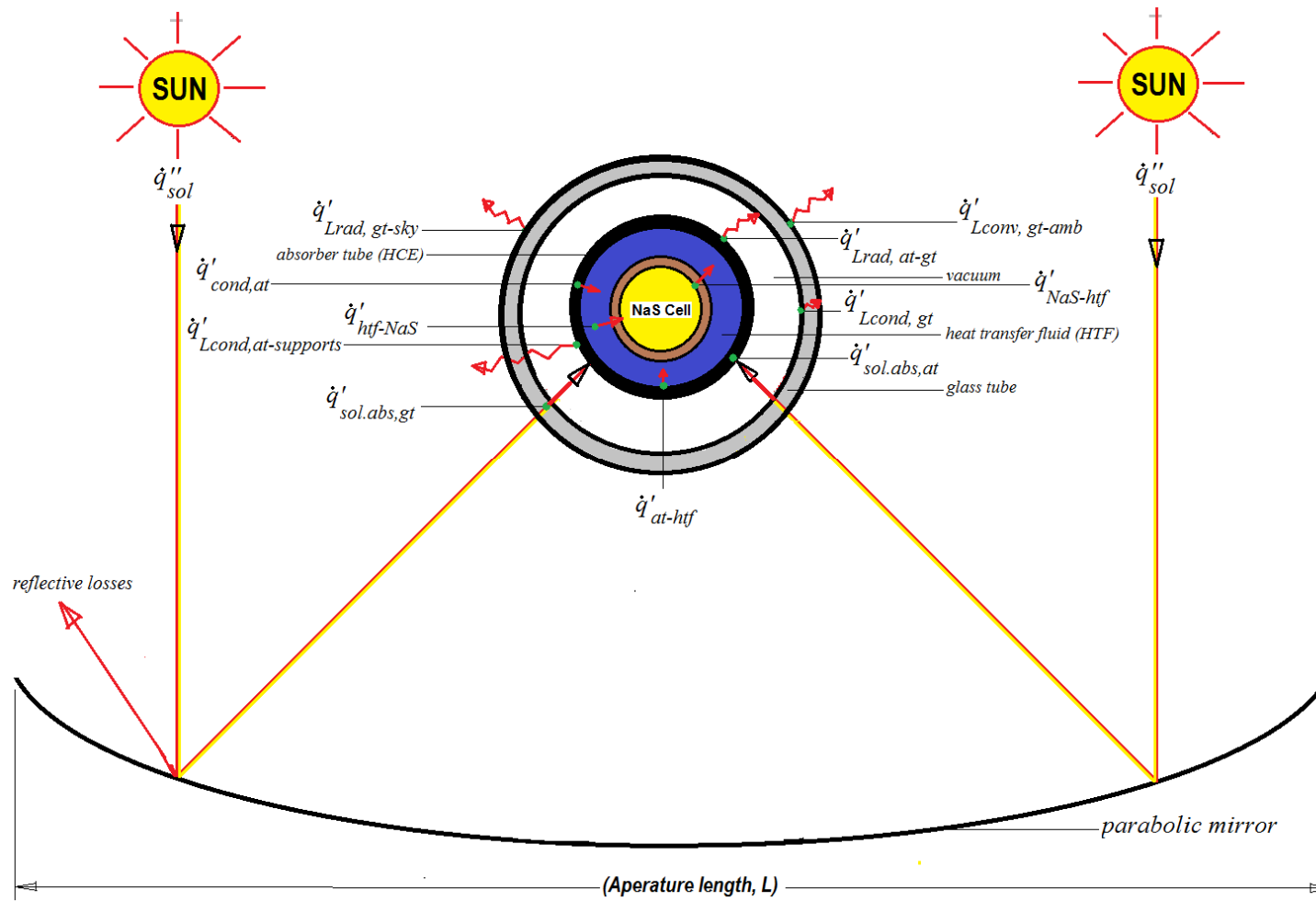


Figure 4-8: Schematic showing heat fluxes in the EES receiver cross section

The heat fluxes described in the model are as follows:

Table 4-1: Definition of Heat Fluxes

Heat Flux (W/m)*	Heat Transfer Method	Heat Transfer Direction	
		From	To
$\dot{q}'_{htf-NaS}$	conduction	heat transfer fluid	NaS cell
$\dot{q}'_{cond,bt}$	conduction	battery tube outer surface	battery tube inner surface
$\dot{q}'_{htf-bt,o}$	convection	heat transfer fluid	battery tube outer surface
\dot{q}'_{at-htf}	convection	absorber tube inner surface	heat transfer fluid
$\dot{q}'_{cond,at}$	conduction	absorber tube outer surface	absorber tube inner surface
$\dot{q}'_{Lrad,at-gt}$	radiation	absorber tube outer surface	glass tube inner surface
$\dot{q}'_{Lcond,gt}$	conduction	glass tube inner surface	glass tube outer surface
$\dot{q}'_{Lconv,gt-amb}$	convection	glass tube outer surface	ambient
$\dot{q}'_{Lrad,gt-sky}$	radiation	glass tube outer surface	sky
$\dot{q}'_{sol.abs,at}$	radiation	sun	Abs. tube outer surface
$\dot{q}'_{sol.abs,gt}$	radiation	sun	glass tube outer surface
$\dot{q}'_{Lgt,tot}$	convection, radiation	sun	ambient
$\dot{q}'_{bt,i-NaS}$	conduction	battery tube inner surface	NaS cell

* per unit length of the EES receiver

Next, the important terms, variables and parameters used for identification and descriptive purposes in the model are given in Table 4-2.

Table 4-2: Definition of key parameters

Parameter	Description	unit	Parameter	Description	unit
A_{col}	Collector mirror area	(m ²)	$\alpha_{conv,gt}$	Convective heat transfer coefficient from glass tube to ambient	(Wm ⁻² K ⁻¹)
ϵ_{at}	Emissivity of absorber tube	none	$\alpha_{conv,at}$	Convective heat transfer coefficient from absorber tube to glass tube	(Wm ⁻² K ⁻¹)
ϵ_{gt}	Emissivity of glass tube	none	$D_{at,o}$	Outer diameter of absorber tube	(m)
τ_{gt}	Transmittance of glass tube	none	$D_{at,i}$	Inner diameter of absorber tube	(m)
α_{at}	Absorptance of absorber tube	none	$D_{gt,o}$	Outer diameter of glass tube	(m)
α_{gt}	Absorptance of glass tube	none	$D_{gt,i}$	Inner diameter of glass tube	(m)
$\mathfrak{F}_{gt,o}$	Shape Factor of glass tube outer surface	none	$D_{bt,o}$	Outer diameter of battery tube	(m)
$\mathfrak{F}_{a,o-gt,i}$	Shape Factor between absorber and glass tubes	none	$D_{bt,i}$	Inner diameter of battery tube	(m)
$K_{\tau\alpha\gamma}$	Incidence angle modifier	none	D_{NaS}	Diameter of the NaS cell's inner sodium electrode	(m)
σ	Boltzman's Constant	(Wm ⁻² K ⁻⁴)	$T_{gt,i}$	Temperature of glass tube inner wall	(K)
k_{ab}	Thermal conductivity of material between "a" and "b".	(Wm ⁻¹ K ⁻¹)	$T_{gt,o}$	Temperature of glass tube outer wall	(K)

Parameter	Description	unit	Parameter	Description	unit
γ	Mirror Shape Factor	none	T_{htf}	Bulk heat transfer fluid temperature	(K)
ρ	Mirror reflectivity	none	T_{sky}	Sky Temperature	(K)
$h_{ann,o}$	Outer annular heat transfer coefficient	(Wm ⁻² K ⁻¹)	T_{amb}	Ambient Temperature	(K)
$h_{ann,i}$	Inner annular heat transfer coefficient	(Wm ⁻² K ⁻¹)	\bar{T}_{NaS}	Average temperature of the NaS cell in lumped model	(K)
E_{cell}	NaS cell voltage w.r.t cell discharge state	(V)	CR	Solar Flux Concentration Ratio	none
I_{cell}	NaS cell current (charging – ve, discharging +ve)	(A)	R_{NaS}	Internal electrical resistance of NaS cell	(Ω)

Now that the key fluxes, terms and parameters for heat transfer have been defined, the dimensionless numbers and correlations used in the model are now defined.

4.3.2 Dimensionless Numbers and Correlations used in the EES Receiver Model

The set of dimensionless numbers associated with the heat transfer analysis as defined by Incopera and Dewitt (1996) ^[192] are as follows:

- The **Nusselt number (Nu)** which is the ratio between the temperature gradient at the heat transfer boundary and the overall temperature difference, defined as:

$$\text{Nu} = \frac{h_{htf} D_h}{k_{htf}} \quad \text{(Equation 4-5)}$$

- b) The **Reynolds number (Re)** which is a ratio of the inertial to viscous forces in the flow and defined as:

$$\text{Re} = \frac{u_{htf} D_h}{\nu_{htf}} \quad \text{(Equation 4-6)}$$

- c) The **Prandtl number (Pr)** which describes the ratio between the diffusion of particle momentum and the diffusion of heat, defined as:

$$\text{Pr} = \frac{c_p \mu_{htf}}{k_{htf}} \quad \text{(Equation 4-7)}$$

- d) The **Grashof number (Gr)** which describes the ratio between the buoyant and viscous forces in the flow, defined as:

$$\text{Gr}_D = \frac{g \beta (T_s - T_\infty) D_{gt,o}^3}{\nu_{air}^2} \quad \text{(Equation 4-8)}$$

where for an ideal gas equation, $\beta = 1/T_\infty$ is assumed for air, T_∞ being the absolute air film temperature.

- e) The **Rayleigh number (Ra)**, a product of the Grashof and Prandtl numbers indicates whether heat transfer in a moving fluid is primarily conductive or convective and is defined as:

$$\text{Ra} = \text{Gr}_D \text{Pr}_{air} \quad \text{(Equation 4-9)}$$

- f) The **Biot number (Bi)** for the ratio of heat transfer resistance inside of and at the surface of a body, defined as:

$$\text{Bi} = \frac{U_o L_c}{k_{process}}, \quad \text{(Equation 4-10)}$$

L_c being the characteristic length of the heat transfer process, $k_{process}$ the combined thermal conductivity along the path of heat flow and U_o , the overall heat transfer coefficient .

4.3.2.1 Turbulent Heat Transfer in the HTF Annulus

Many correlations exist for describing turbulent heat transfer in annular ducts. The widely used correlations for turbulent Nusselt number developed by Petukhov and Kirolov ^[193] and those of Petukhov and Roizen ^[194-195] for analyzing turbulent annular gaseous flows were recently revised in the year 2009 by Gnielinski for modelling turbulent annular flow in ducts. Gnielinski ^[196] recommends the following new correlations when calculating the turbulent flow ($Re > 10^4$) Nusselt numbers for concentric annuli:

$$Nu_{ann,o} = F_{ann,o} \left[\frac{(f_{ann}/8)RePr}{\{C_1 + 12.7\sqrt{(f_{ann}/8)(Pr^{2/3}-1)}\}} \right] \times \left[1 + \left(\frac{d_h}{L}\right)^{2/3} \right] \times K_t \quad \text{(Equation 4-11)}$$

$$Nu_{ann,i} = F_{ann,i} \left[\frac{(f_{ann}/8)RePr}{\{C_1 + 12.7\sqrt{(f_{ann}/8)(Pr^{2/3}-1)}\}} \right] \left[1 + \left(\frac{d_h}{L}\right)^{2/3} \right] \times K_t \quad \text{(Equation 4-12)}$$

where the equation constant C_1 , the annular friction factor f_{ann} , the modified Reynolds number Re^* , and the annular diameter ratio are given as:

$$C_1 = 1.07 + \frac{900}{Re} - \frac{0.63}{(1 + 10Pr)} \quad \text{(Equation 4-13)}$$

$$f_{ann} = (1.8 + \log_{10} Re^* - 1.5)^{-2} \quad \text{(Equation 4-14)}$$

$$Re^* = Re \frac{(1 + a^2)\ln(a) + (1 - a^2)}{(1 - a^2)\ln(a)} \quad \text{(Equation 4-15)}$$

$$a = \frac{D_{bt,o}}{D_{at,i}} \text{ so that, } 0 \leq a \leq 1 \quad \text{(Equation 4-16)}$$

K_t , the factor which corrects for the variation of fluid properties with temperature is given as:

$$K_t = \left(\frac{\text{Pr}}{\text{Pr}_w} \right)^{0.11} \quad \text{(Equation 4-17)}$$

where Pr and Pr_w are the Prandtl numbers evaluated at bulk fluid and wall temperature respectively.

The annular heat transfer factors are:

$F_{ann,o} = 0.9 - 0.15a^{0.6}$, describing heat transfer from the outer tube to the HTF, with the inner insulated and:

$F_{ann,i} = 0.75a^{-0.17}$, describing heat transfer from the inner tube to the HTF, with the outer insulated.

In the case of the EES receiver model, this flux is negative because, it passes from the HTF into the NaS cells.

The hydraulic diameter of the annulus is given as:

$$\begin{aligned} D_h &= \frac{4 \times A_{flow}}{P} = \frac{4 \times \left(\frac{\pi(D_{at,i}^2 - D_{bt,o}^2)}{4} \right)}{\pi(D_{at,i} + D_{bt,o})} = \frac{(D_{at,i}^2 - D_{bt,o}^2)}{(D_{at,i} + D_{bt,o})} \\ &= \frac{(D_{at,i} + D_{bt,o})(D_{at,i} - D_{bt,o})}{(D_{at,i} + D_{bt,o})} = (D_{at,i} - D_{bt,o}) \end{aligned} \quad \text{(Equation 4-18)}$$

The HTF velocity u_{htf} (m/s), in the annulus can be defined in terms of mass flow, density and the cross sectional area of flow as:

$$u_{htf} = \frac{\dot{M}}{\rho A_{flow}} = \frac{\dot{M}}{\rho \left[\frac{\pi(D_{at,i}^2 - D_{bt,o}^2)}{4} \right]} = \frac{4\dot{M}}{\rho\pi(D_{at,i}^2 - D_{bt,o}^2)} \quad \text{(Equation 4-19)}$$

Thus the Reynolds number in the EES receiver annulus can be defined in terms of the HTF mass flow \dot{M} (kg/s), the hydraulic diameter D_h and the HTF properties as:

$$\begin{aligned}
 \text{Re}_h &= \frac{uD_h}{\nu} = \frac{4\dot{M}}{\rho\pi(D_{at,i}^2 - D_{bt,o}^2)} \times (D_{at,i} - D_{bt,o}) && \text{(Equation 4-20)} \\
 &= \frac{4\dot{M} \times (D_{at,i} - D_{bt,o})}{\pi(D_{at,i}^2 - D_{bt,o}^2)\mu} \\
 &= \frac{4\dot{M} \times (D_{at,i} - D_{bt,o})}{\pi(D_{at,i} + D_{bt,o})(D_{at,i} - D_{bt,o})\mu} = \frac{4\dot{M}}{\pi(D_{at,i} + D_{bt,o})\mu}
 \end{aligned}$$

The fully developed turbulent nature of the projected flow at typical operating temperatures (over 300°C), can be evinced with the evaluation of the Re number. This is calculated using the annular diameters (in metres) of the conceptual receiver, the typical mass flow and an average temperature of 350°C.

$$\text{Re}_h = \frac{4\dot{M}}{\pi(D_{at,i} + D_{bt,o})\mu_{HTF}} = \frac{4 \times 9 \text{ kg/s}}{\pi(0.154 + 0.114)0.177 \times 10^{-3}} = 241,570$$

For this fully developed turbulent flow the annular heat transfer coefficients are given by the following equations as:

$$h_{ann,o} = \frac{\text{Nu}_{ann,o} \times k_{htf}}{D_h} \quad \text{(Equation 4-21)}$$

and

$$h_{ann,i} = \frac{\text{Nu}_{ann,i} \times k_{htf}}{D_h} \quad \text{(Equation 4-22)}$$

4.3.2.2 Convective Heat Transfer to the Ambient

For both natural heat convection from the horizontal glass absorber cover to the ambient with no wind, the correlation ^[197] recommended by Churchill and Chu (1975) for horizontal tubes is used.

$$\text{Nu}_{\text{free-conv,gt,o}} = \left(\frac{0.6 + 0.387\text{Ra}_D^{1/6}}{[1 + (0.559/\text{Pr})^{9/16}]^{8/27}} \right)^2 \quad \text{(Equation 4-23)}$$

which is valid for $0 \leq Pr \leq \infty$ and $10^{-5} \leq Ra \leq 10^{12}$

For the case of a cross flow wind, the Churchill and Berstein (1977) correlation as recommended by Incopera and Dewitt (1996) ^[192] is used to estimate the Nusselt number as:

$Nu_{\text{forced-conv,gt,0}} =$ **(Equation 4-24)**

$$0.3 + \frac{0.62Re_D^{1/2}Pr^{1/3}}{[1 + (0.4/Pr)^{2/3}]^{1/4}} \times \left[1 + \left(\frac{Re_D}{282,000} \right)^{5/8} \right]^{4/5}$$

which is valid for $Re_D Pr \geq 0.2$

All temperature dependent properties of dry air are evaluated at T_∞ , using appropriate correlations obtained from relevant handbooks and publications ^[198-200].

This sub-section concludes both the presentation of key model correlations used in this work and also the ends section describing the system of models. The modelling of the heat transfer processes is now presented in the next section.

4.4 Modelling of Heat Transfer to the NaS Cell

This section, the most important of the chapter, now presents the mathematical models that represent the key processes used for simulating the operation of the conceptual EES receiver in a typical PTC solar field. As is customary, all the assumptions that have been made for the sole purpose of model simplification and easier computation are now given in the brief sub-section that here follows.

4.4.1 Assumptions used in Heat Transfer Modelling

The following assumptions were made for the purpose of simplifying the system of mathematical models. It was assumed that:

1. A vacuum exist between the absorber tube and glass cover of the EES receiver. Therefore convective heat loss can be neglected.

2. Conductive losses from the tube supports are negligible and therefore can be ignored.
3. The NaS cells and battery tube combination have infinite conductance, with no axial or radial temperature gradients. Therefore, this allows the use of an average cell temperature \bar{T}_{NaS} , in all calculations.
4. Variation in HTF temperature is one-dimensional, and occurs only in the axial (HTF flow) direction. Therefore the HTF has no radial temperature gradients and an average HTF temperature \bar{T}_{htf} , can be used in all calculations.
5. Both the inner sodium and outer sulphur electrodes change phase at a common temperature of 115°C, representing the solid–liquid phase change temperature for the “entire NaS cell”. This greatly simplified computation and is permissible due to the fact that the inner sodium electrode (which melts at roughly 100°C) is heated from the outer sulphur electrode which melts at approximately 115.21°C. * (This “bulk” phase change temperature value of 115°C was confirmed as appropriate based on experimental data from the EES receiver rig)

With the model assumptions stated, the first modelling sub-section which now follows, presents the lumped capacitance model and the modes of nodular heat transfer within the EES receiver system.

4.4.2 The NaS Cell Lumped Capacitance Model and Nodular Heat Transfer within the EES Receiver System

For the purpose of simplicity, but still to provide a useful model of the internal heat transfer, the NaS cell is considered to have infinite internal conductance and lumped thermal capacitance (Figure 4-9). The actual thermal resistances inside the cell, theoretically considered as being external, are used to calculate an overall heat transfer coefficient $U_{o,NaS}$, between the moving HTF and the NaS cell.

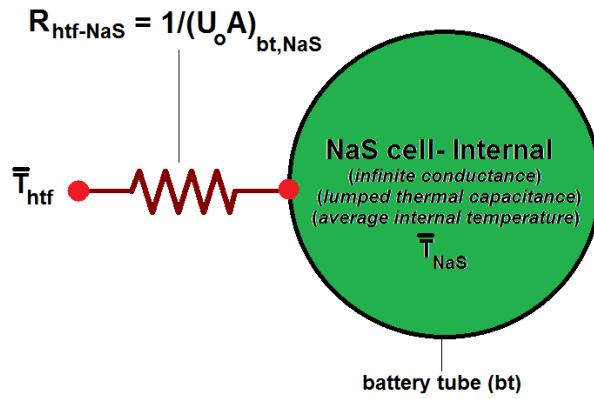


Figure 4-9: Schematic illustrating lumped thermal capacitance of NaS cell

The calculation of the overall heat transfer coefficient $U_{o,NaS}$ was effected by considering the entire set of layers involved in heat transfer to the NaS cell, and depicted in a simplified longitudinal section of the most widely used “central sodium” NaS cell (Figure 4-10).

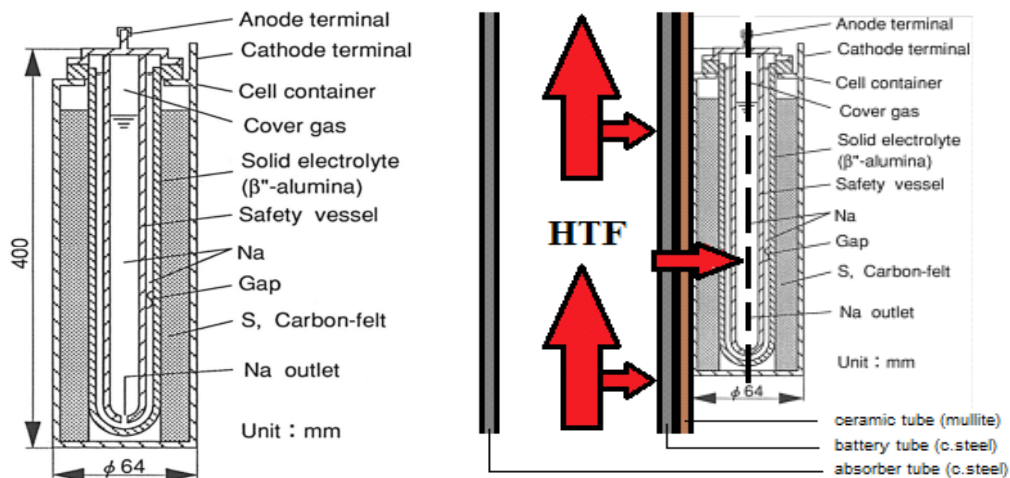


Figure 4-10: Schematic showing inner construction and heat transfer to a 300 Ah central sodium NaS cell (Adapted:^[201])

The equation concerning heat transfer to the NaS cell is given as follows:

$$\dot{q}'_{conv,htf-NaS} = U_{o,NaS} \pi D_{bt,o} (T_{htf} - \bar{T}_{NaS}) \quad \text{(Equation 4-25)}$$

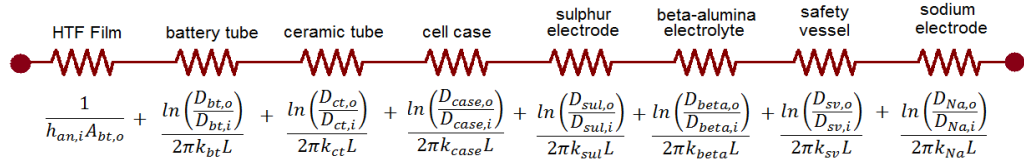


Figure 4-11: Schematic showing thermal resistance between HTF and NaS Cell

With reference to the resistance network (Figure 4-11), the overall heat transfer coefficient $U_{o,NaS}$ was derived as follows:

$$\frac{1}{U_{o,NaS}A_{bt,o}} = \left[\frac{1}{h_{ann,i}A_{bt,o}} + \frac{\ln\left(\frac{D_{bt,o}}{D_{bt,i}}\right)}{2\pi k_{bt}L} + \frac{\ln\left(\frac{D_{ct,o}}{D_{ct,i}}\right)}{2\pi k_{ct}L} + \frac{\ln\left(\frac{D_{case,o}}{D_{case,i}}\right)}{2\pi k_{case}L} + \frac{\ln\left(\frac{D_{sul,o}}{D_{sul,i}}\right)}{2\pi k_{sul}L} + \frac{\ln\left(\frac{D_{beta,o}}{D_{beta,i}}\right)}{2\pi k_{beta}L} + \frac{\ln\left(\frac{D_{sv,o}}{D_{sv,i}}\right)}{2\pi k_{sv}L} + \frac{\ln\left(\frac{D_{Na,o}}{D_{Na,i}}\right)}{2\pi k_{Na}L} \right] \quad \text{(Equation 4-26)}$$

$$U_{o,NaS} = \left[\frac{1}{h_{ann,i}} + \frac{D_{bt,o}}{2} \left\{ \frac{\ln\left(\frac{D_{bt,o}}{D_{bt,i}}\right)}{k_{bt}} + \frac{\ln\left(\frac{D_{ct,o}}{D_{ct,i}}\right)}{k_{ct}} + \frac{\ln\left(\frac{D_{case,o}}{D_{case,i}}\right)}{k_{case}} + \frac{\ln\left(\frac{D_{sul,o}}{D_{sul,i}}\right)}{k_{sul}} + \frac{\ln\left(\frac{D_{beta,o}}{D_{beta,i}}\right)}{k_{beta}} + \frac{\ln\left(\frac{D_{sv,o}}{D_{sv,i}}\right)}{k_{sv}} + \frac{\ln\left(\frac{D_{Na,o}}{D_{Na,i}}\right)}{k_{Na}} \right\} \right] \quad \text{(Equation 4-27)}$$

Jefferson (1972) recommended a correction correlation that was used to improve the accuracy of the overall heat transfer coefficient $U_{o,NaS}$ in the lumped capacitance model. It yields a modified coefficient $U_{o,NaS*}$ which brings the results of the lumped capacitance approach into closer agreement (Figure 4-12) with a transient conduction model. This correlation is given as [202].

$$\frac{1}{U_{o,NaS*}} = \frac{1 + Bi/5}{U_{o,NaS}} \quad \text{(Equation 4-28)}$$

where the Biot number, $Bi = \frac{U_{o,NaS}L_c}{k_{NaS}}$; and L_c the characteristic length, defined as the ratio of the battery tube's internal volume to surface area is given as:

$$L_c = \frac{Volume_{bt}}{Area_{bt,o}} = \frac{\pi (D_{bt,o})^2 / 4 \times L_{NaS}}{\pi D_{bt,o} L_{NaS}} = \frac{D_{bt,o}}{4} \quad \text{(Equation 4-29)}$$

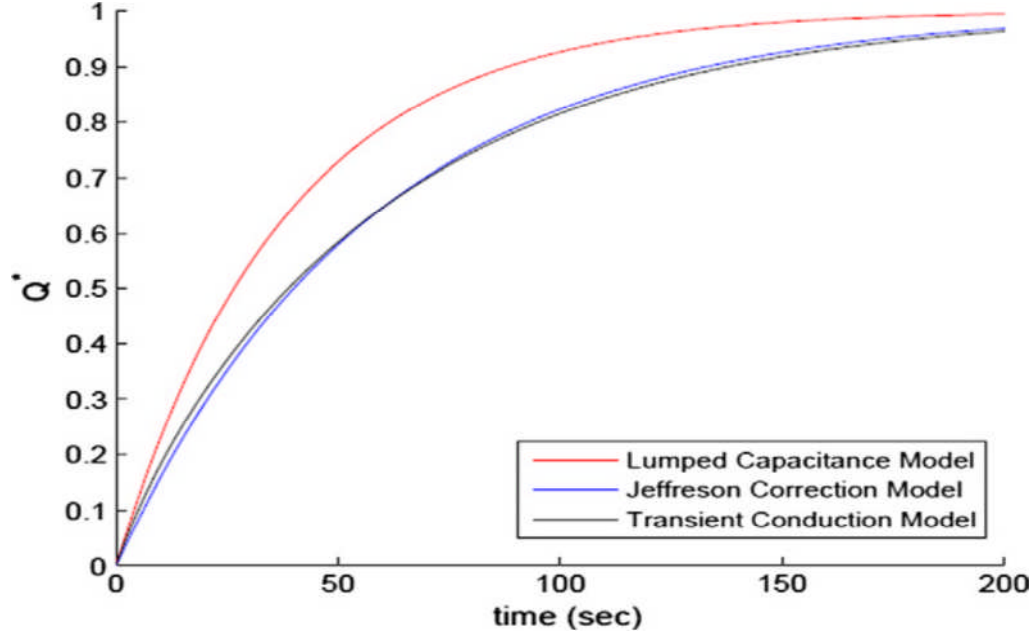


Figure 4-12: Schematic illustrating comparison between Jefferson correction model, exact transient heat conduction and lumped capacitance model for heat transfer to solid object in a fluid

Time dependent temperature variation in the Tepco T5 NaS cell modelled in this work is due to sensible heat transfer with the HTF, as well as entropic heat generation (exothermic and endothermic during cell discharging and charging respectively) within the NaS cell. As given by Gibbard (1978), the total heat energy generated or absorbed by the NaS cell can be therefore represented as ^[203] :

$$\begin{aligned} \dot{Q}_{NaS} &= \dot{Q}_{joule_heating} + \dot{Q}_{reaction_entropy} & \text{(Equation 4-30)} \\ &= I_{NaS} \left(\eta - \bar{T}_{NaS} \frac{dE_{NaS}}{d\bar{T}_{NaS}} \right) \end{aligned}$$

where η is the battery polarization and $\bar{T}_{NaS} \frac{dE_{NaS}}{d\bar{T}_{NaS}}$ is the entropy term.

The battery polarization $\eta = I_{NaS} \times R_{NaS}$ with R_{NaS} , the internal cell resistance found by the difference between the “rated” open circuit voltage

at full charge and the cell voltage at a given time “t”, all divided by the current flow at that same time .

$$R_{NaS} = \frac{(E_{NaS,oc} - E_{NaS,@I_{NaS}})}{I_{NaS}} \quad \text{(Equation 4-31)}$$

As stated earlier, it is here assumed that the NaS cell has no axial or radial temperature gradients and that the whole 0.5 m length of the T5 cell is at one common temperature. This simplified approach allows the temperature variation to be time dependent only and represented by the first order partial differential equation given as:

$$\frac{\partial \bar{T}_{NaS}}{\partial t} = \frac{h_{ann,i} \pi D_{NaS} l_{NaS} (T_{htf} - \bar{T}_{NaS}) + I_{NaS} \left(\eta - \bar{T}_{NaS} \frac{dE_{NaS}}{dT_{NaS}} \right)}{(mc_p)_{NaS}} \quad \text{(Equation 4-32)}$$

Here heat gain from the HTF is given by the $h_{ann,i}$ term and heat generated within the cell during charge/discharge operations by the I_{NaS} and $\frac{dE_{NaS}}{dT}$ terms.

The direction of daytime heat flows can be visualized using the thermal resistance network of Figure 4-13.

At nodes 1-3: (Heat transfer from HTF to NaS Cell)

Since the battery polarization $\eta = I_{NaS} \times R_{NaS}$, Equation 4-32 can be rewritten as follows:

$$\frac{\partial \bar{T}_{NaS}}{\partial t} = \frac{h_{ann,i} \pi D_{NaS} l_{NaS} (T_{htf} - \bar{T}_{NaS}) + I_{NaS} \left(I_{NaS} \times R_{NaS} - \bar{T}_{NaS} \frac{dE_{NaS}}{dT_{NaS}} \right)}{(mc_p)_{NaS}} \quad \text{(Equation 4-33)}$$

When only the initial heating of the NaS cells to operating temperature is considered, the current term is zero and the partial differential equation can be simplified as follows:

$$\frac{\partial \bar{T}_{NaS}}{\partial t} = \frac{U_{o,NaS} \pi D_{bt,o} l_{NaS} (T_{htf} - \bar{T}_{NaS})}{(mc_p)_{NaS}} \quad \text{(Equation 4-34)}$$

where U_{o,NaS^*} , is the overall heat transfer coefficient from the HTF to the NaS cells, developed earlier and modified with the Jefferson correction.

At nodes 3 - 4: (Heat transfer between Battery Tube and HTF)

Like the NaS cell, a uniform HTF temperature is assumed with no radial temperature gradients. In the case of heating the cells to working temperature, heat is expected to flow into the NaS cells from the HTF. However, heat may also flow from the NaS cells into to HTF, during night time or poor sunlight conditions when the NaS battery banks are being discharged.

Therefore overall battery temperature change may be due to solar heat gain through the inner wall of the absorber tube (given by $\alpha_{ann,o}$), or by heat gained from the NaS cell through the outer battery tube wall (given by $\alpha_{ann,i}$). This is represented in Equation 4-35 as:

$$\left(\frac{\partial T_{htf}}{\partial x} + \frac{1}{\bar{u}_{htf}} \frac{\partial T_{htf}}{\partial t}\right) = \frac{h_{ann,o}\pi D_{at}(T_{at}-T_{htf})+U_{o,NaS}\pi D_{bt,o}(T_{NaS}-T_{htf})}{(Mc_p)_{htf}} \quad \text{(Equation 4-35)}$$

Further, the flux conducted through the NaS battery tube wall from the HTF is given by Equation 4-36 as:

$$\dot{q}'_{cond,bt} = \frac{2\pi k_{bt}(T_{bt,o} - T_{bt,i})}{\ln \left[\frac{D_{bt,o}}{D_{bt,i}} \right]} \quad \text{(Equation 4-36)}$$

This is the same flux convected from the HTF to the NaS battery tube, and is given by Equation 4-37 as:

$$\begin{aligned} \dot{q}'_{conv,htf-bt} &= \dot{q}'_{cond,bt} \\ &= h_{ann,i}\pi D_{bt,o}(T_{htf} - T_{bt,o}) \end{aligned} \quad \text{(Equation 4-37)}$$

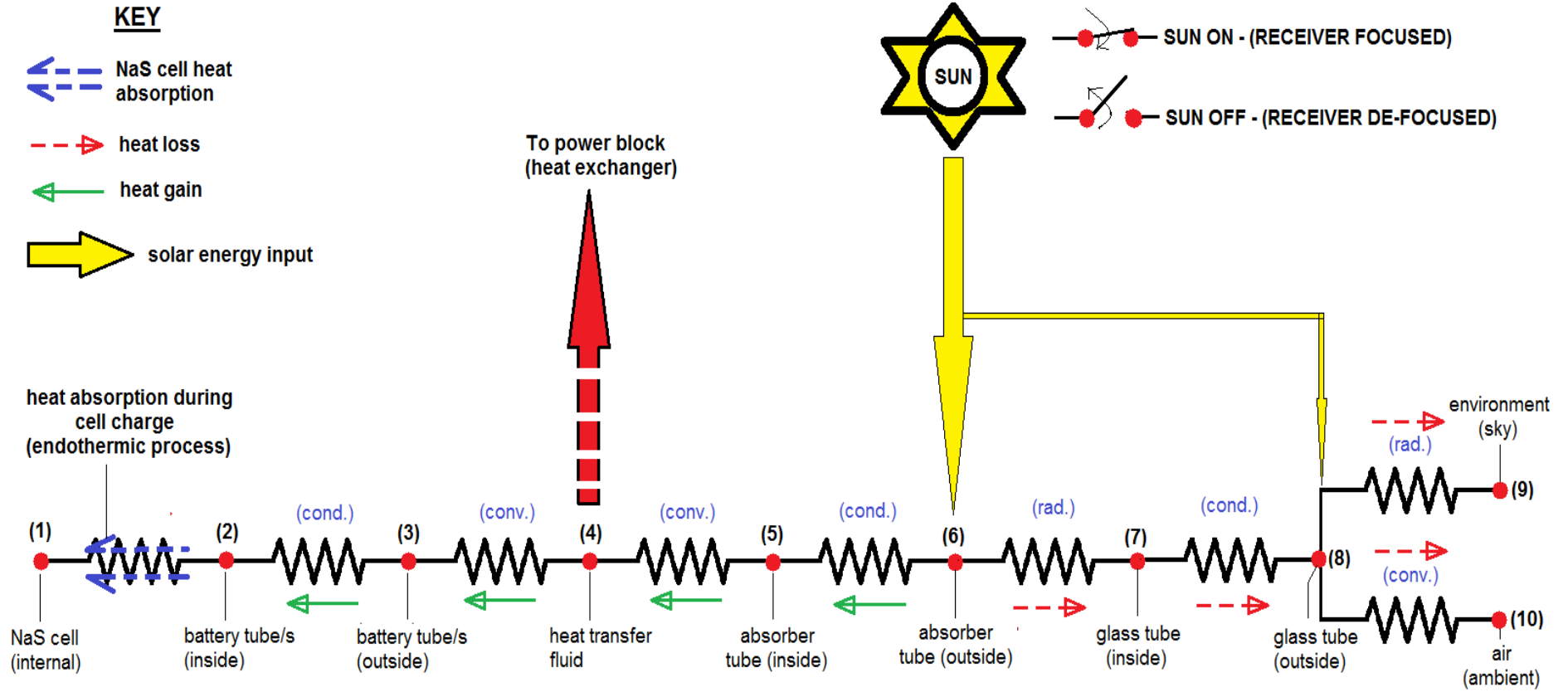


Figure 4-13: Thermal resistance model of heat flow in the EES receiver (day time)

At nodes 4-5: (Heat transfer from Absorber Tube to HTF)

At node 4, heat flux enters the HTF by convective heat transfer at the inner wall of the EES absorber tube, being conducted from the outer wall which is the focused to concentrated solar flux. This heat flux is given by Equation 4-38 as:

$$\dot{q}'_{conv,at-htf} = h_{ann,o} \pi D_{at,i} (T_{at,i} - T_{htf}) \quad \text{(Equation 4-38)}$$

The heat flux conducted through the absorber tube (node 5 of Figure 4-13) is equal to the heat flux convected into the HTF and is given by Equation 4-39 as:

$$\begin{aligned} \dot{q}'_{cond,at} &= \dot{q}'_{conv,at-htf} & \text{(Equation 4-39)} \\ &= \frac{2\pi k_{at} (T_{at,o} - T_{at,i})}{\ln \left[\frac{D_{at,o}}{D_{at,i}} \right]} \end{aligned}$$

At nodes 6-7: (Heat balance at the absorber tube)

The heat flux conducted through the absorber tube wall is equal to the solar energy absorbed by the receiver, less the radiative and convective losses at outer surface of the glass cover. This is given by Equation 4-40 as:

$$\dot{q}'_{cond,at} = \dot{q}''_{sol.abs,at} \pi D_{at,o} - (\dot{q}'_{Lrad,at-gt} + \dot{q}'_{Lconv,at-gt}) \quad \text{(Equation 4-40)}$$

$$\dot{q}'_{cond,at} = \dot{q}''_{sol.abs,at} \pi D_{at,o} - \dot{q}'_{Lrad,at-gt} \quad \text{(Equation 4-41)}$$

where

$$\dot{q}'_{Lrad,at-gt} = \mathfrak{S}_{at,o-gt,i} \sigma \pi D_{at,o} (T_{at,o}^4 - T_{gt,i}^4) \quad \text{(Equation 4-42)}$$

and

$$\mathfrak{S}_{at,o-gt,i} = \left[\frac{1}{F_{at,gt}} + \left(\frac{1}{\varepsilon_{at}} - 1 \right) + \frac{D_{at}}{D_{gt,i}} \left(\frac{1}{\varepsilon_{gt}} - 1 \right) \right]^{-1} \quad \text{(Equation 4-43)}$$

The fluxes $\dot{q}'_{Lcond,gt}$ and $\dot{q}'_{sol.abs,gt}$ are given as:

$$\dot{q}'_{Lcond,gt} = \frac{2\pi k_{gt}(T_{gt,i} - T_{gt,o})}{\ln \left[\frac{D_{gt,o}}{D_{gt,i}} \right]} \quad \text{(Equation 4-44)}$$

$$\dot{q}'_{sol.abs,gt} = \dot{q}''_{sol.const} \rho_m \gamma_m K_{\theta} \alpha_{gt} \pi D_{gt,o} \quad \text{(Equation 4-45)}$$

At nodes 9-10: (Heat loss from the glass tube to the external environment)

The heat flux conducted through the glass cover is finally lost by radiation to the sky and convection to the ambient. This is represented in Equation 4-46 as follows:

$$\dot{q}'_{Lcond,gt} = \dot{q}'_{Lrad,gt-sky} + \dot{q}'_{Lconv,gt-amb} \quad \text{(Equation 4-46)}$$

$$\dot{q}'_{Lrad,gt-sky} = \mathfrak{S}_{gt-sky} \sigma \pi D_{gt,o} (T_{gt,o}^4 - T_{sky}^4)$$

$$\text{and } \dot{q}'_{Lconv,gt-amb} = h_{conv,gt} \pi D_{gt,o} (T_{gt,o} - T_{amb}) \quad \text{(Equation 4-47)}$$

Now that the equations modelling both lumped capacitance and the modes of nodular heat transfer for the EES receiver have been presented, the next sub-section outlines the process developed to solve the key set of steady state algebraic equations in the system.

4.4.3 Solving the Steady-State System of Equations

Solving the quasi-transient system of equations consisted of a process of precedence ordering and back substitution of the steady state equations to formulate a very nonlinear algebraic equation in the absorber wall heat flux $\dot{q}'_{cond,at}$. This was then solved at each node of the model's two discretized transient equations.

The ten “*steady state*” equations which describe the basic heat transfer processes in the EES receiver are given as follows.

$$\begin{aligned} \dot{q}'_{Lcond,gt} + \dot{q}''_{sol.abs,gt}\pi D_{gt,o} & \quad \text{(Equation 4-48)} \\ & = h_{conv,gt}\pi D_{gt,o}(T_{gt,o} - T_{amb}) \\ & + \mathfrak{S}_{gt,o}\pi D_{gt,o}\sigma(T_{gt,o}^4 - T_{sky}^4) \end{aligned}$$

$$\begin{aligned} \dot{q}'_{Lrad,at-gt} + \dot{q}'_{Lconv,at-gt} & = \dot{q}'_{Lcond,gt} & \quad \text{(Equation 4-49)} \\ & = \frac{2\pi k_{gt}(T_{gt,i} - T_{gt,o})}{\ln \left[\frac{D_{gt,o}}{D_{gt,i}} \right]} \end{aligned}$$

$$\begin{aligned} \dot{q}'_{Lrad,at-gt} + \dot{q}'_{Lconv,at-gt} & \quad \text{(Equation 4-50)} \\ & = \mathfrak{S}_{at,o-gt,i}\sigma\pi D_{a,o}(T_{at,o}^4 - T_{gt,i}^4) \\ & + h_{conv,at}\pi D_{at,o}(T_{at,o} - T_{gt,i}) \end{aligned}$$

$$\begin{aligned} \dot{q}'_{cond,at} & = \dot{q}''_{sol.abs,at}\pi D_{at,o} - (\dot{q}'_{Lrad,at-gt} & \quad \text{(Equation 4-51)} \\ & + \dot{q}'_{Lconv,at-gt}) \end{aligned}$$

$$\dot{q}'_{cond,at} = \frac{2\pi k_{at}(T_{at,o} - T_{at,i})}{\ln \left[\frac{D_{at,o}}{D_{at,i}} \right]} \quad \text{(Equation 4-52)}$$

$$\dot{q}'_{cond,at} = h_{ann,o}\pi D_{at,i}(T_{at,i} - T_{htf}) \quad \text{(Equation 4-53)}$$

$$h_{ann,o} = fxn(\dot{q}'_{at}) \quad \text{(Equation 4-54)}$$

$$h_{ann,i} = fxn(\dot{q}'_{at}) \quad \text{(Equation 4-55)}$$

$$\begin{aligned} \dot{q}'_{cond,bt} & = \frac{2\pi k_{bt}(T_{bt,o} - T_{bt,i})}{\ln \left[\frac{D_{bt,o}}{D_{bt,i}} \right]} = \dot{q}'_{htf-NaS} & \quad \text{(Equation 4-56)} \\ & = \dot{q}'_{bt,i-NaS} \end{aligned}$$

$$\dot{q}'_{Lgt,tot} = \dot{q}'_{Lcond,gt} + \dot{q}''_{sol.abs,gt}\pi D_{gt,o} \quad \text{(Equation 4-57)}$$

The first step in the solution process was the precedence ordering and back substitution of Equations 4-46 to 4-55, to obtain a single non-linear equation in $\dot{q}'_{cond,at}$.

In order to develop this single equation, Equation 4-51 was re-arranged to make $T_{at,i}$ the subject and substituting for $\alpha_{ann,o}$ gives:

$$T_{at,i} = \frac{\dot{q}'_{cond,at}}{h_{ann,o}\pi D_{at,i}} + T_{htf} \quad \text{(Equation 4-58)}$$

Substituting for $T_{at,i}$ in Equation 4-58 gives:

$$T_{at,i} = \frac{\dot{q}'_{cond,at}}{h_{ann,o}\pi D_{at,i}} + T_{htf} \quad \text{(Equation 4-59)}$$

$$\dot{q}'_{cond,at} = \frac{2\pi k_{at} \left[T_{at,o} - \left[\frac{\dot{q}'_{cond,at}}{h_{ann,o}\pi D_{at,i}} + T_{htf} \right] \right]}{\ln \left[\frac{D_{at,o}}{D_{at,i}} \right]} \quad \text{(Equation 4-60)}$$

Solving Equation 4-60 for $T_{at,o}$ gives:

$$T_{at,o} = \left\{ \frac{\dot{q}'_{cond,at} \times \ln \left[\frac{D_{at,o}}{D_{at,i}} \right]}{2\pi k_{at}} + \left[\frac{\dot{q}'_{cond,at}}{h_{ann,o}\pi D_{at,i}} + T_{htf} \right] \right\} \quad \text{(Equation 4-61)}$$

From Equation 4-49:

$$T_{gt,o} = T_{gt,i} - \frac{\dot{q}'_{Lcond,gt} \times \ln \left[\frac{D_{gt,o}}{D_{gt,i}} \right]}{2\pi k_{gt}} \quad \text{(Equation 4-62)}$$

Substituting for $T_{gt,o}$ in Equation 4-48, gives:

$$\dot{q}'_{Lgt,tot} = h_{conv,gt}\pi D_{gt,o} \left(\left[T_{gt,i} - \frac{\dot{q}'_{Lcond,gt} \times \ln \left[\frac{D_{gt,o}}{D_{gt,i}} \right]}{2\pi k_{gt}} \right] - T_{amb} \right) \quad \text{(Equation 4-63)}$$

$$+ \mathfrak{S}_{gt,o}\pi D_{gt,o}\sigma \left\{ \left[T_{gt,i} - \frac{\dot{q}'_{Lcond,gt} \times \ln \left[\frac{D_{gt,o}}{D_{gt,i}} \right]}{2\pi k_{gt}} \right]^4 - T_{sky}^4 \right\}$$

Since it is assumed that $\dot{q}'_{Lconv,at} = 0$, then from Equation 4-49,

$$\dot{q}'_{Lrad,at} = \dot{q}'_{Lcond,gt}$$

Also Equation 4-50 only bears the radiative loss term and simplifies to become:

$$\dot{q}'_{Lrad,at} = \mathfrak{S}_{at,o-gt,i}\sigma\pi D_{at,o}(T_{at,o}^4 - T_{gt,i}^4) = \dot{q}'_{Lcond,gt} \quad \text{(Equation 4-64)}$$

Rearranging Equation 4-64 and solving for $T_{gt,i}$ gives:

$$(T_{at,o})^4 - \frac{\dot{q}'_{Lrad,at}}{\mathfrak{S}_{a,o-gt,i}\sigma\pi D_{at,o}} = (T_{gt,i})^4 \quad \text{(Equation 4-65)}$$

$$T_{gt,i} = \sqrt[4]{(T_{at,o})^4 - \frac{\dot{q}'_{Lrad,at}}{\mathfrak{S}_{a,o-gt,i}\sigma\pi D_{at,o}}} = \sqrt[4]{(T_{a,o})^4 - \frac{\dot{q}'_{Lcond,gt}}{\mathfrak{S}_{a,o-gt,i}\sigma\pi D_{at,o}}} \quad \text{(Equation 4-66)}$$

Substituting for $T_{gt,i}$ in Equation 4-66 gives:

$$\dot{q}'_{Lgt,tot} = h_{conv,gt}\pi D_{gt,o} \left(\left[\sqrt[4]{(T_{at,o})^4 - \frac{\dot{q}'_{Lrad,at}}{\mathfrak{S}_{a,o-gt,i}\sigma\pi D_{at,o}}} - \frac{\dot{q}'_{Lcond,gt} \times \ln \left[\frac{D_{gt,o}}{D_{gt,i}} \right]}{2\pi k_{gt}} - T_{amb} \right] + \right. \quad \text{(Equation 4-67)}$$

$$\left. \mathfrak{S}_{gt,o}\pi D_{gt,o}\sigma \left\{ \left[\sqrt[4]{(T_{at,o})^4 - \frac{\dot{q}'_{Lrad,at}}{\mathfrak{S}_{a,o-gt,i}\sigma\pi D_{at,o}}} - \frac{\dot{q}'_{Lcond,gt} \times \ln \left[\frac{D_{gt,o}}{D_{gt,i}} \right]}{2\pi k_{gt}} \right]^4 - T_{sky}^4 \right\} \right)$$

Substituting Equation 4-61 for $T_{at,o}$ gives:

$$\begin{aligned} \dot{q}'_{Lgt,tot} = & \hspace{15em} \text{(Equation 4-68)} \\ & h_{conv,gt}\pi D_{gt,o} \left(\left[\sqrt[4]{\left\{ \frac{\dot{q}'_{cond,at} \times \ln\left[\frac{D_{at,o}}{D_{at,i}}\right]}{2\pi\lambda_{at}} + \left[\frac{\dot{q}'_{cond,at}}{h_{ann,o}\pi D_{at,i}} + T_{htf} \right]} \right\}^4 - \frac{\dot{q}'_{Lrad,at}}{\mathfrak{S}_{a,o-gt,i}\sigma\pi D_{at,o}}} \right] - \right. \\ & \left. \frac{\dot{q}'_{Lcond,gt} \times \ln\left[\frac{D_{gt,o}}{D_{gt,i}}\right]}{2\pi k_{gt}} - T_{amb} \right) + \\ & \mathfrak{S}_{gt,o}\pi D_{gt,o}\sigma \left\{ \left[\sqrt[4]{\left\{ \frac{\dot{q}'_{cond,at} \times \ln\left[\frac{D_{at,o}}{D_{at,i}}\right]}{2\pi k_{at}} + \left[\frac{\dot{q}'_{cond,at}}{h_{ann,o}\pi D_{at,i}} + T_{htf} \right]} \right\}^4 - \frac{\dot{q}'_{Lrad,at}}{\mathfrak{S}_{a,o-gt,i}\sigma\pi D_{at,o}}} \right] - \right. \\ & \left. \frac{\dot{q}'_{Lcond,gt} \times \ln\left[\frac{D_{gt,o}}{D_{gt,i}}\right]}{2\pi\lambda_{gt}} - T_{\infty}^4 \right\} \end{aligned}$$

From Equation 4-57:

$$\dot{q}'_{Lgt,tot} = \dot{q}'_{Lcond,gt} + \dot{q}''_{sol.abs,gt}\pi D_{gt,o}$$

Therefore:

$$\begin{aligned} \dot{q}'_{Lcond,gt} + \dot{q}''_{sol.abs,gt}\pi D_{gt,o} = & \hspace{15em} \text{(Equation 4-69)} \\ & h_{conv,gt}\pi D_{gt,o} \left(\left[\sqrt[4]{\left\{ \frac{\dot{q}'_{cond,at} \times \ln\left[\frac{D_{at,o}}{D_{at,i}}\right]}{2\pi k_{at}} + \left[\frac{\dot{q}'_{cond,at}}{h_{ann,o}\pi D_{at,i}} + T_{htf} \right]} \right\}^4 - \frac{\dot{q}'_{Lrad,at}}{\mathfrak{S}_{a,o-gt,i}\sigma\pi D_{at,o}}} \right] - \right. \\ & \left. \frac{\dot{q}'_{Lcond,gt} \times \ln\left[\frac{D_{gt,o}}{D_{gt,i}}\right]}{2\pi k_{gt}} - T_{amb} \right) + \\ & \mathfrak{S}_{gt,o}\pi D_{gt,o}\sigma \left\{ \left[\sqrt[4]{\left\{ \frac{\dot{q}'_{cond,at} \times \ln\left[\frac{D_{at,o}}{D_{at,i}}\right]}{2\pi k_{at}} + \left[\frac{\dot{q}'_{cond,at}}{h_{ann,o}\pi D_{at,i}} + T_{htf} \right]} \right\}^4 - \frac{\dot{q}'_{Lrad,at}}{\mathfrak{S}_{a,o-gt,i}\sigma\pi D_{at,o}}} \right] - \right. \\ & \left. \frac{\dot{q}'_{Lcond,gt} \times \ln\left[\frac{D_{gt,o}}{D_{gt,i}}\right]}{2\pi k_{gt}} - T_{sky}^4 \right\} \end{aligned}$$

Finally, from Equation 4-51, $\dot{q}''_{sol.abs,at}\pi D_{at,o} - \dot{q}'_{cond,at} = \dot{q}'_{Lrad,at}$

Also recall that $\dot{q}'_{Lrad,at} = \dot{q}'_{Lcond,gt}$ since $\dot{q}'_{Lconv,at} = 0$

Substituting for $\dot{q}'_{Lrad,at}$ and $\dot{q}'_{Lcond,gt}$ in Equation 4-69 gives:

$$\dot{q}''_{sol,abs,at}\pi D_{at,o} + \dot{q}''_{sol,abs,gt}\pi D_{gt,o} - \dot{q}'_{cond,at} = \quad \text{(Equation 4-70)}$$

$$h_{conv}\pi D_{gt,o} \left(\sqrt[4]{\left\{ \frac{\dot{q}'_{cond,at} \times \ln\left[\frac{D_{at,o}}{D_{at,i}}\right]}{2\pi k_{at}} + \left[\frac{\dot{q}'_{cond,at}}{h_{ann,o}\pi D_{at,i}} + T_{htf} \right] \right\}^4 - \frac{\dot{q}''_{sol,abs,at}\pi D_{at,o} - \dot{q}'_{cond,at}}{\mathfrak{S}_{a,o-gt,i}\sigma\pi D_{a,o}}} \right) - \left(\frac{\dot{q}''_{sol,abs,at}\pi D_{at,o} - \dot{q}'_{cond,at} \times \ln\left[\frac{D_{gt,o}}{D_{gt,i}}\right]}{2\pi k_{gt}} + T_{amb} \right) + \mathfrak{S}_{gt,o}\pi D_{gt,o}\sigma \left\{ \left[\sqrt[4]{\left\{ \frac{\dot{q}'_{cond,at} \times \ln\left[\frac{D_{at,o}}{D_{at,i}}\right]}{2\pi k_{at}} + \left[\frac{\dot{q}'_{cond,at}}{h_{ann,o}\pi D_{at,i}} + T_{htf} \right] \right\}^4 - \frac{\dot{q}''_{sol,abs,at}\pi D_{at,o} - \dot{q}'_{cond,at}}{\mathfrak{S}_{a,o-gt,i}\sigma\pi D_{a,o}}} \right]^4 - \frac{\dot{q}''_{sol,abs,at}\pi D_{at,o} - \dot{q}'_{cond,at} \times \ln\left[\frac{D_{gt,o}}{D_{gt,i}}\right]}{2\pi k_{gt}} - T_{sky}^4 \right\}$$

Re-writing $\dot{q}''_{sol,abs,at}$ in terms of the solar constant \dot{q}''_{sol} and optical PTC parameters defined earlier ($\rho_m, \gamma_m, \tau_{gt}, K_\theta, \alpha_{at}, \alpha_{gt}$), gives:

$$\dot{q}''_{sol} \times CR \times \rho_m \gamma_m \tau_{gt} K_\theta (\alpha_{at}\pi D_{at,o} + \alpha_{gt}\pi D_{gt,o}) - \dot{q}'_{cond,at} = \quad \text{(Equation 4-71)}$$

$$h_{conv,gt}\pi D_{gt,o} \left(\sqrt[4]{\left\{ \frac{\dot{q}'_{cond,at} \times \ln\left[\frac{D_{at,o}}{D_{at,i}}\right]}{2\pi k_{at}} + \left[\frac{\dot{q}'_{cond,at}}{h_{ann,o}\pi D_{at,i}} + T_{htf} \right] \right\}^4 - \frac{(\dot{q}''_{sol, const} \times \rho_m \gamma_m \tau_{gt} K_\theta \alpha_{at}\pi D_{at,o} - \dot{q}'_{cond,at})}{\mathfrak{S}_{a,o-gt,i}\sigma\pi D_{at,o}}} \right) - \left(\frac{(\dot{q}''_{sol} \times \rho_m \gamma_m \tau_{gt} K_\theta \alpha_{at}\pi D_{at,o} - \dot{q}'_{cond,at}) \times \ln\left[\frac{D_{gt,o}}{D_{gt,i}}\right]}{2\pi k_{gt}} - T_{amb} \right) + \mathfrak{S}_{gt,o}\pi D_{gt,o}\sigma \left\{ \left[\sqrt[4]{\left\{ \frac{\dot{q}'_{cond,at} \times \ln\left[\frac{D_{at,o}}{D_{at,i}}\right]}{2\pi k_{at}} + \left[\frac{\dot{q}'_{cond,at}}{h_{ann,o}\pi D_{at,i}} + T_{htf} \right] \right\}^4 - \frac{(\dot{q}''_{sol} \times \rho_m \gamma_m \tau_{gt} K_\theta \alpha_{at}\pi D_{at,o} - \dot{q}'_{cond,at})}{\mathfrak{S}_{a,o-gt,i}\sigma\pi D_{at,o}}} \right]^4 - \frac{(\dot{q}''_{sol} \times \rho_m \gamma_m \tau_{gt} K_\theta \alpha_{at}\pi D_{at,o} - \dot{q}'_{cond,at}) \times \ln\left[\frac{D_{gt,o}}{D_{gt,i}}\right]}{2\pi k_{gt}} - T_{sky}^4 \right\}$$

This is the final implicit and non-linear equation in terms of useful heat flux through the absorber tube walls into the HTF, $\dot{q}'_{cond,at}$. For convenience,

the goal seek tool in Microsoft Excel was employed to find the value of the heat flux.

To corroborate the accuracy of the MS Excel results, a binary search (see Appendix F) was conducted to check the MS Excel output. Both results were found to be in agreement and the resulting values were identical to a tolerance of 10^{-4} . With $\dot{q}'_{cond,at}$ computed, the other fluxes and temperatures across the cross section (which are functions of $\dot{q}'_{cond,at}$) were easily determined. The next sub-section outlines the reference frame transformation of the two partial differential equations used in the model.

4.4.4 Reference Frame Transformation for the Transient Equations of the Heat Transfer Model

The second step in the process of solving the system of equations was the transformation of the transient equations 4-72 and 4-73 from a Eulerian to a Lagrangian flow reference frame.

$$\left(\frac{\partial T_{htf}}{\partial x} + \frac{1}{v_{htf}} \frac{\partial T_{htf}}{\partial t} \right) = \frac{h_{ann,o} \pi D_{at} (T_{at} - T_{htf}) + h_{ann,i} \pi D_{bt} (\bar{T}_{NaS} - T_{htf})}{(\dot{M} c_p)_{htf}} \quad \text{(Equation 4-72)}$$

$$\frac{\partial \bar{T}_{NaS}}{\partial t} = \frac{h_{ann,i} \pi D_{NaS} l_{NaS} (T_{htf} - \bar{T}_{NaS}) + I_{NaS} \left(I_{NaS} R_{NaS} - \bar{T}_{NaS} \frac{dE_{NaS}}{dT_{NaS}} \right)}{(m c_p)_{NaS}} \quad \text{(Equation 4-73)}$$

With respect to the HTF, temperature change may be due to solar heat transfer through the inner wall of the absorber tube (given by $\alpha_{ann,o}$) or through the outer battery tube wall from the NaS cell (given by $\alpha_{ann,i}$).

The advantage of a Eulerian to Lagrangian flow transformation is that it allows effective separation of the time and position derivatives of the partial differential equations (P.D.E's) and manipulates them for solution similar to the method of characteristics. The process produces partial derivatives in "x" or "t" only (partial derivatives $\frac{\partial T_{htf}}{\partial x}$ and $\frac{\partial T_{htf}}{\partial t}$) and allows the observer to "move with the flow".

Lagrangian time (t') and position x' are given as:

$$t' = t - \frac{x}{v} \quad \text{(Equation 4-74)}$$

$$x' = x/L \quad \text{(Equation 4-75)}$$

Where v = HTF velocity; L = Flow loop length; t and x being Eulerian time and position respectively.

If T_{htf} is considered as a function of Lagrangian time and position only, then the total differential of T_{htf} is:

$$dT_{htf} = \frac{\partial T_{htf}}{\partial x'} \Big|_{t'} \times dx' + \frac{\partial T_{htf}}{\partial t'} \Big|_{x'} \times dt' \quad \text{(Equation 4-76)}$$

Dividing Equation 4-76 by dx , yields an expression for the Eulerian partial derivative $\frac{\partial T_{htf}}{\partial x}$ as follows:

$$\frac{dT_{htf}}{dx} = \frac{\partial T_{htf}}{\partial x} \Big|_t = \frac{\partial T_{htf}}{\partial x'} \Big|_{t'} \frac{dx'}{dx} \Big|_t + \frac{\partial T_{htf}}{\partial t'} \Big|_{x'} \frac{dt'}{dx} \Big|_t \quad \text{(Equation 4-77)}$$

Similarly, dividing Equation 4-76 by dt , yields an expression for the Eulerian partial derivative $\frac{\partial T_{htf}}{\partial t}$ as follows:

$$\frac{dT_{htf}}{dt} = \frac{\partial T_{htf}}{\partial t} \Big|_x = \frac{\partial T_{htf}}{\partial x'} \Big|_{t'} \frac{dx'}{dt} \Big|_x + \frac{\partial T_{htf}}{\partial t'} \Big|_{x'} \frac{dt'}{dt} \Big|_x \quad \text{(Equation 4-78)}$$

To obtain expressions for the derivative terms of Equation 4-78, the equations for Lagrangian time and position were differentiated as follows:

$$\frac{dt'}{dt} \Big|_x = 1; \quad \frac{dt'}{dx} \Big|_t = -\frac{1}{v}; \quad \frac{dx'}{dx} \Big|_t = \frac{1}{L}; \quad \frac{dx'}{dt} \Big|_x = 0$$

Substituting the values for these derivatives in Equations 4-79 and 4-80 gives:

$$\frac{dT_{htf}}{dx} = \frac{\partial T_{htf}}{\partial x} \Big|_t = \frac{1}{L} \frac{\partial T_{htf}}{\partial x'} \Big|_{t'} - \frac{1}{v} \frac{\partial T_{htf}}{\partial t'} \Big|_{x'} \quad \text{(Equation 4-79)}$$

$$\frac{dT_{htf}}{dt} = \frac{\partial T_{htf}}{\partial t} \Big|_x = \frac{\partial T_{htf}}{\partial t'} \Big|_{x'} \quad \text{(Equation 4-80)}$$

Recall that:

$$\left(\frac{\partial T_{htf}}{\partial x} + \frac{1}{v} \frac{\partial T_{htf}}{\partial t}\right) = \frac{h_{ann,o}\pi D_{at}(T_{at}-T_{htf})+h_{ann,i}\pi D_{at}(\bar{T}_{NaS}-T_{htf})}{(\dot{M}c_p)_{htf}} \quad \text{(Equation 4-81)}$$

Substituting Equations 4-79 and 4-80 into Equation 4-81 gives:

$$\left\{\frac{1}{L} \frac{\partial T_{htf}}{\partial x'} \Big|_{t'} - \frac{1}{v} \frac{\partial T_{htf}}{\partial t'} \Big|_{x'}\right\} + \frac{1}{v} \frac{\partial T_{htf}}{\partial t'} \Big|_{x'} = \frac{h_{ann,o}\pi D_{at}(T_{at}-T_{htf})+h_{ann,i}\pi D_{at}(\bar{T}_{ssc}-T_{htf})}{(\dot{M}c_p)_{htf}} \quad \text{(Equation 4-82)}$$

This simplifies to give:

$$\frac{1}{L} \frac{\partial T_{htf}}{\partial x'} \Big|_{t'} = \frac{h_{ann,o}\pi D_{at}(T_{at}-T_{htf})+h_{ann,i}\pi D_{bt,o}(\bar{T}_{NaS}-T_{htf})}{(\dot{M}c_p)_{htf}} \quad \text{(Equation 4-83)}$$

Using the same manipulation Equation 4-73 can also be rewritten as:

$$\frac{\partial \bar{T}_{NaS}}{\partial t} = \frac{\partial \bar{T}_{NaS}}{\partial t'} \Big|_{x'} = \frac{h_{ann,i}\pi D_{NaS}L'_{NaS}(T_{htf}-\bar{T}_{ssc})+I_{NaS}\left(I_{NaS}R_{NaS}-\bar{T}_{NaS}\frac{dE_{NaS}}{d\bar{T}_{NaS}}\right)}{(mc_p)_{NaS}} \quad \text{(Equation 4-84)}$$

The transformed equations in Lagrangian coordinates are now given as:

$$\frac{\partial \bar{T}_{NaS}}{\partial t'} \Big|_{x'} = \frac{h_{ann,i}\pi D_{NaS}L'_{NaS}(T_{htf}-\bar{T}_{NaS})+I_{NaS}\left(E_{NaS}-\bar{T}_{NaS}\frac{dE_{NaS}}{d\bar{T}_{NaS}}\right)}{(mc_p)_{NaS}} \quad \text{(Equation 4-85)}$$

$$\frac{1}{L_{flow\ loop}} \frac{\partial T_{htf}}{\partial x'} \Big|_{t'} = \frac{h_{ann,o}\pi D_{at}(T_{at}-T_{htf})+h_{ann,i}\pi D_{at}(\bar{T}_{ssc}-T_{htf})}{(\dot{M}c_p)_{htf}} \quad \text{(Equation 4-86)}$$

For the initial heating-up phase of the receiver where no electrical charge or discharge occurs, the electrical current is zero and the transformed equations simplify as follows:

$$\frac{\partial \bar{T}_{NaS}}{\partial t'} \Big|_{x'} = \frac{h_{ann,i}\pi D_{NaS}L'_{NaS}(T_{htf}-\bar{T}_{NaS})}{(mc_p)_{NaS}} \quad \text{(Equation 4-87)}$$

$$\frac{\partial T_{htf}}{\partial x'} \Big|_{t'} = L_{flow\ loop} \times \left\{ \frac{h_{ann,o}\pi D_{at}(T_{at}-T_{htf})+h_{ann,i}\pi D_{at}(\bar{T}_{NaS}-T_{htf})}{(\dot{M}c_p)_{htf}} \right\} \quad \text{(Equation 4-88)}$$

The next sub-section now describes the discretization of the P.D.E's for numerical solution using a finite differences approach.

4.4.5 Discretization and Numerical Solution of the Partial Differential Equations

The transformed P.D.E's Equations 4-85 and 4-86 were discretized for solution via a finite differences numerical scheme comprising a first order forward difference (predictor), and a second order modified central difference (corrector).

Using the forward difference predictor, the HTF partial derivative was re-written as follows:

$$\frac{\partial T_{htf}}{\partial x'} \Big|_{t'} = \frac{T_{htf_{i+1}} - T_{htf_i}}{\Delta x'} \quad \text{(Equation 4-89)}$$

and

$$\frac{\partial \bar{T}_{NaS}}{\partial t'} \Big|_{x'} = \frac{\bar{T}_{NaS_{i+1}} - \bar{T}_{NaS_i}}{\Delta t'} \quad \text{(Equation 4-90)}$$

At the first increment $i = 1$ using the first order predictor:

$$T_{htf(1)} = T_{htf(0)} + \Delta x' \times L_{flow\ ch.} \left[\frac{\alpha_{ann,o} \pi D_{at} (T_{at} - T_{htf}) + \alpha_{ann,i} \pi D_{at} (\bar{T}_{NaS,initial} - T_{htf})}{(\dot{M}c_p)_{htf}} \right]_0 \quad \text{(Equation 4-91)}$$

Modifying this result using the second order corrector gives:

$$T'_{htf(1)} = T_{htf(0)} + \frac{\Delta x' \times L_{flow\ ch.}}{2} \left\{ \left[\frac{h_{ann,o} \pi D_{at} (T_{at} - T_{htf}) + h_{ann,i} \pi D_{at} (\bar{T}_{NaS} - T_{htf})}{(\dot{M}c_p)_{htf}} \right]_0 + \left[\frac{h_{ann,o} \pi D_{at} (T_{at} - T_{htf}) + h_{ann,i} \pi D_{at} (\bar{T}_{NaS} - T_{htf})}{(\dot{M}c_p)_{htf}} \right]_1 \right\} \quad \text{(Equation 4-92)}$$

Programme code for a Visual Basic macro was written in Microsoft Excel to implement the numerical solution of the system of equations. The predictor and corrector calculations were iterated until the difference

between predicted and corrected values was within a given tolerance of $1 \times 10^{-4} \text{ } ^\circ\text{C}$. The value of the absorber tube temperature used in these calculations was derived from the solution (using a Microsoft goalseek tool) of the precedence ordered non-linear equation (Equation 4-71) that was given in terms of the heat flux $\dot{q}'_{cond,at}$.

The other transient equation (Equation 4-93) regarding the sodium sulphur battery temperature \bar{T}_{NaS} , was solved analytically at the same increment using the “final corrected value” of HTF temperature obtained from the finite difference approximation to the solution.

$$\left. \frac{\partial \bar{T}_{NaS}}{\partial t'} \right|_{x'} = \frac{h_{ann,i} \pi D_{bt,o} L'_{NaS} (T_{htf} - \bar{T}_{SSC})}{(mc_p)_{SSC}} \quad \text{(Equation 4-93)}$$

Since x' is invariant at $(0, t')$, then Equation 4-93 becomes the ordinary differential Equation 4-94:

$$\frac{d\bar{T}_{NaS}}{dt'} = \frac{h_{ann,i} \pi D_{bt,o} L'_{NaS} (T_{htf} - \bar{T}_{NaS})}{(mc_p)_{NaS}} \quad \text{(Equation 4-94)}$$

The method by which this equation was solved analytically at $(x, t') = (0, t'_1)$ is given as follows:

$$\text{Firstly, let } C = \frac{h_{ann,i} \pi D_{bt,o} L'_{NaS} T_{htf}|_{0,t'_0}}{(mc_p)_{NaS}} \text{ and } A = \frac{c}{T_{htf}|_{0,t'_0}}$$

Equation 4-95 can now be re-written as:

$$\frac{d\bar{T}_{NaS}}{C - A\bar{T}_{NaS}} = dt' \quad \text{(Equation 4-95)}$$

Integrating both sides gives:

$$\int \frac{d\bar{T}_{NaS}}{C - A\bar{T}_{NaS}} \Big|_{0,t'} = \int dt' \quad \text{(Equation 4-96)}$$

The above integral is of the general form:

$$\int \frac{1}{ax + b} dx = \frac{1}{a} \ln|ax + b| + Constant \quad \text{(Equation 4-97)}$$

Therefore Equation 4-97 becomes:

$$-\frac{1}{A} \ln(C - A\bar{T}_{Nas}) = t' + Constant \quad \text{(Equation 4-98)}$$

At $t' = 0$, $\bar{T}_{Nas}|_{0,t'} = \bar{T}_{Nas}|_{0,0}$, and:

$$Constant = -\frac{1}{A} \ln(C - A\bar{T}_{Nas}|_{0,0}) \quad \text{(Equation 4-99)}$$

Therefore substituting for the constant term in Equation 4-97 gives:

$$-\frac{1}{A} \ln(C - A\bar{T}_{Nas}|_{0,t'}) = t' - \frac{1}{A} \ln(C - A\bar{T}_{Nas}|_{0,0}) \quad \text{(Equation 4-100)}$$

With ordinary algebraic manipulation, the Equation 4-100 can now be expressed with \bar{T}_{Nas} as the subject by use of the following steps:

$$\ln(C - A\bar{T}_{Nas}|_{0,t'}) = \ln(C - A\bar{T}_{Nas}|_{0,0}) - At' \quad \text{(Equation 4-101)}$$

$$\ln(C - A\bar{T}_{Nas}|_{0,t'}) - \ln(C - A\bar{T}_{Nas}|_{0,0}) = -At' \quad \text{(Equation 4-102)}$$

$$\ln \frac{(C - A\bar{T}_{Nas}|_{0,t'})}{(C - A\bar{T}_{Nas}|_{0,0})} = -At' \quad \text{(Equation 4-103)}$$

$$\frac{(C - A\bar{T}_{Nas}|_{0,t'})}{(C - A\bar{T}_{Nas}|_{0,0})} = \exp^{-At'} \quad \text{(Equation 4-104)}$$

$$(C - A\bar{T}_{Nas}|_{0,t'}) = \exp^{-At'}(C - A\bar{T}_{Nas}|_{0,0}) \quad \text{(Equation 4-105)}$$

$$\frac{[C - (C - A\bar{T}_{Nas}|_{0,0})\exp^{-At'}]}{A} = \bar{T}_{Nas}|_{0,t'} \quad \text{(Equation 4-106)}$$

$$\bar{T}_{Nas}|_{0,t'} = \frac{[C + (A\bar{T}_{Nas}|_{0,0} - C)\exp^{-At'}]}{A} \quad \text{(Equation 4-107)}$$

$$\bar{T}_{NaS}|_{0,t'} = \frac{[C - C \exp^{-At'} + A\bar{T}_{NaS}|_{0,0} \exp^{-At'}]}{A} \quad \text{(Equation 4-108)}$$

$$\bar{T}_{NaS}|_{0,t'} = \frac{C}{A} + \left(\bar{T}_{NaS}|_{0,0} - \frac{C}{A} \right) \exp^{-At'} \quad \text{(Equation 4-109)}$$

Since $\frac{C}{A} = T_{htf}|_{0,t'_0}$

$$\bar{T}_{NaS}|_{0,t'_1} = T_{htf}|_{0,t'_0} + \left(\bar{T}_{NaS}(0,t'_0) - T_{htf}|_{0,t'_0} \right) \exp^{-A(t'_1 - t'_0)} \quad \text{(Equation 4-110)}$$

where the time value at the next increment is given as:

$$t'_1 = \frac{\Delta x}{u_{htf}} - t_0. \quad \text{(Equation 4-111)}$$

Since $t_0 = t'_0$, then also:

$$t'_1 = \frac{\Delta x}{u_{htf}} - t'_0 \quad \text{(Equation 4-112)}$$

For $(x', t') = (0, t'_1)$, both C and $T_{htf}(0, t'_1)$ are evaluated using the properties of the HTF and NaS cell coded into the MS Excel macro at $(x', t') = (1, 0)$.

With this solution of the average cross sectional NaS cell temperature \bar{T}_{NaS} , all the temperature profiles along the EES receiver length are now defined. Thus the full mathematical model of the system has been presented. Although this model does assume an average temperature for both HTF and NaS cells in all computations performed, it still provides useful insights into the nature of expected heat transfer processes during operation of the conceptual EES receiver in a typical PTC solar field.

4.4.6 Assessment of the Numerical Method

The final section of this chapter comments on the numerical scheme used in solution of the system of equations. The standard in this respect is to evaluate the compatibility, convergence and stability of a numerical method. It must be first stated that investigation of the method's

compatibility was not possible as in this case there is no analytical solution for comparison.

However, convergence of the finite difference approximation to the partial differential equations was confirmed by directly varying the computational step size Δx , and indirectly varying the time step size Δt , through the HTF velocity. The nominal step size for Δx , was 0.5 m, the length of a typical T5 NaS cell. In the cases where the step size was both doubled and halved, the computation converged (Appendix I) with the difference between the finite difference approximations decreasing with step size.

Though a stability analysis was not possible, owing to the non-linear nature of the system of equations, research conducted by Cockcroft ^[204] confirmed stability of the numerical approach used in this work (a combination forward and modified central differences) in a linear system. Table 4-3 summarizes these findings for a film resistance model in both Eulerian and Lagrangian flow reference frames.

Table 4-3: A summary of the stability of Linear Finite Difference Schemes

Finite Difference Approximation to Derivative		Film Resistance Model	
Time (t)	Position (x)	Eulerian	Lagrangian
Forward	Forward	Conditionally stable	Conditionally stable
Forward	Backward	Conditionally stable	Conditionally stable
Forward	Central	Conditionally stable	Conditionally stable
Backward	Forward	Conditionally stable	Stable
Backward	Backward	Conditionally stable	Stable
Backward	Central	Conditionally stable	Stable
Central	Forward	Conditionally stable	Stable
Central	Backward	Conditionally stable	Stable
Central	Central	Conditionally stable	Stable

With regards to these findings, the forward and central difference combination (highlighted) was found to be completely stable in the Lagrangian reference frame. This is one of the primary reasons for the reference frame transformation described earlier in the previous section.

Though the complexity and non-linearity of the models ruled out compatibility and stability analyses, the general convergence observed in the numerical scheme, its validity for linear systems and the fact that model predictions closely follow experimental/model validated data are indications of reliability. The main points of this chapter are now recapped in the chapter summary which here follows.

Chapter Summary

In this chapter, the system of mathematical models used to describe the heat transfer processes and electrical current flow in the conceptual EES receiver of Chapter 3 have been presented. This quasi-transient system of 10 steady state and 2 transient equations was given in terms of the important nodular temperatures and heat fluxes of the EES receiver.

It was shown that the steady state equations were combined to produce a highly non-linear equation in $\dot{q}'_{cond,at}$, the heat flux conducted through the absorber wall flux, which was solved using the goalseek tool available in Microsoft Excel. The solution to this “*main*” equation served as the backbone of a Visual Basic macro coded in Microsoft Excel for the incremental solution of discretized transient equations along the axial length of the HTF flow path.

Next, in Chapter 5, the mathematical models here presented are used to simulate the initial heating operation of the conceptual EES receiver, in the solar field of a standard 50 MW_e PTC power plant.

Chapter 5

Simulation of the operation of the Conceptual EES Receiver in a typical 50 MWe PTC Power Plant

Introduction

This chapter explores the initial heating-up process of a conceptual EES receiver solar field, using the mathematical models just presented in Chapter 4. The solar field parameters are chosen to reflect those of the 50 MWe Andasol-1 PTC power plant (Figure 5-1) in Granada, Spain (latitude 37°).

As measured weather data for the Andasol-1 site was not readily available, weather data from the SEGS VI PTC plant at Kramer Junction, California, USA (Latitude 35°) ^[205] was used in the simulations. Though the solar radiation in Granada is slightly less than of the Kramer Junction site, the latitudes are similar and the Kramer Junction data should still provide a reasonable idea of the expected solar field performance.



Figure 5-1: South facing view of the 50 MWe Andasol-1 Solar PTC plant in Granada, Spain (Source: ^[206])

This chapter is divided into three sections. The first section compares key model outputs with respect to credible test data and the recognized heat transfer models of key researchers in the field. The second introduces the model set up parameters and physical dimensions used for the simulations to be presented in this chapter. The third and final section presents the results of simulations performed to investigate the initial heating of the conceptual EES receiver solar field, up to operating temperature above 300°C. The chapter then closes with a summary of the key points presented.

5.1 Key Comparisons of the EES Receiver Model Outputs

Heat transfer in the EES receiver is composed primarily of two “*useful energy*” producing processes: (a) heat transfer to the HTF and (b) heat transfer to the NaS batteries. It is the second aspect of this heat transfer process that constitutes the fundamental difference between this current model and all the other PTC receiver models developed to date.

Despite this difference however, it is still possible to compare the outputs of the EES receiver model with both credible PTC test data and with recognized models of key researchers. This can be achieved if the NaS cells are modelled under adiabatic conditions so that useful solar energy is transferred only to the HTF, as in the case of a standard PTC receiver.

By the process of setting the inner annular heat transfer co-efficient (for the NaS cells) to zero, changing the outer annular diameter to the standard internal diameter of a typical PTC receiver tube and making the inner one infinitesimally small, the required comparisons were realized.

Four key performance metrics of the conceptual EES solar receiver were evaluated, namely:

- a) Receiver heat loss per metre length with absorber temperature
- b) Collector efficiency with HTF temperature
- c) Useful energy gain of the HTF with temperature
- d) Tube temperature with loop position in metres

Forristall [3] and Dudley [207] are both prominent researchers in the field who have modelled the heat transfer processes in commercial PTC receivers. Forristall developed numerical 1-D and 2-D models which were solved in Engineering Equation Solver [208]. Dudley's model on the other hand was one dimensional and analytical.

Of the two models, the Forristall model [3] was chosen for most of the comparative simulations performed, as the simulation parameters used were the most explicit. The following operating conditions were used in all comparative simulations:

- DNI (Direct normal insolation) = 950 W/m^2
- HTF = Therminol VP-1 @ 2.58 m/s
- Collector = LS-2
- Receiver = Schott PTR-70
- $T_{\text{sky}} = 14^\circ\text{C}$; $T_{\text{amb}} = 22^\circ\text{C}$

The results of these comparisons are now presented in the next subsection.

5.1.1 Receiver Heat Loss per metre length (W/m)

In the first comparison, the EES model was used to simulate heat loss characteristics of a receiver with physical dimensions similar to that of a standard PTC receiver.

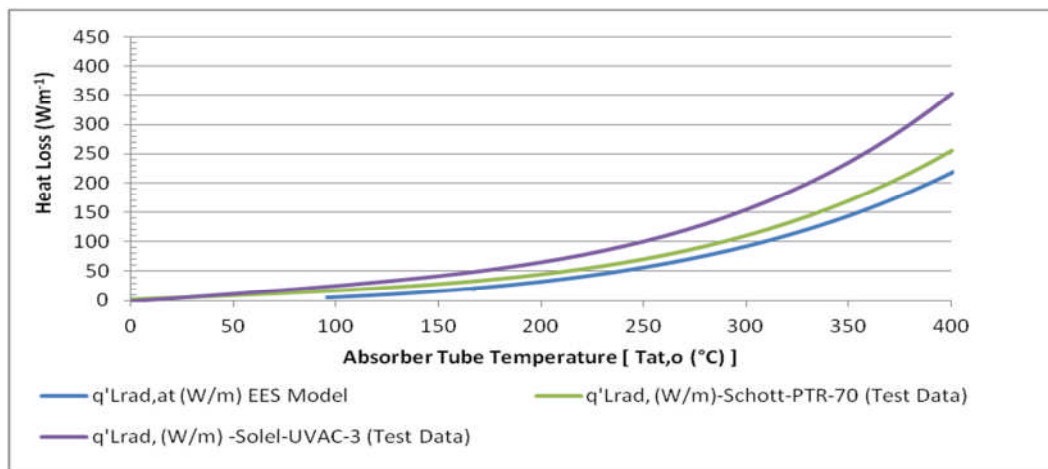


Figure 5-2: Absorber heat loss per metre length vs. absorber tube temperature

The predicted heat loss, as a function of absorber temperature is plotted in Figure 5-2, along with experimental data obtained from test results conducted at the National Renewable Energy Laboratory (NREL) USA. These test results were obtained from NREL test reports by Burkholder and Kutscher [2, 209].

It was observed that the EES model under predicts the actual absorber heat loss. This results from the fact that it assumes a perfect vacuum between absorber and glass tubes, thus ignoring the convective heat exchange in the annulus. However of the two receivers, the Schott PTR-70 test results most closely approximated those of the idealized condition predicted by the EES receiver model. In the next sub-section, the collector efficiency output of the model is compared with validated models and experimental data of researchers Forristall and Dudley.

5.1.2 Collector Efficiency with HTF Temperature above Ambient

The predicted EES collector efficiency was compared against the Forristall model [3] and the experimental results from Dudley [207]. Like the Forristall model, the EES model used Therminol VP-1 as the circulating HTF, and simulated performance under similar operating conditions. As expected, the EES model predicted slightly higher collector efficiency for the same operating temperature, as a result of the ignored heat losses previously mentioned.

However, the efficiency curve can be seen to follow the general shape of the Forristall model by a fixed value of approximately 5-6 % (Figure 5-3) owing primarily to the fact that the same HTF was modelled in both cases. The efficiency “*fall-off*” in the experimental data reported by Dudley [207] however, differed from the other two curves. This resulted from the fact that Syltherm 800 HTF was instead used and the tests conditions were also slightly different.

In the next, sub-section, the “*useful energy gain*” model output is comparatively evaluated.

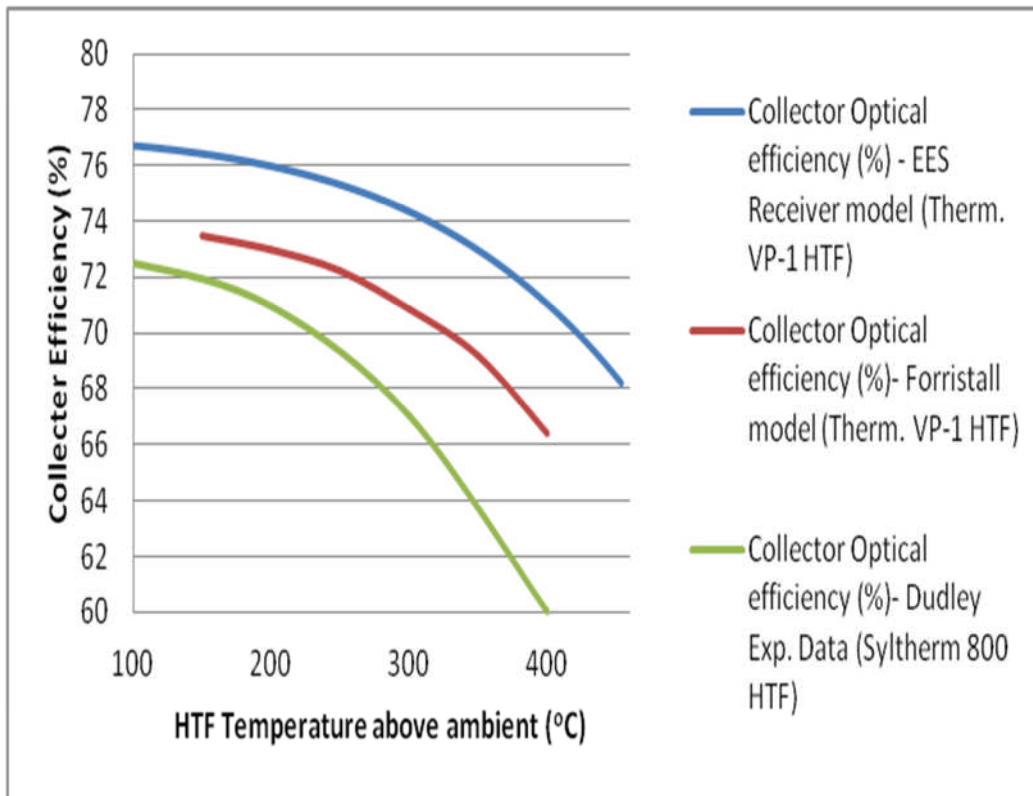


Figure 5-3: Collector efficiency vs. HTF temperature above the ambient (°C)

5.1.3 Useful Energy Gain of the HTF

The useful energy gain of the HTF with operating temperature along with the 1D model of Forristall [3] is given in Figure 5-3. The model also over predicts the useful energy gain due to the ignored losses stated earlier (convective heat loss between absorber and glass cover and the conductive heat loss from the tube support points along the receiver tube length).

Although Forristall's model simulated performance over only a small temperature range, the EES model curve nevertheless follows the general trend of the Forristall model (Figure 5-4) but exceeds each value by approximately 200 W/m. This value is representative of the combined heat losses (convective and conductive) per metre length of receiver, ignored by EES receiver model and gives a rough idea of the magnitude of these losses.

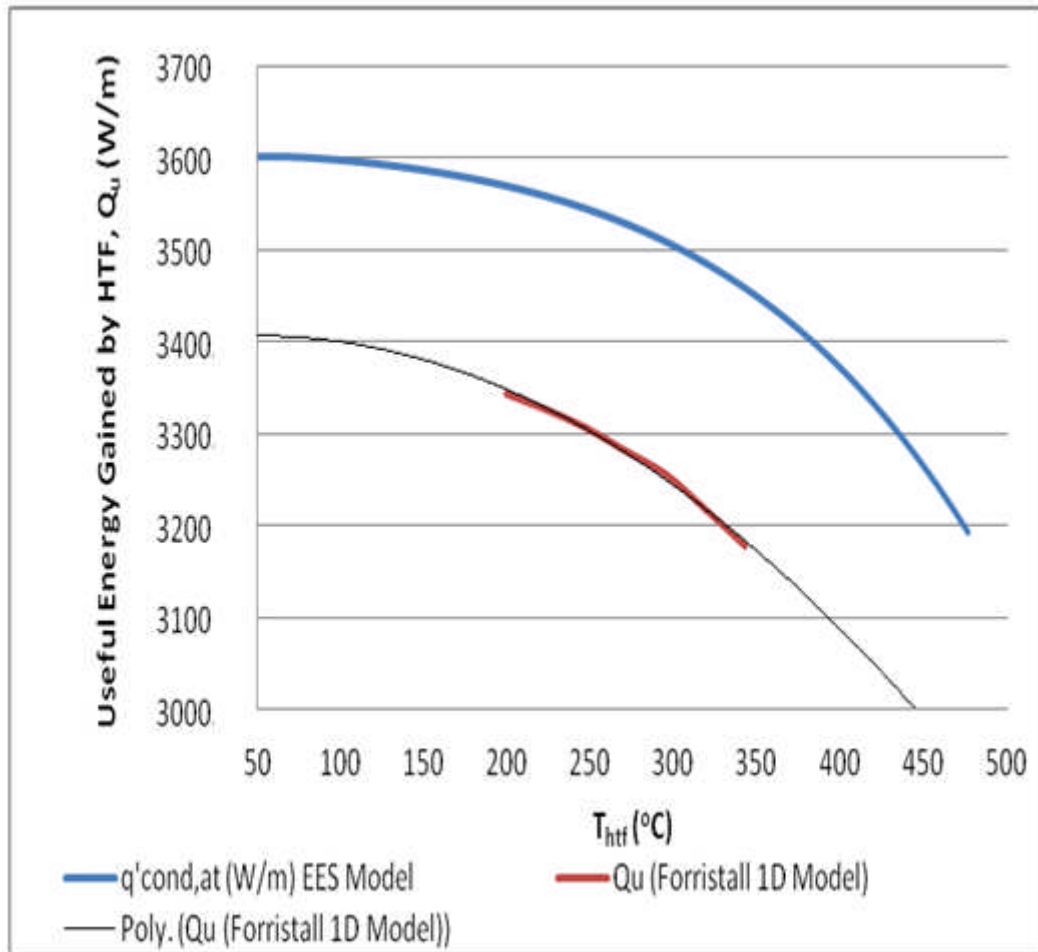


Figure 5-4: Useful energy gain of the HTF with operating temperature

The final comparison presented in the next-subsection concerns the HTF temperature profile along the length of the flow path.

5.1.4 HTF Temperature Profile along Flow Loop

The final key comparison concerned the HTF temperature profile along the flow loop as predicted by the EES receiver. This was compared with the predicted profile of the Forristall 2-D model^[3] by setting the inner heat transfer coefficient of the NaS cell to zero. Results revealed that the EES temperature profile closely followed the Forristall model at lower operating temperatures (Figure 5-5) but slightly over predicted the final HTF outlet temperature.

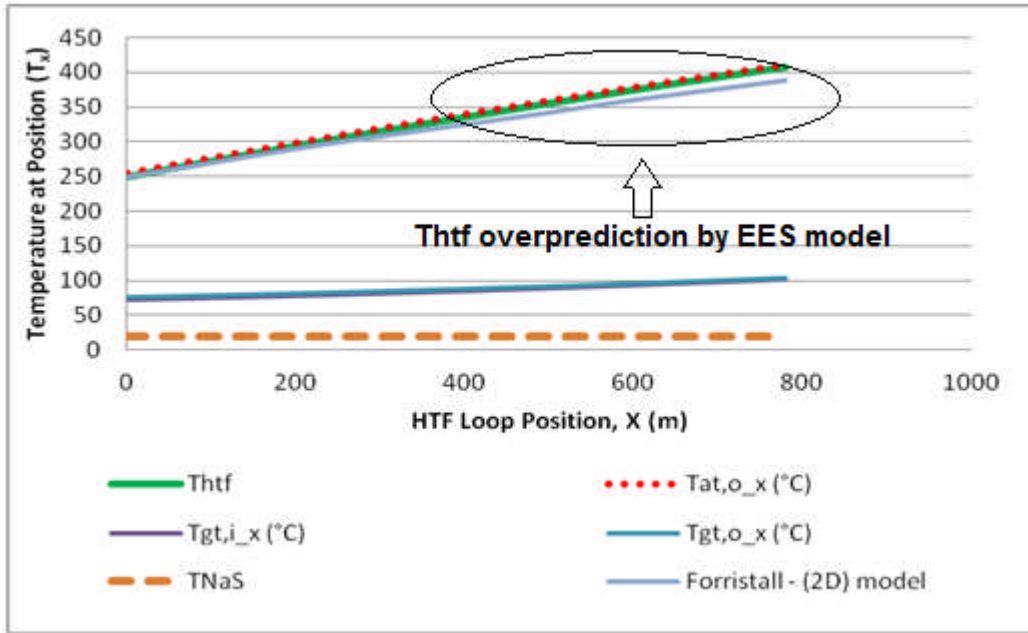


Figure 5-5: Simulated tube temperature profiles with HTF loop position

Based on the results of the comparative simulations, the EES model has been shown to closely follow the model predictions of other key researchers and also of valid test data, albeit from an idealized perspective. This is suggestive of general model reliability for simulating the theoretical performance of the conceptual EES solar field. It has been deduced that the EES model over predicts solar field efficiency by roughly 5-6% and that a predicted useful energy gain of between 3200 – 3600 W/m (over the 0 - 400°C operating range) contained an ignored heat loss in the order of 200 W/m.

Now that all the important comparative simulations have been presented, the next sub-section evaluates with experimental data the phase change temperature assumption made in Chapter 4 for the NaS cell.

5.1.5 Phase Change Temperature Validation using Experimental Data from the constructed prototype EES Receiver

The reader will recall that though sodium and sulphur have phase change temperatures of 98°C and 115°C respectively, a decision was taken in

Chapter 4, to use the higher melting point of sulphur ($\approx 115^{\circ}\text{C}$) as the official phase change temperature of the NaS cell. This is due to the fact that the outer sulphur electrode, a poor thermal conductor must first be heated before the inner sodium electrode can melt.

Experimental data obtained from the EES heating rig confirmed this value as a good choice. An examination of the temperature profiles for HTF, absorber and NaS cells (Figure 5-6) revealed a relatively steady temperature increase until a temperature of approximately 116°C was reached. At this point, the temperature profiles became unstable and subject to oscillation. This instability results from the thermocouples inside the EES receiver prototype, simultaneously experiencing the “*temperature reducing effect*” of absorbed phase change energy combined with sustained heat transfer from a band heaters around the pipework.

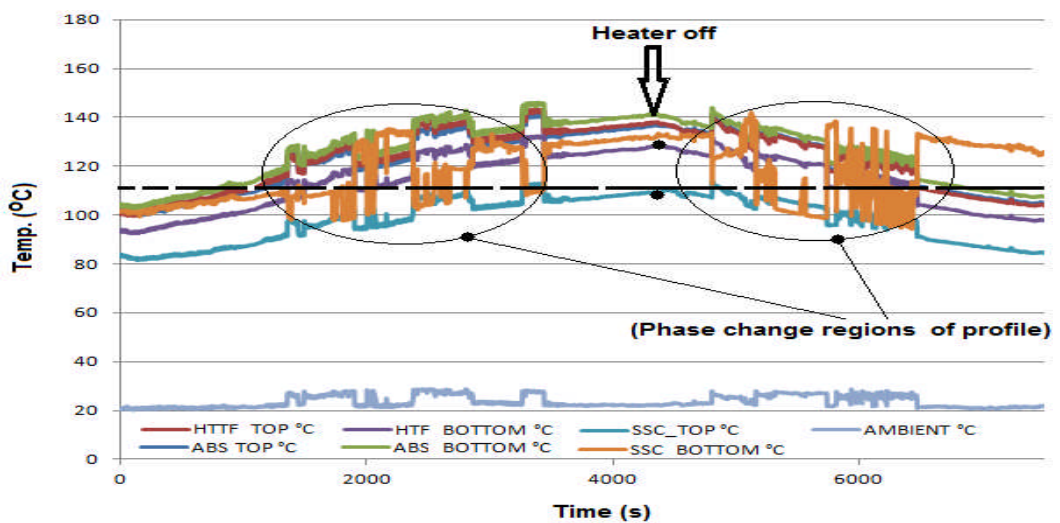


Figure 5-6: Tube temperature profiles along the experimental EES receiver

One other key observation from the experimental data is the significant temperature difference that exists between the HTF and NaS cell during the initial stages of the heating-up process (Figure 5-7). Within the $0 - 150^{\circ}\text{C}$ temperature range, results from the experimental rig showed this temperature difference to be $10 - 20^{\circ}\text{C}$ on average.

A similar difference was also found in the simulations which follow in this chapter. However, the temperature difference is larger because of the significantly lower heat losses between the receiver and the ambient, in the case of the EES receiver model.

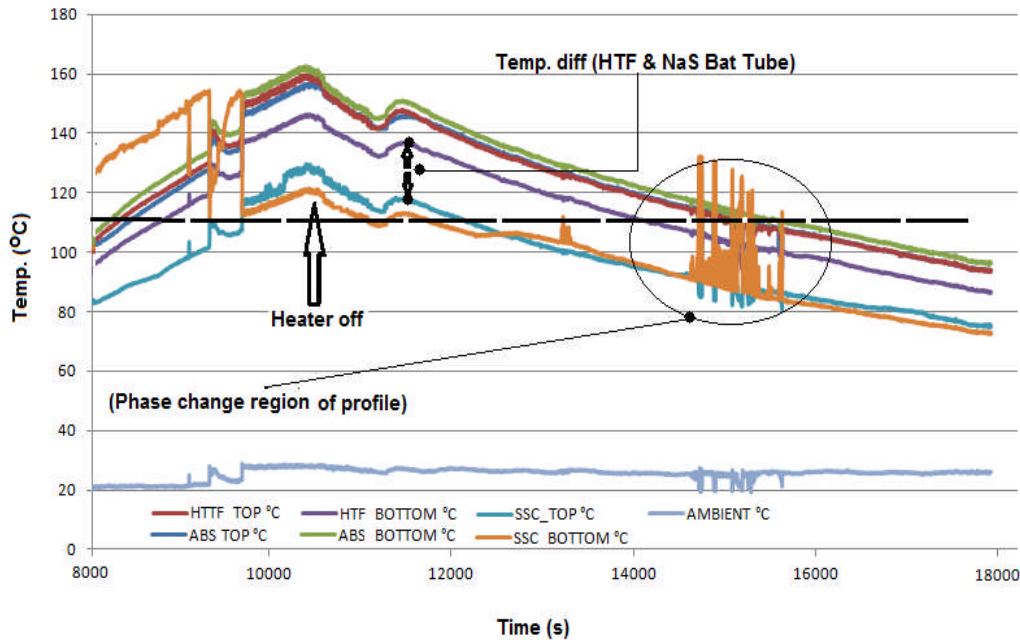


Figure 5-7: Plot illustrating temperature difference between HTF and NaS temperatures

This now concludes the chapter section of comparative simulations for the key outputs of the ESS model. The next section presents the important model set-up parameters and physical dimensions used in the initial heating simulations to be presented in the final section of this chapter.

5.2 Setting up the Model for the Solar Field of the Conceptual EES Receiver

This section describes the associated model set-up parameters and physical dimensions for simulating the initial heating operation of the EES receiver in an Andasol-1 type PTC solar field (Figure 5-8). It is important to note that the EES receiver is intended to operate in a complementary mode with standard molten salt tank storage, for 24 hours using 8 hours of molten salt thermal storage and 4 hours of NaS cell electrical energy storage.

In this regard, thermal energy from the solar field HTF is assumed to be theoretically transferred to a “hot” molten salt tank, so as to reduce the thermal gradient exposure of the NaS cells.

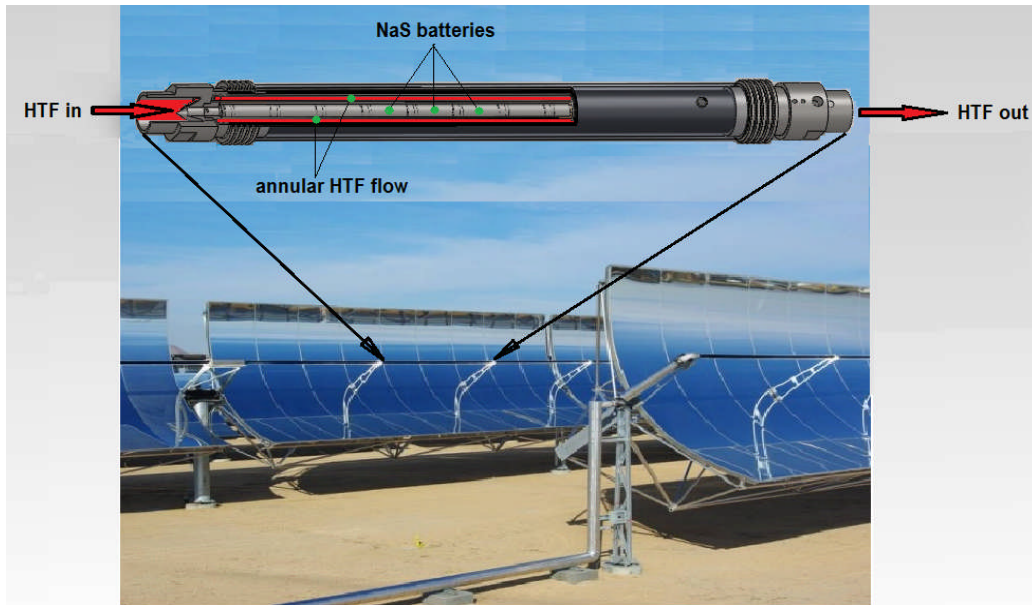


Figure 5-8: Illustration of the integration of the EES receiver in a typical PTC solar field. (Adapted: PVTECH)

The sub-section which now follows specifies the important physical dimensions of the system used in the simulations.

5.2.1 Physical Specifications of the Simulated EES Receiver and Collector

For the simulation of the conceptual EES receiver, a 1.2 kWh TEPCO/NGK T5 NaS cell was used. Using key data from Wen ^[210], a cross sectional sketch (Figure 5-9) was made to show the key internal dimensions of this cell. The cell is approximately 91 mm in diameter and 516 mm in length. However since the “*reactive or working*” cell length is determined by the length of the solid internal β –alumina electrolyte, a length of 500 mm (0.5 m) was used in all simulations.

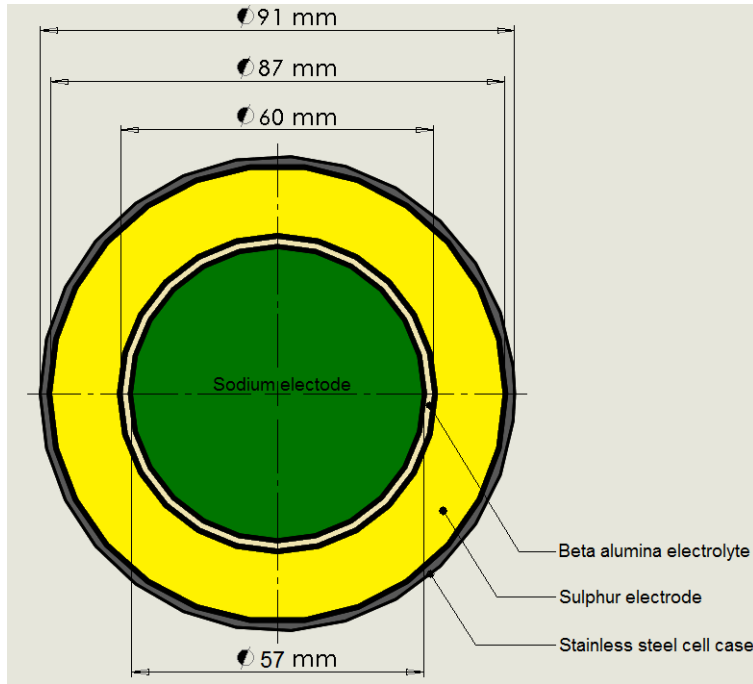


Figure 5-9: Sketch of cross section through a typical Tepco T5 NaS cell

The dimensions presented for the T5 cell (Figure 5-9) now make it possible to specify the physical dimensions of the conceptual EES receiver to be simulated. One of the main challenges presented here was to limit the size of the absorber tube, as flux concentration ratio falls and heat losses increase with larger absorber diameters.

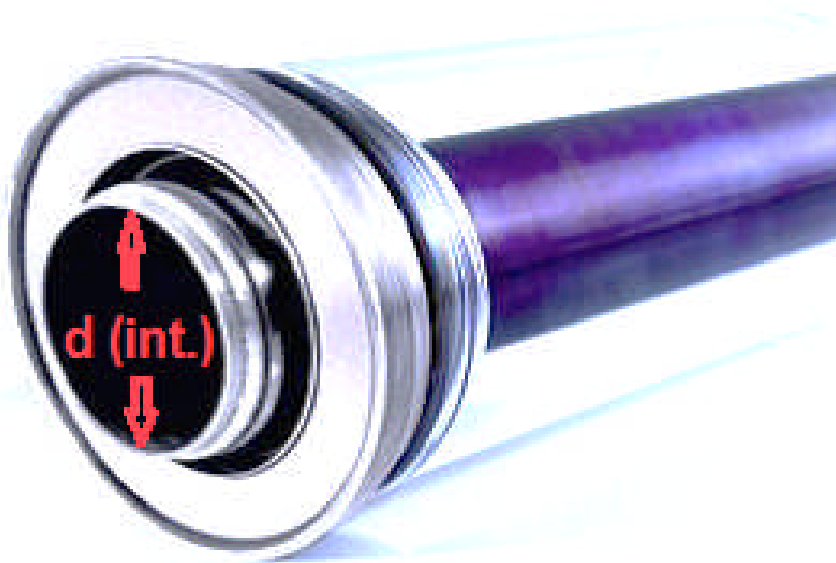


Figure 5-10: Image showing the end of the industry standard Schott PTR-70 PTC receiver tube (Source: Schott Solar)

In this regard, the internal diameter of the conceptual EES receiver must be of such to accommodate not only the T5 cell (91 mm in diameter), but also provide adequate annular space for the flow of HTF.

Since standard PTC receivers such as the Schott PTR-70 and the Solel UVAC-3 all have internal diameters ($d_{int.}$) of approximately 66 mm (Figure 5-10), their physical dimensions could not be used in the conceptual system. Although use of a smaller diameter NaS cell (eg. Tepco T4.1 or T4.2 cells [211]) would allow use of a standard receiver tube, the resulting lower storage capacity of these cells could prove uneconomical for the system.

As standard receiver dimensions could not be used to accommodate the T5 cell, a conceptual receiver cross section was constructed using readily available commercial pipe/tube sizes. Given the constraint of minimizing the absorber tube diameter, while still accommodating the T5 NaS cell along with an adequate HTF annulus, tube sizes (Figure 5-11) were chosen to allow a slightly smaller, yet reasonable annular HTF flow diameter (40 mm compared to standard of 66 mm).

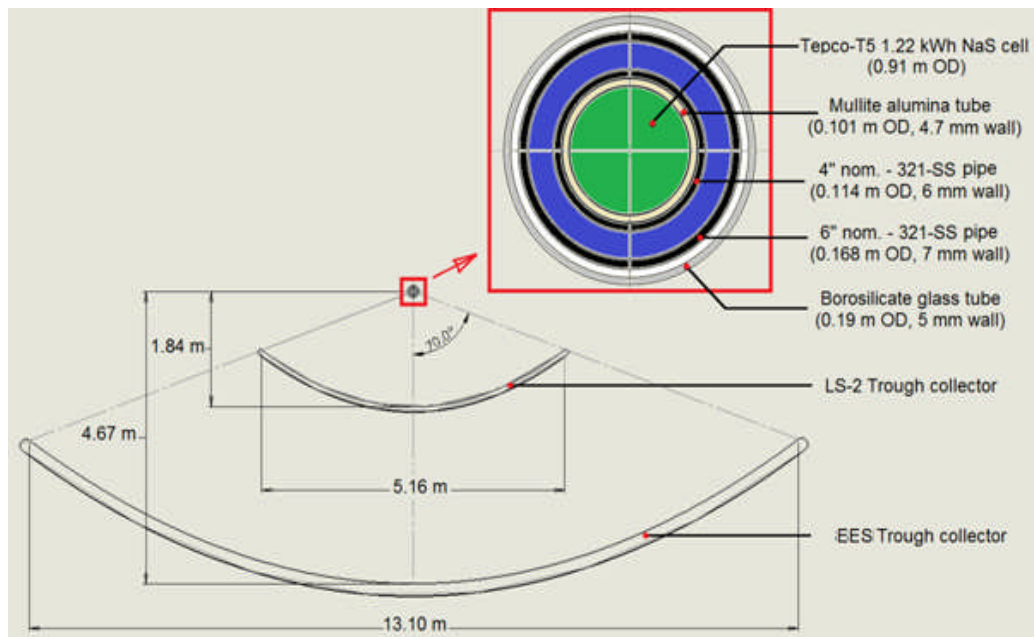


Figure 5-11: Schematic showing cross section of the conceptual EES Receiver/Collector system

Data on alumina [212], glass [213] and steel tube dimensions [214] was obtained from “sentotech.com”, “glass-solutions.co.uk” and “onlinemetals.com” websites respectively.

As previously mentioned, both the flux concentration ratio reduction and increased heat losses that accompany a larger receiver diameter are unavoidable when implementing the EES receiver concept. However these are insignificant compared to the storage benefits that could be achieved from the system. In regards to flux concentration ratio, using a LS-2 collector and PTR-70 receiver system as reference (Figure 5-12), it was revealed that for traditional flux concentration ratios, an EES collector aperture of approximately 13.1 m was required.

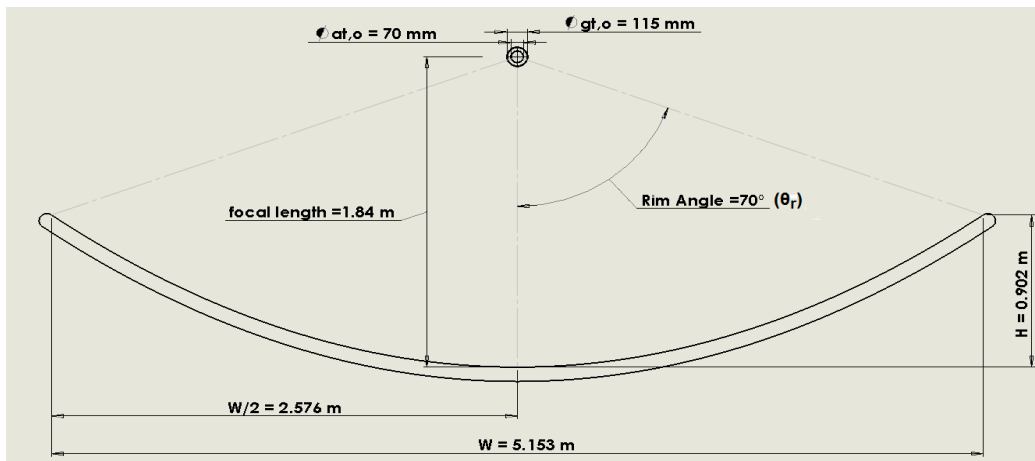


Figure 5-12: Schematic showing cross section of a standard PTR-70 Receiver and LS-2 Collector combination

Analysis of the economics of this increase requires further investigation that is outside the scope of this work. However, the simulations presented in this chapter revealed that using current PTC collector specifications (eg. LS-3/E-100/E-150), good results for system performance were still obtainable.

Simulations of the conceptual EES solar field were therefore performed on a conceptual collector of dimensions similar to that of LS-3/E-100/E-150 specifications (Figure 5-13).

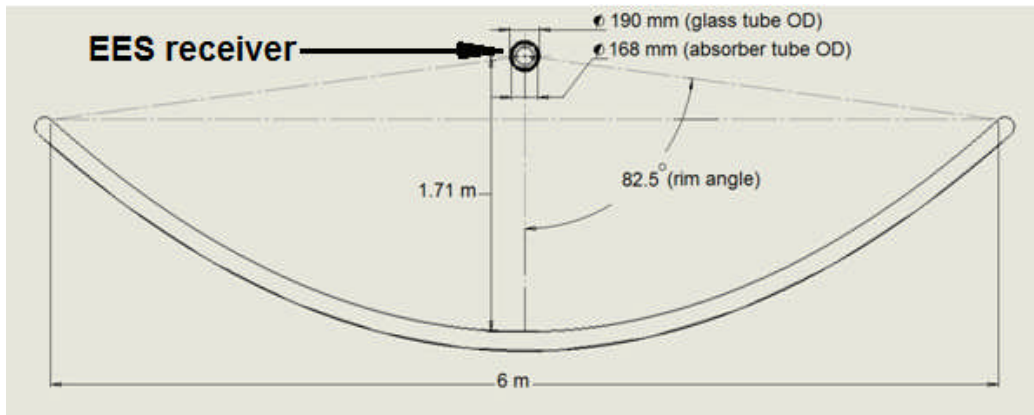


Figure 5-13: Collector dimensions used in simulation of the EES Receiver solar field

Now that the physical dimensions of the EES receiver/collector have been specified, the next section presents the parameters used to set up the various model simulations.

5.2.2 Setting up the EES Receiver Model

The simulation parameters used in the EES receiver model are given below in Table 5-1. The EES receiver dimensions are those mentioned in the previous section and the solar field specifications are similar to those of the Andasol-1 PTC power plant.

Table 5-1: Model parameters used in EES Receiver solar field simulation

EES Receiver solar field model property (Unit)	Value
Absorber tube outer diameter, [wall] (m)	0.168, [0.007]
Glass tube outer diameter, [wall] (m)	0.190, [0.005]
NaS battery tube outer diameter, [wall] (m)	0.114, [0.006]
HTF annulus diameter, (m)	0.040
HTF loop length, (m)	576
Number of HTF loops	156
Tepco - T5 NaS cell diameter, (m)	0.0916

EES Receiver solar field model property (Unit)	Value
Therminol VP-1 HTF mass flow (kg/s)	3-9
HTF inlet temperature (°C)	20
Initial NaS battery temperature (°C)	20
Ambient temperature (°C)	(SEGS VI data file, July 11, 1991)
Sky Temperature (°C) ^[184, 215]	$0.05525 \times T_{amb}^{1.5}$
Start-up time of day	6:30 am
(Latitude, Longitude)- SEGS Solar Plants, USA- <i>[Used for weather data]</i>	(35°N, 117°W)
(Latitude, Longitude)- 50 MW _e Andasol-1 Solar Plant, Granada, Spain <i>[Used for solar field specifications in this model]</i>	(37°N, 73°W)
DNI @ start-up (W/m ²)	(SEGS VI data file, July 11, 1991)
Flux concentration ratio	12.37
Receiver incidence angle	0°
Collector/receiver parameters $\tau, \alpha, \rho, \varepsilon, \gamma, K_{\theta}$ <i>(transmittance, absorbance, reflectivity, emissivity, mirror shape factor, and incidence angle modifier respectively)</i>	$\tau_{glass} = 0.97; \alpha_{at} = 0.98; \alpha_{gt} = 0.03; \rho_{mirror} = 0.9; \varepsilon_{at} \text{ (correlation)}^9; \varepsilon_{gt} = 0.9; \gamma = 0.9; K_{\theta} = 1$
Collector types applicable for comparison in this model	LS-3, E-100, E-150

One of the set-up parameters listed in Table 5-1, identified the industry standard Therminol VP-1, as the HTF chosen for simulation. The temperature dependent fluid properties for this HTF are now given as follows:

$$\lambda_{Therminol\ VP-1} = 0.137743 - 8.19477 \times 10^{-5}(T_{htf}) - 1.92257 \times 10^{-7}(T_{htf})^2 + 2.5034 \times 10^{-11}(T_{htf})^3 - 7.2974 \times 10^{-15}(T_{htf})^4 \text{ [W/mK]}$$

$$c_{pTherminol\ VP-1} = 1498 + 0.002414 \times (T_{htf}) + 5.9591 \times 10^{-6}(T_{htf})^2 - 2.9879 \times 10^{-8}(T_{htf})^3 + 4.4172 \times 10^{-11}(T_{htf})^4 \text{ [J/kg.K]}$$

$$\rho_{Therminol\ VP-1} = 1083.25 - 0.90797 \times (T_{htf}) + 0.00078116 \times (T_{htf})^2 - 2.367 \times 10^{-6}(T_{htf})^3 \text{ [kg/m}^3\text{]}$$

$$\nu_{Therminol\ VP-1} = e^{\left(\frac{544.149}{(T_{htf})+114.43} - 2.59578\right)} \times 10^{-6} \text{ [m}^2\text{/s]}$$

For HTF performance comparisons with Therminol VP-1, simulations of solar field performance using Dowtherm A (used in Andasol-1 solar field) and Syltherm 800 HTF's were also effected. Since temperature dependent equations for the fluid properties of these HTF's could not be found, but were required for simulations, polynomial fits made in Microsoft Origin-Pro 8.1 software to tabular manufacturer's data. These equation based fits were found to produce very good estimates and details on their accuracy (e.g R² values), are provided in Appendices R through U of this thesis.

For Syltherm 800:

$$\lambda_{syltherm\ 800} = 0.13877 - 1.88021 \times 10^{-4}(T_{htf}) - 1.56094 \times 10^{-10}(T_{htf})^2 \text{ [W/mK]}$$

$$c_{p_{syltherm\ 800}} = 1574.27947 + 1.7072 \times (T_{htf}) + 1.56094 \times 10^{-7}(T_{htf})^2 \text{ [J/kg.K]}$$

$$\rho_{syltherm\ 800} = 953.16424 - 0.91658 \times (T_{htf}) + 4.21141 \times 10^{-4}(T_{htf})^2 - 1.67059 \times 10^{-6}(T_{htf})^3 \text{ [kg/m}^3\text{]}$$

$$\mu_{syltherm\ 800} = 0.01533 - 3.79993 \times 10^{-4}(T_{htf}) + 7.03717 \times 10^{-6}(T_{htf})^2 - 9.78061 \times 10^{-8}(T_{htf})^3 + 9.14537 \times 10^{-10}(T_{htf})^4 - 5.50071 \times 10^{-12}(T_{htf})^5 + 2.08325 \times 10^{-14}(T_{htf})^6 - 4.78395 \times 10^{-17}(T_{htf})^7 + 6.07105 \times 10^{-20}(T_{htf})^8 - 3.26206 \times 10^{-23}(T_{htf})^9 \text{ [Pa.s]}$$

For Dowtherm A:

$$c_{p_{Dowtherm\ A}} = 1515.74506 + 2.79199 \times (T_{htf}) + 0.00212 \times (T_{htf})^2 - 2.74935e - 05 \times (T_{htf})^3 + 1.49289e - 07 \times (T_{htf})^4 - 3.91739e - 10 \times (T_{htf})^5 + 4.09815e - 13 \times (T_{htf})^6 \text{ [J/kg.K]}$$

$$\lambda_{Dowtherm\ A} = 0.1419 - 1.59976 \times 10^{-4}(T_{htf}) - 4.03066 \times 10^{-11}(T_{htf})^2 \text{ [W/mK]}$$

$$\rho_{DowthermA} = 1076.50757 - 0.83565 \times (T_{htf}) + 3.09141 \times 10^{-4}(T_{htf})^2 - 1.73931 \times 10^{-6}(T_{htf})^3 \text{ [kg/m}^3\text{]}$$

$$\mu_{DowthermA} = 7.195 - 0.17379 \times (T_{htf}) + 0.00198 \times (T_{htf})^2 - 1.20115 \times 10^{-5}(T_{htf})^3 + 3.97125 \times 10^{-8}(T_{htf})^4 - 6.72827 \times 10^{-11}(T_{htf})^5 + 4.56618 \times 10^{-14}(T_{htf})^6 \text{ [mPa.s]}$$

This now concludes the second section of this chapter, which outlined the important physical dimensions and set-up parameters used in the EES model simulations. The third and final section now presents the results of these simulations.

5.3 Model Simulations of the initial heating-up of the EES Receiver Solar Field

The simulation of the initial heating of the EES receiver is considered using a “single HTF loop”, the basic building block of every PTC solar field. In order to obtain a more accurate picture of the expected receiver operation, DNI and ambient test data (Figure 5-14) from the SEGS VI PTC plant at Kramer Junction, California USA on the summer day July 18, 1991 was used. Use of this data was motivated by the fact that test results from these plants have been a reference point for PTC plant analysis and optimization since their construction in the early 1980’s.

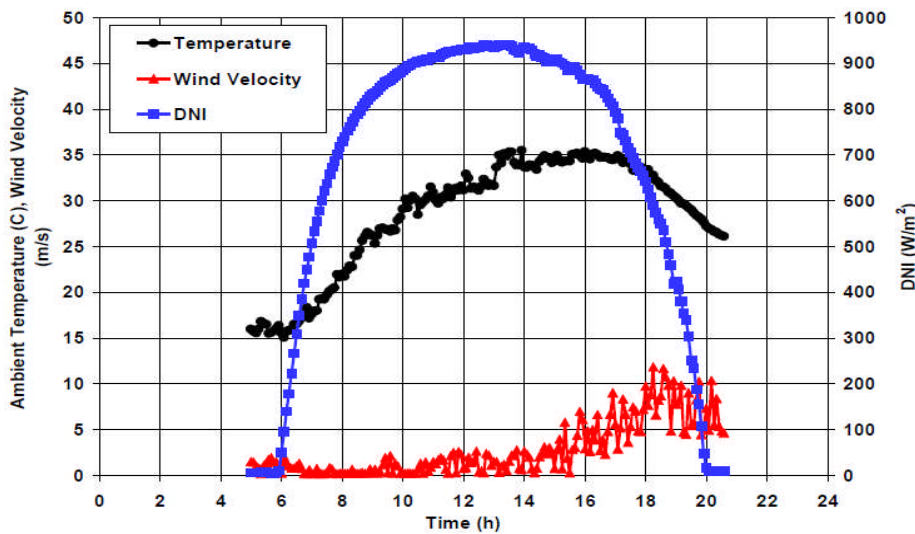


Figure 5-14: Weather data at SEGS VI power plant, Kramer Junction, California on July 18, 1991 (Source:^[205])

Although there is nothing special about this data set, it is typical of a “good” summer day and provides information for DNI, ambient temperature and wind speed all in a single graph. Microsoft OriginPro 8.6 software was used to produce polynomial fits to the test data, which was later integrated into the Visual Basic code used for simulations. Details of these fits are provided in the Appendices J, K and L.

For the model start-up, NaS battery temperatures along the HTF loop are held at their initial cold temperature of 20°C. This is referred as the “zero pass” through the system (Figure 5-15). The HTF was thus allowed to heat up as it flows through the loop at a relatively low mass flow of 2.5 kg/s, a value chosen to reduce the pumping power expended during initial heating and at the same time allow a HTF temperature rise above 100°C. Model results predicted an exit temperature of 140°C, or a temperature rise of 120°C. This value is close to the standard temperature rise of 100°C, typical of all solar fields operating with synthetic oil, at fully rated mass flows.

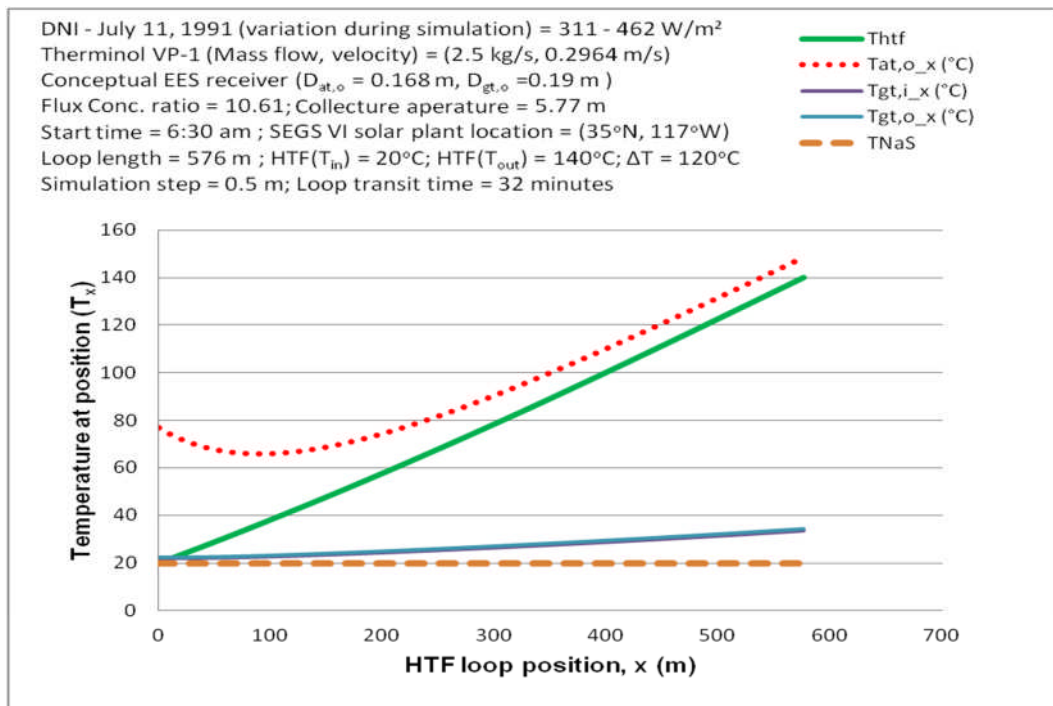


Figure 5-15: Temperature profiles during the “zero pass” through the HTF loop

After the “zero” pass was used to establish the initial temperature profile of the HTF, heat transfer was thereafter allowed with the NaS cells during on the “first pass” of the HTF through the loop. As expected, heat transfer to the NaS cells resulted in a slight fall in HTF temperature ($\approx 130^{\circ}\text{C}$) when compared to the outlet temperature of the “zero pass” profile (140°C).

This fall would have been greater had it not been for the relatively high series internal thermal resistance of the NaS cells, a value largely influenced by the thermal resistances of the sulphur electrode (0.205 W/mK)^[216] and β -alumina electrolyte (3 W/mK)^[217] respectively.

Another important observation is the large difference (Figure 5-16) between the absorber tube and HTF temperatures at start-up. This large difference results from the impact of concentrated solar radiation on an initially cold absorber tube, and the time delay in effecting heat transfer to the HTF (absorber thermal inertia). It was also seen that this difference is significantly reduced as the HTF heats up along the HTF flow path.

The glass cover temperature change was seen to be nonlinear, but is at a significantly lower value compared to the NaS and HTF temperatures. Also, owing to incident concentrated solar radiation passing “into” the receiver, the outer glass surface was seen to be slightly hotter than the inner one.

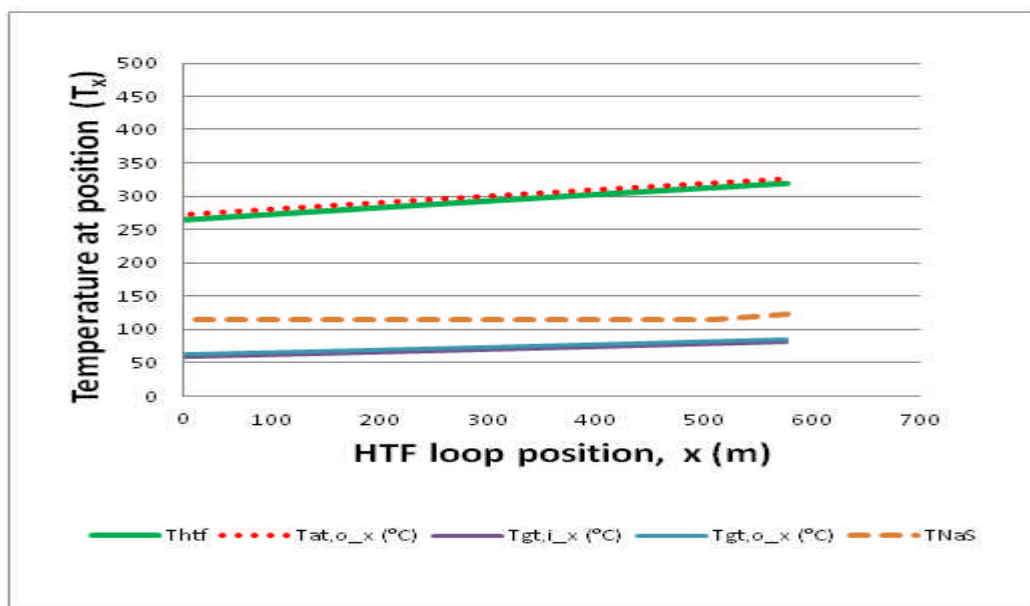


Figure 5-16: Temperature profiles during the “first pass” through the HTF loop

It is important to mention that heat transfer from the HTF to the NaS cells occurs only “after one residence time through the total power plant flow circuit” (comprising solar field loop, header, runner and the pipework of the storage/power block) and only if the solar field HTF “return temperature” exceeds the initial cold temperature of the NaS cell bed. Therefore, depending on the initial temperatures of the NaS cells and other sections of the flow circuit, it is possible that the NaS cells could be “cooled” rather than heated, on return of the HTF to the solar field.

In order to continue analysis, it was important to develop a rough estimate of the maximum time delay between HTF exit and re-entry, in a representative HTF loop. A schematic depicting the layout typical of the Andasol-1 power plant layout (Figure 5-17) was therefore used to estimate the HTF flow distance between the power block and one of the HTF loops furthest from it (loop 117). Based on a “rough” calculation, the average distance the HTF travels to and from this loop, is approximately 2000 m.

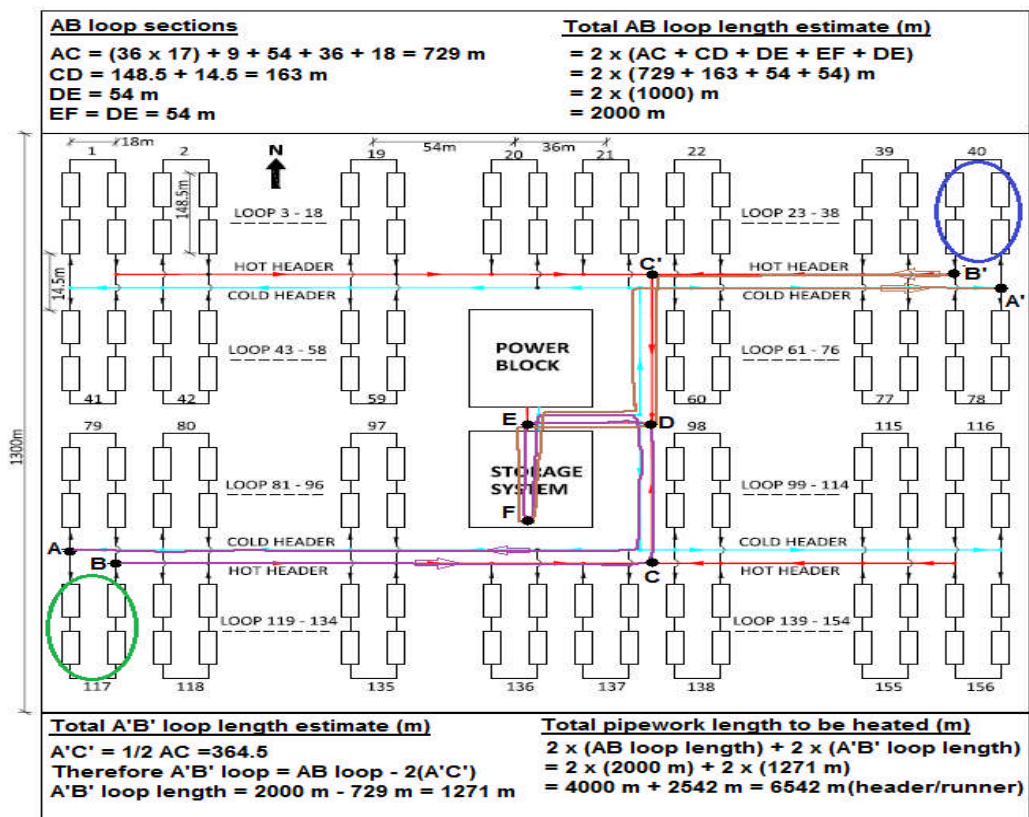


Figure 5-17: Schematic illustrating the layout of an Andasol-1 type PTC solar field (Adapted:^[218])

Further, for estimation of the time delay associated with HTF's exit and re-entry into the solar field, it is also necessary to know the average HTF velocity through this "*estimated 2000 m of pipework*". In the System Advisor Model (SAM) '*Technical Manual for the Physical Trough Model*'^[219], Wagner and Gilman of NREL, USA refer to PTC plants as having three different pumps for the HTF flow loop. These pumps are used to connect the three main piping sections of the plant, (power block, solar field and header/runners). Therefore as different flows are typical across the three main sections of HTF flow circuitry, it was inappropriate to apply the same flow velocity of 0.2964 m/s used previously for the "*first pass*" through the solar field, to the rest of pipework in the system.

According to Wagner and Gilman, the design-point HTF velocity used for PTC plants in SAM software is 1.85 m/s. Using this velocity as a "*rough estimate*", the maximum expected time delay between solar field HTF exit and re-entry into the chosen representative loop was evaluated as follows:

$$\text{Time delay} = \frac{\text{Total distance}}{\text{design point velocity}} = \frac{2000 \text{ m}}{1.85 \text{ m/s}} = 1081 \text{ s} \approx 18 \text{ mins}$$

In the first pass, simulations revealed an HTF loop exit temperature of approximately 130°C. As stated earlier in this chapter, the EES receiver operates in conjunction standard thermal storage, but before the storage system can be charged, the "*entire 2000 m length of pipe work*" must be heated up by the "*entire solar field*".

This requires determination of the mc_p value of the pipe work. For a worst case scenario, the physical properties and dimensions of of the largest pipe work section (runners) in a standard PTC plant were used to estimate the mc_p value of the entire 2000 m length of pipe work. Wagner and Gilman^[219] give the largest pipe size used in the SAM model as 72" schedule D steel pipe with an internal diameter of 1.778 m and a wall thickness of 34.5 mm.

The volume of a 2000 m length of this pipe is calculated as follows:

$$volume = \pi(D_o - D_i)^2 \times L_{pipe} = \pi(1.847 \text{ m} - 1.778 \text{ m})^2 \times 6542 \text{ m} = 97.84 \text{ m}^3$$

Based on the work of Kelly and Kearney ^[220] the pipe work is here assumed to be ASTM A106, Grade B, seamless carbon steel pipe. The density ^[221] of this carbon steel is given in an industry datasheet as 7870 kg/m³.

Therefore the mass of pipework to be heated is given as:

$$Mass = Density \times Volume = 7870 \text{ kg/m}^3 \times 97.84 \text{ m}^3 = 7.7 \times 10^5 \text{ kg} = 770 \text{ tonnes}$$

The mass of absorber pipework in the entire solar field must also be heated up, before heat transfer can begin to the HTF or NaS cells. Using the “real” HTF loop length of 600 m, the total length of the 156 loops in the solar field is calculated as: $600 \text{ m} \times 156 = 93,600 \text{ m}$

The solar field absorber pipe volume can therefore be calculated as follows:

$$volume = \pi(D_o - D_i)^2 \times L_{pipe} = \pi(0.168 \text{ m} - 0.154 \text{ m})^2 \times 93600 \text{ m} = 57 \text{ m}^3$$

Using the same density value as for ASTM A106, Grade B, seamless carbon steel pipe, the mass of absorber pipe to be heated is given as:

$$Mass = Density \times Volume = 7870 \text{ kg/m}^3 \times 57.634 \text{ m}^3 = 454 \times 10^3 \text{ kg} = 454 \text{ tonnes}$$

Therefore the total mass of power plant pipe work to be heated is given as:

$$Mass \text{ total} =$$

$$Mass \text{ (solar field pipe work} + \text{ pipework connecting to power block)} \text{ [tonnes]}$$

$$Mass \text{ total} = 454 + 770 = 1224 \text{ tonnes}$$

Now, the energy captured by the HTF as it moves through the each flow loop of the solar field can be calculated as:

$$Energy \text{ captured (J)} = \dot{M}_{HTF} \text{ [kg/s]} \times C_{p,HTF} \text{ [J/kgK]} \times \Delta T \text{ (K)} \times t \text{ [s]}$$

The C_p value for Therminol VP-1 increases with temperature. Therefore in order to remain conservative, the “cold temperature” C_p value of 1548

J/kgK at the 20°C start-up temperature was used in calculation. The ΔT for this calculation is 110 K ([130 – 20]°C), but a value of 100°C was used for calculation purposes. From the model simulation, the time required for one pass of the HTF through the 576 m loop at a mass flow of 2.5 kg/s (flow velocity of 0.2964 m/s) is 32 minutes. Therefore the energy captured by the HTF flow through the single representative loop is:

$$\text{Energy captured} = 2.5 \text{ kg/s} \times 1548 \text{ J/kg.K} \times 100\text{K} \times (32 \times 60)\text{s} = 743 \text{ MJ}$$

An Andasol-1 type solar field consists of 156 loops. Therefore assuming the same mass flow in all 156 loops the total energy capture of the entire solar field during this time can be estimated to be:

$$\text{Solar field energy capture} = (743.04 \times 156)\text{MJ} = 116 \text{ GJ}$$

It was already estimated that it would take approximately 18 minutes for the HTF to pass through the 2000 m of header/runner pipe work in the AB flow path (Figure 5-17) and this time is used as representative of all field loops for simulation purposes. Therefore it can be concluded that on average every 18 minutes, the 2000 m length of pipe work would receive 115.914 GJ of energy from the entire solar field. This translates to a rate heat transfer rate of:

$$\text{Heat transfer rate} = \frac{115.914 \text{ GJ}}{(18 \times 32 \times 60)\text{s}} = 3.354 \text{ MJ/s}$$

The “Engineering Toolbox” website gives the specific heat of carbon steel as 0.49 kJ/kg.K. Therefore, the energy required to heat up the entire 1224 tonnes of pipe work also by 100 K is calculated as:

$$\text{Required Pipe work Heat Energy (J)} = m_{\text{pipe work}} \times C_{p,c\text{-steel}} \times \Delta T$$

$$\text{Required Pipe work Heat Energy (J)} = 1224000 \text{ kg} \times 490 \text{ J/kg.K} \times 100\text{K} = 59.95 \text{ GJ}$$

If the heat transfer rate to the pipe work is 107.33 MJ/s as calculated earlier, then the total time required to reach an equilibrium temperature of 130°C is given as:

$$\text{Heating time (s)} = \frac{\text{Required Pipe work Heat Energy (J)}}{\text{Heat transfer rate (J/s)}}$$

$$\text{Heating time (s)} = \frac{59.95 \text{ GJ}}{3.354 \text{ MJ/s}} = 17875 \text{ s} = 4.97 \text{ h}$$

This translates to a time of approximately 5 hours, a value which may prove conservative as during this time, the actual solar (DNI value W/m^2) would have been increased beyond the maximum value of the range used in the initial 32 minute simulation.

However this time delay does provide a useful point in time from which to continue with the initial heating-up of the solar field from beyond the 130°C value. Since simulation began at 6:30 am, adding 5 hrs to this time would allow simulation to continue from the 130°C temperature value with a new start time of approximately 11:30 am and with HTF and NaS temperature profiles as depicted by the “first pass” (Figure 5-16). This simulation produced the “second pass” profile shown below.

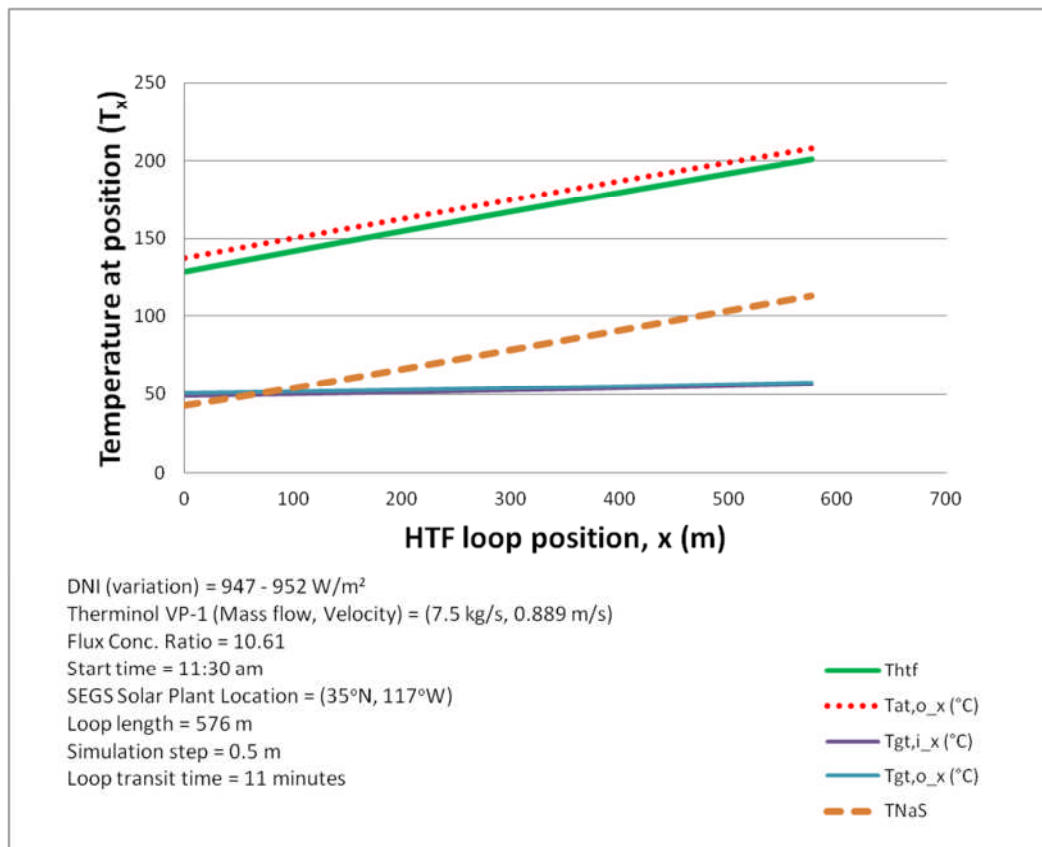


Figure 5-18: Second pass of Therminol VP-1 HTF through a representative loop in the solar field

In the “second pass” (Figure 5-18), the HTF which had been previously held at 130°C until it had brought the entire plant pipe work up to temperature, is now passed through the 576 m flow loop. As the DNI value at this time of day (11:30 am) has now approached the rated (solar noon) value, the mass flow was increased to a rated 7.5 kg/s resulting in a shorter transit time of 11 minutes. The outlet HTF temperature was seen to rise to a new value of approximately 200°C during this transit time.

At this point, it is important to point out, that this new HTF outlet temperature of 200°C will not be seen again at the HTF loop inlet until the entire PTC plant pipework has been heated to this temperature. Based on the 5 hour time delay calculated for a 100K rise, it is evident that with only 12 hours of solar radiation per day, it is impossible to heat up the entire plant from a cold temperature of 20°C to a power cycle temperature of approximately 400°C in one day without utilizing a gas fired boiler to initially heat up the system.

This is actually what has to be done when commissioning new plants, and the previous calculations served mainly to show the level of delay that could be encountered when heating up the conceptual solar field. From this point onward, it is assumed that all plant pipe work has already been heated up to the power cycle temperature of 400°C. However the 18 minute delay between HTF loop exit and re-entry in the solar field will still be observed for simulations. Observing this delay, the “*third pass*” start time for HTF flow through the solar field (Figure 5-19) was calculated as follows:

3rd pass start time = 11:30am (2nd pass start time) + (11 mins in solar field transit time) + (18 mins delay for return to solar field) = 11:58 am.

Thus 11:58 am was used as the start time of the “*3rd HTF pass*” through the solar field. Results of this pass are provided in Figure 5-19 (see overleaf).

At the end of the fourth pass (Figure 5-20), the simulation shows that the NaS cells in the first half of the loop would have been undergoing phase

change, with only a few cells near the end of the loop having fully completed phase change.

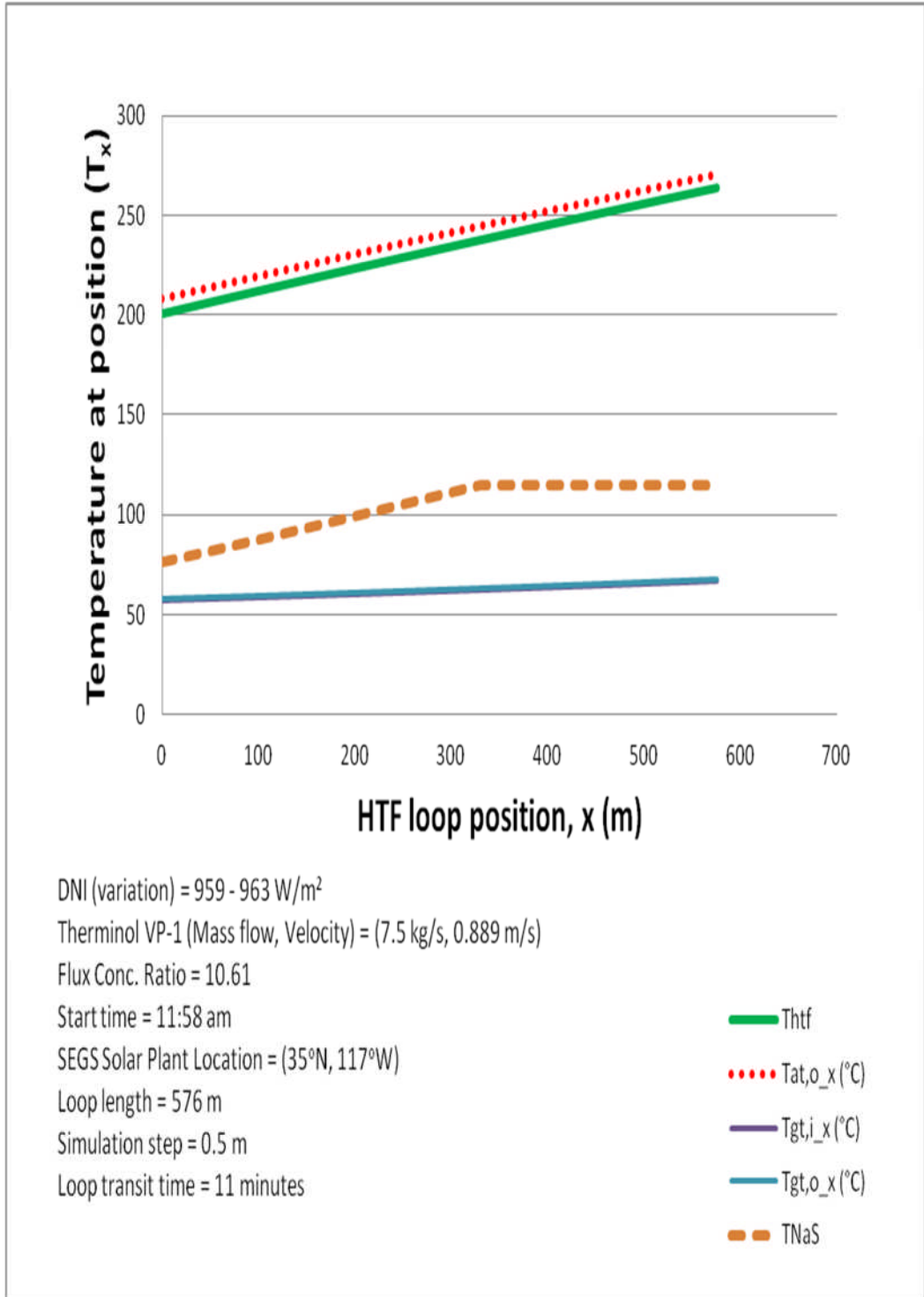


Figure 5-19: Third pass of Therminol VP-1 HTF through a representative loop in the solar field

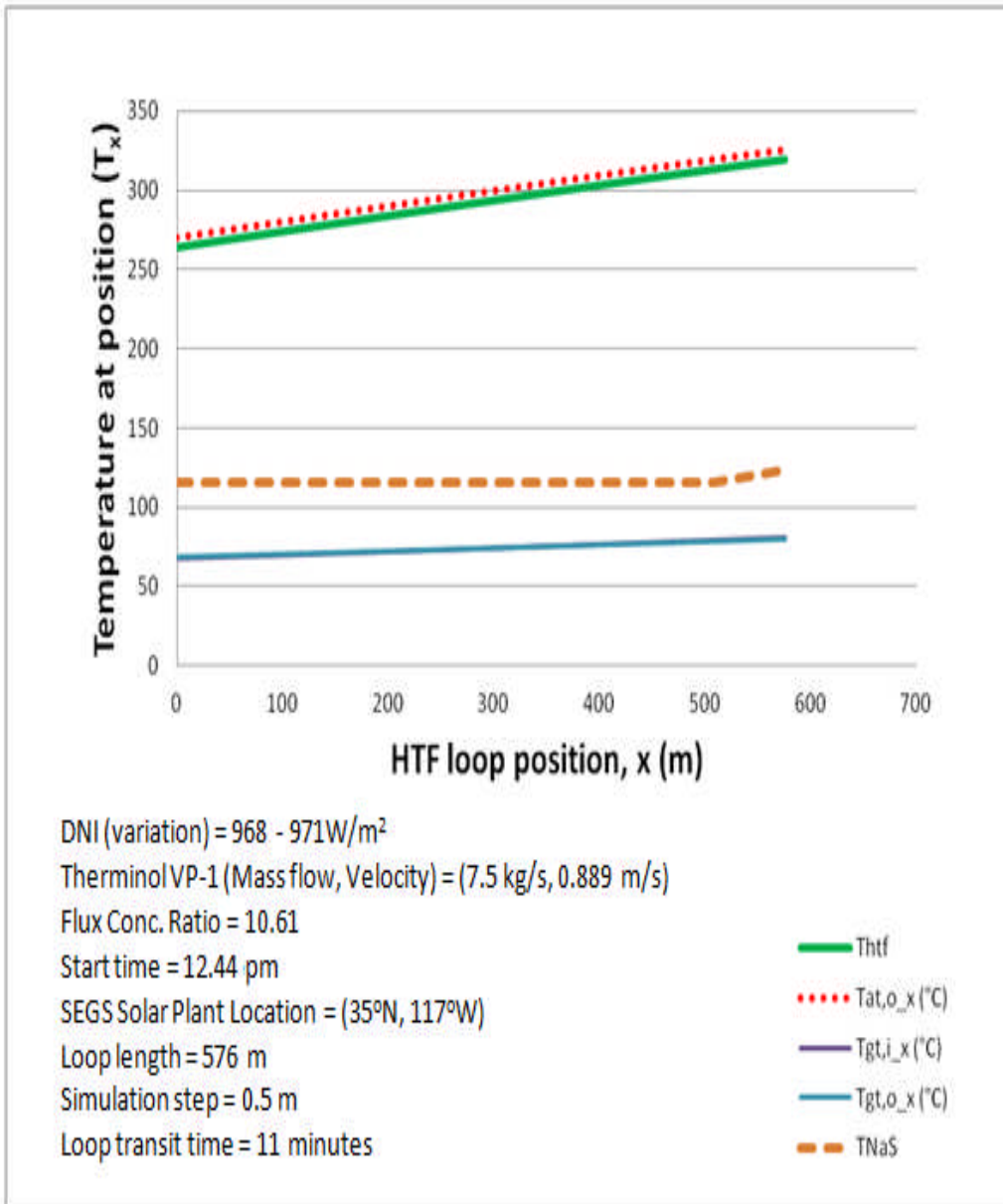


Figure 5-20: Fourth pass of Therminol VP-1 HTF through a representative loop in the solar field

By the time of the fifth pass (Figure 5-21), most of the NaS cells in the loop would have passed through phase change and would have again begun to experience temperature rise. It can be seen that there is a slight fall in the gradient of the slope near the end of this profile. This was influenced by the previous gradient at the end of the fourth pass, resulting in a lower driving force for heat transfer to the NaS cells during the fifth pass.

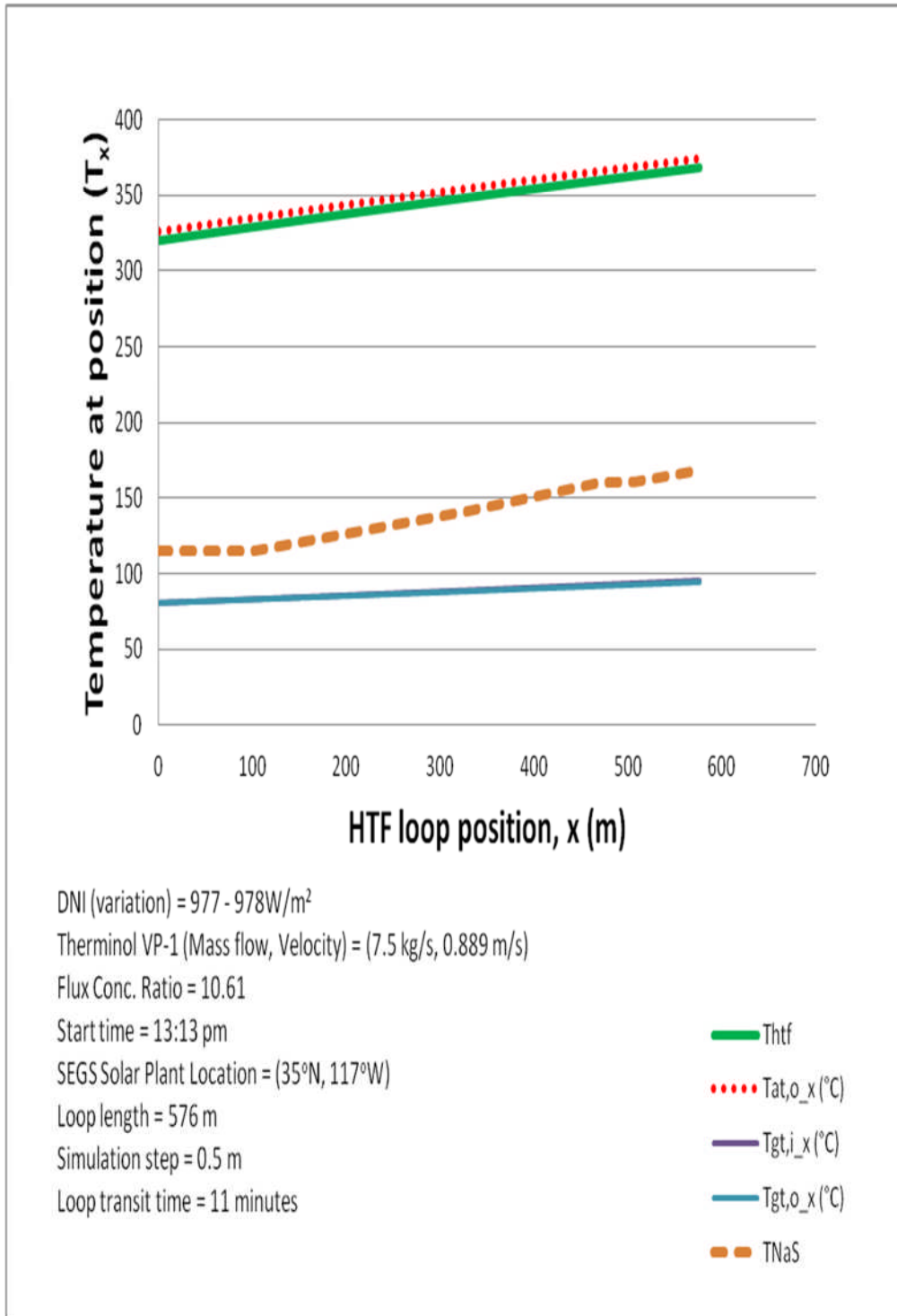


Figure 5-21: Fifth pass of Therminol VP-1 HTF through a representative loop in the solar field

At the time of the sixth pass (Figure 5-22), simulations revealed that all the NaS cells would have completed phase change, and that cell temperatures would continue to rise, approaching that of the average HTF temperature.

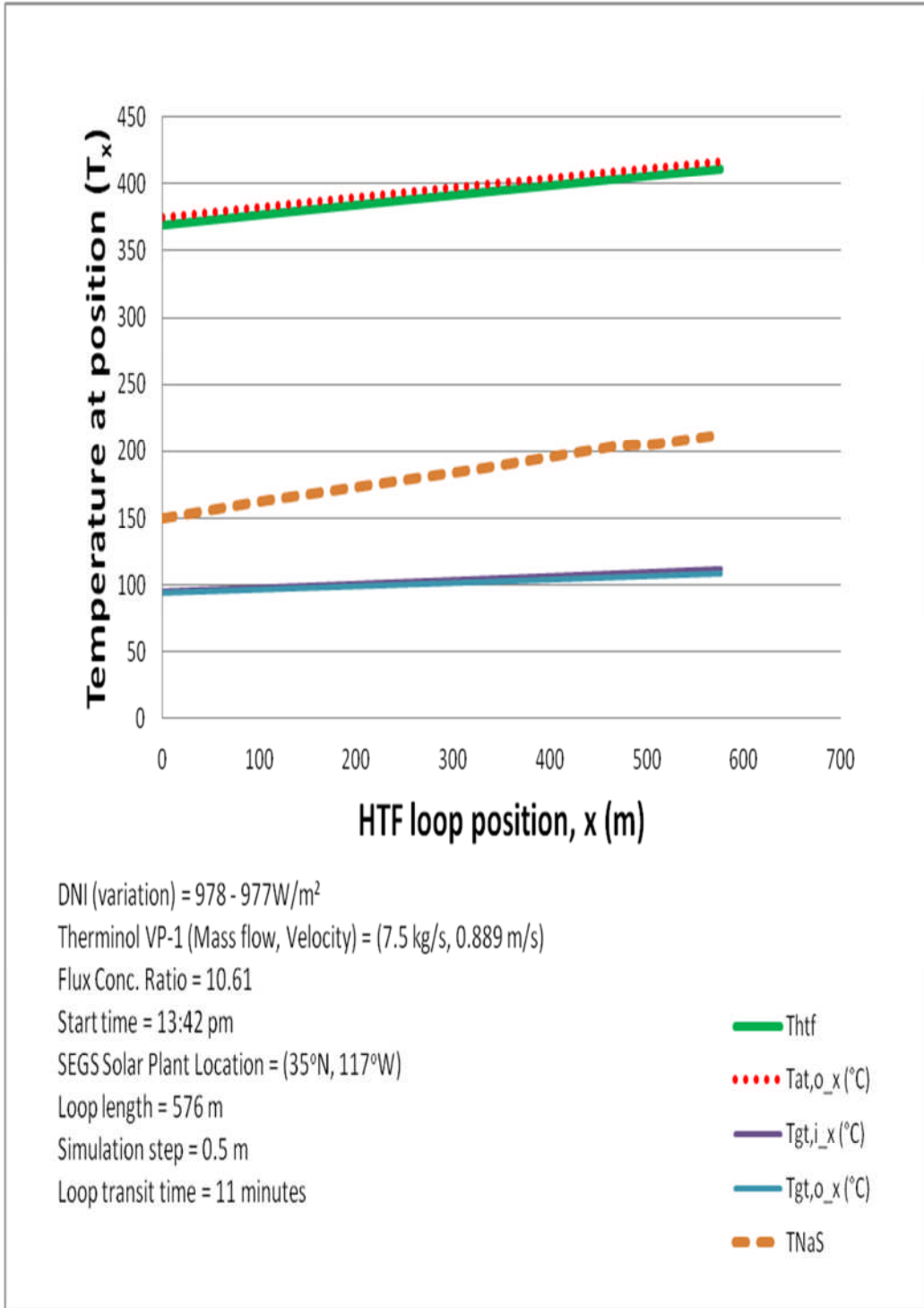


Figure 5-22: Sixth pass of Therminol VP-1 HTF through a representative loop in the solar field

For the 7th to 13th passes, (Figures 5-23 to 5-29) results show the NaS battery temperature gradually approaching that of the HTF. In all these passes the HTF is assumed to be “cooled down” by heat transfer in the

plant's thermal storage system and returned to the solar field at a fairly constant temperature of 300°C.

The simulated temperature profiles for the 7th to 13th passes of HTF through a representative the solar field loop are now presented as follows:

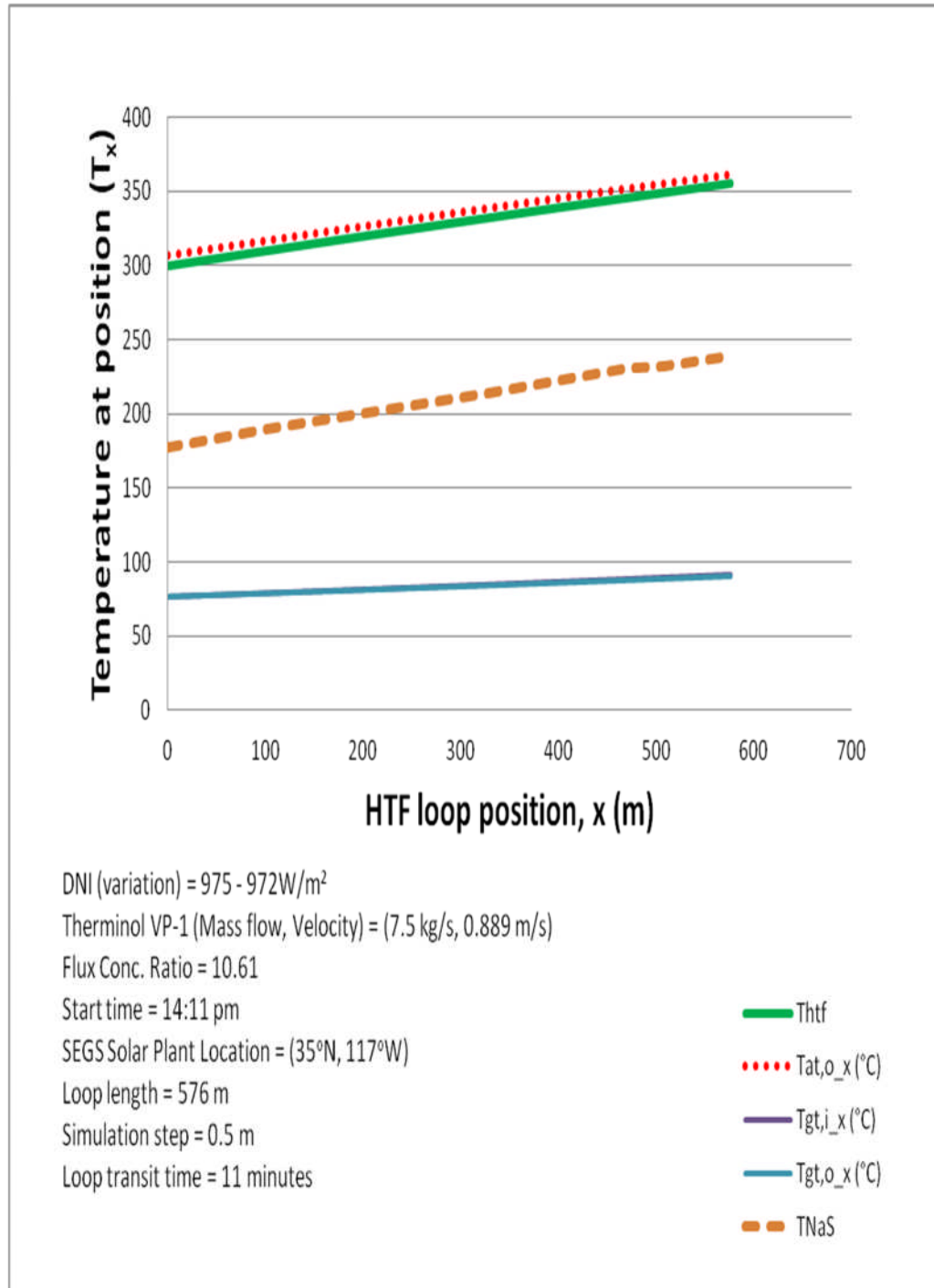


Figure 5-23: Seventh pass of Therminol VP-1 HTF through a representative loop in the solar field

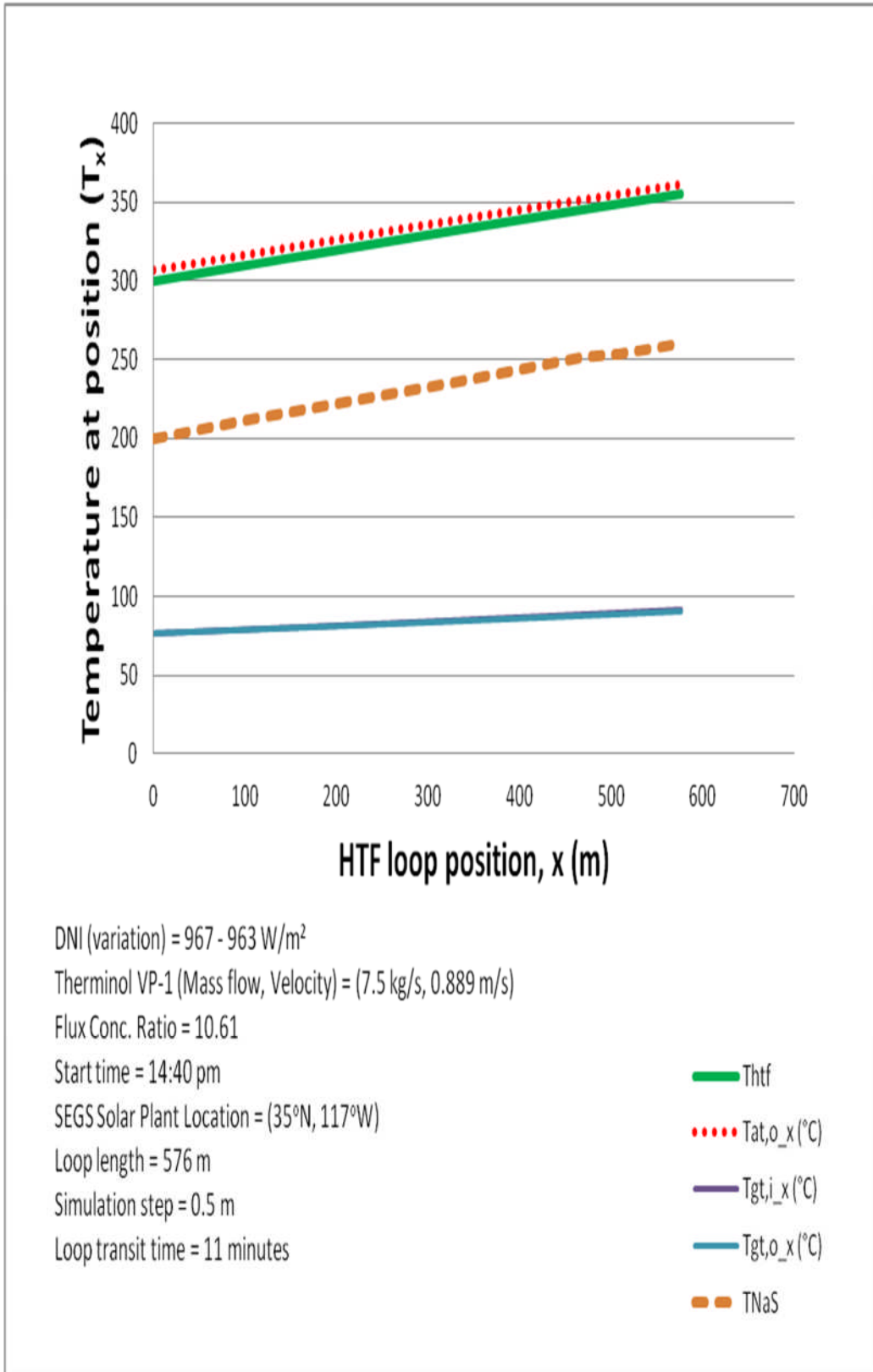


Figure 5-24: Eighth pass of Therminol VP-1 HTF through a representative loop in the solar field

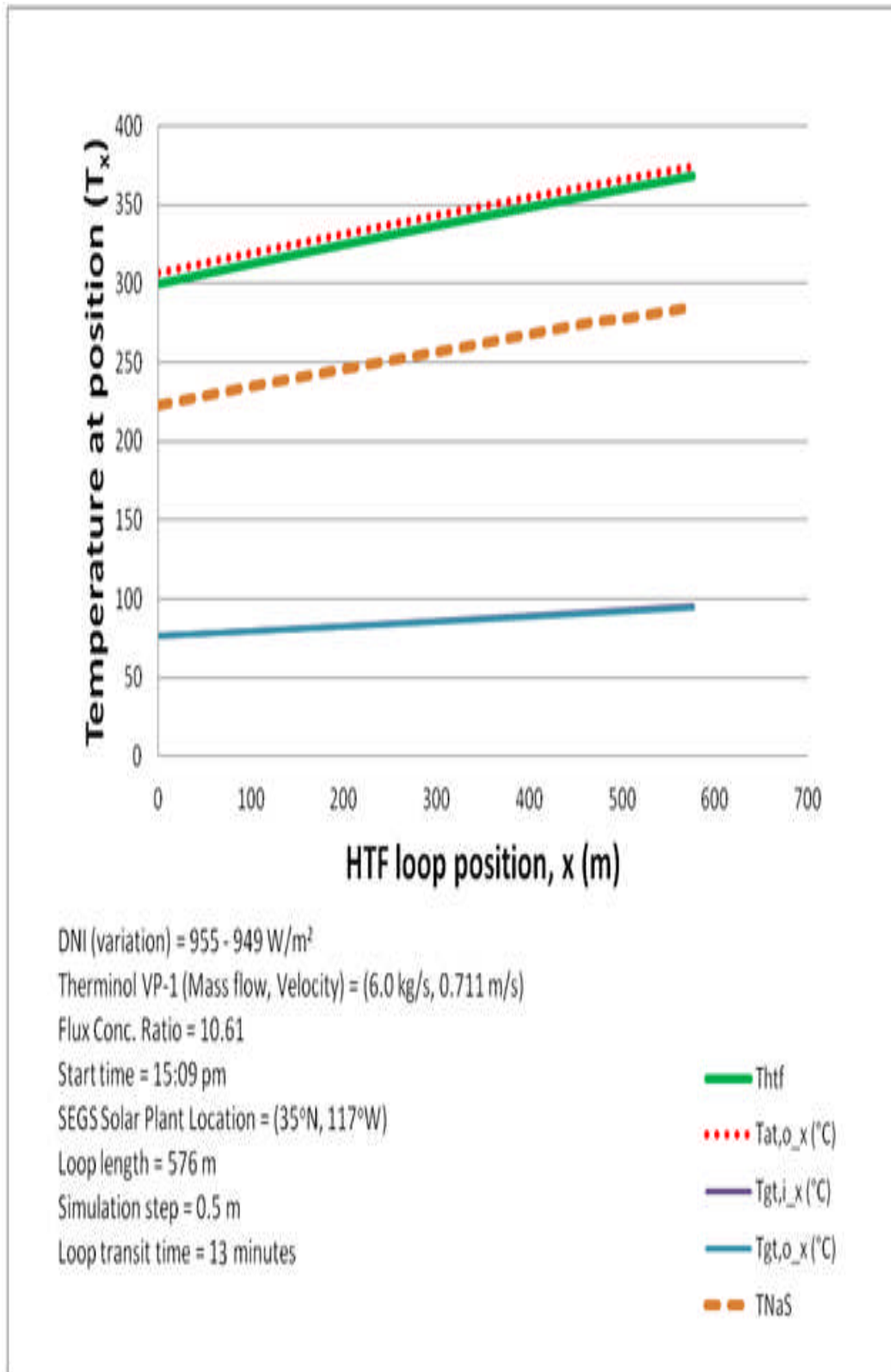


Figure 5-25: Ninth pass of Therminol VP-1 HTF through a representative loop in the solar field

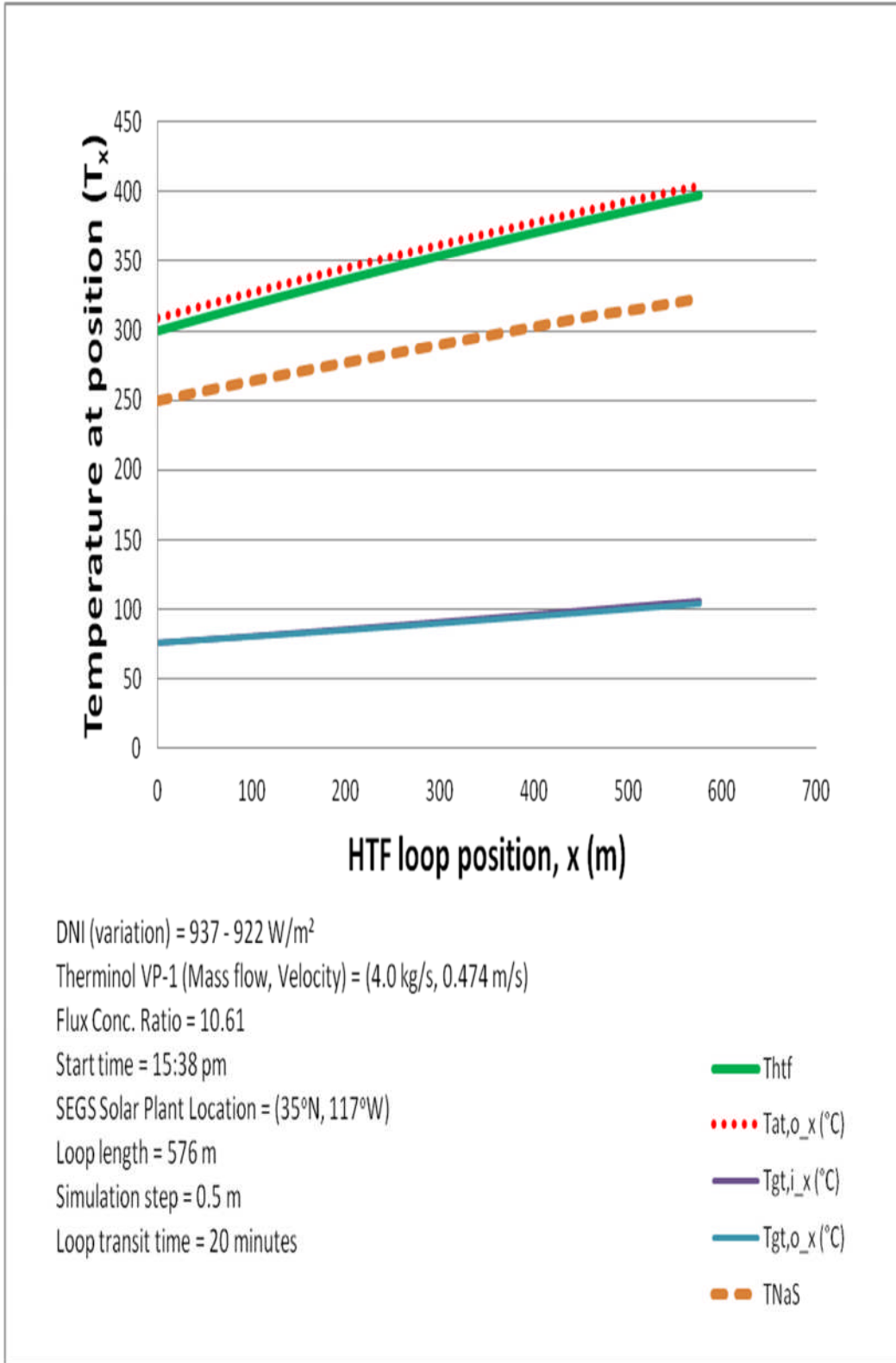


Figure 5-26: Tenth pass of Therminol VP-1 HTF through a representative loop in the solar field

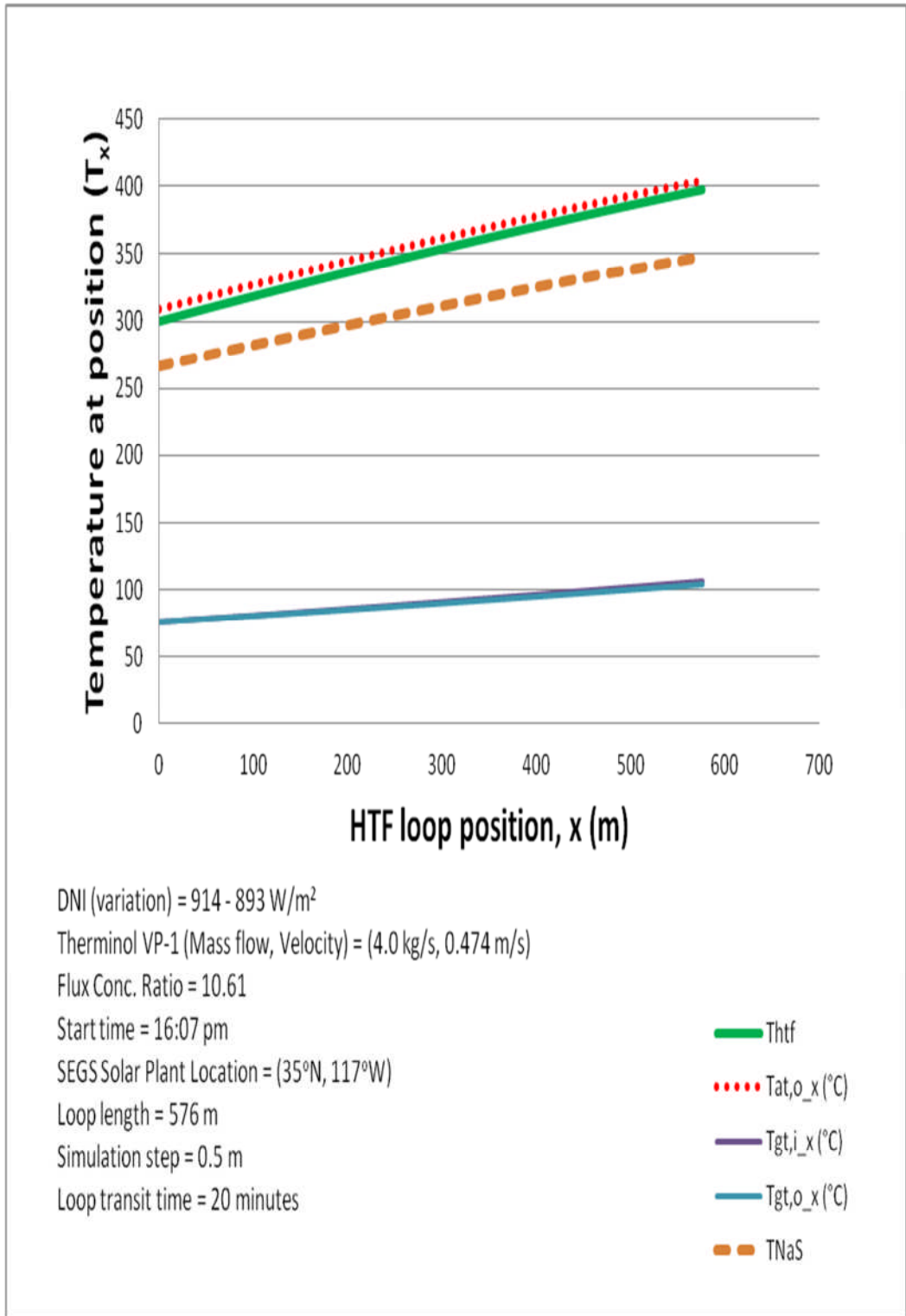


Figure 5-27: Eleventh pass of Therminol VP-1 HTF through a representative loop in the solar field

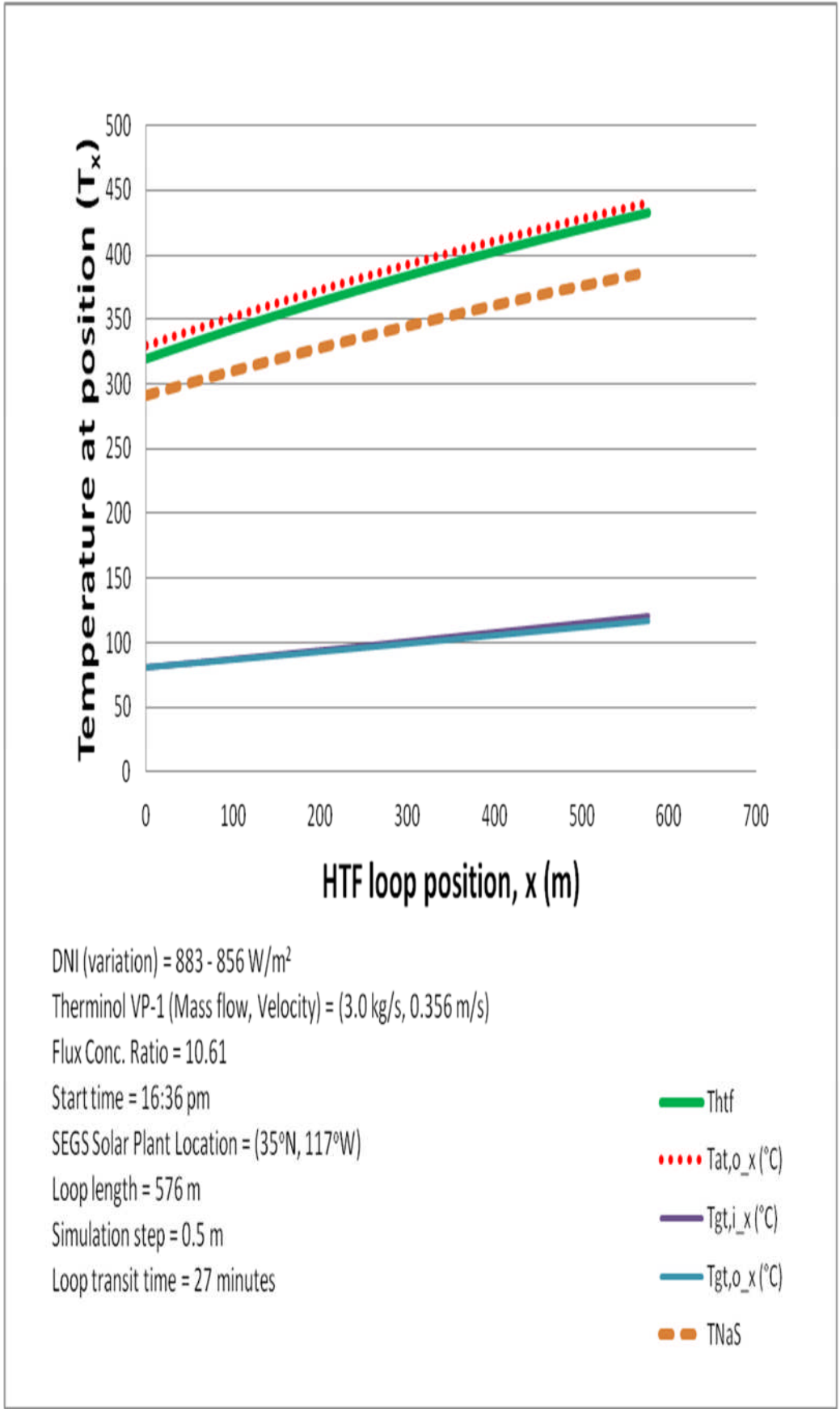


Figure 5-28: Twelfth pass of Therminol VP-1 HTF through a representative loop in the solar field

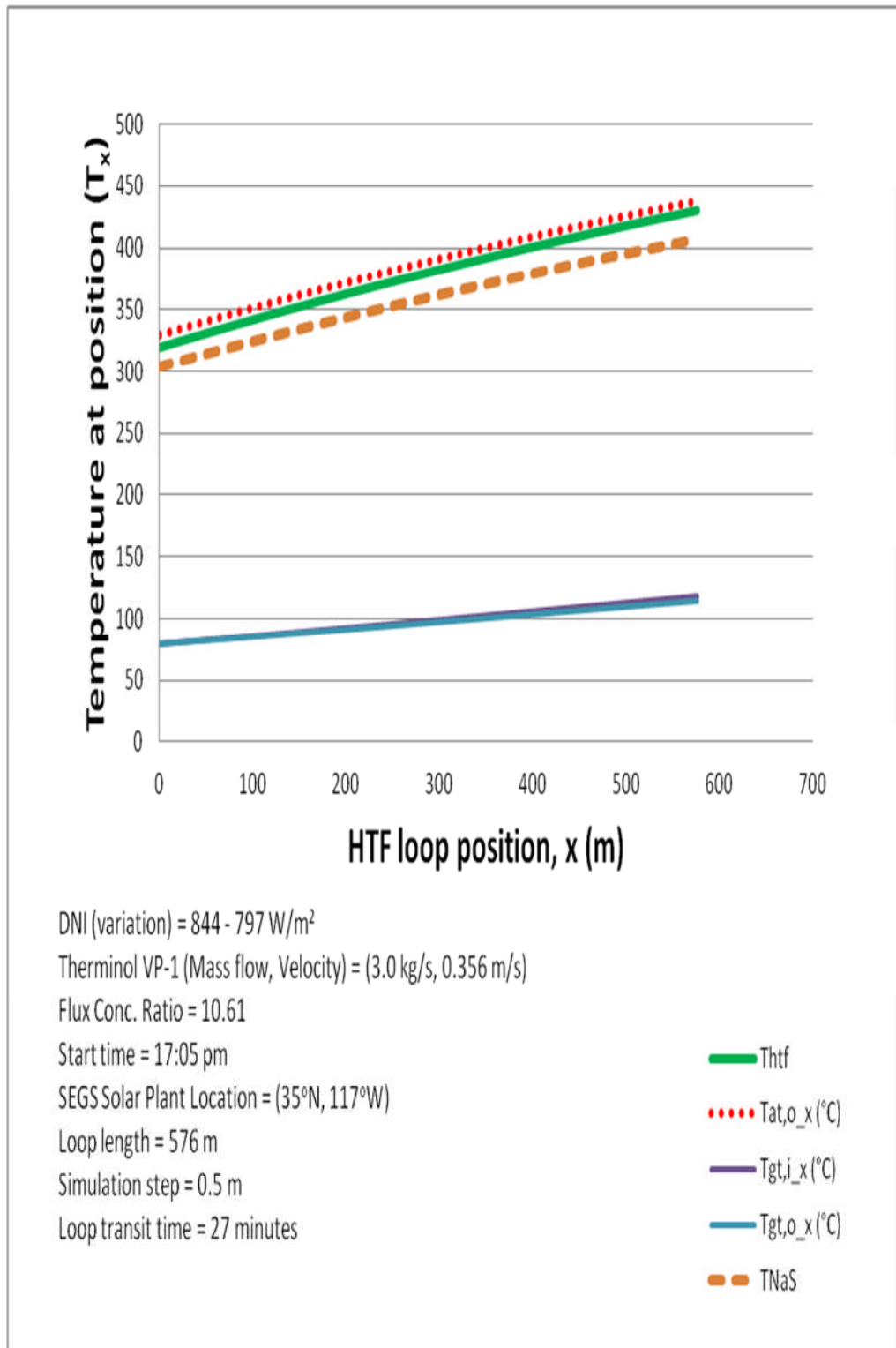


Figure 5-29: Thirteenth pass of Therminol VP-1 HTF through a representative loop in the solar field

At the time of the fourteenth pass, the NaS cells would have reached thermal equilibrium with the HTF (Figure 5-30) and be ready for charging.

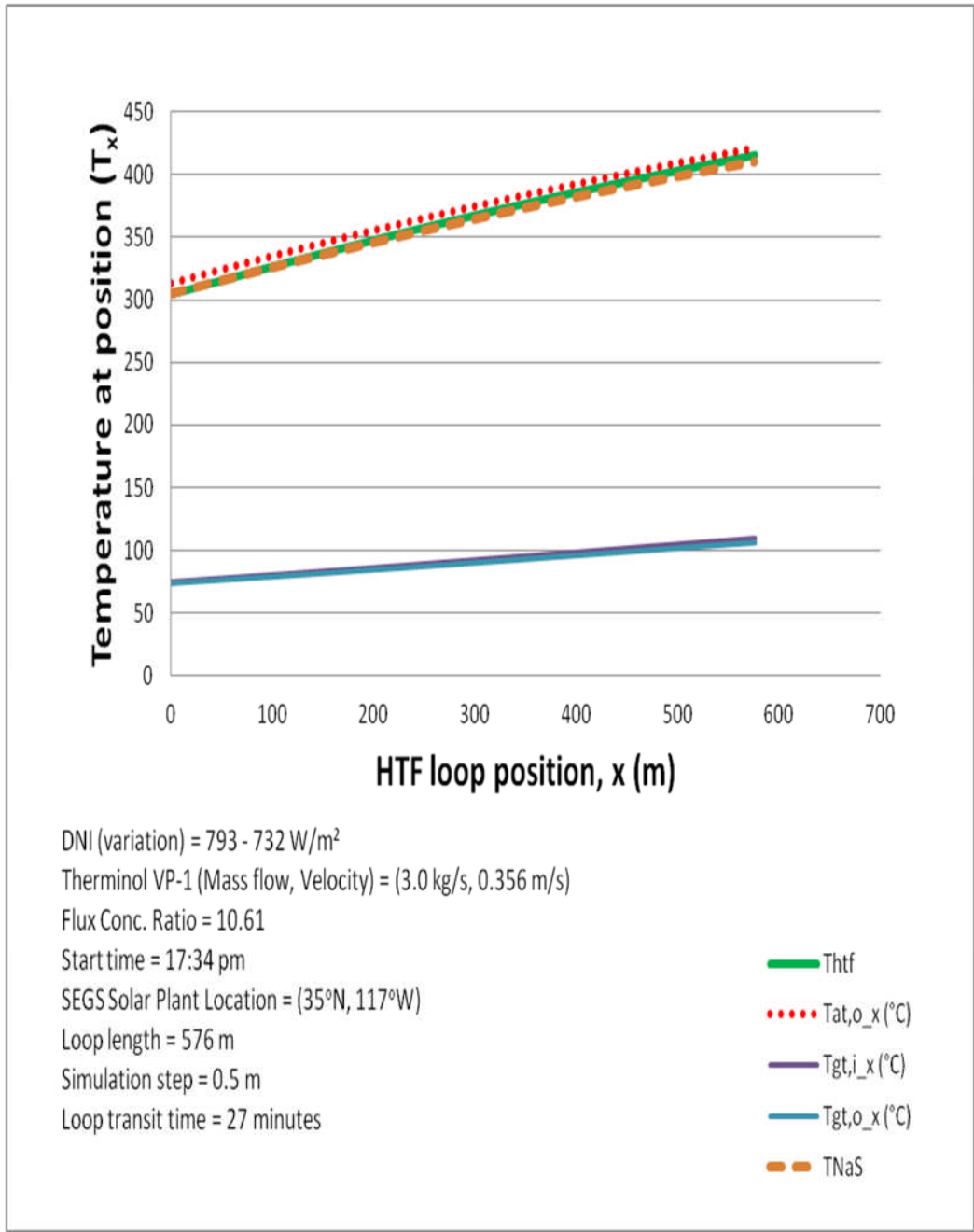


Figure 5-30: Fourteenth and final pass of Therminol VP-1 HTF through a representative loop in the solar field

The final sub-section which next follows, presents the operating profiles for the heat losses, efficiency and useful energy gain connected with the use of selected HTF's in the EES receiver at a given temperature. It therefore serves to provide the reader with a comparative idea of how some widely used solar HTF's would perform during the initial heating process.

5.3.1 Operating Profiles for Heat loss, Efficiency and Useful Energy Gain for selected HTF's at rated temperature

This final chapter section compares the use of common commercial heat transfer fluids in the conceptual EES receiver and provides plots of tube temperatures, useful energy gains, collector efficiencies and heat losses, for these HTF's.

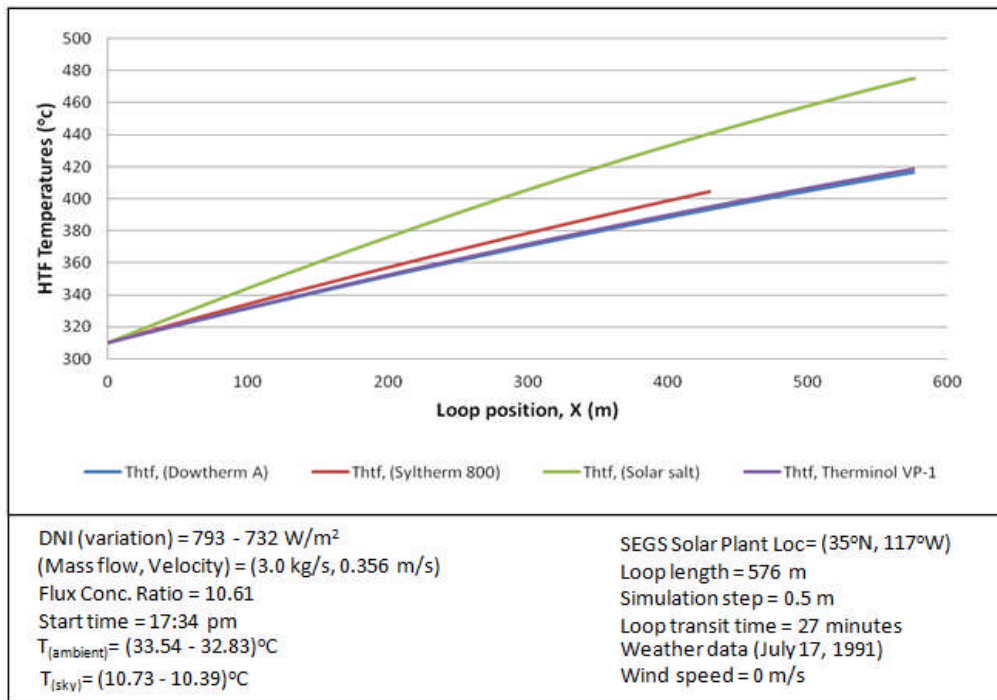


Figure 5-31: Tube temperature profiles along HTF loop length

A simulation of the tube temperature profile of the EES solar field (Figures 5-31 to 5-33) over the 300-400°C operating range was done using four standard heat transfer fluids: Therminol VP-1, Dowtherm A, Syltherm 800 and Solar Salt. Three of the HTF's produced very similar temperature profiles, and it was found that Therminol VP-1 and Dowtherm A have the closest operational performance.

However, Solar Salt was found to achieve a higher loop outlet temperature for the same loop length because of its lower specific heat capacity. Also glass tube temperature profiles (Figure 5-33), were highest for Solar Salt which is directly attributed to this HTF producing the highest

heat losses (Figure 5-34) and the lowest useful energy gain (Figure 5-35) of all the simulated HTF's.

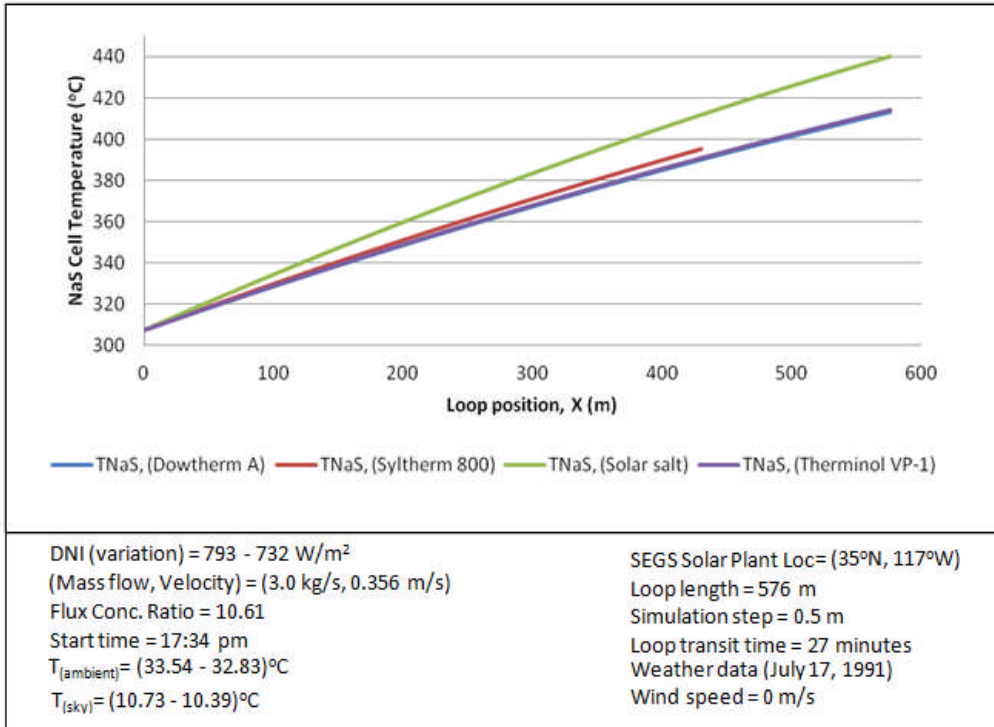


Figure 5-32: NaS cell temperature profile along HTF loop length

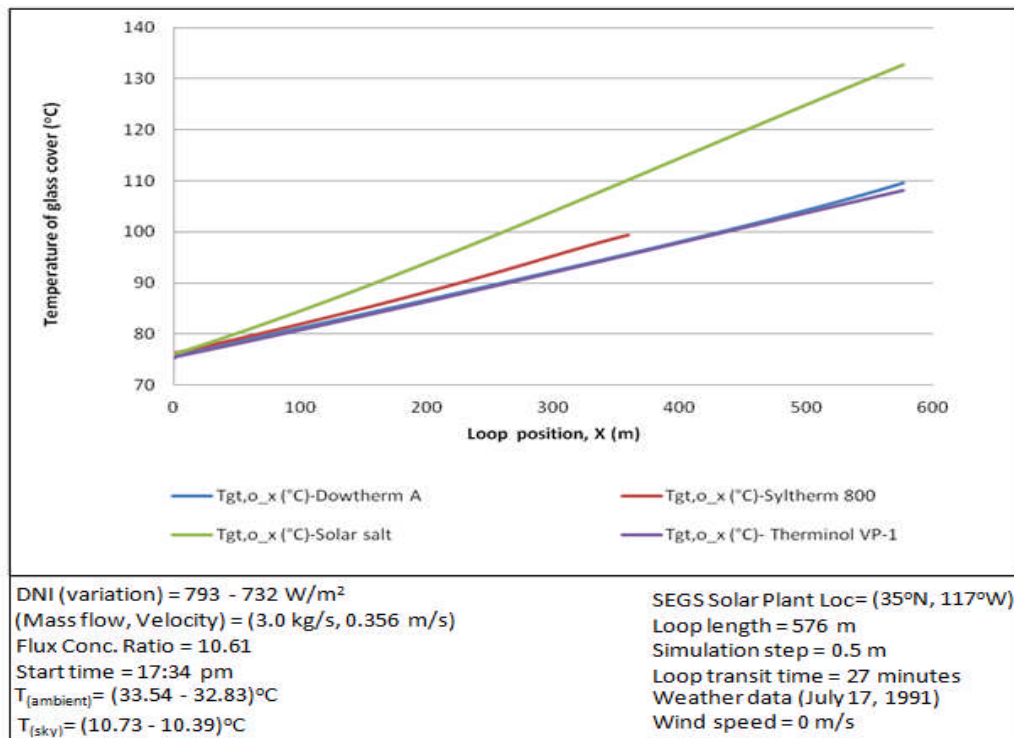


Figure 5-33: Glass tube temperature profiles for use of various HTF's in the EES receiver.

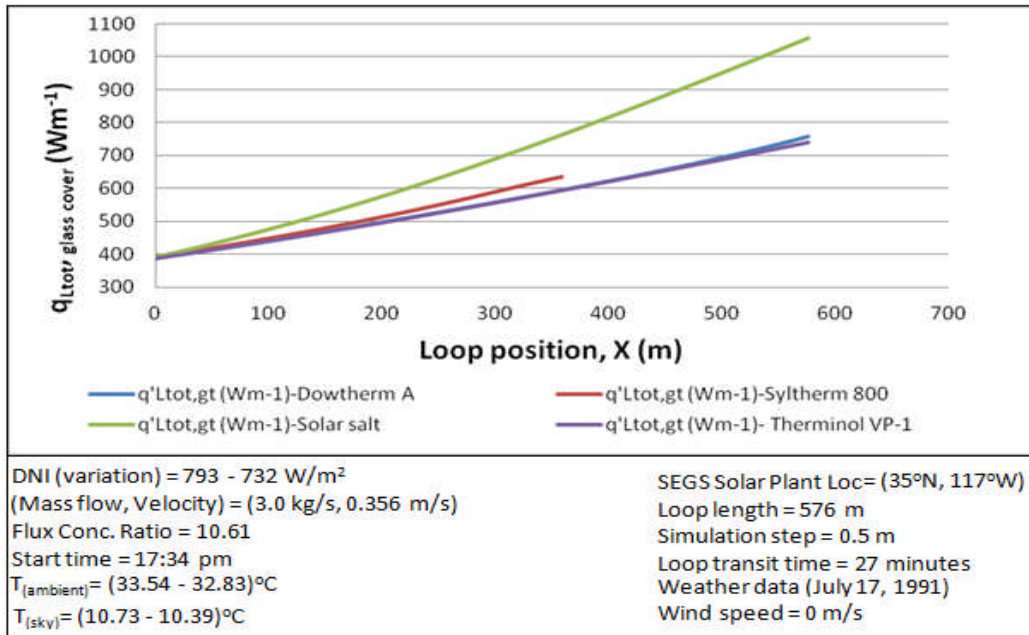


Figure 5-34: Glass tube heat losses along HTF loop

Compared to a standard 70 mm PTC receiver, it can be seen (Figure 5-34) that the heat losses from the conceptual EES receiver (at HTF entry temperature of 310°C) are approximately 400 W/m. This value is more than double the value of about 125 W/m obtained for the earlier simulation of the 70 mm PTR-70 tube performance (Figure 5-2), a result of the unavoidable increase of absorber tube diameter to accommodate both the internal NaS cells and an HTF flow annulus.

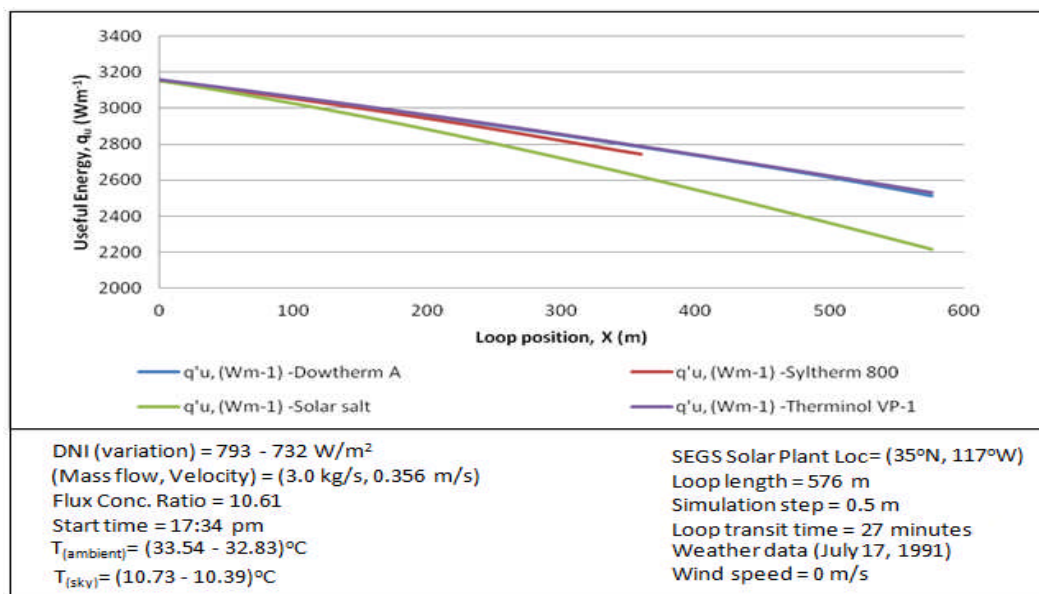


Figure 5-35: Useful energy gain of the various HTF's used in simulation

With regards to collector efficiency, solar salt was seen to produce the lowest value, as depicted in Figure 5-36.

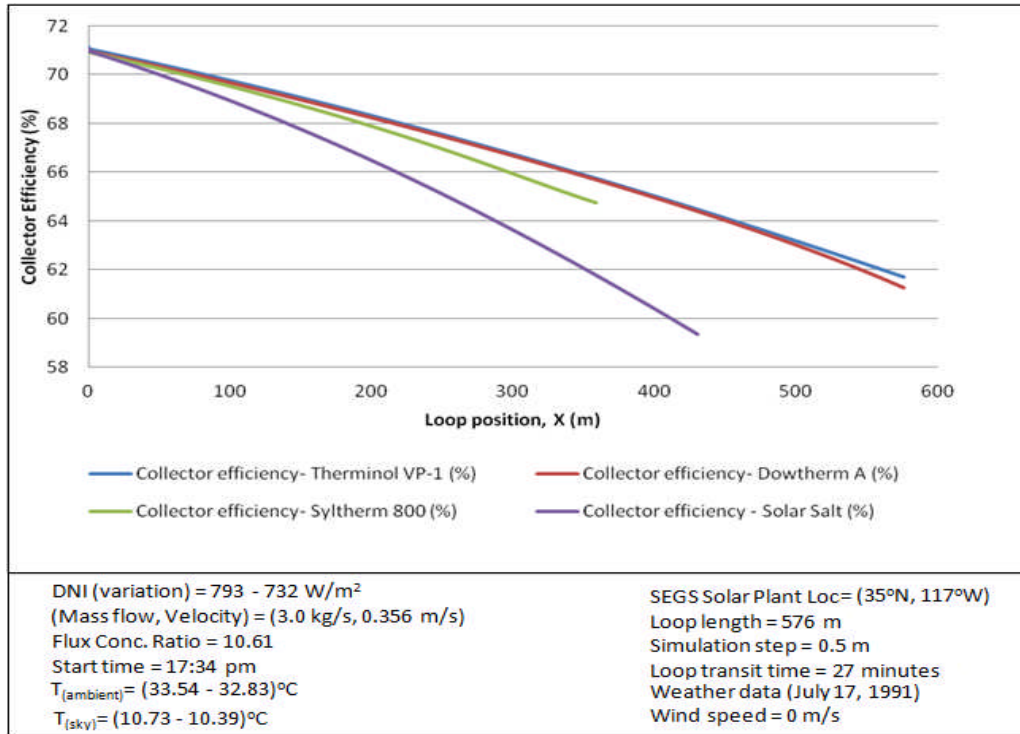


Figure 5-36: EES collector efficiency for the various HTF's used in simulation

Of important note is the fact that for all of these key simulations, (Figures 5-31 to 5-36) the performances of Therminol VP-1 and Dowtherm A are identical in almost every respect. This implies that one could easily replace the other for any given solar field application.

This now concludes the presentation of the initial heating simulations of this chapter. A chapter summary now follows.

Chapter Summary

In this chapter, the initial heating to operating temperature of the conceptual EES receiver solar field has been presented. Both test results and validated models of other researchers were used to assess model predictions. It was found that the model generally provides valid predictions of the key operating parameters, but over, or under predicts these parameters slightly because of the idealistic heat transfer conditions

assumed (e.g. ignoring annular convective losses in glass cover and conductive losses from the absorber tube). It was also seen that the EES receiver exhibits a relatively higher heat loss, which is directly influenced by its much larger absorber surface area and consequently lower flux concentration ratio. Despite these factors however, the results are generally encouraging, as key plant performance indicators (at working temperatures of 300-400°C) such as useful energy gain (3000-4000 W/m) and collector efficiency (75 – 61%) are still within the general range obtained for standard solar fields.

The main objective of the chapter was to provide an idea of the initial heating up of the EES receiver solar field. Based on the calculations, an entire day would not be enough to heat-up the complete plant from ambient to operating temperature using solar radiation only. Consequently fossil fired heaters, as is the case in real world plants would be required in order to achieve this.

As the results obtained from these initial simulations are encouraging, the next chapter (Chapter 6) explores the conceptual charge/discharge operation of the EES receiver at operating temperatures above 300°C.

Chapter 6

Charge and Discharge Simulation in the Conceptual EES Receiver: Results and Discussion

Introduction

In this chapter, the basic charge/discharge operation of the conceptual EES receiver is simulated. Battery charging or discharging is a temperature dependent operation that can only begin when the receiver has been heated up to an operating temperature above 300°C. Charging of the receiver is an endothermic process, and NaS cells will tend to “cool” internally during this operation. It therefore should occur during the available sunshine hours. The discharging of the receiver on the other hand is an exothermic process and should occur during night time or no-sun hours to prevent overheating of the cells.

Before battery charge or discharge can be explored, the temperature dependent nature of these processes must first be established. The important differential equation which describes this relationship was already presented in chapter 4 as follows:

$$\frac{\partial \bar{T}_{NaS}}{\partial t} = \frac{h_{an,i} \pi D_{NaS} L_{NaS} (T_{htf} - \bar{T}_{NaS}) + I_{NaS} \left(I_{NaS} R_{NaS} - \bar{T}_{NaS} \frac{dE_{NaS}}{d\bar{T}_{NaS}} \right)}{(mc_p)_{NaS}} \quad \text{(Equation 6-1)}$$

Clearly, any change in NaS battery temperature is a direct result of heat transfer with the HTF and also due to heat generation from the charge/discharge operation. The current related heating term is:

$$\dot{Q}_{current} = I_{NaS} \left(I_{NaS} R_{NaS} - \bar{T}_{NaS} \frac{dE_{NaS}}{d\bar{T}_{NaS}} \right) \quad \text{(Equation 6-2)}$$

This term was ignored during the initial heating simulations presented in chapter 5, but will be used in this chapter to develop an insight into the potential charging and discharging of the receiver. It can be broken into two parts, namely: (i) a Joule heating ($P_{NaS} = I^2_{NaS}R_{NaS}$) and (ii) an entropy term ($I_{NaS} \times \bar{T}_{NaS} \frac{dE_{NaS}}{dT_{NaS}}$) related to the endothermic or exothermic heat associated with the chemistry of the cell reaction [222].

In order to evaluate this heating term, the cell voltage, current, cell temperature and temperature coefficient of the cell EMF (voltage) are all required. The voltage and temperature coefficient relationships are normally given with respect to the battery state of charge or depth of discharge (D.O.D).

In order to develop a profile for NaS battery EMF with respect to the D.O.D, data points obtained from a profile developed by Sudworth [223] was plotted in Microsoft Excel. A simple polynomial trend line (Figure 6-1) was fitted to this data, and was found to have fairly good accuracy ($R^2 > 0.998$) for most of the data range when values were compared with original data. This polynomial equation was implemented as part of the Visual Basic code used to generate cell open circuit voltage levels for any given state of charge or discharge.

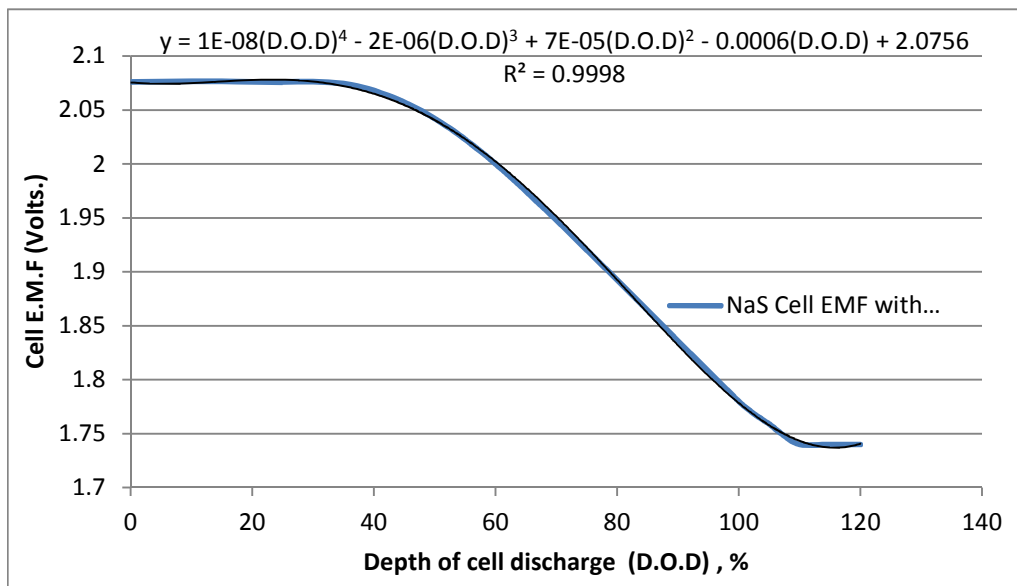


Figure 6-1: NaS cell EMF with depth of discharge (D.O.D)

In order to determine the heating properties of the system with charge/discharge, the temperature coefficient of cell voltage (dE/dT) of the NaS cell is also required. The most widely recognized profile was produced by Knodler ^[222] in 1984. Therefore is profile was obtained from the published work on the NaS battery edited by Sudworth ^[217] and digitized with “*Getdata Graph Digitizer*” software. A very accurate reproduction (Figure 6-2) of the original plot was thereby obtained in Microsoft Excel.

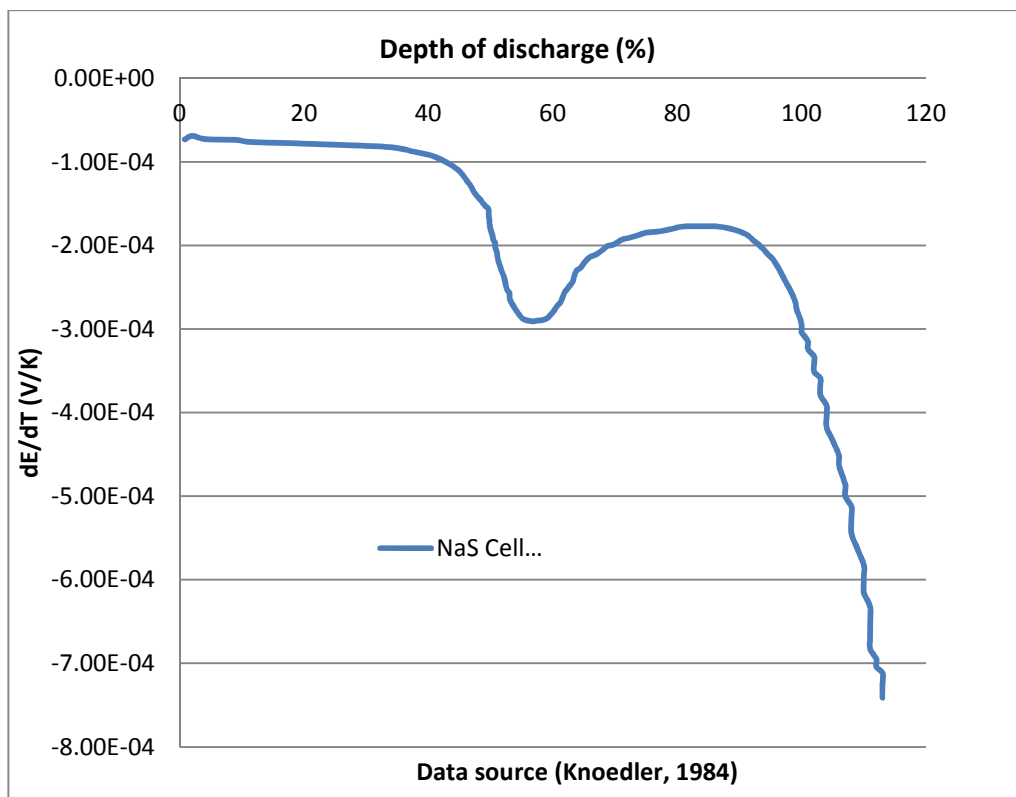


Figure 6-2: NaS cell voltage temperature coefficient with depth of discharge (D.O.D)

For implementation into the charge/discharge model, a mathematical model had to be fitted to the reproduction of the empirically derived plot. However, the significant non-linearity of the profile made it impossible to accurately fit a single mathematical model to the profile. It was therefore decided to split the profile into sections and to fit separate models to each part. With trial and error, three profile divisions (Figure 6-3) were

established that allowed a very good mathematical representation of the empirical data.

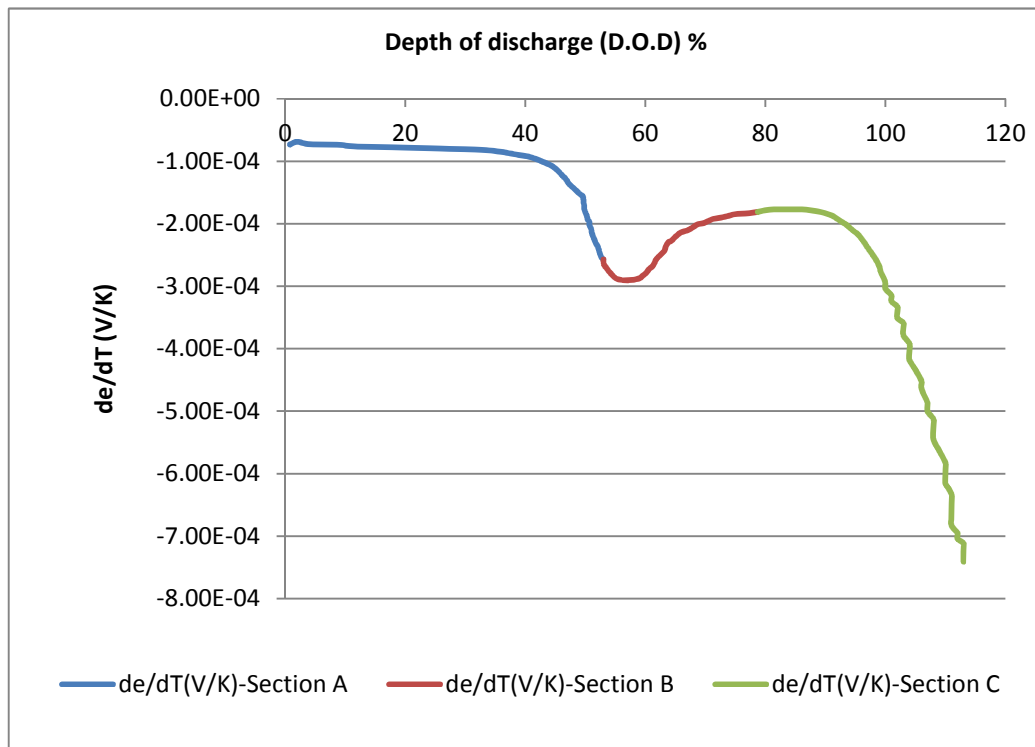


Figure 6-3: Plot showing the three sections of the original dE/dT profile used for fitting of a mathematical model

As the polynomial fits produced in Microsoft Excel proved inaccurate when tested, OriginPro 8.6 software was used to find more accurate fits for the three sections of the reproduced dE/dT plot and details regarding their accuracy are provided in the Appendices M, N and O.

The mathematical fits developed for the three sections were implemented in the Visual Basic code using an "IF" condition to select the appropriate profile section with regards to the battery D.O.D. With both the voltage and the voltage-temperature coefficients fitted with mathematical equations, it became possible to model the current related term of the NaS battery heating equation and to simulate the charge/discharge operation of the NaS cells in the EES receiver.

With this background information covered, four main sections now follow in this chapter. The first presents the conceptual design of a

charge/discharge system that could be used in the EES receiver solar field. The second presents the results of simulations regarding the charging of the batteries during daylight hours, under concentrated radiation and the third presents the discharging of the batteries during no-sun or night time conditions. The fourth section presents a possible approach to cooling or *“levelling the temperature gradient”* developed in the NaS batteries within the HTF loop, and is followed by the usual chapter summary.

6.1 The Charge/Discharge Concept for the EES Receiver Solar Field

In this work, the EES solar field is conceptualized to be charged by the process of *“re-absorbing a portion of the power it produces back from the grid over the available daylight hours, and storing this electrical energy in the field’s NaS batteries”*.

In order to understand how this could be done, a typical PTC solar field is considered for discussion. A PTC solar field is made up of structures known as solar collector assemblies (SCA’s) arranged in loops. An SCA (Figure 6-4) is a mechanical structure consisting of individual collector modules with parabolic reflecting mirrors for concentrating solar radiation onto heat collecting elements along its central axis.

In the case of an Andasol-1 type PTC plant, each loop consists of four SCA units of 144 m length and each SCA unit is made up of 12 individual collector modules of 12 m length. The standard heat collecting element (HCE) used in most PTC plants is typically 4 m long. Therefore each collector module supports 3 heat collecting elements connected in series. The NaS cells used in the analysis are 0.5 m in length, which implies that each collector module would hold 24 NaS cells and at 2.076 VDC per cell, a collector module’s *“end to end”* voltage would be approximately 50 VDC.

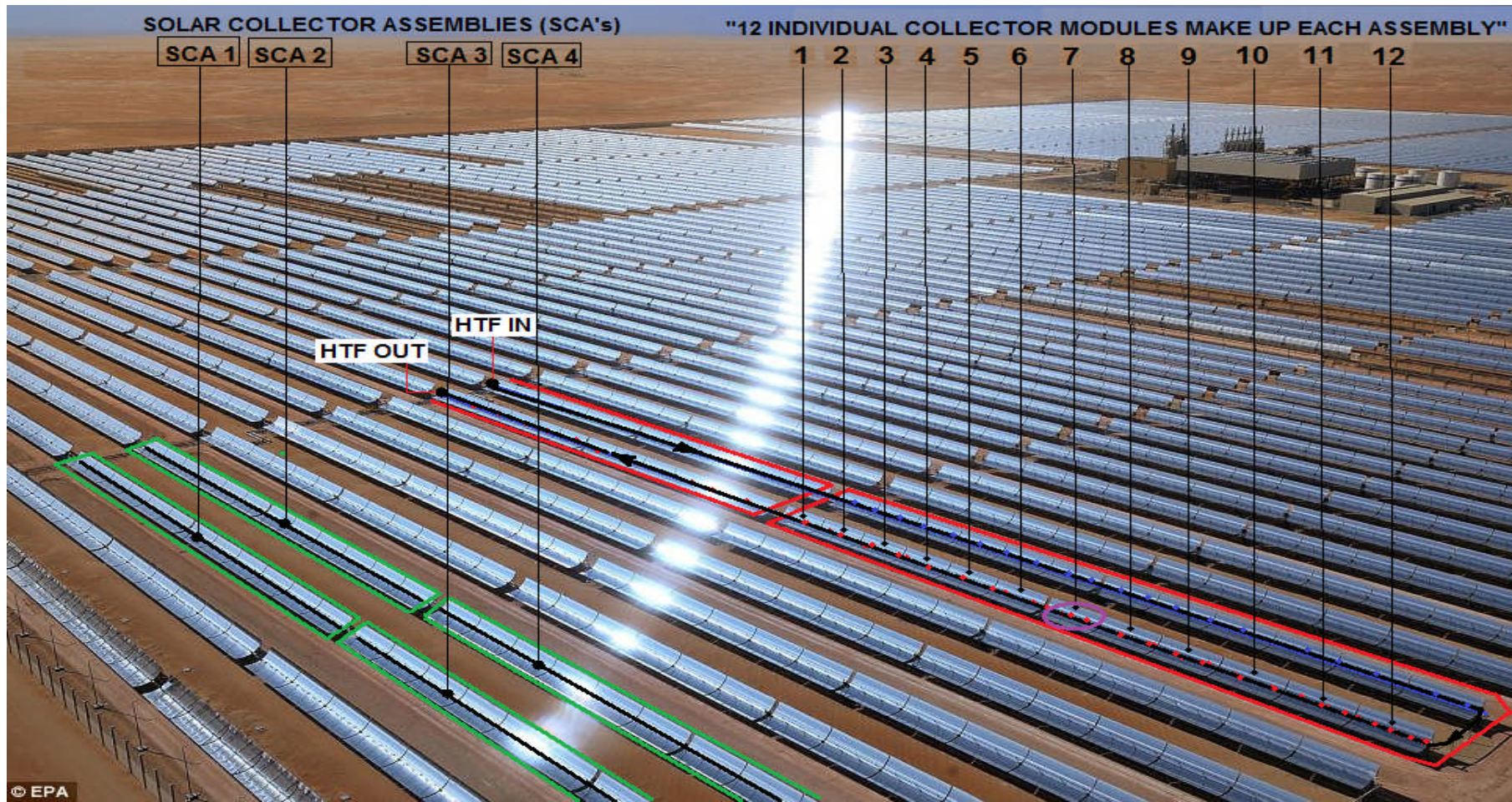


Figure 6-4: A PTC receiver solar field showing SCA loops (Source: SHAMS-1 PTC power plant)

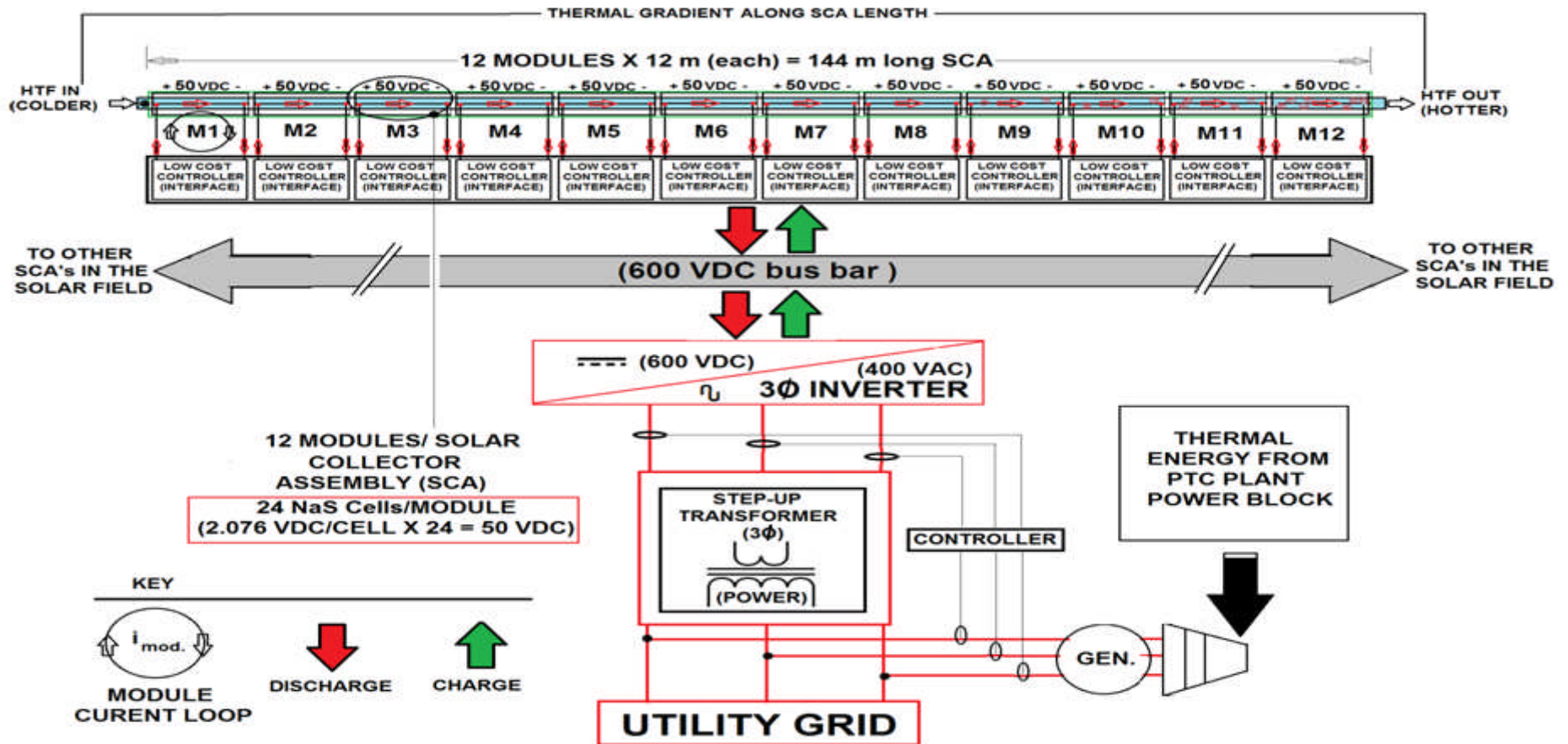


Figure 6-5: Schematic illustrating a conceptual setup for the EES receiver charge/discharge control operation in a typical solar field.

The charging of the NaS cells from the plant output/utility grid would be achieved using suitable power inverters (electronic devices for converting from DC to AC power) and low cost electronic interface controllers, along with a power transformer.

As each collector module is expected to have a terminal voltage of 50 VDC, an SCA assembly of 12 modules would then have a terminal voltage of approximately 600 VDC (Figure 6-5). Each SCA would be “tied” by an electronic controller to this 600 VDC bus. As this work only provides an initial concept, further optimization, modelling and economic investigation would be required to determine the maximum number of SCA’s that should be connected to each 600 VDC bus, an undertaking that is outside the scope of this work.

Power from the 600 VDC bus could then be converted to 400VAC by a three phase inverter. A step-up/down power transformer in conjunction with appropriate controllers, would link the EES solar field inverters with the high voltage utility line (eg. 150 KVA) to effect power transfer during charge or discharge operations. With the exception of the “*charging function*” required in the EES solar field, modern grid connected photovoltaic (PV) power plants use a similar set-up for connecting with the power grid.

6.1.1 The Potential Energy Storage Capacity of the Tepco T5 NaS Cells.

Each of the SCA’s in a single loop of a conceptual EES solar field would contain contains 288 Tepco T5 NaS cells, each cell of 632 Ah capacity and EMF of 2 V.

$$\Rightarrow \text{Total electrical storage capacity per SCA} \\ = IV \times t = 632 \text{ Ah} \times 2 \text{ V} \times 288 \text{ cells} = 364.032 \text{ kWh}$$

Each Plant Loop contains 4 SCA’s

$$\Rightarrow \text{Total electrical storage capacity per plant Loop} \\ = \text{No. SCA's/Loop} \times \text{SCA Capacity}$$

$$= 4 \times 364.032 \text{ kWh} = 1.456 \text{ MWh}$$

Each Plant contains 156 loops

$$\begin{aligned} \Rightarrow \text{Total electrical storage capacity of Plant} \\ &= 1.274 \text{ MWh per Loop} \times 156 \text{ loops} \\ &= 227.16 \text{ MWh} \end{aligned}$$

The number of hours for a full rated power output of 50 MW_e by the solar plant, solely from the battery storage is given as:

$$\text{No. of hours} = \frac{\text{Solar field storage capacity battery (MWh)}}{\text{Rated power output (MW}_e\text{)}}$$

$$\text{No. of hours} = 227.16 \text{ MWh} / 50 \text{ MWe} = 4.5 \text{ hours}$$

Thus, a 50 MW_e power plant with a Andasol-1 footprint would be able to provide “full rated power” for at least four (4) hours after dusk from battery storage alone. Operating in complementary mode with this electrical energy storage (provided by the conceptual EES receiver solar field), such a plant (with a standard 7.5 – 8 hours of thermal storage capacity) could therefore “theoretically” operate without fossil fuel input over the entire 12 hour time period, typical after dusk.

In this regard, 24 hour operation of the conceptual EES plant would be possible from a “theoretically 100% green” perspective. More importantly, the large host of ancillary, reserve, back-up and power conditioning capabilities that come with NaS battery storage systems would be available to the PTC power plant. Consequently, some of the traditional costs incurred in securing many of the usual reserve generators and other ancillary power support systems could be effectively eliminated using this hybrid storage approach. Exploration of these and other related concepts are beyond the scope of this work, but definitely worthy of future investigation.

This concludes a brief description of the model set-up process for charge/discharge simulations and of one possible design approach for implementing charge/discharge of the NaS batteries in a conceptual EES receiver solar field. The next chapter section presents results of

charging simulations for the NaS batteries during daylight hours under concentrated solar radiation.

6.2 Charging of the NaS Batteries during daylight hours under Concentrated Solar Radiation

In this section the results of selected simulations regarding the charging operation of NaS batteries in the conceptual EES receiver are now presented. With regards to the entropic aspect of the cell reaction, charging of the NaS cells is by nature endothermic and therefore tends to create a “cooling” or “*internal temperature reducing effect*” within the cell.

This is a very important factor which makes possible charging of the NaS batteries during the available daylight hours. During a typical summer day, 12 sunshine hours are available for the battery charging operation. The Tepco T5 cells modelled in the simulations are roughly of 600 Ah capacities. This implies that if fully discharged cells were to be charged over a 12 hour time duration, they must be charged at a 50 A rate. However in other cases, it may be required to charge cells up more quickly, over shorter time durations. In such cases, significantly higher charge currents would be required. A 52 kW Tepco T5 battery module for example, has a current rating of 726 A at 58 VDC and 363 A at 116 VDC, and therefore currents of over 700 A could be expected in these cases.

In the first set of simulations presented, a charging current of 600 A was used in order to evaluate the temperature profile of the cells at current value close to the maximum rated charge current of a T5 module (726 A)^[190]. This high current value (600 A) was chosen to reduce the number of simulations for a full battery charge, and also evaluate battery temperature stability at a high charge rate.

In all the simulations that were done, Solar Salt HTF was used. A temperature change value of approximately 200 K was allowed along the solar loop, corresponding to HTF entering the loop at 350°C and leaving at or near 550°C. As explained in an earlier chapter, the EES receiver solar field is conceptualized to operate with a 7.5 – 8 hour thermal storage

system and therefore it is assumed that when not operating the power block, the 550°C HTF is cooled down to 350°C by heat exchange with the hot storage tank.

Using a initial charging current of 600 A, and solar radiation values around the time of solar noon, the first four simulations (Figures 6-8 to 6-12). show that the 600 Ah NaS cells would have attained full charge in 1 hour (approximately 4 cycles). The current is negative (to represent the charging condition) and for the last flow through the loop, it was reduced from 600 to 216 A so as not to overcharge the cells (theoretically).

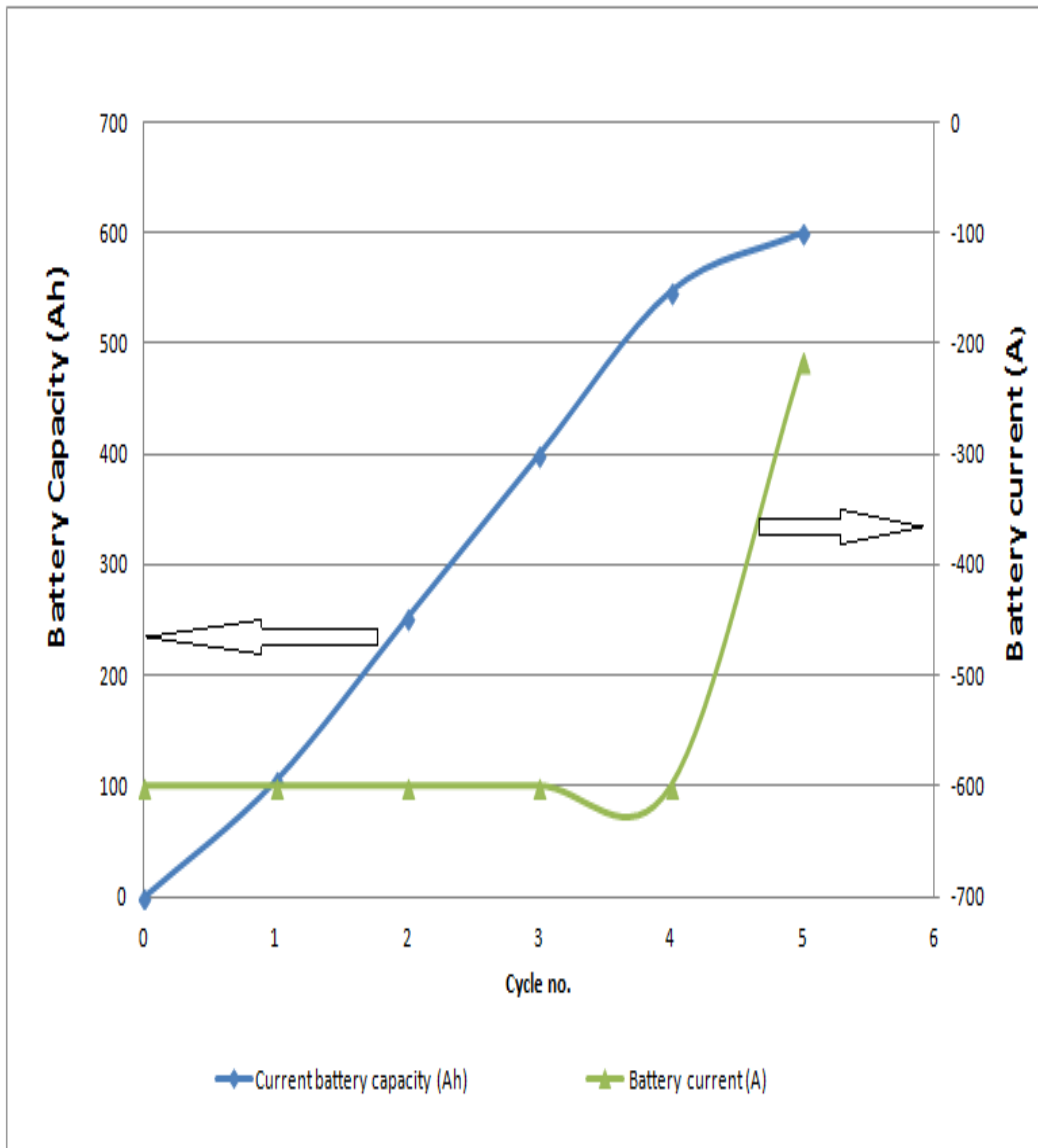


Figure 6-6: Battery charge capacity and current with charging cycles

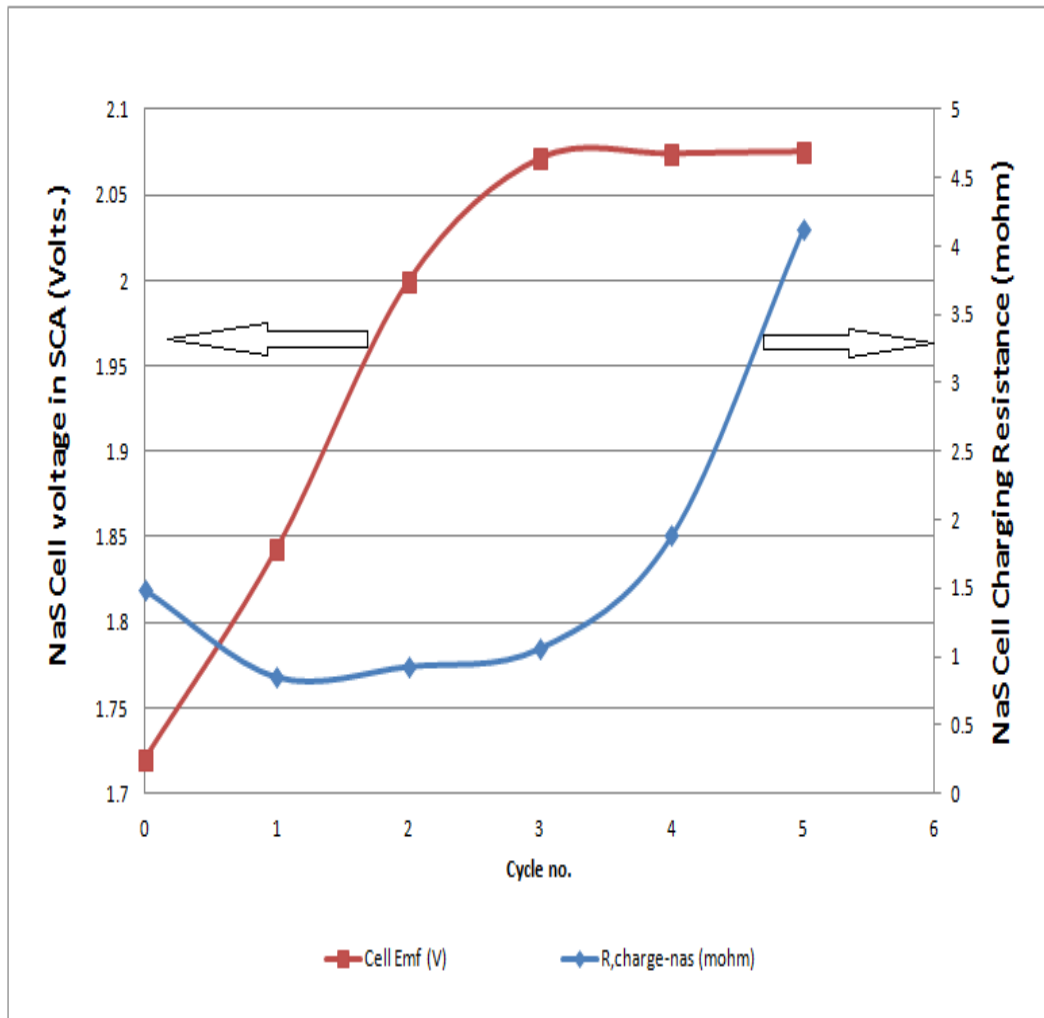


Figure 6-7: A representative NaS battery charging profile and the associated cell charging resistance within a single SCA

The magnitude of the charging current is determined by the typical T5 cell voltage and internal resistance profile that would be expected during charging as given in Figure 6-7. These profiles are therefore directly linked to the internal joule heating of the NaS battery current.

An examination of the main simulation results (Figures 6-8 to 6-12) reveal that the HTF should be able to maintain a fairly constant inlet/outlet temperature, an important factor for normal operation of the plant's power block. The graphed results of these charging simulations are now given. (See overleaf)

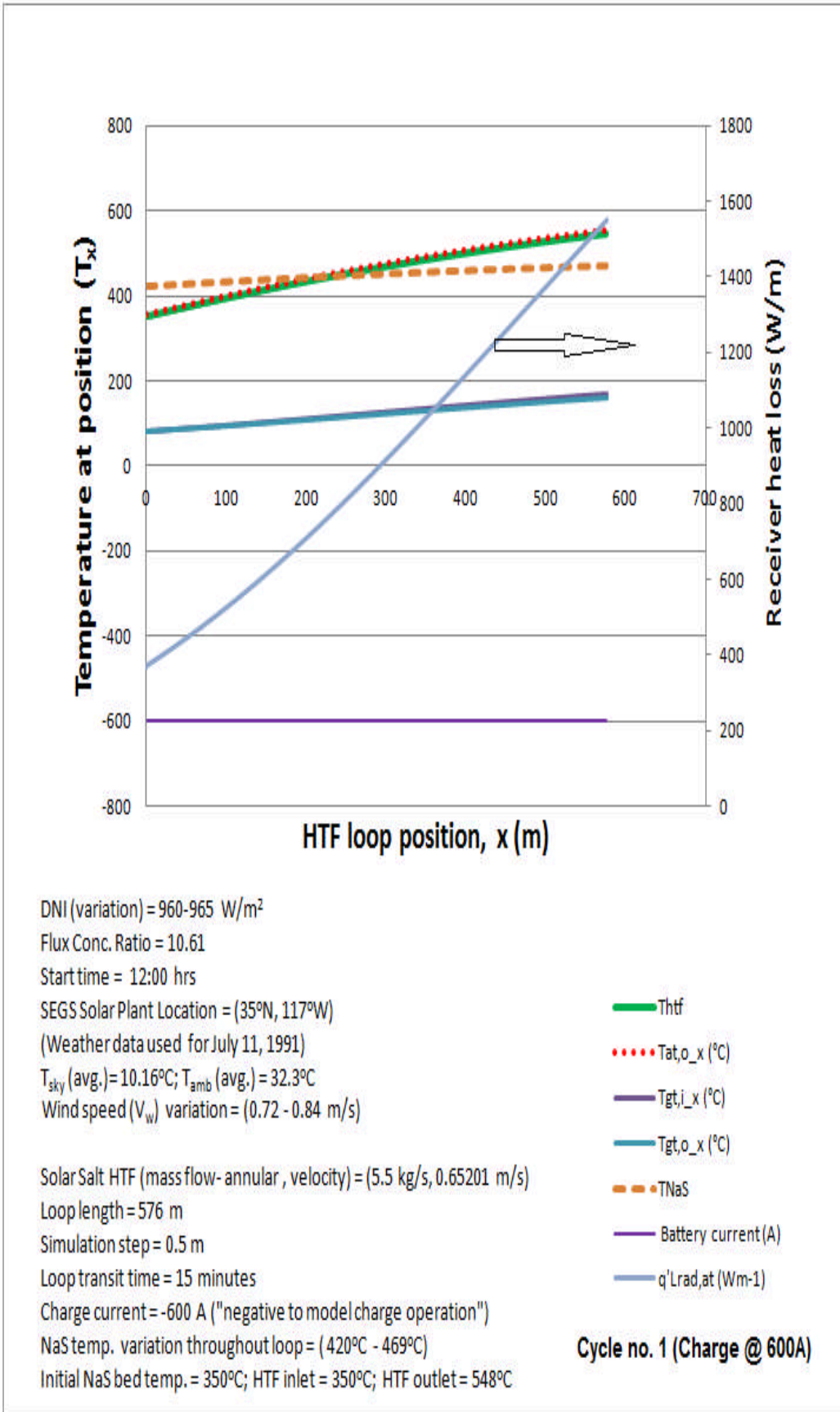


Figure 6-8: Simulated profiles results for 1st NaS battery charge cycle at 600 A.

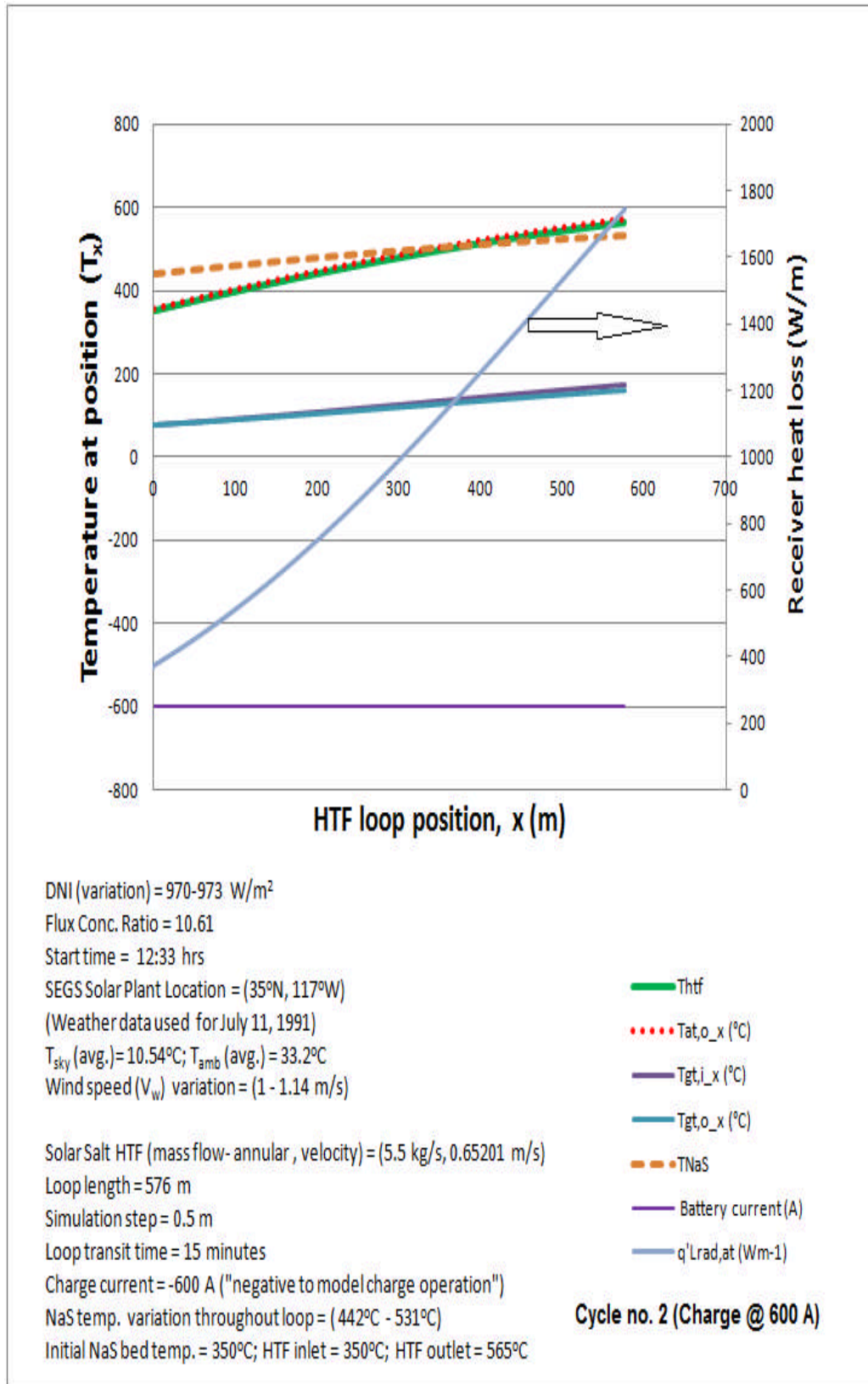


Figure 6-9: Simulated profiles results for 2nd NaS battery charge cycle at 600 A.

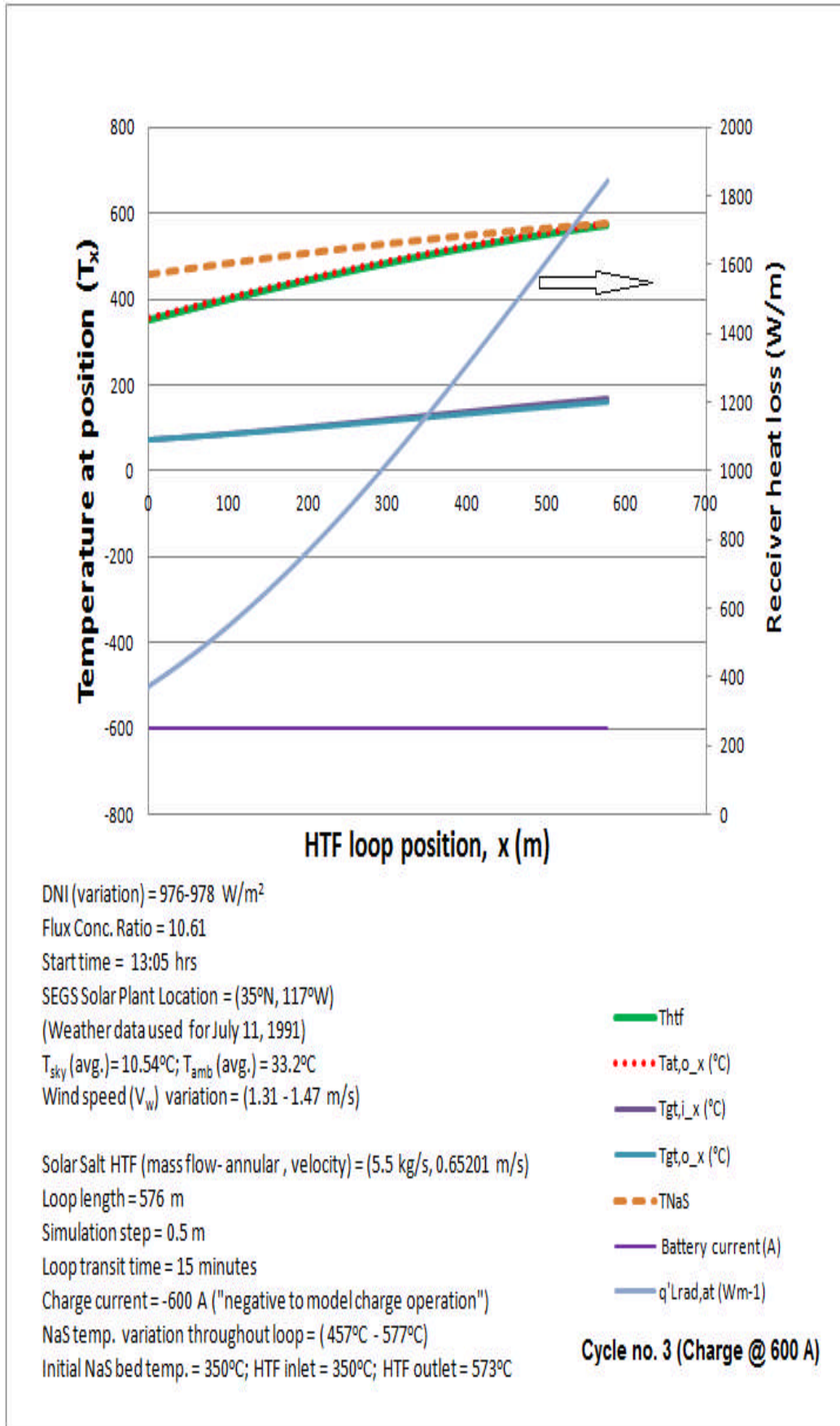


Figure 6-10: Simulated profiles results for 3rd NaS battery charge cycle at 600 A.

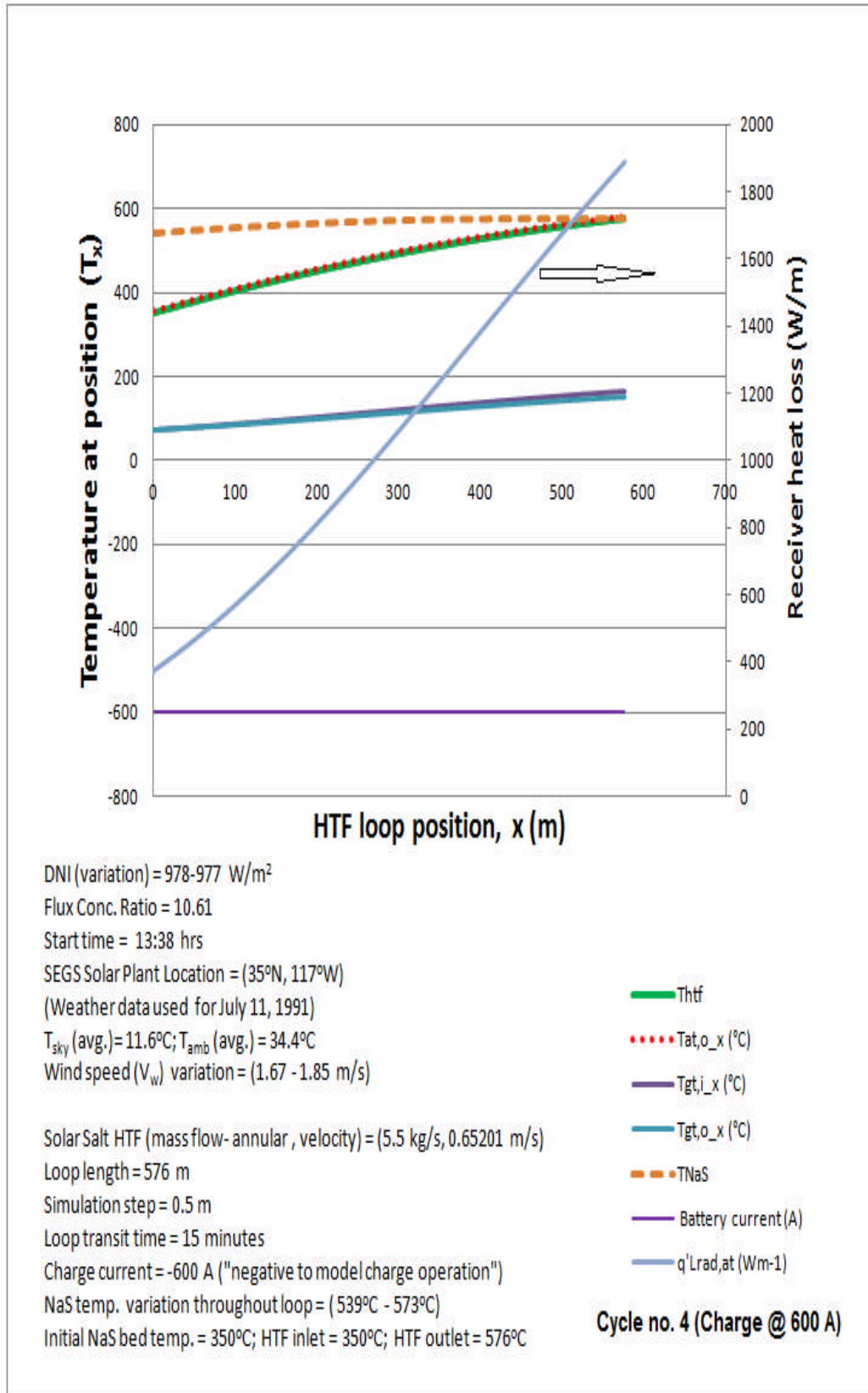


Figure 6-11: Simulated profiles results for 4th NaS battery charge cycle at 600 A.

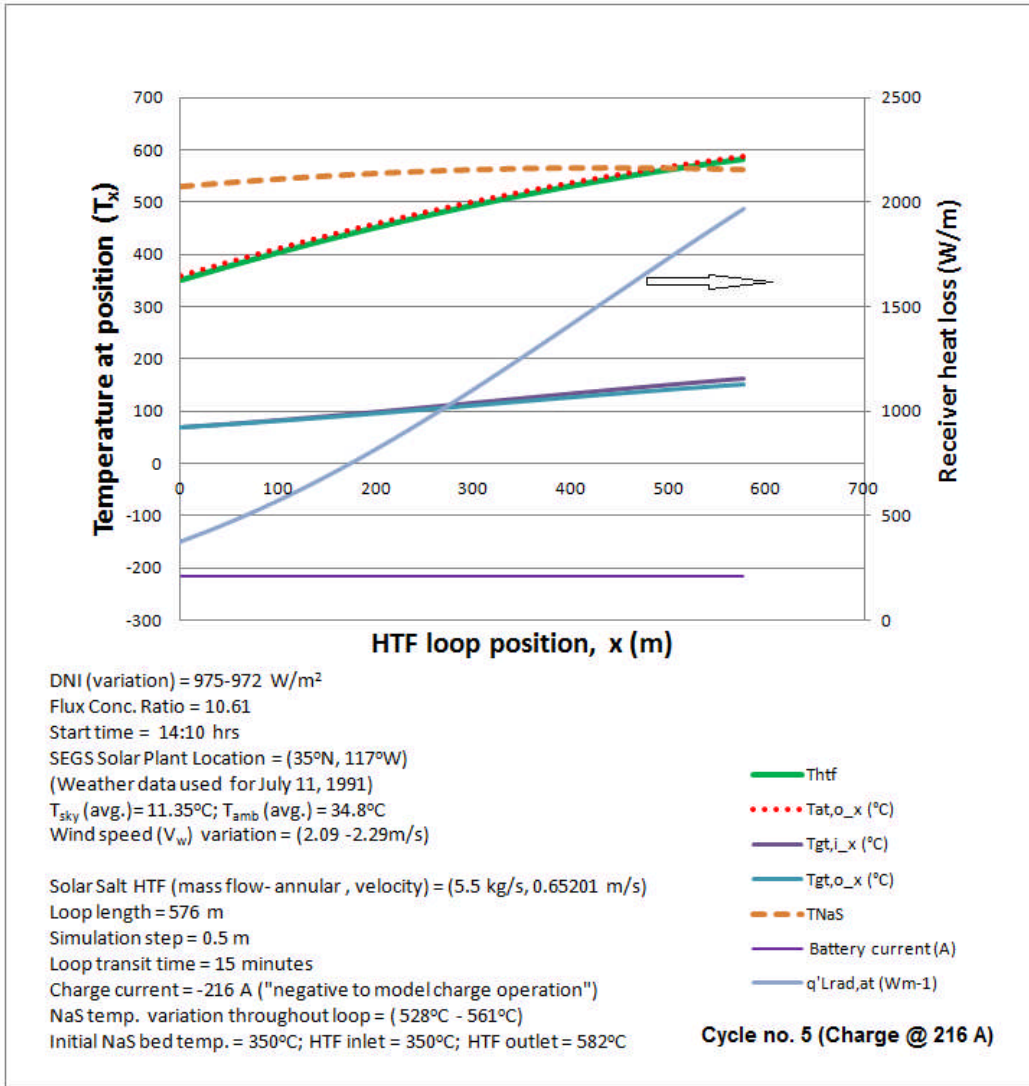


Figure 6-12: Simulated profiles results for 5th NaS battery charge cycle at 216 A.

These results show that the NaS cells, initially at a temperature of 350°C developed a gradient ranging from 420 – 469°C along the 576 m length of the loop at the end of the first cycle. Most of the temperature rise in the cells is caused by the “joule heating effect” of the 600 A charge current. This is evinced (Figure 6-8) as the NaS cell temperature is seen to rise significantly above the HTF temperature at the loop inlet, only being exceeded by the HTF temperature midway through the loop. The low level of heat exchange between the NaS cell and the HTF is also demonstrated by the significant temperature difference (due to a relatively low overall NaS cell thermal conductivity) that develops towards the end of the loop.

The other cycles 2, 3 and 4 (Figures 6-9 to 6-12) all show the NaS battery temperature increasing significantly over a HTF temperature profile, which was essentially constant over all the cycles. As mentioned earlier, during the last cycle, the charge current was reduced to 216 A, as this current level was required to complete charging of the batteries over the 1 hour charge cycle time.

Although the charging operation of the NaS cell is an endothermic one, these results indicate that at high current levels, there is a danger of cell temperatures reaching unsafe levels, without appropriate temperature controls. After an hour of simulated charging, the fully charged NaS cells would have reached an average internal temperature of 550°C, (up from 350°C) which is close to their maximum operating temperature limit of 600°C. A potential method for controlling NaS battery temperature using the circulating HTF will be discussed later in this chapter.

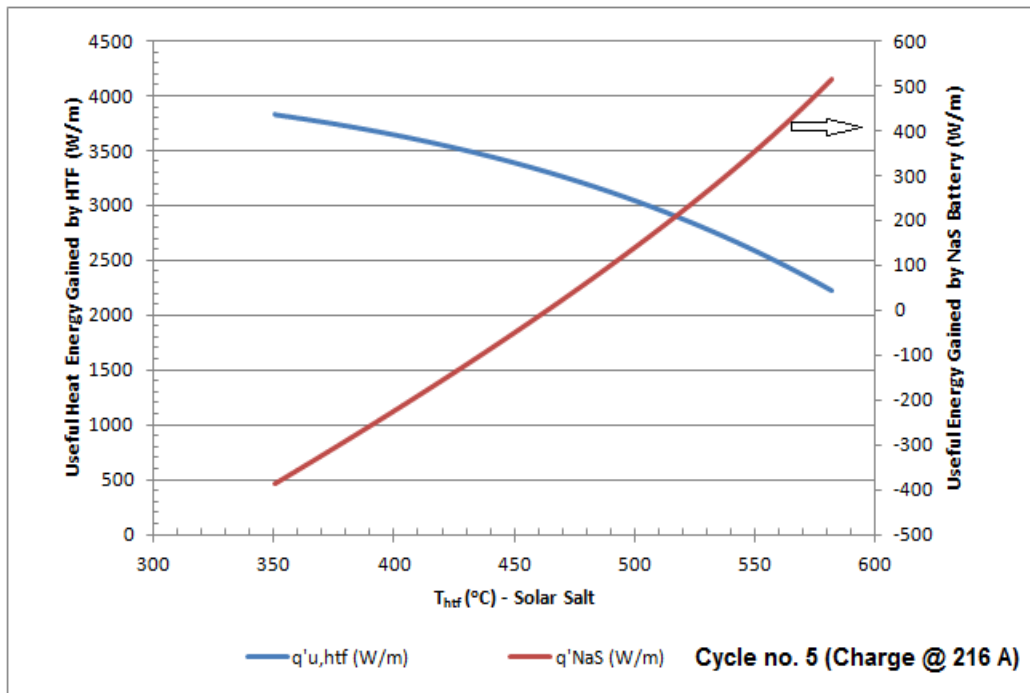


Figure 6-13: Simulated useful energy gain profiles results for NaS battery and HTF during the 5th charge cycle at 216 A.

Other important simulations were the useful energy gains of both the HTF and NaS battery, along with the expected collector efficiency (Figures 6-13 and 6-14). It was observed that the useful energy gain of the HTF

comprises a range typical of standard PTC solar fields, a positive sign in context of the plant's ability to supply the typical rated power to the electric grid.

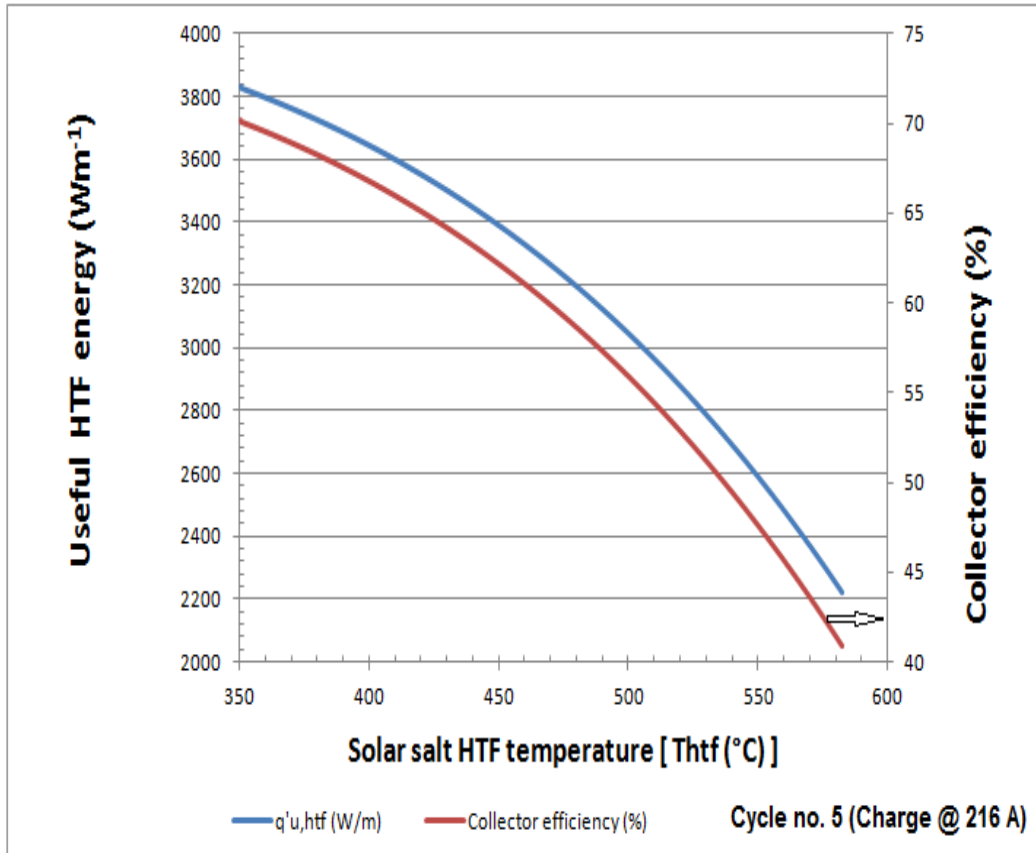


Figure 6-14: Simulated collector efficiency of EES collector using solar salt HTF

The useful energy gain of the NaS batteries was seen to be positive or negative depending on the value of the battery temperature in relation to the HTF temperature. In the final charge cycle for example, the useful energy gain of the batteries was negative, indicating they were losing heat to the HTF, being at a higher temperature. This value only became positive near the end of the cycle when the HTF temperature exceeded the battery temperature.

Useful energy gain of the batteries is generally an order of magnitude smaller than that of the HTF. This indicates that the batteries heat up at a significantly slower rate than the HTF, and this is caused primarily by the

high thermal resistance presented by the battery internals, to the path of heat.

Collector efficiency (Figure 6-14) simulations revealed that solar field efficiency drops below 60% when operating at HTF temperatures over 500°C. Since collector efficiency has the largest impact on overall plant efficiency, it would be therefore recommended that HTF loop outlet temperature be limited to a maximum value below 500°C.

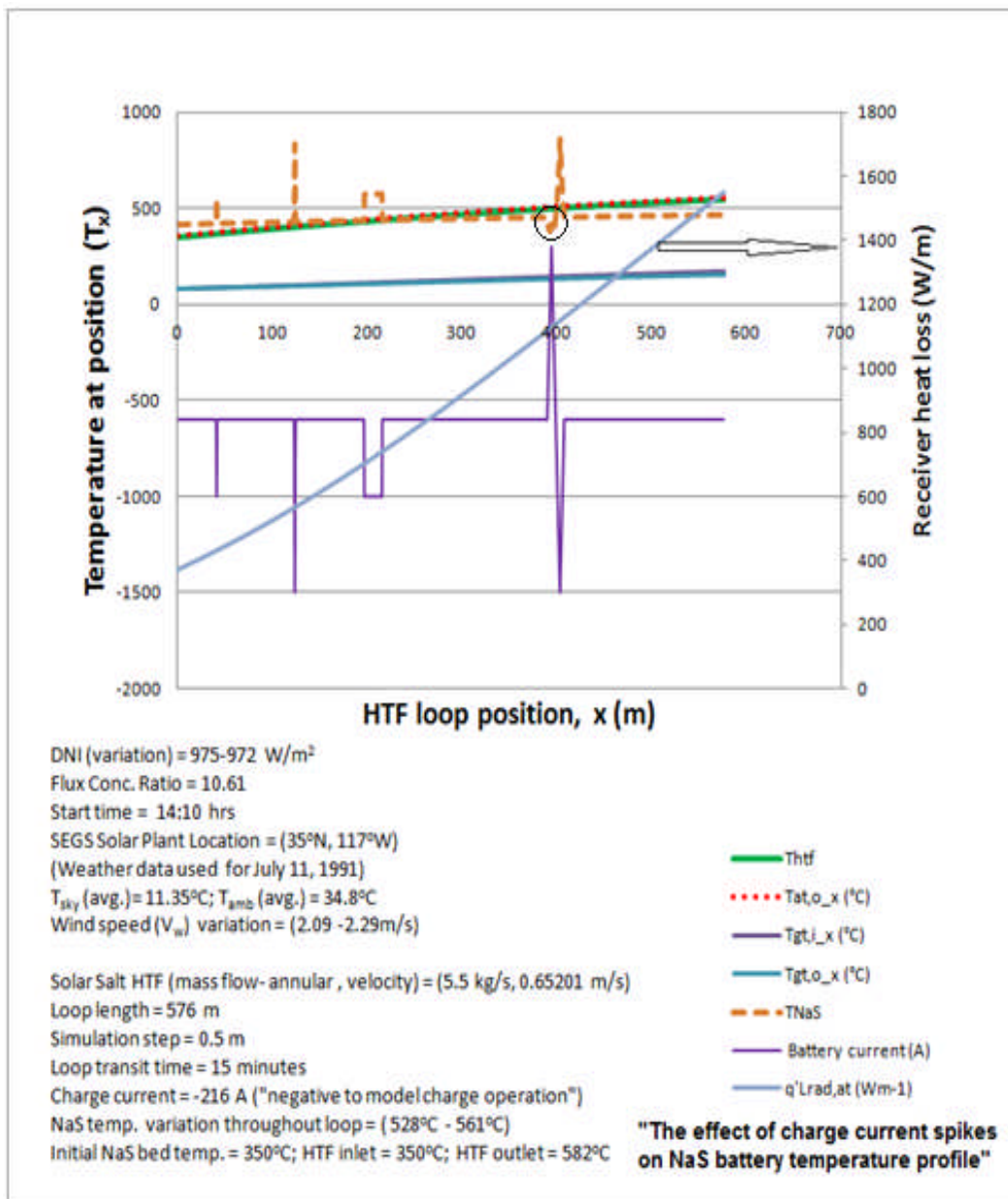


Figure 6-15: The effect of current spikes on the NaS battery temperature profile

The effect of current spikes on the NaS temperature profile was also briefly explored. Results (Figure 6-15) indicate that the battery temperature profile is affected by spikes in the negative direction. Negative current is charging current, and consequently a current increase in the negative direction corresponds to an increase in charging current.

The temperature of the NaS batteries was seen to increase with these spikes due to the fact that the charge operation is endothermic. The cell reaction therefore does not release the joule heating generated in the charging process, and though some of this heat is “*cooled off*” by the energy absorbed in the entropy of the cell charging reaction, the joule heating (being significantly greater), still contributes to a notable spike in temperature. This is because cell “*absorbs*” heat during the charging mode.

Conversly, the spike in the positive current direction (discharging direction) was seen to produce a battery temperature reducing effect, due to the exothermic nature of the battery discharge process. In this regard, heat flux generated by the current spike is transferred outward from the battery in the direction of the HTF, representing a heat loss and consequently a temperature reduction.

However, the temperature reducing effect was seen to be very small (“*small circle*” in Figure 6-15), owing to the fact that the spike is dampened as it travels outward from the centre of the cell by the combined thermal inertia of the ceramic and battery tubes between the battery and the HTF. Further, the thermal capacitance of the HTF is such that the small perturbation produced in the NaS temperature profile produced no obvious variation in the HTF temperature profile.

6.3 Discharging of the NaS cells during no-sun or night time hours

One of the reasons for using a molten salt HTF in these charge/discharge simulation was to explore the operation of the solar field at temperatures higher than that of traditional fields using synthetic oil HTF’s. A molten salt

such as Solar Salt can operate up to 550°C and results in a higher power cycle ΔK ($\Delta K = 200$, compared to the standard $\Delta K = 100$). However if the maximum HTF temperature has to be limited to 450°C in order to reduce increased heat losses at higher temperatures a different molten salt with a freezing point below 200°C (eg. calcium nitrate, HITEC) would be required.

The discharging of the NaS cells was simulated to occur during no-sun or night time hours. In order to obtain a picture of the natural “*temperature fall-off*” effect of night time temperatures on the solar field, the first simulation was done with the NaS cells held under adiabatic conditions.

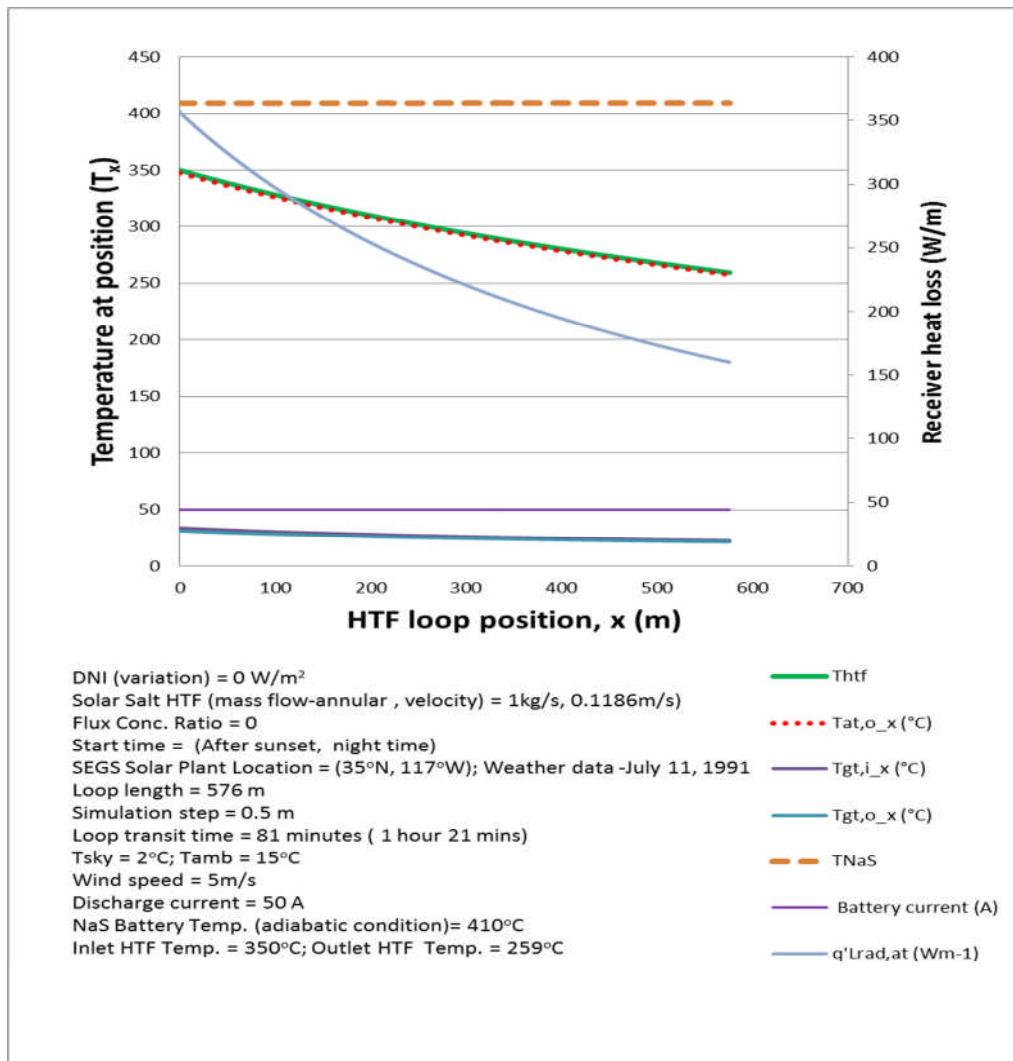


Figure 6-16: Plot showing natural HTF temperature decay during night time hours with NaS cells held under adiabatic conditions

The results (Figure 6-16) reveal an exponential decay of the HTF temperature with loop position and consequently with respect to time. Over a time of roughly one hour and twenty minutes, the HTF temperature would have fallen by close to 100°C from an initial value of 350°C. This is because of significant radiative heat loss from the receiver to the sky (at 2°C) which on average is in the region of 200 – 300 W/m (Figure 6-17) for HTF temperatures in the 300 – 400°C range. In support of this simulation, the fall-off in molten salt temperature overnight has also been shown by Kearney *et.al* [224] to be exponential (Figure 6-18).

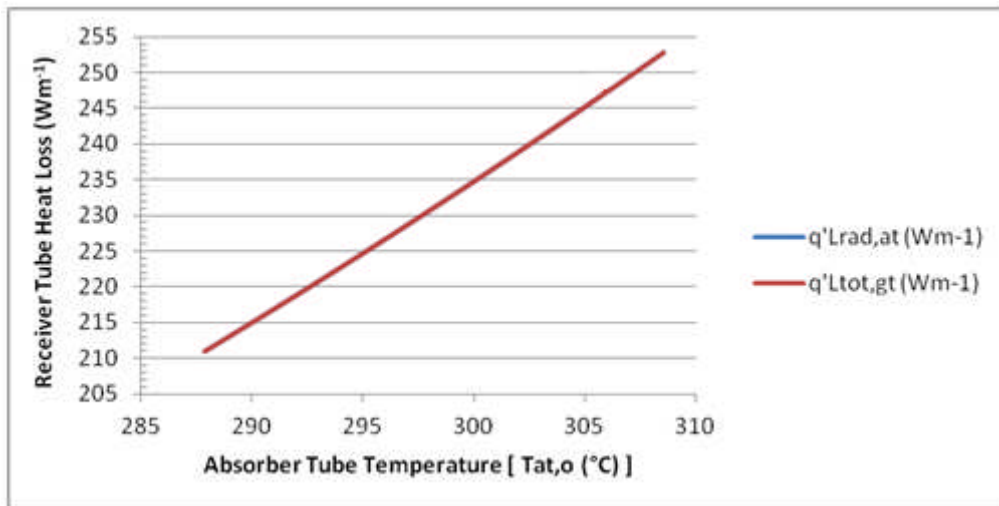


Figure 6-17: Heat losses from EES receiver during night-time operation

More importantly, one major benefit that could be provided by the EES receiver is helping with solar field freeze protection when using a molten salt HTF. The ability of the EES receiver to help reduce HTF temperature fall-off at night time using the exothermic nature of the NaS cell discharge reaction was therefore investigated.

For batteries initially at 410°C and an inlet HTF temperature of 350°C (Figure 6-19), heat transfer from the NaS cells does produce a “*lifting effect*” on the HTF temperature profile, but the NaS cells cool significantly (by close to 100 K), in the process.

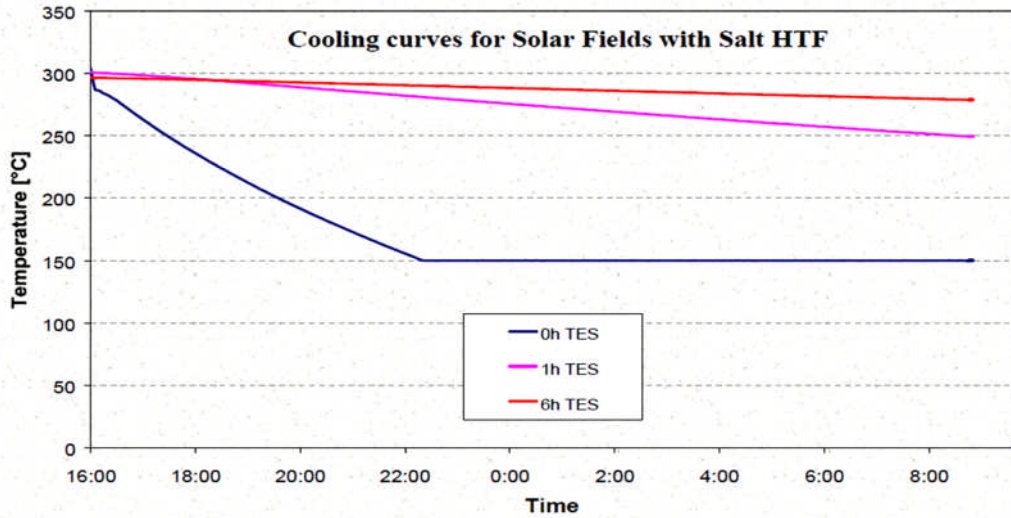


Figure 6-18: Overnight fall-off in molten salt HTF temperature with plant storage capacity (Source:^[224])

This is largely owing to the significantly higher specific heat capacity (c_p) value of the HTF (1524 J/kg.K_[avg.]) compared to the NaS battery (744.2 J/kg.K_[model calc.]) and the large driving force developed from the difference between the HTF, ambient and sky temperatures.

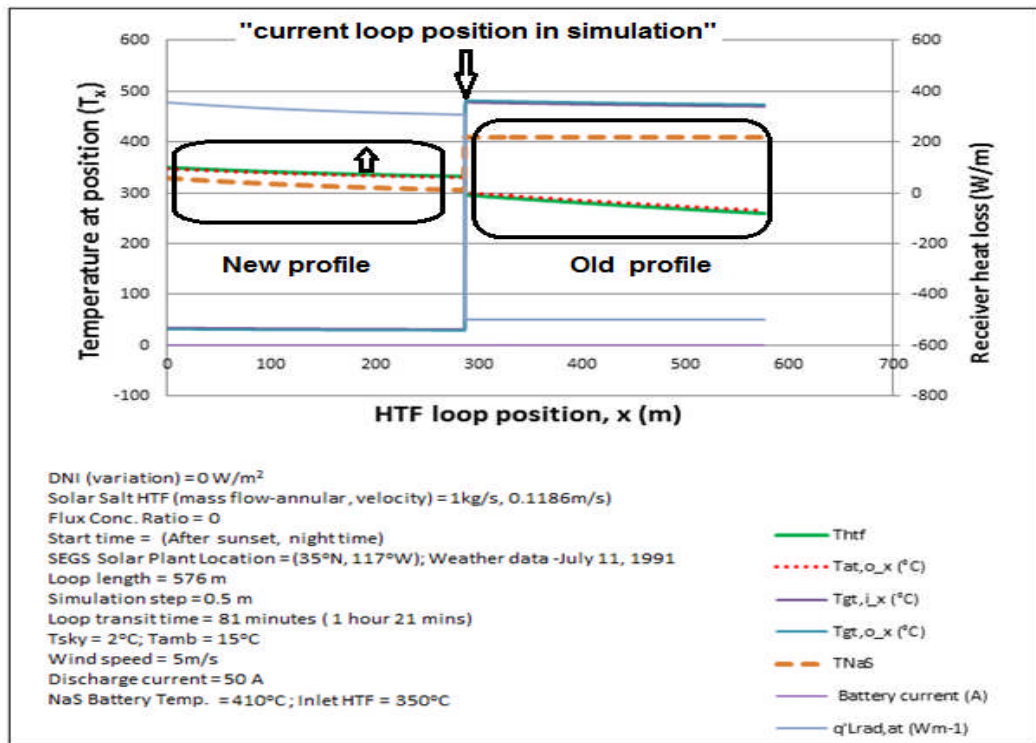


Figure 6-19: Effect of NaS cell thermal capacitance in reducing HTF temperature fall-off

Based on work done by Kearney *et.al* [224], it has been suggested that a PTC power plant with only 6 hours of thermal storage (Figure 6-18) is able by virtue of the “hot salt tank thermal capacitance of alone”, to maintain the temperature of the circulating HTF above freezing point overnight. This freeze protection is therefore further complemented in the conceptual EES receiver solar field, by the thermal energy stored in the thermal capacitance of the batteries and also by the exothermic nature of the associated battery discharge night time operation.

6.3.1 Simulation of the Discharging Operation

In the conceptual EES PTC solar field, the NaS batteries in the receivers would be required to provide 4 hours of continuous power output at 50 MW_e, in conjunction with a standard 7.5 - 8 hour molten salt thermal salt storage system.

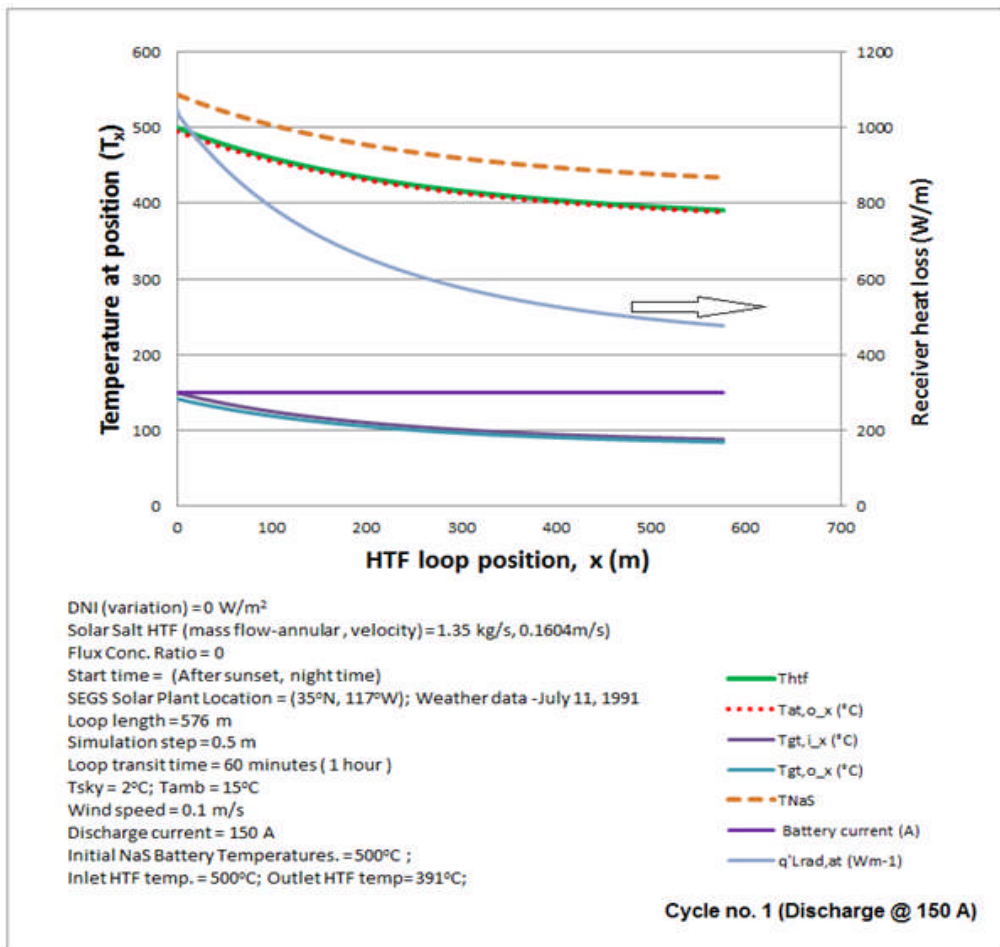


Figure 6-20: Simulated profile results for the 1st NaS battery discharge cycle at 50 A

For this 4 hour duration, it is important that battery temperature does not fall below the minimum charge/discharge temperature of 300°C and that the salt temperature is maintained well above freezing point. Simulations were therefore performed to investigate these operating conditions and the related results are displayed in Figures 6-20 to 6-23.

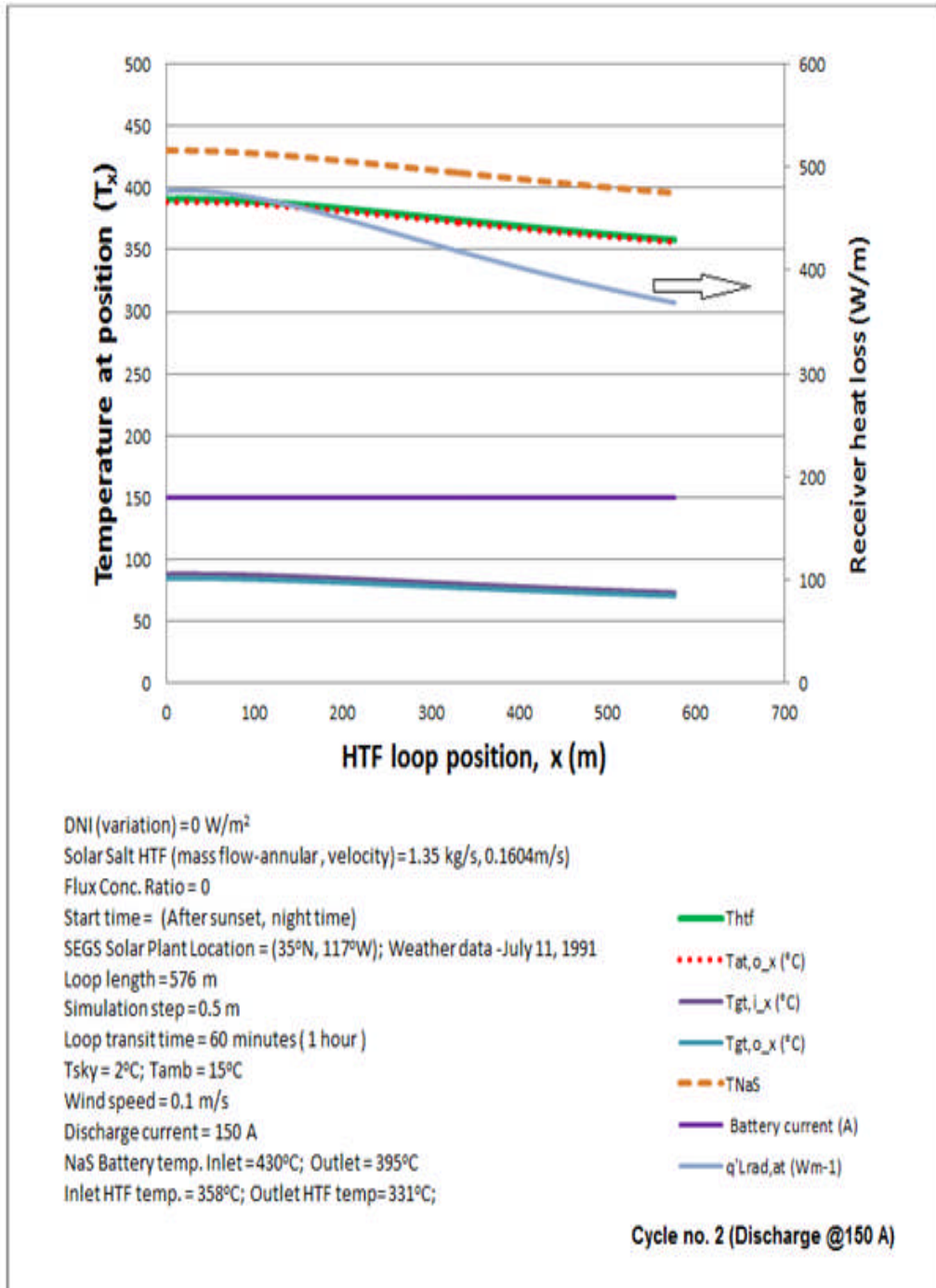


Figure 6-21: Simulated profile results for the 2nd NaS battery discharge cycle at 50 A

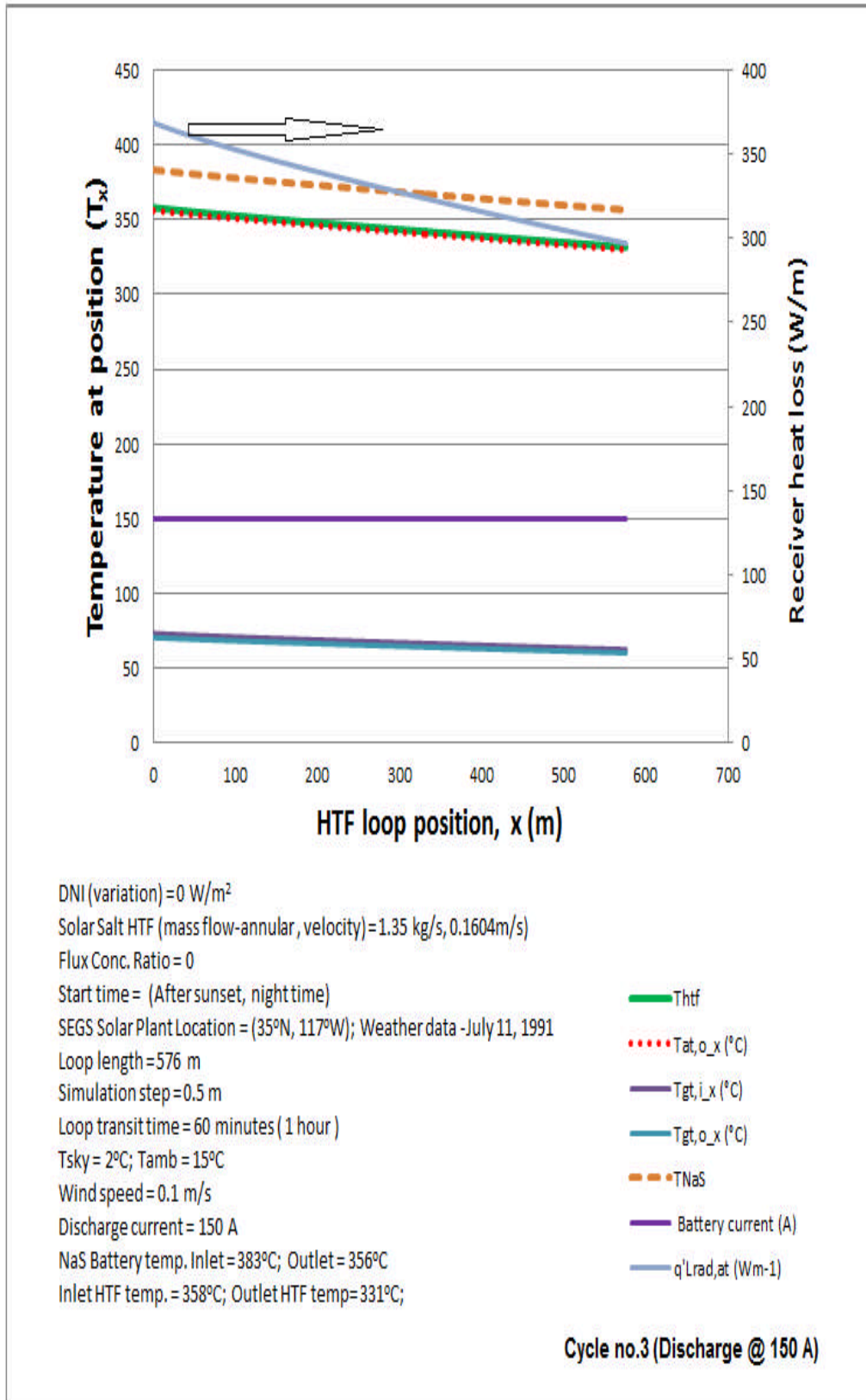


Figure 6-22: Simulated profile results for the 3rd NaS battery discharge cycle at 50 A

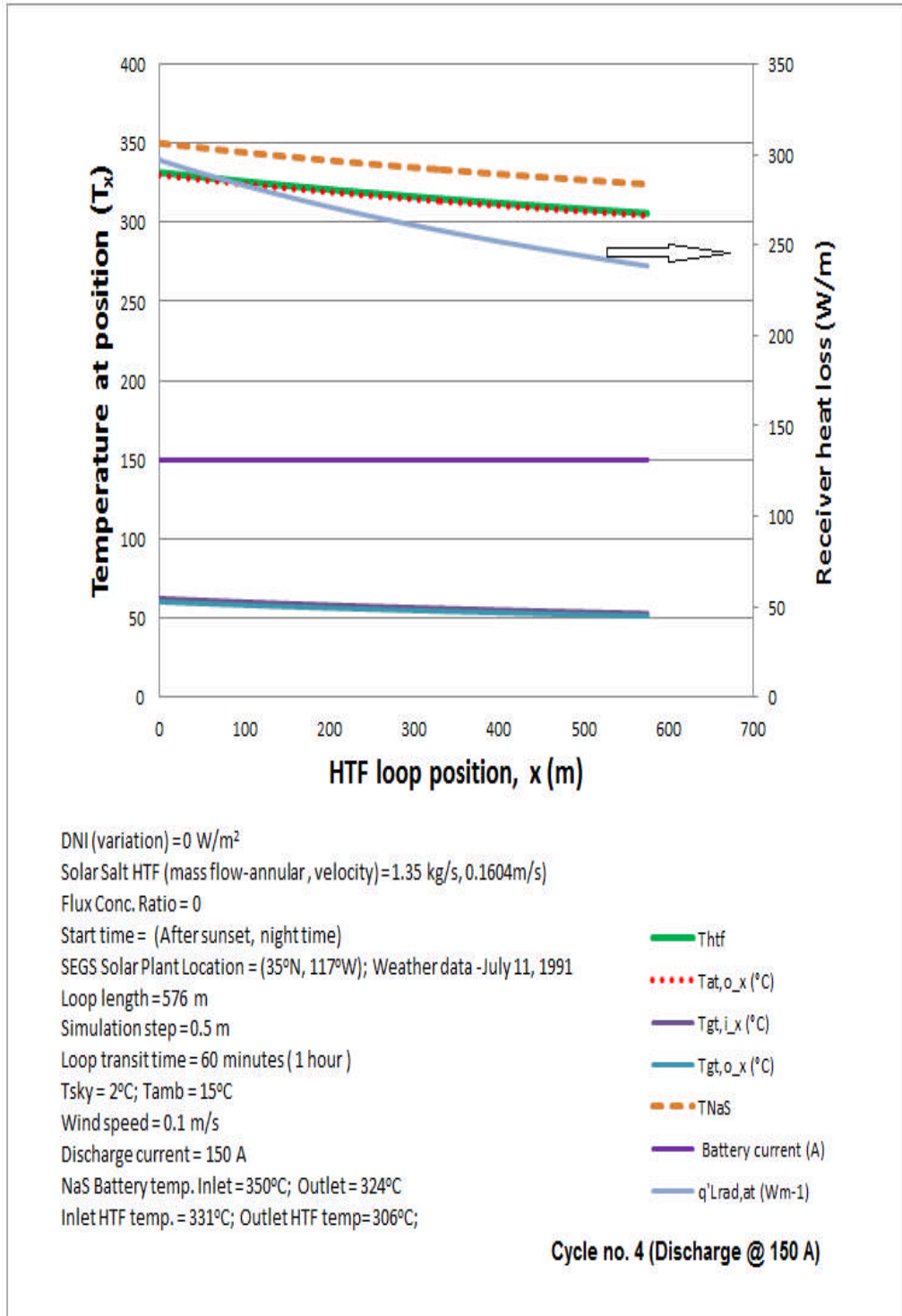


Figure 6-23: Simulated profile results for the 4th NaS battery discharge cycle at 50 A

For the simulated 600 Ah Tepco T5 NaS cell (632 Ah actual cell), a current flow of 150 A would be required to totally discharge the batteries in

4 hours. Consequently, this current level used in the first set of discharging simulations (Figures 6-20 to 6-23).

In all these simulations, the loop transit time was one hour and it was assumed that the NaS batteries and the Solar Salt HTF had achieved a uniform daytime equilibrium temperature of 500°C, using appropriate temperature and flow control mechanisms.

In discharge cycle number 1 (Figure 6-20), the battery temperature is seen to jump upwards by approximately 50°C at start-up (caused by joule heating from the discharge current and the entropy of the reaction) and to fall steeply to 430°C over the one hour time duration. During this time, the salt HTF also cools down to just under 400°C and is seen to follow the cooling pattern of the battery temperature profile, indicating heat transfer from the batteries to the Solar Salt HTF.

For cycles 2-4 (Figures 6-21 to 6-23), the salt HTF temperature fall-off is less steep, and the *“lifting effect”* of heat transfer from the batteries is more evidently seen. The results showed that after 4 hours of night time discharge at ambient and sky temperatures of 15°C and 2°C respectively, both the HTF and battery temperatures still exceed 300°C.

However wind speeds in these simulations were close to 0 m/s and higher heat losses (a greater cool down effect) would be expected at higher wind speeds in the region of 5 -10 m/s. In such cases, battery and HTF temperatures could fall below 300°C and other approaches to reducing these losses, presently outside the scope of this work would need to be explored.

After cycle 4, the batteries are fully discharged. Therefore in cycle number 5, the battery current was set to zero. In this cycle (Figure 6-24) the visible temperature difference between batteries and HTF has disappeared and an equilibrium temperature was reached. This clearly demonstrated that the *“heat evolved from battery charging”* was solely responsible for the temperature difference between battery and HTF.

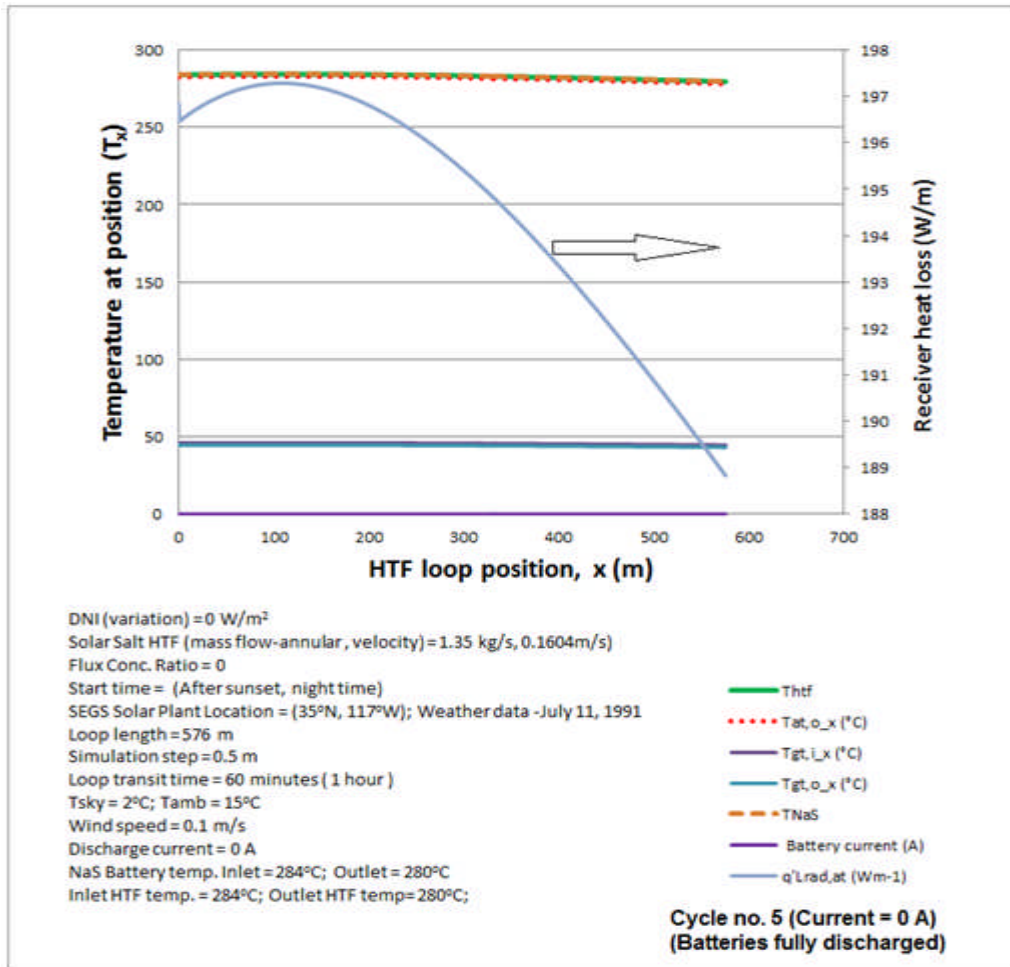


Figure 6-24: Simulated profile results for the 5th NaS battery discharge cycle at 0 A

In the discharge simulations just presented, the NaS batteries were fully discharged over a 4 hour duration at a current level of 150 A. However, it is important to note that the batteries could be discharged over any number of hours. One possible approach could be to discharge the batteries at a 50 A current level over the 12 hour “no-sun” period, and “simultaneously supply plant output power” from a combination of battery and salt tank energy storage over this entire time period.

This now concludes the section on battery discharge simulations. The final section which follows, discusses a potential approach to “battery temperature cooling” or “temperature gradient reduction” along the loop of NaS cells.

6.4 An Approach to cooling the NaS batteries during Charge or Discharge Operations

Temperature control of the NaS batteries will always be a crucial factor in the operation of a solar field based on the EES receiver concept outlined in this work. Two simple approaches to “cooling down” the cells if they get too hot are “defocusing the SCA from the concentrated radiation”, through the SCA tracking control system or introducing a “cold” HTF stream into the loop. The first option is essentially not ideal and should be used only in emergency situations, since it results in an unrecoverable loss of useful thermal energy to the power plant. Also, the second option of introducing a colder HTF stream is not always possible and may not be convenient at all times during the plant’s operation.

From the simulations performed when running the EES model, it was realized that control and equalization of the NaS batteries temperatures can be effected by “reversing or varying the direction of HTF flow through the loop” (Figure 6-25). Although this is not done in standard PTC plants, it is an option that could be considered in the case of this concept. It would require that loop hydraulics (valves and pumps) allow bi-directional HTF flow and the additional cost incurred in this regard could be the subject of future work, though it is not expected to be a very significant capital cost.

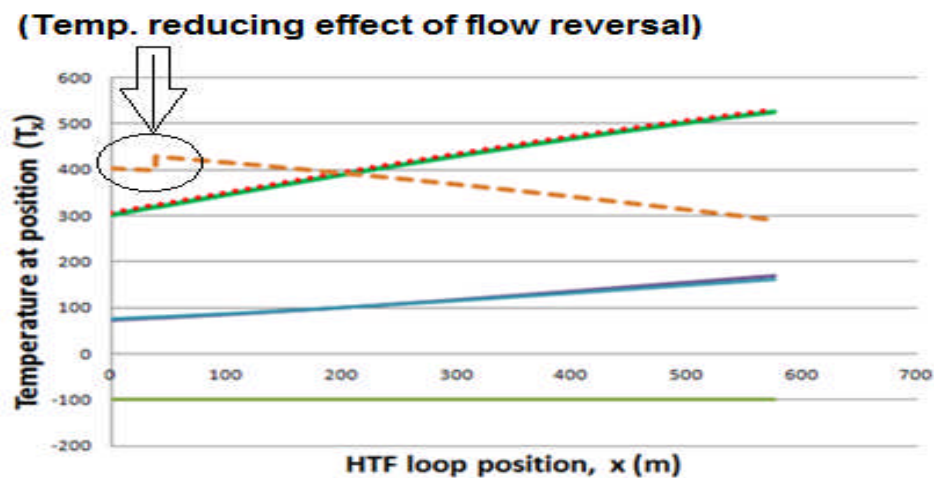


Figure 6-25: The temperature reducing effect of flow reversal

The cooling effect is enhanced due to the heat capacity of the HTF being more than double that of the batteries, and consequently the HTF is able to “soak-up” heat from the batteries.

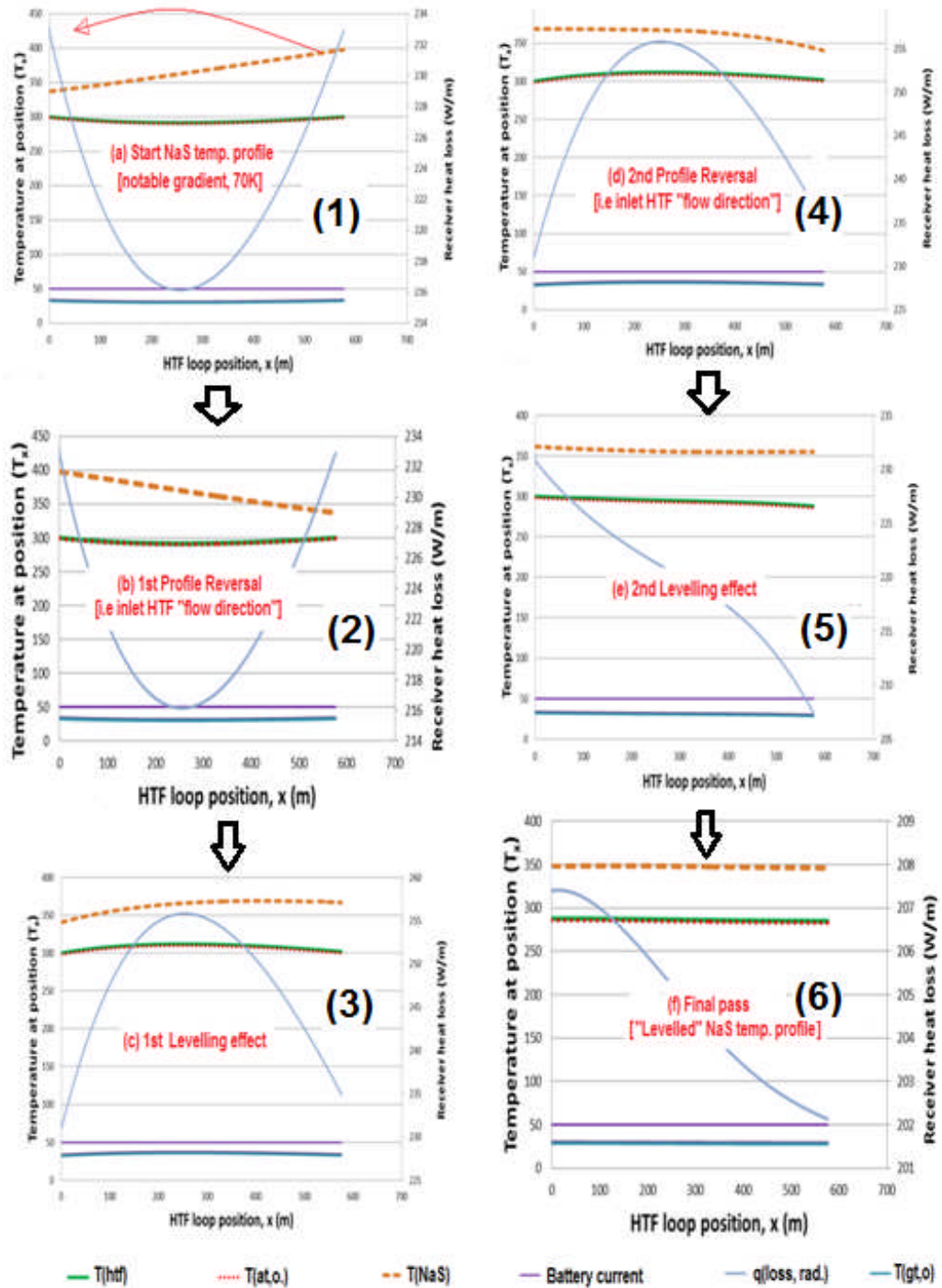


Figure 6-26: Plots illustrating the NaS temperature profile equalization effect of two flow reversals

This cooling effect is further illustrated using an arbitrary NaS and HTF temperature profile combination (Figure 6-26) from a previous simulation. Following steps 1 through to 6, the original NaS temperature profile which had a notable starting gradient was “*cooled down*” without use of colder HTF stream “*external to the loop*”. Rather battery temperature was lowered by reversing the flow of the same HTF in the loop, with the HTF entering from the “*hot end*” of the flow channel. This effect served to create a greater driving force for heat transfer from the NaS batteries to the passing HTF.

After two cycles of flow reversal, the notable battery temperature gradient at the start of the simulations was seen to disappear and a “*levelled*” battery temperature profile was realized.

This section served only to provide an elementary idea of the possibility of a flow reversal cooling approach. Consequently much further and more detailed investigation is required, especially in regards to quantification of the extra pumping power required and the economics of the method. Bearing all these points in mind, the chapter summary now follows.

Chapter Summary

In this chapter, simulations of basic charge/discharge operations in the conceptual EES receiver solar field were presented. Based on the simulations, charge and discharge operations in the conceptual receiver would be possible provided that an appropriate temperature control strategy is developed for the NaS batteries.

It was also seen that heat from the discharge operation during night time hours helps to reduce the temperature fall-off in HTF temperature, and that both HTF and battery temperatures remained above 300°C during a 4 hour period of night time discharge. During this 4 hour time period, the stored NaS battery power alone would have supported the full 50 MW_e output of the power plant.

Finally, combined with a 7.5 - 8 hour molten salt storage system, and with molten salt HTF circulating throughout the field at night time, joule heating from the discharging NaS batteries combined with the heat stored in their thermal capacitance, would be enough to completely ensure HTF freeze protection in the solar field.

This chapter has now concluded the essential work concerning both the modelling and simulation of the conceptual EES receiver described in this thesis. The next and final chapter of this work will summarize for the reader all the key findings, present some important recommendations for future research and will posit the general conclusions that have been deduced from this study.

Chapter 7

Thesis Summary, Recommendations, and Conclusion

Introduction

In this thesis, the modelling and simulation of a conceptual energy storage solar receiver referred as the “Electrical Energy Storage (EES) receiver” has been presented along with the design of an experimental rig for the purpose of testing this concept. Based on the simulations undertaken and the experimental data presented, the concept could one day prove promising and is therefore worthy of further investigation by other researchers in the solar thermal field.

One of the important recommendations for future work, (found in the list of recommendations given in the next section of this chapter), is the need for a thorough economic analysis of the concept. Although this is generally outside the scope of this current work, NREL’s System Advisor Model (SAM 2011) software (*developed by NREL, for use by engineers, researchers and the general public*) was used to obtain some idea of the key economic parameters of the conceptual plant. Details of these simulations for the purpose of the reader can be found in Appendix G.

From the basic SAM results (Appendix G), it was estimated that the levelized cost of the energy (LCOE) produced by for the EES receiver PTC plant is almost double the value obtained in the Andasol – 1 case study ^[225], (An LCOE of 50.81 ¢/kWh versus of 30 ¢/kWh in US cents) which is typical of a standard PTC power plant. The reader must note however that this estimate is not authoritative as the SAM software could not be adapted to model and quantify the benefits of the “*electrical aspects of the hybrid storage system*”.

Nevertheless, the high LCOE value is not surprising and is directly attributable to the significant capital cost of the NaS cells inside the

receiver. Further, the LCOE would become slightly higher if costs involved in manufacturing, fabricating and deploying the conceptual EES receiver are taken into account. A much more detailed economic analysis is therefore required for future work, along with a method of modifying the SAM software code to accommodate electrical energy storage for purposes of analysis.

An initial exploration of the EES receiver concept as found in this work, definitely exposes the need for a more thorough investigation into keys aspects of the system's operation. Consequently, in the next section of this chapter, some important recommendations for further study are presented. These recommendations are then followed by a summary of the key findings and a general conclusion to the thesis.

7.1 Thesis Summary

This thesis presented the conceptualization, design and simulated operation of electrical energy storage (EES) receiver for potential use in PTC power plants. A hybridization of sodium sulphur (NaS) and parabolic trough collector (PTC) technologies, the receiver would provide PTC plants with built in electrical energy storage capabilities, and could one day provide them with the capacity for higher cycle efficiencies when used with a molten salt HTF.

For a succinct recap of the six previous chapters in this thesis, the reader would recall that Chapter 1 was used to provide an overview of the general scope and focus of this work, while Chapter 2 positioned the same in the context of related field research. In Chapter 3 the physics of conceptual EES receiver was presented along with the design of an associated heating rig for experimentation with the concept.

Chapter 4 presented the mathematical models used to represent the system's operation, while chapters 5 and 6 presented experimental and simulated results in respect of the initial heating and charge/discharge operation of the system respectively.

It has been shown through simulations that with the appropriate temperature and current controls, the EES receiver:

- a) Should operate successfully in charging mode during daylight hours in a solar field under concentrated radiation with appropriate temperature and flow control mechanisms.
- b) Should operate successfully in a discharging mode during night time hours in a solar field, in the absence of concentrated solar radiation due to the exothermic nature of the discharge operation.
- c) Provide freeze protection to molten salt HTF's, potentially enabling synthetic oil plants to eventually switch over to the use of a molten salt HTF.
- d) Must be made physically larger than standard receivers to accommodate an internal NaS cell and a HTF flow annulus. The larger absorber tube size more than doubles the associated radiative and convective heat losses but this unavoidable condition is insignificant when compared to the general benefits the receiver could provide.
- e) When combined with an 8 hour thermal storage system could make it possible to "*theoretically*" operate a 50 MW_e PTC power plant at full power for 24 hours without fossil fuel input.
- f) Is expected to have a LCOE value (based on current prices) that could double that of a standard plant, due solely to the current high cost of NaS battery storage and system integration. However this cost could be significantly reduced in coming years with a combination of falling battery prices and technological enhancements to this storage concept.

7.2 Recommendations for Future Work

Successful implementation and operation of the conceptual EES receiver in a pilot plant or in a test solar field will be a far more complicated operation than of a traditional PTC receiver. This is due to the added task of controlling the operational parameters of the NaS cell. As seen from the

simulations in chapter 6, one of the main challenges will be to develop a fast, robust and effective temperature/current control system for the EES receivers in the solar field. Ensuring operational safety will also be critical, especially when dealing with the combination of high system temperatures, HTF pressures and batteries containing sodium metal.

Some areas on which future researchers could focus are:

- a) Developing an appropriate temperature control strategy/system for EES receivers in a solar field.
- b) Developing an appropriate charging/discharging control strategy/system for EES receivers in a solar field.
- c) Re-engineering the NaS cell to achieve better heat transfer with the circulating HTF or developing heat transfer enhancement mechanisms in the EES receiver in order to achieve this.
- d) Modelling the operation of the complete EES receiver PTC plant, including the storage and power blocks.
- e) A detailed economic analysis of the potential of the concept in context of the present day, especially.
- f) Development of a more detailed heat transfer model, based on transient heat conduction, CFD and/or multi-dimensional numerical analysis of the EES receiver cross section
- g) A detailed analysis of the prospects for complementary operation of NaS battery storage combined with standard molten salt thermal storage over an operating range of 350 – 550°C.
- h) A quantization and evaluation of the power quality and ancillary power benefits of an EES receiver field to the power plant from a generation perspective.
- i) A detailed evaluation of the operation of the EES receiver field with molten salt HTF and its effectiveness in freeze protection of the HTF over 12 hour of night time.
- j) Analysis and design of appropriate plant hydraulics, especially in relation to the concept of allowing “*flow reversal*” as required, for “*levelling*” of the NaS battery temperature profile.

These are only a few of the many topics open to investigation. It is generally hoped that this preliminary work will engender significant thought on this very interesting and challenging concept, prompting further investigation by sagacious researchers in this area of solar thermal technology.

Concluding Remarks for this Thesis

In this work the conceptual EES receiver which has been presented was developed as part of a potential chain of solutions for improving the performance of PTC power plants and for making "*green even greener*".

By use of both experimental results and model simulations, the most important parameters that describe the potential operation of the EES receiver have been evaluated. From these results, it can be generally concluded that the concept is technically feasible, and implementable. However the anticipated cost in developing a plant based on this concept are significantly higher than the current costs of developing standard PTC power plants. This is due primarily to the high costs of the NaS batteries (\$500/ kWh) and the expected costs in fabricating the EES receiver.

Also the inability of the SAM software to incorporate the benefits of electrical storage into its performance-economics calculations leaves the question on the "*cost-effectiveness*" of this concept partially unanswered and therefore this area requires detailed future analysis.

On a positive note however, since the NaS cell is constructed from very cheap and readily available materials, in future years it is very possible that with mass production, cells could become as cheap, or cheaper than standard lead-acid batteries. Should this occur at some future point, the concept could prove a very competitive storage option.

Further yet, one possible means of supporting system development especially in a pilot plant, could be a cost sharing approach where battery manufacturers (such as TEPCO, Japan and Ionotec, U.K) provide PTC

plant developers a significant reduction in battery costs, in exchange for a stake in plant ownership and/or revenue streams.

In conclusion, it can be said that the main object of this thesis in obtaining a *“basic understanding of the operation of a purely conceptual EES receiver in a conceptual PTC power plant”* has been achieved. This work has only scratched the surface of this concept and has shown that there is significant scope for future research on this idea. Though some may cavil at the current challenge of high battery prices (which may only be ephemeral), the EES receiver concept itself carries merit, due largely to its capacity as a novel energy storage solution, its potential for robust ancillary power support services and its potential to help create a *“24 hour renewable energy”* PTC power plant.

Therefore with a combination of further research, engineering and falling component costs, this conceptual receiver or some modified form of it, may one day become a standard component of all PTC power plants in a 100% renewables future power grid.

References Section

References

1. Streicher W. Solar Thermal Heating Systems - Lecture Book; 2012.
2. Brurkholder F, Kutscher, C. Heat Loss Testing of Schott's 2008 PTR70 Parabolic Trough Receiver. NREL/TP-550-45633. U.S.A.: National Renewable Energy Laboratory (NREL); 2009.
3. Forristall R. Heat Transfer Analysis and Modelling of a Parabolic Trough Solar Receiver Implemented in Engineering Equation Solver; 2003.
4. Kalogirou SA. Solar thermal collectors and applications. Progress in Energy and Combustion Science 2004;30(3):231-95.
5. Beltran H, Perez E, Aparicio N, Rodriguez P. Daily Solar Energy Estimation for Minimizing Energy Storage Requirements in PV Power Plants. Sustainable Energy, IEEE Transactions on 2012;PP(99):1-8.
6. (CSPA) CSPA. The Economic and Reliability Benefits of CSP with Thermal Energy Storage: Recent Studies and Research Needs; 2012. p. x-xx,86.
7. Ela E, Milligan, M., Kirby, B. Operating Reserves and Variable Generation; 2011. p. 21,48.
8. Tamme R. Thermal Energy Storage: Concrete and Phase Change TES. Parabolic Trough Technology Workshop 2006; 2006.
9. Steinmann W-D, Tamme R. Latent heat storage for solar steam systems. Paper presented at, 2008; 3 Park Avenue, New York, NY 10016-5990, United States.
10. Ming L, Saman W, Bruno F. Review on storage materials and thermal performance enhancement techniques for high temperature phase change thermal storage systems. Renewable and Sustainable Energy Reviews 2012;16(4):2118-32.

11. Michels H, Pitz-Paal R. Cascaded latent heat storage for parabolic trough solar power plants. *Solar Energy* 2007;81(6):829-37.
12. Medrano M, Gil A, Martorell I, Potau X, Cabeza LF. State of the art on high-temperature thermal energy storage for power generation. Part 2—Case studies. *Renewable and Sustainable Energy Reviews* 2010;14(1):56-72.
13. Madaeni SH, Sioshansi R, Denholm P. How Thermal Energy Storage Enhances the Economic Viability of Concentrating Solar Power. *Proceedings of the IEEE* 2012;100(2):335-47.
14. Luzzi A, Lovegrove K, Filippi E, Fricker H, Schmitz-Goeb M, Chandapillai M. Base-load solar thermal power using thermochemical energy storage. *Journal De Physique. IV : JP* 1999;9(3):Pr3-105 - Pr3-10.
15. Liu M, Saman W, Bruno F. Review on storage materials and thermal performance enhancement techniques for high temperature phase change thermal storage systems. *Renewable and Sustainable Energy Reviews* 2012;16(4):2118-32.
16. Laing D, Steinmann WD, Viebahn P, Gräter F, Bahl C. Economic Analysis and Life Cycle Assessment of Concrete Thermal Energy Storage for Parabolic Trough Power Plants. *Journal of Solar Energy Engineering* 2010;132(4):041013-13.
17. Laing D, Bahl C, Bauer T, Fiss M, Breidenbach N, Hempel M. High-temperature solid-media thermal energy storage for solar thermal power plants. Paper presented at: SPECIAL ISSUE: The Intermittency Challenge: Massive Energy Storage in a Sustainable Future, 2012; 445 Hoes Lane / P.O. Box 1331, Piscataway, NJ 08855-1331, United States.
18. Kreith F, West RE. THERMAL ENERGY STORAGE FOR SOLAR SYSTEMS. Paper presented at: Extended Abstracts - Fall Meeting (168th Society Meeting), the Electrochemical Society., 1985; Las Vegas, NV, USA.

19. Kintner-Meyer M, Jin C, Balducci P, Elizondo M, Guo X, Nguyen T, et al. Energy storage for variable renewable energy resource integration - A regional assessment for the Northwest Power Pool (NWPP). Paper presented at, 2011; Phoenix, AZ.
20. Kerestes RJ, Reed GF, Sparacino AR. Economic analysis of grid level energy storage for the application of load leveling. Paper presented at, 2012; San Diego, CA.
21. IRENA, editor. Renewable Energy Cost Analysis - Concentrating Solar Power; 2012;Vol. 1.
22. Harries DN, Paskevicius M, Sheppard DA, Price TEC, Buckley CE. Concentrating solar thermal heat storage using metal hydrides. Paper presented at: SPECIAL ISSUE: The Intermittency Challenge: Massive Energy Storage in a Sustainable Future, 2012; 445 Hoes Lane / P.O. Box 1331, Piscataway, NJ 08855-1331, United States.
23. Gill S, Ault GW, Kockar I. The optimal operation of energy storage in a wind power curtailment scheme. Paper presented at, 2012; San Diego, CA.
24. Gil A, Medrano M, Martorell I, Lazaro A, Dolado P, Zalba B, et al. State of the art on high temperature thermal energy storage for power generation. Part 1: concepts, materials and modellization. Renewable and Sustainable Energy Reviews 2010;14(1):31-55.
25. Feldhoff JF, Benitez D, Eck M, Riffelmann K-J. Economic potential of solar thermal power plants with direct steam generation compared with HTF plants. Journal of Solar Energy Engineering, Transactions of the ASME 2010;132(4).
26. Elkind EN. The Power of Energy Storage: How to Increase Deployment in California to Reduce Greenhouse Gas Emissions: Bank of America, Berkley Law Center for Law and Energy, UCLA Environmental Law Center; 2010.

27. Díaz-González F, Sumper A, Gomis-Bellmunt O, Villafáfila-Robles R. A review of energy storage technologies for wind power applications. *Renewable and Sustainable Energy Reviews* 2012;16(4):2154-71.
28. Cabeza LF, Sole C, Castell A, Oro E, Gil A. Review of Solar Thermal Storage Techniques and Associated Heat Transfer Technologies. *Proceedings of the IEEE* 2012;100(2):525-38.
29. Alliance CSP. The Economic and Reliability Benefits of CSP with Thermal Energy Storage: Recent Studies and Research Needs. CSP Alliance Report 2012 2012.
30. Muller-Steinhagen H, Trieb, F. Concentrating Solar Power: A Review of the technology: DLR; 2004.
31. NREL. Concentrating Solar Power Projects in the United States; 2013. Retrieved on July 29, 2013 from URL:
http://www.nrel.gov/csp/solarpaces/by_country_detail.cfm/country=US
32. NREL. Martin Next Generation Solar Energy Center; 2013. Retrieved on July 29, 2013 from URL:
http://www.nrel.gov/csp/solarpaces/project_detail.cfm/projectID=267
33. NREL. Gaskell Sun Tower; 2011. Retrieved on July 29, 2013 from URL:
http://www.nrel.gov/csp/solarpaces/project_detail.cfm/projectID=82
34. NREL. Archimede; 2012. Retrieved on July 29, 2013 from URL:
35. NREL. Holaniku at Keahole Point; 2013. Retrieved on July 29, 2013 from URL:
http://www.nrel.gov/csp/solarpaces/project_detail.cfm/projectID=71
36. NREL. Kimberlina Solar Thermal Power Plant; 2013. Retrieved on July 29, 2013 from URL:
http://www.nrel.gov/csp/solarpaces/project_detail.cfm/projectID=37

37. NREL. Nevada Solar One. 2013. Retrieved on July 29, 2013 from URL:
http://www.nrel.gov/csp/solarpaces/project_detail.cfm/projectID=20
38. NREL. Saguaro Power Plant; 2013. Retrieved on July 29, 2013 from URL:
http://www.nrel.gov/csp/solarpaces/project_detail.cfm/projectID=24
39. NREL. SEGS I-IX Plants; 2013. Retrieved on July 29, 2013 from URL: http://www.nrel.gov/csp/solarpaces/by_project.cfm
40. NREL. Sierra Sun Tower; 2013. Retrieved on July 29, 2013 from URL:
http://www.nrel.gov/csp/solarpaces/project_detail.cfm/projectID=63
41. NREL. Palen Solar Electric Generating System; 2013. Retrieved on July 29, 2013 from URL:
http://www.nrel.gov/csp/solarpaces/project_detail.cfm/projectID=53
42. NREL. Rice Solar Energy Project; 2013. Retrieved on July 29, 2013 from URL:
http://www.nrel.gov/csp/solarpaces/project_detail.cfm/projectID=61
43. NREL. Tooele Army Depot; 2013. Retrieved on July 29, 2013 from URL:
http://www.nrel.gov/csp/solarpaces/project_detail.cfm/projectID=265
44. NREL. Crescent Dunes Solar Energy Project. 2013. Retrieved on July 29, 2013 from URL:
http://www.nrel.gov/csp/solarpaces/project_detail.cfm/projectID=60
45. NREL. Concentrating Solar Power Projects in Spain; 2013. Retrieved on July 29, 2013 from URL:
http://www.nrel.gov/csp/solarpaces/by_country_detail.cfm/country=ES
46. Herrmann U, Kearney DW. Survey of thermal energy storage for parabolic trough power plants. *Journal of Solar Energy Engineering, Transactions of the ASME* 2002;124(2):145-52.

47. REN21.2013. Renewables Global Futures Report 2013 (Paris: REN21). 2013. p. 57.
48. Libby C. Program on Technology Innovation: Evaluation of Concentrating Solar Thermal Energy Storage Systems. 1018464. Electric Power Research Institute (EPRI),3420 Hillview Avenue, Palo Alto, CA 94304: EPRI; 2009.
49. Libby C. Program on Technology Innovation: Evaluation of Concentrating Solar Thermal Energy Storage Systems: Electric Power Research Institute (EPRI); 2009.
50. Libby C, Bedard, R. New Mexico Central Station Solar Power:Summary Report: Electric Power Research Institute (EPRI); 2008.
51. Bauer T, et al. Overview of Molten Salt Storage Systems and Materials Development for Solar Thermal Power Plants. ASES Solar 2012; 2012.
52. Pavlovic TM, Radonjic IS, Milosavljevic DD, Pantic LS. A review of concentrating solar power plants in the world and their potential use in Serbia. Renewable and Sustainable Energy Reviews 2012;16(6):3891-902.
53. Kearney D, Herrmann U, Nava P, Kelly B, Mahoney R, Pacheco J, et al. Assessment of a molten salt heat transfer fluid in a parabolic trough solar field. Journal of Solar Energy Engineering, Transactions of the ASME 2003;125(2):170-76.
54. Pacheco JE, Showalter SK, Kolb WJ. Development of a molten-salt thermocline thermal storage system for parabolic trough plants. Journal of Solar Energy Engineering, Transactions of the ASME 2002;124(2):153-59.
55. Bayon R, Rojas E. Simulation of thermocline storage for solar thermal power plants: From dimensionless results to prototypes and real-size tanks. International Journal of Heat and Mass Transfer 2013;60(1):713-21.

56. Herrmann U, Kelly B, Price H. Two-tank molten salt storage for parabolic trough solar power plants. *Energy* 2004;29(5-6):883-93.
57. Yang Z, Garimella S.V. Molten-salt thermal energy storage in thermoclines under different environmental boundary conditions. *Applied Energy* 2010;87(11):3322-29.
58. Yang Z, Garimella S.V. Cyclic operation of molten-salt thermal energy storage in thermoclines for solar power plants. *Applied Energy* 2013;103:256-65.
59. Bradshaw RW, Siegel NP. Molten nitrate salt development for thermal energy storage in parabolic trough solar power systems. Paper presented at: 2008 2nd International Conference on Energy Sustainability, ES 2008, August 10, 2008 - August 14, 2008, 2009; Jacksonville, FL, United states.
60. Gomez JC, Calvet N, Starace AK, Glatzmaier GC. $\text{Ca}(\text{NO}_3)_2$ - NaNO_3 - KNO_3 molten salt mixtures for direct thermal energy storage systems in parabolic trough plants. *Journal of Solar Energy Engineering, Transactions of the ASME* 2013;135(2).
61. Wang T, Mantha D, Reddy RG. High thermal energy storage density LiNO_3 - NaNO_3 - KNO_3 - KNO_2 quaternary molten salt for parabolic trough solar power generation. Paper presented at: Energy Technology 2012: Carbon Dioxide Management and Other Technologies - TMS 2012 Annual Meeting and Exhibition, March 11, 2012 - March 15, 2012, 2012; Orlando, FL, United states.
62. Wang T, Mantha D, Reddy RG. Thermal stability of the eutectic composition in LiNO_3 - NaNO_3 - KNO_3 ternary system used for thermal energy storage. *Solar Energy Materials and Solar Cells* 2012;100:162-68.
63. Hussain ST, Saqlain MA, Siddiq M. Synthesis and characterization of nano heat transfer fluid (NHTF). *Current Nanoscience* 2012;8(2):232-38.

64. Moens L, Blake DM, Rudnicki DL, Hale MJ. Advanced thermal storage fluids for solar parabolic trough systems. *Journal of Solar Energy Engineering, Transactions of the ASME* 2003;125(1):112-16.
65. Moens L, Blake DM. Advanced heat transfer and thermal storage fluids. Paper presented at: *Solar Engineering 2005*, August 2, 2005 - August 6, 2005, 2005; Orlando, FL, United states.
66. Reddy RG, Zhang Z, Arenas MF, Blake DM. Thermal Stability and Corrosivity Evaluations of Ionic Liquids as Thermal Energy Storage Media. *High Temperature Materials and Processes* 2003;22(2):87-94.
67. Valkenburg MEV, Vaughn RL, Williams M, Wilkes JS. Thermochemistry of ionic liquid heat-transfer fluids. Paper presented at, 2005.
68. Gabbrielli R, Zamparelli C. Optimal design of a molten salt thermal storage tank for parabolic trough solar power plants. *Journal of Solar Energy Engineering, Transactions of the ASME* 2009;131(4):0410011-04100110.
69. Yang Z, Garimella SV. Thermal analysis of solar thermal energy storage in a molten-salt thermocline. *Solar Energy* 2010;84(6):974-85.
70. Flueckiger SM, Zhen Y, Garimella SV. Thermomechanical simulation of the Solar One thermocline storage tank. *Journal of Solar Energy Engineering* 2012;134(4):041014 (6 pp.).
71. Li P, Van Lew J, Karaki W, Chan C, Stephens J, Qiuwang W. Generalized charts of energy storage effectiveness for thermocline heat storage tank design and calibration. *Solar Energy* 2011;85(9):2130-43.
72. Brosseau D, Hlava, P., Kelly, M. Testing Thermocline Filler Materials and Molten-Salt Heat Transfer Fluids for Thermal Energy

Storage Systems used in Parabolic Trough Solar Power Plants; 2004.

73. Flueckiger SM, Yang Z, Garimella SV. Review of molten-salt thermocline tank modeling for solar thermal energy storage. *Heat Transfer Engineering* 2013;34(10):787-800.
74. Kolb GJ, Hassani Vahab. TRYNSYS Modelling of a 1 MWe Saguaro Plant: SNL & NREL 2006.
75. Dunn R. Report on the 2012 SolarPACES Conference, . Marrakech, Morocco; 2012.
76. Querol P, et al. Single Tank Thermal Storage Prototype. Paper presented at: 18th SolarPACES Conference, Marrakech, Morocco; September 2012, 2012.
77. Laing D. Thermal Energy Storage for Concentrated Solar Power: State of Art and Developments: DLR- German Aerospace Center; 2011.
78. Li P, Van Lew J, Chan C, Karaki W, Stephens J, O'Brien JE. Similarity and generalized analysis of efficiencies of thermal energy storage systems. *Renewable Energy* 2011;39(1):388-402.
79. Flueckiger SM, Garimella SV. Second-law analysis of molten-salt thermal energy storage in thermoclines. *Solar Energy* 2012;86(5):1621-31.
80. Karaki W, Van Lew JT, Li P, Chan CL, Stephens J. Heat transfer in thermocline storage system with filler materials: Analytical model. Paper presented at: ASME 2010 4th International Conference on Energy Sustainability, ES 2010, May 17, 2010 - May 22, 2010, 2010; Phoenix, AZ, United states.
81. Kolb GJ, Hassani V. Performance analysis of thermocline energy storage proposed for the 1 MW Saguaro solar trough plant. Paper presented at: Solar 2006: Renewable Energy - Key to Climate Recovery, Including 35th ASES Annual Conference, 31st ASES National Passive Solar Conference, 1st ASES Policy and

Marketing Conference and ASME Solar Energy Division
International Solar Energy Conference, July 9, 2006 - July 13,
2006, 2006; Denver, CO, United states.

82. Kelly B. Arizona Public Service SOLar Power Plant Saguaro Power Plant Thermal Storage Design Options: NEXTANT (Under contract to NREL); 2004.
83. Kelly B. Technical Specification for the Thermocline Thermal Storage Tank, Arizona Public Service Saguaro Project, Rev.0: NEXTANT (under contract to NREL); 2004.
84. Company MDA. 10 MWe Solar Thermal Central Receiver Pilot Plant Mode 5 (Test 1150) and Mode 6 (Test 1160) Test Report; 1986.
85. Faas SE, et. al. 10 MWe Solar Thermal Central Receiver Pilot Plant: Thermal Storage Subsystem Evaluation - Final Report: Sandia National Laboratories; 1986.
86. Van Lew JT, Li P, Chan CL, Karaki W, Stephens J. Transient heat delivery and storage process in a thermocline heat storage system. Paper presented at: 2009 ASME International Mechanical Engineering Congress and Exposition, IMECE2009, November 13, 2009 - November 19, 2009, 2010; Lake Buena Vista, FL, United states.
87. Van Lew JT, Peiwen L, Cho Lik C, Karaki W, Stephens J. Analysis of Heat Storage and Delivery of a Thermocline Tank Having Solid Filler Material. Journal of Solar Energy Engineering 2011;133(2):021003 (10 pp.).
88. Valmiki MM, Karaki W, Li P, Lew JV, Chan C, Stephens J. Experimental investigation of thermal storage processes in a thermocline tank. Journal of Solar Energy Engineering, Transactions of the ASME 2012;134(4).

89. Flueckiger S, Yang Z, Garimella SV. An integrated thermal and mechanical investigation of molten-salt thermocline energy storage. *Applied Energy* 2011;88(6):2098-105.
90. Igari T, Wada, H., Ueta M. Mechanism-based evaluation of thermal ratcheting due to travelling temperature distribution. *ASME Journal of Pressure Vessel Technology* 2000;122:130-38.
91. Rusell-Stevens M. TR, Papakyriacou M. Thermal expansion behaviour of ultra-high modulus carbon fibre reinforced magnesium composite during thermal cycling. *Journal of Material Science* 2006;41(19):6228-36.
92. Qin FGF, Yang X, Ding Z, Zuo Y, Shao Y, Jiang R, et al. Thermocline stability criterions in single-tanks of molten salt thermal energy storage. *Applied Energy* 2012;97:816-21.
93. Laing D, Steinmann W-D, Tamme R, Richter C. Solid media thermal storage for parabolic trough power plants. *Solar Energy* 2006;80(10):1283-89.
94. Tamme R. Concrete Storage: Update on the German concrete TES program: DLR - German Aerospace Center, Institute of Technical Thermodynamics; 2003.
95. Geyer M. CONTEST: Concrete Thermal Energy Storage for Parabolic Trough Plants: DLR Germany, Plataforma Solar de Almeria, Spain; 1999.
96. Tamme R. Phase Change Storage Systems: DLR - German Aerospace Institute; 2003.
97. Laing D, Steinmann W-D, Fi M, Tamme R, Brand T, Bahl C. Solid media thermal storage development and analysis of modular storage operation concepts for parabolic trough power plants. Paper presented at, 2008; 3 Park Avenue, New York, NY 10016-5990, United States.
98. Laing D, Lehmann D, Fi M, Bahl C. Test results of concrete thermal energy storage for parabolic trough power plants. *Journal of Solar*

Energy Engineering, Transactions of the ASME

2009;131(4):0410071-76.

99. Mathur A. Latent Heat Storage for Concentrating Solar Power: Terrafore; 2009.
100. Mathur A. Heat Transfer and Latent Heat Storage in Inorganic Molten Salts for Concentrating SOLar Plants: Terrafore; 2011.
101. Nomura T, Okinaka N, Akiyama T. Technology of Latent Heat Storage for High Temperature Application: A Review. ISIJ International 2010;50(9):1229-39.
102. Sokolov. K. Performance indicators for solar pipes with phase change storage. Solar Energy 1991:339-46.
103. Sharma A, Tyagi VV, Chen CR, Buddhi D. Review on thermal energy storage with phase change materials and applications. Renewable and Sustainable Energy Reviews 2009;13(2):318-45.
104. Lane GA. Solar Heat Storage: Latent Heat Material. Volume II: CRC Press, ; 1986.
105. Felix Regin A, Solanki SC, Saini JS. An analysis of a packed bed latent heat thermal energy storage system using PCM capsules: Numerical investigation. Renewable Energy 2009;34(7):1765-73.
106. Steinmann W-D, Laing D, Tamme R. Latent heat storage systems for solar thermal power plants and process heat applications. Journal of Solar Energy Engineering, Transactions of the ASME 2010;132(2):0210031-35.
107. Microtek Laboratories I. Encapsulated Phase Change Materials; 2012.
108. Bauer T, Tamme, R., Christ, M., Ottinger, O. PCM-Graphite Composites for High Temperature Thermal Energy Storage. Tenth International Conference on Thermal Energy Storage. Atlantic City; 2006.

109. DLR P. The DISTOR Project: German Aerospace Center (DLR); 2013.
110. Pincemin S, Py X, Olives R, Christ M, Oettinger O. Elaboration of conductive thermal storage composites made of phase change materials and graphite for solar plant. *Journal of Solar Energy Engineering* 2008;130(1):1-5.
111. Morisson V, Rady M, Palomo E, Arquis E. Thermal energy storage systems for electricity production using solar energy direct steam generation technology. *Chemical Engineering and Processing: Process Intensification* 2008;47(3):499-507.
112. Kenisarin MM. High-temperature phase change materials for thermal energy storage. *Renewable and Sustainable Energy Reviews* 2010;14(3):955-70.
113. Dinter F, Geyer, M., Tamme, R., . Thermal Energy Storage for Commercial Application (TESCA), a feasibility study on economic storage systems. : Springer-Verlag, Berlin; 1991.
114. Hanslett RA, Kosson, R.L., Ferrara, A.A., Roukis, J.G., . Thermal Energy Storage in Heat Exchanger Design. Paper presented at: ASME Aeorspace Division: Conference on Environmental Systems, ; July 10-13, 1978; San Diego, USA
115. Steiner D, Nonnenmacher, A., 1982. Studie u"ber thermische Energiespeicher fu" r den Temperaturbereich 200°C bis 500°C. *BMFT-FB-T* 1982(82):105.
116. Carden P. A large scale solar pplant based on the dissociation and synthesis of ammonia: Dept. Eng. Phys., RSPHYS, Australian National University; 1974.
117. Carden P. Energy corradiation using the reversible ammonia reaction. *Soalr Energy* 1977;19:365-78.
118. Wright J, Lenz, T. Solar energy collection using the reversible ammonia dissociation. Paper presented at: 15th Intersoc. Energy Conv. Eng. Conf., , 1980; Fort Collins, CO.

119. Dunn R, Lovegrove K, Burgess G. A Review of Ammonia-based Thermochemical Energy Storage for Concentrating Solar Power. Proceedings of the IEEE 2012;100(2):391-400.
120. Lovegrove KM. High pressure ammonia dissociation experiments for solar energy transport and storage. International Journal of Energy Research 1996;20(11):[d]965-78.
121. Lovegrove K. The potential role for ammonia based thermochemical energy transport and storage in large scale solar thermal systems. Paper presented at: Energy and the Environment. Into the 1990s. Proceedings of the 1st World Renewable Energy Congress, 23-28 Sept. 1990, 1990; Oxford, UK.
122. Lovegrove K. Thermodynamic limits on the performance of a solar thermochemical energy storage system. International Journal of Energy Research 1993;17(9):817-29.
123. Lovegrove K. Thermodynamic limits on the performance of a solar thermochemical energy storage system. International Journal of Energy Research 1993;17(9):817-29.
124. Lovegrove K. Exergetic optimization of a solar thermochemical energy storage system subject to real constraints. International Journal of Energy Research 1993;17(9):831-45.
125. Lovegrove K, Kreetz H, Luzzi A. The first ammonia based solar thermochemical energy storage demonstration. Paper presented at: 9th SolarPACES International Symposium on Solar Thermal Concentrating Technologies. STCT 9, 22-26 June 1998, 1999; France.
126. Lovegrove K, Luzzi A. Endothermic reactors for an ammonia based thermochemical solar energy storage and transport system. Solar Energy 1996;56(4):361-71.
127. Lovegrove K, Luzzi A, Kreetz H. A solar-driven ammonia-based thermochemical energy storage system. Solar Energy 1999;67(4-6):309-16.

128. Lovegrove K, Luzzi A, McCann M, Freitag O. Exergy analysis of ammonia-based solar thermochemical power systems. *Solar Energy* 1999;66(2):103-15.
129. Lovegrove KM. Experimental simulation of solar energy storage via ammonia dissociation: preliminary results. Paper presented at: Living in the Greenhouse. Proceedings of the Australian and New Zealand Solar Energy Society Conference, 28 Nov.-1 Dec. 1990, 1990; Auckland, New Zealand.
130. Lovegrove K, Burgess G, Pye J. A new 500m² paraboloidal dish solar concentrator. *Solar Energy* 2011;85(4):620-26.
131. Schaub F, Worner A, Tamme R. High Temperature Thermochemical Heat Storage for Concentrated Solar Power Using Gas-Solid Reactions. *Journal of Solar Energy Engineering* 2011;133(3):031006 (7 pp.).
132. Meier A, Sattler, C. Solar Fuels from Concentrated Sunlight- Solar PACES: International Energy Agency (IEA); 2009.
133. Kodama T, Gokon N. Thermochemical Cycles for High-Temperature Solar Hydrogen Production. *Chemical Reviews* 2007;107(10):4048-77.
134. Thomey D, De Oliveira L, Sack J-P, Roeb M, Sattler C. Development and test of a solar reactor for decomposition of sulphuric acid in thermochemical hydrogen production. Paper presented at, 2012; Langford Lane, Kidlington, Oxford, OX5 1GB, United Kingdom.
135. Tarquini P, Giaconia A, Grena R, Lanchi M, Liberatore R. Hydrogen/methanol production by sulfur-iodine thermochemical cycle powered by combined solar/fossil energy. *International Journal of Hydrogen Energy* 2007;32(4):469-81.
136. Alvani C, Bellusci M, La Barbera A, Padella F, Pentimalli M, Seralessandri L, et al. Reactive pellets for improved solar hydrogen production based on sodium manganese ferrite thermochemical

- cycle. *Journal of Solar Energy Engineering, Transactions of the ASME* 2009;131(3):0310151-55.
137. Roeb M, Sattler C, Kluser R, Monnerie N, de Oliveira L, Konstandopoulos AG, et al. Solar hydrogen production by a two-step cycle based on mixed iron oxides. *Transactions of the ASME. Journal of Solar Energy Engineering* 2006;128(2):125-33.
 138. Charvin P, Abanades S, Beche E, Lemont F, Flamant G. Hydrogen production from mixed cerium oxides via three-step water-splitting cycles. *Solid State Ionics, Diffusion & Reactions* 2009;180(14-16):1003-10.
 139. Neises M, Roeb M, Schmucker M, Sattler C, Pitz-Paal R. Kinetic investigations of the hydrogen production step of a thermochemical cycle using mixed iron oxides coated on ceramic substrates. *International Journal of Energy Research* 2010;34(8):651-61.
 140. Diver RB, Miller JE, Allendorf MD, Siegel NP, Hogan RE. Solar thermochemical water-splitting ferrite-cycle heat engines. Paper presented at, 2008; 3 Park Avenue, New York, NY 10016-5990, United States.
 141. Karagiannakis G, Agrafiotis CC, Pagkoura C, Konstandopoulos AG, Thomey D, De Oliveira L, et al. Hydrogen production via sulfur-based thermochemical cycles: Part 3: Durability and post-characterization of silicon carbide honeycomb substrates coated with metal oxide-based candidate catalysts for the sulfuric acid decomposition step. *International Journal of Hydrogen Energy* 2012;37(10):8190-203.
 142. Villafan-Vidales HI, Abanades S, Caliot C, Romero-Paredes H. Heat transfer simulation in a thermochemical solar reactor based on a volumetric porous receiver. *Applied Thermal Engineering* 2011;31(16):3377-86.
 143. Abanades S, Legal A, Cordier A, Peraudeau G, Flamant G, Julbe A. Investigation of reactive cerium-based oxides for H₂ production

- by thermochemical two-step water-splitting. *Journal of Materials Science* 2010;45(15):4163-73.
144. Coker EN, Ambrosini A, Rodriguez MA, Miller JE. Ferrite-YSZ composites for solar thermochemical production of synthetic fuels: In operando characterization of CO₂ reduction. *Journal of Materials Chemistry* 2011;21(29):10767-76.
 145. Neises M, Tescari S, de Oliveira L, Roeb M, Sattler C, Wong B. Solar-heated rotary kiln for thermochemical energy storage. *Solar Energy* 2012;86(10):3040-8.
 146. Krishnan S, Palo DR, Wegeng RS. Cycle evaluations of reversible chemical reactions for solar thermochemical energy storage in support of concentrating solar power generation systems. Paper presented at: 8th Annual International Energy Conversion Engineering Conference, July 25, 2010 - July 28, 2010, 2010; Nashville, TN, United states.
 147. Steinfeld A, Brack M, Meier A, Weidenkaff A, Wuillemain D. A solar chemical reactor for co-production of zinc and synthesis gas. *Energy* 1998;23(10):803-14.
 148. Levy M. Studies in closed and open loop solar chemical heat pipes. Paper presented at: 6th International Symposium on Solar Thermal Concentrating Technology; 28 September - 2 October 1992, 1993; Mojacar, Spain.
 149. Rodat S, Abanades S, Flamant G. Co-production of hydrogen and carbon black from solar thermal methane splitting in a tubular reactor prototype. *Solar Energy* 2011;85(4):645-52.
 150. Anikeev VI, Bobrin AS, Ortner J, Schmidt S, Funken KH, Kuzin NA. Catalytic thermochemical reactor/receiver for solar reforming of natural gas: design and performance. *Solar Energy* 1998;63(2):97-104.

151. Kodama T, Kiyama A, Shimizu KI. Catalytically activated metal foam absorber for light-to-chemical energy conversion via solar reforming of methane. *Energy and Fuels* 2003;17(1):13-17.
152. Diver RB. Solar test of an integrated sodium reflux heat-pipe receiver/reactor for thermo- chemical energy transport. Paper presented at: 4th International Symposium on Solar Thermal Technology, 1990.
153. Steinfeld A. *Solar Energy* 1978;78:603.
154. Tescari S, Neveu P, Mazet N. Thermochemical solar reactor: Simplified method for the geometrical optimization at a given incident flux. *International Journal of Chemical Reactor Engineering* 2010;8.
155. Kaushika ND, Mishra A, Chakravarty M. Thermal analysis of solar biomass hybrid co-generation plants. *International Journal of Sustainable Energy* 2005;24(4):175-86.
156. Birnbaum J, Eck M, Fichtner M, Hirsch T, Lehmann D, Zimmermann G. A direct steam generation solar power plant with integrated thermal storage. *Journal of Solar Energy Engineering, Transactions of the ASME* 2010;132(3):0310141-45.
157. Feldhoff JF, Schmitz K, Eck M, Schnatbaum-Laumann L, Laing D, Ortiz-Vives F, et al. Comparative system analysis of direct steam generation and synthetic oil parabolic trough power plants with integrated thermal storage. *Solar Energy* 2012;86(1):520-30.
158. Guo CX, Zhang WJ. Numerical simulation and parametric study on new type of high temperature latent heat thermal energy storage system. *Energy Conversion and Management* 2008;49(5):919-27.
159. Laing D, Bauer T, Ehmann D, Bahl C. Development of a thermal energy storage system for parabolic trough power plants with direct steam generation. *Journal of Solar Energy Engineering, Transactions of the ASME* 2010;132(2):0210111-18.

160. Laing D, Bahl C, Bauer T, Lehmann D, Steinmann W-D. Thermal energy storage for direct steam generation. *Solar Energy* 2011;85(4):627-33.
161. Zhuang J, Fengwu B, Ershu X. Performance analysis of two-stage thermal energy storage system of solar power tower plant. Paper presented at: 2011 Asia-Pacific Power and Energy Engineering Conference (APPEEC 2011), 25-28 March 2011, 2011; Piscataway, NJ, USA.
162. Adinberg R, Zvegilsky D, Epstein M. Heat transfer efficient thermal energy storage for steam generation. *Energy Conversion and Management* 2010;51(1):9-15.
163. Naish Cea. Outlook of Energy Storage Technologies. European Parliament, Committee on Industry Research and Energy (ITRE); 2008.
164. Park ISE. Capturing the power of nature; 2013.
165. Green B. Types of Hydro Power Systems; 2013.
166. Min JK, Lee C-H. Numerical study on the thermal management system of a molten sodium-sulfur battery module. *Journal of Power Sources* 2012;210(0):101-09.
167. Ding M, Xu N, Bi R, Chen Z, Luo Y, Song Z. Modeling and comparative study on multiple battery energy storage systems. *Dianli Xitong Zidonghua/Automation of Electric Power Systems* 2011;35(15):34-39.
168. Gully BH, Webber ME, Seepersad CC, Thompson RC. Energy storage analysis to increase large ship fuel efficiency. Paper presented at, 2009; San Francisco, CA.
169. Kintner-Meyer M, Jin C, Balducci P, Elizondo M, Guo X, Nguyen T, et al. Energy storage for variable renewable energy resource integration - A regional assessment for the Northwest Power Pool (NWPP). Paper presented at: 2011 IEEE/PES Power Systems

Conference and Exposition, PSCE 2011, March 20, 2011 - March 23, 2011, 2011; Phoenix, AZ, United states.

170. Laing D, Steinmann WD, Viebahn P, Grater F, Bahl C. Economic analysis and life cycle assessment of concrete thermal energy storage for parabolic trough power plants. *Journal of Solar Energy Engineering* 2010;132(4):041013 (6 pp.).
171. Madaeni SH, Sioshansi R, Denholm P. Estimating the Capacity Value of Concentrating Solar Power Plants With Thermal Energy Storage: A Case Study of the Southwestern United States. *Power Systems, IEEE Transactions on* 2012;PP(99):1-1.
172. Nandi BR, Bandyopadhyay S, Banerjee R. Analysis of high temperature thermal energy storage for solar power plant. Paper presented at: 3rd IEEE International Conference on Sustainable Energy Technologies, ICSET 2012, September 24, 2012 - September 27, 2012, 2012; Kathmandu, Nepal.
173. Oro E, Gil A, de Gracia A, Boer D, Cabeza LF. Comparative life cycle assessment of thermal energy storage systems for solar power plants. *Renewable Energy* 2012;44:166-73.
174. Roberts B. Capturing grid power. *IEEE Power and Energy Magazine* 2009;7(4):32-41.
175. Shakib AD, Balzer G. Energy storage design and optimization for power system with wind feeding. Paper presented at: 2010 IEEE 11th International Conference on Probabilistic Methods Applied to Power Systems, PMAPS 2010, June 14, 2010 - June 17, 2010, 2010; Singapore, Singapore.
176. Sioshansi R, Denholm P. The Value of Concentrating Solar Power and Thermal Energy Storage. *Sustainable Energy, IEEE Transactions on* 2010;1(3):173-83.
177. Sundararagavan S, Baker E. Evaluating energy storage technologies for wind power integration. *Solar Energy* 2012;86(9):2707-17.

178. Wagner SJ, Rubin ES. Economic implications of thermal energy storage for concentrated solar thermal power. 2012.
179. Wen Z, Hu Y, Wu X, Han J, Gu Z. Main challenges for high performance NAS battery: Materials and interfaces. *Advanced Functional Materials* 2013;23(8):1005-18.
180. Zalba B, Marín JM, Cabeza LF, Mehling H. Review on thermal energy storage with phase change: materials, heat transfer analysis and applications. *Applied Thermal Engineering* 2003;23(3):251-83.
181. Zhou Z, Benbouzid M, Charpentier JF, Sculler F, Tang T. Energy storage technologies for smoothing power fluctuations in marine current turbines. Paper presented at, 2012; Hangzhou.
182. Zhou Z, Benbouzid M, Frédéric Charpentier J, Sculler F, Tang T. A review of energy storage technologies for marine current energy systems. *Renewable and Sustainable Energy Reviews* 2013;18:390-400.
183. Millennium S. The parabolic trough power plants Andasol 1 to 3: Solar Millennium; 2008.
184. García-Valladares O, Velázquez N. Numerical simulation of parabolic trough solar collector: Improvement using counter flow concentric circular heat exchangers. *International Journal of Heat and Mass Transfer* 2009;52(3–4):597-609.
185. Rolim MM, Fraidenraich N, Tiba C. Analytic modeling of a solar power plant with parabolic linear collectors. *Solar Energy* 2009;83(1):126-33.
186. Plaza S. Top 10 World's Most Efficient Solar PV Modules (Monocrystalline); 2011.
187. Millennium S. Andasol -1 thermo solar energy; 2008.
188. Kearney D, Kelly B, Herrmann U, Cable R, Pacheco J, Mahoney R, et al. Engineering aspects of a molten salt heat transfer fluid in a trough solar field. *Energy* 2004;29(5–6):861-70.

189. Price H, Lupfert E, Kearney D, Zarza E, Cohen G, Gee R, et al. Advances in parabolic trough solar power technology. Transactions of the ASME. Journal of Solar Energy Engineering 2002;124(2):109-25.
190. Hussien ZF, Cheung LW, Siam MFM, Ismail AB. Modelling of Sodium Sulfur Battery for Power System Applications. Elekrika 2007; 9 (2):66-72.
191. Kalogirou SA. Solar Energy Engineering: Processes and Systems. 1 ed: Academic Press, Elsevier; 2009.
192. Incopera FP, Dewitt, D.P. Fundamentals of Heat and Mass Transfer. 4 ed: John Wiley & Sons; 1996.
193. Petukhov BS, Kirillov, V.V. On Heat Exchange at Turbulent Flow of Liquids in Pipes. Teploenergetika 1958;4:63-68.
194. Petukhov BS, Roizen, L.I. An Experimental Investigation of Heat Transfer in a Turbulent Flow of Gas in Tubes of Annular Section. High Temperature 1963;1:373-80.
195. Petukhov BS, Roizen, L.I. Generalized Relationships for Heat Transfer in Turbulent Flow of Gas in Tubes of Annular Section. High Temperature 1964;2:65-68.
196. Gnielinski V. Heat Transfer Coefficients for Turbulent Flow in Concentric Annular Ducts. Heat Transfer Engineering 2009;30(6):431- 36.
197. Springer Handbook of Mechanical Engineering: Springer; 2009.
198. Rohsenow WM, Hartnett, J.P., Cho Y.I. Handbook of Heat Transfer. 3 ed: McGraw-Hill; 1998.
199. McQuillan FJ, Culham, J.R., Yovanovich, M.M. . Properties of Dry Air at One Atmosphere; 1984.
200. Tsilingiris PT. Thermophysical and transport properties of humid air at temperature range between 0 and 100°C. Energy Conversion and Management 2008;49(5):1098-110.

201. Tokoi H, Watahiki N, Izumi S, Satoh K. Evaluation of sodium sulfur cell characteristics using an in situ X-ray computed tomogram system. *Journal of the Electrochemical Society* 1999;146(11):4005-08.
202. Jefferson CP. Prediction of breakthrough curves in packed beds: 1. Applicability of single parameter models. *American Institute of Chemical Engineers* 1972;18(2):409-16.
203. Gibbard HF. Thermal properties of battery systems. *Journal of the Electrochemical Society* 1978(125):353-58.
204. Cockcroft CS. Investigation of a Thermally Regenerative Reactor System [Doctor of Philosophy]. Leeds: University of Leeds; 1976.
205. Jones SA, Pitz-Paal, P.S., Blair, N., Cable, R. TRNSYS Modelling of the SEGS VI Parabolic Trough Solar Electric Generating System. Paper presented at: Solar Energy: The Power to Choose, Proceedings of Solar Forum 2001, 2001; Washington DC.
206. Vincent J. *The Future of Energy is Now*: Greenpeace; 2009.
207. Dudley VE. Test Results: SEGS LS-2 Solar Collector: National Renewable Energy Laboratory (NREL); 1994.
208. Klein SA. *Engineering Equation Solver*; 2002.
209. Burkholder F, Kutscher, C.,. Heat Loss Testing of Solel's UVAC3 Parabolic Trough Receiver: National Renewable Energy Laboratory (NREL); 2008.
210. Wen Z, et. al. Research on sodium sulphur battery for energy storage. *Solid State Ionics* 2008;179:1697-701.
211. Kamihayashi M. Advanced sodium sulfur (NaS) Battery system: TEPCO; 2001.
212. Technology ST-HTP. Alumina Tubes: ST-3625; 2013.
213. Solutions G. *Glass Tubing and Rod Cutting*; 2013.
214. Metals O. SCHEDULE 40 STAINLESS STEEL PIPE T-304/304L; 2013.

215. Padilla RV, Demirkaya G, Goswami DY, Stefanakos E, Rahman MM. Heat transfer analysis of parabolic trough solar receiver. *Applied Energy* 2011;88(12):5097-110.
216. Research W. Technical data for sulphur. Mathematica's ElementData; 2013.
217. Sudworth JL, Tiley AR, editors. *The Sodium Sulphur Battery*. New York: Chapman and Hall; 1985.
218. Khaled A. *Technical and Economic Performance of Parabolic Trough in Jordan* [Masters]: Universitat Kassel; 2012.
219. Wagner MJ, Gilman, P. *Technical Manual for the Physical Trough model*. System Advisor Model Documentation: NREL; 2011.
220. Kelly B, Kearney, D. *Parabolic Trough Solar System Piping Model*: NREL; 2006.
221. Corp. MI. *Density of Steel Pipes*; 2013.
222. Knodler R. Thermal properties of sodium-sulphur cells. *Journal of Applied Electrochemistry* 1984;14:36-46.
223. Sudworth J. Sodium metal chloride batteries with beta alumina electrolyte. *Chemistry and Industry (London)* 1988(3):77-79.
224. Kearney D, Kelly, B., Cabe. R., Potrovitza, N. Overview on use of a Molten Salt HTF in a Trough Solar Field. NREL Parabolic Trough Thermal Energy Storage Workshop Golden CO.; 2003.
225. NREL. *System Advisor Model (SAM) Case Study: Andasol - 1*; 2012.
226. Crowe R. Energy storage grows to integrate Wind, Solar.: *Renewable Energy World..Com*; 2011.

Appendices Section

Loop 1 Analysis

Moving “anti-clockwise” from the pump discharge point “p”.

Using Bernoulli’s principle:

The total head at “p” and “m” respectively are given as:

$$H_p = \frac{P_p}{\rho g} + \frac{u_p^2}{2g} + z_p \quad \text{(Equation 0-1)}$$

$$H_m = \frac{P_m}{\rho g} + \frac{u_m^2}{2g} + z_m \quad \text{(Equation 0-2)}$$

But

$$H_p = H_m + h_{f,p-m} + h_{l,p-m} \quad \text{(Equation 0-3)}$$

where $h_{f,p-m}$ and $h_{l,p-m}$ are the frictional and local pipe work losses respectively along the path from “p” to “m”.

Therefore:

$$H_p = \frac{P_p}{\rho g} + \frac{u_p^2}{2g} + z_p = \frac{P_m}{\rho g} + \frac{u_m^2}{2g} + z_m + h_{f,p-m} + h_{l,p-m} \quad \text{(Equation 0-4)}$$

Rearranging gives:

$$\frac{P_p - P_m}{\rho g} = \frac{u_m^2 - u_p^2}{2g} + z_m - z_p + h_{f,p-m} + h_{l,p-m} \quad \text{(Equation 0-5)}$$

$$P_p - P_m = \left(\frac{u_m^2 - u_p^2}{2g} + z_m - z_p + h_{f,p-m} + h_{l,p-m} \right) \rho g \quad \text{(Equation 0-6)}$$

$$\Delta P_{p-m} = \left(\frac{u_m^2 - u_p^2}{2g} + z_m - z_p + h_{f,p-m} + h_{l,p-m} \right) \rho g \quad \text{(Equation 0-7)}$$

$$\Delta P_{p-m} = (z_m - z_p + h_{f,p-m} + h_{l,p-m}) \rho g \quad \text{(Equation 0-8)}$$

$$\Delta P_{p-m} = (\Delta z_{m-p} + h_{f,p-m} + h_{l,p-m}) \rho_{htf} g \quad \text{(Equation 0-9)}$$

Since pipe diameter is constant between “p” and “m”, $u_m^2 = u_p^2$, so reduces to:

Since each length of pipe work considered will be of constant diameter, this relationship will be used to derive the pressure drops around Loop 1 and 2 in the hydraulic network.

Similarly the other pressure drops in Loop 1 are defined as:

$$\Delta P_{m-k} = (\Delta z_{m-k} + h_{f,m-k} + h_{l,m-k})\rho_{htf}g$$

$$\Delta P_{k-j} = (\Delta z_{k-j} + h_{f,k-j} + h_{l,k-j})\rho_{htf}g$$

$$\Delta P_{j-v1} = (\Delta z_{j-v1} + h_{f,j-v1} + h_{l,j-v1})\rho_{htf}g$$

$$\Delta P_{u-q} = (\Delta z_{q-u} + h_{f,u-q} + h_{l,u-q})\rho_{htf}g$$

The Pump pressure ΔP is equal to the sum of the pressure drops around Loop 1. Moving “anti-clock wisely” around loop 1:

$$\Delta P = \Delta P_{m-k} + \Delta P_{k-j} + \Delta P_{j-v1} + \Delta P_{u-q}$$

.....(1)

Loop 2

From Loop 2:

$$\Delta P_{j-v2} = \Delta P_{j-v1}$$

.....(2)

Also $Q_{TOT} = Q_1 + Q_2$ where $Q_{TOT} = Q_{Pump}$, $Q_1 = Q_{Bypass}$ and $Q_2 = Q_{Process}$

From calculations and explanations given earlier in this report, to ensure fully developed turbulent flow within the PECT receiver, $Q_{Process} \geq 10^{-4} m^3/s$. The chosen flow regime is:

$$10^{-4} m^3/s \leq Q_{Process} \leq 10^{-3} m^3/s$$

However, before the pressure drops can be calculated, h_f and h_l for each pressure drop must be determined. In terms of flow Q and pipe diameter D, these head losses (metres) are defined as:

$$h_f = \frac{fLQ^2}{3.03D^5} \text{ and } h_l = \frac{k_l Q^2}{12.1D^4}$$



Figure 0-2: EES Rig Geometry approximations for pressure drop calculations

The worst case scenario is used to work out the equivalent pipe lengths and pressure drops within the PECT receiver.

The PECT receiver assembly is modelled to begin at (1) and the end at (4)

- Geometry 1-2 is modelled as a *0.116m length of 2" pipe*
- The reduction at 2 is modelled as a sudden reduction ($d/D = \frac{1}{4}$) for a 2" pipe
which is: *l = 0.75 m of 2" pipe*
- Geometry 2-3 is modelled as a 1m pipe length with pipe diameter $D_p = D_h = (0.056 - 0.040) = 0.016 \text{ m} \approx \text{nominal } \frac{1}{2}'' \text{ pipe}$
Therefore geometry 2 -3 is modelled as 1 m of 1/2" pipe
- The enlargement at 3 is modelled as a sudden enlargement ($d/D = \frac{1}{4}$) for a 1/2" pipe, which is: *l = 0.3 m of 1/2" pipe*
- Geometry 3-4 is modelled as a *0.116 m length of 2" pipe*

Steps in calculation of pressure drops and flows

- The pressure drop across the Loop 2 branch was computed using the relationship $\Delta P_{x-y} = (\Delta z_{y-x} + h_{f,x-y} + h_{l,x-y})\rho_{htf}g$ and desired value of $Q_{process}$.
- The bypass branch's pressure drop was set equal to the "Process Branch's" pressure drop since it is in parallel. Q_{bypass} was then calculated by developing the relationship outlined below:

$\Delta P_{bypass} = \Delta P_{process} = (\Delta z_{TOT} + h_{f,TOT} + h_{l,TOT})\rho_{htf}g$, where "TOT" implies the total of all corresponding terms along the bypass branch

$$\Delta P_{bypass} = \left[\sum_{i=1}^n (\Delta Z_{bypass}) + \sum_{i=1}^n (h_{f,bypass}) + \sum_{i=1}^n (h_{l,bypass}) \right] \rho_{htf}g$$

$$\Delta P_{bypass} = \left[\sum_{i=1}^n (\Delta Z_{i,bypass}) + \sum_{i=1}^n \left(\frac{f L_i Q_{bypass}^2}{3.03 D_i^5} \right) + \sum_{i=1}^n \left(\frac{k_L Q_{bypass}^2}{12.11 D_i^4} \right) \right] \rho_{htf} g$$

$$\frac{\Delta P_{bypass}}{\rho_{htf} g} = \sum_{i=1}^n (\Delta Z_{i,bypass}) + \sum_{i=1}^n \left(\frac{f L_i Q_{bypass}^2}{3.03 D_i^5} \right) + \sum_{i=1}^n \left(\frac{k_L Q_{bypass}^2}{12.11 D_i^4} \right)$$

$$\frac{\Delta P_{bypass}}{\rho_{htf} g} - \sum_{i=1}^n (\Delta Z_{i,bypass}) = \sum_{i=1}^n \left(\frac{f L_i Q_{bypass}^2}{3.03 D_i^5} \right) + \sum_{i=1}^n \left(\frac{k_L Q_{bypass}^2}{12.11 D_i^4} \right)$$

$$\frac{\Delta P_{bypass}}{\rho_{htf} g} - \sum_{i=1}^n (\Delta Z_{i,bypass}) = Q_{bypass}^2 \left[\sum_{i=1}^n \left(\frac{f L_i}{3.03 D_i^5} \right) + \sum_{i=1}^n \left(\frac{k_L}{12.11 D_i^4} \right) \right]$$

$$\frac{\Delta P_{bypass}}{\rho_{htf} g} - \sum_{i=1}^n (\Delta Z_{i,bypass}) = Q_{bypass}^2 \times \sum_{i=1}^n \left[\frac{f \times L_i}{3.03 D_i^5} + \left(\frac{k_L}{12.11 D_i^4} \right) \right]$$

$$Q_{bypass}^2 = \frac{\frac{\Delta P_{bypass}}{\rho_{htf} g} - \sum_{i=1}^n (\Delta Z_{i,bypass})}{\sum_{i=1}^n \left[\frac{f \times L_i}{3.03 D_i^5} + \left(\frac{k_L}{12.11 D_i^4} \right) \right]} = \frac{\frac{\Delta P_{process}}{\rho_{htf} g} - \sum_{i=1}^n (\Delta Z_{i,bypass})}{\sum_{i=1}^n \left[\frac{f \times L_i}{3.03 D_i^5} + \left(\frac{k_L}{12.11 D_i^4} \right) \right]}$$

$$Q_{bypass} = \sqrt{\frac{\frac{\Delta P_{process}}{\rho_{htf} g} - \sum_{i=1}^n (\Delta Z_{i,bypass})}{\sum_{i=1}^n \left[\frac{f \times L_i}{3.03 D_i^5} + \left(\frac{k_L}{12.11 D_i^4} \right) \right]}}, (m^3/s)$$

- Next, Q_{Pump} was calculated as, $Q_{Pump} = Q_{Process} + Q_{Bypass}$
- The pressure drops in the line of Q_{Pump} were then calculated.
- Finally, the pump ΔP was calculated by summing the pressure drops around the PECT Receiver hydraulic network.

The equations were implemented in a simple MS Excel spread sheet and the calculated results indicated that for a maximum flow of 1 kg/s through the main pump loop, with EES receiver. With the heat exchanger bypass branch valves closed off (no flow) calculations showed that the total pressure drop around the HTF loop for 1" pipe-work would be approximately 2.00 bar. Calculations showed that changing the pipe size to ¾" resulted in a higher pressure drop of 2.36 bar, for the same flow. Therefore it was decided that 1" piping would be used in the rig design. A plot of the pressure drop around the hydraulic circuit (Figure 0-3 and Figure 0-4) with respect to the flow resistance network (Figure 0-1) given earlier was generated from the calculations performed in the MS Excel sheet.

However the vapour pressure of the HTF to be used (Therminol 66) is approximately 0.3 bar at 300°C the intended operating temperature. Therefore the pump suction pressure needed to exceed this value in order to avoid cavitation problems. Since the total pressure drop around the loop at operating temperature conditions was 2.0 bar, with a pump suction pressure of 0.5 bar chosen to provide a margin of safety, the required pump discharge pressure was therefore $2.0 + 0.5 = 2.5$ bar.

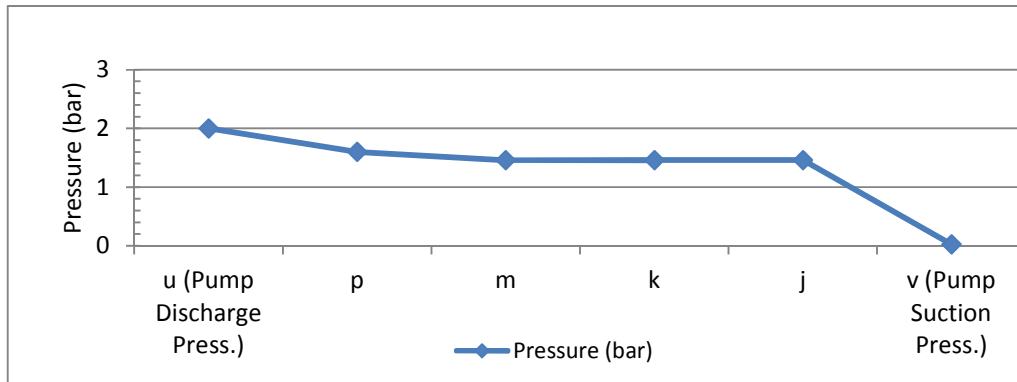


Figure 0-3: Pressure drop around main flow loop with pump

Table 0-1: Pressure Profile (Around Main Pump Loop --> Bypass)

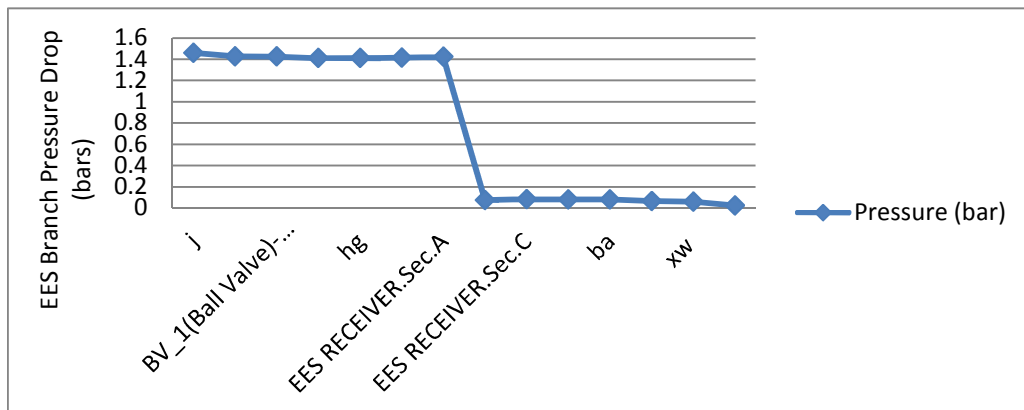


Figure 0-4: Pressure drop across EES receiver tube branch

Using the 1" piping, the required N₂ gas pressure at point "l" was 1.96 bars. This was calculated by subtracting the pressure drop of section "um" from the required pump discharge pressure of 2.5 bars.

Appendix B

Calculating the Volume of Fluid in Hydraulic Circuit

The volume of fluid in a pipe section = Avg. cross section area x length

Relevant Data

- Inner CSA of $\frac{3}{4}$ " Carbon Steel pipe = $\pi \times D_i^2/4 = \pi \times (0.02112)^2/4 = 3.503 \times 10^{-4} \text{ m}^2$
- Length of Arc of $\frac{3}{4}$ " pipe elbows = 0.072m
- Tee Dimensions ($L_1-0.055 \times L_2-0.015$)m
- Cross Dimensions ($L_1-0.055 \times L_2-0.014$)m
- Concentric Reducer ($D_1-0.053 \times D_2-0.020 \times L_3-0.041 \times L_4-0.0193 \times L_5-0.037$) m
- Flanges ($D_1-0.060 \times L_2-0.046$) m
- PECT Receiver ($D_i-0.052 \times L_1-0.064 \times D_{at}-0.064 \times D_{bt}-0.047 \times L_2-0.035 \times L_{ann}-0.96$)m
- Expansion Tank ($D_i-0.154 \times L-0.3$) m

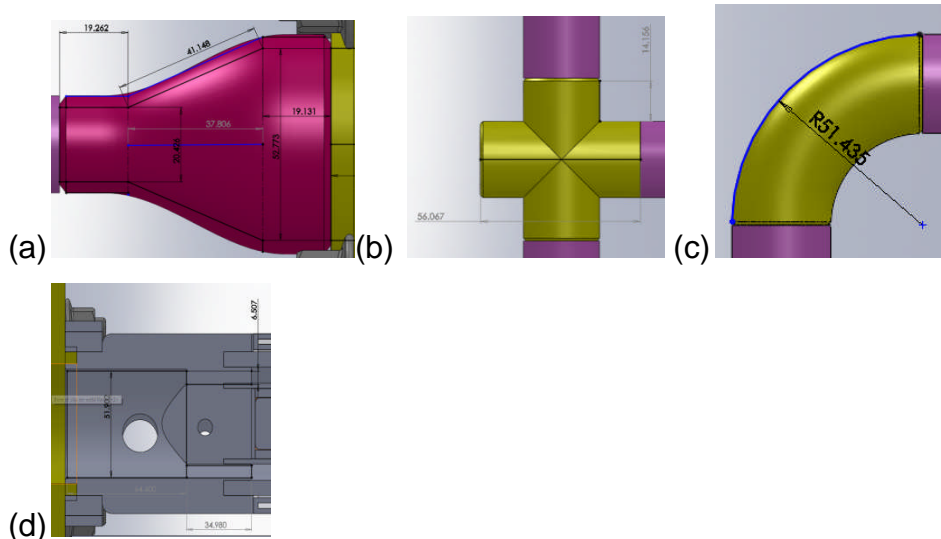


Figure 0-1: Important hydraulic loop sections: (a) Reducer (b) Junction (c) 90° Elbow (d) EES Receiver Inlet

Fluid in 1" Pipework

$$\text{Vol. } -ab = \text{Pipe-CSA} \times L = (3.503 \times 10^{-4} \text{ m}^2) \times (0.034 \text{ m}) = 1.19 \times 10^{-5} \text{ m}^3$$

$$\text{Vol. } -gh = \text{Pipe-CSA} \times L = (3.503 \times 10^{-4} \text{ m}^2) \times (0.113 \text{ m}) = 3.96 \times 10^{-5} \text{ m}^3$$

$$\text{Vol. } -ij = \text{Pipe-CSA} \times L = (3.503 \times 10^{-4} \text{ m}^2) \times (0.087 \text{ m}) = 3.05 \times 10^{-5} \text{ m}^3$$

$$\text{Vol. } -jk = \text{Pipe-CSA} \times L = (3.503 \times 10^{-4} \text{ m}^2) \times (0.091 \text{ m}) = 3.19 \times 10^{-5} \text{ m}^3$$

$$\text{Vol. } -mn = \text{Pipe-CSA} \times L = (3.503 \times 10^{-4} \text{ m}^2) \times (0.048 \text{ m}) = 1.68 \times 10^{-5} \text{ m}^3$$

$$\text{Vol. } -op = \text{Pipe-CSA} \times L = (3.503 \times 10^{-4} \text{ m}^2) \times (0.435 \text{ m}) = 15.2 \times 10^{-5} \text{ m}^3$$

$$\text{Vol. } -qt = \text{Pipe-CSA} \times L = (3.503 \times 10^{-4} \text{ m}^2) \times (1.07 \text{ m}) = 37.5 \times 10^{-5} \text{ m}^3$$

$$\text{Vol. } -qp \text{ (Pump)} = \text{Pipe-CSA} \times L = (3.503 \times 10^{-4} \text{ m}^2) \times (0.223 \text{ m}) = 7.81 \times 10^{-5} \text{ m}^3$$

$$\text{Vol. } -uv = \text{Pipe-CSA} \times L = (3.503 \times 10^{-4} \text{ m}^2) \times (0.106 \text{ m}) = 3.71 \times 10^{-5} \text{ m}^3$$

$$\text{Vol. } -wx = \text{Pipe-CSA} \times L = (3.503 \times 10^{-4} \text{ m}^2) \times (0.087 \text{ m}) = 3.05 \times 10^{-5} \text{ m}^3$$

$$\text{Vol. } -yz = \text{Pipe-CSA} \times L = (3.503 \times 10^{-4} \text{ m}^2) \times (1.58 \text{ m}) = 55.3 \times 10^{-5} \text{ m}^3$$

$$\text{Total Pipe work Volume for } \frac{3}{4} \text{'' pipe} = 135.64 \times 10^{-5} \text{ m}^3$$

The ratio of 1" to $\frac{3}{4}$ " pipe cross sectional areas is:

$$(5.75 \times 10^{-4} \text{ m}^2 / 3.503 \times 10^{-4} \text{ m}^2) = 1.643$$

$$\begin{aligned} \text{Therefore total pipe-work Volume for 1'' pipe} &= (135.64 \times 10^{-5} \text{ m}^3) \times 1.643 \\ &= 222.86 \times 10^{-5} \text{ m}^3 \end{aligned}$$

Fluid in 1" Fittings

$$\begin{aligned} \text{Vol. } - \text{Elbow } - xa &= \text{Pipe-CSA} \times \text{length of Arc} = (3.503 \times 10^{-4} \text{ m}^2) \times 0.072 \text{ m} \\ &= 2.52 \times 10^{-5} \text{ m}^3 \end{aligned}$$

$$\begin{aligned} \text{Vol. } - \text{Elbow } - hi &= \text{Pipe-CSA} \times \text{length of Arc} = (3.503 \times 10^{-4} \text{ m}^2) \times 0.072 \text{ m} \\ &= 2.52 \times 10^{-5} \text{ m}^3 \end{aligned}$$

$$\begin{aligned} \text{Vol. } - \text{Elbow } - on &= \text{Pipe-CSA} \times \text{length of Arc} = (3.503 \times 10^{-4} \text{ m}^2) \times 0.072 \text{ m} \\ &= 2.52 \times 10^{-5} \text{ m}^3 \end{aligned}$$

$$\text{Vol - Elbow} - ut = \text{Pipe-CSA} \times \text{length of Arc} = (3.503 \times 10^{-4} \text{ m}^2) \times 0.072 \text{ m} \\ = 2.52 \times 10^{-5} \text{ m}^3$$

$$\text{Vol - Tee} - jz = \text{Pipe-CSA} \times L_1 + \text{Pipe-CSA} \times L_2 \\ = (3.503 \times 10^{-4} \text{ m}^2) \times 0.055 \text{ m} + (3.503 \times 10^{-4} \text{ m}^2) \times 0.014 \text{ m} \\ = 1.93 \times 10^{-5} \text{ m}^3 + 4.9 \times 10^{-6} \text{ m}^3 = 2.42 \times 10^{-5} \text{ m}^3$$

$$\text{Vol - Cross} - wvy = \text{Pipe-CSA} \times L_1 + 2 \times \text{Pipe-CSA} \times L_2 \\ = (3.503 \times 10^{-4} \text{ m}^2) \times 0.055 \text{ m} + 2 \times (3.503 \times 10^{-4} \text{ m}^2) \times 0.014 \text{ m} \\ = 1.93 \times 10^{-5} \text{ m}^3 + 2 \times 4.9 \times 10^{-6} \text{ m}^3 = 2.91 \times 10^{-5} \text{ m}^3$$

$$\text{Vol - Reducer} - bc = \text{Pipe-CSA} \times L_4 + 0.33 \times \pi \times (D_1^2/4 + D_1/2 \times D_2/2 + \\ D_2^2/4) \times 0.037 + \pi \times D_1^2/4 \times L_4 \\ = (3.503 \times 10^{-4} \text{ m}^2) \times 0.0193 \text{ m} + 0.33 \times \pi \times \\ (0.053^2/4 + 0.053/2 \times 0.020/2 + 0.020^2/4) \times 0.037 + \pi \times 0.053^2/4 \times 0.193 = \\ 6.76 \times 10^{-6} + 4.09 \times 10^{-5} + 4.25 \times 10^{-4} = 47.3 \times 10^{-5} \text{ m}^3$$

$$\text{Vol - Reducer} - fg = \text{Pipe-CSA} \times L_4 + 0.33 \times \pi \times (D_1^2/4 + D_1/2 \times D_2/2 + \\ D_2^2/4) \times 0.037 + \pi \times D_1^2/4 \times L_4 \\ = (3.503 \times 10^{-4} \text{ m}^2) \times 0.0193 \text{ m} + 0.33 \times \pi \times \\ (0.053^2/4 + 0.053/2 + 0.020/2 + 0.020^2/4) \times 0.037 + \pi \times 0.053^2/4 \times 0.193 = \\ 6.76 \times 10^{-6} + 4.09 \times 10^{-5} + 4.25 \times 10^{-4} = 47.3 \times 10^{-5} \text{ m}^3$$

$$\text{Vol} - 2'' \text{ Flanges} - cd = \pi \times D_1^2/4 \times L_2 = \pi \times 0.060^2/4 \times 0.046 \\ = 13.0 \times 10^{-5} \text{ m}^3$$

$$\text{Vol} - 2'' \text{ Flanges} - ef = \pi \times D_1^2/4 \times L_2 = \pi \times 0.060^2/4 \times 0.046 \\ = 13.0 \times 10^{-5} \text{ m}^3$$

$$\text{Total Fittings Volume for } 3/4'' = 136.01 \times 10^{-5} \text{ m}^3$$

$$\text{The ratio of } 1'' \text{ to } 3/4'' \text{ pipe cross sectional areas are : } (5.75 \times 10^{-4} \text{ m}^2/3.503 \\ \times 10^{-4} \text{ m}^2) = 1.643$$

$$\text{Therefore Total Fittings Volume for } 1'' = (136.01 \times 10^{-5} \text{ m}^3) \times 1.643 = 223.45 \\ \times 10^{-5} \text{ m}^3$$

Fluid inside EES Receiver

$$\begin{aligned} \text{Vol} - \text{End Cap 1} &= \pi D_i^2/4 \times L_1 + \pi(D_{at}^2/4 - D_{bt}^2/4) \times L_2 \\ &= \pi \times 0.052^2/4 \times 0.064 + \pi (0.064^2/4 - 0.047^2/4) \times 0.035 = 1.36 \times 10^{-4} + 5.19 \\ &\quad \times 10^{-5} \\ &= 18.8 \times 10^{-5} \text{ m}^3 \end{aligned}$$

$$\begin{aligned} \text{Vol} - \text{End Cap 2} &= D_i \times L_1 + \pi(D_{at}^2/4 - D_{bt}^2/4) \times L_2 \\ &= \pi \times 0.052^2/4 \times 0.064 + \pi (0.064^2/4 - 0.047^2/4) \times 0.035 = 1.36 \times 10^{-4} + 5.19 \\ &\quad \times 10^{-5} \\ &= 18.8 \times 10^{-5} \text{ m}^3 \end{aligned}$$

$$\begin{aligned} \text{Vol} - \text{HTF annulus} &= \pi(D_{at}^2/4 - D_{bt}^2/4) \times L_{ann} = \\ &= \pi (0.064^2/4 - 0.047^2/4) \times 0.96 = 143 \times 10^{-5} \text{ m}^3 \\ \text{Total PECT Receiver Volume} &= 180.6 \times 10^{-5} \text{ m}^3 \end{aligned}$$

Fluid inside ¼ Full Tank

$$\begin{aligned} \text{Vol} &= \pi D_{tnk}^2/4 \times L/4 \\ &= \pi (0.154^2/4) \times 300/4 = 140 \times 10^{-5} \text{ m}^3 \end{aligned}$$

Therefore, the total volume of fluid in the PECT Hydraulic Loop is:

Total Volume = Pipe work Vol. + Fittings Vol. + PECT Receiver Vol. +
Exp. Tank Vol.

$$= 222.86 \times 10^{-5} \text{ m}^3 + 223.45 \times 10^{-5} \text{ m}^3 + 180.6 \times 10^{-5} \text{ m}^3 + 140 \times 10^{-5} \text{ m}^3$$

Total Hydraulic Loop Volume = 766.91 x 10⁻⁵ m³ ≈ 0.0077m³ = 7.7 L

Calculating HTF Expansion Volume – (Therminol 66 HTF)

Coefficient of Thermal Expansion (CoTE) - *Therminol 66 HTF* =
0.0009/°C

$$\text{At } 350 \text{ } ^\circ\text{C} \Rightarrow 350^\circ\text{C} \times 0.0009/^\circ\text{C} = 0.315 = 31.5\%$$

Therefore Expansion Volume at 350°C = 32% of Total Hydraulic Loop Volume

$$\text{Expansion Volume} = 32\% \times 7.7 \text{ L} = 2.46 \text{ L}$$

The expansion tank must be large enough to accommodate this expansion. At the maximum operating temperature of 350°C the tank should be no more than $\frac{3}{4}$ full.

Since the tank was originally $\frac{1}{4}$ full, then the increase tank volume would have increased by $\frac{1}{2}$

We now need to check that $\frac{1}{2}$ Tank Volume \geq Expansion Volume

Check

$$\frac{1}{2} \text{ Tank Volume} = \pi D_{\text{tnk}}^2 / 4 \times L / 2 = \pi (0.154^2 / 4) \times 300 / 2 = 280 \times 10^{-5} \text{ m}^3 = 0.0028 \text{ m}^3 = 2.8 \text{ L}$$

Therefore the design is adequate since " $\frac{1}{2}$ Tank Volume" > "Expansion Volume"

Appendix C

Heating Design Calculations for the EES Heating Rig

To calculate the heater requirements, the following must be determined.

- a) Total mass of pipe work and fittings that will be brought up to operational temperature
- b) Total mass of heat transfer fluid to be heated to operational temperature

Specifications for Pipe work to be used in Rig Design are as follows

- Main pipe work → 5m of Schedule 40 Carbon steel 3/4" pipe; Weight = 1.13 lbs per foot (1.68 kg per 1m), Wall thickness – 2.79mm
- DPHX → 0.4m of Schedule 40 2" Carbon steel pipe – 3.65 lbs per foot (5.44 kg per 1m) – Wall thickness 3.91 mm
- PECT RECEIVER absorber tube → 3" Aluminium T- 6061 Round Tube, OD – 76.2 mm, Weight = 2.54 lbs per foot (3.79 kg per 1m), Wall thickness 6.35 mm
- PECT RECEIVER battery tube → 1.875" Aluminium T- 6061 Round Tube, OD – 47.63mm, Weight = 0.3894 lbs per foot (0.58 kg per 1m), Wall thickness 1.47 mm

To work out heat load, the mass/volume and density specifications for the following fittings are required

- PECT RECEIVER Screw On End Piece (T-6061 AL) x 1
- PECT RECEIVER Weld On End Piece (T-6061 AL) x 1
- PECT RECEIVER Internal Tube spacer (T-6061 AL) x 2
- 3/4" 90 degree carbon steel elbow x 7
- 3/4" Carbon Steel straight cross x 1
- 3/4" Carbon Steel Tee x 1
- 3/4" Carbon Steel ANSI -150 Flange x 2
- 2" Carbon Steel ANSI -150 Flange x 4
- 2" Aluminium ANSI -150 Flange x 2
- 2 – 3/4" Concentric Reducer x 2
- 6" Carbon Steel pipe (0.3 m) x 1
- 6" Carbon Steel ANSI -150 Flange x 2

Estimated Pipe work Mass

Mass of Pipe -Schedule 40 SS Base loop – $(1.2\text{m} \times 2 + 1\text{m} \times 2) = 4.4\text{m}$;
 $4.4\text{m} \times 5.41 \text{ kg/ m} = 23.8 \text{ kg}$

Mass of Flexi-Verticals – $1\text{m} \times 2$ (Using Schedule 40 SS as estimate)= $1\text{m} \times 2 = 2\text{m}$; $2\text{m} \times 5.41\text{kg/m} = 10.82 \text{ kg}$

Mass Receiver (Schedule 80 SS) – 1m ; $1\text{m} \times 11.81\text{kg/m} = 11.81 \text{ kg}$

Mass of Battery tube (Schedule 40 SS) - 1m ; $1\text{m} \times 3.43 \text{ kg/m} = 3.43 \text{ kg}$

Ends Volume = $\pi r^2 L = \pi \times 0.052^2 \times 0.095\text{m} = 8.07 \times 10^{-4} \text{ m}^3$

Density of 304 SS = $8000\text{kg/m}^3 \Rightarrow$

Mass of the two Ends = $\rho \times V \times 2 = 8 \times 10^3 \times 8.07 \times 10^{-4} \times 2 = 13 \text{ kg}$

Total mass of Steel to be heated = $23.8 + 10.82 + 11.81 + 3.43 + 13 = 62.86 \text{ kg}$

For 20% over design, New Mass = Design mass $\times 1.2 = 62.86 \times 1.2 \approx 75 \text{ kg}$

Estimated Fluid Mass

Mass of Therminol 66 Heat Transfer fluid = 20kg

For 20% over design, New Mass = Design mass $\times 1.2 = 20 \text{ kg} \times 1.2 = 24\text{kg}$, use $\approx 25 \text{ kg}$

Heating Requirement

a) Heating Steel Pipe work from 10 to $330 \text{ }^\circ\text{C}$; $C_{p,304SS} = 500 \text{ J/kg/K}$
 $Q = mC_p\Delta T = 75 \text{ kg} \times 500 \text{ J/kg/K} \times 320 \text{ K} = 12 \text{ MJ}$

b) Heating HTF from 10 to $320 \text{ }^\circ\text{C}$; Avg- $C_{p,TH66} = 900 \text{ J/kg/K}$
 $Q = mC_p\Delta T = 25 \text{ kg} \times 900 \text{ J/kg/K} \times 310 \text{ K} = 6.98 \text{ MJ}$

Total Heating required = $18.98 \text{ MJ} \approx 19 \text{ MJ}$

Time required to heat up system = $3 \text{ hours} = 3 \times 3600 \text{ s} = 10,800 \text{ s}$

Power = Heat Energy Transferred/ Time taken = $19 \times 10^6 \text{ J} / 10,800 \text{ s} = 1759.3 \text{ W}$

Therefore a 2 kW heater is adequate for heating up the system within 3hrs.

Appendix D

Calculation of the required Pipe-work Insulation for the EES Heating Rig at an Operating Temperature of 350°C

The purpose of the insulation is to introduce a high resistance in the path of heat flow from pipe work to ambient, thereby significantly reducing heat loss, while providing a safe working surface temperature. In approaching this calculation, the first step was to draw a resistance model (Figure 0-1) for the heat flow path between the Heat Transfer Fluid (HTF) in the pipe work and the ambient.

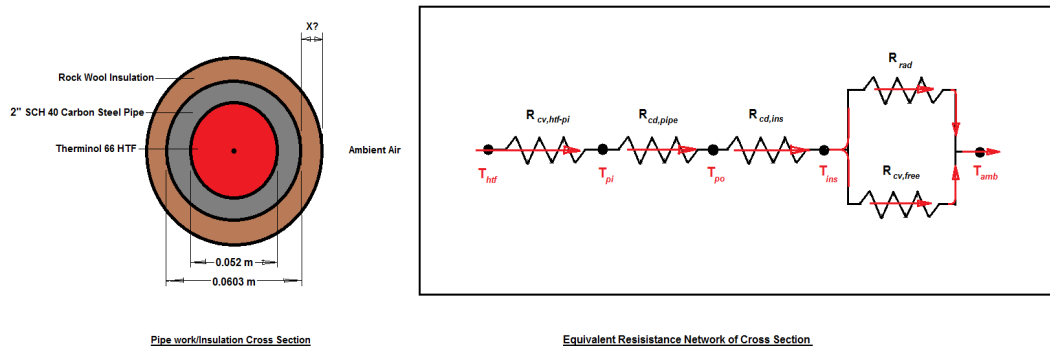


Figure 0-1 Schematic diagram of Heat Flow Model for Pipe work Cross Section using Resistance Network

The driving force for this cross sectional heat flow is the temperature difference between the HTF (T_{htf}), and the laboratory room (T_{amb}). For purposes of calculation T_{HTF} is made to assume a steady state value of 350°C, while T_{amb} assumes a value of 20°C.

The four steps that will be used to calculate the insulation thickness are as follows:

1. The type of insulation will be chosen, and a value will be set for the maximum radial heat loss ($\dot{q}'_{L,max}$) allowed from the pipe work.
2. The value of $\dot{q}'_{L,max}$, the driving temperature difference ($T_{htf} - T_{amb}$) and the constant heat exchanging area ($A_{p,o}$) of the outer

pipe surface, will be used to calculate the overall heat loss coefficient (U_L), between the HTF and the ambient.

3. The heat transfer coefficient inside the HTF pipe, along with the convective and radiative heat loss coefficients at the insulation surface will then be computed and used to find the value of the required insulation resistance (R_{ins}).
4. Finally the required insulation thickness (X_{ins}) will be calculated from R_{ins} .

The following steps were used to calculate the insulation thickness:

Step 1: Choosing insulation type and setting maximum permissible radial heat loss ($Q_{L,max}$)

The insulation type chosen for the PECT Rig is “Rockwool Mineral Insulation”, which is rated up to 700°C, with a thermal conductivity of 0.037 W/mK. It consists of half sections which will be placed around the pipe work and bonded by a reflective foil adhesive of emissivity 0.04. (See: <http://www.insulationexpress.co.uk/Pipe-Insulation/Rocklap-Pipe-Sections-.htm>)

The maximum permissible radial heat loss per meter length chosen for the pipe work is:

$\dot{q}'_{L,max} = 80 \text{ W/m}$ (This economical value was chosen to be 4% of 2 kW heat input)

Step 2: Calculating the Overall Heat Loss Coefficient (U_L)

The overall heat loss coefficient (U_L), can be calculated from the overall equation for heat loss given below as:

$$\dot{Q}_{L,max} = U_L A_{p,o} (T_{htf} - T_{amb}) \quad \text{(Equation 0-1)}$$

If the heat loss is considered per unit length, then:

$$\dot{q}'_{L,max} = U_L \pi d_{p,o} (T_{htf} - T_{amb}) \quad \text{(Equation 0-2)}$$

Rearranging for U_L we have:

$$U_L = \frac{\dot{q}'_{L,max}}{\pi d_{p,o} (T_{htf} - T_{amb})} \quad \text{(Equation 0-3)}$$

Substituting the values for $\dot{q}'_{L,max} = 80 \text{ W/m}$; $(T_{htf} - T_{amb}) = \Delta T = (350 - 20) \text{ K} = 330 \text{ K}$; and $d_{p,o} = 0.0603 \text{ m}$, we have :

$$U_L = \frac{80 \text{ W/m}}{\pi \times 0.0603 \text{ m} \times 330 \text{ K}} = 1.28 \text{ W/m}^2 \text{ K}$$

Step 3: Calculating the required Insulation Resistance (R_{ins})

The overall heat loss coefficient can be found by calculating the overall flow resistance ($\frac{1}{U_L A_{p,o}}$) along the path of heat loss.

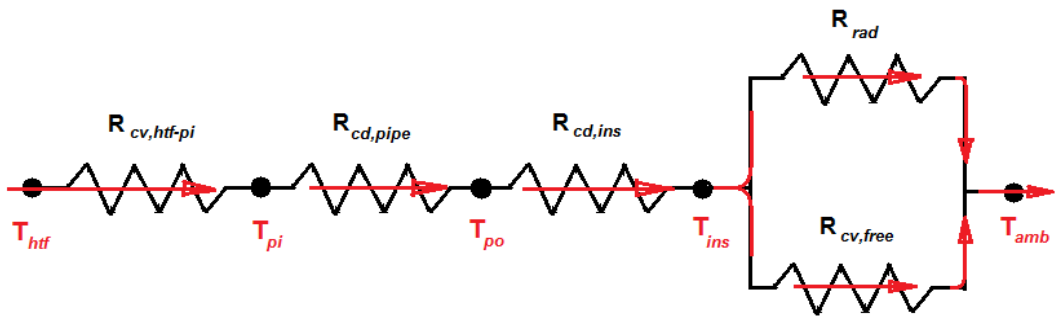


Figure 0-2; Schematic diagram of Cross Sectional Resistance Network

Considering the resistance network (Figure 0-2) , we have:

$$\frac{1}{U_L A_{p,o}} = R_{cv,htf-pi} + R_{cd,pipe} + R_{cd,ins} + \left(\frac{1}{R_{rad}} + \frac{1}{R_{cv,free}} \right) \quad \text{(Equation 0-4)}$$

$$\frac{1}{U_L A_{p,o}} = \frac{1}{h_{htf-pi} A_{p,i}} + \frac{\ln\left(\frac{d_{p,o}}{d_{p,i}}\right)}{2\pi k_{pipe} L} + \frac{\ln\left(\frac{d_{ins}}{d_{p,o}}\right)}{2\pi k_{ins} L} + \left[\frac{1}{(h_{rad} + h_{cv,free}) A_{ins,o}} \right] \quad \text{(Equation 0-5)}$$

Multiplying by $A_{p,o}$ gives:

$$\frac{1}{U_L} = \frac{A_{p,o}}{h_{htf-pi}A_{p,i}} + \frac{A_{p,o} \times \ln\left(\frac{d_{p,o}}{d_{p,i}}\right)}{2\pi k_{pipe}L} + \frac{A_{p,o} \times \ln\left(\frac{d_{ins}}{d_{p,o}}\right)}{2\pi k_{ins}L} + \left[\frac{A_{p,o}}{(h_{rad} + h_{cv,free})A_{ins,o}} \right] \quad \text{(Equation 0-6)}$$

The outer insulation diameter (d_{ins}) = $d_{p,o} + 2X_{ins}$ where $d_{p,o}$ is the outer diameter of the carbon steel pipe and X_{ins} is the insulation thickness. Re-writing gives:

$$\frac{1}{U_L} = \frac{A_{p,o}}{h_{htf-pi}A_{p,i}} + \frac{A_{p,o} \ln\left(\frac{d_{p,o}}{d_{p,i}}\right)}{2\pi k_{pipe}L} + \frac{A_{p,o} \ln\left(\frac{d_{p,o} + 2X_{ins}}{d_{p,o}}\right)}{2\pi k_{ins}L} + \left[\frac{A_{p,o}}{(h_{rad} + h_{cv,free})A_{ins,o}} \right] \quad \text{(Equation 0-7)}$$

Substituting the expressions for the “Areas” gives:

$$\frac{1}{U_L} = \frac{\pi d_{p,o}L}{h_{htf-pi}\pi d_{p,i}L} + \frac{\pi d_{p,o}L \times \ln\left(\frac{d_{p,o}}{d_{p,i}}\right)}{2\pi k_{pipe}L} + \frac{\pi d_{p,o}L \times \ln\left(\frac{d_{p,o} + 2X_{ins}}{d_{p,o}}\right)}{2\pi k_{ins}L} + \left[\frac{\pi d_{p,o}L}{(h_{rad} + h_{cv,free}) \times \pi(d_{p,o} + 2X_{ins})L} \right] \quad \text{(Equation 0-8)}$$

Simplifying gives:

$$\frac{1}{U_L} = \frac{d_{p,o}}{h_{htf-pi}d_{p,i}} + \frac{d_{p,o} \times \ln\left(\frac{d_{p,o}}{d_{p,i}}\right)}{2k_{pipe}} + \frac{d_{p,o} \times \ln\left(\frac{d_{p,o} + 2X_{ins}}{d_{p,o}}\right)}{2k_{ins}} + \frac{d_{p,o}}{(h_{rad} + h_{cv,free}) \times (d_{p,o} + 2X_{ins})} \quad \text{(Equation 0-9)}$$

To find the heat transfer coefficients h_{htf-pi} , h_{rad} and $h_{cv,free}$, the Reynold's number Re must be first calculated:

$$\begin{aligned} \text{(Input Data: } M = 1 \text{ kg/s; } \mu = 3.24 \times 10^{-4} \text{ kg.ms; } d_{p,i} = 0.052 \text{ m; } c_p \\ = 2766 \text{ J/kgK; } k_{htf} = 0.088 \text{ W/mK)} \end{aligned}$$

$$Re = \frac{4M}{\pi d_{p,i} \mu} = \frac{4 \times 1}{\pi \times 0.052 \times 3.24 \times 10^{-4}} = 75,572; \quad Pr = \frac{c_p \times \mu}{k_{htf}} = \frac{2766 \times 3.24 \times 10^{-4}}{0.088} = 10.18$$

$$a) \quad h_{htf-pi} = \frac{Nu_i \times k_{htf}}{d_{p,i}}, \quad \text{where } Nu = \frac{(f/2) Re Pr}{1.07 + 12.7(f/2)^{0.5} (Pr^{2/3} - 1)} \quad \text{and where}$$

$$f = \frac{1}{4(1.82 \log(Re) - 1.64)^2} = \frac{1}{4(1.82 \log(75,572) - 1.64)^2} = 4.771 \times 10^{-3}$$

$$Nu = \frac{(f/2) Re Pr}{1.07 + 12.7(f/2)^{0.5} (Pr^{2/3} - 1)} = \frac{(4.771 \times 10^{-3} / 2) \times 75,572 \times 10.18}{1.07 + 12.7(4.771 \times 10^{-3} / 2)^{0.5} (10.18^{2/3} - 1)}$$

$$Nu = 545.69$$

$$a) \quad h_{htf-pi} = \frac{Nu \times k_{htf}}{d_{p,i}} = \frac{545.69 \times 0.088}{0.052} = 923.472 \text{ W/m}^2\text{K}$$

b) The radiation coefficient can be approximated as $h_{rad} = \sigma \varepsilon (T_{ins}^2 + T_{amb}^2) (T_{ins} + T_{amb})$ where T_s = surface temperature of the insulation. Given that the maximum permissible value of $T_{ins} = 45^\circ\text{C} = 318 \text{ K}$ and ambient temperature is $20^\circ\text{C} = 293 \text{ K}$:

$$\sigma = 5.673 \times 10^{-8} \text{ W/m}^2\text{K}^4, \quad \varepsilon_{rockwool_ins_foil} = 0.04$$

$$h_{rad} = 5.673 \times 10^{-8} \times 0.04(318^2 - 293^2)(318 + 293) = 0.26 \text{ W/m}^2\text{K}$$

c) We now seek to calculate the free convection heat transfer coefficient.

$$Nu = \exp[-2.95 + 1.02 \ln(PrGr) - 0.0829[\ln(PrGr)]^2 + 0.0267[\ln(PrGr)]^3]$$

Where $Gr = \frac{\beta d_{ins}^3 \rho_{air}^2 (T_{ins} - T_{amb})}{\mu_{air}^2}$; @ $T = \left[\frac{45+20}{2} \right]^\circ\text{C}$ or 305.5 K , $\mu_{air} \approx 1.88 \times 10^{-5} \text{ kg/ms}$;

$$\rho_{air} = 1.16 \text{ kg/m}^3; \quad \beta = \frac{1}{T_{amb}} = \frac{1}{293 \text{ K}} = 3.41 \times 10^{-3} / \text{K}; \quad c_{p,air} = 1.006 \times 10^3 \text{ J/kgK}; \quad k_{air} = 0.0267 \text{ W/mK}$$

$$\text{Therefore Gr} = \frac{3.41 \times 10^{-3} (0.063 + 2X_{ins})^3 \times 1.16^2 (45 - 20)}{(1.88 \times 10^{-5})^2} = (3.246 \times 10^8) \times (d_{ins})^3$$

Evaluating an initial value for Gr with an estimate of $d_{ins} = (d_{p,o} + 0.04) = 0.063 + 0.04 = 0.103 \text{ m}$, gives: $\text{Gr} = (3.246 \times 10^8) \times (0.103)^3 = 354,655$

$$\text{Pr} = \frac{c_{p,air} \times \mu_{air}}{k_{air}} = \frac{1.006 \times 10^3 \times 1.88 \times 10^{-5}}{0.02656} = 0.71$$

Therefore initial estimate of the Nusselt number is:

$$\text{Nu}_{cv,free} = \left[0.825 + \frac{0.387(\text{GrPr})^{1/6}}{[1 + (0.492/\text{Pr})^{9/16}]^{8/27}} \right]^2$$

$$\text{Nu}_{cv,free} = \left[0.825 + \frac{0.387(354,655 \times 0.71)^{1/6}}{[1 + (0.492/0.71)^{9/16}]^{8/27}} \right]^2$$

$$\text{Nu}_{cv,free} = 11.58$$

$$h_{cv,free} = \frac{\text{Nu}_{cv,free} \times k_{air}}{d_{ins}} = \frac{11.58 \times 0.02656}{0.103} = 2.99 \text{ W/mK}$$

Recall that:

$$\frac{1}{U_L} = \frac{d_{p,o}}{h_{htf-pi} d_{p,i}} + \frac{d_{p,o} \times \ln\left(\frac{d_{p,o}}{d_{p,i}}\right)}{2k_{pipe}} + \frac{d_{p,o} \times \ln\left(\frac{d_{p,o} + 2X_{ins}}{d_{p,o}}\right)}{2k_{ins}}$$

$$+ \frac{d_{p,o}}{(h_{rad} + h_{cv,free}) \times (d_{p,o} + 2X_{ins})}$$

Therefore

$$\frac{1}{1.27} = \frac{0.0603}{955.65 \times 0.052} + \frac{0.0603 \times \ln\left(\frac{0.0603}{0.052}\right)}{2 \times 43}$$

$$+ \frac{0.0603 \times \ln\left(\frac{0.0603 + 2X_{ins}}{0.0603}\right)}{2 \times 0.037}$$

$$+ \frac{0.0603}{(0.259 + 2.71) \times (0.0603 + 2X_{ins})}$$

$$\Rightarrow 0.7874 = 1.213 \times 10^{-3} + 1.038 \times 10^{-4} + 0.815 \times \ln\left(\frac{0.0603 + 2X_{ins}}{0.0603}\right) + \frac{0.02031}{(0.0603 + 2X_{ins})}$$

$$\Rightarrow 0.7874 - 1.213 \times 10^{-3} - 1.038 \times 10^{-4} = 0.815 \times \ln\left(\frac{0.0603 + 2X_{ins}}{0.0603}\right) + \frac{0.02031}{(0.0603 + 2X_{ins})}$$

$$\Rightarrow 0.786 = 0.815 \times \ln\left(\frac{0.0603 + 2X_{ins}}{0.0603}\right) + \frac{0.02031}{(0.0603 + 2X_{ins})}$$

$$\Rightarrow 0.965 = \ln\left(\frac{0.0603 + 2X_{ins}}{0.0603}\right) + \frac{0.02492}{(0.0603 + 2X_{ins})}$$

$$\Rightarrow 0.965 = \ln(0.0603 + 2X_{ins}) - \ln(0.0603) + \frac{0.02492}{(0.0603 + 2X_{ins})}$$

$$\begin{aligned} \Rightarrow 0.965 \times (0.0603 + 2X_{ins}) &= \ln(0.0603 + 2X_{ins}) \times (0.0603 + 2X_{ins}) - \ln(0.0603) \\ &\times (0.0603 + 2X_{ins}) + 0.02492 \end{aligned}$$

$$\Rightarrow 0.0577 + 1.929X_{ins} = [\ln(0.0603 + 2X_{ins}) - \ln(0.0603)] \times (0.0603 + 2X_{ins}) + 0.02492$$

$$\Rightarrow 0.0582 + 1.929X_{ins} = \ln\left(\frac{0.0603 + 2X_{ins}}{0.0603}\right) \times (0.0603 + 2X_{ins}) + 0.0249$$

$$\Rightarrow 0.0328 + 1.929X_{ins} = \ln(1 + 33.17X_{ins}) \times (0.0603 + 2X_{ins})$$

$$\Rightarrow \frac{(0.0328 + 1.929X_{ins})}{(0.0603 + 2X_{ins})} = \ln(1 + 33.17X_{ins})$$

The easiest way to solve is to let LHS = g(x) and RHS = f(x).

Plotting these two functions in MS Excel yields the solution which is the point where f(x) = g(x). This occurs at a value of:

$$X_{ins} = 0.035 \text{ m}$$

Table 0-1: Table of selected values of g(x) and f(x) functions

x(m)	g(x)	f(x)
0	0.543946932	0
0.01	0.648692403	0.286456

0.02	0.711665005	0.508864
0.03	0.753699086	0.690694
0.04	0.783749109	0.844494
0.05	0.806300686	0.977762

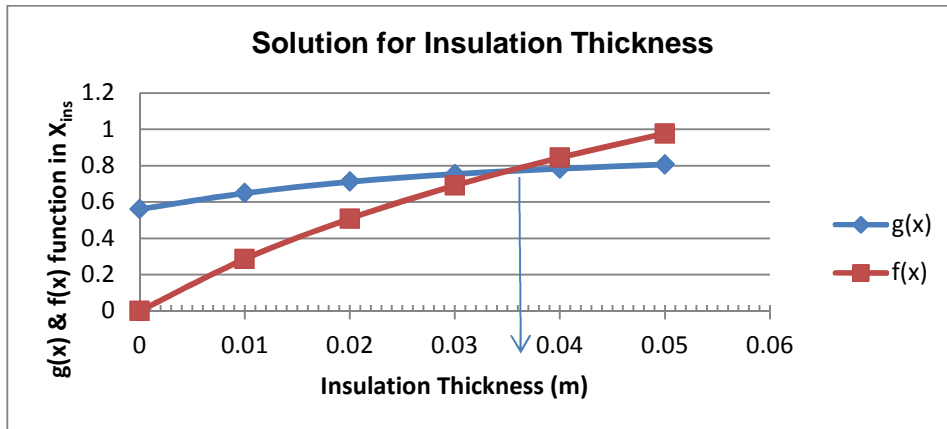


Figure 0-3; Solution of equations for insulation thickness

Since the first value is an approximation which was obtained using a reasonable guess, then d_{ins} must be recalculated starting with the new value of $d_{ins} = (0.0603 + 2 \times 0.035) = 0.1303$. we begin by finding the Gr number.

$$Gr = (3.246 \times 10^8) \times (0.1303)^3 = 718,094$$

Next the Nusselt number for free convection over the insulation's surface is calculated as follows:

$$Nu_{cv,free} = \left[0.825 + \frac{0.387(GrPr)^{1/6}}{[1+(0.492/Pr)^{9/16}]^{8/27}} \right]^2$$

$$Nu_{cv,free} = \left[0.825 + \frac{0.387(718,094 \times 0.71)^{1/6}}{[1 + (0.492/0.71)^{9/16}]^{8/27}} \right]^2$$

$$Nu_{cv,free} = 13.87$$

Next we evaluate:

$$h_{cv,free} = \frac{Nu_{cv,free} \times k_{air}}{d_{ins}} = \frac{13.87 \times 0.0259}{0.1303} = 2.76 \text{ W/mK}$$

Recall that:

$$\frac{1}{U_L} = \frac{d_{p,o}}{h_{htf-pi} d_{p,i}} + \frac{d_{p,o} \times \ln\left(\frac{d_{p,o}}{d_{p,i}}\right)}{2k_{pipe}} + \frac{d_{p,o} \times \ln\left(\frac{d_{p,o} + 2X_{ins}}{d_{p,o}}\right)}{2k_{ins}} + \frac{d_{p,o}}{(h_{rad} + h_{cv,free}) \times (d_{p,o} + 2X_{ins})}$$

Therefore

$$\frac{1}{1.27} = \frac{0.0603}{955.65 \times 0.052} + \frac{0.0603 \times \ln\left(\frac{0.0603}{0.052}\right)}{2 \times 43} + \frac{0.0603 \times \ln\left(\frac{0.0603 + 2X_{ins}}{0.0603}\right)}{2 \times 0.037} + \frac{0.0603}{(0.259 + 2.76) \times (0.0603 + 2X_{ins})}$$

$$\Rightarrow 0.7874 = 1.213 \times 10^{-3} + 1.038 \times 10^{-4} + 0.815 \times \ln\left(\frac{0.0603 + 2X_{ins}}{0.0603}\right) + \frac{0.0199}{(0.0603 + 2X_{ins})}$$

$$\Rightarrow 0.7874 - 1.213 \times 10^{-3} - 1.038 \times 10^{-4} = 0.815 \times \ln\left(\frac{0.0603 + 2X_{ins}}{0.0603}\right) + \frac{0.0199}{(0.0603 + 2X_{ins})}$$

$$\Rightarrow 0.786 = 0.815 \times \ln\left(\frac{0.0603 + 2X_{ins}}{0.0603}\right) + \frac{0.0199}{(0.0603 + 2X_{ins})}$$

$$\Rightarrow 0.965 = \ln\left(\frac{0.0603 + 2X_{ins}}{0.0603}\right) + \frac{0.02442}{(0.0603 + 2X_{ins})}$$

$$\Rightarrow 0.965 = \ln(0.0603 + 2X_{ins}) - \ln(0.0603) + \frac{0.02442}{(0.0603 + 2X_{ins})}$$

$$\begin{aligned} \Rightarrow 0.965 \times (0.0603 + 2X_{ins}) &= \ln(0.0603 + 2X_{ins}) \times (0.0603 + 2X_{ins}) - \ln(0.0603) \\ &\times (0.0603 + 2X_{ins}) + 0.0249 \end{aligned}$$

$$\Rightarrow 0.0577 + 1.929X_{ins} = [\ln(0.0603 + 2X_{ins}) - \ln(0.0603)] \times (0.0603 + 2X_{ins}) + 0.02442$$

$$\Rightarrow 0.0582 + 1.929X_{ins} = \ln\left(\frac{0.0603 + 2X_{ins}}{0.0603}\right) \times (0.0603 + 2X_{ins}) + 0.0244$$

$$\Rightarrow 0.0338 + 1.929X_{ins} = \ln(1 + 33.17X_{ins}) \times (0.0603 + 2X_{ins})$$

$$\Rightarrow \frac{(0.0338 + 1.929X_{ins})}{(0.0603 + 2X_{ins})} = \ln(1 + 33.17X_{ins})$$

Solving as was done before produces no observable change in the plot so:

$$X_{ins} = 0.035 \text{ m (will be round up to 0.04 m)}$$

Recall that the outside diameter of the 2" carbon steel pipe is: $d_{p,o} = 0.0603 \text{ m}$

$$\Rightarrow \text{Insulation diameter : } d_{ins} = d_{p,o} + 2X_{ins} = 0.143 \text{ m} = 143 \text{ mm}$$

and

$$\Rightarrow \text{Insulation Thickness } X_{ins} = 0.04 \text{ m} = 40 \text{ mm}$$

Appendix E

Solving the Quartic Glass Tube Temperature Equation

Recall from equation (4-44) that:

$$\dot{q}'_{Lcond,gt} = \mathfrak{S}_{at,o-gt,i} \sigma \pi D_{at,o} (T_{at,o}^4 - T_{gt,i}^4) + h_{conv,at-gt} \pi D_{at,o} (T_{at,o} - T_{gt,i}) - \dot{q}''_{sol} K_{lumped} \alpha_{gt} \pi D_{gt,o}$$

This equation will be solved for $T_{gt,i}$

Expanding brackets gives:

$$\begin{aligned} \dot{q}'_{Lcond,gt} = & \mathfrak{S}_{at,o-gt,i} \sigma \pi D_{at,o} T_{at,o}^4 - \mathfrak{S}_{at,o-gt,i} \sigma \pi D_{at,o} T_{gt,i}^4 + h_{conv,at-gt} \pi D_{at,o} T_{at,o} - \\ & h_{conv,at-gt} \pi D_{at,o} T_{gt,i} - \dot{q}''_{sol} K_{lumped} \alpha_{gt} \pi D_{gt,o} \end{aligned}$$

Therefore:

$$\begin{aligned} \mathfrak{S}_{at,o-gt,i} \sigma \pi D_{at,o} T_{gt,i}^4 + h_{conv,at-gt} \pi D_{at,o} T_{gt,i} = & -\dot{q}''_{sol} K_{lumped} \alpha_{gt} \pi D_{gt,o} \\ + \mathfrak{S}_{at,o-gt,i} \sigma \pi D_{at,o} T_{at,o}^4 + h_{conv,at-gt} \pi D_{at,o} T_{at,o} - \dot{q}'_{Lcond,gt} \end{aligned}$$

Dividing through by $\mathfrak{S}_{at,o-gt,i} \sigma \pi D_{at,o}$ gives:

$$\begin{aligned} T_{gt,i}^4 + \frac{h_{conv,at-gt} \pi D_{at,o}}{\mathfrak{S}_{at,o-gt,i} \sigma \pi D_{at,o}} T_{gt,i} = & \\ \frac{-\dot{q}''_{sol} K_{lumped} \alpha_{gt} \pi D_{gt,o} + \mathfrak{S}_{at,o-gt,i} \sigma \pi D_{at,o} T_{at,o}^4 + h_{conv,at-gt} \pi D_{at,o} T_{at,o} - \dot{q}'_{Lcond,gt}}{\mathfrak{S}_{at,o-gt,i} \sigma \pi D_{at,o}} \end{aligned}$$

$$\text{Let } A = \frac{-\dot{q}''_{sol} K_{lumped} \alpha_{gt} \pi D_{gt,o} + \mathfrak{S}_{at,o-gt,i} \sigma \pi D_{at,o} T_{at,o}^4 + h_{conv,at-gt} \pi D_{at,o} T_{at,o} - \dot{q}'_{Lcond,gt}}{\mathfrak{S}_{at,o-gt,i} \sigma \pi D_{at,o}}$$

$$\text{and } B = \frac{h_{conv,at-gt} \pi D_{at,o}}{\mathfrak{S}_{at,o-gt,i} \sigma \pi D_{at,o}}$$

$$\Rightarrow T_{gt,i}^4 + B T_{gt,i} = A$$

Re-arranging gives:

$$T_{gt,i}^4 + BT_{gt,i} - A = 0$$

Let $T_{gt,i} = x$. Therefore eqn. () becomes:

$$x^4 + Bx - A = 0$$

To solve this quadratic, we will first make the assumption that:

$$x^4 + Bx - A = (x^2 + px + q)^2 - (rx + s)^2 = 0$$

Expanding RHS gives:

$$x^4 + px^3 + qx^2 + px^3 + p^2x^2 + pqx + qx^2 + pqx + q^2 - r^2x^2 - 2rsx - s^2 = 0$$

Simplifying gives:

$$x^4 + 2px^3 + (2q + p^2 - r^2)x^2 + (2pq - 2rs)x + q^2 - s^2 = 0$$

Therefore:

$$x^4 + 2px^3 + (2q + p^2 - r^2)x^2 + (2pq - 2rs)x + q^2 - s^2 = x^4 + Bx - A = 0$$

Equating coefficients gives:

$$2p = 0 \Rightarrow p = 0$$

$$(2q + p^2 - r^2) = 0 \Rightarrow 2q = r^2 \tag{1}$$

$$(2pq - 2rs) = B \Rightarrow rs = \frac{-B}{2} \tag{2}$$

$$q^2 - s^2 = -A \Rightarrow A + q^2 = s^2 \tag{3}$$

$$2q(A + q^2) = \frac{B^2}{4} \Rightarrow q^3 + Aq - \frac{B^2}{8} = 0$$

Therefore multiplying (1) and (3) gives the auxillary cubic equation:

Let the auxillary cubic equation be of the form:

$$q^3 + \lambda q + \mu = 0 \tag{4}$$

$$\text{where } \lambda = A \text{ and } \mu = -\frac{B^2}{8}$$

$$\text{Trying } q = u + v \text{ gives: } q^3 = u^3 + 3u^2v + 3uv^2 + v^3$$

$$\Rightarrow q^3 = u^3 + 3uv(u + v) + v^3$$

$$\Rightarrow q^3 = u^3 + 3uvq + v^3$$

$$\text{Therefore, } q^3 - 3uvq = v^3 + u^3$$

Comparing with (4), it can be seen that:

$$\lambda = -3uv \text{ and } \mu = -(v^3 + u^3)$$

$$\text{Therefore } uv = \frac{\lambda}{-3} = \frac{A}{-3} \text{ and } v^3 + u^3 = -\mu = \frac{B^2}{8}. \text{ Also } \Rightarrow u^3 v^3 = -\frac{A^3}{27}$$

Let u^3 and v^3 be solutions to the quadratic $t^2 + \mu t - \frac{A^3}{27}$

Then $(u^3 - v^3)^2 = (u^3)^2 + (v^3)^2 - 2u^3 v^3$ which can be rewritten as:

$$(u^3 - v^3)^2 = (u^3)^2 + (v^3)^2 + 2u^3 v^3 - 4u^3 v^3$$

$$(u^3 - v^3)^2 = (u^3 + v^3)^2 - 4u^3 v^3 \tag{5}$$

Since $(v^3 + u^3) = -\mu = \frac{B^2}{8}$ then, $\mu^2 = (v^3 + u^3)^2 = \frac{B^4}{64}$, therefore (5)

becomes:

$$(u^3 - v^3)^2 = \frac{B^4}{64} + \frac{4A^3}{27}$$

$$\text{Therefore: } (u^3 - v^3) = \sqrt{\frac{B^4}{64} + \frac{4A^3}{27}} \text{ and also recall that } u^3 + v^3 = \frac{B^2}{8}$$

Adding the two expressions gives:

$$(u^3 - v^3) + (u^3 + v^3) = 2u^3 = \sqrt{\frac{B^4}{64} + \frac{4A^3}{27}} + \frac{B^2}{8}$$

$$\text{Therefore } u = \sqrt[3]{\frac{\sqrt{\frac{B^4}{64} + \frac{4A^3}{27}} + \frac{B^2}{8}}{2}}$$

$$\text{Recall that } uv = \frac{A}{-3} \Rightarrow v = -\frac{A}{3u} = -\frac{A}{3 \times \left\{ \sqrt[3]{\frac{\sqrt{\frac{B^4}{64} + \frac{4A^3}{27}} + \frac{B^2}{8}}}{2} \right\}}$$

$$\text{Therefore the auxillary cubic variable } = u + v, \text{ and } q = \left\{ \sqrt[3]{\frac{\sqrt{\frac{B^4}{64} + \frac{4A^3}{27}} + \frac{B^2}{8}}{2}} \right\} -$$

$$\left\{ A / \left[3 \times \left(\sqrt[3]{\frac{\sqrt{\frac{B^4}{64} + \frac{4A^3}{27}} + \frac{B^2}{8}}}{2} \right) \right] \right\}$$

$$\text{Recall from (1) that } r^2 = 2q \Rightarrow r = \sqrt{2q}$$

Therefore:

$$r = \sqrt{2 \times \left\{ \sqrt[3]{\frac{B^4 + 4A^3 + B^2}{\sqrt{64 + \frac{4A^3}{27} + \frac{B^2}{8}}}} \right\} - \left\{ A / \left[3 \times \left(\sqrt[3]{\frac{B^4 + 4A^3 + B^2}{\sqrt{64 + \frac{4A^3}{27} + \frac{B^2}{8}}}} \right) \right] \right\}}$$

Also recall from (2) that $rs = \frac{-B}{2} \Rightarrow s = -\frac{B}{2r}$

Therefore:

$$s = -B / \left(2 \times \sqrt{2 \times \left\{ \sqrt[3]{\frac{B^4 + 4A^3 + B^2}{\sqrt{64 + \frac{4A^3}{27} + \frac{B^2}{8}}}} \right\} - \left\{ A / \left[3 \times \left(\sqrt[3]{\frac{B^4 + 4A^3 + B^2}{\sqrt{64 + \frac{4A^3}{27} + \frac{B^2}{8}}}} \right) \right] \right\}} \right)$$

Recall that

$$x^4 + Bx - A = (x^2 + px + q)^2 - (rx + s)^2 = 0$$

$$\Rightarrow (x^2 + px + q)^2 - (rx + s)^2 = (x^2 + px + q + rx + s)(x^2 + px + q - rx - s) = 0$$

Therefore either:

$$[x^2 + (p + r)x + q + s] = 0, \quad \text{or} \quad [x^2 + (p - r)x + q - s] = 0$$

If $[x^2 + (p + r)x + q + s] = 0$, then:

$$x = \frac{-(p+r) \pm \sqrt{(p+r)^2 - 4(q+s)}}{2}, \text{ and since we already know } p = 0, \text{ then:}$$

$$x = \frac{-r \pm \sqrt{r^2 - 4(q+s)}}{2}$$

Alternately, if $[x^2 + (p - r)x + q - s] = 0$, then:

$$x = \frac{-(p-r) \pm \sqrt{(p-r)^2 - 4(q-s)}}{2}, \text{ which reduces to } x = \frac{r \pm \sqrt{r^2 - 4(q-s)}}{2}$$

Therefore the solutions for x are:

$$x = \frac{-r \pm \sqrt{r^2 - 4(q+s)}}{2} \text{ or } x = \frac{r \pm \sqrt{r^2 - 4(q-s)}}{2}$$

Since $T_{gt,i} = x$, then:

$$T_{gt,i} = \frac{-r \pm \sqrt{r^2 - 4(q+s)}}{2} \text{ or } T_{gt,i} = \frac{r \pm \sqrt{r^2 - 4(q-s)}}{2}$$

where :

$$q = \left\{ \sqrt[3]{\frac{B^4 + 4A^3 + B^2}{64 + 27 + 8}} - \left\{ A / \left[3 \times \left(\sqrt[3]{\frac{B^4 + 4A^3 + B^2}{64 + 27 + 8}} \right) \right] \right\} \right\}$$

$$r = \sqrt{2 \times \left\{ \sqrt[3]{\frac{B^4 + 4A^3 + B^2}{64 + 27 + 8}} - \left\{ A / \left[3 \times \left(\sqrt[3]{\frac{B^4 + 4A^3 + B^2}{64 + 27 + 8}} \right) \right] \right\} \right\}}$$

and

$$s = -B / \left(2 \times \sqrt{2 \times \left\{ \sqrt[3]{\frac{B^4 + 4A^3 + B^2}{64 + 27 + 8}} - \left\{ A / \left[3 \times \left(\sqrt[3]{\frac{B^4 + 4A^3 + B^2}{64 + 27 + 8}} \right) \right] \right\} \right\} \right)$$

With the constant A and B being defined as follows:

$$A = \frac{-q''_{sol} K_{lumped} \alpha_{gt} \pi D_{gt,o} + \mathfrak{I}_{at,o-gt,i} \sigma \pi D_{at,o} T_{at,o}^4 + h_{conv,at-gt} \pi D_{at,o} T_{at,o} - q'_{Lcond,gt}}{\mathfrak{I}_{at,o-gt,i} \sigma \pi D_{at,o}}$$

$$\text{and } B = \frac{h_{conv,at-gt} \pi D_{at,o}}{\mathfrak{I}_{at,o-gt,i} \sigma \pi D_{at,o}}$$

Appendix F

Sample Check of the MS Excel calculation by a Binary Search Method

A sample of the “primary” model input parameters (table 1) are given below. These inputs were used to evaluate other important secondary input parameters such as temperature dependent fluid properties (eg. viscosity, density, conductivity) and flow dependent terms (eg. heat transfer coefficients, dimensionless flow numbers).

Table 0-1: Sample Model Input Data (Primary)

$T_{amb}(^{\circ}\text{C})$	$T_{\infty}(^{\circ}\text{C})$	$T_{htf}(^{\circ}\text{C})$	$D_{at,o}(\text{m})$	$D_{at,i}(\text{m})$	$D_{gt,o}(\text{m})$	$D_{gt,i}(\text{m})$	$k_{at}(\text{Wm}^{-1}\text{K}^{-1})$	ε_{at}	ε_{gt}
25	6	20	0.076	0.063	0.1	0.090	40	0.1	0.89

$\dot{M}_{htf}(\text{kgs}^{-1})$	$\dot{q}''_{sol}(\text{Wm}^{-2})$	$\sigma(\text{Wm}^{-2}\text{K}^{-4})$	$SF_{gt,o-sky}$	$VF_{gt,o-sky}$	$VF_{at,o-gt,i}$	$W_{PTC}(\text{m})$	$k_{gt}(\text{Wm}^{-1}\text{K}^{-1})$
9	1000	5.67×10^{-8}	1	1	1	6	1.40

Results presented in this section are derived from the MS Excel “goal seek” solution to Equation 11. To check these results, a binary search was conducted using the data in table 1, to determine the value of the required heat flux $\dot{q}'_{cond,at}$.

Table 0-2– Sample Model Output Data (Primary)

Input Parameters	Output Flux Value
Table. 1 Values	$\dot{q}'_{cond,at}$ (MS Excel, goal seek)
	$2684.67 \text{ Wm}^{-1}\text{K}^{-1}$

In the binary search check given below, equation 11 is solved iteratively by substituting an initial guess for the flux into both the right hand side (R.H.S) and (L.H.S) of the equation, and computing the difference. The

closer the substituted value comes to the solution, the smaller this difference becomes. Ideally the difference would be zero at the solution value of the $\dot{q}'_{cond,at}$. However, like all numerical methods, an analytic solution is not possible and so the actual value of the flux can only be approximated subject to some tolerance. The tolerance chosen in this calculation was $L.H.S - R.H.S \leq 0.0001 \text{ Wm}^{-1}\text{K}^{-1}$.

Table 0-3– Binary search calculation

Input Parameters	Output Flux Value	R.H.S (Eqn.11)	L.H.S (Eqn.11)	(L.H.S – R.H.S)
	$\dot{q}'_{cond,at}$ (initial guess)			
	3000 $\text{Wm}^{-1}\text{K}^{-1}$	9894.03	2794.38	-7099.65
	$\dot{q}'_{cond,at}$ (new guess)			
	2675 $\text{Wm}^{-1}\text{K}^{-1}$	2024.79	2794.38	769.60

We observe that the difference between L.H.S and R.H.S has now become positive. Thus, we have trapped the root between the values of 2675 $\text{Wm}^{-1}\text{K}^{-1}$ and 3000 $\text{Wm}^{-1}\text{K}^{-1}$. We now continue our search within this range for the value of $\dot{q}'_{cond,at}$ that will result in the difference (L.H.S – R.H.S) approaching zero subject to our tolerance.

Table 0-4 – Binary search calculation (continued)

Input Parameters	Output Flux Value	R.H.S (Eqn.11)	L.H.S (Eqn.11)	(L.H.S – R.H.S)
	$\dot{q}'_{cond,at}$ (new value)			
	2700 $\text{Wm}^{-1}\text{K}^{-1}$	3453.35	2794.38	-658.97

The root is now trapped between the values of 2675 $\text{Wm}^{-1}\text{K}^{-1}$ and 2700 $\text{Wm}^{-1}\text{K}^{-1}$. We now continue our search within this range for the value of $\dot{q}'_{cond,at}$

Table 0-5– Binary search calculation (continued)

Input Parameters	Output Flux Value	R.H.S (Eqn.11)	L.H.S (Eqn.11)	(L.H.S – R.H.S)
	$\dot{q}'_{cond,at}$ (new value)			
	2690 Wm ⁻¹ K ⁻¹	3055.42	2794.38	-261.04
	$\dot{q}'_{cond,at}$ (new value)			
	2680 Wm ⁻¹ K ⁻¹	2506.98	2794.38	287.40

We notice that with $\dot{q}'_{cond,at} = 2680 \text{ Wm}^{-1}\text{K}^{-1}$, the difference again becomes positive. The root is now trapped between the values of $2680 \text{ Wm}^{-1}\text{K}^{-1}$ and $2690 \text{ Wm}^{-1}\text{K}^{-1}$. Our next test value of $2685 \dot{q}'_{cond,at} = \text{Wm}^{-1}\text{K}^{-1}$ gives:

Table 0-6– Binary search calculation (continued)

Input Parameters	Output Flux Value	R.H.S (Eqn.11)	L.H.S (Eqn.11)	(L.H.S – R.H.S)
	$\dot{q}'_{cond,at}$ (new value)			
	2685 Wm ⁻¹ K ⁻¹	2812.38	2794.38	-17.99

The root is now trapped between the values of $2680 \text{ Wm}^{-1}\text{K}^{-1}$ and $2685 \text{ Wm}^{-1}\text{K}^{-1}$.

Table 0-7– Binary search calculation (continued)

Input Parameters	Output Flux Value	R.H.S (Eqn.11)	L.H.S (Eqn.11)	(L.H.S – R.H.S)
	$\dot{q}'_{cond,at}$ (new value)			
	2684.5 Wm ⁻¹ K ⁻¹	2785.40	2794.38	8.98
	$\dot{q}'_{cond,at}$ (new value)			
	2684.6 Wm ⁻¹ K ⁻¹	2790.84	2794.38	3.54
	$\dot{q}'_{cond,at}$ (new value)			
	2684.65Wm ⁻¹ K ⁻¹	2793.56	2794.38	0.827

Input Parameters	Output Flux Value	R.H.S (Eqn.11)	L.H.S (Eqn.11)	(L.H.S – R.H.S)
	$\dot{q}'_{cond,at}$ (new value)			
	2684.66 Wm ⁻¹ K ⁻¹	2794.09	2794.38	0.285
	$\dot{q}'_{cond,at}$ (new value)			
	2684.67 Wm ⁻¹ K ⁻¹	2794.64	2794.38	-0.257

The root is now trapped between the values of 2684.66 Wm⁻¹K⁻¹ and 2684.67 Wm⁻¹K⁻¹. We now try values within this range. For the sole purpose showing the agreement between both sides of the calculation, the decimal places

Table 0-8– Binary search calculation (continued)

Input Parameters	Output Flux Value	R.H.S (Eqn.11)	L.H.S (Eqn.11)	(L.H.S – R.H.S)
	$\dot{q}'_{cond,at}$ (new value)			
	2684.665 Wm ⁻¹ K ⁻¹	2794.369	2794.383	0.014
	$\dot{q}'_{cond,at}$ (new value)			
	2684.6651 Wm ⁻¹ K ⁻¹	2794.375	2794.383	0.0088
	$\dot{q}'_{cond,at}$ (new value)			
	2684.652 Wm ⁻¹ K ⁻¹	2794.380	2794.383	0.0033
	$\dot{q}'_{cond,at}$ (new value)			
	2684.6525 Wm ⁻¹ K ⁻¹	2794.3832	2794.3839	0.0007
	$\dot{q}'_{cond,at}$ (new value)			
	2684.6526 Wm ⁻¹ K ⁻¹	2794.3839	2794.3839	9.99E-09

We now end the iteration with $\dot{q}'_{cond,at} = 2684.65 \text{ Wm}^{-1}\text{K}^{-1}$ as this is now within our required tolerance of $\text{L.H.S} - \text{R.H.S} \leq 0.0001$ and is also identical to the solution produced by MS Excel.

Appendix G

System Advisor Model (SAM) – Exploring system costs

One of the important recommendations for future work, found in the list of recommendations of chapter 7, is the need for a thorough economic analysis of the concept. Although this is generally beyond the scope of this current work, NREL's System Advisor Model (SAM 2011) software (*developed by NREL, for use by engineers, researchers and the general public*) was used to obtain some idea of the key economic parameters of the conceptual plant.

The typical physical parameters and the capital costs describing PTC receiver and collectors were adjusted in SAM 2011 software to reflect those of the EES receiver. Where possible, the input values used for the SAM model were the values used in the "SAM - Andasol case study" by NREL^[225]. The NaS battery capital costs were represented using the "Fossil back-up" parameter, which was normally set zero in standard simulations. According to Crowe^[226], NaS batteries typically cost around \$500 USD per kWh_e, and therefore this value was used in the SAM simulation as the "Fossil back-up" parameter. The relevant system parameters used in all of the SAM simulations which now follow.

Table 0-1: Physical trough model input parameters for the solar field and storage system used the Andasol case study (Source:²²⁵)

Page	Variable	Default Value	Andasol-1
Climate	Location	AZ Tucson (TMY2)	Granada (EPW)
Solar Field	Field aperture (Option 2)	861590 m ²	510120 m ²
	Irradiation at design	950 W/m ²	700 W/m ²
	Field HTF fluid	Therminol VP-1	User-defined (below)
	Design loop outlet temp	391°C	393°C
	Number of SCA per loop	8	4
Collector (SCAs)	Configuration name	Solargenix SGX-1	EuroTrough ET150
Receivers (HCEs)	Configuration name (Type 2)	No library match	Solel UVAC 3
Power Cycle	Capacity - Design gross output	111 MW	55 MW
	Rated cycle conversion efficiency	0.3774	0.381
	Aux heater outlet set temp	391°C	393°C
	Fossil dispatch mode	Minimum backup	Supplemental operation
Thermal Storage	Full load hours of TES	6 hr	7.5 hr
	Tank height	20 m	14 m
	Dispatch schedule	Summer Peak	Summer Peak
	TOD factor	Different values	All of them change to 1
	Fossil fill fraction (Period 1)	0	0.15
	Fossil fill fraction (Period 2)	0	0.20
Performance Adjustment	Fossil fill fraction (Period 3)	0	0.45
	Year-to-year decline in output	0	0.5

Table 0-2: Physical trough model input parameters for cost and plant financing used the Andasol case study (Source:²²⁵)

Page	Variable	Default Value	Andasol-1
Trough System Costs	Site Improvements	30.00 \$/m ²	28.00 \$/m ²
	HTF System	80.00 \$/m ²	78.00 \$/m ²
	Storage	80.00 \$/kWht	78.00 \$/kWht
	Fossil Backup	0.00 \$/kWe	60.00 \$/kWe
	Power Plant	830.00 \$/kWe	850.00 \$/kWe
	Balance of plant	110.00 \$/kWe	105.00 \$/kWe
	Fixed Cost by Capacity	65.00 \$/kW-yr	66.00 \$/kW-yr
	Variable Cost by Generation	4.00\$/MWh	3.00\$/MWh
	Fossil Fuel Cost	0.00 \$/MMBTU	6.00 \$/MMBTU
Financing	Minimum Required IRR	15%	12%
	PPA Escalation Rate	1%	0%
	Loan Rate	8%	7%
	Real Discount Rate	8.20%	8%
	Federal Income Tax	35%	30%
	State Income Tax	7%	0%
	Insurance Rate	0.5%	1%
	Up-front Fee	1%	3.5%
	Construction Period - Months	24	28
	Annual Interest Rate	5%	5.5%
Depreciation	Allow SAM to pick debt fraction	<input type="checkbox"/>	<input checked="" type="checkbox"/>
	Federal	5-yr MACRS	Straight line (25 yr)
	State	5-yr MACRS	No depreciation

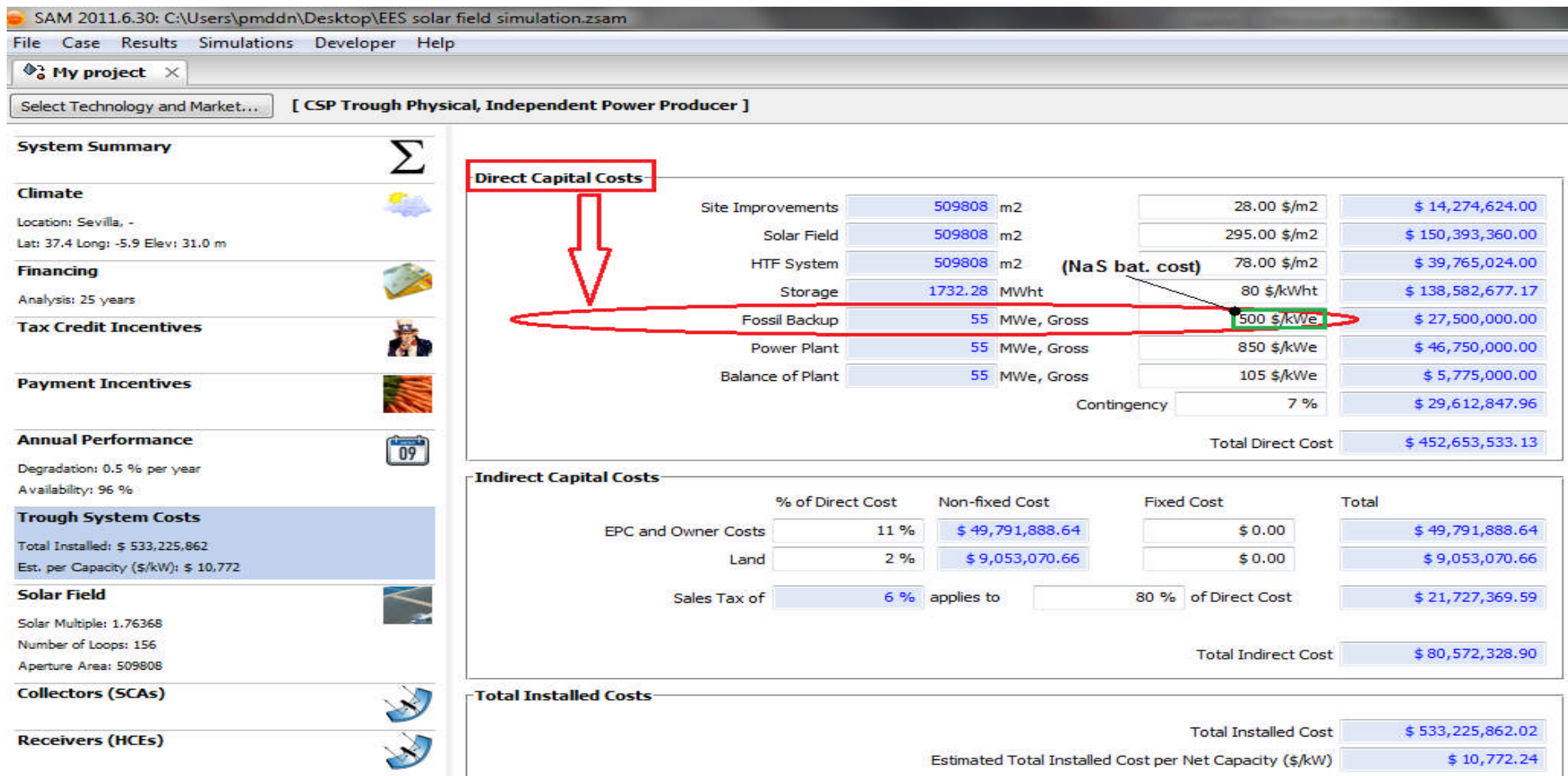


Figure 0-1: SAM window illustrating modification made to the “Fossil back-up” parameter of the “Trough System Costs” tab in the SAM 2011 programme.

Receiver (HCE) Type 1

Configuration name: No library match. Choose receiver from library...

Receiver Geometry

Absorber tube inner diameter	0.154 m	Absorber flow plug diameter	0.114 m
Absorber tube outer diameter	0.168 m	Internal surface roughness	4.5e-005
Glass envelope inner diameter	0.18 m	Absorber flow pattern	Annular flow
Glass envelope outer diameter	0.19 m	Absorber material type	304L

Parameters and Variations

	Variation 1	Variation 2	Variation 3	Variation 4*
Variant weighting fraction*	0.985	0.01	0.005	0
Absorber Parameters:				
Absorber absorptance	0.96	0.96	0.8	0
Absorber emittance	Table...	0.65	0.65	0
Envelope Parameters:				
Envelope absorptance	0.02	0.02	0	0
Envelope emittance	0.86	0.86	1	0
Envelope transmittance	0.963	0.963	1	0
	<input type="checkbox"/> Broken Glass	<input type="checkbox"/> Broken Glass	<input checked="" type="checkbox"/> Broken Glass	<input type="checkbox"/> Broken Glass
Gas Parameters:				
Annulus gas type	Hydrogen	Air	Air	Hydrogen
Annulus pressure (torr)	0.0001	750	750	0
Heat Loss at Design:				
Estimated avg. heat loss (W/m)	150	1100	1500	0
Optical Effects:				
Bellows shadowing	0.96	0.96	0.96	0.963
Dirt on receiver	0.98	0.98	1	0.98

Note: *The variant weighting fractions and Variation 4 inputs are not part of the library.

Figure 0-2: SAM window showing the EES receiver tube specifications used in the SAM simulation

Collector (SCA) Type 1

Configuration name: No library match. Choose collector from library...

Collector Geometry

Reflective aperture area	817 m ²	Number of modules per assembly	12
Aperture width, total structure	5.77 m	Average surface-to-focus path length	1.8 m
Length of collector assembly	144 m	Piping distance between assemblies	1 m

Optical Parameters

Incidence angle modifier coeff 1	1	Geometry effects	0.98
Incidence angle modifier coeff 2	0.0506	Mirror reflectance	0.935
Incidence angle modifier coeff 3	-0.1763	Dirt on mirror	0.95
Tracking error	0.994	General optical error	0.99

Optical Calculations

Length of single module	12 m	End loss at design	0.998515
Incidence angle modifier	1.00148	Optical efficiency at design	0.856609

Figure 0-3: SAM window showing the EES collector specifications used in the SAM simulation

Storage System

Full load hours of TES	12 hr	Aux heater outlet set temp	500
Storage volume	11236.2 m ³	Tank heater capacity	25 MWt
TES Thermal capacity	1732.28 MWt	Tank heater efficiency	0.98
Parallel tank pairs	1	Hot side HX approach temp	5 °C
Tank height	14 m	Cold side HX approach temp	7 °C
Tank fluid min height	1 m	Heat exchanger derate	1
Tank diameter	31.9669 m	Initial TES fluid temp	300 °C
Min fluid volume	802.585 m ³	Storage HTF fluid	Solar Salt
Tank loss coeff	0.4 W/m ² -K	User-defined HTF fluid	Edit...
Estimated heat loss	0.335702 MWt	Fluid Temperature	400 °C
Cold tank heater set point	250 °C	TES fluid density	1835.6 kg/m ³
Hot tank heater set point	365 °C	TES specific heat	1.5118 kJ/kg-K
Fossil dispatch mode	Supplemental operation		

Figure 0-4: SAM window showing thermal storage specifications used in the simulation

Plant Capacity

Design gross output	55 MWe
Estimated gross to net conversion factor	0.9
Estimated net output at design (nameplate)	50 MWe

Note: Parasitic losses typically reduce net output to approximately 90 % of design gross power

Power Block Design Point

Rated cycle conversion efficiency	0.381
Design inlet temperature	500 °C
Design outlet temperature	300 °C
Boiler operating pressure	100 bar
Fossil backup boiler LHV efficiency	0.9
Steam cycle blowdown fraction	0.02

Plant Control

Low resource standby period	2 hrs
Fraction of thermal power needed for standby	0.2
Power block startup time	0.5 hr
Fraction of thermal power needed for startup	0.2
Minimum required startup temp	300 °C
Max turbine over design operation	1.05
Min turbine operation	0.25
Minimum power block restart time	1 hr
Turbine Inlet Pressure Control	Fixed pressure

Cooling System

Condenser type	Evaporative	Hybrid Dispatch	
Ambient temp at design	20 °C	Period 1:	0
Ref. Condenser Water dT	10 °C	Period 2:	0
Approach temperature	5 °C	Period 3:	0
ITD at design point	16 °C	Period 4:	0
Condenser pressure ratio	1.0028	Period 5:	0
Min condenser pressure	1.25 inHg	Period 6:	0
Cooling system part load levels	2	Period 7:	0
		Period 8:	0
		Period 9:	0

Note: Hybrid dispatch control parameters refer to the dispatch periods defined on the thermal storage page.

Figure 0-5: SAM window showing the power block specifications used in the simulation

Parasitics				Design Point Totals				
Piping thermal loss coefficient	<input type="text" value="0.45"/>	W/m ² -K						
Tracking power	<input type="text" value="125"/>	W/sca		Tracking	<input type="text" value="78000"/> W			
Required pumping power for HTF through power block	<input type="text" value="0.55"/>	kJ/kg						
Required pumping power for HTF through storage	<input type="text" value="0.15"/>	kJ/kg						
Fraction of rated gross power consumed at all times	<input type="text" value="0.0055"/>			Fixed	<input type="text" value="0.3025"/> MWe			
			Factor	Coeff 0	Coeff 1	Coeff 2		
Balance of plant parasitic	<input type="text" value="0"/>	MWe/MWcap	<input type="text" value="1"/>	<input type="text" value="0.483"/>	<input type="text" value="0.517"/>	<input type="text" value="0"/>	BOP	<input type="text" value="0"/> MWe
Aux heater, boiler parasitic	<input type="text" value="0.02273"/>	MWe/MWcap	<input type="text" value="1"/>	<input type="text" value="0.483"/>	<input type="text" value="0.517"/>	<input type="text" value="0"/>	Aux	<input type="text" value="1.25015"/> MWe

Figure 0-6: Window showing collector specifications used in the simulation

System Summary	
Nameplate Capacity	<input type="text" value="49500"/> kW
Total Direct Cost	<input type="text" value="452,653,533.13"/> \$
Total Installed Cost	<input type="text" value="533,225,862.02"/> \$
Total Installed Cost per Capacity	<input type="text" value="10,772.24"/> \$/kW
Analysis Period	<input type="text" value="25"/> years
Inflation Rate	<input type="text" value="2.5"/> %
Real Discount Rate	<input type="text" value="8"/> %

Figure 0-7: A summary of important plant data

Before results obtained from SAM 2011 software are evaluated, it is important to point out that they only serve to provide “a basic idea of plant economics” as a thorough economic analysis is outside the scope of this work. It must also be noted that in the SAM simulations, all of the 12 storage hours were represented as thermal, due to the inability of the software to model electrical storage.

In reality, the NaS cells would provide four hours of full rated power at 50 MWe, and the effect of this benefit cannot be seen in the simulations due to the mentioned software limitations. However the effect of the EES receiver’s physical construction, annular flow characteristics and NaS battery cost were successfully integrated into the SAM software

simulation, and this still allows the simulations to be of some worth in assessing the “basic economics” of the conceptual plant.

One of the most important results for comparison with the Andasol -1 case study was the LCOE value. From the SAM results, it can be seen that the cost of the energy produced by for the EES receiver PTC plant the plant is almost double the value that obtained in the Andasol – 1 case study. A LCOE real value of 50.81 ¢/kWh (USD) was obtained (Figure 0-8) compared to a value of approximately 30 ¢/kWh (USD) obtained in the case study and representative of a standard Andasol -1 type PTC plant.

This is not surprising due to the significant cost of the NaS cells into the receiver a value which would be even higher if the costs involved in manufacturing and deploying the hybridized EES receiver are taken into account. Other important power production and plant cost results obtained from the SAM 2011 software are given in Figure 0-9 to Figure 0-13 of this appendix.

Results – SAM software simulations of EES Receiver based PTC Power Plant

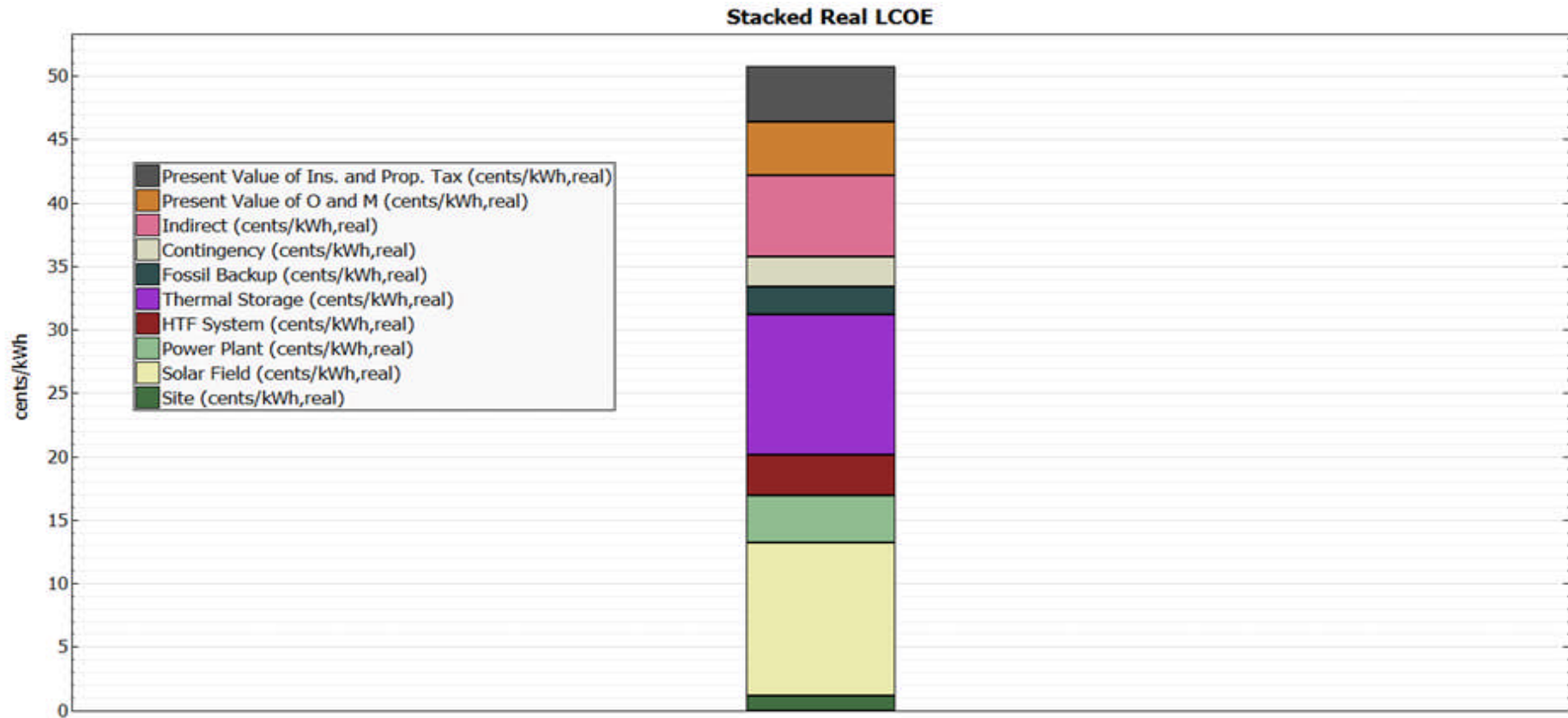


Figure 0-8: Simulated stacked real levelized cost of energy (LCOE) for EES receiver PTC plant (SAM)

Results – SAM software simulations of EES Receiver based PTC Power Plant

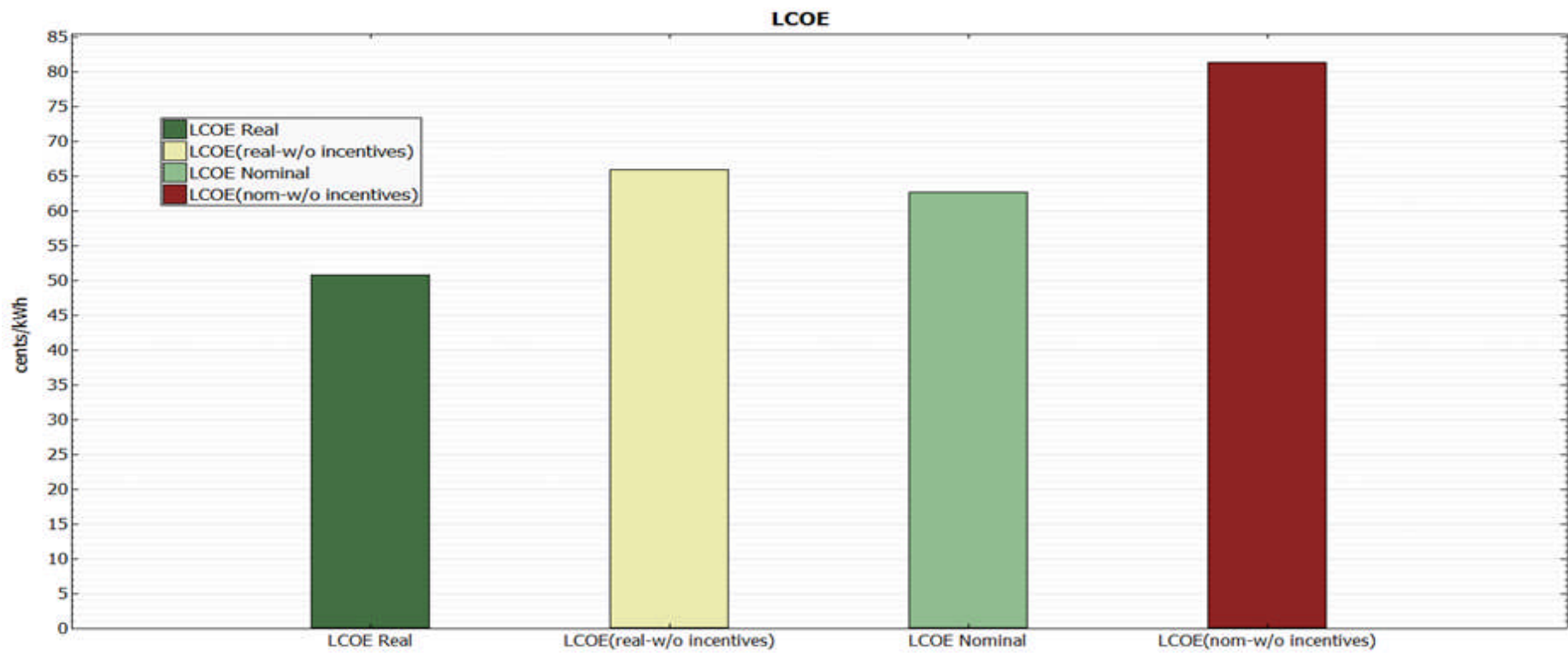


Figure 0-9: Simulated levelized cost of energy (LCOE) for EES receiver PTC plant (SAM)

Results – SAM software simulations of EES Receiver based PTC Power Plant

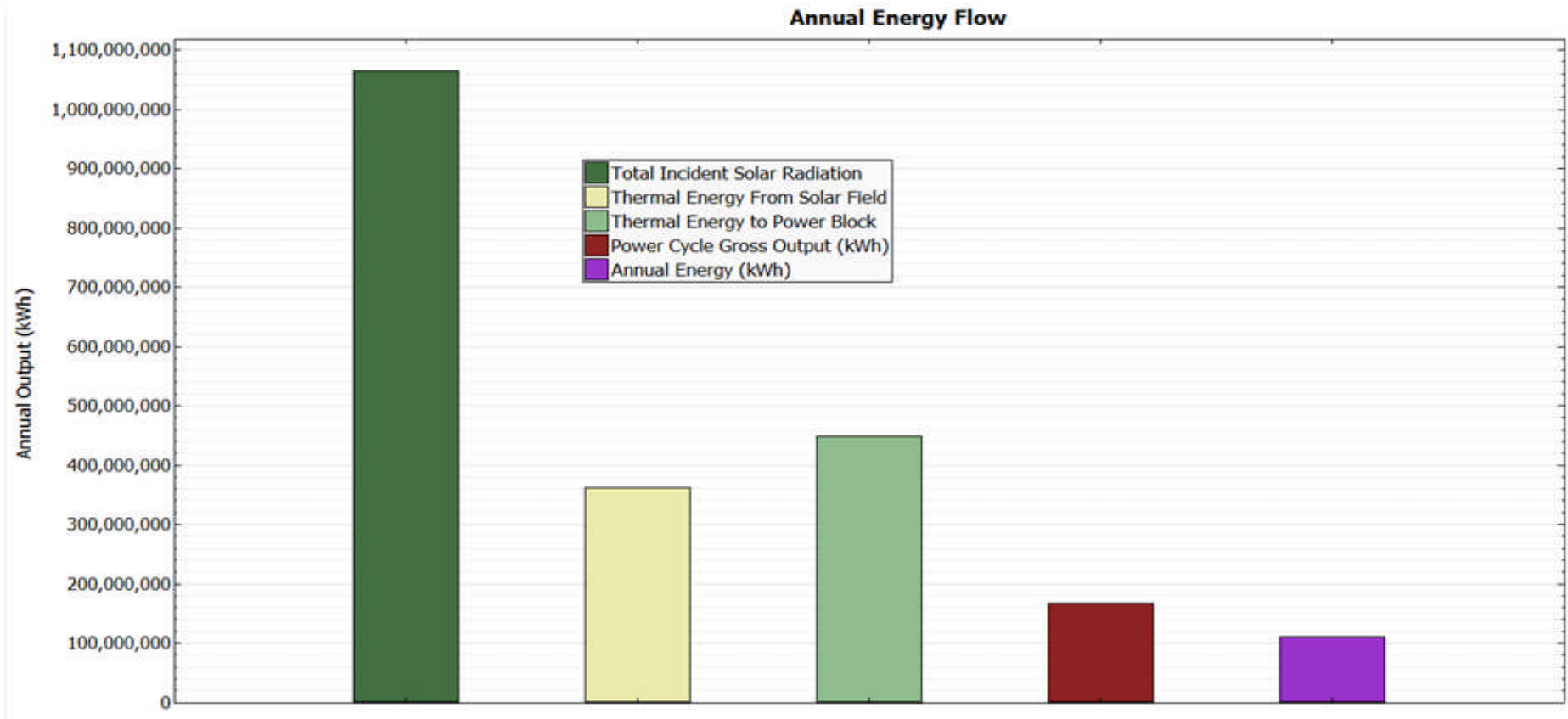


Figure 0-10: Simulated annual energy flow for EES receiver PTC plant (SAM)

Results – SAM software simulations of EES Receiver based PTC Power Plant

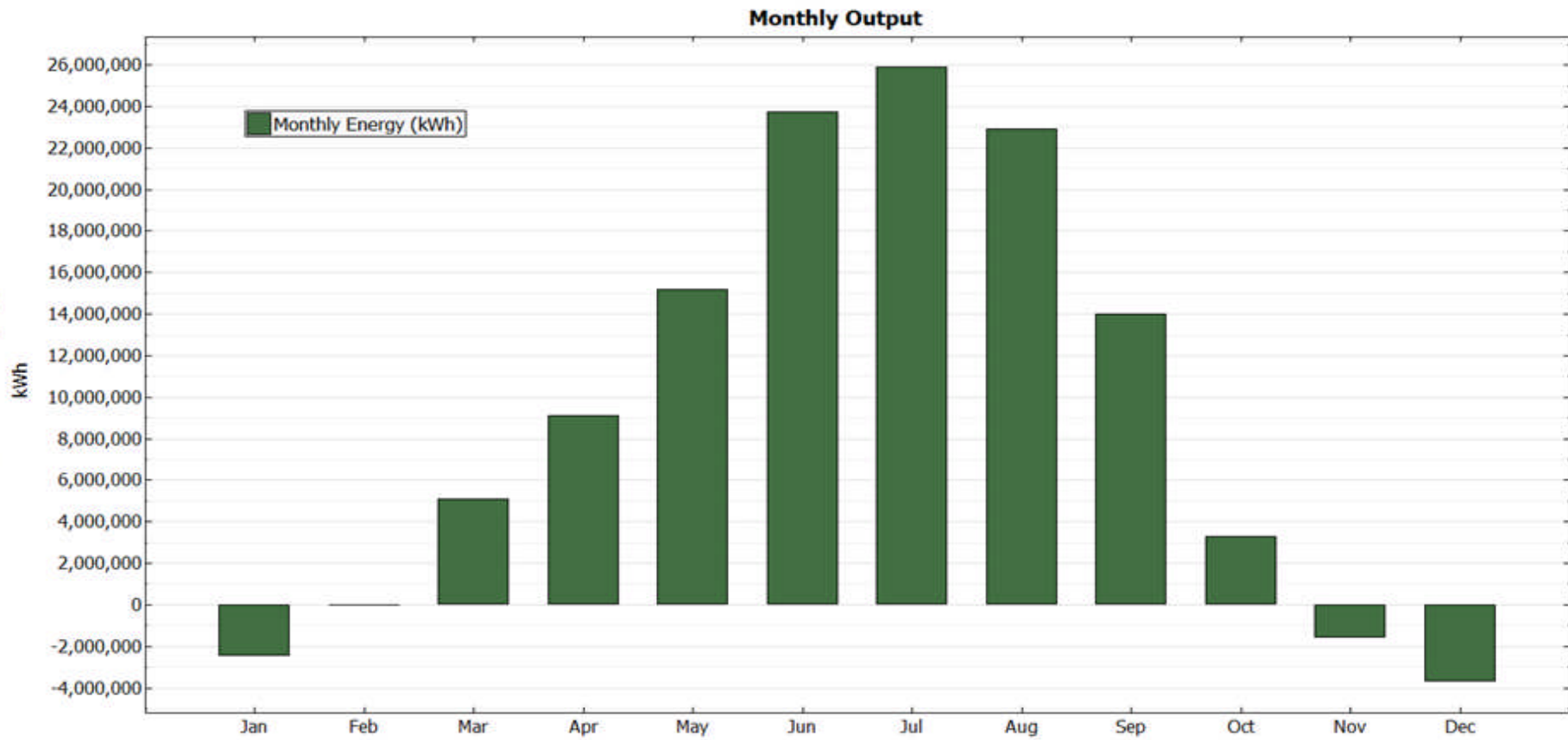


Figure 0-11: Simulated monthly energy output for EES receiver PTC plant (SAM)

Results – SAM software simulations of EES Receiver based PTC Power Plant

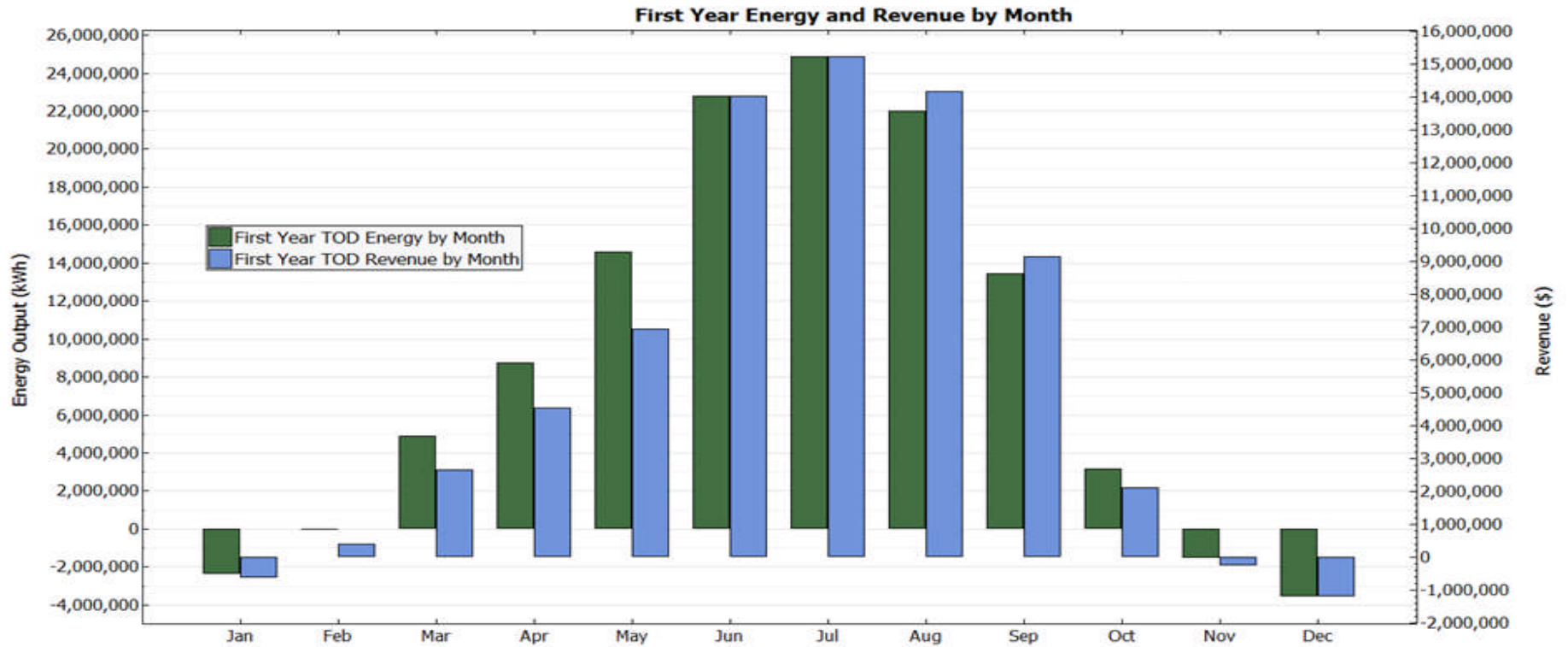


Figure 0-12: Simulated first year revenue by month, for EES receiver PTC plant (SAM)

Results – SAM software simulations of EES Receiver based PTC Power Plant

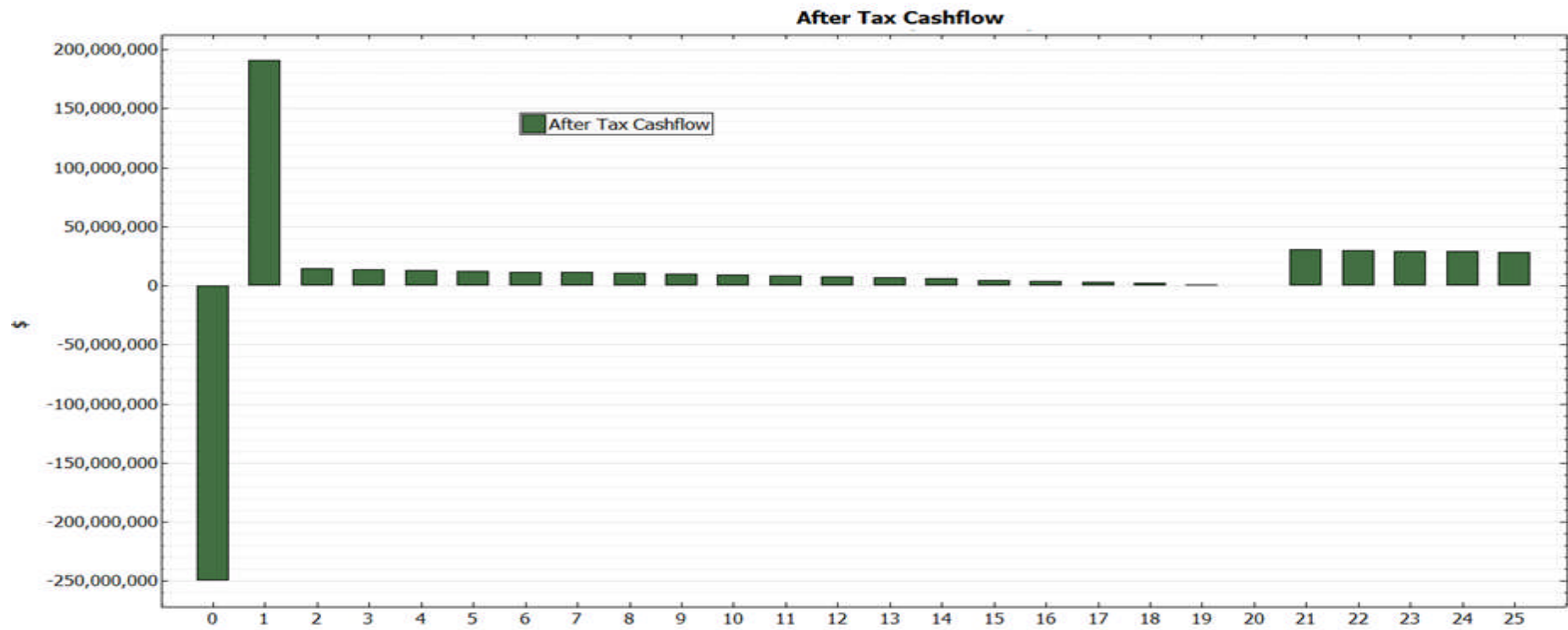


Figure 0-13: Simulated after tax cashflow for EES receiver PTC plant for 25 years (SAM)

Appendix H

Microsoft Visual Basic (VB) Code used for Model Solution

Sub Macro4()

,

'USER INFORMATION: This code calculates the temperature profiles of both HTF and NaS cell along the cross sectional profile of a hybrid SECT PTC receiver tube using a Forward difference "PREDICTOR" and a Modified central difference "CORRECTOR"

'SECTION 1: DECLARATIONS

Dim startnumber As Integer *'Declaration of start number integer*
Dim endnumber As Integer *'Declaration of end number integer*
Dim rangeCell *'Declaration of range of MS Excel cells used for computation*
Dim changeCell *'Declaration of "changing cell" used in MS goalseek*
Dim cyclenumber *'Declaration of the HTF cycle number being simulated*
Dim Thtf_init *'Declaration of initial HTF temperature at given step*
Dim Tnas_init *'Declaration of initial NaS battery temperature at given step*
Dim Thtf_start *'Declaration of starting HTF temperature for each line of calculation*
Dim Tnas_start *'Declaration of starting NaS battery temperature for each line of calculation*
Dim Thtf_diff *'Declaration of difference between the predicted and corrected HTF temperature*
Dim Tnas_diff *'Declaration of difference between the predicted and corrected battery temperature*
Dim Tnas_cold *'Declaration of "cold" battery temperature*

Dim deltaThtf_1 *'Declaration of the predicted change in HTF temperature per increment*

Dim deltaTnas_1 *'Declaration of the predicted change in battery temperature per increment*

Dim deltaThtf_2 *'Declaration of the corrected HTF temperature change per increment*

Dim deltaTnas_2 *'Declaration of the corrected battery temperature change per increment*

Dim Thtf_pred *'Declaration of value of the predicted HTF temperature*

Dim Tnas_pred *'Declaration of value of the predicted battery temperature*

Dim Thtf_mod *'Declaration of value of the modified HTF temperature*

Dim Tnas_mod *'Declaration of value of the modified battery temperature*

Dim phase_change_energy *'Declaration of current value of battery phase change energy*

Dim absorbed_heat_nas *'Declaration of current value of heat energy absorbed by battery*

Dim converge_tolerance *'Declaration of convergence tolerance for finite difference approximation of the*
PDE'S

Dim start_htf_cell *'Declaration of start cell for HTF temperature calculation*

Dim start_nas_cell *'Declaration of start cell for battery temperature calculation*

Dim Thtf_init_next *'Declaration of the initial HTF temperature for next increment*

Dim htf_vel *'Declaration of HTF velocity*

Dim increment *'Declaration of step size used in computation*

Dim htf_loop_time *'Declaration of HTF loop transit time*

Dim cell_offset *'Declaration of offset for copy/paste of results in new worksheet at end of*
computation

```
Dim cell_select           'Declaration of variable used for selection of worksheet results
Dim unabs_latent_heat_energy 'Declaration of unabsorbed latent heat energy for use in next cycle
Dim latent_heat_energy    'Declaration of variable representing latent heat value of cell in computation
Dim nas_mCp_liquid        'Declaration of liquid "mcp" value of battery
Dim nas_mCp_solid         'Declaration of solid "mcp" value of battery

Dim temp_diff             'Declaration of temperature difference between battery and phase change
temperatures

Dim delta_t_pc            'Declaration of loop transit time associated with absorbing phase change energy
Dim delta_t_sh            'Declaration of loop transit time associated with absorbing specific heat energy

converge_tolerance = Range("B28") 'Definition of tolerance
cyclenumber = Range("D28")         'Initialization of cyclenumber
Tnas_cold = Range("J28")           'Initialization of Nas cold temperature
Thtf_cold = Range("G28")           'Initialization of htf cold temperature
startnumber = Range("C28")         'Initialization of startnumber
endnumber = 1185                   'Initialization of endnumber
htf_vel = Range("AI10")            'Loading of htf velocity value
increment = Range("AH3")           'Loading of increment value
htf_loop_time = Range("A1186")     'Loading of htf loop time (minutes)
```

```
nas_phase_change_energy = Range("H22") 'Loading of battery phase change value  
nas_mCp_liquid = Range("CD14") 'Loading of battery "mcp-liquid" value  
nas_mCp_solid = Range("F22") 'Loading of battery "mcp-solid" value
```

```
'*****  
***
```

```
'START OF MAIN CODE _ WITHIN A "FOR LOOP"
```

```
For Each cell In Range("L32:L1185") 'Definition of range of computation
```

```
    rangeCell = "L" & startnumber 'Definition of rangeCell
```

```
    changeCell = "Q" & startnumber 'Definition of changeCell
```

```
    start_htf_cell = "E" & startnumber
```

```
    start_nas_cell = "AE" & startnumber
```

```
    nas_heat_flux = "BD" & startnumber
```

```
    latent_heat_energy = "BJ" & startnumber
```

```
'*****  
***
```

```
'INITIALIZATIONS WITHIN THE "FOR LOOP"
```

```
If startnumber = 32 Then
```

```
    Thtf_start = Thtf_cold
Else
    Thtf_init = "E" & startnumber           'Initilization of Thtf (collecting historical temp values)'
    Thtf_start = Range(Thtf_init)         'Initialization of Thtf_start (collecting historical temp  
values)'
End If

    Tnas_init = "AE" & startnumber         'Initilization of Tnas (collecting historical temp values)'
    Tnas_start = Range(Tnas_init)         'Initialization of Tnas_start (collecting historical temp  
values)'

    Range(start_htf_cell) = Thtf_start    'Loading Thtf_start into active cell  
(starting value for each calculation-subject to change)'

    Range(start_nas_cell) = Tnas_start    'Loading Tnas_start into active cell  
(starting value for each calculation-subject to change)'

    Thtf_diff = 1                         'Initialization of Thtf_diff'
    Tnas_diff = 1                         'Initialization of Tnas_diff'

'*****
***
'Start of MAIN CODE's, "IF condition"
```

```
If cyclenumber = 0 And Tnas_start < 115.21 Then 'Code for Zero-Pass profile
    Range("AE32:AE1184") = Tnas_cold 'Tnas cold temperature is written to entire AE column in range

'Loop for achieving defined Temperature tolerance
Do while Thtf_diff > converge_tolerance
    Range(rangecell).GoalSeek Goal:=0, ChangingCell:=Range(changece11)
    'Perform a goalseek calculation to obtain "deltaThtf_1"
    deltaThtf_1 = "BH" & startnumber
    'Loading the variable deltaThtf_1, the "First calculated change in HTF temp" with value from cell in
    "CC" column
    Thtf_pred = Thtf_start + Range(deltaThtf_1) 'Calculation of the predicted HTF temperature
    'Predicted HTF temperature is written to "E" column cell, VERWRITING "Thtf_start"
    Range(start_htf_cell) = Thtf_pred
    Range(rangecell).GoalSeek Goal:=0, ChangingCell:=Range(changece11)
    'Perform a goalseek calculation to obtain "deltaThtf_2" Loading the variable deltaThtf_2, the
    "Second" calculated change in HTF in "CC" column
deltaThtf_2 = "BH" & startnumber
'HTF Temp corrector
    'Calculation of the modified HTF temperature
    Thtf_mod = Thtf_start + 0.5 * (Range(deltaThtf_1) + Range(deltaThtf_2))
```

'Calculation of the absolute value of Temp. difference between "predicted" and "modified" HTF temperature

Thtf_diff = Math.Abs(Thtf_pred - Thtf_mod)

'Modified HTF temperature is written to "E" column cell, OVERWRITING "Thtf_pred"

Range(start_htf_cell) = Thtf_mod

Thtf_init_next = "E" & startnumber + 1

Range(Thtf_init_next) = Thtf_mod

Loop

'Starting number is incremented by one

startnumber = startnumber + 1

'Display of current row computation in user window

Range("E28") = "ROW " & startnumber & " OF " & endnumber

'End of code for Zero-Pass profile

'*****

'PERIOD FROM START-UP TO NaS PHASE CHANGE TEMPERATURE OF 115.21 deg.C

ElseIf cyclenumber > 0 **Then**

'Loop for achieving defined Temperature tolerance

Do while Thtf_diff And Tnas_diff > converge_tolerance

'Perform a goalseek calculation to obtain "deltaThtf_1"

Range(rangecell).GoalSeek Goal:=0, ChangingCell:=Range(changece11)

'Loading the variable deltaThtf_1, the "First calclated change in HTF temp" with value from cell in "CC" column

deltaThtf_1 = "CC" & startnumber

If Tnas_start > 115.21 **Then**

 deltaTnas_1 = "BI" & startnumber

Else

 deltaTnas_1 = "BE" & startnumber

End If

'Loading the variable deltaTnas_1, the "First calculated change in NaS temp" with value from cell

deltaTnas_1 = "BE" & startnumber

'Calculation of the predicted HTF temperature

Thtf_pred = Thtf_start + Range(deltaThtf_1)

'Calculation of the predicted HTF temperature

Tnas_pred = Tnas_start + Range(deltaTnas_1)

'Predicted HTF temperature is written to "E" column cell, OVERWRITING "Thtf_start"

Range(start_htf_cell) = Thtf_pred

'Predicted HTF temperature is written to "E" column cell, OVERWRITING "Thtf_start"

Range(start_nas_cell) = Tnas_pred

'Perform a goalseek calculation to obtain "deltaThtf_2"

Range(rangecell).GoalSeek Goal:=0, ChangingCell:=Range(changeCell)

'Loading the variable deltaThtf_2, the "Second" calculated change in HTF & NaS temp with value from cell in "CC" & "BE" columns

deltaThtf_2 = "CC" & startnumber

If Tnas_start >= 115.21 **Then**

 deltaTnas_2 = "BI" & startnumber

Else

 deltaTnas_2 = "BE" & startnumber

End If

'HTF Temp corrector

Thtf_mod = Thtf_start + 0.5 * (Range(deltaThtf_1) + Range(deltaThtf_2)) *'Calculation-modified HTF temperature*

'Calculation of absolute value of Temperature difference between "predicted" and "modified" HTF temperature

`Thtf_diff = Math.Abs(Thtf_pred - Thtf_mod)`

'Modified HTF temperature is written to "E" column cell, OVERWRITING "Thtf_pred"

`Range(start_htf_cell) = Thtf_mod`

`Thtf_init_next = "E" & startnumber + 1`

`Range(Thtf_init_next) = Thtf_mod`

'NaS Temp corrector

'Calculation of the modified HTF temperature

`Tnas_mod = Tnas_start + 0.5 * (Range(deltaTnas_1) + Range(deltaTnas_2))`

'Calculation of the absolute value of Temp. difference between "predicted" and "modified" HTF temperature

`Tnas_diff = Math.Abs(Tnas_pred - Tnas_mod)`

'Modified HTF temperature is written to "E" column cell, OVERWRITING "Thtf_pred"

`Range(start_nas_cell) = Tnas_mod`

Loop

'Temperature increase over residence time in loop

`Tnas_mod = Tnas_start + (Range(deltaTnas_2) * (htf_vel / increment) * htf_loop_time * 60)`

`Range(start_nas_cell) = Tnas_mod`

If Tnas_mod >= 115.21 And Range(latent_heat_energy) >= 0 **Then**

temp_diff = Tnas_mod - 115.21

Range(start_nas_cell) = 115.21

'Calculation of unabsorbed latent heat energy

unabs_latent_heat_energy = Range(latent_heat_energy) - (temp_diff * nas_mCp_liquid)

'Writing of the "unabsorbed energy value" back to the address cell in MS Excel

Range(latent_heat_energy) = unabs_latent_heat_energy

If unabs_latent_heat_energy < 0 **Then**

delta_T_pc = Math.Abs(Range(latent_heat_energy) / (Range(nas_heat_flux) * 60))

delta_t_sh = htf_loop_time - delta_t_pc

'Writing of the "unabsorbed energy value" of zero back to the address cell in MS Excel

Range(latent_heat_energy) = 0

Tnas_mod = 115.21 + (Range(deltaTnas_2) * (htf_vel / increment) * delta_T_pc *

60)

Range(start_nas_cell) = Tnas_mod

ElseIf Range(latent_heat_energy) = 0 **Then**

```
Range(latent_heat_energy) = 0.0001
delta_T_pc = Math.Abs(Range(latent_heat_energy) / (Range(nas_heat_flux) * 60))
    'Temperature increase over residence time in loop
Tnas_mod = 115.21 + (Range(deltaTnas_2) * (htf_vel / increment) * delta_T_pc * 60)
Range(start_nas_cell) = Tnas_mod
Range(latent_heat_energy) = 0
```

End If

End If

```
startnumber = startnumber + 1    'Starting number is incremented by one
Range("E28") = "ROW " & startnumber & " OF " & endnumber    'Display of current row
```

'End of initial heating up section

```
'*****
***
```

Else

End If

Next

If startnumber = endnumber **Then**

'Writing the final HTF value to G28 for the Thtf cold of the next cycle

Range("G28") = Thtf_mod

Range("A31:CC1186").Select

Selection.Copy

Sheets("Sheet7").Select

cell_offset = cyclenumber * 1189

cell_select = "A1" & cell_offset

Range(cell_select).Select

Selection.PasteSpecial Paste:=xlPasteValues, Operation:=xlNone, SkipBlanks _
:=False, Transpose:=False

Selection.PasteSpecial Paste:=xlPasteFormats, Operation:=xlNone, _
SkipBlanks:=False, Transpose:=False

End If

cyclenumber = cyclenumber + 1

Range("D28") = cyclenumber

End Sub

Appendix I

Convergence check for temperature calculation with decreasing step size

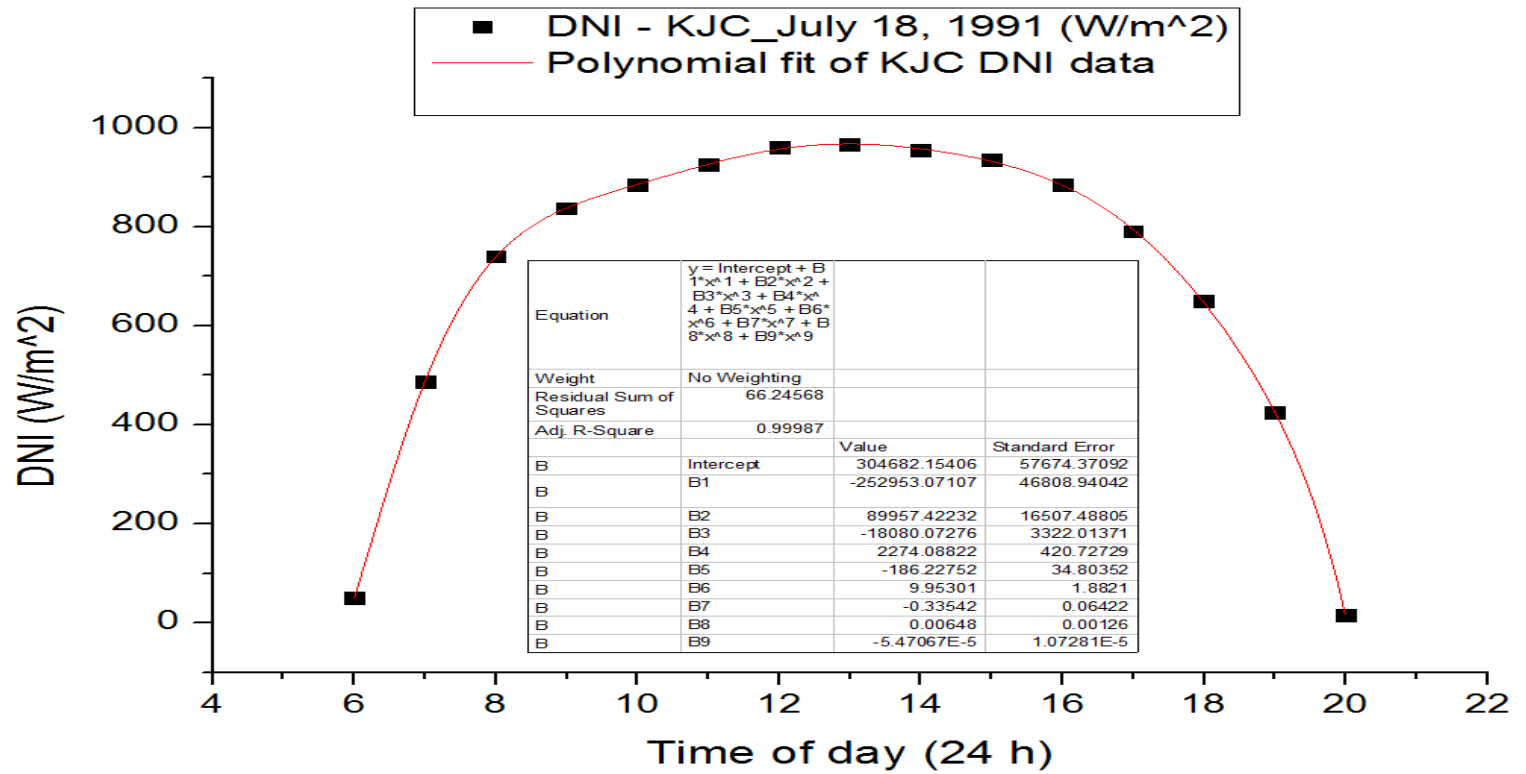
Loop Position, X (m)	Lagrangian Time, t' (s)	Cp (htf), JKg ⁻¹ K ⁻¹	T _{htf, Therminol VP-1}
0	0	2338.060779	310.4488828
1	2.811831534	2339.298192	310.8967061
2	5.623663067	2340.535426	311.3439271

Loop Position, X (m)	Lagrangian Time, t' (s)	Cp (htf), JKg ⁻¹ K ⁻¹	T _{htf, Therminol VP-1}
0	0	2337.132843	310.1127096
0.5	1.405915767	2337.443511	310.225292
1	2.811831534	2337.754247	310.3378655
1.5	4.217747301	2338.065152	310.4504663

Loop Position, X (m)	Lagrangian Time, t' (s)	Cp (htf), JKg ⁻¹ K ⁻¹	T _{htf, Therminol VP-1}
0	0	2336.899671	310.0281887
0.25	0.702957883	2336.977377	310.0563578
0.5	1.405915767	2337.055117	310.0845372
0.75	2.10887365	2337.132891	310.1127267
1	2.811831534	2337.210698	310.1409264

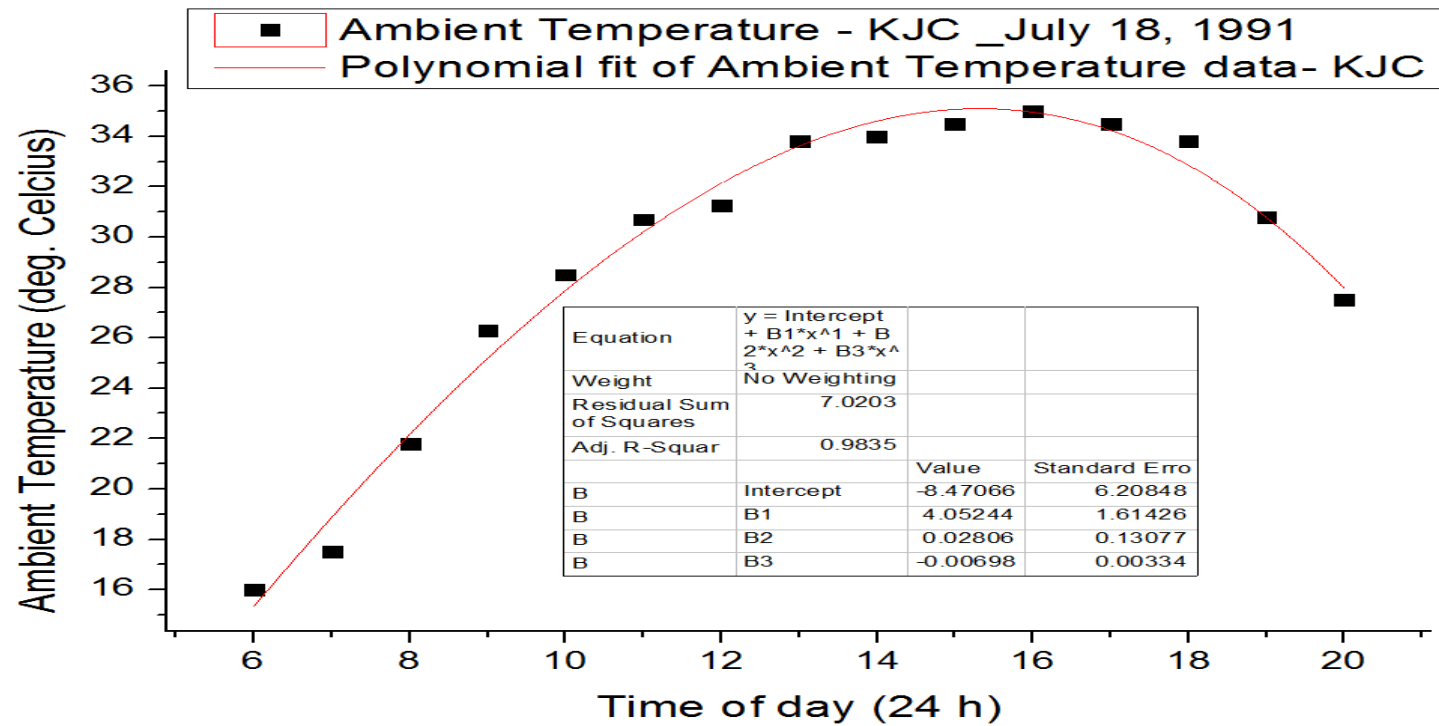
Appendix J

DNI Data used in Simulation – Kramer Junction, USA



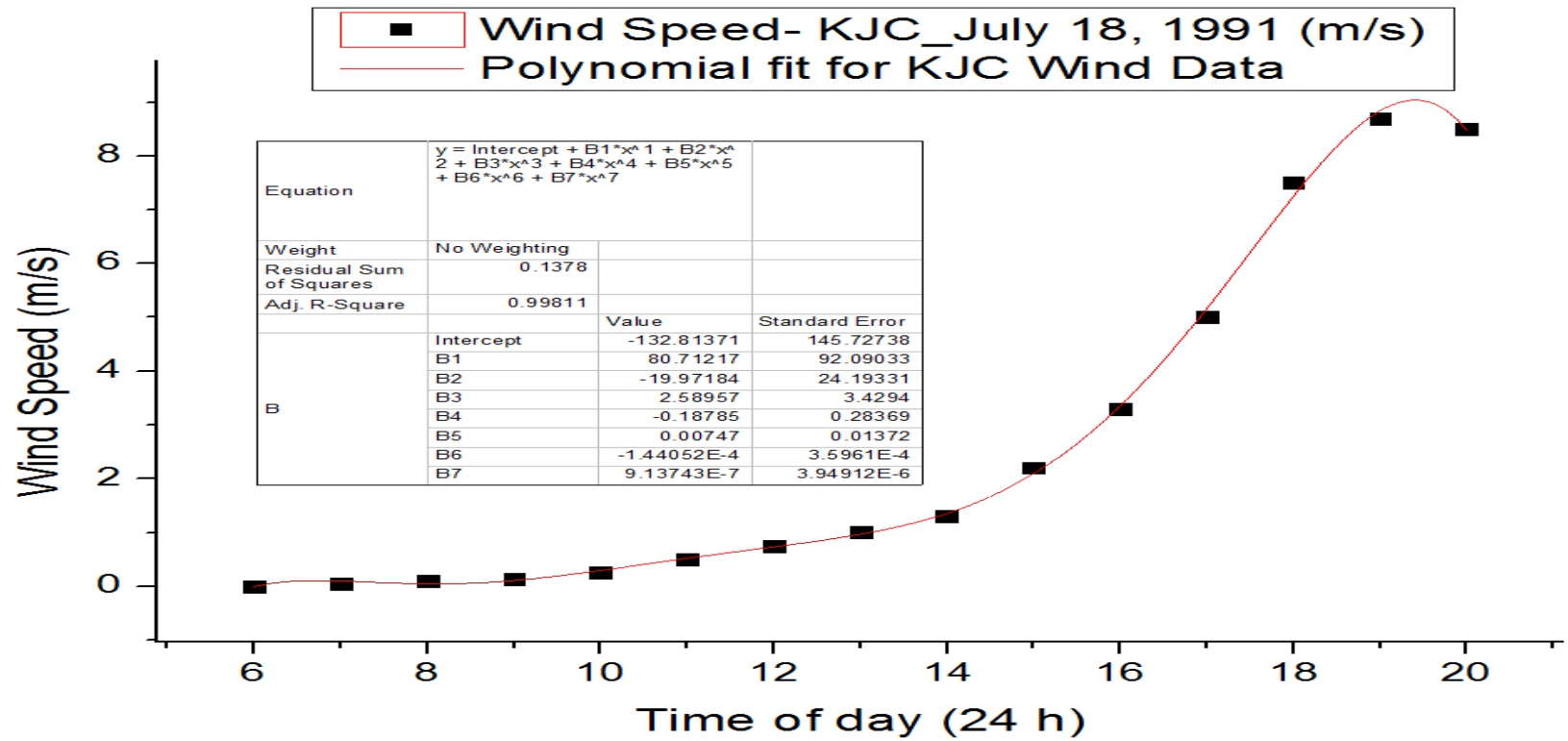
Appendix K

Ambient Temperature Data used in Simulation – Kramer Junction, USA



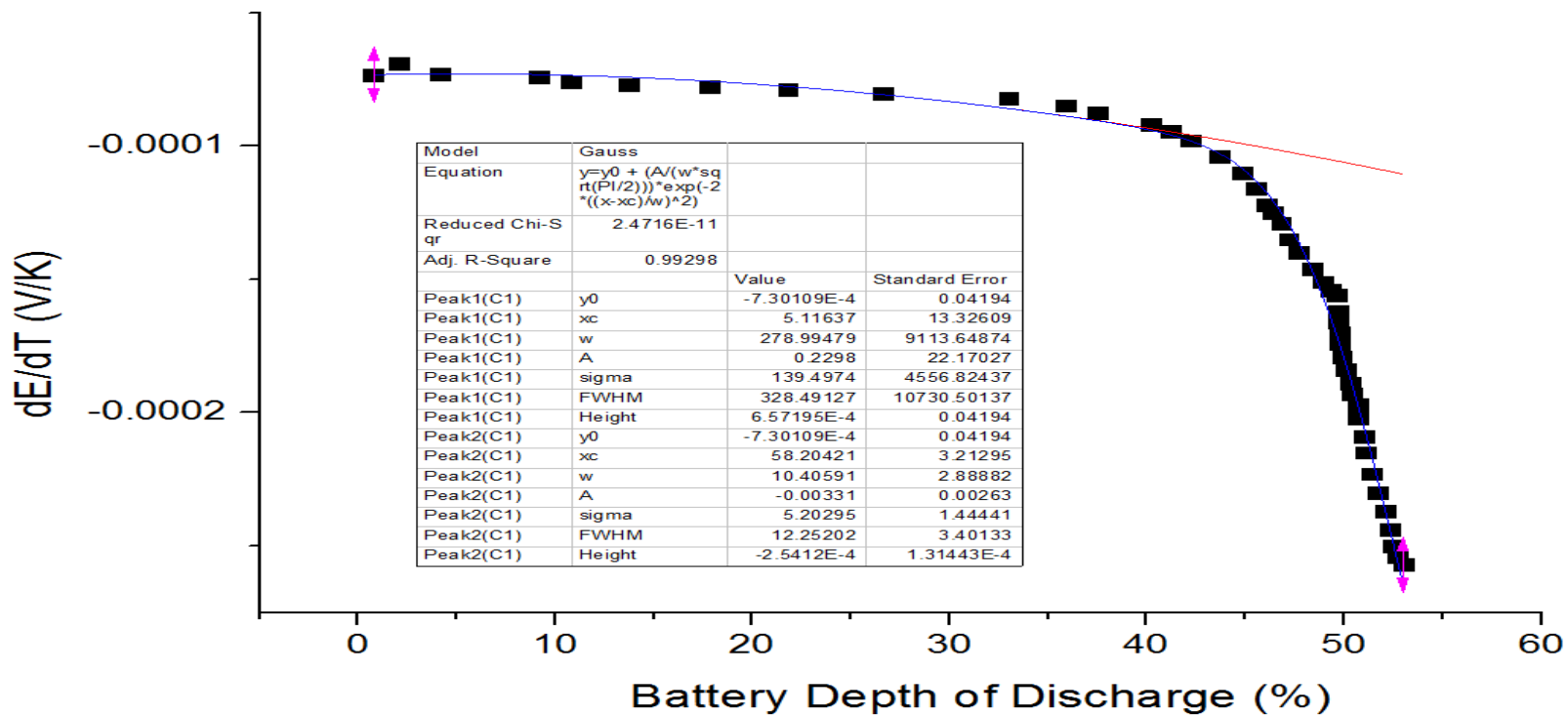
Appendix L

Wind Speed Data used in Simulation – Kramer Junction, USA



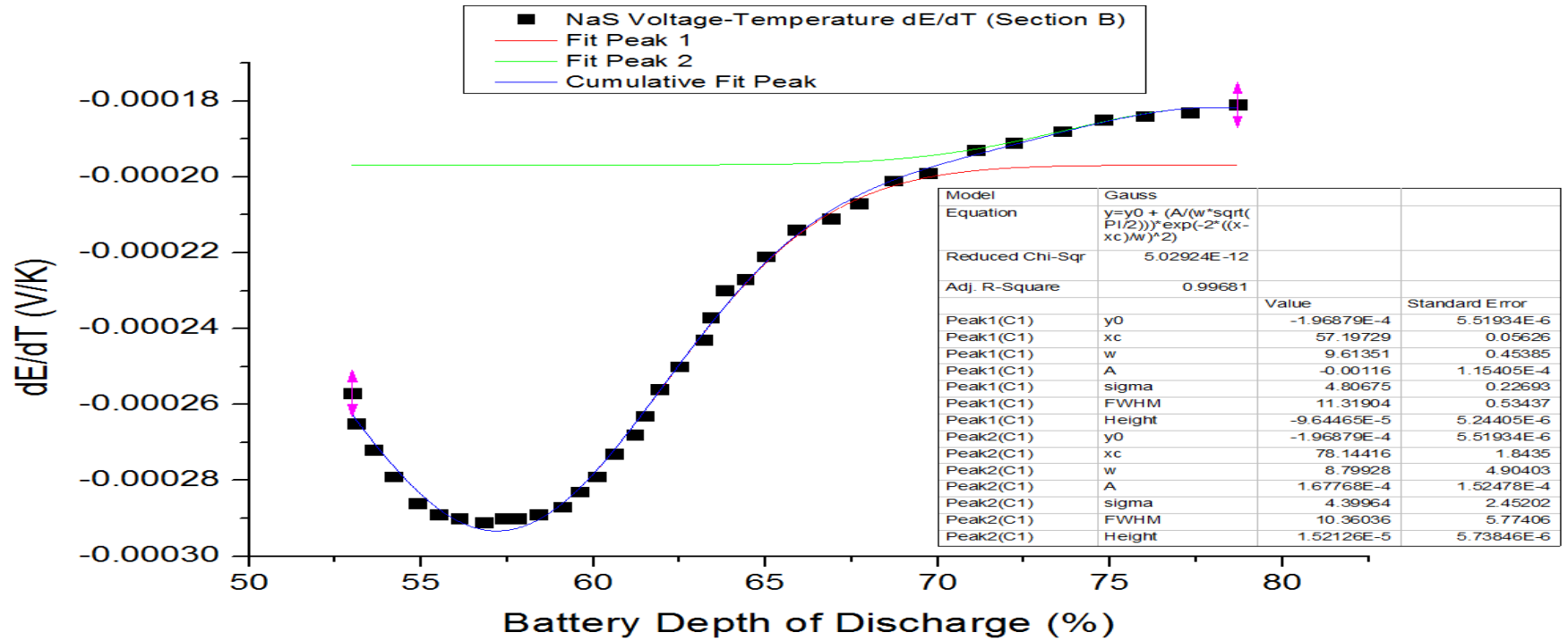
Appendix M

Section A, Graph of NaS Cell Temperature Coefficient of Cell Voltage (Data source: ²¹⁷)



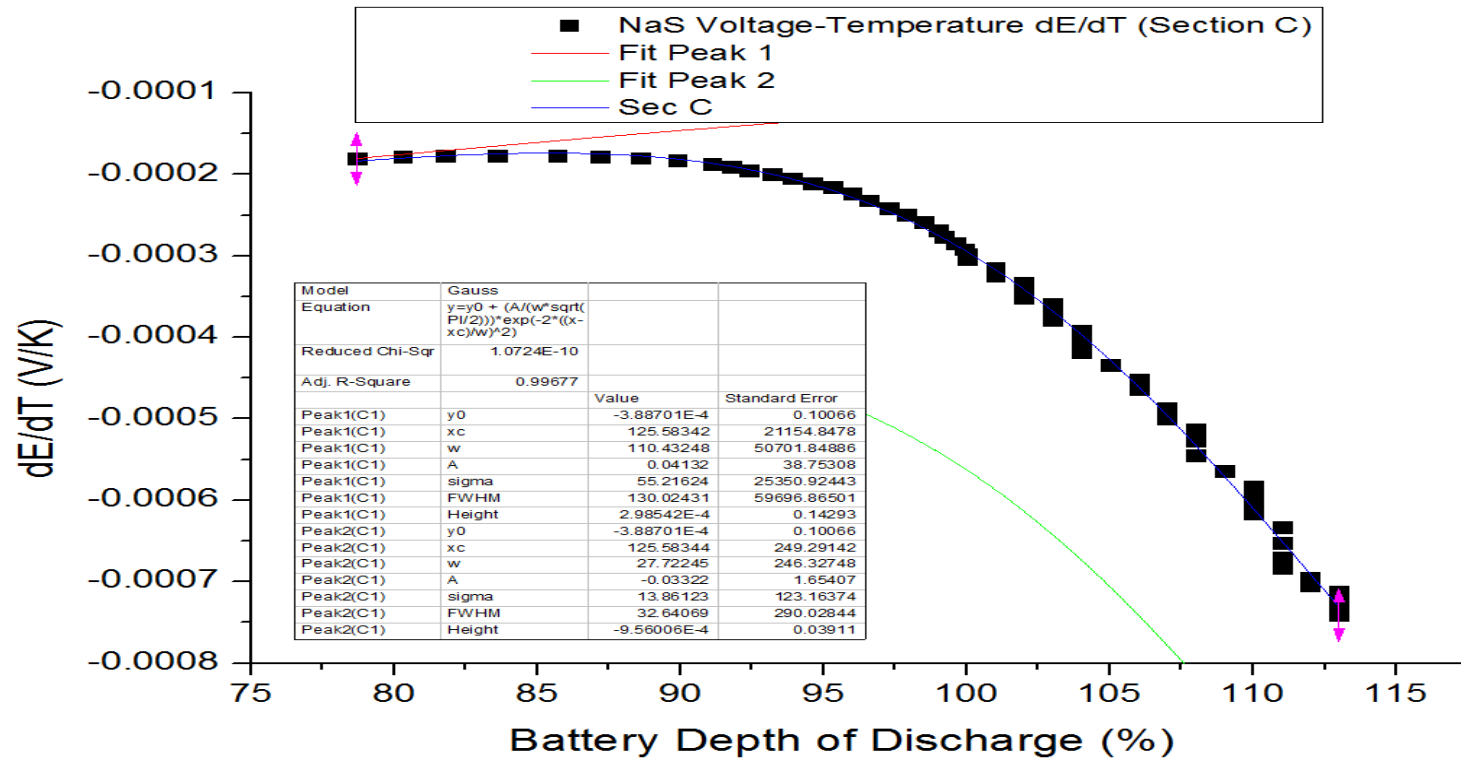
Appendix N

Section B, Graph of NaS Cell Temperature Coefficient of Cell Voltage (Data source: ²¹⁷)



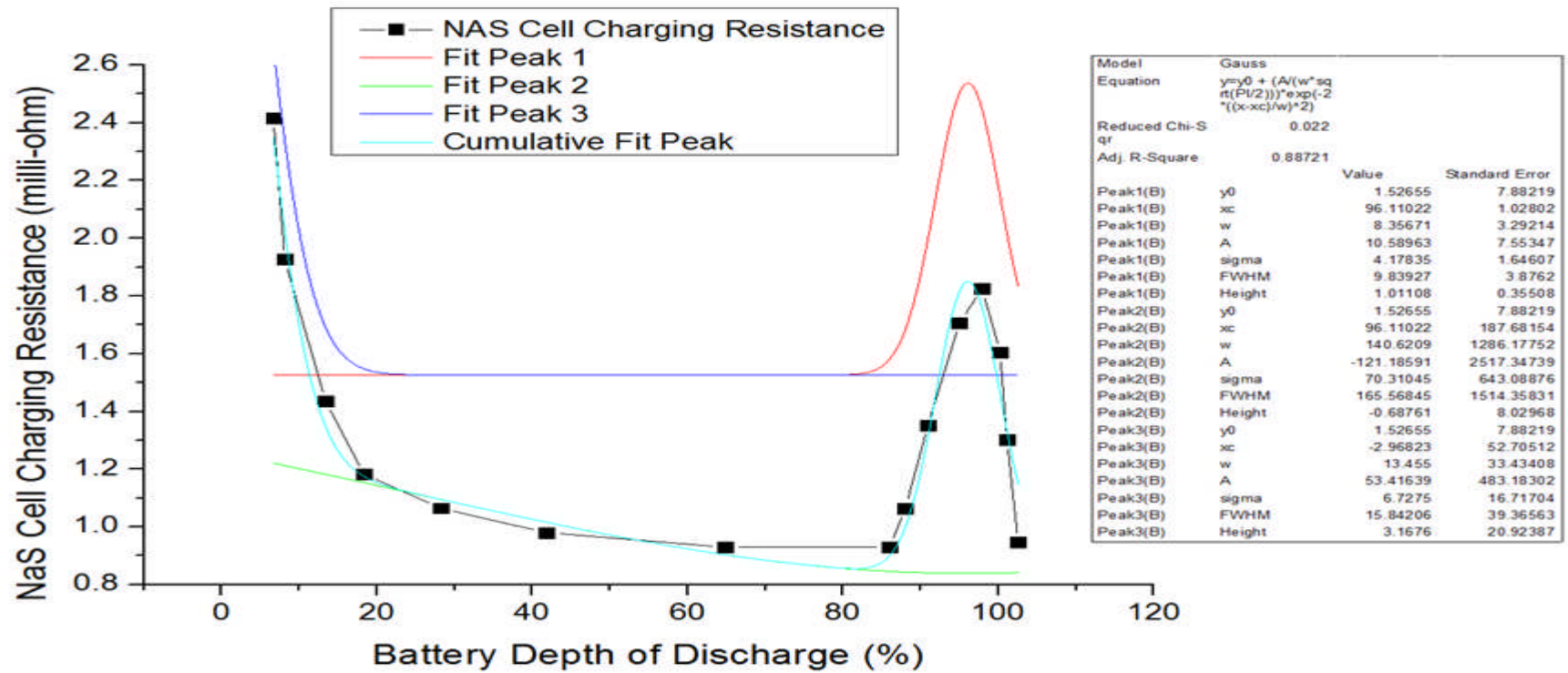
Appendix O

Section C, Graph of NaS Cell Temperature Coefficient of Cell Voltage (Data source: ²¹⁷)



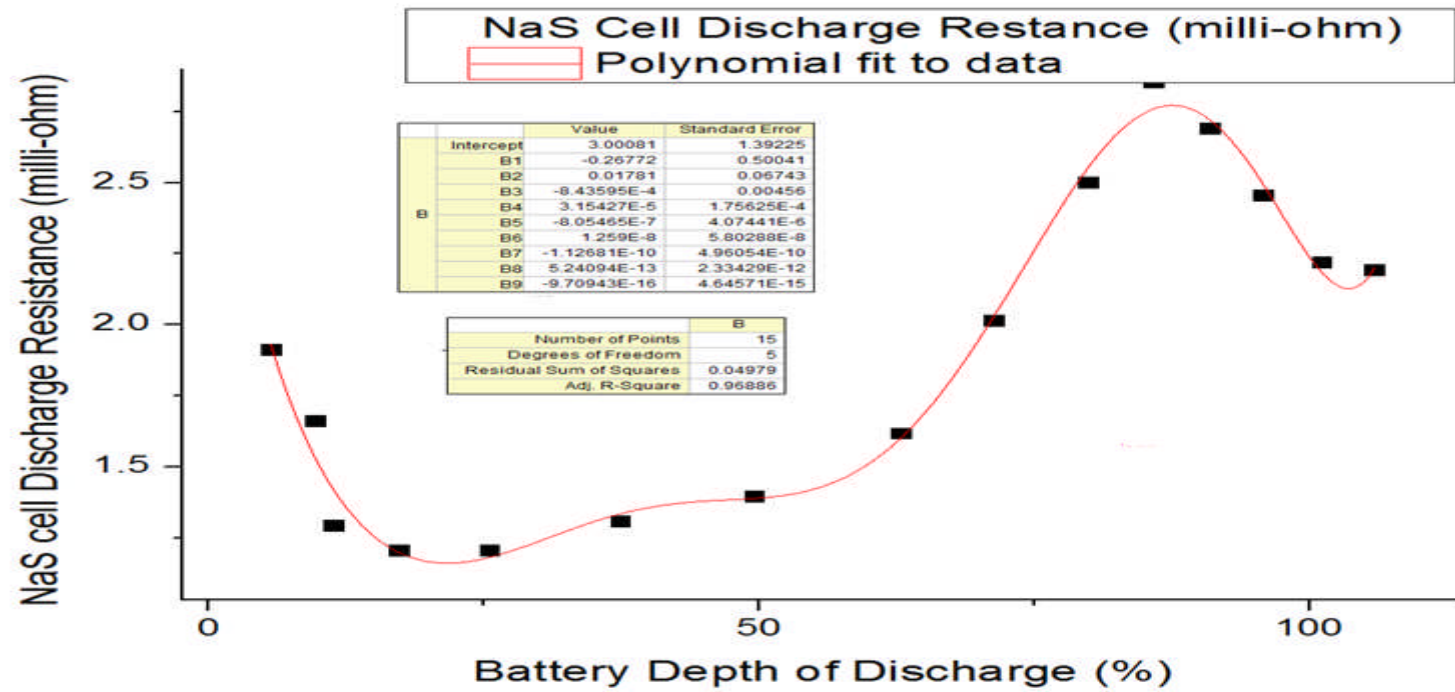
Appendix P

Graph of Tepco T5 NaS Cell Charge Resistance with Depth of Discharge (Data source:¹⁹⁰)



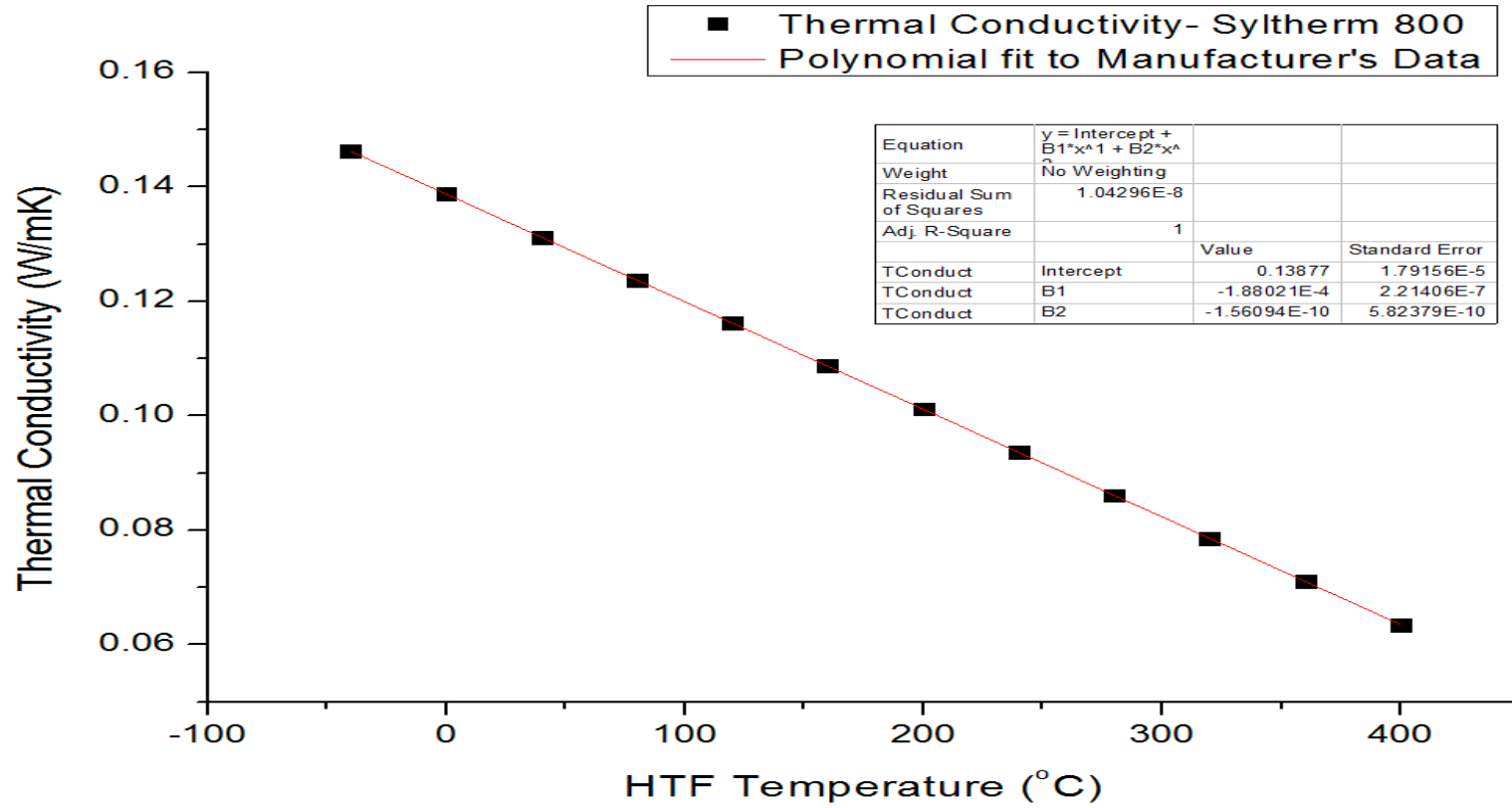
Appendix Q

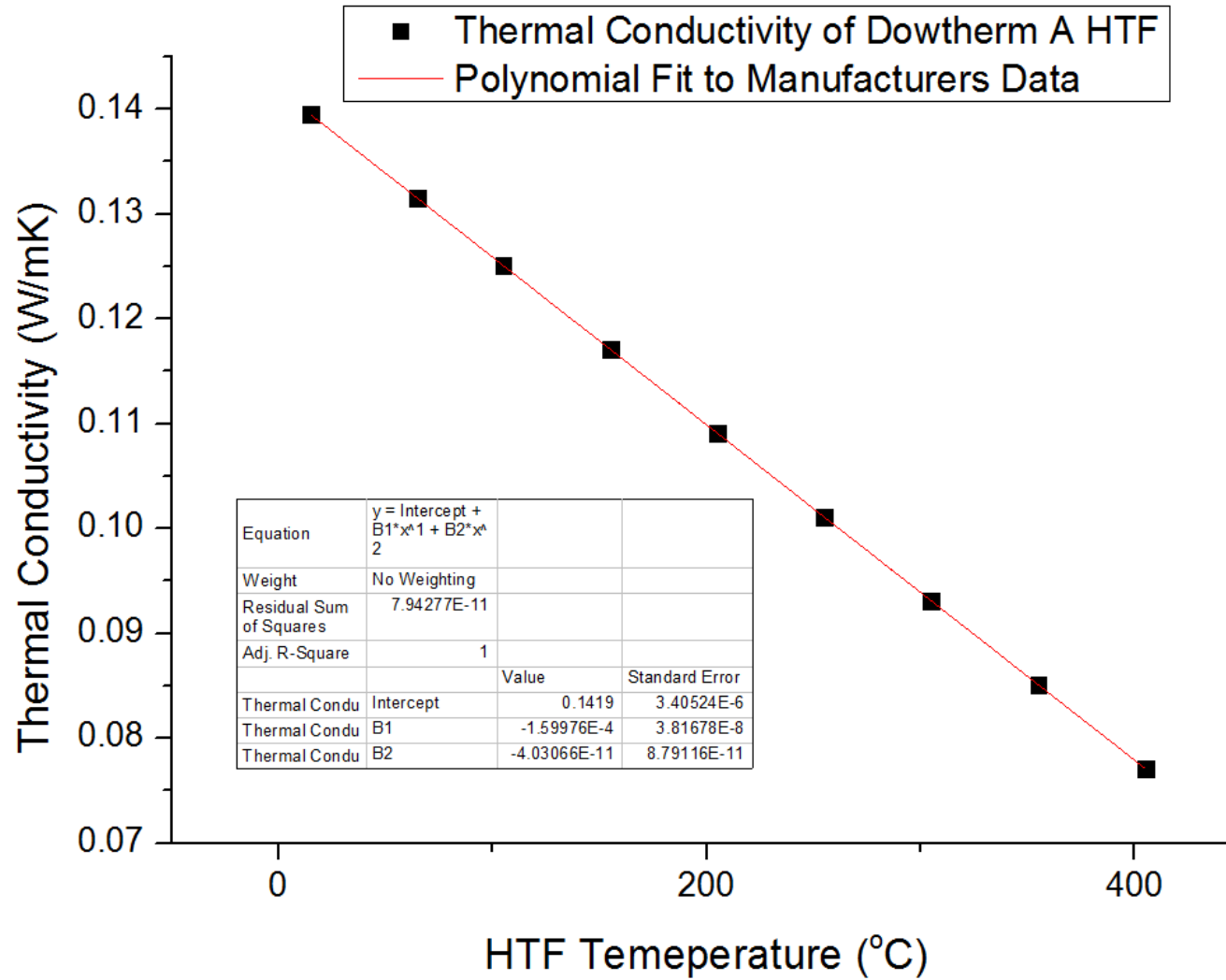
Graph of Tepco T5 NaS Cell Charge Resistance with Depth of Discharge (Data source:¹⁹⁰)



Appendix R

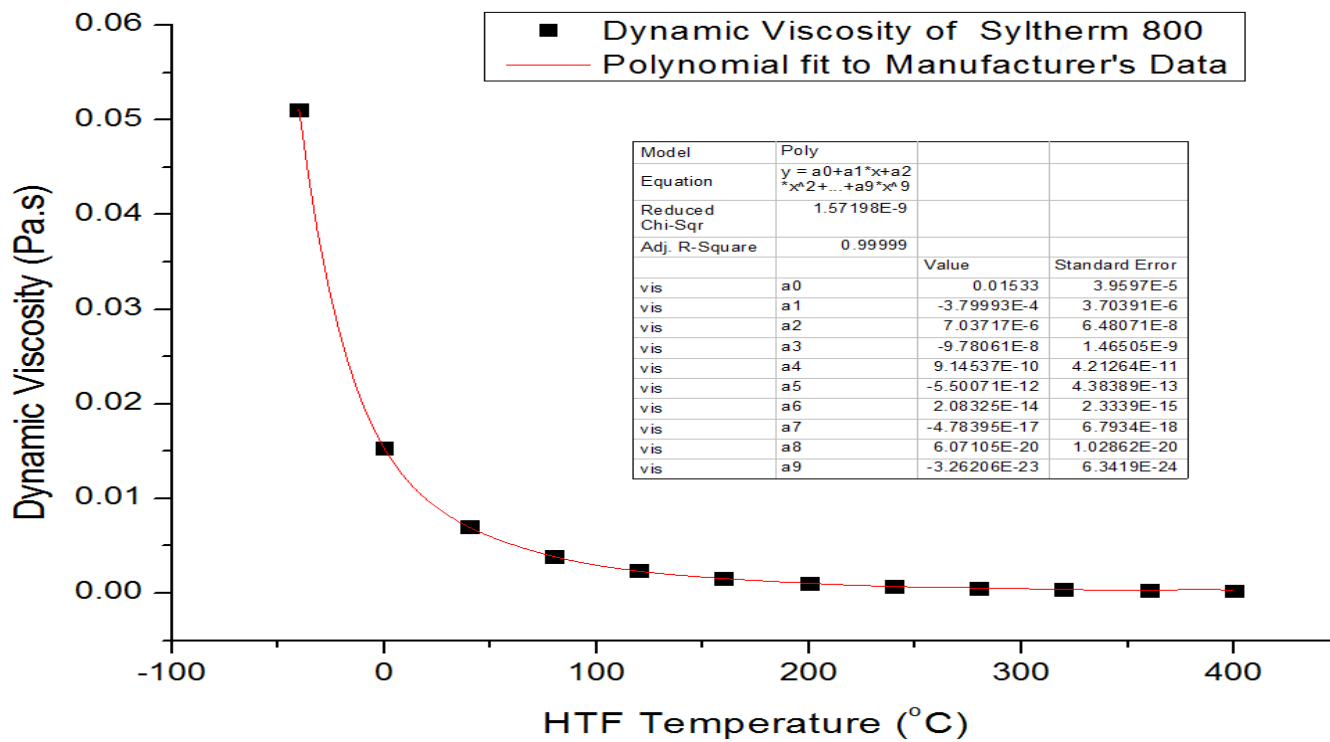
Physical properties (Thermal conductivity) data for Syltherm 800 and Dowtherm A HTF's





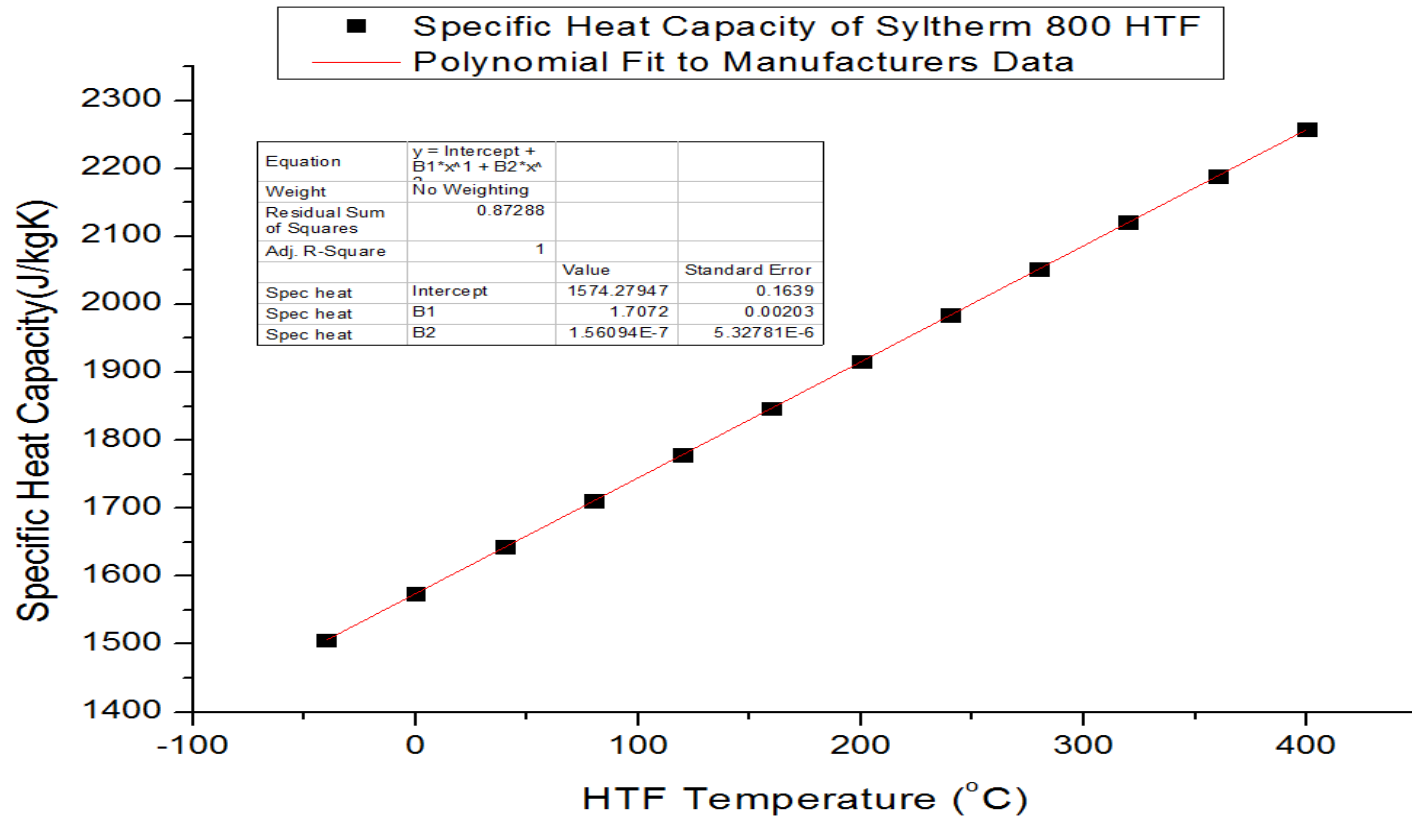
Appendix S

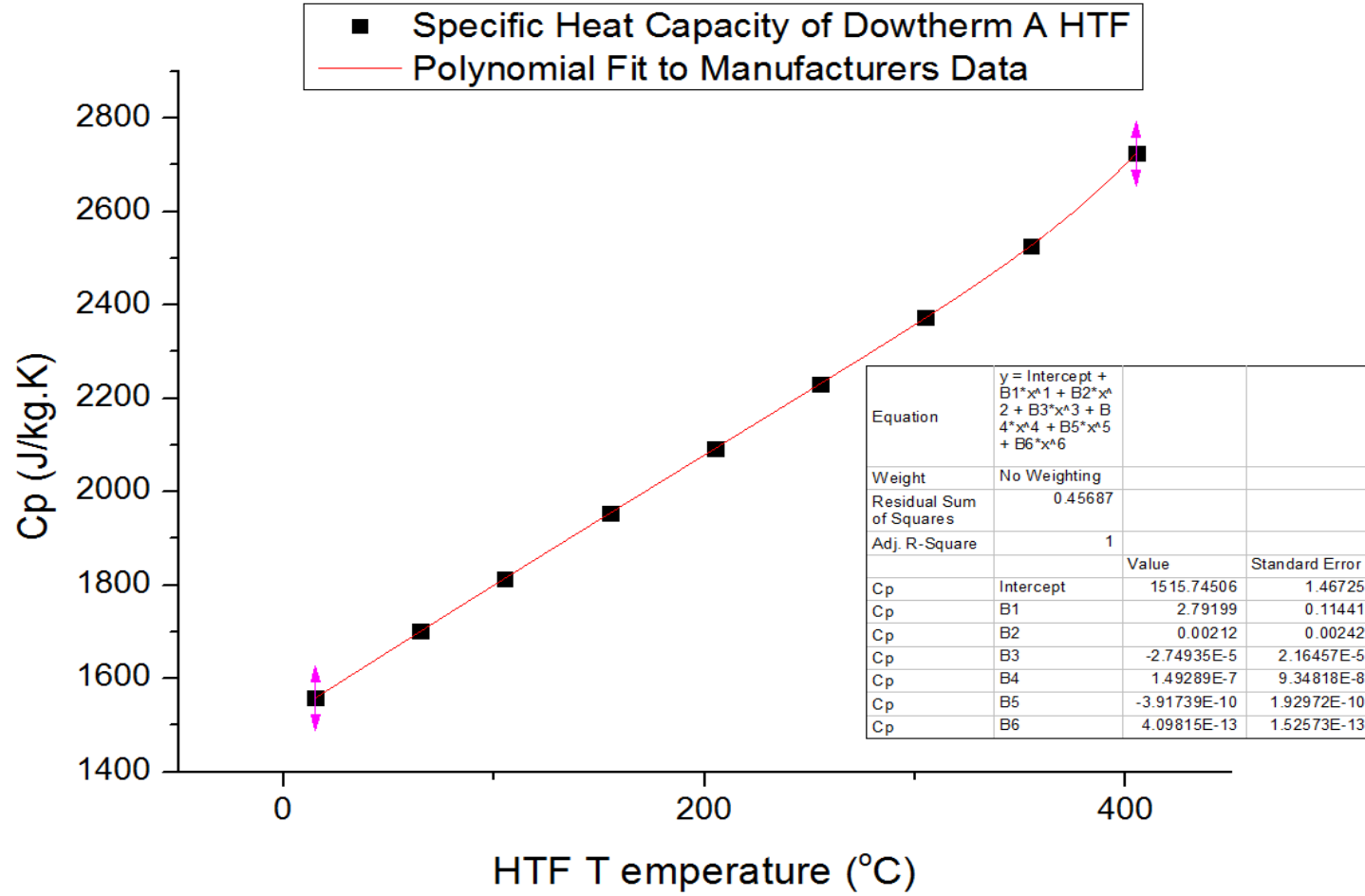
Physical properties (Dynamic Viscosity) data for Syltherm 800 HTF



Appendix T

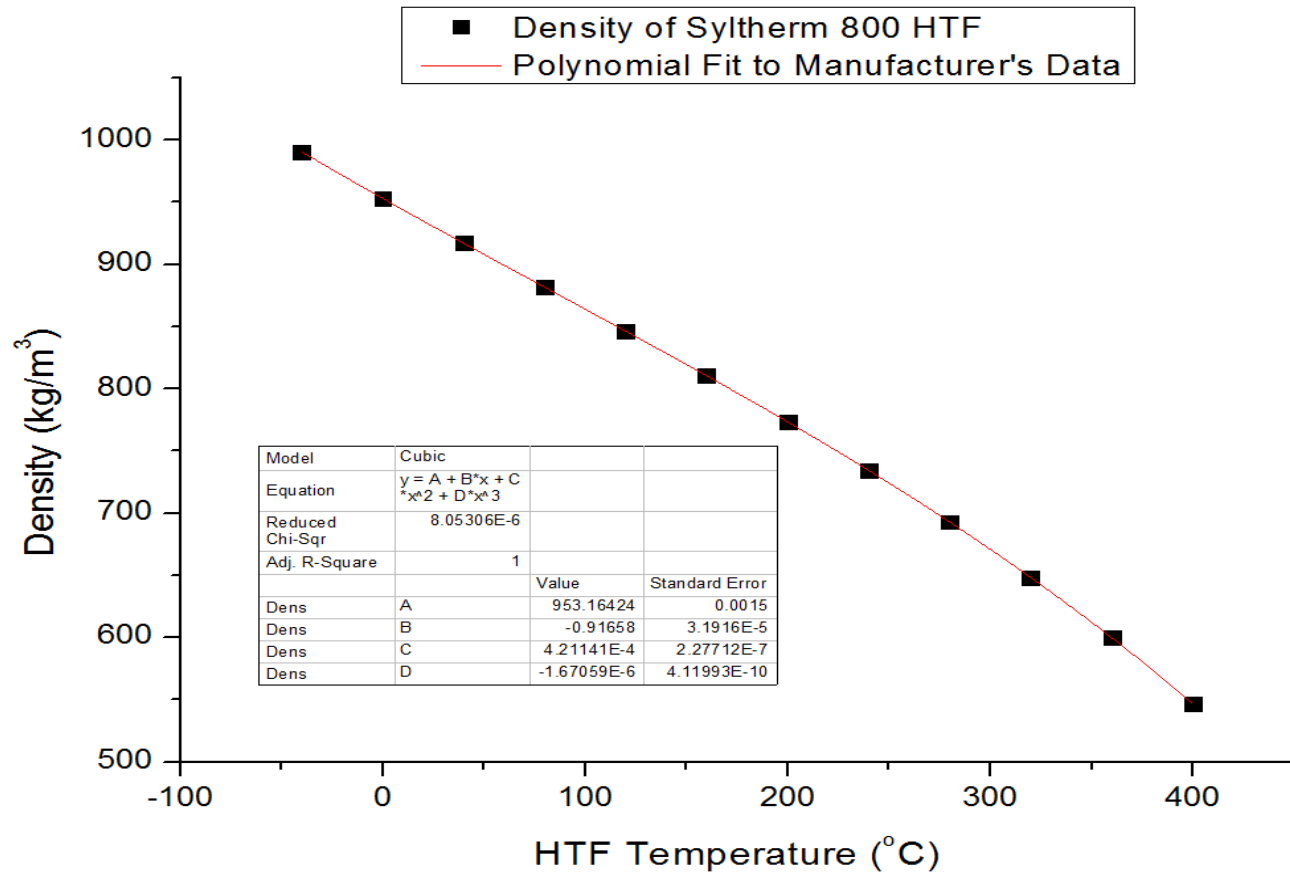
Physical properties (Specific Heat Capacity) data for Syltherm 800 and Dowtherm A HTF's



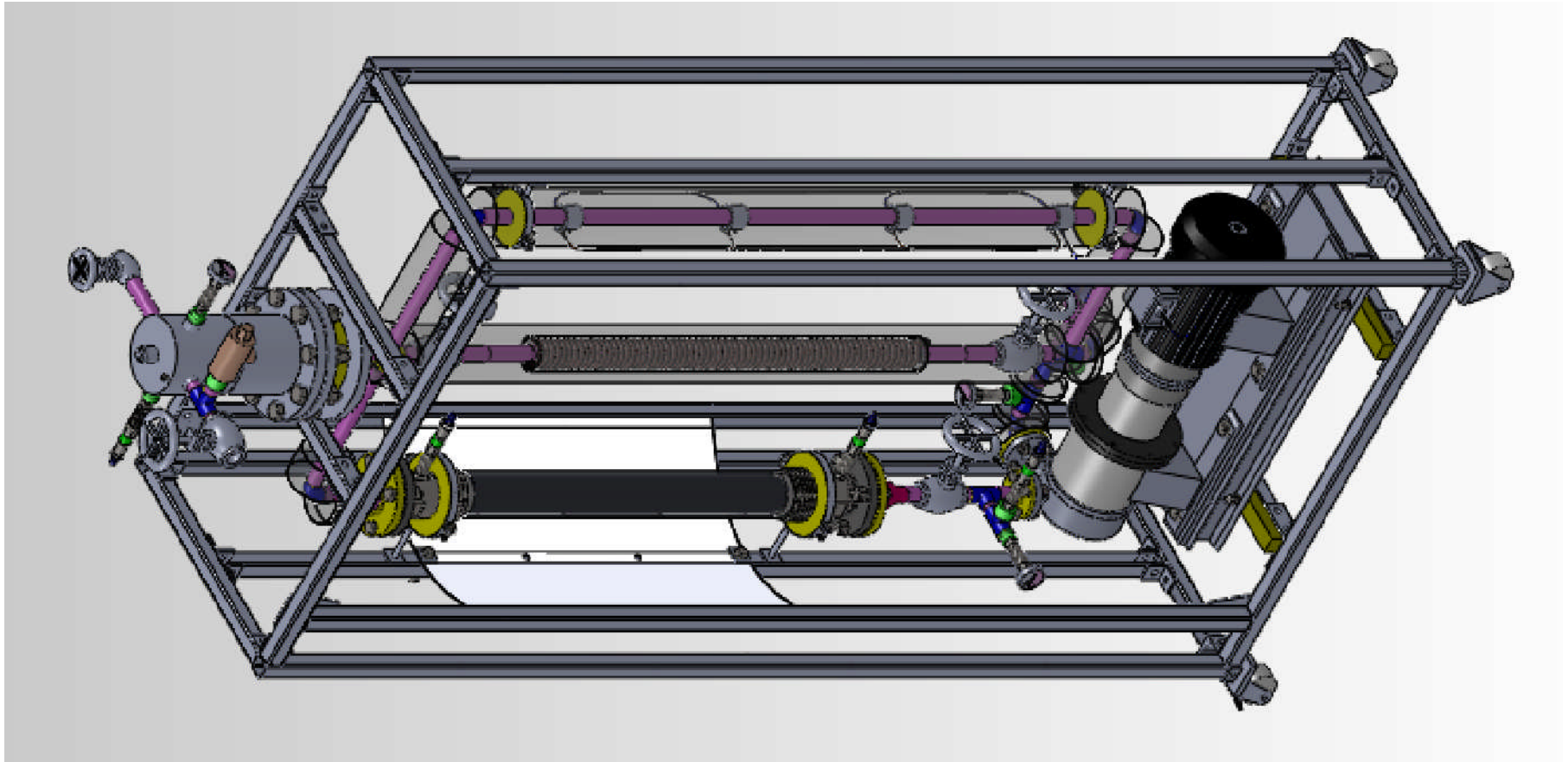


Appendix U

Physical properties (Density) data for Syltherm 800 HTF

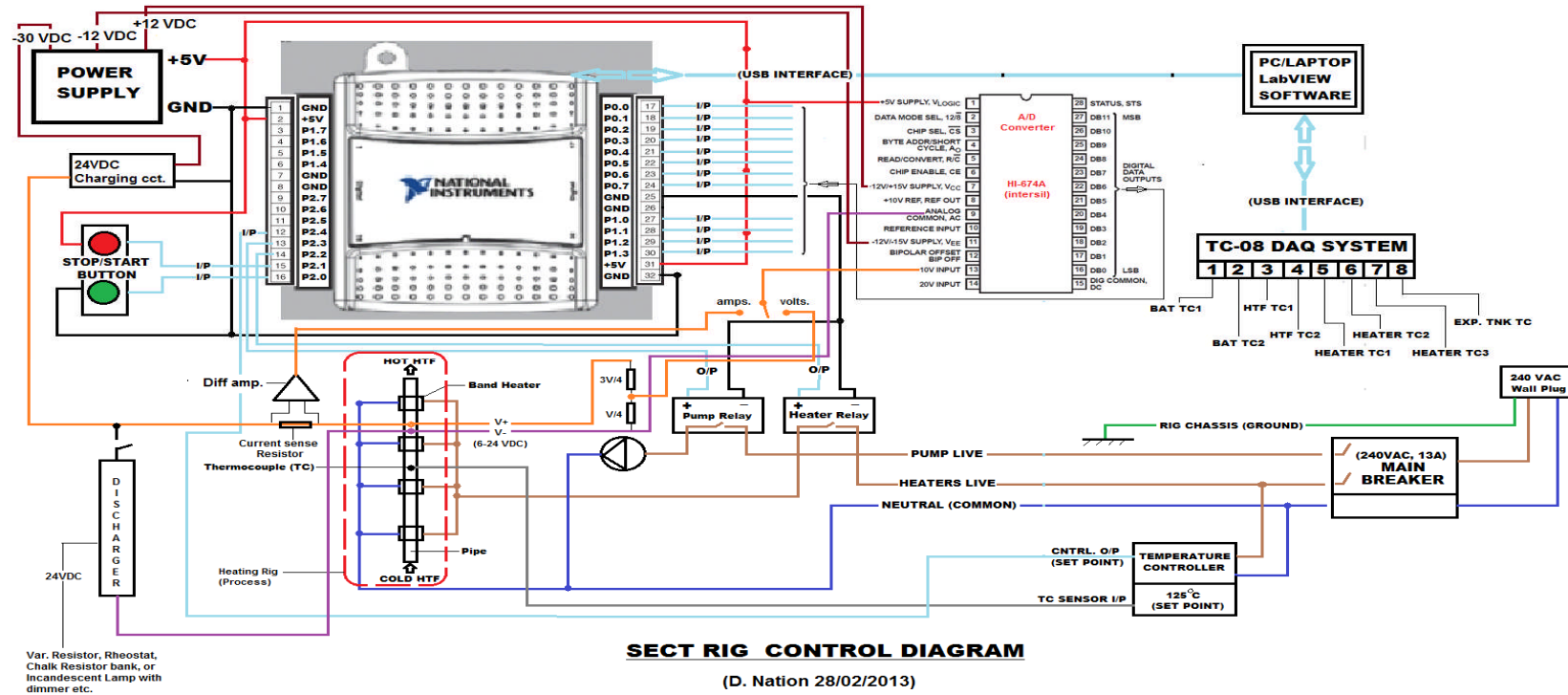


Angled View of the Experimental EES Receiver Rig Assembly (Designed with SolidWorks 2011 CAD Programme)



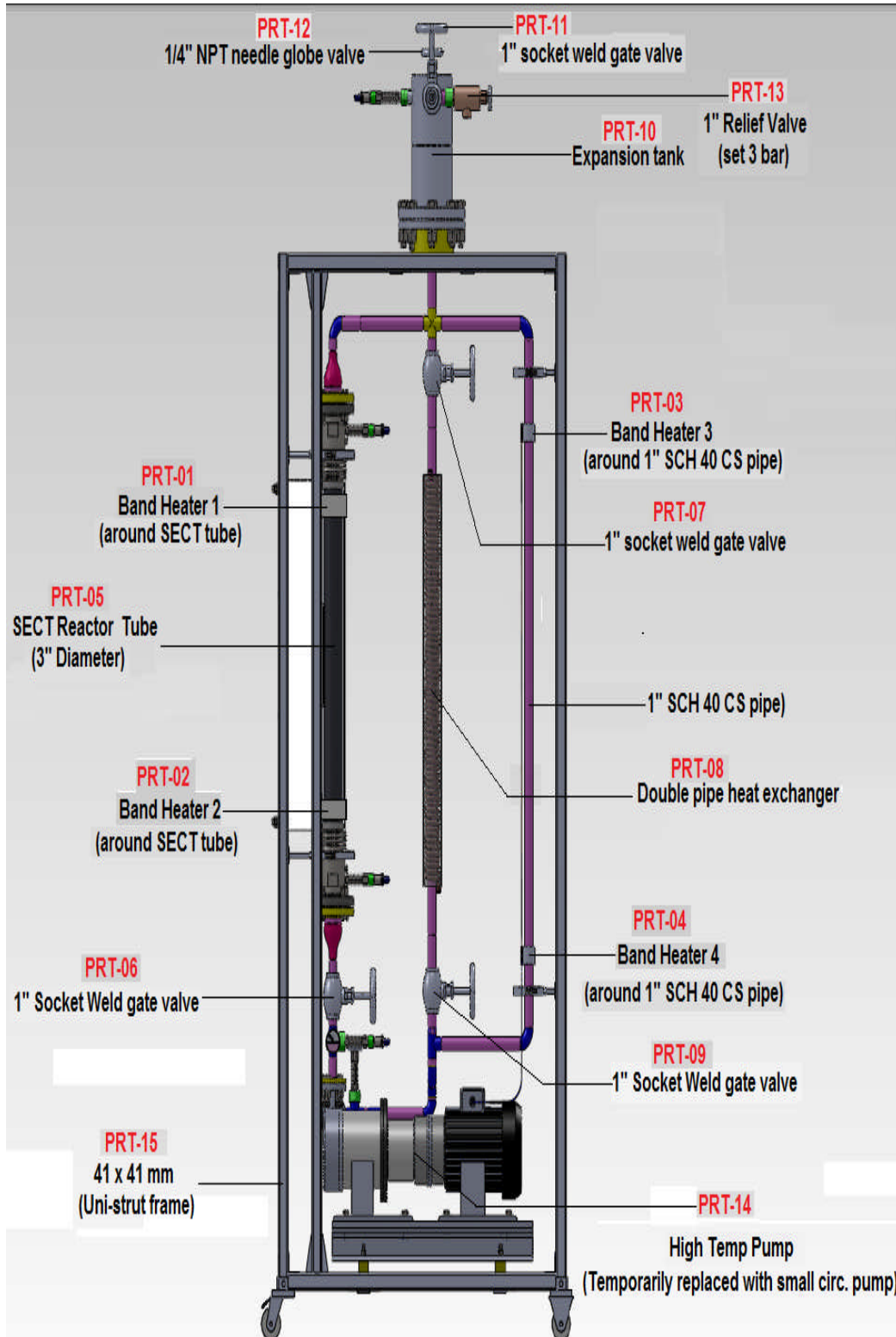
Appendix X

Electrical Wiring Plan and Main Parts Information for Experimental Rig



Appendix Y

Main Parts Information Sheet for EES Experimental Rig



Part No.	Description	Function	Vendor	Vendor Part No./URL
PRT-01	Band heater 1 (70 mm, 360 W)	Heats oil in pipes	TC Direct	TC Part No. 924-474 http://www.tcdirect.co.uk/Default.aspx?level=2&department_id=300/3
PRT-02	Band heater 2 (70 mm, 360 W)	Heats oil in pipes	TC Direct	TC Part No. 924-474 http://www.tcdirect.co.uk/Default.aspx?level=2&department_id=300/3
PRT-03	Band heater 3 (30 mm, 155W)	Heats oil in pipes	TC Direct	TC Part No. 924-408 http://www.tcdirect.co.uk/Default.aspx?level=2&department_id=300/3
PRT-04	Band heater 4 (30 mm, 155W)	Heats oil in pipes	TC Direct	ORDER NO. 924-408 http://www.tcdirect.co.uk/Default.aspx?level=2&department_id=300/3
PRT-05	SECT Reactor Tube	Houses NaS batteries under test	Fabricated, Lowe Engineering (Materials BSS)	N/A
PRT-06	OMB-1"-GATE VALVE BOLTED BONNET REDUCED BORE-CLASS 800-BODY ASTM A105N- TRIM 13% CHROME	Manual isolation for SECT tube flow	MRC Transmark	MRC Part No: 10010100810201 http://66.18.210.80/manuals/OMB/OMBForgedSteelGateGlobeCheck.pdf
PRT-07	OMB-1"-GATE VALVE BOLTED BONNET REDUCED BORE-CLASS 800-BODY ASTM A105N- TRIM 13%		MRC Transmark	MRC Part No: 10010100810201 http://66.18.210.80/manuals/OMB/OMBForgedSteelGateGlobeCheck.pdf

Part No.	Description	Function	Vendor	Vendor Part No./URL
CHROME				
PRT-08	Double Pipe Heat Exchanger	Cooling the oil in pipes (will not be used at this time)	Fabricated, Lowe Engineering (Materials BSS)	N/A
PRT-09	OMB-1"-GATE VALVE BOLTED BONNET REDUCED BORE-CLASS 800-BODY ASTM A105N-TRIM 13% CHROME	Manual isolation for heat exchanger flow	MRC Transmark	MRC Part No: 10010100810201 http://66.18.210.80/manuals/OMB/OMBForgedSteelGateGlobeCheck.pdf
PRT-10	Expansion Tank	Allows for fluid expansion/air venting	Fabricated, Lowe Engineering (Materials BSS)	N/A
CHROME				
PRT-11	OMB-1"-GATE VALVE BOLTED BONNET REDUCED BORE-CLASS 800-BODY ASTM A105N-TRIM 13% CHROME	Manual isolation for heat exchanger flow	MRC Transmark	MRC Part No: 10010100810201 http://66.18.210.80/manuals/OMB/OMBForgedSteelGateGlobeCheck.pdf
PRT-12	OMB-1/4"-GLOBE VALVE NEEDLE TYPE BOLTED BONNET FULL BORE-CLASS 800-BODY	Isolation/connection for N ₂ gas supply	MRC Transmark	MRC Part no: 10002200830001 http://66.18.210.80/manuals/OMB/OMBForgedSteelGateGlobeCheck.pdf

Part No.	Description	Function	Vendor	Vendor Part No./URL
	ASTM A105N- TRIM 13% CHROME			
PRT-13	1" Relief Valve- GRESWELL	Safety Relief	Collister & Glover	C&G. Part No. GRESG55M25 http://www.colglo.co.uk/product.php?product=GRESG55M25
PRT-14	Circulating Pump	Circulates HTF in pipework	Collister & Glover	C&G. Part No. DABVA60117941 http://www.colglo.co.uk/product.php?product=DABVA60117941
PRT-15	SLOTTED 41mm X 41mm X 3m CHANNEL 2.5mm PRE- GALV (TO BS6946 1988) UNISTRUT	Makes up the rig frame	Jack Pennington	J.P. Part No. P1000T http://www.jpldirect.co.uk/catalog/Pre_Galv_Slotted_Channel_B10051.html
PRT -16	25 Amp SS Relay	Turn heaters on/off	Farnell	Farnell Part No. 7229010 http://uk.farnell.com/opto-22/240d25-17/ssr-25a-240vac/dp/7229010?Ntt=7229010
PRT-17	PID Temperature controller with SSR output	Controls heater temperature	TC Direct	TC Part No. 309-103 http://www.tcdirect.co.uk/Default.aspx?level=2&department_id=100/9

Appendix Z

Risk Assessment for EES Experimental Rig

(Health & Safety Requirement)

Risk assessment

For

EES Experimental Test Rig

Prepared by : Deju Nation

(ERI)

Date: March 26, 2013

RISK ASSESSMENT FORM - SAMPLE

RISK ASSESSMENT DETAILS		DEGREE OF RISK		RISK RATING MATRIX																																																												
Faculty/School/Service	Engineering/ SPEME	<table border="1"> <thead> <tr> <th colspan="2">LIKELIHOOD (L)</th> </tr> </thead> <tbody> <tr> <td>5</td> <td>Inevitable</td> </tr> <tr> <td>4</td> <td>Highly Likely</td> </tr> <tr> <td>3</td> <td>Possible</td> </tr> <tr> <td>2</td> <td>Unlikely</td> </tr> <tr> <td>1</td> <td>Remote Possibility</td> </tr> </tbody> </table>		LIKELIHOOD (L)		5	Inevitable	4	Highly Likely	3	Possible	2	Unlikely	1	Remote Possibility	<table border="1"> <thead> <tr> <th colspan="2" rowspan="2"></th> <th colspan="5">SEVERITY</th> </tr> <tr> <th>1</th> <th>2</th> <th>3</th> <th>4</th> <th>5</th> </tr> </thead> <tbody> <tr> <th rowspan="5">LIKELIHOOD</th> <th>1</th> <td>1</td> <td>2</td> <td>3</td> <td>4</td> <td>5</td> </tr> <tr> <th>2</th> <td>2</td> <td>4</td> <td>6</td> <td>8</td> <td>10</td> </tr> <tr> <th>3</th> <td>3</td> <td>6</td> <td>9</td> <td>12</td> <td>15</td> </tr> <tr> <th>4</th> <td>4</td> <td>8</td> <td>12</td> <td>16</td> <td>20</td> </tr> <tr> <th>5</th> <td>5</td> <td>10</td> <td>15</td> <td>20</td> <td>25</td> </tr> </tbody> </table>								SEVERITY					1	2	3	4	5	LIKELIHOOD	1	1	2	3	4	5	2	2	4	6	8	10	3	3	6	9	12	15	4	4	8	12	16	20	5	5	10	15	20	25
LIKELIHOOD (L)																																																																
5	Inevitable																																																															
4	Highly Likely																																																															
3	Possible																																																															
2	Unlikely																																																															
1	Remote Possibility																																																															
		SEVERITY																																																														
		1	2	3	4	5																																																										
LIKELIHOOD	1	1	2	3	4	5																																																										
	2	2	4	6	8	10																																																										
	3	3	6	9	12	15																																																										
	4	4	8	12	16	20																																																										
	5	5	10	15	20	25																																																										
Team	ERI																																																															
Risk Assessment Title	Set-up of a Solar Photo-Electro-Chemical Thermal (PECT) Receiver Experimental Rig																																																															
Risk Assessment Log Reference																																																																
Date	8.3.13																																																															
				PERSONS AT RISK																																																												

Name of Assessors	Dr. D.W. Dixon-Hardy, Prof. P.J. Heggs, Mr. Peter Thompson, Mr. Ed Woodhouse		SEVERITY (S)		<table border="1"> <thead> <tr> <th data-bbox="1599 264 1991 336">PERSONS AT RISK</th> </tr> </thead> <tbody> <tr> <td data-bbox="1599 336 1991 400">Employees</td> </tr> <tr> <td data-bbox="1599 400 1991 464">Students</td> </tr> <tr> <td data-bbox="1599 464 1991 528">Clients</td> </tr> <tr> <td data-bbox="1599 528 1991 592">Contractors</td> </tr> <tr> <td data-bbox="1599 592 1991 655">Members of the public</td> </tr> <tr> <td data-bbox="1599 655 1991 719">Work Experience students</td> </tr> <tr> <td data-bbox="1599 719 1991 783">Other Persons</td> </tr> </tbody> </table>	PERSONS AT RISK	Employees	Students	Clients	Contractors	Members of the public	Work Experience students	Other Persons
PERSONS AT RISK													
Employees													
Students													
Clients													
Contractors													
Members of the public													
Work Experience students													
Other Persons													
Manager Responsible	Dr Darron Dixon-Hardy	5	Very High -Multiple Deaths										
Location		4	High - Death, serious injury, permanent disability										
<p><u>Details of Activity</u></p> <p>The Rig is designed to simulate the operation of a Solar Thermal Power Plant incorporating direct electrical energy storage via solar assisted charging of high capacity Sodium Sulphur (NaS) Thermal batteries. An outer absorber tube (reactor) encloses the NaS cells in a sealed inner tube, with Therminol 66 HTF flowing through the annular space between the tubes. The HTF is heated indirectly via band heaters attached to the pipework, and monitored by a temperature control system to a maximum temperature of 120°C. It is important to note that the rig is NOT currently pressurized, draws a nominal current of only 5A @ 240VAC (heaters and pump) and that pump operation is inaudible.</p> <p>Experimental work will involve recording NaS cell temperatures and voltages during heating up and cooling cycles, and the rig will be attended at all times, during operation. <i>(Based on rough tests done at the rig fabrication firm, a typical 120°C heating/cooling cycle should take about 5-6 hrs under normal ambient temperature</i></p>		3	Moderate - RIDDOR over 3 days										
		2	Slight - First Aid treatment										
		1	Nil - Very Minor										

conditions of 20°C.)

NB: At some future point it may be required to operate the rig at 300°C for further testing, and at such time this document will be reviewed and updated.

Other assessments which might also be required, if needed:

- Manual Handling REF
- COSHH REF
- Personal Protective Equipment (PPE) REF
- Noise REF
- Other REF

REVIEW DATES

RISK
RATING
SCORE

ACTION

					1 - 4	Broadly Acceptable - No action required	
					5 - 9	<u>Moderate - Reduce risks if reasonably practicable</u>	
					10 -15	<u>High Risk - Priority Action to be undertaken</u>	
					16 -25	Unacceptable <u>-Action must be taken</u> <u>IMMEDIATELY</u>	
HAZARD AND RELATED ACTIVITIES e.g. trip, falling objects, fire, explosion, noise, violence etc.	PERSONS AT RISK e.g. Employees, Customers, Contractors, Members of the public	POSSIBLE OUTCOME	RISK RATING BEFORE CONTROLS (LxS)	EXISTING CONTROLS e.g. Guards, Safe Systems of Work, Training, Instruction, Authorised Users, Competent Persons, Personal Protective Equipment (PPE)	RISK RATING AFTER CURRENT CONTROLS (LxS)	FURTHER CONTROLS REQUIRED?	RISK RATING AFTER ADDITIONAL CONTROLS (LxS)
Hot Oil/Vapour	Student	Burns to body	3 x 4	Any leak potential has been minimized due to welding	1 x 4	Not likely	1 x 4

leakage/ spray				<p>and testing all joints; using carbon steel pipework which is suited for the duty, use of cast steel globe valves for high temp, use appropriate PPE.</p> <p>NOTE: Perspex screens will be placed around the rig to contain spraying oil in the event of a leak.</p>			
Explosion of NaS Cells	Student	Auto-ignition of HTF and development of fire, burns to	3 x 4	NaS cells are housed in sealed aluminium tube, and this aluminium tube is contained within a carbon steel absorber tube, adding	1 x 4	Not likely	1 x 4

		body, fire damage to equipment/room		another layer of protection; a functional temp. control system with automatic over temperature shutdown; over voltage shutdown; manual backup emergency shutdowns by experimenter for any breached safety parameter; safety isolation valve for HTF supply to Receiver tube; use of high temperature mica electrical insulation between NaS and battery tube wall to prevent any short circuit. NOTE: a pipe will be attached to the outlet of the			
--	--	-------------------------------------	--	---	--	--	--

				pressure relief valve that drains into a tank.			
Electric Shock	Student	Death, Burns	3 x 4	Earthing all metal parts or the rig; observing necessary BS electrical wiring regulations; having all electrical mains wiring and circuitry inspected, tested and approved before system commission; fuse protecting of individual band heaters as an extra protection.	1 x 4	Not likely	1 x 4
Hot piping/ surfaces	Student	Burns	3 x 3	Use of high temperature Rockwool pipe insulation to	1 x 3	Not likely	1 x 3

COMMUNICATION OF RISK ASSESSMENT FINDINGS TO STAFF				
	METHOD	YES	DATE	COMMENTS
REFERENCE OF FORMAL COMMUNICATION TO STAFF	Copy of risk assessment issued to staff			
	Controls covered in team procedure issued to staff			
	Staff Handbook issued to staff			
	Other -			
ADDITIONAL	Induction			

METHODS OF COMMUNICATION	Toolbox Talk			
	Team Meeting			
	E-mail circulation			
	Other -			

COMMENTS AND INFORMATION

(Use this section to record any dynamic risk assessment comments and information)

The system will be constantly monitored by the experimenter during operation, will not be left unattended and will only be **operated when experimenter is onsite**. Also, any potential improvements conceptualized or realized during initial operations which are capable of producing even greater operational safety, will be recommended to ERRI lead technician Ed Woodhouse for implementation.

**Do additional controls adequately
lower high risk activities to an**

YES / NO

SIGNATURE OF MANAGER

"The risks identified in this assessment are controlled so far as is reasonably practicable"

acceptable level?	If NO explain in comments box above	Signature:	Date:
--------------------------	--	------------	-------

DATE OF REASSESSMENT (Every two years minimum)	ARE THERE ANY CHANGES TO THE ACTIVITY SINCE THE LAST ASSESSMENT?	SIGNATURE OF MANAGER

LOCATION OF CURRENT	
----------------------------	--

SIGNED RISK ASSESSMENT	
-------------------------------	--

RISK ASSESSMENT LOG - SAMPLE

RISK ASSESSMENT LOG											
Directorate:						Area:					
Section/Team	Risk Assessment Title	Version No.	Risk Assessment Category	Code /Location	Risk Assessor	Manager responsible for signing off risk assessment	Date assessment signed off	Review Due	Review Date	Outstanding Controls/Actions Yes/No	Comments

(This page is intentionally left blank)